

Table of Contents

INVITED TALKS: MOX	1
MOX01 - FRIB operations: first three years.....	1
INVITED TALKS: MOY	8
MOY01 - Status of the HIAF accelerator facility in China.....	8
CONTRIBUTED TALKS: MOB	12
MOB01 - First RIB production with SPES Exotic Beam Facility at INFN-LNL.....	12
INVITED TALKS: MOZ	16
MOZ03 - High power targetry devices at FRIB: challenges, status and plan.....	16
CONTRIBUTED TALKS: MOC	22
MOC01 - Commissioning of the S3 Spectrometer : advances, challenges and [...]..	22
MONDAY POSTER SESSION: MOP	26
MOP01 - Computation model for space charge effect for bunched beam in [...]....	26
MOP04 - Monte Carlo simulation analysis for radiation damage on Glidcop [...]..	30
MOP05 - Thermal-hydraulic analysis of a 20 kW beam power water-cooled [...]....	34
MOP07 - Control of microphonics for a superconducting radio-frequency [...]....	38
MOP11 - Design and fabrication of FRIB normal conducting cavities.....	42
MOP14 - Mechanical vibration study of low-energy superconducting linear [...]..	46
MOP18 - Extending JuTrack's capabilities to the FRIB accelerator to [...].....	50
MOP19 - Budget-friendly defense against radiation-induced camera damage.....	54
MOP21 - Physics applications in support of FRIB beam tuning and [...].....	58
MOP29 - Updated magnetic rigidity calibration of ARIS.....	62
INVITED TALKS: TUX	65
TUX01 - Future challenges for CERN's ion injector complex.....	65
TUX03 - Maintaining optimal beam brightness and luminosity using machine [...]..	71
TUX05 - Boost of ALPI superconducting linac performances using AI [...].....	77
INVITED TALKS: TUY	83
TUY01 - Recirculating and energy recovery ion linear accelerators.....	83
CONTRIBUTED TALKS: TUB	89
TUB01 - A single-slice rotating graphite target at FRIB.....	89
INVITED TALKS: TUZ	93
TUZ01 - Innovation for Sustainable Accelerator Systems (The European iSAS [...]..	93
TUZ02 - Primary beam development for FRIB experiments.....	98
CONTRIBUTED TALKS: TUC	104
TUC04 - Development of the first 1 GHz Niobium-Tin quarter-wave cavity.....	104
TUESDAY POSTER SESSION: TUP	107
TUP01 - Optimization of a mini-channel beam dump for FRIB operation.....	107
TUP03 - Study on synergistic irradiation effects of nuclear materials [...]....	111
TUP04 - Design and experimental thermal validation of the mini-channel [...]....	114
TUP05 - Application of ASME BPVC Section VIII, Division-2, design by [...]....	118
TUP09 - Development of automatic beam tuning system using Bayesian [...].....	122
TUP11 - Application of ML tools for extraction of BPM-Q and transverse [...]....	126
TUP13 - FRIB multi-gap buncher conditioning up to 30 kW.....	130
TUP14 - Avoiding beam instabilities and resonances with circular modes.....	133
TUP16 - Development of High Temperature Ovens for solid ion beam [...].....	137

TUP18 - Computational analysis of MP activation and suppression in 325 [...]	141
TUP19 - The 120 kW solid state amplifier system for the FRIB RFQ.....	145
TUP21 - Study on properties of NEG deposited on the titanium alloy lined [...]	148
TUP23 - Design and operational experience of FRIB magnet and [...]	151
TUP24 - Feasibility study of plasma processing for the FRIB energy [...]	154
TUP25 - High resolution current control from switched mode power supply.....	158
TUP27 - Assessment of magnetic quadrupole pick-up structure at FRIB.....	162
TUP29 - FRIB chopper monitor system calibration process.....	164
TUP30 - Superconducting multipole triplets magnets commissioning for the [...]	167
INVITED TALKS: WEX.....	171
WEX01 - Status of High Performance ECR ion sources: achievements and [...]	171
WEX05 - Measurement of forward-directed neutrons generated by an inverse [...]	177
INVITED TALKS: WEY.....	180
WEY02 - High intensity Ti-50 beam production for superheavy element [...]	180
INVITED TALKS: WEZ.....	184
WEZ01 - Single-bunch extraction at the 88-Inch Cyclotron.....	184
WEZ02 - Advances in transverse beam halo characterization and [...]	188
CONTRIBUTED TALKS: WEC.....	194
WEC02 - The beam dynamics case of Beam-Beam Wire Compensators for the [...]	194
WEDNESDAY POSTER SESSION: WEP.....	198
WEP03 - Mitigating the thermal challenges in carbon stripper: test bench [...]	198
WEP06 - Image mapping for multiple charge state beams using a beam [...]	201
WEP07 - Beam loss detection and mitigation at FRIB.....	204
WEP08 - Beam intensity prediction for ECR ion source using machine [...]	207
WEP09 - JuTrack, a Julia-based tool for accelerator modeling and tracking [...]	211
WEP10 - Machine-Learning-Assisted Rapid Beam Energy Change at the ATLAS [...]	214
WEP11 - Design improvement of a minichannel beam dump wing through [...]	217
WEP12 - Enhancing ALPI-PIAVE performance at INFN-LNL with advanced [...]	220
WEP19 - Study of ponderomotive instability in the FRIB beta=0.53 [...]	224
WEP20 - Multi-q beam studies at FRIB: simulations and measurements.....	228
WEP24 - Variable wedge for ARIS.....	232
INVITED TALKS: THX.....	236
THX03 - High energy ion implantation at BNL.....	236
CONTRIBUTED TALKS: THA.....	240
THA03 - Six-dimensional beam matching with linear accelerator structures.....	240
INVITED TALKS: THY.....	244
THY01 - NEWGAIN project at GANIL: construction of the new heavy ion [...]	244
THY02 - Demonstration of cavity field mapping by falling drops of liquid.....	249
THY03 - Operation of a pulsed gas stripper during regular user beam time [...]	254
THY04 - RF power limits of 4-rod RFQs.....	260
INVITED TALKS: FRX.....	264
FRX01 - A charge stripper ring for RIBF.....	264
CONTRIBUTED TALKS: FRA.....	270
FRA01 - Rare isotope beam tuning in FRIB.....	270
FRA02 - Rare-isotope production optics of ARIS preseparator.....	274
FRA03 - Particle identification using trajectory reconstruction with the [...]	277

FRA04 - The SPES-ISOLPHARM beamline for the production of medical [...]	281
FRA05 - Reaccelerating long-lived Rare Isotopes at FRIB	285

FRIB OPERATIONS: FIRST THREE YEARS*

J. Wei[†], C. Alleman, H. Ao, B. Arend, D. Barofsky, S. Beher, J.S. Berryman, G. Bollen, J. Brandon, N. Bultman, F. Casagrande, W. Chang, H. Cheng, Y. Choi, S. Cogan, P. Cole, C. Compton, M. Cortesi, J. Curtin, K. Davidson, S. Di Carlo, A. Dombos, X. Du, K. Elliott, B. Ewert, A. Facco¹, F. Ferrell, A. Fila, K. Fukushima, A. Gade, V. Ganni, A. Ganshyn, T. Ginter, T. Glasmacher, A. Gonzalez, J. Guo, E. Gutierrez, Y. Hao, W. Hartung, N. Hasan, M. Hausmann, K. Holland, H. C. Hseuh, M. Ikegami, R. Iwai, D. Jager, S. Jones, N. Joseph, D. Kahl, T. Kanemura, J. Kim, S. H. Kim, C. Knowles, T. Konomi, B. Kortum, N. Kulkarni, E. Kwan, T. Lange, M. Larmann, T. Larter, K. Laturkar, M. LaVere, R. E. Laxdal², G. Lee, J. LeTourneau, Z.-Y. Li, S. Lidia, G. Machicoane, P. Manwiller, F. Marti, T. Maruta, D. McNanney, E. Metzgar, S. Miller, Y. Momozaki³, A. C. Morton, M. Mugerian, D. Morris, P. Nariyoshi, I. Nesterenko, D. Newhart, C. Nguyen, S. Noji, P. Ostroumov, M. Patil, A. Plastun, L. Popielarski, M. Portillo, A. Powers, J. Priller, X. Rao, M. Reaume, S. Rodriguez, S. Rogers, K. Saito, B. M. Sherrill, M. K. Smith, J. Song, M. Steiner, A. Stolz, O. Tarasov, G. Timko, B. Tousignant, E. Wakai, R. Walker, J. Wan, L. Wang, X. Wang, J. Wenstrom, G. West, M. Wright, T. Xu, M. Yeck, R.G.T. Zegers, D. Zhang, T. Zhang, Q. Zhao, S. Zhao

Facility for Rare Isotope Beams, Michigan State University, East Lansing, MI, USA

P. Hurh, Fermi National Accelerator Laboratory, Batavia, IL, USA

S. Prestemon, T. Shen, Lawrence Berkeley National Laboratory, Berkeley, CA, USA

¹also at INFN - Laboratori Nazionali di Legnaro, Legnaro (Padova), Italy

²also at TRIUMF, Vancouver, BC, Canada

³also at Argonne National Laboratory, Lemont, IL, USA

Abstract

The paper summarizes the operational experience and challenges during the first three years of FRIB user operations, covering accelerator improvement projects, expansions in user stations, and plans for facility upgrades.

INTRODUCTION

Upon completion of the Facility for Rare Isotope Beams (FRIB) construction project in April 2022, the scientific user program started in May 2022. During the first three years of user operations, the FRIB complex has safely accelerated more than a dozen different primary beams ranging from ^{16}O to ^{238}U to beam energies ~ 200 MeV/u (Fig. 1). The primary beam power has increased by a factor of 20, from the initial 1 kW to the present 20 kW, including the uranium beam (Fig. 2). More than 410 kinds of rare isotopes have been delivered to the user experiments. During the past year, the accelerator complex operated more than 6000 beam hours with $\sim 95\%$ availability serving both scientific and industrial users.

THE FRIB SCIENCE PROGRAM

At FRIB, the short-lived nuclei produced via fragmentation or fission can be used directly as fast beams for reactions; they can be stopped in a detection system that measures their decays, or they can be slowed down in a gas

stopper and used in precision experiments or made into reaccelerated beams with energies ranging from hundreds of keV to well above the Coulomb barrier. Thanks to this unique scheme, FRIB provides isotopes of any element lighter than U for studies as fast, stopped, and reaccelerated beams. These complementary experimental opportunities allow users to directly address three of the four science challenges put forward in the 2023 Long Range Plan for Nuclear Science [1]. They also open up new avenues for the applications of rare isotopes for the benefit of the nation and society. The published experimental results from FRIB already address a wide variety of topics, including new-isotope discovery [2], the determination of a variety of nuclear observables obtained from nuclear decays [3–5] and reactions [6], and have reached the proton dripline for the precision mass measurements [7], for example.

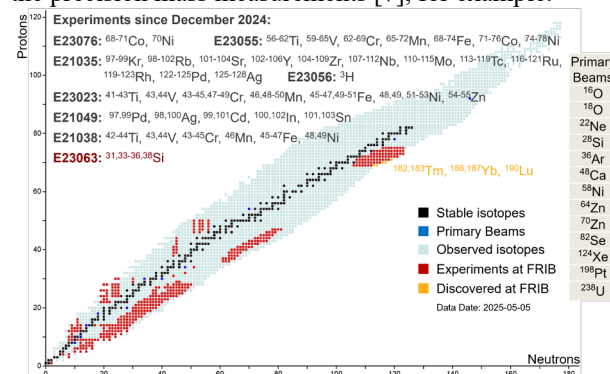


Figure 1: Rare isotopes delivered to scientific users of FRIB, and primary beams used in the driver linac [8].

* Work supported by the U.S. Department of Energy Office of Science under Cooperative Agreement DE-SC0023633, the State of Michigan, and Michigan State University.

[†]wei@frib.msu.edu

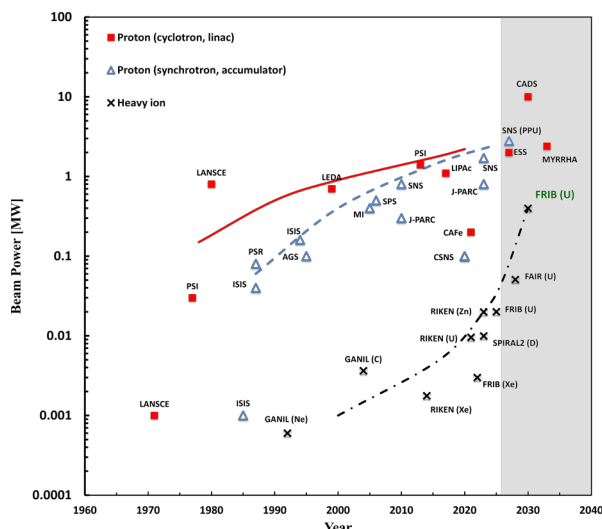


Figure 2: Beam power on target as a function of time for attained (as of March 2025) and planned power-frontier accelerator facilities.

USER OPERATIONS

During the first three years of user operations, a series of Accelerator Readiness Reviews (ARR) and Instrument Readiness Reviews (IRR) were conducted, allowing the safe increase of beam power and the extension to newly completed user vaults, as shown in Table 1.

Table 1: FRIB Major Milestones for User Operations [8]

Milestone	Date
ARR7 for 1 kW beam operations	Jan 2022
Construction project completion, CD-4	Apr 2022
Start of user operation at 1 kW power	May 2022
ARR8 for 3 kW beam operations	Jul 2022
S3 Vault S800 IRR	Jul 2022
ARR9 for 5 kW beam operations	Jan 2023
ARR10 for 10 kW beam operations	Oct 2023
HRS-HTBL CD-2/CD-3 Review	Oct 2024
ARR11 for 20 kW beam operations	Oct 2024
S1 Vault IRR	Mar 2025
S2 Vault IRR	Apr 2025

Scientific User Operations

FRIB is required to schedule 4200 hours of beam time annually with $> 85\%$ availability for scientific operations. FRIB has met the requirement with $> 90\%$ availability. Figure 3 shows the downtime of the facility by system category during Fiscal Years 2023 and 2024. Leading downtime incidents include failures of the legacy cryogenics cold box and legacy SC magnets, the auxiliary cooling system for the RFQ, and a liquid lithium charge stripper gasket.

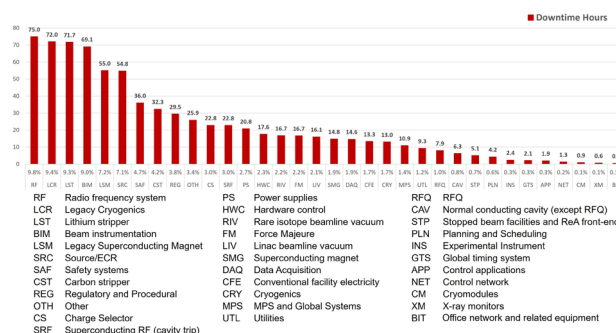


Figure 3: FRIB facility downtime hours during scientific user operations by system category from October 2022 to September 2024. The overall availability of the facility is 93%.

Industrial User Operations

The FRIB single event effect (FSEE) facility annually delivers ~ 2000 beam hours with a dedicated beamline downstream of Segment 1 of the driver linac. Figure 4 shows the current beam list and the offered ion cocktails [9].

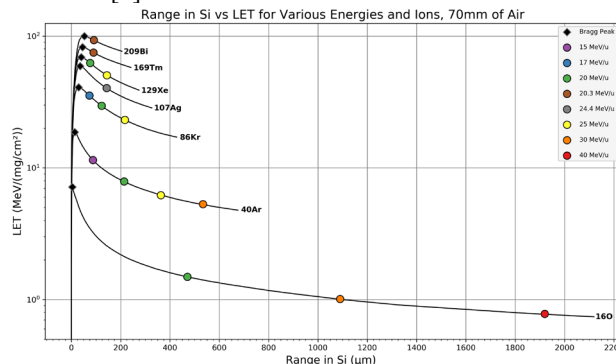


Figure 4: Ion range and linear energy transfer offered by the FSEE facility.

OPERATIONAL EXPERIENCE AND CHALLENGES

Uncontrolled Beam Loss near Charge Stripping

The revolutionary thin-film liquid lithium technology [10] (Fig. 5) and the multi-charge-state simultaneous acceleration [11] allow charge stripping at a high efficiency of 83% for uranium beams. However, the variation in film thickness over time causes uncontrolled beam loss. Feedback controls operating on both 0.1-second timescale by energy compensation and multi-second timescale by shifting of the impact point were implemented [12]. A Machine Protection Systems Threshold Configuration Tool (MPS TCT) was deployed to optimally set the fast MPS and automatically configure the corresponding beam loss monitors (BLM), ensuring a fast signal response time of 150 μ s for this beam power level.

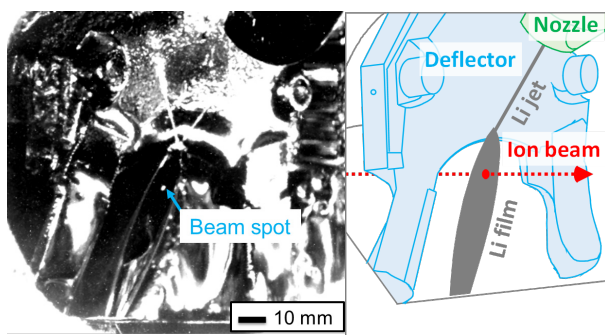


Figure 5: Image of the uranium beam on the liquid lithium charge stripper film. The beam-on-target power is 20 kW. The relatively poor image quality is due to radiation damage to the camera imaging sensor.

Science Demands on Rare Isotope Beams

The FRIB science program is not solely focused on the most exotic rare isotope beams for which the rigidities deviate significantly from the primary beam, but also on high-intensity rare isotope beams close in rigidity to the primary beam. As shown in Fig. 6, under such conditions, the beam loss is incurred along the entire ARIS (Advanced Rare Isotope Separator) [13] beamline. The case illustrated in the figure is for production of ^{34}Si from a ^{48}Ca primary beam at 215 MeV/u. This distribution of power is typical when the rigidity of the fragment is close to the rigidity of the beam. In this case, 120 W of fragments pass the beam dump at a primary beam power of 20 kW. At 400 kW this will be nearly 2.5 kW of fragments. A thorough analysis of how to collect fragments and handle significant fragment power indicates that several system upgrades are needed.

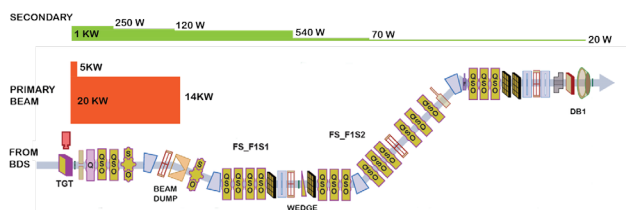


Figure 6: Typical ARIS beam loss with high-intensity rare isotope beams close in rigidity to the 20 kW primary beam.

Beam Intercepting Systems Challenges

Beam intercepting systems both in the target hall (the production target and the beam dump) and in the linac (collimators and charge selector) are currently limiting the performance of the FRIB accelerator.

A rotating single-slice graphite target has been used to produce rare isotopes (Fig. 7). Complications have primarily been due to coating and bearing lubrication that sustain thermal and radiation impacts [14]. A rotating multi-slice graphite target is planned for beam power beyond 50 kW.

The beam dump downstream of the production target absorbs up to 70% of the primary beam power and is the most challenging system confronting FRIB's power ramp up. The static beam dump went through several iterations of improvements (Fig. 8): reducing the incident beam

angle from 20° to 6° to reduce the surface power deposition density, and improvements to the bi-metal material and the cooling efficiency [15]. A rotating thin shell water beam dump is planned for beam power beyond 50 kW.

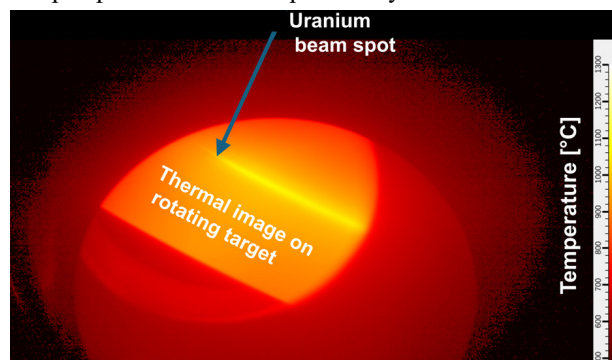


Figure 7: Thermal optical image of the uranium beams on the rotating production target during the 20 kW run. The 2.1 mm thick graphite target disc rotates counterclockwise at 500 rpm. The maximum temperature reached on the target is 1200 °C.

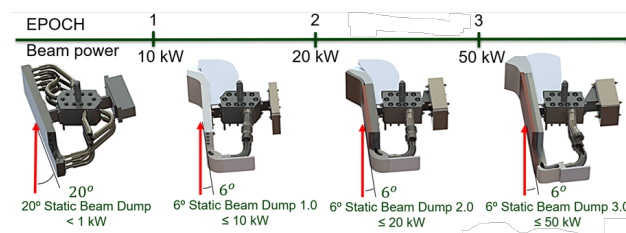


Figure 8: Improvements to static beam dump since the start of FRIB user operations. The Epoch 2 version is currently used for 20 kW operations.

Personnel Protection Challenges

Because FRIB is built on a university campus, stringent radiation containment measures must be applied to comply with public radiation limits, both during normal operation and under all possible fault scenarios (Fig. 9) [16]. Radiation protection currently includes the radiation control system, consisting of fast neutron monitors and fast beam inhibit devices, shielding, and the access control system. A fast beam containment system (FBCS) based on ion chambers is in the process of being credited.

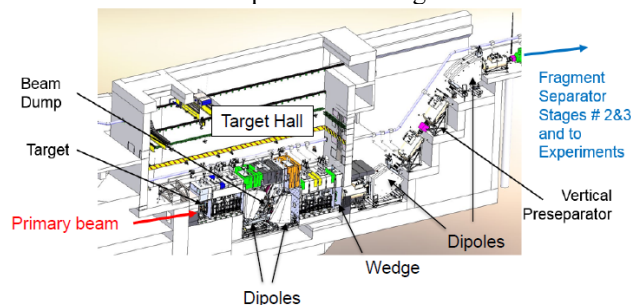


Figure 9: Most vulnerable fault scenario when uncontrolled loss occurs after a high-power primary beam produced from the underground tunnel passes along the ARIS and rises to the ground level.

ACCELERATOR IMPROVEMENTS

Persistent accelerator improvements are key to reliable operations and performance ramp up. The work is organized as individual sub-projects covering accelerator improvement (AIP), capital equipment investment (ACE), and operations spares (AOP) to mitigate operations risks.

Accelerator Improvements & Operation Spares

The superconducting (SC) ECR ion source is now equipped with high temperature ovens [17] running > 2000 °C and now powered by both a gyrotron operating at 28 GHz and a klystron operating at 18 GHz (Fig. 10), offering $^{238}\text{U}^{35+}$ at >100 eμA. A second SC ion source is being developed [18], which eventually enables three ion sources to meet user demands [8].

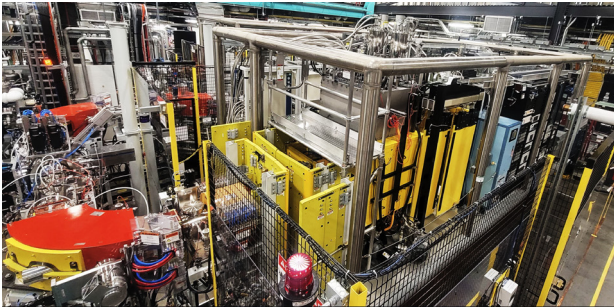


Figure 10: 28 GHz SC ECR ion source mounted on a 100 kV high voltage platform at the FRIB front end.

FRIB in general uses solid-state amplifiers (SSA) to power SC cavities in the linac for high system availability, except that a tube amplifier is used to power the normal conducting (NC) RFQ due to the high-power requirement. A new SSA system has been developed that combines 8 amplifier racks to replace the tube amplifier [19] (Fig. 11).

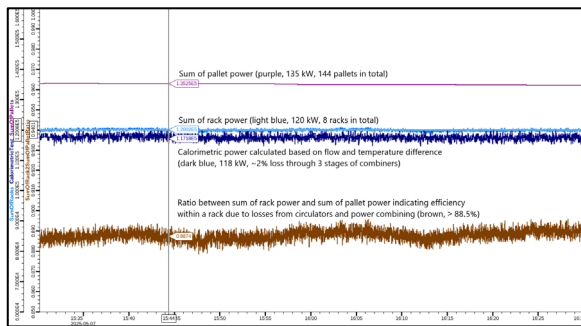


Figure 11: In-rack power combining efficiency considering losses from circulators and power combiners is greater than 88.5%. The combining efficiency of the three stages of external hybrid couplers is ~98% resulting in an overall efficiency of 86.7% with 120 kW output power.

The non-conventional utility (NCU) system plays a vital role in both cooling the high-power targetry system and in removing trapped radionuclides. The cooling loops consist of the target loop with cooling water through the target, NC magnet coils and SC magnet thermal shields, and the beam dump loop. The hydrogen recombiner system has been commissioned after comprehensive catalyst testing and system validation. The polishing loop filtration was

upgraded for maintainability. As shown in Fig. 12, the overall NCU system demonstrates operational readiness to meet the challenges of stopping the primary beam inside the water beam dump.

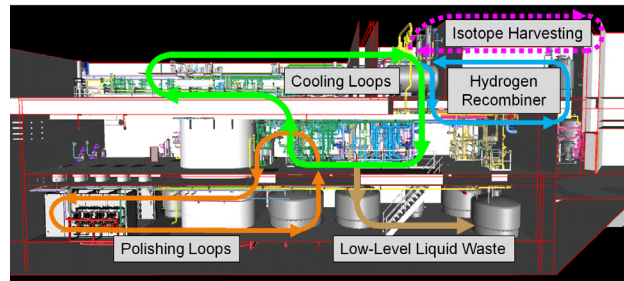


Figure 12: NCU system with cooling loops, polishing loops, hydrogen recombiner and low-level liquid waste. Isotope harvesting capability was recently added.

The remote handling (RH) system is routinely used for maintenance of the targetry system including target and wedge changes between different user experiments. A second set of RH manipulators was added to enhance remote handling capabilities (Fig. 13).



Figure 13: Two sets of remote handling manipulators for the FRIB target hall.

Legacy System Renovation

The aging legacy systems inherited from the NSCL cyclotron facility contribute significantly to the downtime of the FRIB facility (Fig. 3). Persistent efforts are underway to refurbish and replace both legacy cryogenic distribution systems [20] and SC magnets [21] (Fig. 14).



Figure 14: A recently built spare S800-style SC quadrupole triplet for the FRIB experimental beamlines.

Epoch 3 Power Ramp Up Roadmap

FRIB has been operating in the Epoch 2 at 20 kW beam power since March 2025. Epoch 3 operations at 50 kW beam power are planned for 2027. The major accelerator improvement projects on the Epoch 3 power ramp up roadmap are shown in Fig. 15 and Table 2, among which are three AIP and ACE tasks associated with mitigation of uncontrolled beam loss in the Folding Segment 1 (FS1) area of charge stripping and collection, four AIP and AOP tasks associated with high-power targetry systems, and an AOP task on FBCS. Installation of these devices is mainly scheduled during 2025 and 2026.



Figure 15: FRIB facility layout with eight tasks on the Epoch 3 beam power ramp up roadmap (Table 2).

Table 2: FRIB Accelerator Sub-Projects for Operations Risk Mitigation with Epoch 3 Beam Power Ramp Up Roadmap

Risk ID	Task	Indicated in Fig. 15
095-AIP	FS1 second harmonic cavity	①
096-AIP	FS1 large bore NC magnets	②
062-ACE	Enhanced FS1D2 dipole chamber	③
104-AOP	Fast beam containment system	④
037-AOP	Rotating target, multi slice	⑤
115-AIP	Post-target shielding	⑥
023a-AIP	Static beam dump for 50 kW	⑦
023b-AIP	Rotating water beam dump, 1-mm wall	⑧

EXPANDING THE AVAILABLE VAULTS FOR EXPERIMENTS

During Epoch 1 operations, user experiments mostly used FRIB's fast and stopped beams. The FRIB Decay Station initiator (FDSi) was the first instrument to receive the FRIB beam for decay spectroscopy (e.g., [3-5]) and was then located in the transfer hall. Reaction experiments with rare isotopes were carried out in the S3 vault with the S800 spectrometer and GREINA (e.g. [6]). Precision mass measurements (see [7]) and laser spectroscopy of

short-lived nuclei were performed with the FRIB-unique stopped beams from the N4 vault. Starting in Epoch 2, the S1 and S2 experimental vaults (Table 1 and Fig. 15) were brought into commission, with the FDSi now permanently housed in S1 and the S2 vault enabling a complementary class of reactions experiment with fast beams. In addition to fast- and stopped-beam experiments, measurements with reaccelerated beams of rare isotopes were performed as well, utilizing the unique FRIB opportunity of stopping the fast beams in N4 and reaccelerating them to Coulomb-barrier energies for experiments complementary to fast-beam measurements.

The High Rigidity Spectrometer (HRS) project [22, 23] funded by the US DOE Office of Science, Office of Nuclear Physics consists of two subprojects: the High Transmission Beamline (HRS-HTBL) and the Spectrometer Section (HRS-SPS). All the overarching scientific motivations for FRIB require experiments using fast rare-isotope beams with magnetic spectrometers. The HRS will have double the magnetic rigidity (8 Tm) of existing spectrometers at FRIB, substantially increasing FRIB's scientific reach [23]. For example, the luminosity for experiments involving the most interesting neutron-rich nuclei, including nuclei that otherwise can only be produced in colliding neutron stars, will increase by a factor of up to 100. Such gains are possible because of the ability of the HRS-HTBL to transport rare-isotope beams from ARIS to the reaction target of the HRS-SPS with near 100% transmission at beam rigidities for which the production rate in ARIS is maximal. In addition, by using high-rigidity beams, thick reaction targets can be used for experiments with the HRS, which would otherwise not be possible. For example, when the HRS is operated together with the Gamma-Ray Energy Tracking Array (GRETA) [24], γ -ray spectroscopy of the key nucleus ^{60}Ca becomes possible, as the luminosity increases by a factor of 35 compared to what is feasible without the HRS. The HRS-SPS will be a unique spectrometer consisting of a large-gap (60 cm) dipole magnet enabling invariant-mass spectroscopy with neutrons, followed by a second dipole magnet enabling high-resolution charged-particle spectroscopy for a wide range of experiment types. Large-acceptance quadrupole magnets, combined with higher-order correctors, enable high-quality and large-acceptance event reconstruction. Recently, the US DOE Office of Science granted Critical Decision 2/3 approval for the start of execution of the HRS-HTBL. The design of the HRS-SPS is also in the advanced stages.

FRIB400 UPGRADE

FRIB400 is the aspired 400 MeV/u energy upgrade of FRIB. The science opportunities provided by FRIB400 feature in the 2023 Long Range Plan for Nuclear Science [1] and are based on the community-authored FRIB400 whitepaper, The Scientific Case for the 400 MeV/u FRIB Energy Upgrade [25]. Space was reserved in the FRIB tunnel for the 11 cryomodules of FRIB400, enabling 400 MeV/nucleon energy for uranium and higher energies for lighter ions. The technology has

been proven, prototypes have been tested, and the team to build FRIB400 is in place. The upgrade can be implemented in stages during regular shutdowns with minimal interruption of the FRIB science program. At each stage, the gain in primary beam energy would translate into increased science potential.

ACKNOWLEDGMENTS

We thank the FRIB Technical Systems Advisory committee, the Targetry Advisory Committee, and colleagues who participated in FRIB accelerator peer reviews for their valuable guidance, including N. Alexander, G. Ambrosio, J. Anderson, J. Aoki, D. Arenius, M. Bai, R. Baartman, C. Barbier, W. Barletta, G. Bauer, G. Biallas, J. Bisognano, W. Blokland, S. Bousson, J. Bramble, P. Brindza, E. Buice, M. Calviani, S. Caspi, M. Champion, A. Chatman, E. Christy, D. Cossairt, J. Creel, M. Crofford, C. Cullen, D. Curry, R. Cutler, B. Davids, M. Dayton, G. Decker, J. Delaysen, J. Delong, G. Dodson, J. Donald, H. Edwards, J. Error, I. Evans, M. Fitton, J. Fuerst, Y. Iwamoto, T. Khabiboulline, F. Kornegay, K. Kurukawa, J. Galambos, J. Galayda, G. Gassner, J. Gates, P. Ghoshal, J. Gilpatrick, C. Ginsburg, K. Gnanvo, A. Gottberg, S. Gourlay, I. Graff, J. Haines, M. Harrison, S. Hartman, S. Henderson, D. Hillis, G. Hoffstaetter, J. Hogan, S. Holmes, M. Howell, R. Kersevan, A. Hodgkinson, N. Holtkamp, H. Horiike, K. Hosoyama, C. Hovater, H. Imao, R. Janssens, R. Keller, J. Kelley, M. Kelly, P. Kelley, J. Kerby, S. H. Kim, A. Klebaner, J. Knobloch, R. Lambiase, M. Lamm, I.-Y. Lee, Y. Li, N. Liyanage, C. LoCocq, C. Luongo, R. Lutha, K. Mahoney, S. Maloy, J. Mammoser, T. Mann, A. P. Marcone, R. May, S. Meigo, W. Meng, T. Michaelides, N. Mokhov, D. Montierth, G. Murdoch, T. Nakamura, J. Nolen, W. Norum, H. Okuno, S. Ozaki, R. Pardo, S. Peggs, C. Peters, R. Petkus, C. Pearson, M. Pearson, F. Pellemoine, I. Peterson, T. Peterson, C. Pillar, D. Potterveld, J. Power, T. Powers, J. Preble, J. Price, J. Randall, D. Raparia, J. Rathke, A. Ratti, M. Reichanadter, T. Roser, M. Ross, C. Roux, R. Ruland, T. Russo, J. Sandberg, R. Schmidt, W. J. Schneider, D. Schrage, P. Schuh, D. Senor, D. Seweryniak, S. Sharma, I. Silverman, K. Smith, J. Sondericker, W. Soyars, C. Spencer, R. Stanek, M. Stettler, M.-H. Stodel, W. C. Stone, J. Stovall, H. Strong, K. Sugita, L. T. Sun, Y. Than, J. Thomason, J. Theilacker, Y. Tian, M. Thuot, J. Tuozzolo, V. Verzilov, K. Vodopivec, R. Vondrasek, P. Wanderer, K. White, D. Winder, M. Wiseman, W. Wohlmuther, P. Wright, H. Xu, K. Yoshida, L. Young, A. Zaltsman and S. Zimmerman; and colleagues who advised and collaborated with the FRIB team including A. Burrill, A. C. Crawford, K. Davis, X. Guan, P. He, Y. He, A. Hutton, P. Kneisel, R. Ma, K. Macha, G. Maler, E. A. McEwen, J. Qiang, T. Reilly, W. Sommer, R. Talman, J. Vincent, X. W. Wang, J. Xia, Q. Z. Xing, and H. H. Zhang.

The FRIB accelerator is operated by a dedicated team in the FRIB Accelerator Systems Division in close

collaboration with the Science Division headed by A. Gade, the Experimental Systems Division headed by F. Garcia, the Conventional Facility and Infrastructure Division, and the Chief Engineer's team, with support from the FRIB project controls, procurement, and ES&H teams. We thank our industrial partners in the USA and worldwide for their support to FRIB commissioning and operations.

REFERENCES

- [1] DOE/NSF Nuclear Science Advisory Committee & Long Range Plan Working Group, "A new era of discovery, 2023 Long Range Plan", US Department of Energy, Washington, DC, United States, 2023. doi:10.2172/2280968
- [2] O. B. Tarasov *et al.*, "Observation of new isotopes in the fragmentation of Pt198 at FRIB", *Phys. Rev. Lett.*, vol. 132, no. 7, p. 072501, Feb. 2024. doi:10.1103/physrevlett.132.072501
- [3] H. L. Crawford *et al.*, "Crossing $N = 28$ toward the neutron drip line: first measurement of half-lives at FRIB", *Phys. Rev. Lett.*, vol. 129, no. 21, p. 212501, Nov. 2022. doi:10.1103/physrevlett.129.212501
- [4] T. J. Gray *et al.*, "Microsecond isomer at the $N=20$ island of shape inversion observed at FRIB", *Phys. Rev. Lett.*, vol. 130, no. 24, p. 242501, Jun. 2023. doi:10.1103/physrevlett.130.242501
- [5] I. Cox *et al.*, "Proton shell gaps in $N = 28$ nuclei from the first complete spectroscopy study with FRIB Decay Station Initiator", *Phys. Rev. Lett.*, vol. 132, no. 15, p. 152503, Apr. 2024. doi:10.1103/physrevlett.132.152503
- [6] A. Gade *et al.*, "In-beam spectroscopy reveals competing nuclear shapes in the rare isotope ^{62}Cr ", *Nat. Phys.*, vol. 21, no. 1, pp. 37–42, Oct. 2024. doi:10.1038/s41567-024-02680-0
- [7] S. E. Campbell *et al.*, "Precision mass measurement of the proton dripline halo candidate Al^{22} ", *Phys. Rev. Lett.*, vol. 132, no. 15, p. 152501, Apr. 2024. doi:10.1103/physrevlett.132.152501
- [8] J. Wei *et al.*, "Technological developments and accelerator improvements for the FRIB beam power ramp-up", *J. Instrum.*, vol. 19, p. T05011, May 2024. doi:10.1088/1748-0221/19/05/t05011
- [9] S. Lidia *et al.*, "A heavy-ion Single-Event Effects Test Facility at Michigan State University", 2022 *IEEE Radiation Effects Data Workshop (REDW) (in conjunction with 2022 NSREC)*, Provo, UT, USA, Jul. 2022, pp. 1-7. doi:10.1109/REDW56037.2022.9921718
- [10] T. Kanemura *et al.*, "Experimental demonstration of the thin-film liquid-metal jet as a charge stripper", *Phys. Rev. Lett.*, vol. 128, p. 212301, 2022. doi:10.1103/PhysRevLett.128.212301
- [11] P. N. Ostroumov *et al.*, "First simultaneous acceleration of multiple charge states of heavy ion beams in a large-scale superconducting linear accelerator", *Phys. Rev. Lett.*, vol. 126, p. 114801, 2021. doi:10.1103/PhysRevLett.126.114801
- [12] T. Kanemura *et al.*, "Liquid lithium charge stripping technology: Achievement and lessons learned", in *Proc. IPAC'25*, Taipei, Taiwan, Jun. 2025, pp. 19-23. doi:10.18429/JACoW-IPAC25-MOYD2

- [13] M. Portillo *et al.*, “Commissioning of the Advanced Rare Isotope Separator ARIS at FRIB”, *Nucl. Instrum. Methods Phys. Res., Sect. B*, vol. 540, pp. 151–157, Jul. 2023. doi:10.1016/j.nimb.2023.04.025
- [14] J. Song *et al.*, “A single-slice rotating graphite target at FRIB”, presented at HIAT’25, East Lansing, MI, Jun. 2025, paper TUB01, this conference.
- [15] S. Miller *et al.*, “Optimization of a mini-channel beam dump for FRIB operation”, presented at HIAT’25, East Lansing, MI, Jun. 2025, paper TUP01, this conference.
- [16] M. Ikegami, “Personnel and machine protection for high power accelerator commissioning, operations, and power ramp up”, in *Proc. IPAC’25*, Taipei, Taiwan, Jun. 2025, pp. 827-832. doi:10.18429/JACoW-IPAC25-TUXD1
- [17] H. Cheng *et al.*, “Development of high temperature ovens (HTOs) for solid ion beam production at Facility for Rare Isotope Beams (FRIB)”, presented HIAT’25, East Lansing, MI, Jun. 2025, paper TUP16, this conference.
- [18] T. Shen *et al.*, “Design and development of a 28 GHz Nb₃Sn ECR ion source superconducting magnet”, *IEEE Trans. Appl. Supercond.*, vol. 34, no. 5, p. 4301105, Aug. 2024. doi:10.1109/tasc.2024.3358767
- [19] E. Gutierrez *et al.*, “The 120 kW solid state amplifier system for the FRIB RFQ”, presented at HIAT’25, East Lansing, MI, Jun. 2025, paper TUP19, this conference.
- [20] N. Hasan *et al.*, “Design, fabrication and installation of the cryogenic distribution system for re-configured FRIB A1900 fragment separator”, in *Proc. ICEC28-ICMC 2022*, Hangzhou, China, Apr. 2022. doi: 10.1007/978-981-99-6128-3_28
- [21] Y. Choi *et al.*, “Overview of fragment separator superconducting magnets in the Facility for Rare Isotope Beams”, *IEEE Trans. Appl. Supercond.*, vol. 33, no. 5, p. 4100305, 2023. doi: 10.1109/TASC.2023.3244141
- [22] S. Noji *et al.*, “Design of the High Rigidity Spectrometer at FRIB”, *Nucl. Instrum. Methods Phys. Res. A*, vol. 1045, p. 167548, Jan. 2023. doi:10.1016/j.nima.2022.167548
- [23] R.G.T. Zegers, “The High Rigidity Spectrometer at the Facility for Rare Isotope Beams”, *Nucl. Phys. News*, vol. 32, no. 4, pp. 16–19, Oct. 2022. doi:10.1080/10619127.2022.2100647
- [24] *The Gamma-Ray Energy Tracking Array (GRETA) Final Design Report*, Lawrence Berkeley National Laboratory, LBNL Report, LBNL-1007254, Apr. 2020. <https://greta.lbl.gov/documents>
- [25] A. Gade *et al.* Eds., “FRIB400: The Scientific Case for the 400 MeV/u Energy Upgrade of FRIB”, FRIB, Michigan State University, East Lansing, MI, USA, Jun. 2019, updated Feb. 2023. https://frib.msu.edu/_files/pdfs/frib400_final.pdf

STATUS OF THE HIAF ACCELERATOR FACILITY IN CHINA*

J. C. Yang[†] and HIAF project team

Institute of Modern Physics of the Chinese Academy of Sciences, Lanzhou, China

Abstract

The High Intensity Heavy-Ion Accelerator Facility (HIAF) is one of the major scientific infrastructures in China. The project is managed by Institute of Modern Physics, Chinese Academy of Sciences, and the construction is started on December, 2018 in Huizhou City of Guangdong Province. The main feature of this facility is to provide high intensity heavy ion beam pulse for various experiments. At present, most of the accelerator equipment has been installed and tested. The beam commissioning is scheduled for the second half of 2025. In this paper, an overview of the status and perspective of the HIAF project is reported.

INTRODUCTION

The High Intensity heavy-ion Accelerator Facility is a new accelerator facility under construction at the Institute of Modern Physics (IMP) in China [1]. It is designed to provide intense primary heavy ion beams for nuclear and atomic physics, as well as other application fields. The ac-

celerator consists mainly of a superconducting electron-cyclotron-resonance (SECR) ion source, a continuous wave (CW) superconducting ion linac (iLinac), a booster synchrotron (BRing) and a high precision spectrometer ring (SRing). A fragment separator (HFRS) is also applied as the beam line to connect BRing and SRing. Six experimental terminals will be built in phase-I at HIAF. The layout of the HIAF accelerator was shown in Fig. 1, and the main parameters are listed in Table 1.

The construction of the HIAF project was started officially in December 23rd, 2018. Up to now, all the construction of the accelerator tunnel and on-ground buildings has been completed. Auxiliary facilities such as cooling water, ventilation and air conditioning, high and low-voltage power distribution, power distribution, and cryogenic systems have been installed and debugged, and are now in operation. Almost all the accelerator components have been installed and online testing has been completed. An updated time schedule of HIAF construction is shown in Fig. 2. The first beam is expected to be launched at BRing in the middle of 2025. The Day-one experiment is proposed around the end of 2025.

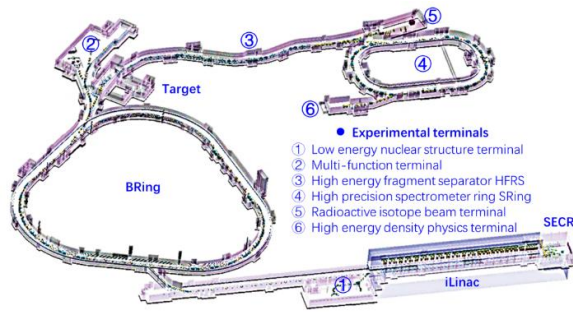


Figure 1: Layout of the HIAF project and the on-site landscape.

Table 1: Main Parameters of the HIAF Accelerators

	SECR	iLinac	BRing	HFRS	SRing
Length / circumference (m)	---	114	569	192	277
Final energy of U (MeV/u)	0.014 (U^{35+})	17 (U^{35+})	835 (U^{35+})	800 (U^{92+})	800 (U^{92+})
Max. magnetic rigidity (Tm)	---	---	34	25	15
Max. beam intensity of U	50 μ A (U^{35+})	28 μ A (U^{35+})	10^{11} ppp (U^{35+})		10^{10} ppp (U^{92+})
Operation mode	DC or pulse	CW or pulse	fast ramping (12T/s, 3Hz)	Momentum- resolution 1100	DC or deceleration
Emittance or Acceptance (H/V, π ·mm·mrad, dp/p)		5 / 5	200/100, 0.5%	± 30 mrad(H)/ ± 15 mrad(V), $\pm 2\%$	40/40, 1.5%, normal mode

* Work supported by the National Development and Reform Commission, China

[†] email address: yangjch@impcas.ac.cn.

2019	2020	2021	2022	2023	2024	2025
Civil construction						
		Electric power, cooling water, compressed air, network, cryogenic, supporting system, etc.				
	ECR design & fabrication	SECR installation and commissioning				
	Linac design & fabrication		iLinac installation and commissioning			
	Prototypes of PS, RF cavity, chamber, magnets, etc.		fabrication	BRing installation & commissioning		
				HFRS & SRing installation & commissioning		
				Terminals installation		
						Day One exp.

Figure 2: Time schedule of the HIAF construction.

FRONT END

Pulsed 50 μA (~ 1 ms) U^{35+} ion beam from SECR is required in the HIAF project, which is 5 times higher than the present records of the 3rd generation ECR ion source. It can only be met by sources operating at higher magnetic field and higher microwave frequency. SECR incorporates with a Nb_3Sn high field superconducting magnet and a quasi-optical 45 GHz gyrotron microwave system, as shown in Fig. 3. The biggest challenge lies in the design and fabrication of the Nb_3Sn magnet [2]. A promising cold mass design has been completed by a collaboration with LBNL, as shown in Fig. 3. Up to now, the full-sized cold-mass have been completed and tested, and the whole system is ready to be installed in this year.



Figure 3: The world's first 45 GHz ECR ion source has been successfully developed and commissioned.

Working at the frequency of 81.25 MHz, the HIAF RFQ aims at accelerating particles with a charge-to-mass ratio of up to 1/7, increasing the energy of particles from 0.014 MeV/u to 0.8 MeV/u in a length of 8.55 m. Depending on the particle type, the RFQ was designed to work in CW or pulse mode, and the KP factor was controlled below 1.6 and 2.0 for the two modes to reduce the RF breakdown rate. The RFQ has been installed in the HIAF accelerator tunnel as shown in Fig. 4, and the first 1 mA $^{16}\text{O}^{6+}$ beam have been successfully commissioned.



Figure 4: HIAF RFQ have been installed and commissioned.

LINAC INJECTOR

The iLinac is used as the injector of BRing and the main accelerator for the low energy nuclear structure terminal. That's why a CW superconducting linac is proposed in HIAF. Two types of accelerating structures in 17 cryomodules are used to achieve the energy of 17 MeV/u for U^{35+} ion beam. The first 6 cryomodules with QWR007 cavities is used to accelerate U^{35+} ions to 5.4 MeV/u. The rest cryomodules are installed with HWR015 cavities. These cavities will be made based on the experience of the CiADS project. A layout of iLinac is shown in Fig. 5, the installation and commissioning of the system will be completed soon this year.

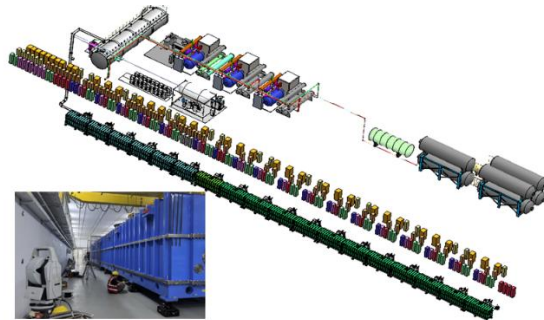


Figure 5: 3-D view of iLinac. SECR locates on left side.

BOOSTER SYNCHROTRON

The Booster Ring (BRing) is the key component of the HIAF project. It is designed with a maximum magnetic rigidity of 34 Tm, which is intended for the storage of U^{35+} ions to an intensity of 2×10^{11} particles with the energy of 835 MeV/u. It has a three-folding symmetry lattice with DBA (double bend achromat) structure. The ionization processes with residual gas particles is the main issue with respect to potential beam loss. Therefore, the lattice design is to localize the beam loss at certain positions to install collimators [3]. BRing offers a transverse H/V acceptance of $200/100 \pi \cdot \text{mm} \cdot \text{mrad}$ to overcome space charge limits of high intensity beams. It is operated below the transition energy to avoid beam loss by transition-energy crossing.

To obtain a high average beam intensity and avoid space charge limits, transverse phase space painting (4-D) is implemented for beam accumulation and a rapid ramping cycle [4] is used to reduce the integral ionization cross section. Related components such as tilted electrostatic septum, ceramic-lined thin-wall vacuum chamber, fast-cycling power supply and magnetic alloy (MA) acceleration cavities are developed for BRing. As shown in Fig. 6, the installation the BRing has been finished and all the supporting systems are undergoing beamless testing. The beam commissioning is scheduled to begin by the end of 2025.

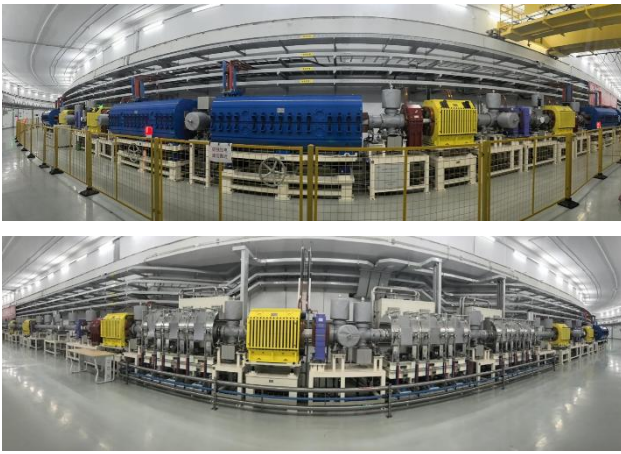


Figure 6: BRing layout in the tunnel.

FRAGMENT SEPARATOR

The High energy Fragment Separator (HFRS) is an in-flight separator at relativistic energy. The schematic layout is shown in Fig. 7. A primary beam from BRing hits the target at PF0. The rare isotopes produced by projectile fragmentation or fission will be collected and purified by the HFRS with the Bp- Δ E-Bp method. The magnetic rigidity up to 25 Tm can be operated in HFRS. The large acceptance including the angular acceptances ± 30 mrad (H) / ± 15 mrad (V) and the momentum acceptance $\pm 2\%$ provides a high collecting efficiency. A two-stage structure is used in HFRS design. The pre-separator is used to dump the primary beams and undesired fragments. The main separator is used to identify the rare isotopes. Details of the HFRS design can be found in Ref. [5]. Currently, the target station and the beam transportation line have been installed, and beamless testing is underway.

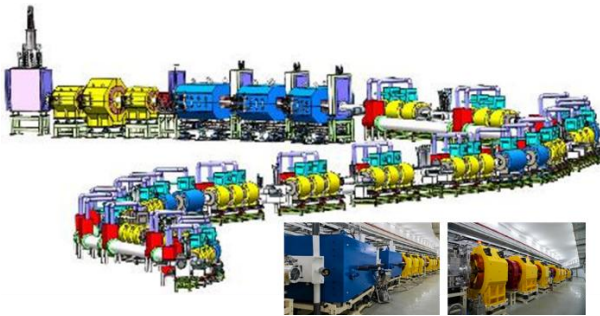


Figure 7: 3-D view of HFRS and on-site photos (partial).

SPECTROMETER RING

SRing is designed as a multi-function experimental storage ring, which can be operated in three modes. Firstly, it will be used as an isochronous mass spectrometer (IMS mode) with two TOF detectors for short-lived neutron-rich nuclei. Secondly, it is used to collect and cool long-lived rare isotopes for nuclear experiments, or accumulate and extract highly-charged stable ions for high energy density physics (normal mode). Thirdly, it can be used to store H-like, He-like or other special charge state ions for internal

target experiments (target mode). Ions can be decelerated to tens MeV in this mode. Details are available in Ref. [6].

A 450 keV magnetized DC electron cooler is used to boost the luminosity of internal target experiments, and proposed to accumulate isotopes combined with stochastic cooling and barrier bucket system [7]. In addition, an electron target system is equipped in SRing for atomic physics, which is similar to the e-cooler and can provide electron beam up to 80 keV.

At present, all components of the SRing accelerator have been installed and tested (Fig. 8). Next, the experimental components are being installed. The Day-one experiment is expected to be carried out at the end the 2025 or early 2026.



Figure 8: SRing layout in the tunnel.

SUBSYSTEMS

The HIAF project has successfully implemented several key technologies through rigorous testing and long-term operation, meeting the design specifications. Notable achievements include the fully-stored fast-cycling power supply system, which has been fully installed and operational, achieving a maximum current of 3,900 A (Fig. 9), a maximum voltage of 4,300 V, and a maximum current rise rate of 38,000 A/s, with a stable operating frequency of 3 Hz. These performance parameters meet the design specifications, and the system has undergone long-term operational testing and precise dynamic calibration of the magnetic field at high frequencies, ensuring a magnetic field error of less than 1 Gauss.

The project has also successfully implemented five high-gradient magnetic alloy high-frequency systems, completing system-wide joint testing. In the most challenging frequency range of 0.29 to 2.1 MHz, the system has achieved an international record of 35 kV/m voltage gradient, with voltage precision better than $\pm 1\%$ (Fig. 10) and phase precision better than $\pm 1^\circ$, marking a leading international standard.

The HIAF project has pioneered the use of titanium alloy skeleton ultra-thin wall vacuum chambers, successfully installed to form the world's largest high-vacuum system for an accelerator, achieving a vacuum level of better than 7×10^{-12} mbar (Fig. 11).

In addition, the project has developed a series of high-end beam diagnostic electronic equipment, achieving full domestic production. Over 1,500 sets of 20 different types

of self-developed electronic devices have been installed, addressing the high-precision, large-dynamic-range, multi-parameter measurement requirements for the HIAF beam, as well as microsecond-level interlock protection.

The HIAF project has also developed a new generation of high-security high-speed communication protocol, CVLink, and a large-scale high-performance accelerator cluster control platform, LACCS. These systems enable precise, intelligent beam control, overcoming key technologies such as the autonomous security of accelerator control software and efficient processing of large datasets. Currently, the LACCS control system has been successfully applied to the HIAF facility.

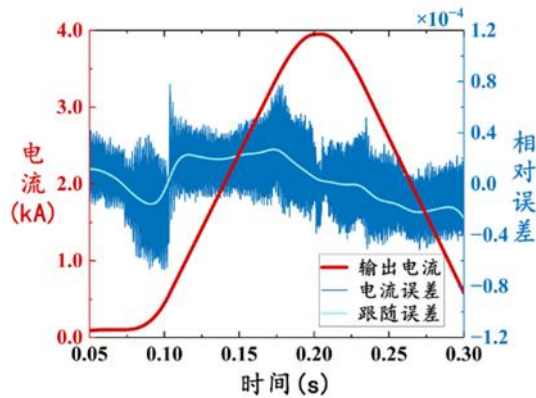


Figure 9: The power system testing result shows that the maximum current can reach 3900A with an accuracy better than $\pm 5 \times 10^{-5}$.

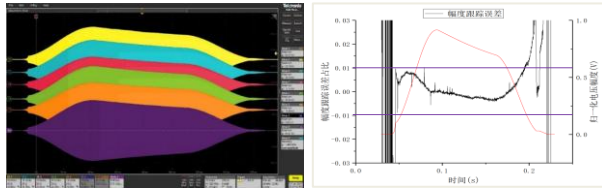


Figure 10: measured voltage (up to 350kV) and accuracy (voltage $\pm 1\%$ and phase $\pm 1^\circ$) for five sets RF.

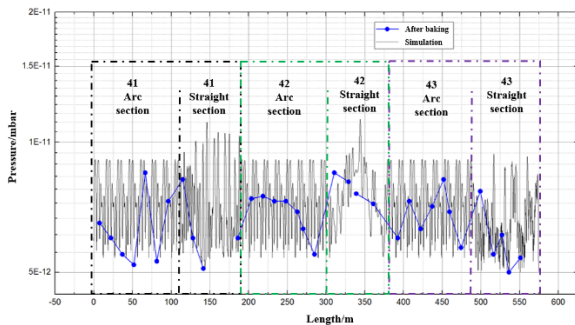


Figure 11: simulation and measurement results of the vacuum pressure in BRing.

CONCLUSION

The HIAF project is the biggest heavy ion accelerator project under-construction in China. There are several challenges related to the ion source, the linac, the RF cavities, the power supplies and so on. In past few years, the HIAF project team have developed several prototypes and obtained test results. The HIAF construction will be benefit on these works. At present, most of the accelerator equipment has been installed and tested. The beam commissioning of the accelerator complex is planned in 2025.

ACKNOWLEDGEMENTS

We thank all the colleagues working on the HIAF project for their valuable contributions on this article.

REFERENCES

- [1] J. C. Yang *et al.*, "High Intensity heavy ion Accelerator Facility (HIAF) in China," *Nucl. Instrum. Methods Phys. Res., Sect. B*, vol. 317, pp. 263-265, Dec. 2013.
doi:10.1016/j.nimb.2013.08.046
- [2] L. Sun *et al.*, "Superconducting magnets for high performance ECR ion sources," *IEEE Trans. Appl. Supercond.*, vol. 28, no. 3, pp. 1-6, Apr. 2018.
doi:10.1109/tasc.2018.2791943
- [3] P. Li *et al.*, "The collimation system design for the Booster Ring in the HIAF project," *Nucl. Instrum. Methods Phys. Res., Sect. A*, vol. 920, pp. 14-21, Mar. 2019.
doi:10.1016/j.nima.2018.12.064
- [4] C. R. Prior and G. H. Rees, "Multiturn injection and lattice design for HIDIF," *Nucl. Instrum. Methods Phys. Res., Sect. A*, vol. 415, no. 1-2, pp. 357-362, Sep. 1998.
doi:10.1016/S0168-9002(98)00406-9
- [5] L. N. Sheng *et al.*, "Ion-optical design of High energy FRagment Separator (HFRS) at HIAF," *Nucl. Instrum. Methods Phys. Res., Sect. B*, vol. 469, pp. 1-9, Apr. 2020.
doi:10.1016/j.nimb.2020.02.026
- [6] B. Wu *et al.*, "The design of the Spectrometer Ring at the HIAF," *Nucl. Instrum. Methods Phys. Res., Sect. A*, vol. 881, pp. 27-35, Feb. 2018.
doi:10.1016/j.nima.2017.08.017
- [7] L. J. Mao *et al.*, "The Electron Cooling System for the HIAF Project in China", in *Proc. COOL'19*, Novosibirsk, Russia, Sep. 2019, pp. 14-17.
doi:10.18429/JACoW-COOL2019-MOZ01

FIRST RIB PRODUCTION WITH SPES EXOTIC BEAM FACILITY AT INFN-LNL

E. Fagotti^{*1}, T. Marchi¹, M. L. Allegrini¹, A. Andrichetto¹, L. Antoniazzi¹, P. Antonini¹, M. Ballan¹, C. Baltador¹, L. Bellan¹, D. Benini¹, G. Benzoni⁴, G. Bisoffi¹, D. Bortolato¹, L. Centofante¹, D. Cittadino⁵, S. Corradetti¹, L. De Dominicis⁶, L. De Ruvo¹, J. Esposito¹, L. Ferrari¹, A. Galatà¹, C. S. Gallo¹, A. Goasduff¹, A. Gottardo¹, F. Gramegna¹, F. Grespan¹, M. Gulmini¹, G. Keppel¹, O. S. Khwairakpam^{1,3}, G. Lilli¹, A. Lombardi¹, M. Maggiore¹, M. Manzolaro¹, P. Mastinu¹, M. Miglioranza¹, P. Modanese¹, M. F. Moisio¹, A. Monetti¹, M. Montis¹, L. Mou¹, Y. K. Ong^{1,2}, A. Palmieri¹, A. Pisent¹, G. Prete¹, G. Pupillo¹, D. Rifuggiato⁵, C. Roncolato¹, M. Rossignoli¹, L. Sarchiapone¹, D. Scarpa¹

¹INFN – Laboratori Nazionali di Legnaro, Legnaro, PD, Italy

²Università La Sapienza, Roma, Italy

³Università di Siena, Siena, Italy

⁴INFN – Sezione di Milano, Milano, Italy

⁵INFN – Laboratori Nazionali del Sud, Catania, Italy

⁶Università degli Studi di Padova, Padova, Italy

Abstract

SPES (Selective Production of Exotic Species) is the INFN (Istituto Nazionale Fisica Nucleare) facility to produce and post-accelerate exotic nuclei for forefront research in nuclear physics and to produce radioisotopes for medical applications. The primary proton beam, extracted by a commercial cyclotron, irradiates targets like SiC, TiC or UCx where the ISOL (Isotope Separation On Line) technique is used to produce and extract exotic nuclei. Those are ionized, selected and either transported to low energy experiments or cooled with an RFQ (Radio-Frequency Quadrupole) cooler, purified from isobars contaminants through a HRMS (High-Resolution Mass Separator), sent to a CB (charge breeder), to increase charge state, injected into a RFQ accelerator and accelerated into ALPI (Acceleratore Lineare Per Ioni) superconducting Linac to finally reach experimental stations. The primary beamline has been fully commissioned, first radioactive beams have been produced and transported to low energy experiments, while the post-accelerator is under installation. A description of the entire facility as well as its commissioning status is given.

INTRODUCTION

SPES is the INFN project to develop an ISOL facility for reaccelerated exotic beams, mainly neutron rich [1]. The project is based on a high-power cyclotron [2] able to accelerate one or two proton beams with a final energy ranging from 35 to 70 MeV and a 750 μ A maximum total current. In case of double extraction, the two proton beams have the same energy, but can have different current values. For example, it is possible to accelerate and extract a very low intensity beam, tens of nanoamps, on one arm of the cyclotron and hundreds of microamps on the other arm.

The cyclotron can supply up to eight users with corresponding beamlines: five on one arm and three on the other arm. Two beamlines are fully operational: one, the BL1 (Beam Line 1), to reach an ISOL target and the other, BL2 (Beam Line 2), to directly irradiate thin targets for nuclear and medical purposes. A third line is currently under installation to irradiate thick targets to be used for radiopharmaceuticals production.

The ISOL beamline is used to transport a 40 MeV 200 μ A maximum current to an ISOL target. Although first beam commissioning are using SiC target, the final configuration will use mainly UCx target, designed to sustain up to 10 kW beam power to produce 10^{13} fissions per second inside target [3]. Reaction products are extracted by thermal process due to high temperature of the TIS (Target-Ion Source) system, in the order of 2000 °C and ionized by three types of ion sources according to requested beam: a SIS (Surface Ionization Source), a PIS (Plasma Ion Source) or a LIS (Laser Ion Source) [4, 5].

Inside the production bunker, a first mass selection is performed with a WF (Wien Filter) with a 1/100 maximum resolution. A LRMS (Low-Resolution Mass Separator), using two 45 deg dipole magnets and placed just outside the production bunker, performs a further mass selection improving resolution to 1/200. Except for WF and LRMS all transport lines are based on electrostatic components to guarantee the same transport to any beam with the same charge state and extracted at the same voltage. RIB (Radioactive Ion Beam) produced in the TIS and roughly selected by WF and LRMS, can follow three different paths:

- It can be transported to low energy experimental hall;
- It can be transported to BC (Beam Cooler) [6], for emittance reduction, that is coupled to HRMS [7] to guarantee a 1/20000 nominal resolution and then transported with electrostatic beam transport line to

* enrico.fagotti@lnl.infn.it

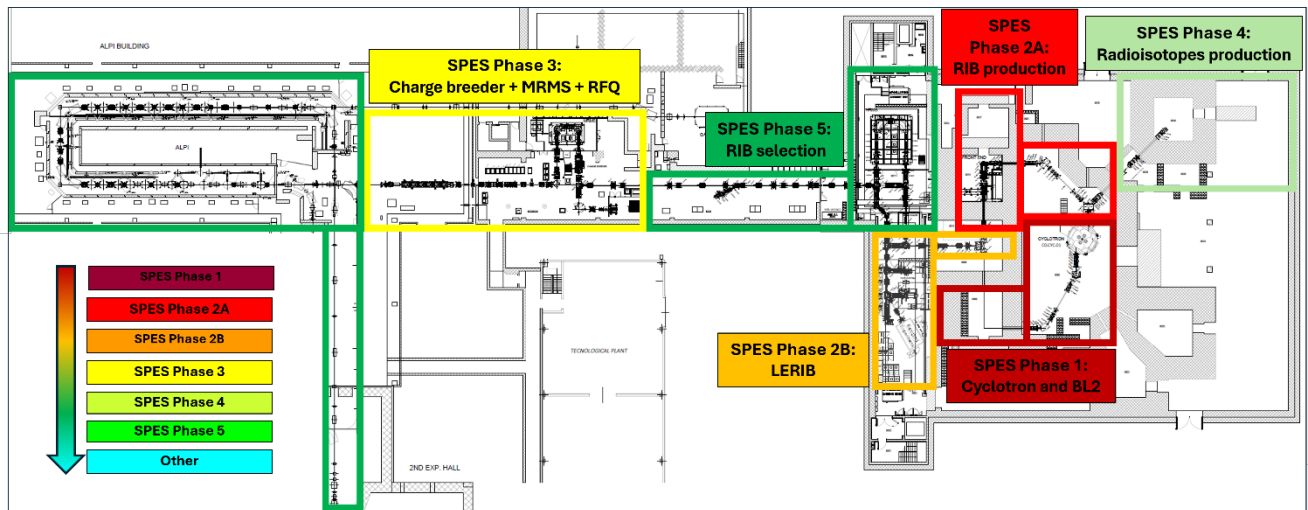


Figure 1: SPES layout – phases approach.

CB [8] for charge state enhancement. CB adds contaminants to the RIB that are removed with a MRMS [9] (Medium Resolution Mass Separator). Pure RIB is then transported by a magnetic transfer line to the RFQ [10, 11] for pre-acceleration, to ALPI linac for reacceleration up to 10 MeV/A and finally to high energy experimental halls;

- It can be transported to reacceleration skipping BC and HRMS in case of selective ionization by a LIS. In this case, beam is directly transported to CB following then the path described in the previous point (CB-MRMS-RFQ-ALPI-experiments).

A new building was built to host the cyclotron, the ISOL bunker for RIBs production, the other bunkers for radioisotopes studies, production and other applications. The new building was connected to an existing one where CB, its injection line, MRMS and transfer line to RFQ replaced the old transfer line used to transport ALPI high energy beams to an experimental area. RFQ itself and its transfer line to ALPI was installed in the ALPI building (Fig. 1).

In the last years, SPES project proceeded in parallel to all other LNL activities. At the end of 2023 there was a paradigm shift: SPES project became first lab priority and it was reorganized into five main phases to be achieved in sequence. Details of phases are the following:

- Phase 1: Cyclotron recommissioning and BL2 test;
- Phase 2: First RIB produced with low current primary beam and transported just outside bunker (Phase 2A) and at the tape station location on the LERIB (Low Energy RIB) experimental area (Phase 2B);
- Phase 3: Installation finalization and beam commissioning with stable beams of the beam line comprising CB, MRMS and RFQ;
- Phase 4: Project finalization, construction, installation and commissioning of all needed to irradiate thick targets for medical radionuclides production;
- Phase 5: RIB selection with BC and HRMS, their transport through CB and MRMS, their pre-acceleration with RFQ, reacceleration with ALPI and transport to high energy experimental halls.

A new time schedule was planned and new delivery time was set for each phase. Just to make an example Phase 1 delivery time was set to April 2024 and it was achieved at the end of May 2024, Phase 2 delivery time was set to March 2025 and it was achieved mid-April 2025. Achievement of Phase 3 is expected to be in March 2026. In the following, Phase 1 and Phase 2 main results will be presented.

PHASE 1

SPES Cyclotron was installed in 2015 and commissioned in 2017-2018 [12] sending beam on a high-power beam dump located in ISOL1 bunker. Concerning the maximum beam power, 35 kW was achieved by delivering 70 MeV protons at 500 μ A. During 2019-2021, tests were mainly related to ion source, cyclotron injection and transport optimization up to 1 MeV due to interference with works on building infrastructures. Between 2021 and 2023 cyclotron operation was stopped for fire prevention authorization upgrade.

Cyclotron maintenance restarted at the end of 2023. Main activities needed to start cyclotron recommissioning concerned ordinary maintenance, control system upgrade, beamlines installation completion, resuming BL1 transport line formerly used for cyclotron commissioning and needed for Phase 2.

In November and December 2023, a water leak was detected inside cyclotron ion source plasma chamber due to a welding failure and traces of corrosion were found on permanent magnets surrounding plasma chamber. After contacting the production company which proposed injector replacement, it was chosen to fix the issue in-house. A new improved design for plasma chamber was ready at the beginning of January 2024 and the final chamber was ready in the same month. A new set of permanent magnets with additional resin coating were delivered at the end of February and the upgraded injector was in operation before the end of March.

Installation and conditioning continued until mid-May when a spark damaged one of the cyclotron RF amplifiers.

Triode dismounting revealed damage in the RF contact fingers silver plating and in the Kapton sheet, where also humidity traces were found. It was also clear that the assembly procedure had to be improved. Even in this case the in-house solution was adopted. An internal solution was implemented and cyclotron was operative at the end of May.

The BL2 line was used to complete SPES Phase 1. Since the requested beam current did not exceed 100 nA, the cyclotron current was reduced by a factor 40 using a pepperpot in the injection line, otherwise the minimum extracted current would not be less than 50 μ A. A target station was set up in ISOL2 bunker and a target sample was positioned in air. A Kapton window, a 75 μ m thick, was placed upstream the target to close the vacuum beamline. A set of graphite collimators and a graphite beam stop were installed to shape the beam on target and finally stop the beam. The cyclotron was optimized for three different proton energies: 35 MeV, 50 MeV and 70 MeV. After each optimization, cyclotron was slightly detuned, working on RF phase, to reduce the maximum beam current on target down to 100 nA. This low current proton beam was used to irradiate thin targets of different materials. As example, in Fig. 2 is reported the production cross section value of the theranostic ^{67}Cu obtained from a natural Zn target in the irradiation with a p-energy 50 MeV.

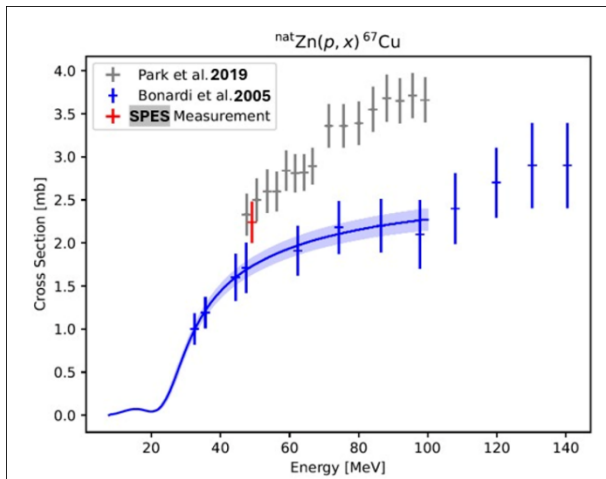


Figure 2: Production cross section value, in red, of the $\text{natZn}(p,x)^{67}\text{Cu}$ nuclear reaction.

PHASE 2

After Phase 1 completion, almost all laboratory human resources were focused on Phase 2. To reduce interferences, Phase 2 was divided in two sub phases:

- Phase 2A: the completion of the installation of the ISOL1 bunker, including cooling plants, pneumatic plants, HV plants, vacuum plants and gas recovery system, control system and MPS (Machine Protection System) (Fig. 3);
- Phase 2B: installation of all beamline's elements up to low energy experiments, including, all plants as for Phase 2A.

For the first RIB production, it was used a 100 nA - 40 MeV primary proton beam accelerated by cyclotron. This time we could profit from cyclotron double extraction,

since both extraction beamlines were operative. In this way no RF detuning was needed. A 4.5 μ A proton beam was extracted on BL2 beam stop while a 100 nA proton beam was spilled and extracted on BL1. Considering the low beam power used for this experiment, a reduced dimension SiC target was used. This target could handle 12.5 μ A proton beam at maximum, but it could profit of a quite uniform power density on its impact surface.

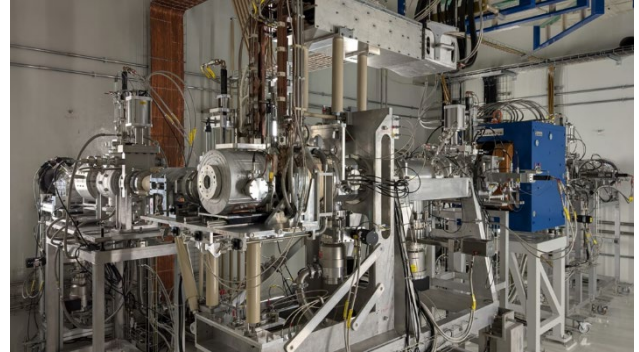


Figure 3: ISOL machine completely installed in the ISOL1 bunker.

After WF characterization it was chosen to select mass 28 for first test. In this configuration HPGe spectrum in coincidence with beta signal revealed $^{28}\text{Si } 2^+ \rightarrow 0^+$ decay and one of the candidates for 2^+ state population is from $^{28}\text{Al } \beta^-$ decay.

The completion of the transfer line up to tape station with Phase 2B confirmed hypothesis made in Phase 2A (Fig. 4).

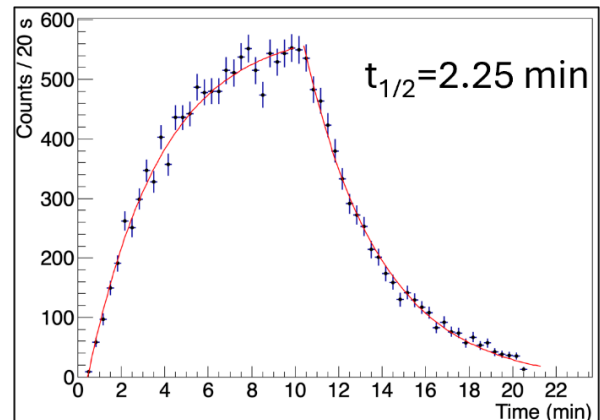


Figure 4: First RIB analysis at tape station revealed half-life of $^{28}\text{Al } \beta^-$ decay.

CONCLUSION

During 2024 and first half of 2025 SPES Project at LNL reached two paramount milestones: Cyclotron recommissioning including BL2 test with irradiation measurements through Phase1 and first RIB produced, delivered and measured at the tape station with Phase2. Nowadays almost all laboratory human resources are focused on Phase 3 that is the completion of line installation between CB and RFQ. RFQ cavity has currently completed tuning process and dummy tuners replacement already started. RFQ conditioning is scheduled for the beginning of next year once all ancillaries will be installed and control system will be

operative. MRMS beamline is installed and we are working on ancillaries' installation. At the end of September, MRMS commissioning will start using CB as injector. First $^{16}\text{O}^{5+}$ stable beam produced by CB, selected by MRMS and accelerated by RFQ is foreseen in March 2026.

REFERENCES

- [1] T. Marchi *et al.*, "The SPES facility at Legnaro National Laboratories," *J. Phys. Conf. Ser.*, vol. 1643, no. 1, p. 012036, Dec. 2020. doi:10.1088/1742-6596/1643/1/012036
- [2] Best Cyclotron System Inc., <http://www.bestcyclo-tron.com/>.
- [3] A. Andrichetto *et al.*, "The SPES multi-foil direct target," *Nucl. Instrum. Methods Phys. Res., Sect. B*, vol. 266, no. 19–20, pp. 4257–4260, Oct. 2008. doi:10.1016/j.nimb.2008.05.134
- [4] M. Manzolaro *et al.*, "Off-line ionization tests using the surface and the plasma ion sources of the SPES project," *Rev. Sci. Instrum.*, vol. 83, no. 2, Feb. 2012. doi:10.1063/1.3666172
- [5] D. Scarpa *et al.*, "New solid state laser system for SPES: selective production of exotic species project at Laboratori Nazionali di Legnaro," *Rev. Sci. Instrum.*, vol. 93, no. 8, Aug. 2022. doi:10.1063/5.0078913
- [6] M. Maggiore *et al.*, "Status of the RFQ Beam Cooler for SPES project at LNL," *EPJ Web of Conferences*, vol. 66, p. 11024, 2014. doi:10.1051/epjconf/20146611024
- [7] M. Comunian, C. Baltador, L. Bellan, M. Cavenago, A. Pisent, and E. Khabibullina, "Design of high-resolution mass spectrometer for SPES", in *Proc. IPAC'18*, Vancouver, Canada, Apr.-May 2018, pp. 3252–3254. doi:10.18429/JACoW-IPAC2018-THPAK021
- [8] A. Galatà *et al.*, "Progresses in the installation of the SPES-charge breeder beam line," *IEEE Open J. Instrum. Meas.*, vol. 13, no. 12, pp. C12009–C12009, Dec. 2018. doi:10.1088/1748-0221/13/12/c12009
- [9] A. Galatà *et al.*, "ADIGE: the radioactive ion beam injector of the SPES project," *J. Phys. Conf. Ser.*, vol. 874, p. 012052, Jul. 2017. doi:10.1088/1742-6596/874/1/012052
- [10] M. Comunian, F. Grespan, A. Palmieri, A. Pisent, "The RFQ injector for the radioactive ion beam of SPES project", in *Proc. LINAC'12*, Tel Aviv, Israel, Sept. 2012, pp. 951–953.
- [11] L. Antoniazzi, E. Fagotti, L. Ferrari, A. Palmieri, and A. Pisent, "Construction, assembly and measurements of the SPES RFQ", in *Proc. IPAC'23*, Venice, Italy, May 2023, pp. 2027–2029. doi:10.18429/JACoW-IPAC2023-TUPL128
- [12] M. Maggiore, P. Antonini, A. Lombardi, L. Pranovi, Z. Filipovsky, "Review and current status of the 70 MeV high intensity cyclotron at LNL", in *Proc. Cyclotrons'19*, Cape Town, South Africa, Sept. 2019, pp. 248–252. doi:10.18429/JACoW-Cyclotrons2019-TUC0

HIGH POWER TARGETRY DEVICES AT FRIB: CHALLENGES, STATUS AND PLAN*

T. Kanemura[†], B. Abdelmegied, N. Bultman, E. Fletcher, T. Ginter, R. Iwai, N. Jockheck, M. LaVere, G. Lee, F. Marti, T. Maruta, S. Miller, Y. Momozaki¹, P. Ostroumov, M. Patil, A. Plastun, R. Quispe-Abad, M. Reaume, D. Simon, J. Song, E. Wakai, X. Wang, J. Wei, Q. Zhao
Facility for Rare Isotope Beams, Michigan State University, East Lansing, MI, USA
¹also at Argonne National Laboratory, Lemont, IL, USA

Abstract

High-intensity heavy-ion accelerators have unique challenges in their beam intercepting devices that originate from the extremely high energy loss per distance traveled by heavy ions traversing their materials. These challenges often prohibit such accelerators from achieving higher beam power and thus determine the accelerator performance. In this paper, the challenges of operation of FRIB beam intercepting devices, as well as their statuses, and their future enhancements are discussed.

INTRODUCTION

The Facility for Rare Isotope Beams (FRIB) is a U.S. Department of Energy Office of Science (DOE-SC) scientific user facility for rare isotope research supporting the mission of the Office of Nuclear Physics in DOE-SC [1]. The ultimate goal is to deliver 400 kW beam power for all ions (especially uranium at an intensity of 8 pA or 5×10^{13} $^{238}\text{U/s}$) to the rare isotope production target at energies >200 MeV/u [2].

Compared to proton-based facilities, lower-energy, heavy-ion-based facilities face challenges, including high power density and high radiation damage in materials where beams are intercepted as discussed later. Heavy-ion facilities have been running at significantly lower beam powers compared to proton-based facilities [3]. FRIB is to push the power frontier of heavy-ion machines to 400 kW, closer to the power level similar to proton-based facilities.

Beam-intercepting devices (BIDs) are used throughout the FRIB facility. As is usually the case in high power accelerator facilities, the performance of the FRIB is currently limited by the capacity of its BIDs. In this paper, the BIDs statuses, their challenges, and their planned enhancements are discussed.

BEAM INTERCEPTING DEVICES AT FRIB

Figure 1 shows a layout of the facility, which consists of three major areas. The first one is the 400 kW superconducting radio-frequency linear accelerator (linac). The second is the rare isotope (RI) production and separation area, where rare isotopes are produced at the target and are transported to experimental areas. And the third is experimental areas.

* This material is based upon work supported by the U.S. Department of Energy, Office of Science, Office of Nuclear Physics and used resources of the Facility for Rare Isotope Beams (FRIB) Operations, which is a DOE Office of Science User Facility under Award Number DE-SC0023633.

[†] kanemura@frib.msu.edu

In the FRIB linac, charge strippers (carbon and lithium strippers) are located in the Folding Segment 1 (FS1). After the first dipole magnet in the FS1, there is a charge selection collimator named the charge selector. The beam is further accelerated to its final energy, and delivered to the RI production target, which is located in the RI production and separation area. The unreacted primary beam is then delivered to the beam dump in the same area. Table 1 shows a list of major BIDs used at FRIB with the beam power and power deposition for full power operations at each BID.

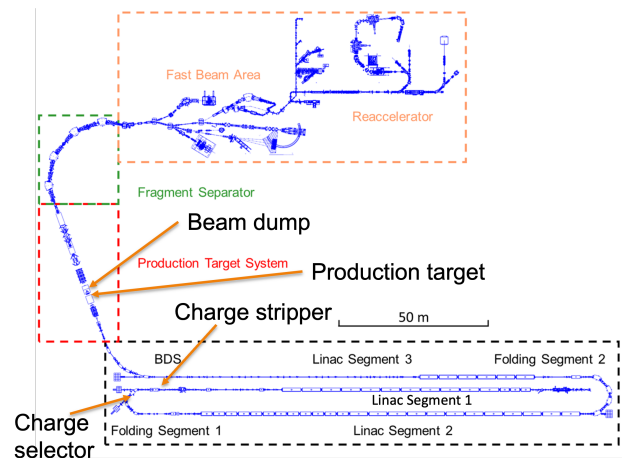


Figure 1: FRIB facility layout and locations of major beam-intercepting devices used in FRIB.

CHALLENGES

There are two major technical challenges in BIDs in heavy ion accelerators in general.

- Extreme thermal load (power density).
- Radiation damage (when a solid material is used).

Thermal Load

Figure 2 shows the energy deposition per unit length in carbon, a popular BID material, as a function of beam energy with selected ion species. Figure 2 illustrates that the heavier the ion is, the higher the energy deposition will be in the material. The energy deposition by ^{238}U is 3 orders of magnitude higher than proton at energies higher than 2 MeV/u. The energy deposition becomes lower with the beam energy. Therefore the interaction between heavy ion beams

Table 1: Major BIDs at FRIB. Beam power and power deposition are for 400 kW full power operations

Area	BID	Beam Energy at BID	Beam Power at BID	Power Deposition into BID
Linac, FS1	Charge stripper	~20 MeV/u	~50 kW	~1 kW
	Charge selector	~20 MeV/u	~50 kW	~10 kW
RI Production & Separation	RI Production	~200 MeV/u	~400 kW	~100 kW
	Target			
	Beam dump	~200 MeV/u	~300 kW	~300 kW

and materials is more severe at lower energies. The energy deposition of ^{238}U at 20 MeV/u is about 4 times higher than that at 200 MeV/u.

As illustrated in Fig. 2, the charge stripper, which is placed where the beam energy is still low to maximize its benefit, is one of the most difficult devices in high-power heavy-ion accelerators. The FRIB's full power ^{238}U beam is expected to deposit thermal load of 60 MW/cm^3 power density in the lithium stripper film.

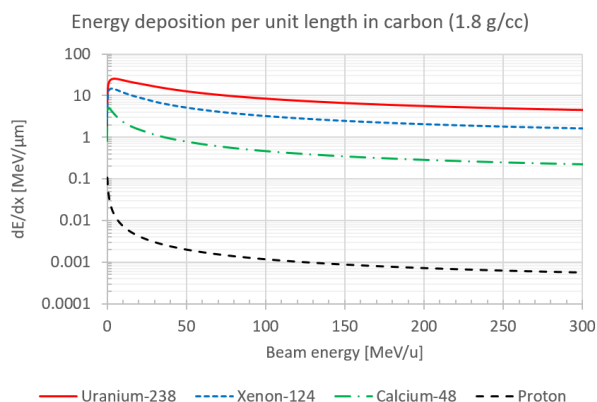


Figure 2: Energy deposition per unit length in carbon as a function of beam energy with selected ion beam species.

Radiation Damage

Figure 3 shows the damage produced by a $^{208}\text{Pb}^{27+}$ beam, 8.1 MeV/u, on Diamond-Like-Carbon (DLC) stripper foils in the National Superconducting Cyclotron Laboratory (NSCL) K1200 Cyclotron. The leftmost photo shows an unused foil, and the middle and rightmost photos show two different foils exposed to the beam [4]. The low-energy Pb beam caused significant damage to the carbon foil. The stripper foils are usually very thin, on the order of μm . Therefore foils are prone to deformation which eventually leads to failures due to displacement damage (displacement of lattice atoms) caused by heavy ions. With this damage the foil became too thin to use for stripping, which made the foil unusable in a short period of time.

As an example of estimated dpa rates, Fig. 4 shows dpa rates as a function of distance from the surface of the charge selector jaws, estimated with the PHITS (Particle and Heavy Ion Transport code System) code [5] assuming the static



Figure 3: Damage produced by a $^{208}\text{Pb}^{27+}$ beam, 8.1 MeV/u, on Diamond-Like-Carbon (DLC) stripper foils in the NSCL K1200 Cyclotron [4].

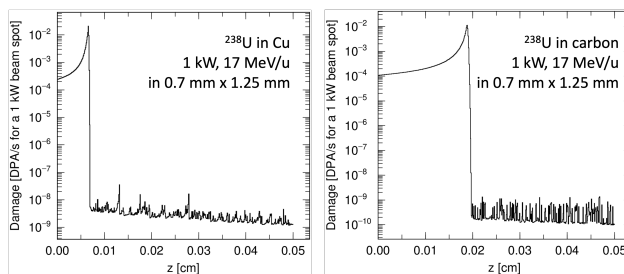


Figure 4: Displacement Per Atom (DPA) rate (per second) caused by 1-kW 17-MeV/u ^{238}U beam in copper (left) and carbon (right). $z = 0$ is the surface of the material.

condition. Here, dpa stands for displacement per atom, a measure of displacement damage in lattice atoms caused by energetic particles. Displacements of lattice atoms alter lattice structure that leads to changes of material properties. The charge selector absorbs the charge states beyond LS2 acceptance, and therefore suffers radiation damage. The beam used for this simulation was 1-kW 17-MeV/u ^{238}U with a spot size of 0.7 mm (horizontal rms) \times 1.25 mm (vertical rms), which is the typical size of one ^{238}U charge state at the charge selector jaws.

As shown in Fig. 4, the stopping range is very short ($< 200 \mu\text{m}$) because of the low energy heavy ion, which results in extremely high thermal loads. Also, the dpa rate is very high (~ 1000 dpa/day at the Bragg peak, ~ 10 dpa/day on the surface with 1 kW power in the beam spot. Note that the dpa rate is linearly scaled by the power received in the spot). With this dpa rate, damage in BID materials is expected to exceed the damage in fusion reactor materials [6]. These challenges require unique BIDs to support FRIB operations.

PHASED APPROACH

Figure 5 shows our phased approach of BID development toward the ultimate beam power of 400 kW. FRIB currently operates at 20 kW. The concept of this approach is to start with proven technologies at low power levels, minimizing risk of failure that is inevitable in complex new systems. This gives us time to mature new technologies that need to be introduced to enable higher power operations.

Passive systems are desired because they are simple and reliable. In the context of BIDs, that means static BIDs (no motion during operations, with, however, some sort of cooling necessary). As shown in Fig. 5, the charge selector and the beam dump still use a passive "static solid" configuration with water cooling. As a matter of fact, the production target was static when the FRIB user operation began at 1 kW in 2022.

Passive BIDs have limitations in the maximum power density that they can handle. At some point as the beam power is ramped up, the power density in BID materials becomes too high to use passive configurations, which necessitates an active configuration to decrease the average power density that the BID materials receive. To achieve it, it is common to use rotation motion to spread out the power deposited in the material by the beam (sometimes it is combined with linear motion as seen in FRIB's rotating carbon stripper). The carbon stripper, intermediate power charge selector and the production target are categorized into this group ("rotating solid" configuration).

Eventually, even with the fast rotating motion of solid BID materials, the power density becomes too high to absorb with the rotating solid configuration. Then "replenishing" configurations become necessary using liquid or gas with circulation, mitigating the radiation damage while still managing the thermal load. The liquid lithium charge stripper (LLCS) [7] and the future water beam dump are categorized into this group ("liquid" configuration). Both are unique to FRIB because of the high intensity of heavy ion beams especially ^{238}U . The LLCS has been established and operational but the water beam dump still needs developments as discussed later.

It is worth noting that from the beginning of the FRIB user operation, the stripper has had no option of using a static configuration because of the technical challenges discussed in the previous section. We used a rotating carbon foil stripper as the main stripper up to 5 kW operation, then switched to the LLCS starting from 10 kW beam power [8]. This is mainly because the carbon stripper had an issue in the rotating mechanism to handle the deposited beam power, which is a thermal management issue, not an inherent bottleneck. Currently this is being addressed [9], and hopefully the carbon stripper will become operational again for light ions, but not for heavy ions (we have seen a carbon foil was damaged due to ^{198}Pt irradiation [10], which is an inherent problem due to physics). All the BIDs other than the LLCS still use either static solid or rotating solid configurations at the current power level of 20 kW.

Finally, this approach makes it possible for us to learn lessons as we ramp up the beam power, and improve systems as we learn.

EPOCH	1	2	3	4	5	6
Beam power	10 kW	20 kW	50 kW	100 kW	200 kW	400 kW
Charge stripper						
- Solid carbon (rotating)						
- Liquid lithium						
Charge selector						
- Low power: static jaws made of Gildcop AL-15						
- Intermediate power: rotating graphite						
- High power: liquid metal option						
Target						
- Single-slice rotating graphite						
- Multi-slice rotating graphite						
Beam dump						
- 6° static beam dump 1.0 (Al absorber)						
- 6° static beam dump 2.0 & 3.0 (bi-metal, mini-channel)						
- Rotating water beam dump (1 mm Ti-6Al-4V shell)						
- Rotating water beam dump (0.5 mm Ti-6Al-4V shell)						

Static solid Rotating solid Liquid (unique to FRIB)

Figure 5: Phased approach of BID development toward the ultimate beam power of 400 kW.

CURRENT STATUS

Strippers

The LLCS has been routinely supporting the FRIB user operations since October 2023 [8]. The LLCS also successfully supported delivering the 20 kW ^{238}U beam to the production target and subsequent user operations. Figure 6 shows the LLCS film while stripping the 17 MeV/u ^{238}U beam while delivering 20 kW ^{238}U beam to the target. The sketch on the right is to illustrate what is seen on the left photo; a round jet of the liquid lithium is produced by the nozzle, which impinges on the edge of a deflector, which transforms the jet into a thin film. The beam goes through the film to be stripped. The beam spot can be seen on the left photo. The beam power lost in the stripper is estimated to be about 60 W. The beam power at the stripper and at the target was 2.2 and 19.5 kW, respectively. To achieve this, lithium stripper film instability needed to be mitigated with two types of feedback control implemented [8, 11, 12]. This double feedback compensation has two different time scales:

- 0.1 s: beam energy feedback using two RF cavities.
- 30 s: beam energy loss feedback using LLCS stage.

The first feedback is to keep the post-stripper beam energy constant and arrival time at the 1st LS2 cavity the same. This significantly reduced beam losses in the post-stripper accelerator. The second one is to keep the beam energy loss in the stripper constant. This utilizes the monotonic film thickness gradient along the flow (see Fig. 2 of [7]); by adjusting the beam position with respect to the film, the desired film thickness can be maintained.

The rotating carbon stripper, which coexists with the LLCS in the FS1 section of the FRIB linac [10], has been undergoing offline thermal testing to improve its thermal management design. Immediately after the beam power was ramped up to 10 kW in October 2023, the rotation motor started stalling presumably because the bearing received

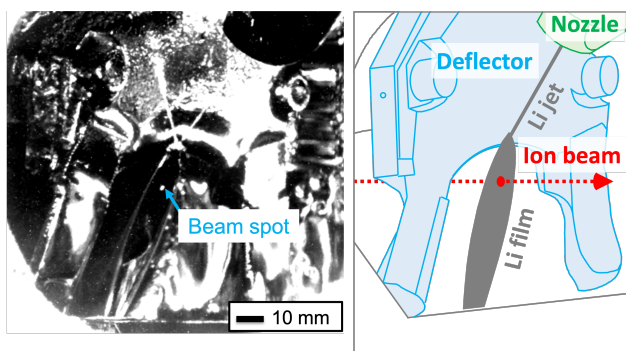


Figure 6: Liquid lithium film stripping 17-MeV/u ^{238}U while delivering 20-kW ^{238}U beam to the target. A bright beam spot on the film is seen on the photo. The right figure is to illustrate what is seen on the left photo.

more heat from the foil and thermally expanded causing additional frictions between bearing balls and casing made of PEEK. To make improvements in the design, we have established an offline test stand with external heat source (high power lasers) to simulate the beam heating in the carbon foil. We started experiments at the same power deposition into the foil at which we observed the rotation stalling in October 2023 [9].

Charge Selector

Currently the Low Power Charge Selector (LPCS) supports the user operation. The LPCS jaws where unwanted charge states are absorbed, are made of Glidcop AL-15. The maximum power that can be absorbed in a spot has been set to 500 W in 0.7 mm (horizontal rms) \times 1.25 mm (vertical rms) through thermo-mechanical simulations, and radiation damage was not considered to set the limit. Figure 7 shows the LPCS model (left) and a photo of the surface of the jaws replaced in Sep. 2024 (right). The drive unit positions the jaws at desired locations. The jaw surface had clear discoloration and damage induced by the beams. We have been studying the mechanism behind this damage and material property changes induced by this damage [13].

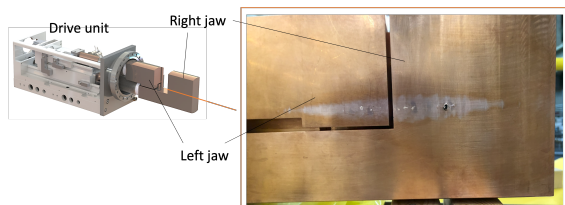


Figure 7: Low Power Charge Selector (LPCS) model (left) and a photo of the surface of the jaws replaced in Sep. 2024 (right) [13].

Thanks to the multi-charge acceleration demonstrated by FRIB [14], the beam loads on the LPCS jaws have been reduced significantly and the LPCS will be able to support 50 kW operations (originally it was thought 10 kW would be the maximum). The more the charge states can be used

simultaneously, the less the beam loads on the jaws become. FRIB has been developing multi-charge acceleration beam tuning for all the ions except for the ones lighter than Ca [15]. With this, the stripping efficiency exceeds 80% for most of the ions. For example, the uranium beam can achieve the remarkable 83% stripping efficiency.

The next version charge selector, called the Intermediate Power Charge Selector (IPCS), has been being designed [16]. Figure 8 shows the latest design model. The 100-mm-diameter rotating wheels as beam absorbers will provide more than 2 orders of magnitude larger irradiation area compared to the one with the LPCS's static jaws, distributing the thermal load as well as the radiation damage. This will significantly increase the acceptable beam loads. Various simulation works support the design. One of them is a vacuum performance simulation [17]. Since the graphite wheel temperature is expected to exceed 1500 °C, its vacuum load to achieve the operating vacuum pressure was a concern. It turned out the load due to the high temperature is manageable.

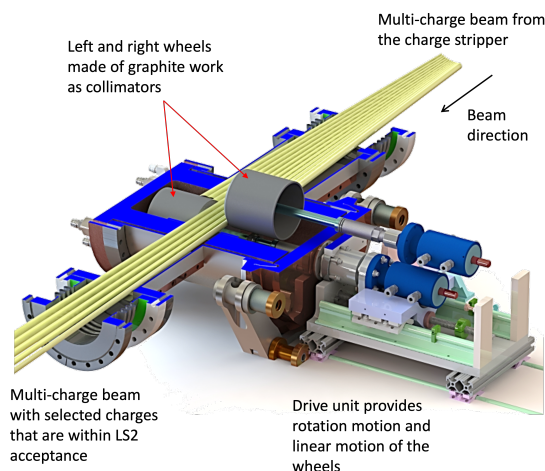


Figure 8: Current design of the Intermediate Power Charge Selector (IPCS).

Production Target

The single-slice target system has been working very well and successfully supporting user operations [18]. Figure 9 shows an optical thermal image of a production target disk taken with the thermal imaging system for the target. A 2.1-mm-thick target disk, rotating counterclockwise at 500 RPM, was irradiated by a 20-kW, 177-MeV/u ^{238}U beam, reaching 1200 °C peak temperature.

Major technical issues that the target system will need to find solutions for beyond the 50 kW beam power are the high-temperature radiation-hardened bearing and lubrication that works at up to 5000 RPM. Also there is an engineering challenge for the multi-slice target, which is the heat exchanger design upgrade to have a capability of remotely replacing target disks without replacing the heat exchanger itself.

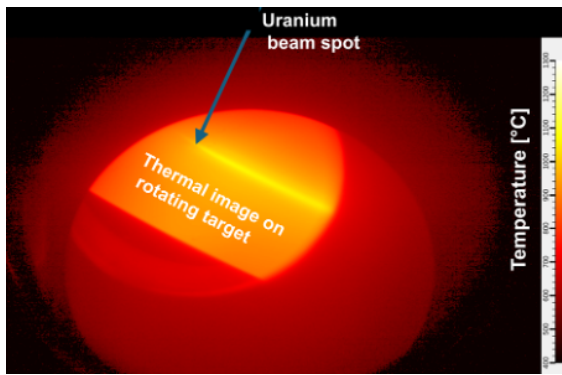


Figure 9: Production target disk irradiated by 20-kW 177-MeV/u ^{238}U .

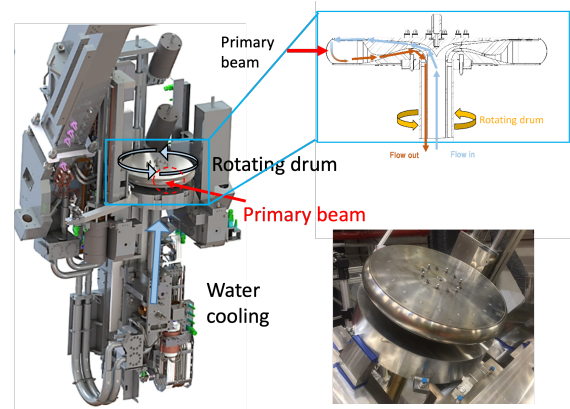


Figure 10: Rotating water beam dump.

Beam Dump

The static beam dump system has been working well too. Currently the 6° static beam dump 2.0 is used to support 20-kW beam operations [19, 20]. This design is backed by thermo-mechanical simulations [21, 22] and thermal performance validation tests [20]. An attempt to apply the machine learning (ML) technique to seek design optimization is also underway [23].

The design upgrade to support 30-kW operations is complete [19]. The current operating temperature limit of the beam dump, which is 250 °C, was set based on the yield strength obtained from literature. To challenge this literature-based limit, we have been carrying out thermal performance validation tests with an e-beam [20]. The preliminary results look promising and most likely we will be able to increase the operating temperature limit.

Beyond the 50-kW operations, we will need to introduce a water beam dump because the power density will become too high to absorb in a static solid material even with the 6° beam incident angle. FRIB's baseline design for the water beam dump is shown in Fig. 10. The water is contained in a thin-wall drum rotating at 600 RPM. The drum is made of the Ti-6Al-4V alloy. The beam passes through the thin-wall shell and stops in the water. The major challenge of this design is to use a rotary water seal on the rotating shaft to seal the water from the beamline vacuum environment, which requires a challenging acceptable water leak rate of 10^{-5} Torr-l/s. Currently we are working on new seal designs as well as seal tests for validation. Another challenge is to maintain the integrity of the drum shell during operations taking into consideration the radiation damage being accumulated in the shell material. The minimum lifetime is set to 1 year (or 4400 hours). Recent research results indicate the loss of ductility of the Ti-6Al-4V alloy at low dpa (≤ 1 dpa) [24].

Availability

Overall, the availability of each FRIB BID is high to support the FRIB user program. The facility availability was 93% during a time period from October 2022 to September 2024 [3]. The device of the lowest availability among the FRIB BIDs was the LLCS, recorded 99.4% availability,

which is considered very high since the LLCS is a state-of-the-art revolutionary device. The downtime analysis is given in Ref. [8]. The second lowest was the carbon stripper, 99.7% availability. The third lowest was the charge selector, 99.8% availability. The production target and beam dump didn't record any downtime during the period. These data backs our phased approach discussed earlier is appropriate to support user operations with high availability.

SUMMARY

FRIB is currently operating at a beam power of 20 kW including the ^{238}U beam. FRIB's BIDs have been supporting high-availability facility operations. The challenges that the FRIB BIDs face stem from the extremely high energy deposition per unit length into BID materials, which creates very high thermal density and radiation damage in the materials. FRIB has been implementing the phased approach to develop and deploy BIDs to support both user operations and power ramp-up, addressing the challenges. This has been proven to work per availability data of each BID.

ACKNOWLEDGEMENTS

The authors would like to thank FRIB's Targetry Advisory Committee (TAC) members, especially, the TAC chair, Patrick Hurh, for their continued support, fruitful discussions, and valuable comments and recommendations to support the FRIB's beam intercepting devices operations and developments.

The authors also would like to thank all the FRIB staff members for their support of operations and upgrades of the beam intercepting devices.

This material is based upon work supported by the U.S. Department of Energy, Office of Science, Office of Nuclear Physics and used resources of the Facility for Rare Isotope Beams (FRIB) Operations, which is a DOE Office of Science User Facility under Award Number DE-SC0023633.

REFERENCES

- [1] T. Glasmacher, A. Gade, G. Bollen, and J. Wei, "The Facility for Rare Isotope Beams: Providing New Opportunities for

- Science”, *Nucl. Phys. News*, vol. 34, no. 3, pp. 5–12, Jul. 2024. doi:10.1080/10619127.2024.2375963
- [2] J. Wei *et al.*, “Technological developments and accelerator improvements for the FRIB beam power ramp-up”, *J. Instrum.*, vol. 19, no. 05, p. T05011, May 2024. doi:10.1088/1748-0221/19/05/t05011
- [3] J. Wei *et al.*, “FRIB operations: first three years”, presented at HIAT’25, East Lansing, USA, June 2025, paper MOX01, this conference.
- [4] J. A. Nolen and F. Marti, “Charge Strippers of Heavy Ions for High Intensity Accelerators”, *Rev. Accel. Sci. Technol.*, vol. 06, pp. 221–236, Jan. 2013. doi:10.1142/s1793626813300107
- [5] T. Sato *et al.*, “Recent improvements of the Particle and Heavy Ion Transport code System - PHITS version 3.33”, *J. Nucl. Sci. Technol.*, vol. 61, pp. 127–135, 2024. doi:10.1080/00223131.2023.2275736
- [6] J. Knaster, A. Moeslang, and T. Muroga, “Materials research for fusion”, *Nat. Phys.*, vol. 12, no. 5, pp. 424–434, May 2016. doi:10.1038/nphys3735
- [7] T. Kanemura *et al.*, “Experimental Demonstration of the Thin-Film Liquid-Metal Jet as a Charge Stripper”, *Phys. Rev. Lett.*, vol. 128, p. 212301, May. 2022. doi:10.1103/PhysRevLett.128.212301
- [8] T. Kanemura *et al.*, “Liquid lithium charge stripping technology: Achievement and lessons learned”, in *Proc. IPAC’25*, Taipei, Taiwan, Jun. 2025, paper MOYD2, p. 19–23. doi:10.18429/JACoW-IPAC25-MOYD2
- [9] B. Abdelmegied *et al.*, “Mitigating the thermal challenges in carbon stripper: test bench simulation to enhance the device stability”, presented at HIAT’25, East Lansing, USA, June 2025, paper WEP03, this conference.
- [10] T. Kanemura *et al.*, “Operational Performance with FRIB Liquid Lithium and Carbon Charge Strippers”, presented at HB’23, Geneva, Switzerland, Oct. 2023, paper WEC212, unpublished.
- [11] S. Zhao *et al.*, “BPM feedback for LLRF energy and phase regulation in charge stripping beamlines”, in *Proc. IPAC’24*, Nashville, TN, USA, May 2024, paper THPG32, p. 3326–3328. doi:10.18429/JACoW-IPAC2024-THPG32
- [12] S. Cogan *et al.*, “Beam loss detection and mitigation at FRIB”, presented at HIAT’25, East Lansing, USA, June 2025, paper WEP07, this conference.
- [13] E. Fletcher *et al.*, “Monte Carlo simulation analysis for radiation damage on Glidcop Al-15 caused by 17–20 MeV/u heavy ions in FRIB”, presented at HIAT’25, East Lansing, USA, June 2025, paper MOP04, this conference.
- [14] P. N. Ostroumov *et al.*, “First Simultaneous Acceleration of Multiple Charge States of Heavy Ion Beams in a Large-Scale Superconducting Linear Accelerator”, *Phys. Rev. Lett.*, vol. 126, p. 114801, Mar. 2021. doi:10.1103/PhysRevLett.126.114801
- [15] T. Maruta *et al.*, “Primary beam development for FRIB experiments”, presented at HIAT’25, East Lansing, USA, June 2025, paper TUZ02, this conference.
- [16] A. Plastun *et al.*, “Advanced charge selector for stripped heavy ion beams”, in *Proc. IPAC’24*, Nashville, TN, USA, May 2024, paper TUPR70, p. 1582–1585. doi:10.18429/JACoW-IPAC2024-TUPR70
- [17] X. Wang *et al.*, “Monte-Carlo simulation of vacuum system for advanced charge selector”, presented at HIAT’25, East Lansing, USA, June 2025, paper TUP06, this conference.
- [18] J. Song *et al.*, “A single-slice rotating graphite target at FRIB”, presented at HIAT’25, East Lansing, USA, June 2025, paper TUB01, this conference.
- [19] S. Miller *et al.*, “Optimization of a mini-channel beam dump for FRIB operation”, presented at HIAT’25, East Lansing, USA, June 2025, paper TUP01, this conference.
- [20] J. Song *et al.*, “Design and experimental thermal validation of the mini-channel beam dump for FRIB”, presented at HIAT’25, East Lansing, USA, June 2025, paper TUP04, this conference.
- [21] M. Patil *et al.*, “Application of ASME BPVC Section VIII, Division-2, design by analysis requirement to FRIB static beam dump”, presented at HIAT’25, East Lansing, USA, June 2025, paper TUP05, this conference.
- [22] R. Quispe-Abad *et al.*, “Thermal-hydraulic analysis of a 20kW beam power water-cooled mini-channel beam dump at Facility for Rare Isotope Beam”, presented at HIAT’25, East Lansing, USA, June 2025, paper MOP05, this conference.
- [23] G. Lee *et al.*, “Design improvements of a minichannel beam dump wing through AI-driven Genetic Algorithms”, presented at HIAT’25, East Lansing, USA, June 2025, paper WEP11, this conference.
- [24] T. Ishida *et al.*, “Tensile behavior of dual-phase titanium alloys under high-intensity proton beam exposure: Radiation-induced omega phase transformation in Ti-6Al-4V”, *J. Nucl. Mat.*, vol. 541, p. 152413, Dec. 2020. doi:10.1016/j.jnucmat.2020.152413

COMMISSIONING OF THE S³ SPECTROMETER: ADVANCES, CHALLENGES AND OUTLOOK

M-H. Stodel^{1*}, M. Aburas¹, M. Authier², A. Drouart², F. Esnault¹, B. Jacquot¹,
N. Lecesne¹, T. Lefrou¹, F. Lutton¹, G. Olivier³, J. Piot¹, H. Savajols¹, C. Stodel¹

¹GANIL, CEA/DRF-CNRS/IN2P3, Caen, France

²Département de Physique Nucléaire, IRFU, CEA, Université Paris-Saclay, Gif-sur-Yvette, France

³ Université Paris-Saclay, CNRS/IN2P3, IJCLab, Orsay, France

Abstract

The S³ spectrometer is a new-generation spectrometer connected to the SPIRAL2 superconducting linear accelerator at GANIL. It aims to provide the nuclear physics community with opportunities to study the products of the fusion-evaporation reaction, producing proton-rich nuclei through to heavy and superheavy nuclei. The project began in 2010 and has now entered its final phase. This paper provides an update on the main equipment developed specifically for the spectrometer, details the challenges we have had to overcome, and looks ahead to the next phases of commissioning.

THE SPECTROMETER DESIGN

In order to take advantage of SPIRAL2's high-intensity beam and study the rare and very rare events produced in the target station, the spectrometer has been designed with 4 main features in mind (Fig. 1): it should accept a 10 kW beam, have a very good rejection rate of the primary beam (selectivity > 10¹³ in the first stage), have a fairly good transmission (> 50%), and also be capable of performing mass selection (> 450) in high-resolution mode.

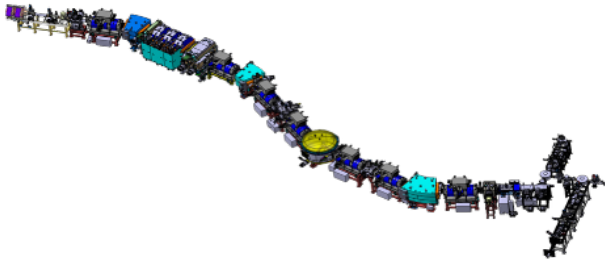


Figure 1: Super Separator Spectrometer overview.

The spectrometer is a symmetrical two-stage design [1]. The first stage, called the momentum achromat, comprises the target station and the main beam dump to get rid of the incoming beam that has not interacted with the target. The second stage, called the mass spectrometer, comprises an electrostatic dipole and a wide-angle magnetic dipole to achieve the appropriate resolution. In total, the spectrometer comprises 8 focusing triplets, 7 of which are superconducting and one of which is an open triplet at room temperature

with a large aperture. At the final focal plane, two detection setups can be placed alternately.

There are two possible modes of operation, depending on whether the objective of the experiment requires good transmission or mass resolution of the reaction products. In the latter case, the aberrations of the 2nd and 3rd order modes will be cancelled by using dedicated sextupoles and octupoles in the superconducting magnets.

DEVICES AND THEIR STATUS

The rotating target station (Fig. 2) has been designed for heavy beams at 10 pμA (thermal heat calculation) at 5 MeV/u [2]. It has a large wheel of 670 mm diameter that supports 18 targets of 21.5 cm². It rotates at a speed up to 3000 rpm. The beam spot is very focused in the horizontal planes with standard deviation of 0.5 mm and 2.5 mm respectively. To ensure the integrity of the target, several sensors detect any damage in the target structure. These include an electron gun, an alpha source and a silicon detector, as well as two Rutherford backscattering detectors. The electronic control is able to synchronize the accelerator beam (using the slow chopper) with the rotation of the target. This prevents damage to the frames. The target station was commissioned off-line, then on-line using a cyclotron beam, and finally qualified with a real SPIRAL2 beam during stage A of the commissioning plan.

After the target the beam is conducted through the dispersive zone (Fig. 3), that comprises a magnetic dipole, a resistive triplet of quadrupoles, and the beam dump. This beam dump is made to withstand a 10 kW power deposit. It comprises two chambers, the upstream chamber and the downstream chamber.

It is made of:

- 11 dump parts (5 fingers, 4 shutters, 2 stationary plates),
- 2 kW / finger (1 kW/cm²). Tungsten/Copper, V shape,
- External and internal lead shielding so that the radiation will decay to 25 μS/h after 24 h cooling time for eventual maintenance in the zone.

The beam dump has been fully developed, produced and tested by CEA/Saclay, and its final installation will take place early 2026.

Another important development for this spectrometer is the Superconducting Multipole Triplet (SMT). There are

* marc-herve.Stodel@ganil.fr



Figure 2: The target station installed on S^3 .

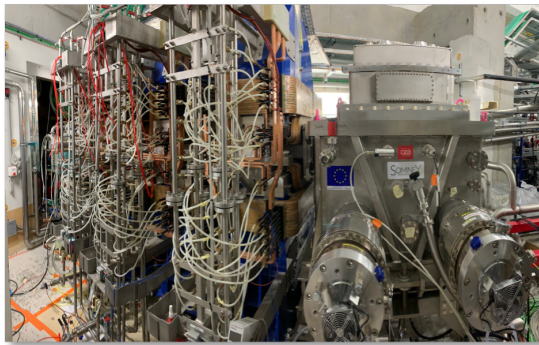


Figure 3: The dispersive zone, installation on-going.

7 of these triplets along the line (Fig. 4). They provide a useful inner diameter for the beam of 336 mm. Inside each SMT the cold mass is made of 3 triplets of quadrupoles, and superimposed are placed high order compensation coils, sextupoles and octupoles. In addition each SMT comprises two different dipolar steerers. The total number of different magnets is therefore 11 per cryostat, and with some optimization for adjacent coils (sharing of current leads), there are 16 current leads per SMT. Each SMT consists of an NbTi wire placed in a precision-machined epoxy glass fiber matrix. The conductor has a critical temperature of 5,65 K, and a peak current of 597 A. Each coil is made of several layers. The 16 current leads are conduction-cooled HTS conductors, including BSCCO and YBCO, and a stainless steel shunt.

The remarkable compactness, as well as the low cryogenic budget per SMT (less than 5 W at 4.2 K LHe), led to a complex design, and the implementation that was not immediately successful on the 7 SMTs. Several magnets had problems with the current leads (mainly delamination), one of the magnets suffered from leaks in the liquid nitrogen

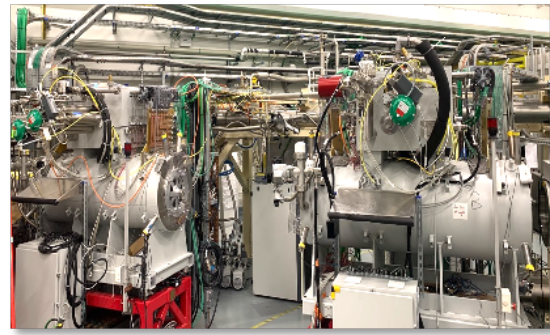


Figure 4: 2 SMTs installed on S^3 .

tank and, finally, one of the SMTs' internal wiring (at 4.2 K) broke. It was later discovered that it was probably not efficiently cooled. All these problems have been solved, and there is a program to improve the design of the HTS current leads, and to add an additional level sensor so that each part of the low-temperature superconducting wire is immersed in the helium bath. Validation of these improvements and repairs is planned for the end of 2025, when the spectrometer will be cooled down. We also plan to minimize the number of thermal cycles for these fragile objects in the future. In addition to the electrical qualification of the superconducting magnets, the magnetic aspects also represented a challenge. All the coils were mapped at room temperature during production. Due to installation constraints and the lack of space along the line, there was only a short sequence to check the quality of the field at high intensity. The first test bench is a long rigid aluminum cylinder placed inside the SMT. It rotates and carries a Hall probe that moves longitudinally. This could not be used at the 7 places. Two other test benches were designed, using Hall probes. The latest uses the fringe fields and will be qualified by the end of 2025.

The qualification of the 7 SMTs was slowed down by the lack of availability of the cryogenic systems during the 2023-2024 period. The 100 W cryogenic system, purchased from Air Liquide, suffered several major failures, resulting in the crash of 4 turbines and more than a year and a half of unavailability. This hampered the magnet qualification program and made it more difficult to understand the problems (broken wires, HTS delaminations, etc.). However, thanks to a new cryogenic maintenance procedure, the cryogenic equipment is operational. The performance of the cryogenic distribution line design, however, may not yet be optimal (>60 W), and this leaves only a small margin in terms of cryogenic load. If we were to operate at maximum current in the future, this line may have to be improved to reduce the load and leave enough cooling power for the magnets.

Another crucial device for the Super Separator Spectrometer is the electrostatic dipole (Fig. 5). This dipole has a large stainless steel enclosure, two titanium electrodes, and is powered by two 300kV commercial of the shelf high voltage power supplies, from Heinzinger company. The commissioning phase of this dipole took some times, because of the many sparks observed in the first phase, the fear to dam-

age the electrodes and a lack of detailed procedure in the bibliography. In addition, due to radiation regulations, the conditioning of the electrostatic dipole should be carried out with no one the S3 cave. This slowed down conditioning.

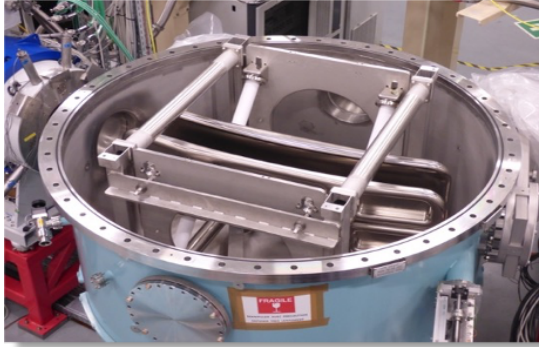


Figure 5: S³ electrostatic dipole open.

The project decided to enlist the help of experts (CERN team), and a modified algorithm was implemented, taking into account the current level, the frequency of sparks, the type of electrode (anode or cathode), and the vacuum level. This algorithm has considerably improved the speed at which the voltage can be increased. A voltage level of + and – 200 kV has been obtained. This level can be reached now rather rapidly, when reconditioning. It is sufficient for Day 1 experiments, and we are confident that we can reach higher levels in the future, if necessary.

As mentioned at the beginning of this article, at the final focal plan can be used alternatively two detection setups. SIRIUS is a system based on decay spectroscopy (Fig. 6). The ions pass through a time-of-flight system, are implanted, and the decay is observed by measurement of the radiation thanks to double sided stripped silicon detectors, and several germanium detectors. All event are recorded and the coincidence are determined offline. This makes it possible to reconstruct the trajectory of the particles and identify them ion by ion. It will mainly be installed for the production of heavy and super-heavy elements, in conjunction with the high-resolution mode spectrometer.

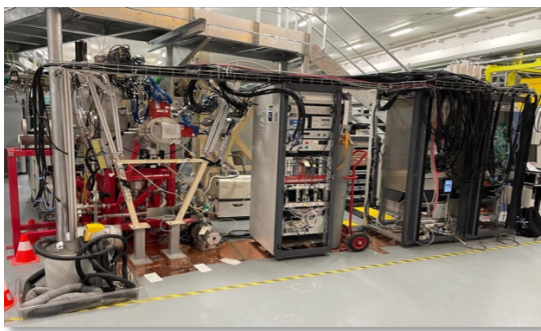


Figure 6: SIRIUS detection system.

The alternative detection system is called S³-LEB (S³ Low Energy Branch) (Fig. 7). It is based on a selective

resonant ionization by lasers. The particles are neutralized, cooled in a gas-jet, then a Laser makes a selective ionization of fusion-evaporation residues, at energies that are signatures of the ions of interest. In addition, in some cases (related to spin parity), an additional scanning Laser can give access to the hyperfine structure of the electronic layers, and provide information on the nuclei structure. After ionization, the ion can be sent for mass identification (MR-TOF MS PILGRIM), or implantation for identification (with the SEASON implantation station), or even to the future installation DESIR. The mass resolution achieved with this setup is above 120000.

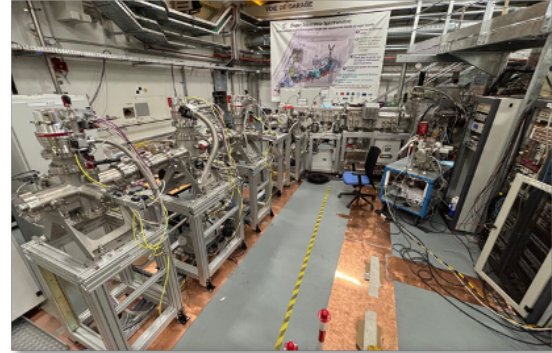


Figure 7: S³-LEB detection system in S³.

COMMISSIONING PHASES

The S3 project has defined 3 commissioning steps. The first step (A), sending the SPIRAL2 beam up to the target station was passed late 2024. The step B consists in sending a direct beam up to the final focal point, to validate the correction behavior and correct performances of each element, with a simple optics. The phase will start by end 2025. In 2026, the last phase (C), consisting in making a real reaction in the target, and making identification of the reaction product, will start during 2026.

Both identification setups, were commissioned off-line, are ready to receive the beam. [3,4]

CONCLUSION

Most of the main elements of the spectrometer are installed and individually validated. The budget is well under control (projected, 28 M€ in 2010 including buildings, actual 34 M€ in 2025). The challenges we had to face on the cryogenics, the superconducting magnets, and to some extent, the electrostatic dipole, gives us in-depth knowledge of these complex systems, and this will be a strength for their operation. We still have to validate the good alignment of the equipment (cold mass of the superconducting magnets), and define a way to efficiently tune the high-resolution mode. The year 2026 will be a crucial year for the project, with the aim to pass the phase B and C. This commissioning will provide the real figures concerning the rejection rate, as well as the transmission toward the final focal plane. We expect to be able to perform real experiments in 2027.

REFERENCES

- [1] F. Déchery *et al.*, “Toward the drip lines and the superheavy island of stability with the Super Separator Spectrometer S^3 ”, *Eur. Phys. J. A*, vol. 51, no. 6, p. 66, Jun. 2015.
doi:10.1140/epja/i2015-15066-3
- [2] Ch. Stodel *et al.*, “High intensity targets stations for S^3 ”, *J. Radioanal. Nucl. Chem.*, vol. 305, no. 3, pp. 761–767, Jan. 2015. doi:10.1007/s10967-015-3936-5
- [3] J. Piot, S^3 coll., “ S^3 : Pushing spectroscopy forward”, *Acta Phys. Pol. B*, vol. 43, no. 2, p. 285, 2012.
doi:10.5506/APhysPolB.43.285
- [4] J. Romans *et al.*, “High-resolution laser system for the S^3 -Low Energy Branch”, *Nucl. Instrum. Methods Phys. Res., Sect. B*, vol. 536, pp. 72–81, Mar. 2023.
doi:10.1016/j.nimb.2022.12.012

COMPUTATION MODEL FOR SPACE CHARGE EFFECT FOR BUNCHED BEAM IN COLLIDER RINGS*

H. Alamprese[†], Y. Hao, Michigan State University, East Lansing, USA

Abstract

In the last two decades, numerical and experimental studies have extensively explored the impact of the space charge on bunched beams in both linear accelerators and storage rings. However, fully accounting for space charge effects over the entire accelerator is computationally intensive, especially in storage rings, where simulations must track beam dynamics over many turns and extended time periods. In many cases, space charge forces cannot be neglected, motivating the development of an alternative computational model. Here, we explore space charge-induced nonlinear dynamics using a model that approximates the Coulomb force by concentrating its effects at discrete locations along the accelerator. This approach enables efficient analyses of the full six-dimensional phase space evolution under space charge effects. Future work will apply this model to further investigate the interplay between space charge and beam-beam interactions in colliders, as well as to assess long-term stability criteria in ring accelerators.

INTRODUCTION

Over the past decades, collective effects have been studied for their role in causing instabilities in accelerators. Several simulation codes have been developed, playing a crucial role in machine design and optimization, as well as in the study of nonlinear beam dynamics, including instabilities and resonances. Currently, the most widely used model is Particle-in-Cell (PIC). However, this approach may be less efficient for circular accelerators due to the extensive demand of computation resources. Moreover, the difficulty in maintaining symplecticity makes it challenging to interpret the results of long-term tracking. A first possible attempt of implementing a symplectic model applicable to accelerators, such as rings and colliders, has been presented in [1]. However, its computational cost scales with the number of Poisson modes and macro particles ($N_{\text{modes}} \times N_{\text{particles}}$), and can become significantly high for simulations of over several thousand turns.

This work adopts a simplified Gaussian beam model to calculate space-charge forces in a proton beam propagating through a periodic FODO cell lattice, and compare two distinct approaches: one based on a two-dimensional (2D) beam phase space and the other on an approximate three-dimensional (2.5D) representation.

The first section presents the theoretical foundations of the implemented model and describes its assumptions in

both the two-dimensional and three-dimensional case. The second section describes the simulation study of a coasting beam, where the two-dimensional method is employed, and a bunched beam in the presence of a radio-frequency (RF) cavity, where the three-dimensional method is applied.

DEVELOPMENT OF A TRANSFER MAP FOR SPACE CHARGE

The space charge force plays a crucial role in collective beam dynamics, as each particle in the bunch experiences the electromagnetic field generated by all other particles in the rest frame. This interaction directly affects the particle's momentum and leads to modifications of their trajectories, resulting in betatron tune and amplitude modulation.

The transverse electric field generated by the beam can be modeled using the 2-D Poisson equation. For a Gaussian beam, the field can be accurately expressed as the Bassetti-Erskine equation, which is derived from the potential of a two-dimensional Gaussian charge distribution. This formulation directly depends on the position of the particle inducing the electric field [2].

Assuming a 2D Gaussian beam distribution, the longitudinal profile is treated as *infinitely uniform*, implying that the electric field is independent of the longitudinal coordinate z . As a result, the transverse momenta is influenced by the electric field as shown in Eq. 1, where $K = 2r_0N/\beta^3/\gamma^3$ defines the perveance in terms of classical radius r_0 and number of particles N in the bunch.

$$dp_{x,y} = \sum_i^n K \cdot E_{x_i,y_i}(x_i, y_i, \sigma_x, \sigma_y) \cdot ds \quad (1)$$

For a bunched beam, the RF cavity compresses the longitudinal beam size, which can also be modeled as a Gaussian distribution (2.5D model). Consequently, the Bassetti-Erskine equation acquires the z -dependence, since the total charge distribution is no longer uniform. The corresponding linear charge density is given by the following.

$$Q\lambda(z) = Q \frac{e^{-\frac{z^2}{2\sigma_z^2}}}{\sqrt{2\pi}\sigma_z} \quad (2)$$

Due to the z -dependence, the transverse momentum kick is proportional to the longitudinal charge distribution, resulting in the following expression for the transverse momentum kick:

$$dp_{x,y} = \sum_i^n \lambda_{z_i} \cdot K \cdot E_{x_i,y_i}(x_i, y_i, \sigma_x, \sigma_y) \cdot ds \quad (3)$$

The circulating beam is subject to its own self-field throughout the entire ring, resulting in a continuous

* Work supported by the U.S. Department of Energy Office of Science under award number DE-SC0024170.

[†] alampres@msu.edu

self-interaction. This complexity makes exact solutions challenging, motivating the use of approximations. A frequently used method involves integrating the space charge force along a reference trajectory. Conceptually, the ring is divided into discrete segments, where the space charge force is evaluated at the end of each segment (interaction points or IPs) to account for its cumulative influence along the preceding length ds , in Eq. 1 and 3. The discretization of the ring for the IP locations is closely linked to the phase advance per turn. To ensure the accuracy of this approximation, the number of interaction points should be greater than — ideally at least twice — the integer part of the machine's phase advance. Although the 2.5D approach accounts for the third dimension, it remains non-symplectic, because it does not consider the variation of energy–momentum and its coupling with the transverse momentum components.

COMPARISON BETWEEN COASTING AND BUNCHED BEAM

Table 1 provides a summary of the beam parameters used in the simulations. The space charge kick is applied either at the end of each FODO cell element or at its midpoint, effectively dividing each element into two segments with the space charge kick applied between them. The two simulation approaches assess the impact of segmenting the structure, revealing that the number of segments was sufficient to ensure convergence.

Table 1: Beam Parameters

Parameter		Value
Beam Energy (GeV)	E	1
Particles bunch	N	0.3×10^{10}
Beam current (A)	I	20
Transverse beam size (μm)	$\sigma_{x,y}$	655, 717
Longitudinal beam size (cm)	σ_z	3
Betatron function (m)	$\beta_{x,y}$	0.75, 0.89
Transverse Emittance ($\mu\text{m rad}$)	$\varepsilon_{x,y}$	57.5
Longitudinal Emittance ($\mu\text{eV s}$)	ε_l	0.23
Transverse tune	$\nu_{x,y}$	0.225, 0.230

2D Approach

The present work focuses on visualizing the negative tune shift the particles experience due to the space charge force, and the nonlinear resonance it could excite. For this purpose, the Frequency Map Analysis (FMA) was computed using the pre-existing Python library routine-NAFFlib. The color map represents the tune diffusion rate of each particle, following the behavior described by Eq. 4 [3].

$$\Delta = \log_{10} \sqrt{(\nu_{x1} - \nu_{x2})^2 + (\nu_{y1} - \nu_{y2})^2} \quad (4)$$

Numerical artifacts, such as horizontal and vertical lines, were observed in the tune diagrams of both the 2D and 2.5D

simulations, as shown in Fig. 1. Increasing the number of macroparticles by a factor of ten, significantly suppresses the horizontal and vertical tune bands, thereby confirming that the observed features were influenced by numerical noise arising from large fluctuations in beam size at each IP. To suppress these undesired effects, a *beam size freezing* technique was applied, to keep the beam size constant at each space charge IP.

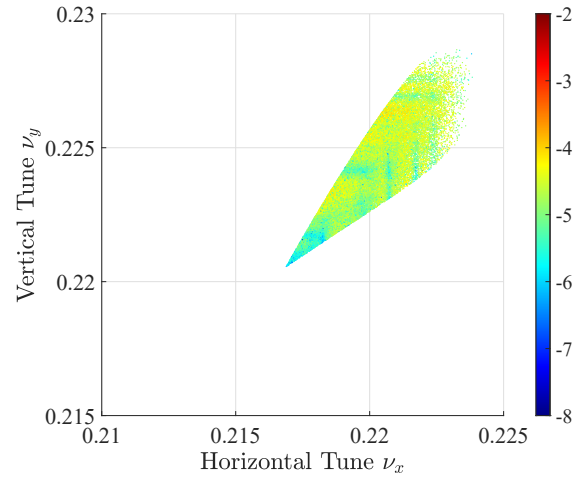


Figure 1: Tune footprint derived from the 2D model simulation. The high tune diffusion rate zones are caused by numerical noise.

The horizontal and vertical tune shift, in Fig. 2, measures approximately 0.01 and confirms the relation with the space charge strength in Eq. 5 [3, 4].

$$\Delta\nu_{x,y} \propto \frac{N \cdot r_0}{\gamma^3 \beta^2 \varepsilon_{x,y}} \quad (5)$$

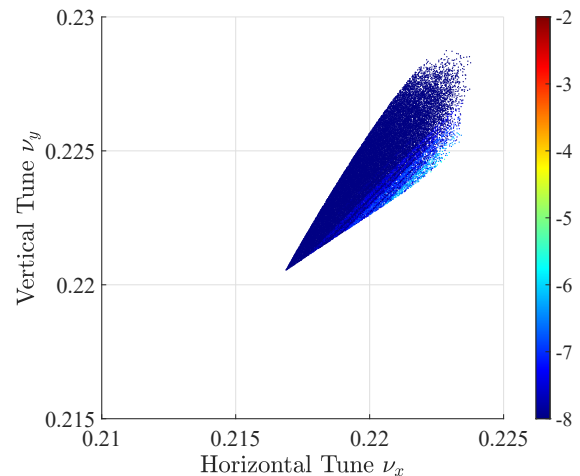


Figure 2: Tune footprint derived from the 2D model simulation, assuming constant beam size.

2.5D Approach

As previously mentioned, the 2.5D approximation incorporates the longitudinal component along which the charge is distributed. The RF field and the associated synchrotron motion of the particles significantly influence the dynamics of the bunched beam. As a result, the betatron frequency couples with the synchrotron tune, potentially leading to nonlinear resonances, as shown in Fig. 3, where the presence of the fifth order resonance is evident.

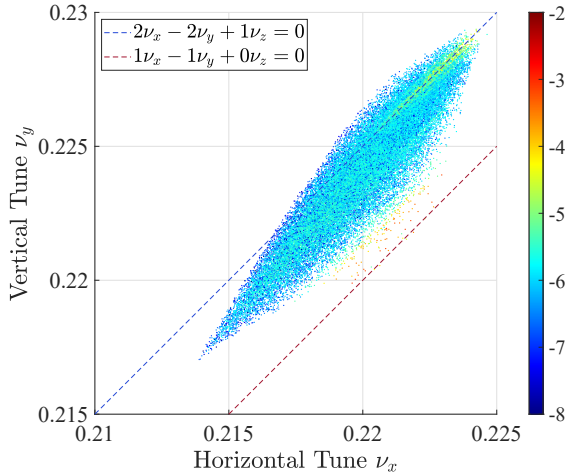


Figure 3: Tune footprint obtained from 2.5D approximation assuming constant beam size. The synchrotron tune is fixed at $\nu_z = 0.01$. Color indicates the logarithmic tune diffusion rate, with warmer colors representing stronger nonlinear behavior.

To highlight the strong interdependence between the transverse and longitudinal tunes, a series of simulations was performed, varying the synchrotron tune, ν_z . Particularly, the synchrotron tune was set at 0.005 to excite the third-order resonance illustrated in Fig. 4, as well as a weaker fifth-order resonance. Furthermore, both the tune spread and the area increase by approximately 10% relative to the 2D approach, indicating that the previous model may underestimate these effects. An especially noteworthy case occurs when the synchrotron tune is $\nu_z = 0.002$, with resonances being excited from the sixth to the ninth order (Fig. 5).

CONCLUSION

The present study demonstrates the limitations of the 2D approximation and emphasizes the importance of including longitudinal-transverse coupling effects. These couplings play a significant role in determining long-term beam stability in high-intensity machines such as colliders and hadron rings, where they can drive particles into resonance conditions, potentially leading to emittance growth or beam losses. Understanding and mitigating such effects is critical for ensuring beam stability and maximizing luminosity. In a more accurate model, the beam size is expected to evolve

under the influence of collective effects. As a consequence, the associated numerical errors will need to be smoothed with a different technique. Therefore, upcoming research will address the application of numerical techniques to suppress such noise.

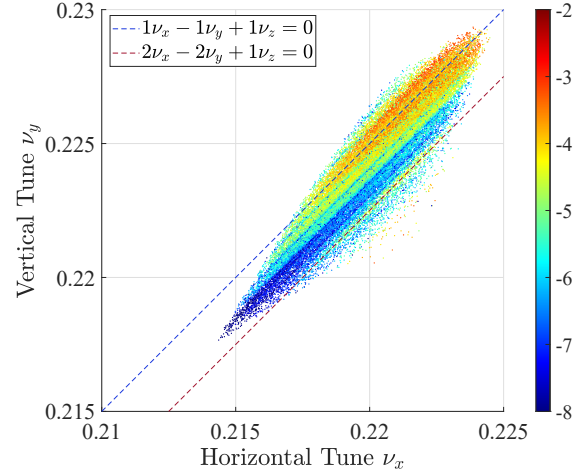


Figure 4: Tune footprint obtained from 2.5D approximation assuming constant beam size. The synchrotron tune is fixed at $\nu_z = 0.005$.

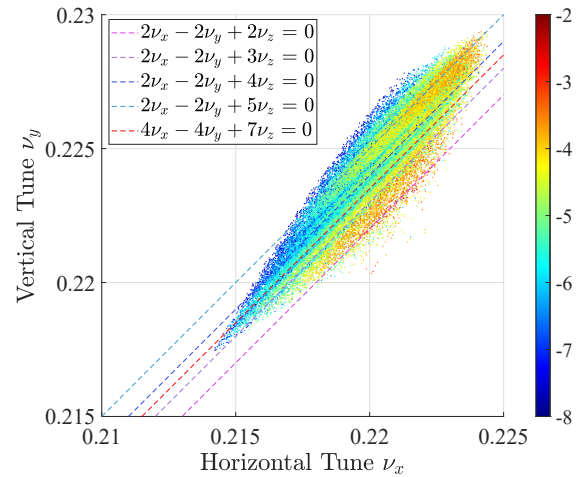


Figure 5: Tune footprint obtained from 2.5D approximation assuming constant beam size. The synchrotron tune is fixed at $\nu_z = 0.002$.

REFERENCES

- [1] J. Qiang, "Symplectic particle-in-cell model for space-charge beam dynamics simulation", *Phys. Rev. Accel. Beams*, vol. 21, no. 5, p. 054201, May 2018.
doi:10.1103/physrevaccelbeams.21.054201
- [2] M. Bassetti and G.A. Erskine, "Closed expression for the electrical field of a two-dimensional Gaussian charge", CERN, Geneva, Switzerland, Rep. CERN-ISR-TH-80-06, Mar. 1980.

- [3] J. Laskar, “Frequency analysis of a dynamical system”, *Celestial Mech. Dyn. Astron.*, vol. 56, no. 1–2, pp. 191–196, Mar. 1993. doi:10.1007/bf00699731
- [4] W. T. Weng, “Space charge effects—Tune shifts and resonances”, *AIP Conf. Proc.*, vol. 153, no. 1, pp. 348–389, Feb. 1987. doi:10.1063/1.36368

MONTE CARLO SIMULATION ANALYSIS FOR RADIATION DAMAGE ON GLIDCOP Al-15 CAUSED BY 17-20 MeV/u HEAVY IONS*

E. Fletcher^{1†}, T. Ginter¹, P. Hurh², T. Kanemura¹, S. Lidia¹, A.S. Plastun¹, E. Wakai¹

¹Facility for Rare Isotope Beams, East Lansing, MI, USA

²Fermi National Accelerator Laboratory, Batavia, IL, USA

Abstract

The Facility for Rare Isotope Beams heavy-ion SRF linear accelerator is designed to accelerate all ions up to Uranium to a maximum beam power of 400 kW. Several beam intercepting devices are essential to the successful operation and maintenance of the accelerator, including a low power charge selector (LPCS) made of copper CONTAINING 0.15% precipitated Aluminum Oxide by weight called Glidcop Al-15. As FRIB ramps up the primary beam power beyond the current 20 kW level, the charge selector must withstand ever increasing heat loads and higher radiation damage rates. Significant beam induced radiation damage—including deformation, (e.g., swelling and blistering with cracking) has already been observed on a recently removed LPCS. We also observed physical features up to about 5.5 mm wide which appear to be deeper than the projected range of any ions.

This paper presents the results of Monte Carlo simulations carried out using the Particle and Heavy Ion Transport code System (PHITS), quantifying the total damage dose caused by ²³⁸U from 2023-2024. Simulating an accurate irradiation history is essential to determining the scope of post irradiation examination (PIE) work. This paper will also present a PIE plan in detail.

INTRODUCTION

The Facility for Rare Isotope Beams (FRIB) linear accelerator (linac) uses a charge stripper to increase the mean charge state of an ion beam, therefore increasing the energy gain of the beam from post-stripper linac cavities. This also creates multiple charge states of the beam. While the FRIB linac can simultaneously accelerate multiple charge states within a $\Delta Q/Q$ of about $\pm 3\%$, it cannot accelerate them all. The low power charge selector [1] (LPCS), as shown in Fig. 1, is a set of moving jaws that act as slits to intercept the lowest intensity charge states that cannot be accelerated and ensure that high-intensity charge states are allowed to pass through a gap between the jaws to be accelerated. This beam interception causes radiation damage due to the displacement of lattice atoms, ion implantation and other irradiation effects such as transmutation. While the effects of radiation damage are observable on the LPCS, there is little data available to show how the combined effects of

different ion species and transmutation products affect damage mechanisms.

The best place to begin understanding the complex interplay between various radiation damage effects is by looking at the contributions of individual ion species, specifically the displacement damage measured in dpa that each species causes. This information can be used to localize regions of interest to perform PIE.

This paper intends to elucidate the process by which individual ion species are evaluated for their contributions to the displacement damage using ²³⁸U as an example and explain how this information will be used to inform future PIE work.



Figure 1: FRIB LPCS with visible radiation damage.

METHODOLOGY

Particle Current Calculations

To calculate the total displacement damage caused by ²³⁸U, we must first calculate the total number of particles that were intercepted by the LPCS. This must be converted from electrical current given by FRIB beam current monitors (BCMs). The conversion is given by:

$$I_p = \frac{I_{euA}}{Q * e} \quad (1)$$

where I_p is the particle current (particles per second or pps), I_{euA} is the charge current in electrical micro amperes, Q is the ionic charge state and e is the elementary charge. Since multiple charge states are intercepted, and each charge state only composes a fraction of the total intercepted beam, Eq. (1) becomes:

$$I_{pi} = \frac{I_{euAi}}{Q_i * e} = \frac{I_{euA} * f_i}{Q_i * e} \quad (2)$$

where f_i denotes the fraction of the contribution of a particular charge state Q_i to the intercepted beam current. Summing over the contribution of all intercepted charge states, we get:

*This material is based upon work supported by the U.S. Department of Energy, Office of Science, Office of Nuclear Physics and used resources of the Facility for Rare Isotope Beams (FRIB) Operations, which is a DOE Office of Science User Facility under Award Number DE-SC0023633 and Office of High Energy Physics, under Award Number DE-SC0018362.

†fletcher@frib.msu.edu

$$I_{p_{total}} = \frac{I_{euA_{total}}}{e} * \sum_i \frac{f_i}{q_i} \quad (3)$$

Measured beam current data was averaged in 6–8-hour intervals, depending on the duration of an experiment using the ^{238}U beam.

To find the total number of particles intercepted, which is necessary for the total dose calculation, simply apply Equation 3 to each 6–8-hour interval and multiply by the corresponding number of seconds in each interval. The total number of intercepted particles is the sum of the number of particles in each time interval or:

$$N_p = \sum_j I_{p_{totj}} * t_{intj} \quad (4)$$

where N_p is the total number of intercepted particles, j represents each 6-8 hour time interval, and t is in seconds.

DPA Calculations

To find the total dose delivered to the LPCS, we used the PHITS Monte Carlo code [2] to calculate the radiation damage caused by ^{238}U . A gaussian energy distribution was assumed for each charge state with a spread (σ) of 20 keV, and assuming cutoffs at $\pm 3\sigma$. However, given that the energy of each charge state is approximately the same (≈ 16.5 MeV/u), only one charge state study with PHITS is required to assess the displacement damage, as the effects of other charge states are assumed to be additive with lateral displacement from dispersion. Ten batches of 10^4 particles of the intercepted 68^+ charge state were used in the simulation for ^{238}U . Table 1 describes the relevant inputs for the PHITS simulation, including the beam energy, spot size in x (horizontal) and y (vertical), and the center position in x from the optical axis for the intercepted charge states seen in Fig. 2. The fractional contribution of each charge state is also included, as it is important in the context of Eq. (3) and the calculation to find the total dpa.

Table 1: Relevant Simulation Inputs for Intercepted Charge States of ^{238}U

Charge State	Fraction f_i	X rms (cm)	Y rms (cm)	Center Position X (cm)
68+	0.0038	0.087	0.604	-7.846
69+	0.0112	0.080	0.554	-6.718
70+	0.0343	0.073	0.497	-5.592
71+	0.1023	0.066	0.437	-4.469
72+	0.2376	0.060	0.379	-3.349
78+	0.4108	0.117	0.164	3.336
79+	0.1354	0.138	0.170	4.447
80+	0.0449	0.161	0.186	5.557
81+	0.0148	0.186	0.208	6.667
82+	0.0050	0.211	0.233	7.777

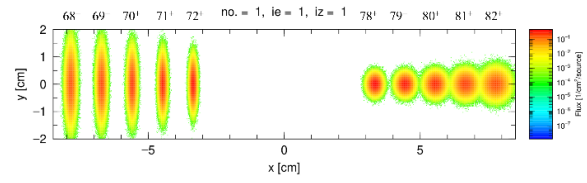


Figure 2: Intercepted charge states (top) of 17 MeV/u ^{238}U beam on the LPCS. The contours show particle flux normalized by the number of incident particles.

PHITS calculates the displacement damage rate in dpa/source, with the source being a singular particle. The displacement damage was calculated using the athermal recombination correction (arc-dpa), which corrects the standard Norgett-Robinson-Torrens dpa calculation's overestimation of the number of stable defects and underestimation of the amount of atomic mixing [3].

Once PHITS completes a simulation, the resulting dpa is output in a graph such as Fig. 3, and the peak dpa can be estimated. PHITS is also capable of calculating the dpa in the xz and yz planes, with z representing the depth of the LPCS. Since the intensity of the beam is highest in the center of the gaussian distribution, the total dpa calculation is based on the peak dpa in this region, as it is expected to be significantly larger than in the 2σ and 3σ regions of the distribution.

The resulting displacement damage rate is then multiplied by the result of Eq. (4) to find the total displacement damage.

RESULTS

Once Eq. (4) was applied to the ^{238}U current data from the years 2023-2024, the total number of particles intercepted is estimated to be 7.3×10^{16} . The PHITS simulation gave the resulting displacement damage rate along the beam axis, as summarized in the Fig. 3.

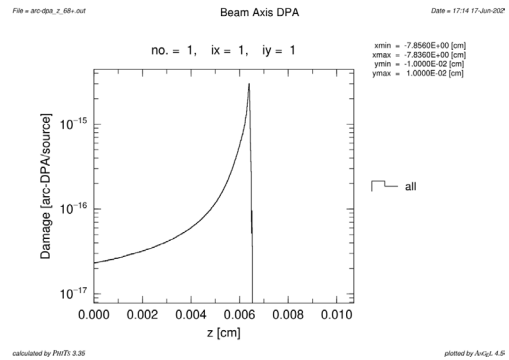


Figure 3: Arc-dpa along the beam axis near the Bragg peak.

PHITS can also calculate the displacement damage in the xz and yz planes, allowing us to approximate the dpa on the surface of the LPCS across the whole beam spot. However, the resolution is low, meaning that the error in the dpa approximation on the surface is higher than when calculating the dpa along the beam axis.

Additionally, PHITS can map the behavior of the beam, as seen in Fig. 4, allowing us to view how the beam and

secondary products such as electrons and neutrons behave as a function of depth.

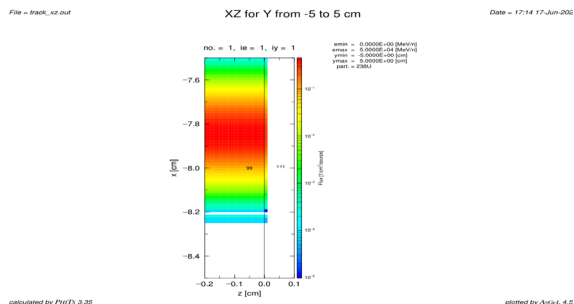


Figure 4: ^{238}U stopping behavior visualized in PHITS.

The estimated peak arc-dpa is 1.145×10^{-15} arc-dpa/source with a range of 0.0065 cm. Multiplying the peak arc-dpa result by the result of Eq. (4) gives us 85.5 arc-dpa in total damage caused by ^{238}U along the beam axis over the lifetime of the removed LPCS.

DISCUSSION

While this study is limited to one singular primary beam, similar studies can be conducted in the same manner for any primary beam used at FRIB. This will allow us to create a comprehensive irradiation history for the LPCS. Compiling such a comprehensive irradiation history will inform decisions regarding the scope and breadth of current and future PIE endeavours. This methodology can also be applied to other components in the FRIB BID infrastructure such as beam dumps.

While beyond the scope of this paper, these results imply that not only can we calculate the total displacement damage, but we can also use Eq. (2) to analyze the damage per charge state as well. This would allow us to create a map of the damage across the LPCS by ion species, allowing us to determine the impact of individual ion species on radiation damage to the LPCS and other BIDs in the FRIB infrastructure, further allowing us to narrow the scope of PIE work, focusing on specific areas of interest due to ion species, amount of displacement damage and the interplay between different ion species that overlapped in the same area.

PIE Planning and Execution

FRIB is currently planning on performing PIE on the removed LPCS. As mentioned previously, it would be impractical to perform PIE on the entire affected region of the LPCS. Thus, upon visual inspection, we chose a region of particular interest as seen in Fig. 5, which appears to have sustained the most significant amount of radiation damage. This damage was likely caused by the ^{48}Ca beam. For the lifetime of the LPCS, the linac could only accelerate the 20^+ charge state of ^{48}Ca , comprising 68% of the total intensity of the beam. The damage area corresponds to approximately where the 19^+ charge state would land and contained 30% of the beam intensity with approximately 500 W of power, the maximum power for which the LPCS is rated.

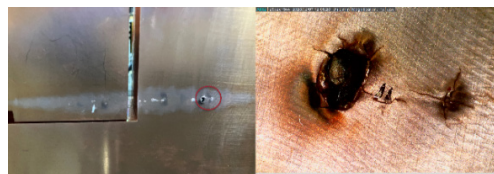


Figure 5: Damage observed on the LPCS jaw surface. The region circled in red is a zoomed in view of the region on which we intend to focus our PIE efforts.

High resolution photos of areas of high interest will be taken. A profilometer will then be used to scan the surface profile to identify areas of interest for microscopy work, and these areas will be sectioned. Once areas of interest are sectioned, SEM/EDS work will be done to find areas of high implanted ion concentration that could lead to more focused TEM work. Once optical and SEM microscopy work is complete, we will utilize nano-indentation to track the radiation hardening behavior of the material, which can help us with tracking ion diffusion into the material. Once significant areas of interest have been identified by optical microscopy and SEM, TEM imaging will be utilized to create cross-sectional images of samples. Additionally, the mechanism behind the discoloration across the LPCS as seen in Fig. 1 is unclear. Microscopy can help us determine the cause of the discoloration.

SUMMARY

Analysis of beam current data and PHITS Monte Carlo simulations allowed us to calculate the total peak displacement damage done along the beam axis by a ^{238}U beam over the lifetime of a recently removed LPCS. In addition, we were able to visualize the charge state distribution across the LPCS using PHITS and visualize the damage along the beam axis. The methods explored in this paper will allow us to perform a similar analysis for all FRIB primary beams and can be extended to any BID in the FRIB linac. Future work should explore the damage dependence on individual charge states and create comprehensive maps of the damage done by all primary beams for comparison to the observable damage on the LPCS. PIE will be performed on the LPCS to determine the interplay between various radiation damage mechanisms and a plan to do so is in effect. These simulations are the first step in correlating these effects to the displacement damage.

ACKNOWLEDGMENTS

The author would like to thank Dr. Ryoto Iwai for compiling the beam current data necessary for performing this analysis. This work was additionally supported by the Accelerator Science and Engineering Traineeship (ASET) at FRIB.

REFERENCES

- [1] A.S. Plastun *et al.*, “Advanced charge selector for stripped heavy ion beams”, in *Proc. IPAC’24*, Nashville, TN, USA, May 2024, pp. 1582-1585.
[doi:10.18429/JACoW-IPAC2024-TUPR70](https://doi.org/10.18429/JACoW-IPAC2024-TUPR70)
- [2] T. Sato *et al.*, “Recent improvements of the particle and heavy ion transport code system – PHITS version 3.33,” *J. Nucl. Sci. Technol.*, vol. 61, no. 1, pp. 127–135, Nov. 2023.
[doi:10.1080/00223131.2023.2275736](https://doi.org/10.1080/00223131.2023.2275736)
- [3] K. Nordlund *et al.*, “Improving atomic displacement and replacement calculations with physically realistic damage models,” *Nat. Commun.*, vol. 9, no. 1, p. 1084, Mar. 2018.
[doi:10.1038/s41467-018-03415-5](https://doi.org/10.1038/s41467-018-03415-5)

THERMAL-HYDRAULIC ANALYSIS OF A 20 kW BEAM POWER WATER-COOLED MINI-CHANNEL BEAM DUMP AT FACILITY FOR RARE ISOTOPE BEAM*

R. Quispe-Abad†, N. Bultman, T. Kanemura, S. Miller, M. Patil, M. Reaume, J. Song, Facility for Rare Isotope Beams, Michigan State University, East Lansing, MI, USA

Abstract

The Facility for Rare Isotope Beams (FRIB) is a high-power heavy-ion accelerator, completed in April 2022 [1], designed to accelerate heavy ions to energies exceeding 200 MeV per nucleon (MeV/u). These ions collide with a rotating graphite target, while the residual beam is absorbed by a water-cooled static beam dump positioned at a 6-degree angle to the beam path. The current beam dump consists of a machined C18150 copper alloy block, explosion-bonded to AL2219 alloy with precision-machined cooling grooves. Cooling water is supplied through 3D-printed Aluminum 6061 inlet and outlet components, facilitating heat dissipation from the beam stopper. This paper examines the thermal-hydraulic performance of the Mini-Channel Beam Dump (MCBD) under both nominal and off-nominal conditions. The MCBD is designed to handle operational beam power up to 20 kW, with planned optimizations to support a power ramp-up to 30 kW.

INTRODUCTION

This work presents the thermal-hydraulic analysis of a 20 kW beam power, water-cooled mini-channel beam dump. The analysis evaluates its performance under normal and off-normal operating conditions, establishing operational limits and guiding further optimizations. FRIB is primarily a nuclear physics research facility that produces rare isotope beams by striking a rotating target. Typically, the beam dump absorbs 75% of the power after the target, and its location is shown in Fig. 1. As FRIB follows a strategy of gradually increasing its beam power, the ultimate design power is 400 kW [2]. The first version of the beam dump had a 20-degree orientation with respect to the incoming beam, designed for a 1 kW primary beam power

on target [3]. With the ramp-up plan, the subsequent version of the beam dump had a 6-degree orientation for a 10 kW beam power [4]. Both early versions of the beam dump absorber were made of Aluminum 2219. The current version of the 20 kW beam dump in operation (Fig. 2) consists of a machined C18150 copper alloy block, explosion-bonded to an AL2219 alloy, with precision-machined cooling grooves measuring 2 mm × 7 mm (Fig. 3), and is analyzed in this work.

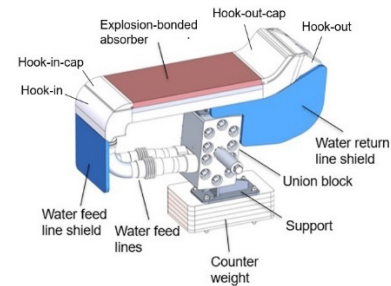


Figure 2: Mini-channel beam dump model (MCBD).

The bi-metal absorber enables higher power operation due to the improved thermal conductivity and strength of the absorber, while also preventing oxidation [4, 5].

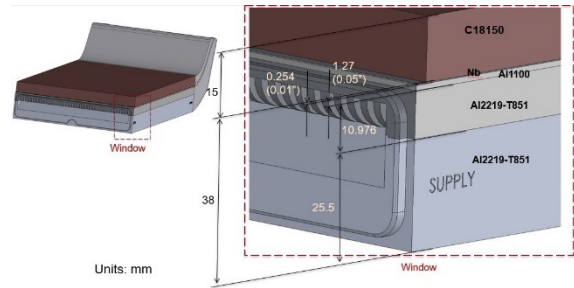


Figure 3: Mini-channel and some interstitial details.

THERMAL-HYDRAULIC ANALYSIS

Computational Fluid Dynamics (CFD) Model

A 3D SolidWorks® model is exported to Ansys Fluent® – Release 22.0, a commercial code based on the finite volume method [6]. The solid region of the absorber uses a structured (hexahedral) mesh, while areas with complex beam dump geometry are meshed using an unstructured grid. The structured mesh has a grid size of 0.75 mm, selected to appropriately capture thermal effects based on the size of a ²³⁸U beam (Table 1). The fluid region within the channels is also meshed using a structured grid. The first layer adjacent to the wall is 0.1 mm thick, with four additional layers included to accurately capture thermal and

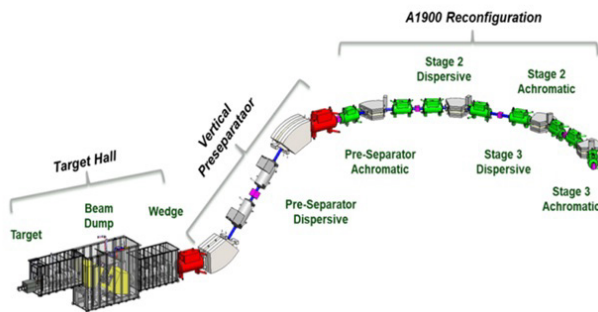


Figure 1: Beam dump location in the target hall [1].

* Work supported by the Department of Energy Contract DE-SC0023633

† quispeab@frib.msu.edu

viscous effects in the boundary layer (BL). The viscous model selected is the k- ω shear-stress transport (SST) RANS model [4]. The thermal-hydraulic simulation solves for the interactions between regions, including solid-to-solid conduction and solid-to-fluid convection.

Table 1: Gaussian Beam Parameters

σ_x [mm]	σ_y [mm]	Beam Power [kW]	Power Deposit [kW]	Depth [mm]
2.32	9.77	20	15	0.28

Hydraulic Analysis

According to the reference point location shown in Fig. 4, the fluid temperature is 28.6 °C, and the flow velocity is 8 m/s. A first grid height of 0.0019 mm is required to achieve a $y^+ \approx 1$ for resolving the viscous sublayer in the inner layer. However, this becomes computationally expensive. An additional algorithm in the k- ω SST RANS model in Ansys Fluent resolves the flow field near the wall region using semi-empirical formulas, known as *wall functions*, to bridge the viscosity-affected region between the wall and the fully turbulent region. In this simulation, the first grid height is 0.1 mm, corresponding to a $y^+ \approx 52$, which falls within the log-law region of the inner layer. The Prandtl number at this location is 5.67, indicating that the thermal boundary layer is thinner than the velocity boundary layer.

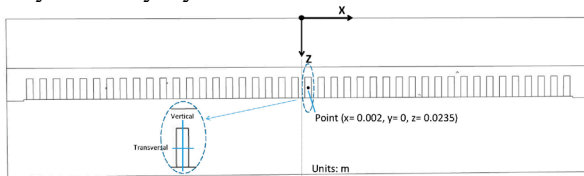


Figure 4: Sketch of cross-section at the center of the absorber.

CFD results confirm the expected boundary layer behavior. Along the transverse axis, as shown in Fig. 4, the velocity boundary layer (BL) thickness is approximately 0.9 mm (~99%), while the thermal BL thickness is about 0.3 mm (~96%), as shown in Fig. 5. Along the vertical axis, the upper wall is hotter than the lower wall, Fig. 6, resulting in different thermal BL behavior on each wall. The velocity BL thickness in this direction is approximately 2.2 mm (~99%), and the thermal BL thickness diffuses closer to the velocity BL thickness. The mesh resolution on the lower wall does not adequately capture the thermal BL thickness; however, this does not significantly affect the calculations, as most of the convective heat transfer occurs on the upper wall. The temperature on the lower wall is approximately 28.14 °C, which is similar to the fluid temperature at the device inlet, 28 °C.

From the analysis, the path-lines indicate that most of the pressure drop occurs within the mini-channels, with a total pressure drop of 13.8 psi from the inlet to the outlet. The average velocity magnitude is approximately 6.48 m/s, with the highest velocities occurring in the mini-channels.

The design requirement of water speed ≤ 4.0 m/s in the impingement areas at a maximum flow rate of 60 GPM is satisfied, as velocities exceeding 4 m/s are confined to the mini-channels, while the flow velocity remains below 4 m/s in the hook-in and hook-out ducts.

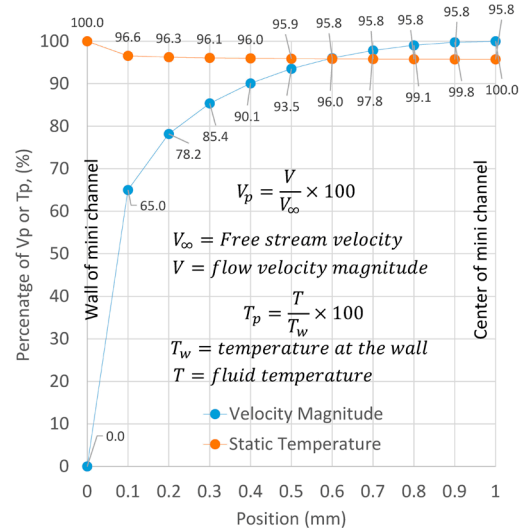


Figure 5: Plot of the change of magnitude velocity (%) and temperature (%) in the boundary layer in the X direction.

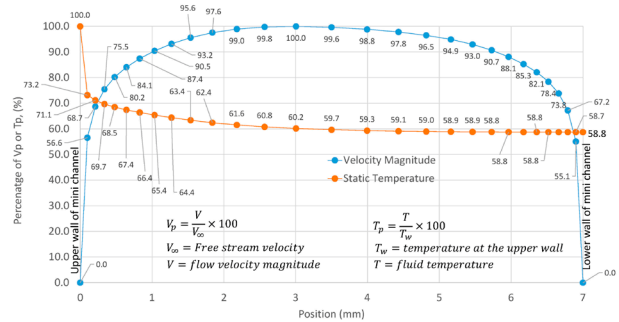


Figure 6: Plot of the change of magnitude velocity (%) and temperature (%) in the boundary layer in the Z direction.

Thermal Analysis

The imprint of the Gaussian beam produces a temperature contour that extends in the Y-direction due to the 6-degree inclination of the absorber relative to the incoming beam. The maximum temperature on the absorber is 245 °C, as shown in Fig. 7. The temperature distribution along the Z-direction at two locations ($X = 0, Y = 0$ and $X = 2$ mm, $Y = 0$) is shown in Fig. 8. In both cases, the temperature decreases from the top (absorber plate) to the bottom (back plate). The back plate does not exhibit any significant temperature change, while the largest temperature gradient ($\Delta T \approx 155$ °) occurs within the absorber, which is made of C18150 copper alloy. The average convection heat transfer coefficient (CHTC) in the channels is approximately 29,000 W/m²·K.

Off-normal Cases during Operation

The analysis of potential off-normal scenarios is essential to understand their effects on the beam dump performance and to determine appropriate remediation actions.

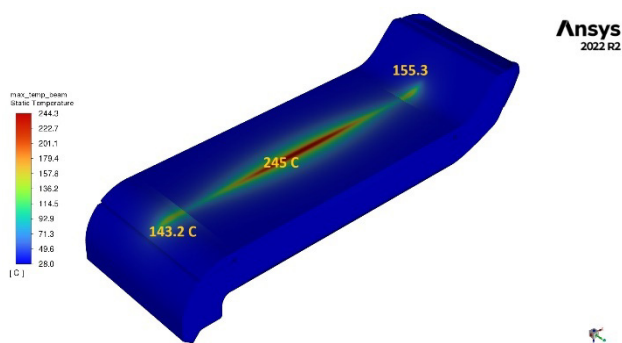
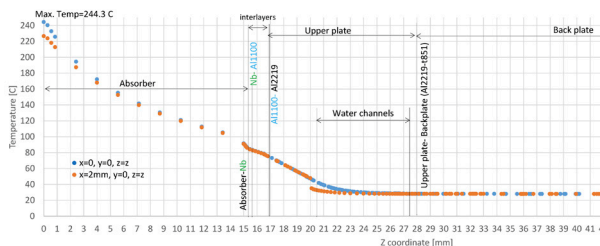


Figure 7: Temperature contours on the MCB.

Figure 8: Temperature distribution along the Z-axis at $X=0$, $Y=0$.

De-bonding in the interlayer (Niobium–Al1100) For power deposition centered in the C18150 absorber ($X = 0$ mm, $Y = 0$ mm, $Z = 0$ mm), a potential off-normal scenario assumes a local de-bonded area in the Nb–Al1100 interlayer, covering approximately 1% of the absorber plate surface. The maximum temperature on the absorber plate increases by 1.2%. The de-bonding introduces a temperature discontinuity across the interlayer due to the loss of thermal contact, preventing heat conduction in the affected region. As a result, the temperature in the niobium plate increases by 27.7% (from 87.1 °C to 111.2 °C).

Thermal conductivity (k) degradation due to high-energy ion irradiation This analysis assumes a reduction in thermal conductivity across the 0.85 mm thickness of the C18150 absorber plate. At each temperature point, k is reduced by 10%, 20%, or 30% from its original value. A 30% reduction in k leads to a 6.8% increase in the maximum temperature on the absorber plate. These temperature increases are localized, dissipating within approximately the first 2 mm, beyond which the temperature converges to the baseline case.

Mini-channel blockage Mini-channels are blocked sequentially, as indicated in Fig. 9, to assess the performance degradation. Blocking one mini-channel results in a temperature increase of 0.6%; blocking two channels increases it by 1.7%, and three channels by 3.1%.

Off-center beams in the X-direction (transversal) Figure 10 shows that a maximum temperature increase of 38.6% occurs when the ^{238}U beam is displaced 84 mm from the center. The maximum temperature on the absorber plate increases with larger off-center distances but begins to decrease as the beam approaches the plate's edge.

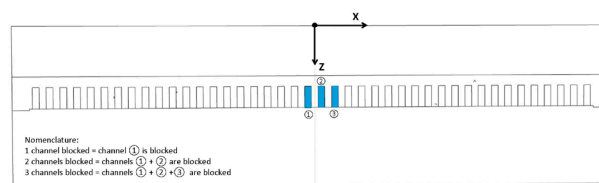
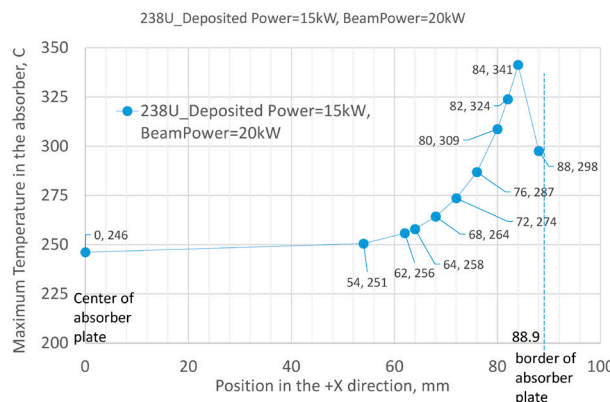


Figure 9: Identification of channels blocked and nomenclature for the number of channels blocked.

Figure 10: Plot of the temperature change when the ^{238}U beam changes position along the +X direction.

Off-center beams in the Y-direction (longitudinal)

The maximum temperature on the absorber plate remains largely unchanged; however, beam displacement in the Y-direction significantly affects other components. For instance, when the beam is positioned at $Y = 50$ mm, the maximum temperature on the hook-out-cap increases by 124.1% compared to the baseline at $Y = 0$ mm, due to increased power deposition in that region.

Beam Dump Optimization

The thermal-hydraulic analysis assumed perfect thermal contact between the hook-caps and hook parts, respectively, see Fig. 2. In the manufacturing process, plug welds were used to achieve this ideal contact condition. However, the process introduced additional residual stresses from welding heat, which led to distortion and weld cracking [2]. Future versions of the optimized beam dump will be fabricated as a single 3D-printed component, eliminating the need for plug welds. Additional improvements include extending the absorber length to accommodate higher power levels, thereby reducing the power density and maximum temperatures on the hook-cap components.

CONCLUSION

A discussion on the hydraulic and thermal analysis of a beam dump under irradiation from a ^{238}U beam at 20 kW beam power was presented, covering both normal and potential off-normal operating scenarios.

REFERENCES

- [1] J. Wei *et al.*, “FRIB transition to user operations, power ramp up, and upgrade perspectives”, in *Proc. SRF'23*,

Grand Rapids, MI, USA, Jun. 2023, pp. 1-8.

doi:10.18429/JACoW-SRF2023-MOIAA01

- [2] S. Miller *et al.*, “Optimization of a mini-channel beam dump for FRIB operation”, presented at HIAT25, East Lansing, MI, Jun. 2025, paper TUP01, this conference.
- [3] M. Portillo *et al.*, “Commissioning of the Advanced Rare Isotope Separator ARIS at FRIB”, *Nucl. Instrum. Methods Phys. Res., Sect. B*, vol. 540, pp. 151–157, Jul. 2023.
doi:10.1016/j.nimb.2023.04.025
- [4] R. Quispe-Abad *et al.*, “Thermal-fluid analysis and operation of a low power water-cooled tilted beam dump at Facility for Rare Isotope Beams”, in *Proc. IPAC'24*, Nashville, TN, USA, May 2024, pp. 3823-3826.
doi:10.18429/JACoW-IPAC2024-THPS40
- [5] J. Song *et al.*, “Design and experimental thermal validation of the mini-channel beam dump for FRIB”, presented at HIAT25, East Lansing, MI, Jun. 2025, paper TUP04, this conference.
- [6] Website of ANSYS, Inc., <http://www.ansys.com/>

CONTROL OF MICROPHONICS FOR A SUPERCONDUCTING RADIO-FREQUENCY PHOTO-INJECTOR CRYOMODULE*

K. M. Villafania^{1,†}, J. Brown¹, W. Chang, S. Kim, T. Xu¹

Facility for Rare Isotope Beams, Michigan State University, East Lansing, MI, USA

¹also at Michigan State University Physics and Astronomy Department, East Lansing, MI, USA

Abstract

A superconducting radio-frequency photo-injector cryomodule is being developed for the high-energy upgrade of the Linac Coherent Light Source (LCLS-II-HE). This effort is a collaboration between the Facility for Rare Isotope Beams at Michigan State University (MSU), Argonne National Laboratory, Helmholtz-Zentrum Dresden-Rossendorf, and SLAC National Accelerator Laboratory. The cryomodule features a 185.7 MHz superconducting quarter-wave resonator (QWR) designed to operate with an RF electric field of 30 MV/m at the photo-cathode. Mechanical vibrations must be controlled for operation with stable amplitude and phase. The first prototype cryomodule was cold-tested at MSU with a QWR, fundamental power coupler, tuner, and cathode stalk. In the first high-power RF cold test, we observed microphonics that made it difficult to control the RF phase at high gradient. The cryogenic circuit was identified as a likely culprit. This paper presents our studies of microphonics during the cryomodule cold test and follow-up investigations at room temperature. Our findings provided valuable feedback for modifications to the cryogenic circuit and a successful second cold test of the cryomodule.

INTRODUCTION

The LCLS-II high energy (HE) upgrade for SLAC adds 23 superconducting cryomodules which will increase the beam energy from 4 GeV to 8 GeV [1]. In addition to these 23 cryomodules, there is consideration of a Low Emittance Injector (LEI) that is parallel to the existing electron source [2]. The addition of this SRF electron source can improve the photon energy from 12.8 keV to 20 keV, which would enable studying dynamics on the atomic scale [3]. This LEI features a 185.7 MHz superconducting quarter-wave resonator (QWR). The cold mass of the cryomodule consisting of the cavity and its ancillary components is shown in Fig. 1. Table 1 has operational parameters of the cryomodule [4].

Constant cavity amplitude and phase is critical to providing uniform acceleration and maintaining accelerator synchronicity. In the case of light sources, this synchronicity is essential to producing high quality, coherent x-rays. Ambient vibrations from cryomodule systems and/or external sources can result in a change in cavity resonant frequency (microphonics), leading to amplitude and phase mismatch without feedback systems.

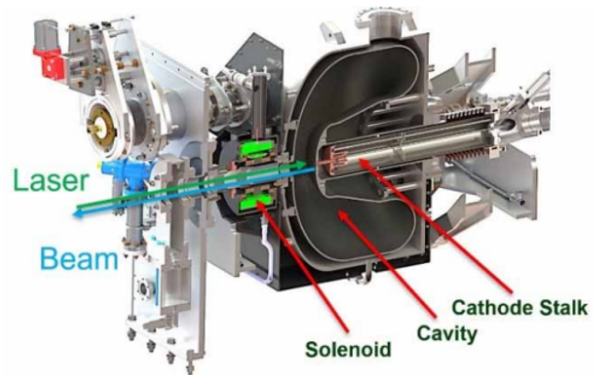


Figure 1: Model of cold mass in cryomodule [4].

Table 1: SRF-PI Cryomodule Performance Parameters [4]

Parameter	Units	Value
Operating Temperature	K	4.2
Cavity Frequency at 4.2 K, 1 bar	MHz	185.7
Cathode Gradient (Nominal/Maximum Operating)	MV/m	>30/35
Integrated E_z Field at 30 MV/m Gradient	MV	>1.6
Captured Dark Current at 30 MV/m Gradient	nA	<10
Cavity Q_0		$>1 \times 10^9$
RF Coupler Q_{ext}^1		10^7
Static Heat Load at 4.5 K	W	<25

¹SLAC Design Values

Mechanical tuners can provide countermeasures to slow detuning effects from variations in bath pressure and temperature or the Lorentz force detuning effect [5]. However, these tuners cannot account for fast changes in cavity resonant frequency. To make up for this, feedback systems for cavity amplitude and phase are implemented into the low-level RF controllers. These control loops do not tune the cavity; they merely provide more power to keep constant cavity amplitude and phase.

FIRST CRYOMODULE TEST

The first cryomodule test was with the QWR without cathode port, fundamental power coupler (FPC), and cathode stalk. During the test, 30 MV/m gradient was successfully reached but relatively strong microphonics were observed; see Fig. 2. The microphonics during testing made it difficult to close the RF phase loop at high accelerating gradient.

* This material is based upon work supported by the Department of Energy Contract DE-AC02-76SF00515 and DE-SC0018362.

[†] villafan@frib.msu.edu

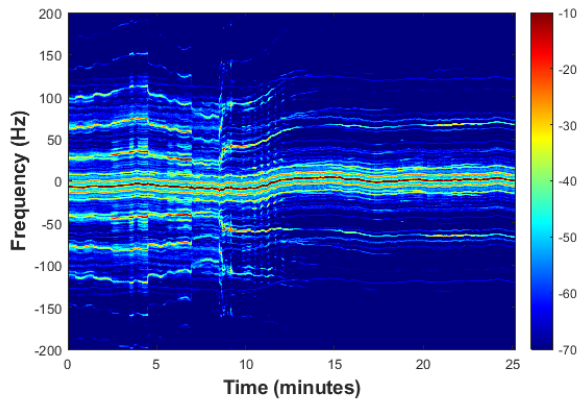


Figure 2: Spectrogram of RF sidebands during first cryomodule test. Accelerating gradient of 30 MV/m.

Joule-Thompson Valve Manipulation

During this first test, it was observed that the RF sideband amplitude and frequency varied with position of the Joule-Thompson valve (JT valve). There was significant reduction in microphonics when this valve was completely shut; see Fig. 3. The JT valve is located in the 4 K cryogenic circuit which supplies liquid helium to the cavity, so it is plausible that a component in this circuit contributed to the microphonics.

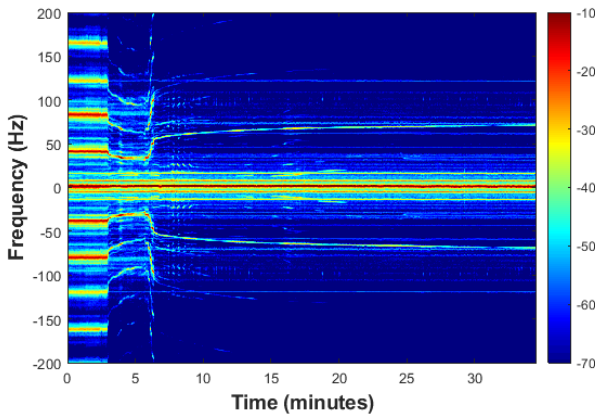


Figure 3: Spectrogram of RF sidebands while closing JT Valve. As the JT valve is closed, the RF sideband amplitudes decreased.

VIBRATION SURVEY

A vibration survey was conducted during the cold test to help diagnose the source of the microphonics. There were 9 accelerometers placed around the outside of the cryomodule. The vibration survey revealed that frequencies in the cavity signal matched frequencies found from the cryogenic piping as well as the FPC. It was concluded that in combination with the information from manipulating the JT valve position, the possible sources of the microphonics were coming from

the 4K cryogenic circuit that supplies liquid helium to the cavity or the excitation of an FPC mechanical mode. Further investigation at room temperature was conducted for the FPC, and a cryomodule rework was done to address potential root cause in 4K circuit.

FUNDAMENTAL POWER COUPLER VIBRATIONAL MODE INVESTIGATION

One possible cause for the strong microphonics was the mechanical modes of the FPC or other ancillary systems. During the cryomodule rework period, access to the FPC and tuner was possible. 6 accelerometers were placed on the FPC structure and 1 on the backside of the cavity near the cathode stalk. This was an effort to determine the mechanical modes of the structures as well as the impact these modes had to the phase modulation of the RF. In order to find the mechanical modes of these structures, the piezo stack in the tuner was used to shake the cavity + FPC structure. The frequency range of 50 Hz to 250 Hz was swept; see Fig. 4.

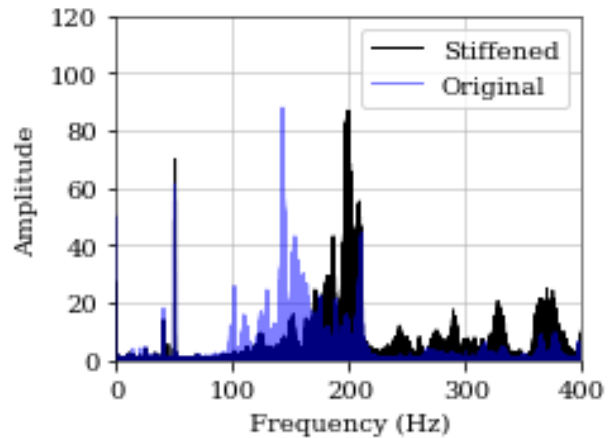


Figure 4: Frequency spectrum of mechanical vibration due to excitation of FPC flange with the piezo stack. Comparison between original FPC and stiffened FPC.

To see if the mechanical modes of the FPC structure were a large contribution to the phase modulation of RF, the FPC was stiffened by placing 3 blocks in between the window flanges to allow less horizontal movement. These stiffeners resulted in the frequencies of the FPC structure to shift upward. While the frequencies of the structure shifted, the RF sidebands frequency and amplitude did not change significantly; see Fig. 5. This allowed the mechanical modes of the FPC and other structures to be ruled out as the source of the microphonics.

CRYOMODULE MODIFICATIONS

The source of vibration has been clearly identified as originating from the 4K cryogenic circuit inside the cryomodule, based on observation and measurement. Two possible causes within this circuit have been identified. First, the SRF gun

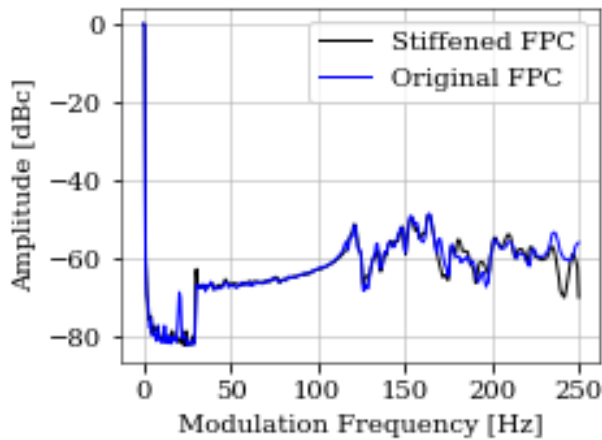


Figure 5: Integrated frequency spectrum of RF sidebands due to excitation of FPC flange with piezo. Comparison between original FPC and stiffened FPC.

module is relatively small, resulting in a low heat load and consequently a low 4K mass flow requirement. The long cryo-distribution line from the helium refrigerator has a sensible heat load comparable to the 4K load of the module. This leads to significant flashing through the JT valve in the module, contributing to the excessive vibration. Second, the initial JT valve chosen is a cryogenic valve with a 400 mm stem. This length was chosen to balance stiffness and heat load without requiring additional support structures. However, the natural frequency of the valve is 50.4 Hz, which may be contributing to the vibration.

Rework has been carried out to mitigate the possible root causes, as no sufficient diagnostic tool was available to pinpoint the exact source. The following changes have been implemented: Additional heat exchange piping was installed in the header to reduce flashing caused by sensible heat from the cryo-distribution line. The cooling of the alignment rail was moved to downstream of the supply valve, instead of upstream. A 600 mm stem cryogenic control valve was selected to replace the existing valve. The lower end of the new valve stem includes a convection break feature to reduce thermal acoustic oscillation along the stem. A 4" OD tube was added as a stiffening support at the constraint midpoint of the valve to increase the natural frequency above 200 Hz.

SECOND CRYOMODULE TEST

Following the conclusion of the cryomodule rework, a second cryomodule test was conducted. In this second test, a significant reduction in microphonics was observed; see Fig. 6. A comparison of the RF sidebands in the first test and second test can be seen in Fig. 7. The reduction of microphonics allowed for successful control of the RF phase at high gradient.

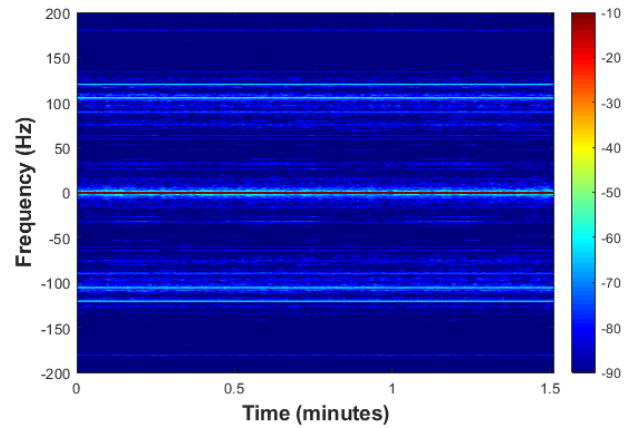


Figure 6: Spectrogram of RF sidebands during second cryomodule test. Operating at 30 MV/m with minimal microphonics.

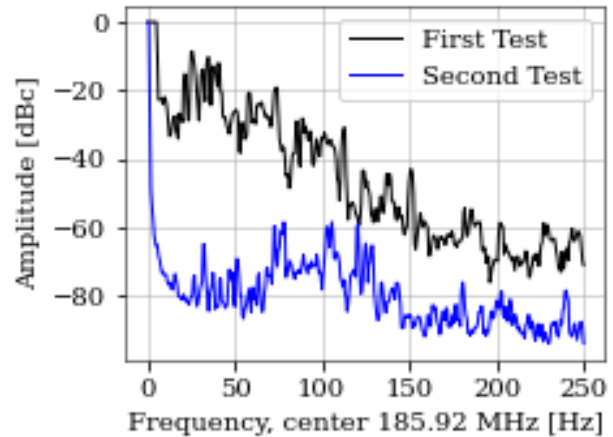


Figure 7: Integrated spectrum of RF sidebands from second cryomodule test compared with first cryomodule test.

CONCLUSION

During the first cryomodule test, there were significant microphonics that affected the ability to control RF phase. Possible sources of vibration in the 4K cryogenics circuit were addressed in a cryomodule rework, and the investigation into FPC vibrational modes concluded that there were no mechanical modes significantly contributing to the microphonics. This effort resulted in a successful second cryomodule test with a significant reduction in microphonics, enabling the cavity amplitude and phase to be locked within specifications.

REFERENCES

- [1] D. A. White, M. Checchin, D. Gonnella, J. Hogan, J. T. Maniscalco, and R. D. Porter, "Cryomodule Storage for LCLS-II HE", in *Proc. SRF'23*, Grand Rapids, MI, USA, Jun. 2023, pp. 282–285. doi: 10.18429/JACoW-SRF2023-MOPMB074
- [2] F. Ji *et al.*, "Beam Dynamics Studies on a Low Emittance Injector for LCLS-II-HE", in *Proc. NAPAC'22*, Albuquerque,

NM, USA, Aug. 2022, pp. 619–622.

doi:10.18429/JACoW-NAPAC2022-WEPA02

- [3] R. W. Schoenlein *et al.*, “LCLS-II High Energy (LCLS-II-HE): a transformative X-ray laser for science”, SLAC National Accelerator Laboratory, Menlo Park, CA, USA, Rep. SLAC-R-1143, 2016.
- [4] S. J. Miller *et al.*, “Status of the SLAC/MSU SRF Gun Development Project”, in *Proc. SRF’23*, Grand Rapids, MI, USA, Jun. 2023, pp. 1003–1010.
doi:10.18429/JACoW-SRF2023-FRIBA07
- [5] C. Contreras-Martinez *et al.*, “Validation of the 650 MHz SRF Cavity Tuner for PIP-II at 2 K”, in *Proc. SRF’21*, East Lansing, MI, USA, Jun.-Jul. 2021, pp. 151–154.
doi:10.18429/JACoW-SRF2021-SUPTEV013

DESIGN AND FABRICATION OF FRIB NORMAL CONDUCTING CAVITIES*

X. Rao[†], N. Bultman, S. Miller, P. Ostroumov, A. Plastun

Facility for Rare Isotope Beams, Michigan State University, East Lansing, MI, USA

Abstract

At FRIB, five unique designs of normal conducting cavities were developed for a 40.25-MHz Multi-Harmonic buncher (MHB), 80.5-MHz quarter-wave cavity MEBT bunchers, 161-MHz H-type cavity bunchers, 322-MHz H-type bunchers, and a quarter-wave 161-MHz buncher for a ReAccelerator (ReA). The paper will cover the main parameters for each type of bunchers, their design/fabrication, cooling design, RF contact design/effectiveness, tuning process, brazing design and fabrication challenges, coupler design, copper-to-stainless steel transitions, etc. The operation status of these bunchers will also be discussed.

INTRODUCTION

The Facility for Rare Isotope Beams (FRIB) started user operation in May 2022 after ~10 years of project design and construction. FRIB since then has been used for scientific experiments for ~3 years successfully [1, 2], with recent achievement of 20 kW Uranium-238 beam on target, which is currently work record [3].

Eight normal conducting cavities with 5 unique designs are under operation along FRIB beamlines, primarily located within the Front End and Folding Segment 1 regions. Six cavities are under operations, and two more are planned summer of 2026.

Figure 1 shows the location of these normal conducting copper cavities: each type and locations.

Normal conducting cavities are made of high-purity copper using high-temperature furnace brazing. They are equipped with motorized tuners for real-time frequency control. An efficient water cooling is provided for CW operation. We have developed and applied a multi-step brazing technique to achieve high dimensional accuracy, reliable RF contacts, and accommodate large stainless steel-to-copper joints.

Superconducting cavities are the primary choice for acceleration because of their distinct advantages. Normal conducting cavities can still be beneficial due to their distinct characteristics and benefits depending on the application:

- Simpler Construction and Infrastructure
 - No cryogenics required
 - If far from other cryogenics devices
- Compact Size: Suitable for Front End

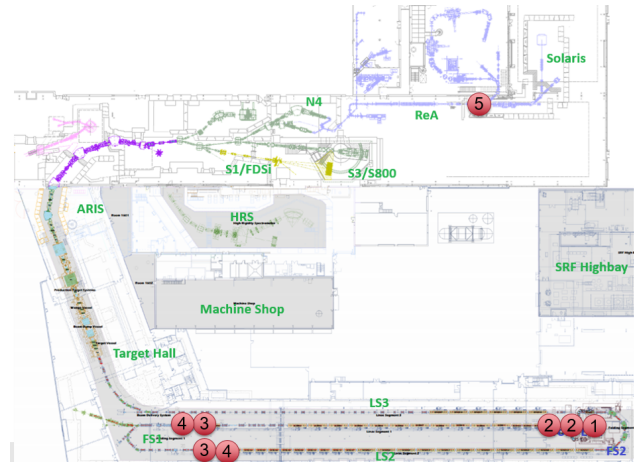


Figure 1: Layout of FRIB Normal Conducting Cavities. Mark 1: MHB at Front End; Mark 2: MEBT Buncher (X2) also at Front End; Mark 3: IH Buncher (X2) at Folding Segment 1 (FS1); Mark 4: 2H Buncher (X2) also at FS1; Mark 5: ReA Buncher.

- Better Protected against Intended or Un-intended Beam Loss
 - Less sensitive to mechanical vibrations
- Lower Cost
 - Drawing count is fewer for lower design cost
 - Fabrication generally quicker
 - Fabrication also generally less expensive
- Quicker Testing and Commissioning
 - Faster testing and conditioning cycles allow for quicker deployment and troubleshooting
- More Potential for RF Power Increase
 - Easy target to be requested for higher RF power
- Benefits for low beta, low duty cycle machine or at low frequency

DESIGN PARAMETERS

Table 1 shows major design parameters for four types of normal conducting cavities, including operating frequency, geometrical beta, aperture diameter, resonator diameter, calculated Q factor, vacuum level, and each cavity's max RF power.

For MHB, model frequencies are 40.25, 80.5 and 120.75 MHz, with total power for MHB is up to 100 Watts [4]. MHB has 3 couplers and 3 tuners. Differences to other cavities are that MHB cavity is on air side, with ceramic break as vacuum interface. Q values measured for MHB are 515, 325 and 244 for the three harmonic. The MHB buncher was manufactured, assembled, tested, installed and commissioned.

* This material is based upon work supported by the U.S. Department of Energy, Office of Science, Office of Nuclear Physics and used resources of the Facility for Rare Isotope Beams (FRIB) Operations, which is a DOE Office of Science User Facility under Award Number DE-SC0023633.

[†] rao@frib.msu.edu

Table 1: Main Parameters of FRIB MEBT/IH/2H/ReA Normal Conducting Cavities

Parameter		Units	MEBT	IH	2H	ReA
Frequency	f	MHz	80.5	161.0	322	161.0
Geometrical β	β_G	-	0.0328	0.185	0.186	0.1
Aperture diameter	$2a$	mm	30	36	36	30
Resonator Dia.	D	m	0.20	0.49	0.24	0.30
Q-factor	Q	-	7300	15620	13037	12855
Tuning Range		MHz	1	1.5	1.8	1.5
Vacuum Level		Torr	10^{-8}	10^{-8}	10^{-8}	10^{-8}
RF Power		kW	2.5	30	4.6	2.7

Tuning of the buncher showed that the two resonators are well decoupled making tuning of the modes easier.

Operation showed that the buncher is able to reach the desirable electrode voltage with available RF power and is stable under a high RF power load, as well as mechanical disturbances.

MEBT Buncher and ReA Buncher

MEBT buncher and ReA buncher are similar type, quarter-wave cavity with center drift and beam ports drift tubes forming 2 gaps, with one motorized tuner, and one fixed tuner. There is mesh at bottom to protect vacuum pump. Cooling to center drift tube through a deep-drilled hole (~900 mm).

Main differences between these two types are that MEBT buncher has 5 radially brazed circular cooling channels, with each ID on the cooling rings smaller from vertical up. And ReA buncher has 4 side vertically brazed cooling plates (cooling of resonator main body also for IH bunchers and 2H bunchers).

IH Buncher and 2H Buncher

IH buncher and 2H buncher are similar Inter-digital H-Mode (IH) drift tube type radio frequency (RF) resonant structure, shown in Fig. 2. Vertical Copper cylindrical resonator with a number of drift tubes to form multiple gaps, so called Multi-Gap Buncher, MGB (7 gaps for IH cavity; 4 gaps for 2H cavity).

2H cavity is needed to eliminate LS2 loss by linearizing the effective voltage of IH Buncher [5]. Each 2H cavity is right downstream of IH cavity.

As operating frequency for 2H cavity is higher, 2H resonator is smaller in dimensions, and at the same time has higher sensitivities due to dimension errors.

Cooling Design

Multi-physics analysis is done to get power density to different heating area, then to optimize cooling design, with investigation on deformation, stress as well frequency change due to temperature increase of the cavity and center stem is conducted. A unique feature for drift tube design is Helix like cooling channel design on center drift tube for max cooling capacity.

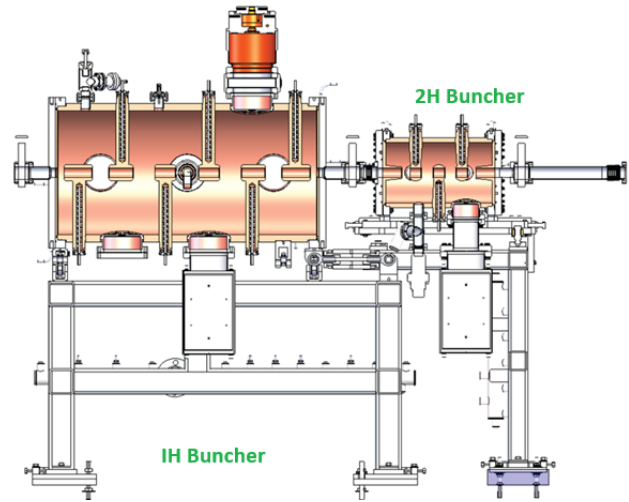


Figure 2: Cross Section View of IH Buncher (left) and 2H buncher (right).

RF Contact

Three types of RF contact are used between non-continuous Copper surfaces: canted coil spring, RF fingers and flapper with C seal. All three types works well, with different applications for each type.

FABRICATION

Overall strategy for FRIB normal conducting cavity fabrication is to locate a qualified vendor with vertical integration of major fabrication processes and be responsible for final product, with capacity to do field tuning as well.

Risk involving brazing is high and many factors can lead to not leak tight after brazing: low quality plating; dimension out of tolerance; improper brazing design; missing brazing alloy, inaccurate over temperature, etc. As for one overall brazement, close to 100 brazing joints need to be leak tight at once.

To help vendor with better understanding dimensional error's impact to the cavity performance, a table of tolerances based on each value's sensitivity is provided to vendor. This also help the cost to be reasonable.

Material

Major components shall be Oxygen Free High Conductivity C101.2 (ASTM F68-10) or equivalent. It is preferred that fabrication vendor to buy the material, and with three material checks (material vendor, fabrication vendor, as well as FRIB). Material from Asia, Europe and US were both used and worked out fine.

End wall functions as both vacuum interface, and RF contact and both functions are critical. Different vacuum seal were used: O ring, Conflat, Delta seal. Normally Stainless Steel portion provides vacuum interface and Copper portion functions as RF contact. Both bi-metal material and brazing are used to form joint in between Stainless Steel portion and Copper portion. Both method work fine (bi-metal may not be available in some markets) and cost/risk for bi-metal is slight lower.

Brazing

As a large brazement has many brazing joints what need to be sealed at the same time, it is beneficial to divide brazing into multiple steps. Benefits includes reduce final number of brazing joints and lower brazing risk, able to check each brazing step, allows use of brazing alloys with descending melting points, and greater flexibility in manufacturing work flow.

Different vendors seem to have different preference related to brazing between circular surfaces or flat surfaces. Both have high success rate with good Q/A process.

Due to planned multi-step brazing, or unexpected repair, a Copper structure may be brazed more than one time. FRIB experience shows max of 4 brazing cycles. There can be risks for multiple brazing cycles: gain size growth with each brazing; each brazing cycle functions as annealing process, and material becomes softer each time; thermal cycling at this high temperature may cause cumulative stress relief and distortion; if brazing oven temperature control is off, earlier joints may experience creep of diffusion, which will reduce joint strength.

Brazing joints between Copper and Copper have much higher success rate than between Copper and Stainless Steel, especially at relatively large dimension. FRIB experiences shows 67% success rate at brazing of Stainless Steel and Copper at 0.5 meter diameter. For the failed brazing resonator, re-brazing doesn't solve the problem. This issue was mitigated by establishing a different vacuum interface resolved the leak issue.

To protect Cryomodule and Superconducting Magnets, it is good practices to avoid water-to-vacuum brazing joints. One way is to move the joints on the airside (e.g. center stem/tuner cooling doesn't have interface to vacuum, and cavity body cooling or end wall cooling from outside, also no interface to vacuum). Another way is to add additional brazing joints, such that one joint is air-to vacuum, and the other joint is air-to water). Couple is only device that can't avoid water-to-vacuum brazing joint.

Cleaning

Cleaning surfaces prior to brazing are key to ensure strong, void-free joints and prevent contamination, with initial mechanical cleaning, degreasing and organic removal, and acid cleaning in ultrasonic bath, rinse and dry.

Cavity right after brazing is as clean as it can get. Machining the cavity after brazing should be avoided. It is a good practice to apply clear paint on outer surface right after leak checking, for cosmetic purpose only and will not impact functionality.

Ultrasonic cleaning was applied to IH buncher once. Results are mixed: Q value increased to higher than calculation, but oxidation happened quickly after cleaning shown in Fig. 3.

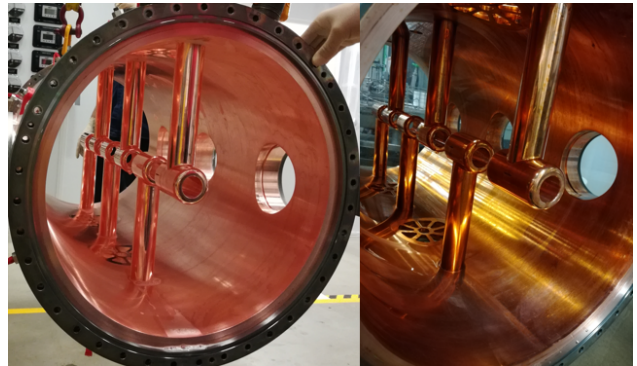


Figure 3: IH buncher cavity right after ultrasonic bath (left), and after another 10 minutes (right).

TUNING PROCESS

A device for each cavity is designed to have extra material to cut during final tuning process, usually fixed tuners, also a plug threaded at bottom of long center stem.

During final tuning, FRIB representative is present at vendor site to witness leak checking (with cavity inside a plastic bag with no leak for at least 15 minutes), and frequency tuning (tuning range by motorized tuners, Q factor value measurement with at least 80% of calculated Q value as target). Usually three steps of tuning are done to cut different length of the tuning device. Normally the intended cut length and actual cut length is within 1 mm, with consideration of vacuum, gravity and ambient temperature.

OPERATIONAL STATUS

The installed normal conducting cavities support FRIB facility beam operation during last few years. There are couple of minor issues during installation, and improvements have been implemented in next device design. These devices have caused no downtime.

AIP project was completed last year to upgrade IH buncher from 18 kW to 30 kW [6]. The upgrade is on RF system only and no changes to cavity side (which shows the advantage of such normal conducting cavity).

Critical spare is identified (IH buncher assembly, motorized tuner assembly, RF contact parts, coupler, motors, etc.) Periodical maintenance is also scheduled to reduce mean time between down.

SUMMARY

This paper presents an overview of the normal-conducting cavities employed at FRIB, including key design parameters, functional characteristics, and principal features of the MHB, MEBT buncher, IH buncher, 2H buncher, and ReA buncher. The discussion also includes insights into their fabrication processes, as well as operational performance and experience gained during commissioning and routine operation.

REFERENCES

- [1] J. Wei *et al.*, “FRIB Operations: First Three Years”, presented at HIAT’25, East Lansing, MI, Jun. 2025, paper MOP01, this conference.
- [2] J. Wei *et al.*, “FRIB Transition to User Operations, Power Ramp Up, and Upgrade Perspectives”, in *Proc. SRF’23*, Grand Rapids, MI, USA, Jun. 2023, pp. 1–8.
doi:10.18429/JACoW-SRF2023-M0IAA01
- [3] P. N. Ostroumov *et al.*, “Acceleration of uranium beam to record power of 10.4 kW and observation of new isotopes at Facility for Rare Isotope Beams”, *Phys. Rev. Accel. Beams*, vol. 27, no. 6, p. 060101, Aug. 2024.
doi:10.1103/physrevaccelbeams.27.060101
- [4] E. Pozdeyev, J. Brandon, N. Bultman, X. Rao, R. York, and Q. Zhao, “Report on Design, Development, and Characterization of a Coaxial Resonator Based Single-gap Gridless Multiharmonic Buncher”, *Office of Scientific and Technical Information (OSTI)*, Feb. 2013. doi:10.2172/1073065
- [5] A. Gonzalez, A. Plastun, and P. Ostroumov, “Mitigation of longitudinal beam losses in the FRIB linac”, in *Proc. LINAC’24*, Chicago, IL, USA, Aug. 2024, pp. 13–16.
doi:10.18429/JACoW-LINAC2024-M0AA002
- [6] H. Ao *et al.*, “FRIB Multi-Gap Buncher Conditioning up to 30 kW”, presented at HIAT’25, East Lansing, MI, Jun. 2025, paper TUP13, this conference.

MECHANICAL VIBRATION STUDY OF LOW-ENERGY SUPERCONDUCTING LINEAR ACCELERATOR (SCL3) IN RAON*

M.O. Hyun[†], O.R. Choi, H. Jang, Y. Kim, J. Shin
Institute for Basic Science (IBS), Daejeon, South Korea

Abstract

Recently, the Institute for Rare Isotope Science (IRIS, previously RISP) in the Institute for Basic Science (IBS), Daejeon, South Korea, finished the first beam commissioning for operating of low-energy superconducting linear accelerator (SCL3). SCL3 is composed of two types of cavity, quarter wave resonator (QWR) which has 81.25 MHz RF frequency and half wave resonator (HWR) which has 162.5 MHz RF frequency. During operation, RF control was very complicated due to many issues including mechanical vibrations coming from vacuum pump, cryogenic valve, or undefined source. In this paper, we will discuss the SCL3 mechanical vibration data measured by laser doppler vibrometer (LDV). In addition, the mechanical vibration of SCL3 cryogenic components such as transfer line and supports will be also described.

INTRODUCTION

IRIS has constructed a low-energy superconducting linac (SCL3) since 2012. Through enormous efforts by many researchers and engineers, SCL3 construction was finished by 2022, and the first beam commissioning was finished by August 2024. During operation, IRIS experienced many issues such as RF or cryogenic control problem, SSPA malfunction, and general utility error. Among them, we are trying to figure out the effect of mechanical vibration to the RF control problem. There are so many sources of mechanical vibration in the SCL3 tunnel, such as vacuum pumps, cryogenic valves, or utility pipes [1–4]. When vibration is excited, it can be transmitted to the connected structure, like rigid support, floor, wall, or cryomodule, and also excite other structures themselves. When this vibration reaches the cavity, then microphonics happen, and RF control can be failed. Therefore, to measure the mechanical vibration of the cryomodule and related connection is undoubtedly crucial for the view of RF control.

VIBRATION MEASUREMENT

First, we planned to measure the whole SCL3 linac region roughly and shortly, because we expected that we could find a tendency of mechanical vibration after two to three measurement. Figure 1 shows the measuring points of SCL3 Linac (Red dots). Three QWR cryomodules (02, 09, 20), two HWRA cryomodules (04, 09), and five HWRB cryomodules (02, 05, 09, 14, 19) were chosen for measuring points. To see the effect of connecting the structure, we

measured both the cryomodule wall and support at each point. We started the measurement of mechanical vibration in December 2023, however, the first measurement became a rehearsal for next measurement, device troubleshooting and solving other technical issues. After troubleshooting, the vibration measurement data was gathered by February, March and September 2024. Table 1 shows the condition of every utility in the SCL3 linac.

Table 1: SCL3 Operating Conditions on Measuring

2024	February	March	September
CM Vacuum	On	On	On
Cavity Vacuum	On	On	On
SSPA	Off	Standby	Standby
Cryogenic	Off	Cooldown	4K Cooling
Water Utility	Running	Running	Running
Air Condition	Running	Running	Running

Figures 2 and 3 show the measurement of the cryomodule wall and stand. We used the Polytec® Portable Digital Vibrometer (PDV) 100 model for the measuring device. Figures 4 and 5 show the measured vibration results for both the cryomodule wall and support by February 2024. In Fig. 5, the main vibration at the support was near 10 Hz (9–12 Hz), and this peak was also shown in Fig. 4. However, near 28 Hz abnormal peak of QWR CM #20 has not been explained yet. We guess this abnormal peak can be excited by unexpected cryogenic valve control. Figures 6 and 7 show the measured vibration results for both the cryomodule wall and support by March 2024.

In Figs. 6 and 7, the main vibration peaks of the cryomodule wall and support were near 10 Hz (9–12 Hz), the same as the results of Feb. 2024. And, both cryomodule wall and support vibration tendencies were also very similar to each other, except for a near 60 Hz peak in support results. However, the magnitude of vibration in the cryomodule wall was greater than the support. We guess that, with Table 1, when the cryogenic system was turned on then the vibration of the cryogenic facility was excited and transmitted through the cryogenic pipeline, and was measured at the cryomodule wall and support. Figures 8 and 9 show the measured vibration results for both the cryomodule wall and support by September 2024.

Compared with previous vibration results, the vibration magnitude was reduced, and the frequency tendency was changed. In Fig. 8, between 10 to 14 Hz vibration peak was

* Work supported by the Institute for Basic Science (IBS-I001-D1)

[†] atikus43@ibs.re.kr

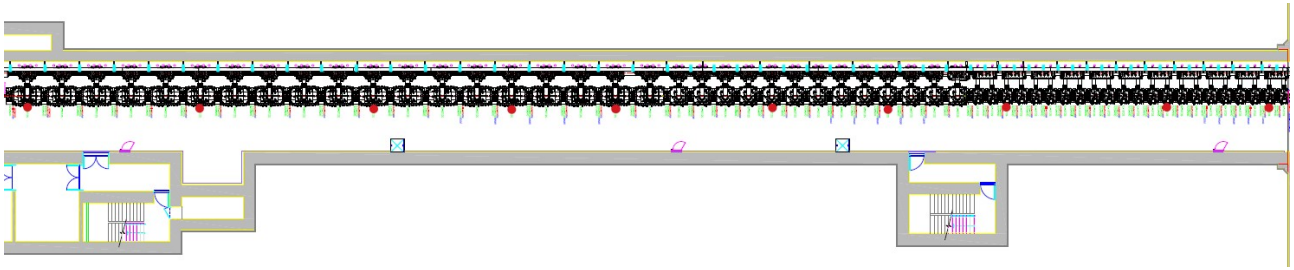


Figure 1: SCL3 tunnel measuring points (red dots).



Figure 2: Cryomodule wall measuring.

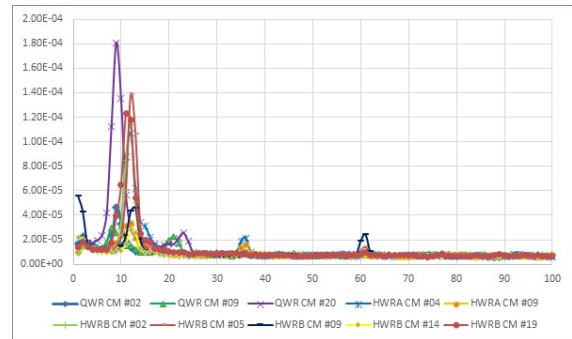


Figure 5: Vibration measurement (Feb. 2024 - Support).



Figure 3: Module support measuring.

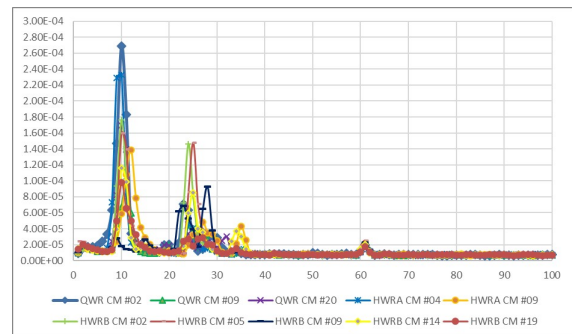


Figure 6: Vibration measurement (Mar. 2024 - CM Wall).

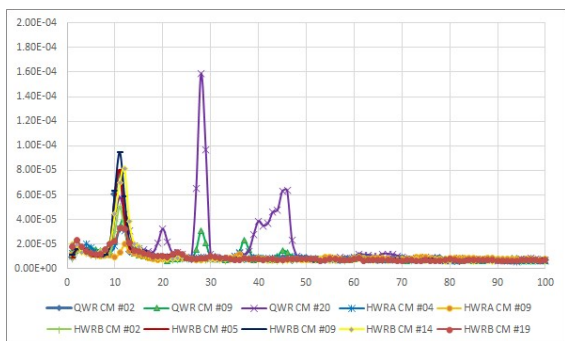


Figure 4: Vibration measurement (Feb. 2024 - CM Wall).

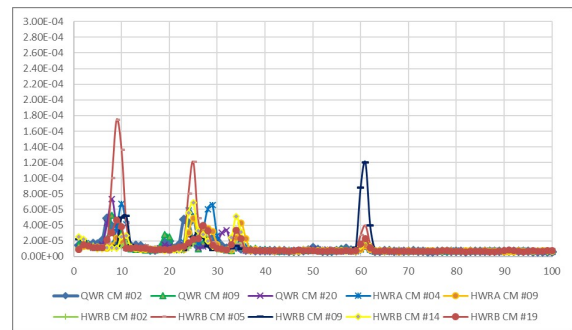


Figure 7: Vibration measurement (Mar. 2024 - Support).

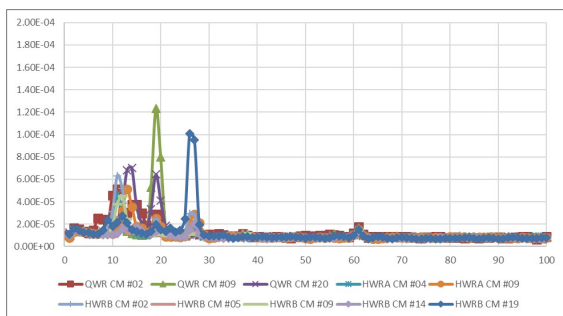


Figure 8: Vibration measurement (Sep. 2024 - CM Wall).

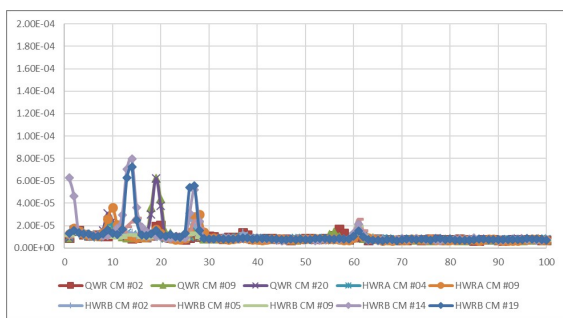


Figure 9: Vibration measurement (Sep. 2024 - Support).

measured, and also a near 20 Hz and 27 Hz vibration peak appeared. This phenomenon could be explained that the initial mechanical vibration was between 10 and 14 Hz, and the next peak was the multiplication of the initial vibration. And, the smaller vibration magnitude could be explained because of cryogenic system was shifted from 2K pumping mode to 4K cool-down mode, preparing for warm-up.

However, nonetheless of SCL3 vibration measurement results and inferences, we could not conclude that the cryogenic system was the main source of mechanical vibration in SCL3. Because, we also measured the vibration of connected cryogenic structures and could not find any similarities. Figure 10 shows the SCL3 cryogenic transfer line (TL) supports measurement, and Fig. 11 shows the vibration measurement results by Sep. 2024. In Fig. 11, the main peak was 60 Hz, and 2X/3X peaks also appeared. An unexpected near 10 Hz vibration appeared in support #1, but did not excite other supports. Figure 12 shows the SCL3 cold-box (CB) vibration measurement, and Fig. 13 shows the measurement results.



Figure 10: SCL3 Transfer Line (TL) measuring.

In Fig. 13, there are higher amplitude peaks such as 7, 18, and 38 Hz. However, this vibration peaks were reduced at the

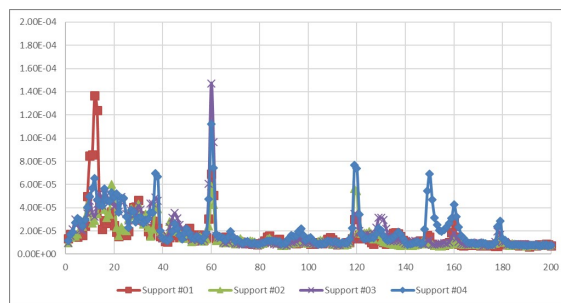


Figure 11: Vibration measurement (Sep. 2024 - TL Sprt.).



Figure 12: SCL3 cold-box (CB) measuring.

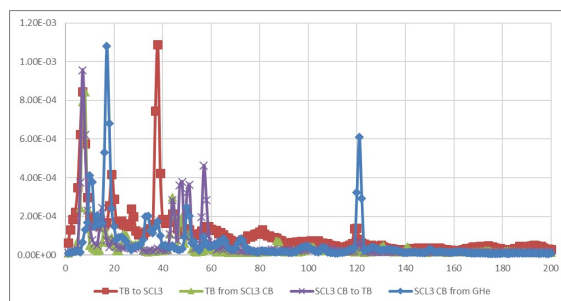


Figure 13: Vibration measurement (Sep. 2024 - CB).

SCL3 TL supports, and not related with SCL3 mechanical vibration results in Fig. 8 and 9. Consequently, the cryogenic system vibration was not related with the SCL3 cryomodule vibration. Therefore, we should proceed the mechanical vibration measurement to the other systems such as HPRF and HVAC.

CONCLUSION

Through the mechanical vibration measurement and analysis, we found that the SCL3 system was so complex that it was hard to define the vibration source. Nevertheless, we will expand the vibration measurement to the HPRF and HVAC utilities to find the main vibration source. Also, to predict the mechanical resonance of SCL3 cryomodule, the resonant frequency measurement will be proceeded with the impact hammer test.

ACKNOWLEDGEMENTS

I thank to Dr. Sungsoo Jung at the KRISS for measuring vibration and giving advices and comments. This work was supported by the Institute for Basic Science (IBS-I001-D1).

REFERENCES

- [1] M. Satoh *et al.*, “Mechanical Vibration Search of Compact ERL Main Linac Superconducting Cavities in Cryomodule”, in *Proc. IPAC'14*, Dresden, Germany, Jun. 2014, pp. 2531–2533. doi:10.18429/JACoW-IPAC2014-WEPRI026
- [2] M. Ge *et al.*, “Measurements and Analysis of Cavity Microphonics and Frequency Control in the Cornell ERL Main Linac Prototype Cryomodule”, in *Proc. LINAC'16*, East Lansing, MI, USA, Sep. 2016, pp. 488–491. doi:10.18429/JACoW-LINAC2016-TUPLR010
- [3] R. D. Porter *et al.*, “Microphonics in the LCLS-II Superconducting Linac”, in *Proc. SRF'23*, Grand Rapids, MI, USA, Jun. 2023, pp. 302–305. doi:10.18429/JACoW-SRF2023-MOPMB081
- [4] Y. Ma *et al.*, “Microphonics Suppression Study in ARIEL e-Linac Cryomodules”, in *Proc. SRF'19*, Dresden, Germany, Jun.-Jul. 2019, pp. 136–140. doi:10.18429/JACoW-SRF2019-MOP036

EXTENDING JuTrack'S CAPABILITIES TO THE FRIB ACCELERATOR TO ENHANCE ONLINE MODELING *

C. T. Ratcliff[†], K. Fukushima, Y. Hao, J. Wan
Facility for Rare Isotope Beams, East Lansing, MI, USA

Abstract

JuTrack is a Julia-based accelerator modeling and tracking package that utilizes compiler-level automatic differentiation (AD) to enable fast and accurate derivative calculations. While JuTrack provides a solid foundation for beam dynamics simulations, its capabilities must be extended to support the Facility for Rare Isotopes (FRIB) linac. This includes modeling heavy-ion linac accelerator components such as the liquid-lithium charge stripper, which facilitates efficient acceleration by remove electrons from heavy isotopes, and incorporating multi-charge state acceleration tracking, which allows for charge-dependent beam dynamics. These extensions address challenges such as the beam matching and optimization of multi charge state through various accelerating structures and beam-material interaction modeling while maintaining the auto differentiation capability. This work focuses on adapting JuTrack to incorporate these elements, enhancing its online modeling abilities. We present modifications to JuTrack's framework and demonstrate their performance in FRIB simulations.

INTRODUCTION

JuTrack is a differentiable accelerator modeling package written in Julia that leverages automatic differentiation for beam dynamics calculations [1]. A comprehensive description of JuTrack's architecture and capabilities can be found in a paper also submitted to this conference [2, 3]. The Facility for Rare Isotope Beams (FRIB) presents unique challenges for beam dynamics modeling due to its multi-charge state acceleration scheme and the presence of charge strippers. This work extends JuTrack to address these specific requirements while maintaining its differentiable nature.

The FRIB accelerator employs charge strippers to increase the charge state of heavy ions, enabling more efficient acceleration. After stripping, multiple charge states are simultaneously transported and accelerated through the downstream beamline. This multi-charge beam dynamics requires specialized tracking capabilities that were not present in the original JuTrack implementation.

FLAME vs. JuTrack APPROACHES

FLAME (Fast Linear Accelerator Model Engine) is an envelope-based beam dynamics code that models beam evolution using second-moment matrices [4]. It solves the envelope equations directly, providing fast computation of beam

sizes and Twiss parameters. However, envelope codes make assumptions about the beam distribution and cannot capture certain nonlinear effects or detailed particle distributions.

In contrast, JuTrack performs element-by-element particle tracking through the accelerator lattice. This approach provides full 6D phase space tracking that captures nonlinear dynamics, unlike envelope methods that rely on linear approximations. JuTrack makes no assumptions about beam distribution shape, allowing it to model arbitrary particle distributions including non-Gaussian beams that may arise.

Most importantly for optimization applications, JuTrack maintains automatic differentiation capability throughout all calculations, enabling efficient gradient-based optimization algorithms with Enzyme, that would be difficult implement with traditional envelope codes [5].

MULTI-CHARGE BEAM IMPLEMENTATION

To support FRIB's multi-charge acceleration scheme, a new MultiChargeBeam class was implemented that manages multiple beam objects with different charge states. Each charge state has its own magnetic rigidity, requiring charge-dependent element parameters. Magnetic elements now scale their fields based on the charge-to-mass ratio relative to the reference beam.

Data Structure

The MultiChargeBeam structure maintains a dictionary of Beam objects indexed by charge state, allowing efficient access to individual charge state properties during tracking calculations. Each charge state has associated magnetic rigidity values ($B\rho$) that determine the particle trajectories through magnetic elements. The structure also stores a reference charge state and its corresponding reference $B\rho$ value, which serve as the baseline for scaling magnetic field effects across all charge states in the beam.

ORBTRIM ELEMENT IMPLEMENTATION

Orbit correction elements (ORBTRIM) were added to support beamline steering. These elements apply angular kicks to the beam:

$$\Delta x'_i = \frac{q_i}{A} \theta_x, \quad \Delta y'_i = \frac{q_i}{A} \theta_y \quad (1)$$

The implementation provides support for both horizontal and vertical kicks, allowing beam steering in both transverse planes. This implementation maintains full integration with JuTrack's automatic differentiation framework, enabling gradient-based optimization of corrector settings for beam trajectory control and orbit correction applications.

* Work supported by the U.S. Department of Energy Office of Science under award number DE-SC0024170 and Cooperative Agreement DE-SC0023633, the State of Michigan, and Michigan State University.

[†] ratcliff@frib.msu.edu

OPERATIONAL METHODS

JuTrack supports two distinct operational methods for beam dynamics calculations, each with specific advantages for different use cases.

Macro Particle Method

The macro particle method tracks a large ensemble of particles through the lattice. Initial particle distributions are generated from FLAME's covariance matrices through random sampling from a 6D Gaussian distribution, followed by transformation to match the desired covariance matrix and addition of charge-dependent momentum offsets that account for the different magnetic rigidities of each charge state.

This method provides full particle distribution information that preserves the statistical properties of the beam throughout the tracking process. The approach naturally handles particle losses by monitoring individual particle trajectories and flagging particles that exceed aperture limits or encounter physical boundaries. Direct calculation of beam moments and emittances from the tracked particle ensemble eliminates the need for analytical approximations inherent in envelope methods.

TPSA Method

The Truncated Power Series Algebra (TPSA) method represents particle coordinates as power series expansions around the reference trajectory [6]. Instead of tracking individual particles, TPSA tracks the polynomial coefficients that describe how particles deviate from the reference.

For a 6D phase space with expansion order 2, each coordinate is represented as:

$$x_i = x_{i,0} + \sum_{j=1}^6 R_{ij} \delta_j + \sum_{j,k} T_{ijk} \delta_j \delta_k + \dots \quad (2)$$

The transfer matrix elements R_{ij} are directly extracted from the first-order coefficients.

FLAME VS. JUTRACK COMPARISONS

Simulation Comparisons

To validate the JuTrack implementation for FRIB applications, detailed comparisons were performed against FLAME calculations using identical lattice configurations and initial beam conditions. Figures 1 and 2 present representative results for the charge state 51 beam tracking through the FRIB beamline.

The beam size comparison demonstrates excellent agreement between the two codes throughout the beamline section. Both the RMS beam sizes and the angular spreads show nearly identical evolution, with JuTrack accurately reproducing the behavior predicted by FLAME. The orbit comparison further validates the implementation, showing that JuTrack accurately tracks beam centroid motion through the lattice elements. The mean beam positions and angles follow identical trajectories in both codes, confirming that

the multi-charge beam implementation correctly handles the magnetic focusing and steering effects for individual charge states.

There are slight discrepancies between the two implementations, mainly in the latter third of the lattice. This is due to how the JuTrack implementation is accounting for the multiple beams, and will be corrected in future use.

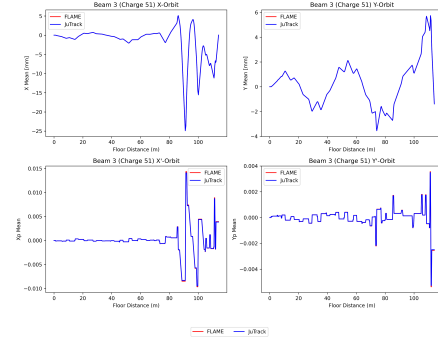


Figure 1: Comparison between the JuTrack TPSA implementation and the FLAME implementation.

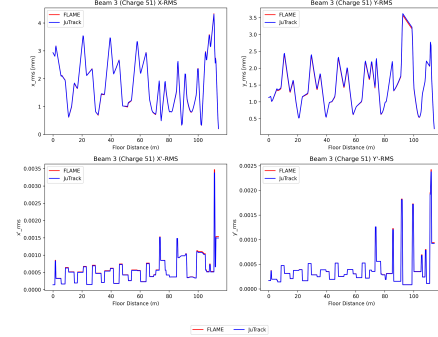


Figure 2: Comparison of the RMS values between the JuTrack TPSA implementation and the FLAME implementation.

Runtime Comparisons

Runtime performance comparisons were conducted across different simulation methods to evaluate computational efficiency. Table 1 presents execution times for tracking through the FRIB beamline section using identical lattice configurations and beam parameters.

The TPSA methods provide an intermediate performance increase compared to the macro particle method, offering potential computational advantages while maintaining higher-order physics modeling capabilities.

These runtime comparisons reflect code maturity differences between the two programs. The JuTrack implementation prioritized physical correctness, automatic differentiation capability, and feature completeness over computational

Table 1: Runtimes Across Different Simulation Methods

Method	Runtime
FLAME	1.16 ms
JuTrack - Macro (10000 particles)	2178 ms
TPSA - 1st Ord.	77.8 ms
TPSA - 2nd Ord.	152 ms

efficiency. Future optimization efforts are expected to substantially reduce these performance gaps while preserving JuTrack's unique advantages for gradient-based optimization and detailed physics modeling.

FUTURE WORK

Optimization Comparison: FLAME vs. JuTrack

To evaluate the performance benefits of JuTrack's differentiable modeling approach, an optimization study is ongoing using a representative tuning scenario in the FRIB beamline. The goal is to adjust quadrupole strengths to meet beam size constraints for multiple charge states while comparing JuTrack with FLAME under identical conditions.

Simulation Setup Initial conditions for the magnet strengths are simulated by varying the given strengths by up to 10%. The same initial distributions are applied in both FLAME and JuTrack simulations to ensure consistent benchmarking.

The tuning objectives are defined with three specific beam size constraints along the beamline. The maximum RMS beam size for all charge states must remain below 3 mm in the first straight section. After the bending section, the maximum beam size must be less than 3.5 mm. At the end of the lattice, the RMS beam size should be approximately 0.3 mm.

Optimization Methodology Let $w_i(z)$ represent the RMS beam size of charge state i at longitudinal position z . The total cost function C is defined as:

$$C = \sum_i \left[\sum_{z \in \mathcal{P}_1} \max(0, w_i(z) - 3)^2 + \sum_{z \in \mathcal{P}_2} \max(0, w_i(z) - 3.5)^2 + (w_i(z_{\text{end}}) - 0.3)^2 \right] \quad (3)$$

where \mathcal{P}_1 and \mathcal{P}_2 denote sets of longitudinal positions in the first straight and post-bend sections, respectively.

Optimization will be performed by varying the strengths of up to 15 quadrupoles surrounding the bending section. The four quadrupoles immediately between the bending magnets will be held fixed in order to preserve the original dispersion design. This optimization is currently ongoing.

Error Propagation for Beam Measurements

A unique, possible application of JuTrack's automatic differentiation capability is the calculation of confidence

intervals for beam parameters derived from measurements. When estimating Twiss parameters from beam size measurements, measurement uncertainties must be propagated through the analysis.

Consider beam size measurements q_1, q_2, \dots, q_n at different locations, each with associated measurement error $\delta q_1, \delta q_2, \dots, \delta q_n$. The Twiss parameter β is determined from these measurements through a fitting procedure. The uncertainty in β can be calculated using standard error propagation:

$$\delta \beta = \sqrt{\sum_{i=1}^n \left(\frac{\partial \beta}{\partial q_i} \delta q_i \right)^2} \quad (4)$$

The challenge is computing the partial derivatives $\frac{\partial \beta}{\partial q_i}$. Traditional approaches require either analytical derivation of these derivatives or numerical differentiation using finite differences. JuTrack's automatic differentiation provides these derivatives exactly at machine precision. The fitting procedure that determines β from the measurements is implemented as a differentiable function, and AD automatically computes all required partial derivatives. This enables uncertainty quantification for beam parameters, optimal placement of diagnostics to minimize parameter uncertainties, and real-time confidence interval estimation during operations.

CONCLUSION

JuTrack has been adapted to address the unique requirements of the FRIB linear accelerator facility. The implementation of multi-charge beam tracking through the Multi-ChargeBeam class enables simultaneous modeling of multiple charge states with charge-dependent magnetic rigidities, accurately representing post-stripper beam transport physics. The addition of orbital trim elements provides essential orbit correction capabilities for operational beamline control.

JuTrack's two existing operational methods were explored for FRIB applications: the macro particle method for detailed particle distribution modeling and the TPSA method for computational efficiency in beam optics calculations. Both methods utilize JuTrack's automatic differentiation framework, preserving the package's key advantage for gradient-based optimization.

ACKNOWLEDGEMENTS

Work supported by the U.S. Department of Energy Office of Science under award number DE-SC0024170 and Cooperative Agreement DE-SC0023633, the State of Michigan, and Michigan State University.

REFERENCES

- [1] J. Bezanson, A. Edelman, S. Karpinski, and V. B. Shah, "Julia: A fresh approach to numerical computing", *SIAM Review*, vol. 59, no. 1, pp. 65–98, 2017. doi:10.1137/141000671

- [2] J. Wan, H. Alamprese, C. Ratcliff, J. Qiang, and Y. Hao, “JuTrack, a Julia-based tool for accelerator modeling and tracking with auto-differentiation”, presented at HIAT’25, East Lansing, MI, Jun 2025, paper WEP09, this conference.
- [3] J. Wan, H. Alamprese, C. Ratcliff, J. Qiang, and Y. Hao, “Ju-track: A julia package for auto-differentiable accelerator modeling and particle tracking”, *Comput. Phys. Commun.*, vol. 309, p. 109497, 2025. doi:10.1016/j.cpc.2024.109497
- [4] Z. He, M. Davidsaver, K. Fukushima, G. Shen, M. Ikegami, and J. Bengtsson, “The fast linear accelerator modeling engine for frib online model service”, *Comput. Phys. Commun.*, vol. 234, pp. 167–178, 2019. doi:10.1016/j.cpc.2018.07.013
- [5] W. S. Moses and V. Churavy, “Instead of rewriting foreign code for machine learning, automatically synthesize fast gradients”, in *Proceedings of the 34th International Conference on Neural Information Processing Systems*, 2020. doi:10.48550/arXiv.2010.01709
- [6] M. Berz, “Differential Algebraic Description of Beam Dynamics to Very High Orders”, *Part. Accel.*, vol. 24, pp. 109–124, 1989. doi:10.2172/6876262

BUDGET-FRIENDLY DEFENSE AGAINST RADIATION-INDUCED CAMERA DAMAGE*

E. Daykin[†], N. Bultman, M. LaVere, S. Lidia, D. McNanney, S. Rodriguez
Facility for Rare Isotope Beams, East Lansing, MI, USA

Abstract

Cameras observing scintillating viewers provide a valuable tool for tuning heavy ion beams. The close placement of these cameras near intense stray neutron and ion radiation, particularly at elements intercepting the primary beam, presents a unique reliability challenge. Commercial solutions are sparse, expensive, and sometimes tightly regulated. We present common failure modes observed at FRIB and propose solutions to extend the lifespan of unspecialized industrial cameras using consumer-grade hardware and open-source software.

INTRODUCTION

Scintillating viewers are a straightforward way to qualitatively observe the alignment and shape of an ion beam. FRIB's primary uranium beam reaches up to 200 MeV/u uranium, and higher energies are achieved for lighter species. The current primary power on target is 20 kW, with the eventual goal of reaching 400 kW. The interaction of this beam with interceptive devices (*e.g.* the charge stripper [1], production target [2], and separator slits [3]) creates stray radiation fields that damage conventional electronics.

This work does not seek to advance any particular state of the art – rather, we present inexpensive, accessible strategies undertaken at FRIB to mitigate the detrimental effects of radiation on cameras, which might apply in equal measure to other sensitive electronic devices.

PROBLEM ANALYSIS

Reactions caused by beam interaction with solid materials induce stray radiation on the order of $1 - 10 \text{ Gy y}^{-1}$ total ionizing dose (TID) [4, 5], neutrons and photons. High-energy photons (X-rays and γ -rays) can cause electrical effects by disrupting electron-hole pairs in silicon, and neutrons can physically displace atoms in semiconductor crystal lattices. Preliminary work [4] estimates the total soft error rate in silicon to be roughly $2 \cdot 10^7 \text{ FIT} \cdot \text{MBit} \cdot \text{cm}^{-2} \cdot \text{s}^{-1}$ at current beam power. That is, for a hypothetical device with a density of 1 Mbit in 1 cm^2 of area, a soft error latch-up would be expected every 50 hours of operation. Empirically, soft errors are seen once per 6 hours of operation at the liquid lithium charge stripper (LLCS), with hard errors and replacement during maintenance necessary after 500-1000 hours of operation on average. Figure 1 depicts typical performance during 20 kW operation.

* Work supported by the U.S. Department of Energy Office of Science under Cooperative Agreement DE-SC0023633, the State of Michigan, and Michigan State University.

[†] daykin@frib.msu.edu

This presents something of a gray area. Specifically designed radiation-hardened cameras are expensive with few existing options on the market, especially with respect to neutrons. Failures are mitigated, to a certain extent, with radiation-tolerant design (*e.g.* CMOS sensors vs. CCD). Other elements are just duplicated for redundancy, which extends the usable lifetime, but does not ultimately prevent radiation-induced failure. However, since these cameras are used primarily for qualitative measurements, sporadic failures are generally acceptable, *provided* the image remains legible and the latch-ups can be cleared remotely without operator intervention.

CONVENTIONAL DESIGN

Hardware

For general-purpose qualitative measurement and some thermographic applications in the near infrared, FRIB uses off-the-shelf general-purpose industrial cameras. Typically, FRIB uses The Imaging Source's 33GX265, featuring a 3.1MP monochrome Sony IMX265 CMOS sensor. It retails for about \$550 USD¹. Lenses are chosen from the Fujinon HF-XA-5M line, with no noticeable darkening in 3 years of operation. The cameras are generally aligned on kinematic mounts between 50 and 100 cm from the object.

Software

Incoming images from the cameras are handled by section of the linac on physical camera servers, with each camera's feed aggregated over a 10-Gigabit Ethernet fiber link. Camera control is accomplished with the camera's firmware implementing the GenICam control standard [6], with network communication implemented by Aravis [7], an open-source emulation of the GigE Vision protocol [8] Aravis, in turn, interfaces with the EPICS supervisory control system [9] via the AreaDetector ADAravis driver [10]. With the detector driver producing images, users may adjust the camera's raw feed and take statistics using the other AreaDetector plugins².

MITIGATING RADIATION DAMAGE

Dead Pixels

Depending on the placement of cameras with respect to interceptive devices, cameras on the beamline will develop dead or "hot" pixels due to radiation damage on the sensor. Visually, this can be mitigated by applying a median filter,

¹ *cf.* similar radiation-hardened models well into the thousands.

² The state machine, along with a sample skeleton EPICS IOC, can be found at <https://github.com/daykin/HIAT25-MOP19>.

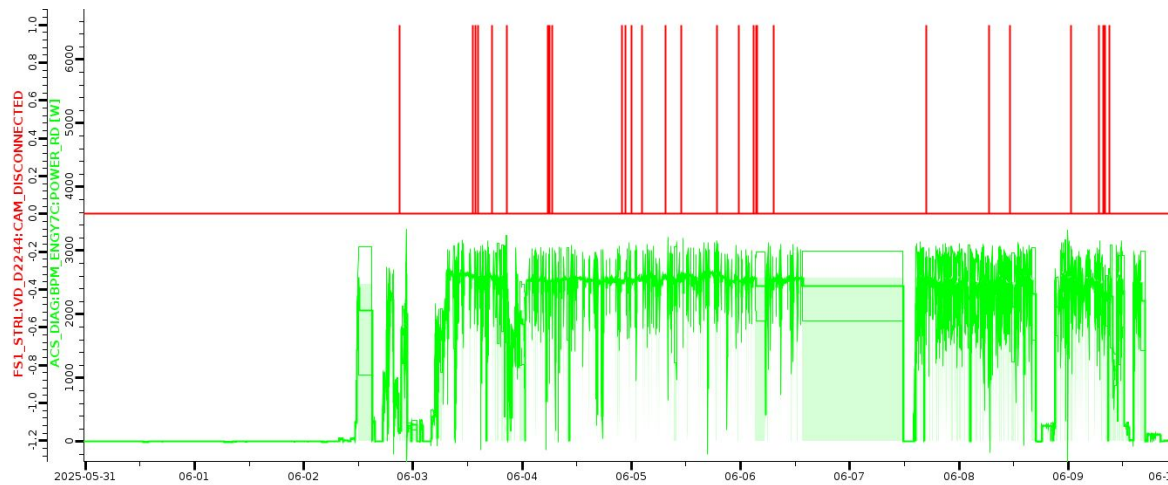


Figure 1: Strip chart of detected soft errors on the LLCs camera during a week-long experiment. The upper trace depicts 27 latch-ups, the lower trace depicts beam power in the area, in Watts.

in which each pixel of the image is replaced by the median of the surrounding 5×5 kernel. OpenCV implements this efficiently with a sliding window and heap strategy, which can accomplish the filtering in $O(nk)$ time, as opposed to $O(nk \log nk)$ for n pixels on a $k \times k$ kernel. Figure 2 shows the difference between the raw and filtered image³. We wrap the OpenCV median filter for use in the control system using a fork of the ADCompVision AreaDetector plugin [11].

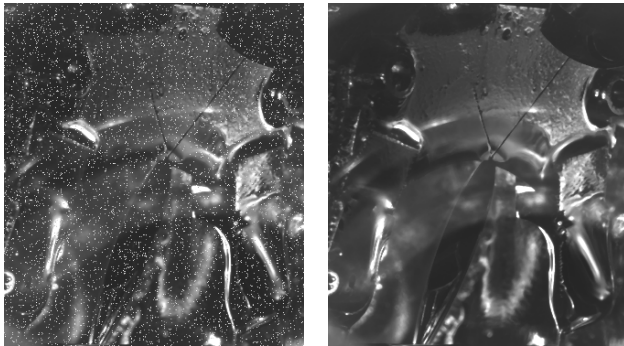


Figure 2: Comparison of the LLCs film image before (left) and after (right) median denoising.

Physical Countermeasures

In areas of particularly high radiation, it becomes reasonably likely that a camera will experience a hard error during active operation, resulting in downtime if it is needed and cannot be brought back up. The only solution, in this case, is to shield and distance the critical components of the camera. This is accomplished by creating a ‘periscope’ of various form factors depending on the environment. This places the active components in shielding away from the most intense radiation. Figure 3 shows an exploded view of one

of these assemblies, placed in this case at the Carbon-foil charge stripper (CCS) used before the LLCs came online. For more complex devices where scale must be preserved, the infrared thermal imaging camera at the target dump features a telecentric lens focused on the dump by a moving series of mirrors, which lengthen or shorten the optical path such that the image is properly focused on the camera’s focal plane array (FPA). This ‘trombone’ assembly is shown in Fig. 4.

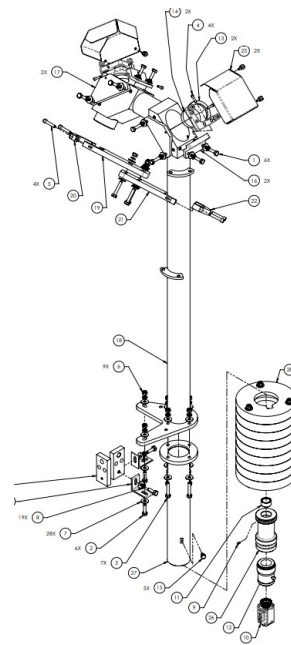


Figure 3: Exploded view of the CCS optical line. The camera itself is shown in the lower-right, and is surrounded by rings of cast iron or borated polyethylene.

³ Additional speckling was rendered onto ‘before’ image before processing to demonstrate effect in print.

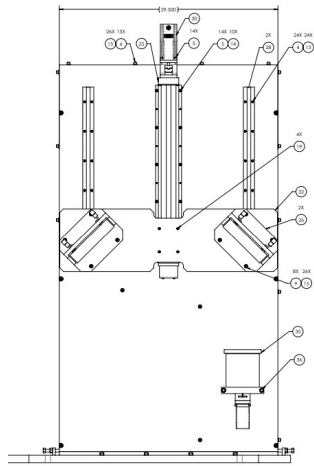


Figure 4: Forward view of the target dump optical line. The camera itself is shown in the lower-right. Angled mirrors move vertically to adjust the apparent distance to the FPA.

Soft Error Recovery

Radiation-induced corruption and latch-up is a more difficult issue to solve. Since the corruption of volatile memory on the device is random by nature, the exact characteristics seen by a remote user are varied. Thus, the device's network stack may still be functioning and the device driver may not recognize the malfunction. In this state, the only way to recover functionality is to physically power down the link.

To solve this, the camera link is shunted with an off-the-shelf Power-over-Ethernet (PoE) injector, powered by a network-controlled power distribution unit (PDU). A finite state machine is implemented on the camera control EPICS server. In short, if the device is nominally 'acquiring', but the frame counter is not incrementing for more than 10 acquisition periods, the server recognizes the camera to be malfunctioning. It will first attempt to send the GenICam a 'Reset' command. If the soft reset does not work (evidenced by the same symptom), it will command the PDU outlet off - first for 5 seconds, then exponentially backing off to 5 minutes switched off, to ensure volatile memory eventually clears. After power-cycling, the application will again check if the camera is successfully transmitting images. The process repeats as long as the state machine is enabled, at longer intervals due to the back-off mechanism.

DISCUSSION

Use-Cases

In the case of FRIB's first three years of operation, hard camera failures induced by radiation have not represented a significant fraction of unscheduled downtime, and maintenance intervals are frequent enough to allow for proactive replacement. However, before the introduction of the above-described methods, sensor damage and soft latch-ups became a significant nuisance. In this operating niche, it is feasible to use remarkably inexpensive methods to automate recovery from the most frequent failures.

Difficulties and Future Work

Some strategies, particularly that of using unspecialized camera hardware, must be carefully considered with respect to the environment in which they will operate. With any installation, it is important to design for the characteristics of stray radiation fields that will be encountered. From this information, a very rough estimate of the mean time between failures can be calculated to determine feasibility. This estimate can be refined on existing installations or test setups with empirical data from commissioning or operation. Failure rates, in turn, can be used to make informed decisions about camera installations in light of the sensor capabilities, operational lifetime, cost of replacement, and cost of related facility downtime.

A particular case in which these strategies are less effective is in the target dump thermal imaging system. This specialized mid-infrared (7–12 μm) camera requires a higher level of care in the harshest environment, due to its potential future role in identifying overheating and uncontrolled beam loss. Despite sitting atop 1.5 meters of cast-iron shielding and retrofitting with 15 cm borated polyethylene, soft failures are still observed between 100 and 1000 hours of operation. We would like to devote future work to in-house modification to relocate all components except the FPA entirely out of the target hot-cell.

CONCLUSION

Placing cameras near devices producing strong prompt radiation is a necessary, but challenging task. Ionizing radiation is particularly damaging to dense semiconductor components, including CMOS sensors and most common forms of volatile and non-volatile memory.

For constrained budgets, we present inexpensive methods of extending the longevity of these devices, and mitigating the most common errors without manual intervention. The most preferable methods involve commercially available, relatively inexpensive hardware, open-source software. If necessary, shielding and distance enclosures are fabricated from commercially available parts and fabrication techniques accessible to most heavy-ion accelerator laboratories.

REFERENCES

- [1] T. Kanemura *et al.*, "Liquid Lithium Charge Stripper Commissioning with Heavy Ion Beams and Early Operations of FRIB Strippers", in *Proc. HIAT'22*, Darmstadt, Germany, Jun.-Jul. 2022, pp. 31–36.
doi:10.18429/JACoW-HIAT2022-M04I2
- [2] J. Song *et al.*, "A single-slice rotating graphite target at FRIB", presented at HIAT'25, East Lansing, MI, USA, Jun. 2025, paper TUB01, this conference.
- [3] M. Hausmann *et al.*, "Design of the Advanced Rare Isotope Separator ARIS at FRIB", *Nucl. Instrum. Methods Phys. Res., Sect. B*, vol. 317, pp. 349–353, Dec. 2013.
doi:10.1016/j.nimb.2013.06.042
- [4] T. Ginter, "Prompt Radiation Conditions in FRIB Target Hall", unpublished.

- [5] R. M. Ronningen, “Levels of Dose Rates around FRIB Charge Stripping Region Activated Components”, unpublished.
- [6] *Standard 1288: Standard for Characterization of Image Sensors and Cameras*, EMVA – European Machine Vision Association, Barcelona, Spain, Sep. 2016.
- [7] Aravis Project, <https://github.com/AravisProject/aravis>
- [8] *GigE Vision: Video Interface Standard for Machine Vision Applications Over Ethernet (Ver. 2.2)*, Association for Advancing Automation, Ann Arbor, MI, USA, Jun. 2022.
- [9] L.R. Dalesio, A.J. Kozubal, and M.R. Kraimer, “EPICS Architecture”, in *Proc. ICALEPCS'91*, Tsukuba, Japan, Nov. 1991, pp. 278–282.
doi:10.18429/JACoW-ICALEPCS1991-S07IC03
- [10] M. Rivers *et al.*, “ADAravis — areaDetector Documentation”, 2025. <https://areadetector.github.io/areaDetector/ADAravis/>
- [11] J. Wlodek *et al.*, “ADCompVision — areaDetector Documentation”, 2025. <https://areadetector.github.io/areaDetector/ADCompVision/ADCompVision.html>

PHYSICS APPLICATIONS IN SUPPORT OF FRIB BEAM TUNING AND OPERATIONS *

T. Zhang[†], K. Fukushima, K. Hwang, T. Maruta, A. Plastun, Q. Zhao, P. Ostroumov
Facility for Rare Isotope Beams, Michigan State University, East Lansing, MI, USA

Abstract

Physics application software plays a crucial role in the tuning and operation of the FRIB linear accelerator (LINAC). The software development began long before the initial commissioning, establishing core capabilities to support early machine setup. Numerous new applications have been created and continuously refined during the past three years of operations through collaboration between engineers and physicists. These efforts have significantly enhanced the beam tuning efficiency and delivery for the user experiments. This paper provides an overview of the status of the development of physics application software, highlights the key applications deployed in operations, and outlines the roadmap for future advancements.

INTRODUCTION

The Facility for Rare Isotope Beams (FRIB) at Michigan State University is a unique modern user facility, featuring a large-scale superconducting LINAC capable of accelerating heavy ion beams from oxygen to uranium. It supports the generation of a wide range of rare isotope beams for nuclear science research [1]. A sophisticated high-level physics control software system has been developed prior to early commissioning, continually refined during staged commissioning phases, and remains under active evolution during user beam operations.

Built on top of the EPICS distributed control system [2], and leveraging efficient physics modeling codes, a systematic software framework named PHANTASY has been designed to address both the immediate and long-term requirements of accelerator commissioning and operation [3]. A model-based virtual accelerator engine was developed to simulate the EPICS environment, enabling early application development independent of hardware availability. The information flow within the accelerator, particularly for essential physics configurations, is carefully abstracted into high-level programming interfaces, allowing applications to operate seamlessly against either virtual or real machines. The Python scripting framework is implemented with consistent unit management to ensure accurate interpretation between machine controls and physics modeling environment.

To better support commissioning, user-friendly graphical interface applications have been developed by encapsulating the validated scripts. Modularized Qt widgets have been

created to handle general use cases ranging from data visualization to the integration of physics models, streamlining the development of Python-based GUI applications.

To manage various types of control system data, multiple libraries and tools have been developed to integrate live and archived data into the Python ecosystem, facilitating the unified interface for advanced data analysis application development.

The rapid advancement of modern computing technologies enables the adoption of powerful new methods into the development workflow. For example, data-driven modeling techniques using machine learning are being actively explored, along with best practices for software engineering to ensure long-term code quality and maintainability.

These combined efforts contribute to the continuously improving efficiency of beam development and delivery at FRIB.

EARLY DEVELOPMENT AND COMMISSIONING SUPPORT

The FRIB accelerator began commissioning in 2017, while development of high-level physics applications started earlier, around 2015. Two critical components emerged during this phase: the physics modeling code and the overall software architecture for physics applications.

Physics Modeling

A key requirement at the time was a simulated EPICS environment with configurable virtual devices to support engineers and physicists in developing and testing applications. To meet this need, and to provide simulation responses more realistic than random noise, FLAME, a fast accelerator simulation engine, was proposed and developed.

FLAME (Fast Linear Accelerator Modeling Engine) is a novel beam envelope tracking code capable of efficiently modeling non-axisymmetric superconducting RF cavities and multi-charge state acceleration [4]. It features matrix-based models for major lattice components such as solenoids, quadrupoles, dipoles (magnetic and electrostatic), charge strippers, and supports misalignment modeling to reflect real-world conditions. Written in C++ for high performance, FLAME also offers native Python bindings for seamless integration with the high-level physics application framework. Its ecosystem continues to grow, with supporting libraries and tools aiding lattice design, optics calculations, and more. Further details are available on the project's GitHub page [5].

* Work supported by the U.S. Department of Energy, Office of Science, Office of Nuclear Physics, and used resources of the FRIB Operations, which is a DOE Office of Science User Facility under Award Number DE-SC0023633 and DE-SC0024707.

[†] zhangt@frib.msu.edu

Software Architecture

The design and initial development of the software architecture for the high-level physics applications were shaped in late 2016, marked by the launch of a Python project called PHANTASY [3, 6]. This project was created to address several key challenges:

- Managing devices while the lattice configuration was still evolving;
- Enabling physics application development prior to machine commissioning;
- Ensuring sustainable and maintainable software development.

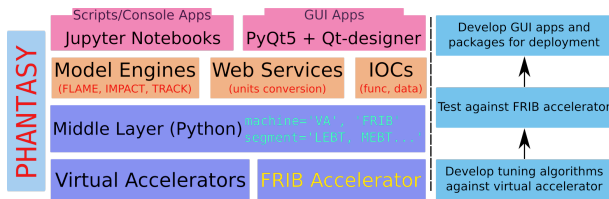


Figure 1: The schematic software architecture of PHANTASY project.

Figure 1 illustrates the major components of physics applications and their relationship to the software development workflow. The architecture is built around a middle layer that abstracts devices and enables object-oriented scripting. This allows access to all devices and lattice information within a Python environment, where machine-agnostic scripts can be developed under specific tuning algorithms to achieve physics objectives.

For example, the FLAME model-driven virtual accelerator provides a consistent control interface to application developers. Device objects are instantiated with machine-specific configuration data, which is separately maintained in a dedicated package (*phantasy-machine*). This separation enables the same scripts to run across different machines, allowing general-purpose physics applications to be developed even before the actual accelerator is operational.

Using this framework, various scripts and applications have been created. Examples include: a GUI for visualizing current lattice data; a general-purpose GUI for studying parameter correlations; an online trajectory correction app using the response matrix method; and a GUI for managing virtual accelerators during development.

To accommodate upstream changes in lattice configurations, often maintained in different formats, the framework includes tools for standardizing and finalizing these configurations within *phantasy-machines*. Each new version reflects upstream updates, while still allowing manual refinements where automated routines may fall short.

EXPANSION DURING OPERATIONS

Initial user operations began in May 2022 [7–10], shortly before the lattice configurations were finalized. With more

complete control signals available via both hardware and software IOCs, the high-level physics applications entered a refinement phase aimed at improving beam development efficiency.

Support IOC and OPI Applications

To enhance integration and user experience, a suite of input/output controller (IOC) applications and operator interface (OPI) pages was developed. These tools interface with the CS-Studio ecosystem, including the Phoebus alarm system, and complement the existing PyQt-based GUI applications used during beam operations.

Frozen features in the GUI apps can be moved to IOC and OPI versions for long-term support and better system integration. While this isn't required, it's helpful and done carefully to avoid affecting beam operations.

Model-based Development

To increase efficiency and reproducibility in beam tuning, model-based tuning algorithms are being actively explored and deployed. A key objective is to prepare optics settings in advance of beam availability. Significant effort has gone into achieving this goal.

Depending on the experimental requirements, a proposed primary beam from the LINAC is first defined. The *Instant Phase Setting* application uses the physics model to rapidly compute SRF cavity field and phase settings. FLAME is then used to generate the corresponding transverse optics solution. These pre-developed configurations are transferred to the control system as device setting snapshots, which can be imported into the *Settings Manager* application. Settings appear as database entries in table format, allowing users to apply them to real devices during beam development.

This workflow is particularly beneficial for tuning different ion species, by either scaling an existing snapshot or creating new ones by combining different parts from multiple snapshots. As the system matures, the time required for beam setup continues to decrease, reflecting the value of prior development efforts.

KEY PHYSICS APPLICATIONS

App Launcher

App Launcher (Fig. 2) provides a unified interface for accessing physics applications using a card-based layout. Each card presents key information consistently; users can launch the app, view its documentation (if available), and access log messages from one place.

As of now, approximately 40 apps are registered in the *App Launcher*. A Git repository is used to manage app configurations, supporting seamless integration with the Linux desktop environment and CS-Studio. The interface is role-aware, showing different sets of applications to regular users and developers.

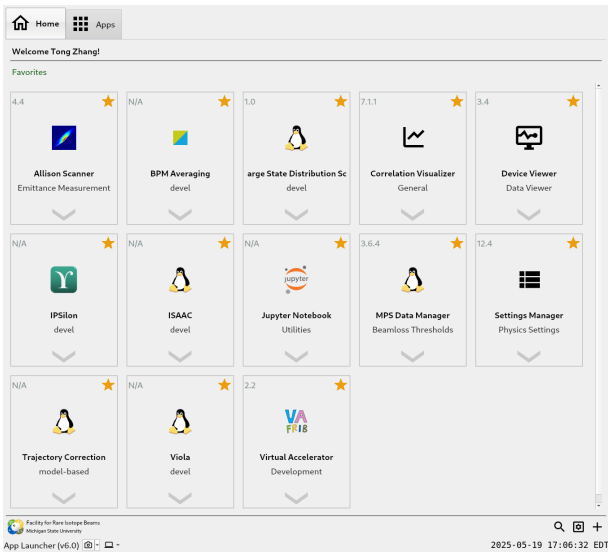


Figure 2: The global entry for all the deployed physics apps.

Settings Manager

Settings Manager is a general-purpose data management tool designed to provide consistent user experience for saving and restoring machine physics settings (Fig. 3). It supports both offline preparation and live control of device settings. Unit conversions between the physics model and device controls are handled internally using core PHANTASY functions. The GUI offers powerful features such as data filtering and comparison, enabling users to quickly identify discrepancies and erroneous settings. It also integrates with the Phoebus alarm system via dedicated IOC and OPI apps. Saved snapshots can be exported with full metadata for use in offline beam development and modeling in various user-friendly data formats [11].

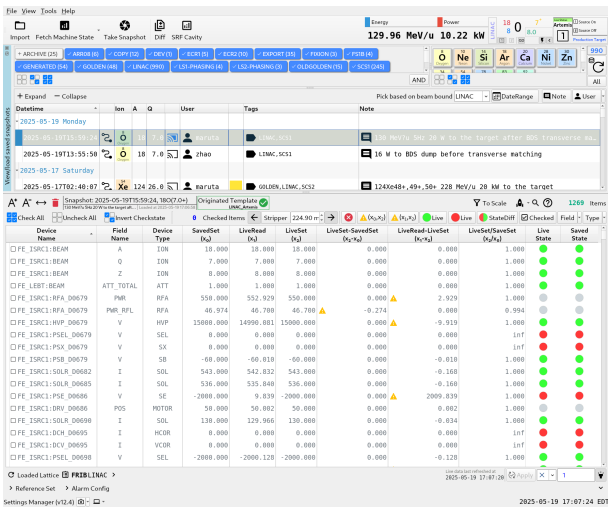


Figure 3: The app manages the physics settings.

Trajectory Correction

Initially, a trajectory correction app based on the trajectory response matrix method was developed. While functional, it

was slow, taking over hours to complete corrections across the full LINAC due to the time required to measure the real BPM responses from superconducting steering correctors.

This has been significantly improved by integrating FLAME-based response matrix calculations. With pre-configured FLAME lattice files available for different LINAC segments, users can now perform trajectory corrections in just minutes by selecting the segment of interest (see the app screenshot shown in Fig. 4).

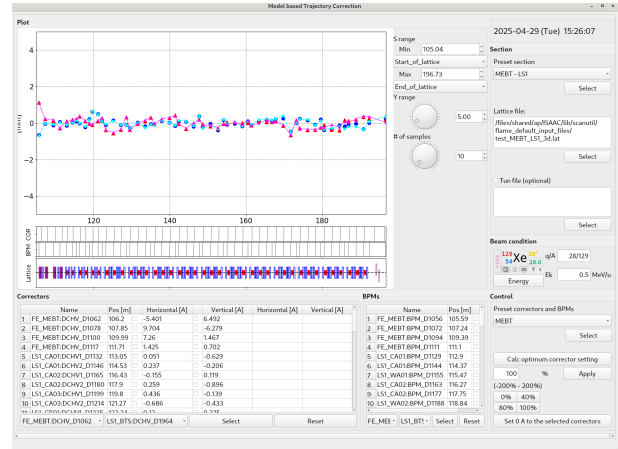


Figure 4: The app corrects the beam central trajectory with FLAME-based response matrix method.

Other Applications

Many additional applications have been developed to support tasks ranging from beam tuning to data management and system diagnostics. These tools aim to automate routine procedures and maximize operational efficiency. The physics applications suite continues to grow, with new tools regularly integrated and existing ones actively improved.

FUTURE DIRECTIONS

The FRIB physics application software continues to evolve, reducing beam development time and improving operational efficiency. As data complexity grows, new challenges arise. To address them, machine learning (ML) approaches are being explored using both historical and live data. Efforts are also underway to enhance the software framework for better ML integration, while maintaining flexibility and long-term sustainability.

ACKNOWLEDGMENTS

The authors would like to thank the FRIB Beam Instrumentation Department for their support and valuable discussions, as well as the Operators Group for reporting software application issues that contributed to ongoing improvements.

REFERENCES

- [1] J. Wei *et al.*, “Advances of the FRIB project”, *Int. J. Mod. Phys. E* 28, 1930003, 2019.
doi:10.1142/S0218301319300030
- [2] <https://epics-controls.org/>
- [3] T. Zhang *et al.*, “High-level physics controls applications development for FRIB”, in *Proc. 17th Int. Conf. on Acc. and Large Exp. Physics Control Systems (ICALEPCS 2019)*, New York, NY, USA, Oct. 2019, pp. 828–834.
doi:10.18429/JACoW-ICALEPCS2019-TUCPR07
- [4] Z. He, Y. Zhang, J. Wei, Z. Liu and R. M. Talman, “Linear envelope model for multicharge state linac”, *Phys. Rev. ST Accel. Beams* 17, no.3, p.034001, 2014.
doi:10.1103/PhysRevSTAB.17.034001
- [5] The GitHub organization for FLAME and other repositories, <https://github.com/flame-simulation>
- [6] T. Zhang, “Physics high-level applications and toolkit for accelerator system”, in *EPICS Collaboration Meeting*, Argonne National Laboratory, IL, USA, Jun. 2018. <https://epics.anl.gov/meetings/2018-06/talks.html>
- [7] P.N. Ostroumov *et al.*, “Beam commissioning in the first superconducting segment of the Facility for Rare Isotope Beams”, *Phys. Rev. Accel. Beams* 22, no.8, p. 080101, 2019.
doi:10.1103/PhysRevAccelBeams.22.080101
- [8] <https://frib.msu.edu/news-center/news/facility-rare-isotope-beams-opens-its-doors-discovery>
- [9] J. Wei *et al.*, “FRIB commissioning and early operations”, in *Proc. 13th Int. Particle Acc. Conf. (IPAC 2022)*, Bangkok, Thailand, pp. 802–807.
doi:10.18429/JACoW-IPAC2022-TUIYGD3
- [10] P. Ostroumov *et al.*, “FRIB from commissioning to operation”, in *Proc. 68th Adv. Beam Dyn. Workshop High-Intensity High-Brightness Hadron Beams, HB2023*, Geneva, Switzerland, pp. 9–15.
doi:10.18429/JACoW-HB2023-MOA1I2
- [11] T. Zhang *et al.*, “Manage the physics settings on the modern accelerator”, in *Proc. 18th Int. Conf. on Acc. and Large Exp. Physics Control Systems (ICALEPCS 2021)*, Shanghai, USA, Oct. 2021, pp. 569–573.
doi:10.18429/JACoW-ICALEPCS2021-WEBL04

UPDATED MAGNETIC RIGIDITY CALIBRATION OF ARIS*

A. C. Dombos[†], K. Fukushima, M. Hausmann, D. Kahl, E. Kwan, M. Portillo,
B. M. Sherrill¹, M. K. Smith, M. Steiner, O. B. Tarasov

Facility for Rare Isotope Beams, Michigan State University, East Lansing, MI, USA

¹also at Department of Physics and Astronomy, Michigan State University, East Lansing, MI, USA

Abstract

The Facility for Rare Isotope Beams (FRIB) enables groundbreaking research in nuclear physics, astrophysics, and fundamental interactions, as well as the societal applications of this work. Critical to the science program at FRIB is the Advanced Rare Isotope Separator (ARIS), which separates, identifies, and purifies fragments produced via projectile fragmentation and fission using a variety of beamline elements, including eight superconducting dipole magnets. An accurate magnetic rigidity calibration of these dipole magnets is crucial for obtaining peak fragment yields with optimal transport conditions in minimal time and comparing to simulations. This work reports on the use of the FRIB linear accelerator to provide charge states of a ^{238}U beam of known energies, with accuracy of 0.1%, to calibrate the ARIS dipole field versus effective bend radius over a range of magnetic rigidities. Due to saturation of the iron in the dipoles, the effective radius varies significantly, especially above about 1.2 T. Details of the procedure and results will be presented.

INTRODUCTION

The Facility for Rare Isotope Beams (FRIB) on the campus of Michigan State University (MSU) is a United States Department of Energy Office of Science user facility that enables a robust science program in fundamental and applied nuclear physics research. The FRIB linear accelerator (linac) currently provides heavy-ion primary beams up to 20 kW with a goal of reaching 400 kW at energies of 200 MeV/u for uranium and higher for lighter ions [1]. After the primary beam interacts with a production target, the resulting fragments, formed through projectile fragmentation or fission, are directed to the Advanced Rare Isotope Separator (ARIS) [2, 3] for the crucial steps of separating, identifying, and purifying the fragments relevant to a particular experiment.

ARIS Layout

ARIS separates fragments in three stages, with the first stage in the so-called preseparator and the second and third stages in the so-called C-Bend. The preseparator consists of four superconducting dipoles (referred to here as SCD1, SCD2, SCD3, and SCD4) that bend the fragments vertically, while the C-Bend has four superconducting dipoles that

bend the fragments horizontally. Fragments of interest for an experiment are selected by their magnetic rigidity, based on $\text{LISE}^{++}_{\text{cute}}$ [4] simulations, after emerging from the target and passing through various detectors and wedge-shaped energy degraders. Therefore, an accurate calibration of these dipoles is crucial for the science program at FRIB.

In addition to dipole magnets, the beamline of ARIS contains six diagnostic boxes (DBs), which house beam-viewer systems. A beam-viewer system is also located in the wedge position in the preseparator. Each beam-viewer system consists of a viewer plate and camera. Hole patterns on the surface of the viewer plate are used to make an absolute position calibration of each viewer in order to accurately measure the beam spot size and position. When the beam strikes the scintillating surface of the viewer plate, light is emitted and captured in a video stream by the camera, thus allowing real-time optimization of the beam spot size and position using the Viola application [5].

A schematic diagram of ARIS showing the eight dipoles, preseparator wedge, and six diagnostic boxes is shown in Fig. 1.

MAGNETIC RIGIDITY CALIBRATION

Modeling

The design of the dipole is such that the reference trajectory experiences an integrated field,

$$K_z(I) = \int dS \cdot B_z = \varphi_0 \chi, \quad (1)$$

for excitation current I , bend angle φ_0 , and $\chi = p/q$ is the magnetic rigidity of a particle of momentum p and charge q . The units of K_z are Tm. An effective radius R_e can be defined such that,

$$\chi = B_{\text{NMR}} R_e(I), \quad (2)$$

where B_{NMR} is the field measured by the NMR, somewhere in the dipole region that gives a reasonably good proportionality to the field integral. The dependence can be measured with beams of known χ in order to establish a calibration.

When beam data is lacking, one can estimate R_e from dipole field data over the path of the trajectory such that,

$$R_e(I) = \frac{K(I)}{\varphi B_{\text{NMR}}}. \quad (3)$$

Field data from 3D models and measured fields along the ideal trajectory have been used to determine R_e over the full

* Work supported by the U.S. Department of Energy Office of Science under Cooperative Agreement DE-SC0023633, the State of Michigan, and Michigan State University.

[†] dombos@frib.msu.edu

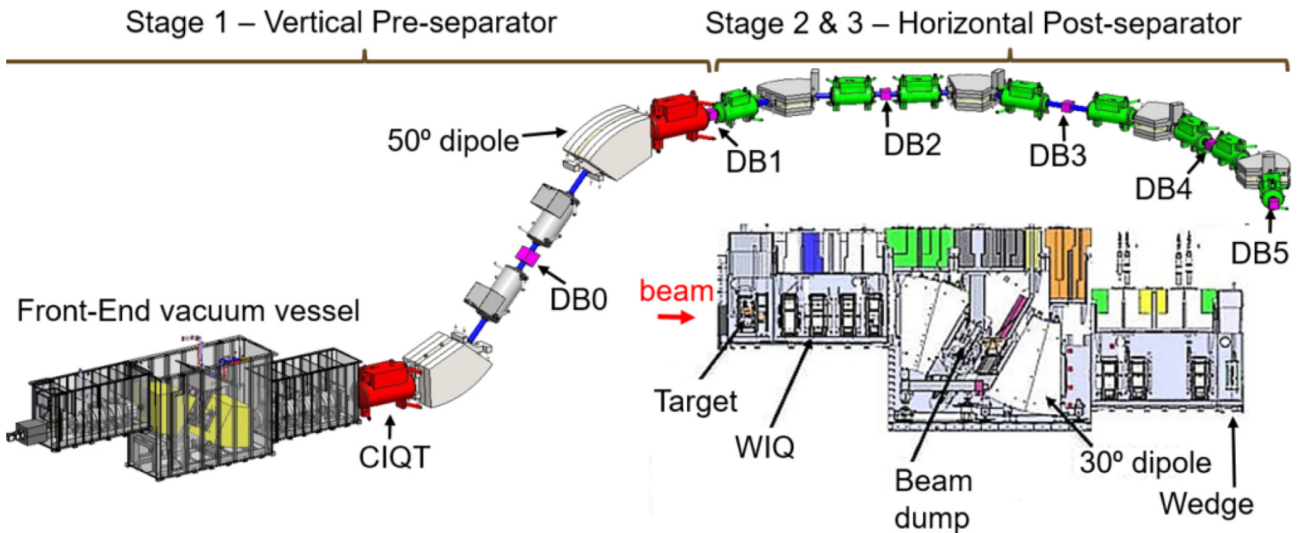


Figure 1: Schematic diagram of ARIS, showing the eight dipole magnets and six diagnostic boxes. The inset shows the inside of the front-end vacuum vessel, which houses the target, SCD1, the preseparator wedge, and SCD2. The horizontal post-separator is also referred to as the C-Bend. Figure adapted from [3].

excitation range of each dipole, and a good fit to the results is obtained by using a fifth-order polynomial of the form,

$$R_e(\chi) = a_0 + a_5\chi^5. \quad (4)$$

Procedure

The magnetic rigidity calibration of ARIS is based on the magnetic field measured at each dipole during the ideal position of the beam on the viewer plate using Viola. The dipole fields are measured with NMR sensors, which have an accuracy of <0.01%. Precise knowledge of the beam rigidity and position at the target position is crucial for the calibration measurements. Primary beam energies from the FRIB linac are known with about a precision of 0.1%. A production target was not inserted during the measurements in order to minimize uncertainties. As such, the thermal imaging system at the target position could not be used to verify the beam position there. The beam trajectory at the target position was optimized using non-intercepting beam-position monitors (BMPs) and minimizing steering (measured with the beam-viewer system at the preseparator wedge position) using quadrupoles closest to the target.

Measurements were performed during October 2024 to improve the magnetic rigidity calibration of ARIS up to DB5. Since the first quadrupole triplet after DB1 was not functioning at the time, it was only possible to calibrate up to DB1 (i.e., dipoles SCD1 through SCD4). A primary beam of ^{238}U of five charge states (73+ to 77+) was developed at 177, 160, 140, and 133 MeV/u to obtain rigidities from approximately 5.3 Tm to 6.5 Tm. No target was installed and the energy of each charge state was measured in the FRIB linac.

To expand the calibration point range for SCD3 and SCD4, additional measurements were performed with an aluminum degrader (nominal 0.020 mm thickness) at the preseparator

wedge position to strip the ^{238}U beam and induce additional change states. In total, 20 calibration points were measured for SCD1 and SCD2, and 26 (20 without stripping, 6 with stripping) were measured for SCD3 and SCD4. For the SCD1 and SCD2 calibration points, the magnetic rigidity of those two dipoles was adjusted to center the beam on the viewer plate at the preseparator wedge position (see Fig. 2 for an example). The fields were scaled by the same factor based on a setting at 4 Tm where the beam is known to be centered between the two dipoles. The preseparator momentum slits were closed down to define the center on the nearby downstream viewer. This defined the optical axis of the beam line. Once centered, the magnetic field of each dipole was recorded and used to calculate the effective radius from the measured magnetic field and the magnetic rigidity referenced to the FRIB linac. A similar procedure was followed for SCD3 and SCD4, adjusting the magnetic rigidity of those two dipoles until the beam was centered on the DB1 viewer.

After the experiment, it was discovered the actual position on the preseparator viewer was 2 mm below the measured position, which in turn meant that the measured magnetic field was low compared to the actual value needed to center the beam on the preseparator viewer (to prevent this from happening in the future, we now check that the drive for the preseparator viewer is calibrated before each beam time so that it is in the correct position). Consequently the measured magnetic field at SCD1 and SCD2 was increased by a percentage equal to $x / (25.6 \text{ mm} / \%)$ where x is the beam's transverse position (in mm) on the preseparator viewer and 25.6 mm / % is the dispersion of ARIS at the preseparator wedge position. This correction was deemed negligible for SCD3 and SCD4.

For SCD3 and SCD4, due to uncertainty in the aluminum degrader thickness, calibration points involving stripping

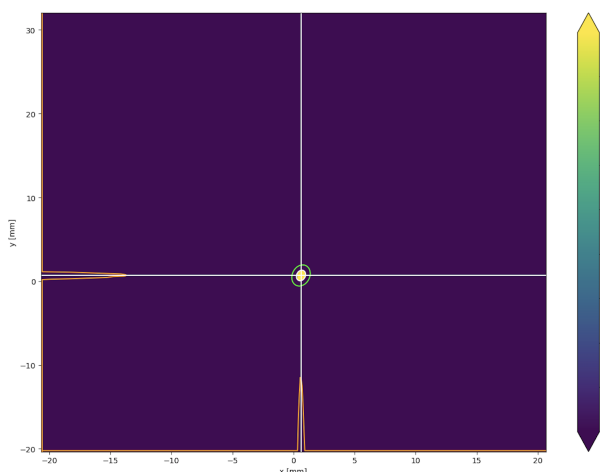


Figure 2: Camera image from Viola of 1.79 W of a 177.4 MeV/u $^{238}\text{U}^{73+}$ beam striking a scintillating viewer plate at the preseparator wedge position. The Y centroid is 0.6864 mm, indicating the beam is centered in the transverse direction. Intensity units are arbitrary.

were excluded from the model fit. For those data points involving stripping, LISE⁺⁺ simulations were performed to determine the necessary aluminum degrader thickness to align the data with the model fit. A thickness of 0.014 mm had the smallest mean squared error (MSE).

Results

The calibration points were fit using Eq. 4. The coefficients of Eq. 4 for SCD1, SCD2, SCD3, and SCD4 of ARIS are shown in Table 1.

Table 1: Best Fit Coefficients for Eq. 4 for the Magnetic Dipoles in the Preseparator of ARIS

Dipole	a_0	a_5
SCD1	4.143	-3.935e-06
SCD2	4.148	-3.935e-06
SCD3	4.126	-3.000e-06
SCD4	4.111	-3.000e-06

As an example, the fitted curve for SCD3 of ARIS is shown in Fig. 3, showing the data is described well by Eq. 4.

SUMMARY

The magnetic rigidity of the first four dipoles of ARIS have been calibrated using a ^{238}U beam from the FRIB

linac. These calibrations are critical for the efficient operation of ARIS, enabling optimized fragment transport and maximal yields, and are essential for accurate comparisons with LISE⁺⁺ simulations. Future work includes calibrating the last four dipoles of ARIS and expanding the calibration point range.

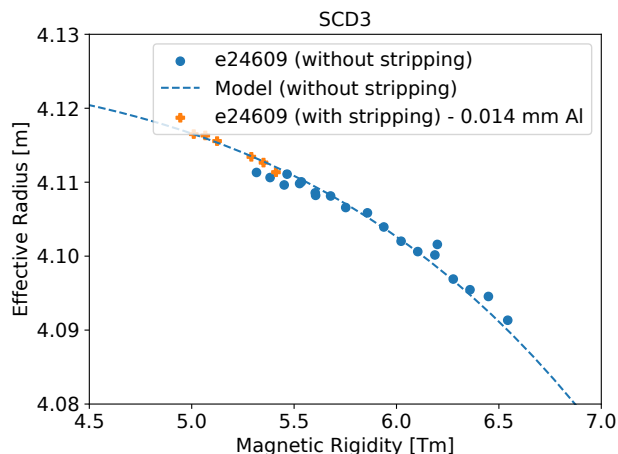


Figure 3: Magnetic rigidity calibration for SCD3 of ARIS.

REFERENCES

- [1] J. Wei *et al.*, “Accelerator commissioning and rare isotope identification at the Facility for Rare Isotope Beams”, *Mod. Phys. Lett. A*, vol. 37, no. 09, p. 2230006, Mar. 2022. doi:10.1142/s0217732322300063
- [2] M. Hausmann *et al.*, “Design of the Advanced Rare Isotope Separator ARIS at FRIB”, *Nucl. Instrum. Methods Phys. Res., Sect. B*, vol. 317, pp. 349–353, Dec. 2013. doi:10.1016/j.nimb.2013.06.042
- [3] M. Portillo *et al.*, “Commissioning of the Advanced Rare Isotope Separator ARIS at FRIB”, *Nucl. Instrum. Methods Phys. Res., Sect. B*, vol. 540, pp. 151–157, Jul. 2023. doi:10.1016/j.nimb.2023.04.025
- [4] O. B. Tarasov *et al.*, “LISE⁺⁺, the latest generation of the LISE⁺⁺ package, to simulate rare isotope production with fragment-separators”, *Nucl. Instrum. Methods Phys. Res., Sect. B*, vol. 541, pp. 4–7, Aug. 2023. doi:10.1016/j.nimb.2023.04.039
- [5] K. Fukushima, “Viola (Online Viewer Application)”, <https://github.com/kryv/viola>

FUTURE CHALLENGES FOR CERN'S ION INJECTOR COMPLEX

M. Slupecki*, D. del Álamo, R. Alemany Fernández, H. Bartosik, G. Bellodi, T. Birtwistle, D. Bodart, R. Bruce, J.M. Cravero, H. Damerau, J.A. Ferreira Somoza, R. García Alía, E. Grenier Boley, A. Huschauer, V. Kain, D. Kuchler, J.B. Lallement, T.M. Lang, A. Lasheen, E. Mahner, A.I. Michet, B. Mikulec, G. Papotti, A. Rossi, F. Roncarolo, S. Ramberger, R. Scrivens, N. Thaus, E. Waagaard¹, A. Waets, B. Woolley, CERN, Geneva, Switzerland
¹also at EPFL, Lausanne, Switzerland

Abstract

The ion injector complex at CERN supplies ions for collisions at the Large Hadron Collider (LHC) and for fixed-target physics programmes at the Super Proton Synchrotron (SPS) and Proton Synchrotron (PS). In recent years, there has been growing interest in experiments with ions lighter than lead within the ion-physics community. The NA61/SHINE collaboration has requested beams of oxygen, magnesium, and boron for Run 4 (2030-2033), while the HEARTS++ project proposal aims to enable switching between four ion species, with each transition occurring within 15 minutes. Additionally, LHC experiments are considering lighter-than-lead ion beams for Run 5 (2036-2041), pending an assessment of which particle species collisions offer higher nucleon-nucleon luminosity. Consolidating these future scenarios demands an evaluation of the light-ion performance of the present injector complex. This contribution discusses the challenges of the present injector complex in view of light-ion operation and a proposed upgrade of the ion complex to address future needs.

ION INJECTOR COMPLEX

The ion injector complex at CERN [1, 2] consists of the ion source, Linac3, Low-Energy Ion Ring (LEIR), Proton Synchrotron (PS) and Super Proton Synchrotron (SPS), which can deliver high-brightness ion beams for the LHC and experimental areas: East Area in PS, and North Area in SPS. The layout of the ion complex is shown in Fig. 1.

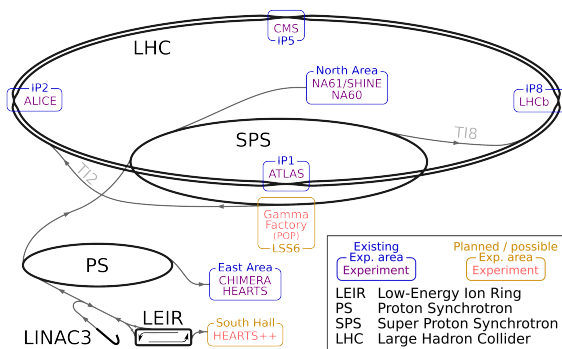


Figure 1: Layout of the ion injector chain, LHC, existing and future experimental areas that operate ion beams.

Ion beams are produced in the Electron Cyclotron Resonance (ECR) [3, 4] ion source of the Grenoble Test Source

* maciej.slupecki@cern.ch

(GTS-LHC) type [5]. It uses a permanent hexapole, resistive solenoids, and 14.5 GHz microwaves to confine and breed highly-charged ions in a plasma, which are ejected from the plasma chamber at 10 Hz repetition rate with pulsed extraction voltage of up to 20 kV. The source design is optimized for lead production, simple maintenance, and quick, non-invasive replacement of material (lead) samples in both of its microovens to minimize the impact on operational availability. During lead operation, the downtime of the source due to oven refills is limited to half a day every month.

Downstream of the source, the beam passes through the Low Energy Beam Transport (LEBT) of Linac3, where a single charge state is selected (Pb^{29+} , O^{4+} , Ne^{5+} , Mg^{7+} , etc.) by a setup composed of spectrometer magnets and a slit. The kinetic energy acceptance of 2.5 keV/u of the subsequent Radio-Frequency Quadrupole (RFQ) defines the extraction voltage used at the source for each ion species. The RFQ bunches and accelerates the beam to 250 keV/u. A set of three interdigital-H cavities further increases the beam energy to 4.2 MeV/u. Here, the beam may be stripped to optimize the ion lifetime in the subsequent accelerators and facilitate transport through the transfer line to LEIR, in which the maximum dipole currents define the minimum transportable charge-to-mass ratio of 0.25. Before reaching LEIR, at the end of Linac3, there are two small RF systems capable of compensating for the evolving beam energy losses due to the ageing of a stripping foil, and ramping beam energy by $\pm 2\%$ along the 300 μs long beam pulse to improve the efficiency of multiturn injection in the LEIR.

In LEIR, up to eight Linac3 beam pulses can be accumulated and cooled with the electron cooler. This is achieved by reducing beam energy spread of each injected pulse, dragging the beam to lower energy, merging it with the circulating stack from the previous injections, and making full phase-space available for the next injection [6]. The coasting beam is then captured by the RF into one, two or three bunches, accelerated to around 70 – 100 MeV/u depending on the ion species and its charge state, and extracted towards the PS. The PS accelerates the beam to the proton-equivalent momentum of 26 GeV/c. Bunch splitting, or batch compression can be performed if the frequency range of PS cavities is suitable for a given ion species and bunch spacing required at SPS and LHC. These RF manipulations are generally useful to reduce the impact of space-charge and intrabeam scattering effects. Splitting the bunches in PS results in lower per-bunch intensity and reduction of associated collective

effects, especially important for the long injection plateau in SPS.

The beam is fully stripped during the transfer from PS to SPS. Up to 14 injections from the LEIR-PS tandem are accumulated in SPS, which can then be slip-stacked to reduce the bunch separation from 100 to 50 ns and hence increase the maximum number of bunches in the LHC. Several of such trains of bunches accelerated to a proton-equivalent momentum of 450 GeV/c are delivered to the LHC.

In addition to the LHC, the ion users comprise SPS North Area experiments: NA61/SHINE and NA60, and PS East Area CHIMERA/HEARTS irradiation facility. All of them foresee upgrades and long-term operation, and request different ions for the future. A new Gamma Factory will also request atypical ions. Together, these experimental requests are described in the next paragraph and Fig. 2. To prepare the injector complex for some of their requests, a series of beam tests has been carried out to evaluate performance reach and stability of operation, as described in Sec. BEAM TEST RESULTS. Finally, the present complex cannot fulfill all expectations of the experiments, hence an Ion Injector Upgrade (ICU) proposal is being prepared to lift the known limitations and expand the capabilities of ion injectors. The preliminary ICU plan is described in Sec. ION COMPLEX UPGRADE STUDY.

FUTURE BEAMS LANDSCAPE

Traditionally, since the completion of the LHC Injectors Upgrade project [1, 2], the ion programme at CERN focused on the heaviest stable nuclei, ^{208}Pb . Recently, the potential of using ions lighter than lead has been identified. Argon and xenon beams were delivered for the NA61/SHINE experiment in 2015 and 2017 respectively. Xenon was also delivered to the LHC in 2017 for a short, 6-hours run [7] and there are plans to send oxygen in July 2025. During these exploratory ion runs, we realized that a coherent plan for future operation with ions is needed. Hence, the Future Ions Working Group (FIWG) was created at CERN in 2023. To drive an informed decision, the FIWG needed to quantify the performance reach for every requested ion, take into account experiment-specific requirements, propose a possible upgrade to meet them, and assess the impact of using more than one ion species on the operation of the complex while exploiting synergies between the requests. The table listing experiments and facilities that ask for different ions proposed (not yet approved) together with their timeline for operation is shown in Fig. 2.

The NA61++/SHINE is the primary requester of new ion beams in the SPS North Area during Run 4. The experiment investigates the critical point of the quark-gluon plasma (QGP). It aims to record the collisions of ion beams on a target made of the same nuclei as the beam, which reduces uncertainties by ensuring symmetric collisions. In addition, the ion species should be light ($Z \lesssim 20$) to enable measurements at the unexplored regions of the QGP phase diagram. The list of ions suitable for both the NA61++/SHINE and the

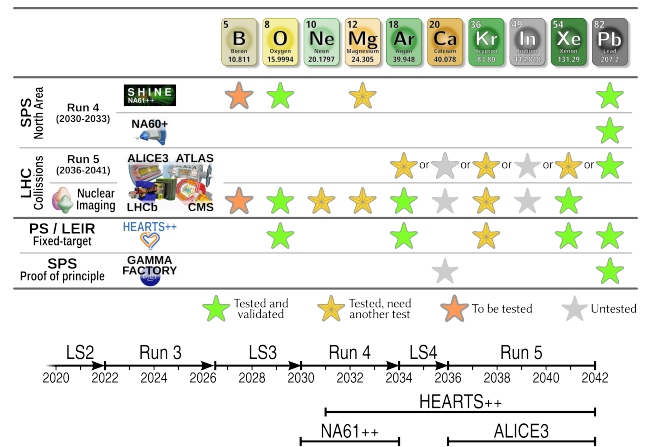


Figure 2: Top: Experiments or facilities and the list of ions they request (not approved). Bottom: Long-term schedule of the ion complex at CERN together with possible operational timelines of future experiments and facilities.

ion injector complex was reduced to three elements: boron, magnesium and oxygen [8]. However, the NA60+ experiment requests a lead beam [9]. To fulfill these mutually exclusive expectations, runs for each of these experiments will need to be scheduled at different times assuming the present operational scheme.

LHC experiments will continue using lead beam throughout Run 4. For Run 5 they request an ion species which maximizes nucleon-nucleon luminosity [10], with preference towards heavier elements. The FIWG launched a study to build an injector simulation model capable of predicting the development of intensities and emittances of beams from the ion source to the LHC for different ion species [11]. The preselected ion candidates for these studies include noble gases (Ar, Kr, Xe), ions with previous operational experience (indium, lead), and calcium, which shows strong synergy with other requests. Besides general tuning based on experimental beam measurements across the ion complex, the injector model needs beam intensity at the ion source for each ion species as input. The source performance is especially difficult to model, thus dedicated tests and measurements are needed. Of this list of ions, only calcium was not tested, mainly because beam intensities are expected to be low compared to noble gases. A dedicated krypton test performed in 2023 at the ion source yielded beam intensity, which when fed into the ion injector complex model [11] could make it the most promising candidate for the LHC Run 5. A follow-up test reaching further down the injector chain, possibly up to the PS, could be foreseen early in Run 4. In addition, LHC experiments recognize potential in short exploratory runs of different ions, such as the ongoing oxygen run and the subsequent neon run [12, 13].

In addition, the High-Energy Accelerators for Radiation Testing and Shielding (HEARTS++) proposal [14] aims to build a facility in the PS East Area or LEIR South Hall, providing radiation testing capabilities for materials and electronics to both scientific and commercial users. HEARTS

requires the capability to (i) deliver four of five different ion species in one day, (ii) switch between ions at user's will, and (iii) perform the transition between any two ions in less than 15 minutes. In addition, high beam intensities (comparable to LHC needs) and the considerable annual operation time (2000 hours) are required. The present ion injector complex cannot fulfill these requirements.

Finally, the Gamma Factory [15, 16] proposal requests partially stripped lead or calcium ions. The project is preparing a proof-of-principle setup for installation in the SPS. If successful, the Gamma Factory may be built at the LHC. In addition to producing intense polarized gamma beam, it may help to increase the ion beam brightness by cooling it down to reach emittances up to five times smaller than currently.

BEAM TEST RESULTS

This section summarizes recent beam tests and operational runs (excluding lead ions) conducted with the accelerator complex. The corresponding injector performance for each ion species is documented in Table 1.

Argon

In 2015 $^{40}\text{Ar}^{11+}$ was produced at the source and fully stripped to $^{40}\text{Ar}^{18+}$ at the transfer between PS and SPS. The run was dedicated to NA61 physics. Only 2.4 s single-injection cycle was used in LEIR. No attempt was made to commission a NOMINAL (longer multi-injection) cycle.

Xenon

Although the xenon run was originally requested by the NA61 experiment, the LHC detectors recognized its potential value and participated in the run as well. Table 1 shows NOMINAL xenon intensities on 12.10.2017, when the beam was injected into the LHC. $^{129}\text{Xe}^{22+}$ from the source was stripped to $^{129}\text{Xe}^{39+}$ at the end of Linac3, then fully stripped to $^{129}\text{Xe}^{54+}$ at PS-SPS transfer.

Krypton

With krypton as a promising LHC Run 5 candidate, a test to characterize the beam performance up to the Linac3 RFQ output was carried out in June 2023. The recorded maximum beam intensity served as input to evaluate expected performance of the injectors and LHC luminosity projections. $^{86}\text{Kr}^{22+}$ proved optimal for production at the source [17].

Magnesium

The magnesium test was performed in spring 2024 in preparation for NA61++/SHINE operation in Run 4. The test identified $^{24}\text{Mg}^{7+}$ as the optimal charge state. Table 1 shows achieved intensities using an improved NOMINAL cycle with four Linac3 injections. While performance was limited by high magnesium consumption (requiring frequent oven refills that disrupt operation and prevent optimal source conditioning), potential upgrades have been developed and will be implemented in the next test campaign [17–19].

Oxygen

At the moment of writing, the oxygen beam commissioning in the injectors for the LHC run is ongoing with the beam having just reached the SPS. Therefore, the oxygen performance shown in Table 1 is not final. In addition, an earlier oxygen test was performed in 2023 [19, 20], but its results are not reported here because they are superseded by the measurements obtained during the present preparations.

Neon

Two neon tests were done in 2025 in preparation for a short LHC run that is scheduled immediately after completion of the LHC oxygen run in July 2025. During the first test, the beam has not left Linac3 (as LEIR was still undergoing hardware commissioning after the yearly shutdown). The first test successfully proved that the ion source can switch relatively quickly between two gaseous ions with very similar rigidity ($^{16}\text{O}^{4+}$ and $^{20}\text{Ne}^{5+}$) and be ready to deliver a stable LHC-quality neon beam within 6 hours after switching with contamination of oxygen below 4%. The second test, between 27–28 May 2025, covered ion injectors up to PS and showed that no significant adaptations of accelerator configurations were needed when switching from $^{16}\text{O}^{4+}$ to $^{20}\text{Ne}^{5+}$, as anticipated. The neon row in Table 1 shows the highest intensities achieved on 27 May 2025 averaged over 20 minutes and should be considered a minimum sustained performance reach for the LHC run. However, at that time, LEIR and PS oxygen configurations, which were reused for neon beams, were not fully optimized. Hence, a major improvement is still expected.

Table 1: Beam currents of ion beam tests or runs achieved at the outputs of linac3 source (BCT05), RFQ (Faraday Cup), Linac3 (BCT41), and total beam intensities per cycle at ejection of LEIR and PS. See the text for specifics of every ion test or run.

Ion	I_b [μA]			Beam intensity [$10^{10} e$]	
	Src	RFQ	Ln3	LEIR	PS
^{40}Ar	140	–	60	2.2	2.0
^{129}Xe	175	–	34	4.0	1.4
^{86}Kr	130	83	–	–	–
^{24}Mg	50	25 [#]	19	1.8	1.0
^{16}O	239	121	93	5.7	3.6
^{20}Ne	181	–	59	2.3	1.4
$^{208}\text{Pb}^*$	182	118 [#]	31	10.3	9.0

[#]Calculated with transmission efficiency measured at different time

*Lead performance from the 2024 LHC ion run shown for reference

Future beam tests

The Linac3 team is preparing for two 4-month test periods in 2026–2027, during Long Shutdown 3 (LS3), a period normally reserved for thorough hardware maintenance

and upgrades, for testing the remaining beams requested by the NA61++/SHINE. Another magnesium test will be performed to validate the selected upgrade to improve the oven lifetime [18]. Moreover, boron beams have never been produced at CERN, so the test is essential to evaluate the efficacy of the boron beam production method at the source, expected performance, and search for possible issues.

In a longer perspective, after LS3, a time slot needs to be found to produce and send the krypton beam through the ion injector complex at least up to the PS. This is essential to collect more input for the injector model and use it to confirm the present uncertain predictions that the LHC nucleon-nucleon luminosity can be significantly higher when using krypton rather than lead beams. The performance reach of the calcium beam should also be tested for the Gamma Factory.

Finally, the HEARTS++ request to choose the beam from a menu of five different ions, with frequent switches between them, and with each transition taking no more than 15 minutes has to be considered and its implementation needs to be tested. This will involve injecting a mixture of several gases into the plasma chamber of the ion source. Up to now only a single operational gas or vapour, and a single buffer gas have been used. With increased number of mixed elements inside the plasma chamber, it is expected that tuning of the source will become more complicated, the intensity reach for each ion will decrease, and plasma stability will be harder to maintain. In such an operational configuration, beam diagnostics that can measure regularly the charge-state composition of the beam from the source will be required.

ION COMPLEX UPGRADE STUDY

While initially ion physics at CERN was only approved until the end of Run 4, it has now been tentatively extended to Run 5. This means that the ion complex will have to be maintained for almost a decade longer, hence the consolidation of ageing equipment needs to be addressed. The development of an extensive upgrade plan that takes advantage of synergies with consolidation and has a long exploitation time perspective became feasible.

Present limitations

The FIWG collected future ions requests and identified the following limitations of the ion injector complex:

- From the beginning of Run 4, the ion complex will be fully committed to operation with no time left to develop and commission new ion beams (assuming that the NA61++/SHINE will be approved for Run 4), including:
 - LHC Run 5 main ion candidates;
 - LHC Run 4 light ions for short runs;
 - Ion mixture needed by HEARTS (O, Ar, Kr, Xe, Pb), switching between these ions and performance evaluation in this mode of operation.
- Limited beam instrumentation leads to costly (in terms of workforce and time) development of new ion beams, and optimization of the existing ones, as we rely on trial and error. In addition, it is an impediment to increasing the automation of source tuning.
- The present single ion source generally allows for sequential operation of only up to 2 different ions (or ion mixtures) per year. Moreover, switching between ions (mixtures) takes weeks of downtime. Only a few specific exceptions are possible.
- There is an unexploited potential to improve the total ion beam intensity delivered by the injectors, translating into higher LHC luminosity, that can be unlocked by:
 - Reducing space-charge and intrabeam scattering losses by injecting higher-energy beam in SPS. Conversely, it requires accelerating the beam to a higher kinetic energy in PS, which is possible with the same accelerator by using an ion species with a higher charge state, necessitating an additional stripping stage between LEIR and PS.
 - Reducing the bunch spacing at SPS ejection from 50 ns to 25 ns with momentum slip-stacking technique, which requires the upstream PS to reduce the bunch spacing at ejection from standard 100 ns to 50 ns with radio-frequency (RF) batch compression manipulation.

Upgrade scope

To overcome these limitations and expand the capabilities of the ion injector complex in view of the next two decades of operation, a comprehensive upgrade plan has been proposed. It can be divided into two major parts:

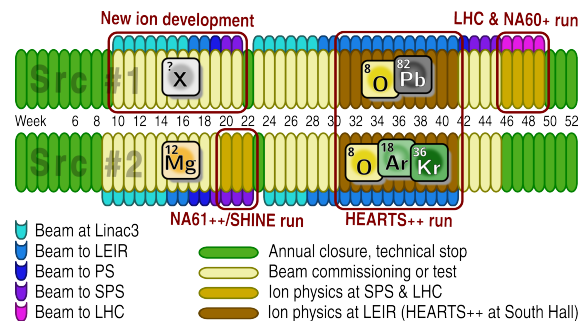


Figure 3: Example of possible ion injectors schedule in Run 4 assuming full ICU approval and realization, and approval of all experimental proposals.

Part 1 is concentrated around Linac3. It comprises the installation of a second ion source and its connection to the linac while ensuring that both sources can be operated in parallel and their performance can be continuously optimized together with a single RFQ. The latter implies the conversion of the DC magnets and other static LEBT components to pulsed versions. The availability of a second source would enable the scheduling of ion beams as in Fig. 3. The

figure shows separate sequences for both sources. Only HEARTS++ demands both sources to deliver beams concurrently. Additional beam development slots become available each year for the LHC or Gamma Factory beam developments, or for improvements of existing beams unrestricted by operational requirements.

Independently of the second source, the upgrade incorporates an improvement in the beam diagnostic capabilities. It includes installation of two new low-energy beam diagnostic lines (one per source) and additional non-beam-destructive instrumentation downstream (beam current transformer, two beam position monitors, and beam energy spread measurement setup), up to the LEIR injection. These upgrades mitigate limitations (a)-(b). The current layout of Linac3 LEBT is shown in Fig. 4 and its ICU version is illustrated in Fig. 5.

Part 2 focuses on lifting the limitation (d). It includes the installation of a new stripper system in the transfer line between PS and LEIR. An update of low-level RF in PS is also necessary to enable synchronization of LEIR-to-PS beam transfer despite a change in PS revolution frequency as a consequence of the energy loss during stripping. Additionally, two new RF cavities must be developed and installed in the PS to cover the RF frequency range required to compress four bunches and reduce the spacing between them to 50 ns.

Efficient implementation of this upgrade programme would aim for the completion of installation at the end of LS3 and before LHC restarts operation into Run 4. However, even if the ICU is approved and funded very soon, implementation during LS3 is very challenging because of the long lead time required for design, integration, and manufacturing, and resource conflict with the High-Luminosity LHC installation. Nevertheless, high-impact infrastructure modifications could still be implemented during LS3. The Part 1 and stripper could be installed in stages during Run 4, and the installation of the rest of Part 2 could be planned for LS4.

SUMMARY AND OUTLOOK

The ion landscape has been evolving at CERN for several years now. The experiments and facilities request beams of new ions that are lighter than lead. Many ion species have been operated to date, including argon, xenon, krypton, oxygen, magnesium, and neon. However, future experimental requests are challenging for the ion injectors, which were originally designed and later optimized to maximize lead performance, but were not built with the flexibility to perform well with different ion species in mind. Thus, extensive preparations are needed well in advance before any new beams can be reliably delivered. After initial feasibility studies, various risk assessments, and implementation of obvious mitigations, actual beam tests are essential to facilitate future operation within accepted schedules and to identify bottlenecks and hard-to-predict operational issues.

However, with the recent increase in the operating time of the complex and handling of more than a single ion species per year, several limitations have been revealed. The com-

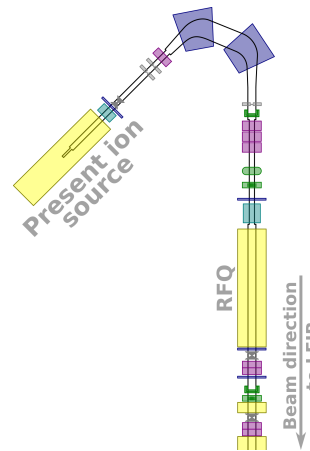


Figure 4: Present layout of the low-energy region of Linac3.

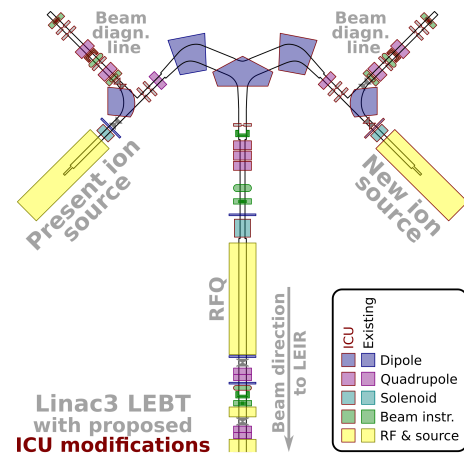


Figure 5: ICU upgrade proposal for the low-energy region of Linac3. The sketch is conceptual – the type and position of the second source is subject to change, as well as the beamline connecting it to the linac.

plex will no longer be able to develop new beams after LS3 because it is fully committed to operation. On the one hand, it shows that there is growing interest in more versatile and extended programmes for ions. On the other hand, the present and future demand exceeds availability and capability. Especially HEARTS++ requirements cannot be realized with the present complex. To overcome these limitations, the ICU proposal is being prepared. It aims at the installation of the second Linac3 source and the improvement of beam instrumentation that leads to better automation in tuning of the sources and the capability to switch ions within 15 minutes. The ICU also plans to improve the ion stripping flexibility, upgrade the PS RF system to reduce beam intensity losses due to collective effects, and to increase the maximum number of bunches in the LHC, and consequently, the luminosity production rate. To profit efficiently from the ICU, the decision on its approval must be taken in 6-12 months.

REFERENCES

- [1] M. Benedikt *et al.*, *LHC Design Report*. CERN, 2004. doi:10.5170/CERN-2004-003-V-3
- [2] J. Coupard *et al.*, “LHC injectors upgrade, technical design report,” CERN, Tech. Rep., 2016. doi:10.17181/CERN.L6VM.UOMS
- [3] G. Melin, A. G. Drentje, A. Girard, and D. Hitz, “Ion behavior and gas mixing in electron cyclotron resonance plasmas as sources of highly charged ions,” *J. Appl. Phys.*, vol. 86, no. 9, pp. 4772–4779, 1999. doi:10.1063/1.371442
- [4] A. Efremov *et al.*, “Performance of the ion source DECRIS-14-2,” *Rev. Sci. Instrum.*, vol. 69, no. 2, pp. 662–664, 1998. doi:10.1063/1.1148567
- [5] C. E. Hill *et al.*, “GTS-LHC: A new source for the LHC ion injector chain,” *AIP Conf. Proc.*, vol. 749, pp. 127–130, 2005. doi:10.1063/1.1893381
- [6] M. Chanel, “LEIR: The low energy ion ring at CERN,” *Nucl. Instrum. Methods Phys. Res., A*, vol. 532, pp. 137–143, 2004. <https://cds.cern.ch/record/557588>
- [7] M. Schaumann *et al.*, “First xenon-xenon collisions in the LHC,” *Proceedings of the International Particle Accelerator Conference (IPAC'18): Vancouver, Canada*, p. 180, 2018. <http://accelconf.web.cern.ch/AccelConf/ipac2018/papers/mopmf039.pdf>
- [8] R. Alemany Fernandez *et al.*, “Future ions in the CERN accelerator complex WG: Post-LS3 NA61/SHINE light ion beam requirements feasibility study: Source operation, radiation protection impact in LINAC 3, LEIR and PS and risk assessment in LEIR,” *CERN-ACC-NOTE-2024-0022*, 2024. <https://cds.cern.ch/record/2916353>
- [9] G. Alocco, “Overview of the NA60+ experiment at the CERN SPS,” *EPJ Web Conf.*, vol. 296, p. 08 005, 2024. doi:10.1051/epjconf/202429608005
- [10] ALICE Collaboration, “Letter of intent for ALICE 3: A next-generation heavy-ion experiment at the LHC,” *arXiv:2211.02491*, 2022. doi:10.48550/arXiv.2211.02491
- [11] E. Waagaard, R. Bruce, R. Alemany-Fernández, H. Bartosik, and J. Jowett, “Charting the luminosity capabilities of the CERN large hadron collider with various nuclear species,” (in preparation), 2025.
- [12] G. Giacalone *et al.*, “The unexpected uses of a bowling pin: Exploiting ^{20}Ne isotopes for precision characterizations of collectivity in small systems,” *arXiv:2402.05995*, 2024. doi:10.48550/arXiv.2402.05995
- [13] G. Giacalone *et al.*, “Anisotropic flow in fixed-target $^{208}\text{Pb}+^{20}\text{Ne}$ collisions as a probe of quark-gluon plasma,” *arXiv:2405.20210*, 2025. doi:10.48550/arXiv.2405.20210
- [14] R. García Alía *et al.*, “The HEARTS EU project and its initial results on fragmented high-energy heavy-ion single-event effects testing,” *IEEE Trans. Nucl. Sci.*, vol. 72, no. 4, pp. 1040–1049, 2025. doi:10.1109/TNS.2025.3530502
- [15] M. W. Krasny, “The Gamma Factory proposal for CERN,” *arXiv:1511.07794*, 2015. doi:10.48550/arXiv.1511.07794
- [16] M. W. Krasny, “Gamma factory,” in *The Future of the Large Hadron Collider*. 2023, ch. Chapter 21, pp. 297–303. doi:10.1142/9789811280184_0021
- [17] D. Küchler, B. Bhaskar, G. Bellodi, M. Slupecki, and R. Scrivens, “Light ions from the GTS-LHC ion source for future physics at CERN,” *26th International workshop on ECR ion sources*, 2024. <https://cds.cern.ch/record/2916870>
- [18] M. Slupecki *et al.*, “CERN ion injector complex performance during 2024 magnesium test,” *CERN-ACC-NOTE-2025-0006*, 2025. <https://cds.cern.ch/record/2929494>
- [19] M. Slupecki *et al.*, “Development of new ion beams at the cern ion injector complex for future physics programmes,” English, in *Proc. IPAC'25, Taipei, Taiwan*, 2025, pp. 704–707. doi:10.18429/JACoW-IPAC25-MOPS047
- [20] M. Slupecki *et al.*, “LHC oxygen run preparation in the CERN injector complex,” *CERN-ACC-NOTE-2024-0001*, 2024. <https://cds.cern.ch/record/2888741>

MAINTAINING OPTIMAL BEAM BRIGHTNESS AND LUMINOSITY USING MACHINE LEARNING*

W. Lin[†], Brookhaven National Laboratory, Upton, NY, USA

Abstract

After many decades of successful operation, human operators have become very good at finding the optimal conditions that maximize the luminosity in the Relativistic Heavy Ion Collider (RHIC). However, since the entire accelerator chain for RHIC is a constantly varying complex system, maintaining such optimal condition is a demanding task. There is also no metric that can measurably determine if those optimal conditions are truly optimal, given the degrees of freedom are very high and there are multiple and competing objectives. In this work we will describe how we use machine learning and improved physics models to build systems for optimizing the beam brightness during injection at the BNL Booster and AGS synchrotrons and efforts to maintain maximum luminosity in RHIC.

INTRODUCTION

Large particle accelerators like the Relativistic Heavy Ion Collider (RHIC) are large systems that require analysis and optimization of thousands of parameters to operate at peak performance. With the more complex Electron-Ion Collider (EIC) planned for future construction, such analysis will quickly become impossible to be performed entirely by human operators. Machine learning (ML) has shown great promise in addressing long-standing challenges in accelerator physics, such as automated tuning and anomaly detection. In this work, we study two major ML techniques and their applications for finding and maintaining optimal beam quality in the RHIC complex: Bayesian optimization (BO) and reinforcement learning (RL).

MACHINE LEARNING METHODS

Bayesian Optimization

Bayesian optimization (BO) is a technique aiming to optimize an objective function f with as few samples as possible. It is particularly useful when the explicit expression of f is unknown and evaluation of f is expensive. Due to its sample efficiency and ability to learn without a preexisting model, BO has been widely implemented to solve complex particle accelerator control problems, as summarized in Algorithm 1 [1]. In general, BO consists of three steps. First, BO constructs a statistical surrogate model of the objective function and if necessary, constraining functions, based on measured data. The model is usually built with Gaussian process (GP) [2]. Second, BO defines an acquisition function based on the GP model, which quantifies the relative

benefit of potential future measurements in input space in order to achieve optimization goals. And finally, BO solves for the point (or set of points) that maximizes the acquisition function, which means it is predicted to provide the most benefit towards the final optimization goals.

Algorithm 1 Bayesian Optimization

Require: Objective function f , observation dataset \mathcal{D}_N , GP prior $M = \mathcal{GP}(\mu(x), k(x, x'))$, acquisition function $\mathcal{A}(\cdot)$.

- 1: **for** $t = 1, 2, \dots$ **do**
- 2: Decide a new sample point $x_{new} = \operatorname{argmax}_x \mathcal{A}(x | \mathcal{D}_N)$.
- 3: Query the objective $y_{new} = f(x_{new}) + \epsilon$.
- 4: Update \mathcal{D}_N and the GP model.
- 5: **end for**

Reinforcement Learning

Reinforcement learning (RL) is a machine learning framework where an agent interacts with an environment and learns to make decisions that maximize a reward [3]. Although less explored than BO, RL has also demonstrated success in accelerator control processes [4]. Despite its dependency on large amount of training data, RL algorithm is more suited for continuous control problems. In general, a RL system consists of several key components: an agent, an environment, a policy, and a reward, as summarized in Algorithm 2. An environment is the system that we want to optimize. A representation of the environment at a specific time is called a state. An agent interacts with the environment, receives observations, and make decisions based on its policy. The decisions made by the agent are called actions. A policy dictates how the agent choose actions, by establish a mapping between the states and the actions. A reward defines the goal of the algorithm. At each step, the environment generates a numerical reward that signals how close it is to the optimal state, and the agent aims to maximize the total reward it receives.

Algorithm 2 Reinforcement Learning

Require: Environment with initial state S_0 , policy \mathcal{P} , reward \mathcal{R} .

- 1: **for** $t = 1, 2, \dots$ **do**
- 2: Agent observes system state S_t .
- 3: Agent chooses an action based on policy $\mathcal{A}_t = \mathcal{P}_t(S_t)$.
- 4: Agent receives a reward \mathcal{R}_t based on action \mathcal{A}_t taken on state S_t .
- 5: Agent updates policy \mathcal{P} .
- 6: **end for**

* Work supported by Brookhaven Science Associates, LLC under Contract No. DE-SC0012704 and No. DE-SC0024287 with the U.S. Department of Energy.

[†] wlin1@bnl.gov

COOLING OPTIMIZATION

The Low Energy RHIC electron Cooler (LEReC) is a non-magnetized cooler of ion beams in RHIC. Electrons are generated by the gun and accelerated to 1.6–2 MeV by the superconducting RF cavity to match the energy of ions in RHIC. The accelerated electron bunches then travel through the transport line to interact with ions in two cooling sections in the “Yellow” and “Blue” RHIC ring (Fig. 1). Ions experience a cooling force from the co-traveling electrons due to Coulomb interaction. As a result, the ion beam has a reduced energy spread and increased phase space density [5]. One of the key factors affecting the cooling performance is the alignment of the electron beam trajectory with respect to the ion beam.

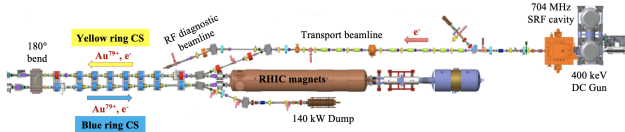


Figure 1: Layout of the LEReC system [6].

The ion beam has a straight trajectory in the LEReC cooling sections due to its high magnetic rigidity. The lower-rigidity electron is controlled by 8 pairs of correctors and is monitored by 8 beam position monitors (BPMs) in each cooling section. We constructed a BO algorithm that tunes the LEReC correctors to maximize cooling rate by optimizing the electron-ion trajectory alignment [6].

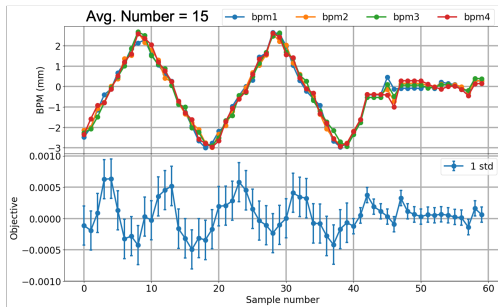


Figure 2: BO results of the LEReC cooling performance [6]. Top: locations of electron trajectory measured at 4 BPMs. Bottom: Cooling rate $-\lambda$ in the LEReC line.

The algorithm objective is to optimize the transverse cooling rate λ , defined as the decreasing speed of the transverse ion beam size δ . It is calculated as $\lambda = (1/\text{avg}(\delta))(\text{avg}(d\delta)/dt)$. More negative λ means faster cooling, so the goal is to maximize $-\lambda$. Averaging over N ion beam size points reduced objective instability due to noise in the ion beam size signals. Optimization results using $N = 15$ are shown in Fig. 2. The BO algorithm was set to begin optimization with the worst possible electron trajectory ($x = -3, y = -3$), but it reached a close neighborhood of the real optimum ($x = 0, y = 0$) in three steps,

and was able to converge and maintain the optimum. The system reaches optimal status when cooling balances growth from intra-beam scattering (IBS), so λ approaches 0 once the system reaches equilibrium.

INJECTION OPTIMIZATION

Electron Beam Ion Source

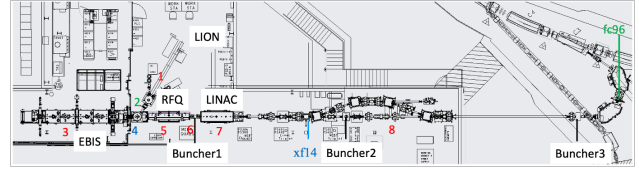


Figure 3: Layout of the EBIS line [7].

Electron Beam Ion Source (EBIS) is a compact heavy ion accelerator developed to serve as pre-injector for both RHIC and NASA Space Radiation Laboratory (NSRL) [8]. It is capable of producing short, high-intensity ion pulses, which are ideal for fast injection and quick species transition. The EBIS system has several beamline sections (Fig. 3), which are LION (Laser Ion Source), EBIS Injection Line, EBIS, EBIS Extraction Line, radio-frequency quadrupole (RFQ), medium energy beam transport (MEBT), Linac, and high energy beam transport (HEBT). Each section has many different control parameters that influence the beam performance, making the entire system difficult to optimize.

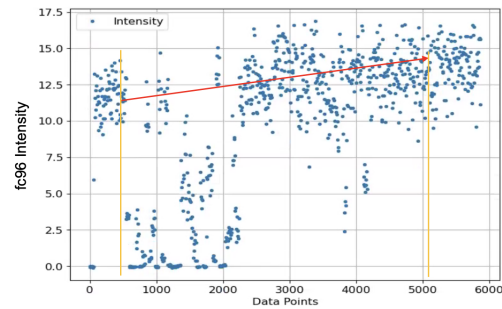


Figure 4: BO results of the EBIS injection line [7].

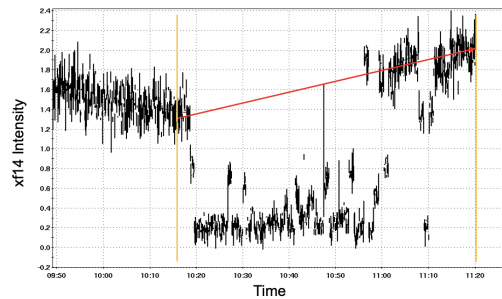


Figure 5: BO results of the EBIS extraction line [7].

In order to optimize EBIS beam intensity, we designed a BO algorithm based on the GPTune package [9] developed

by LBNL. For injection line optimization, beam intensity is measured at Faraday-cup FC96, and 9 control parameters are used. For extraction line optimization, beam intensity is measured at current transformer XF14, and 10 control parameters are used [7]. Figure 4 shows the FC96 beam intensity signal during the injection optimization process (between the two vertical lines). The algorithm improved the average intensity by 22%. Similarly, Fig. 5 shows the XF14 beam intensity signal during the extraction optimization process. The algorithm improved the average intensity by 43%.

Linac to Booster Transfer Line

For polarized proton operation at RHIC, H⁻ beam is created at the Optically Pumped Polarized Ion Source (OPPI) and accelerated to 200 MeV in the Linac, and transported to the Booster through the Linac to Booster (LtB) transfer line [10]. After the beam enters the Booster, it is scraped intentionally in both horizontal and vertical planes to reduce the emittance and intensity to RHIC requirements. There are 13 quadrupoles and 16 correctors in the LtB line used to optically match the incoming beam into the Booster ring (Fig. 6). Booster injection process sets maximum beam brightness for rest of acceleration through RHIC.

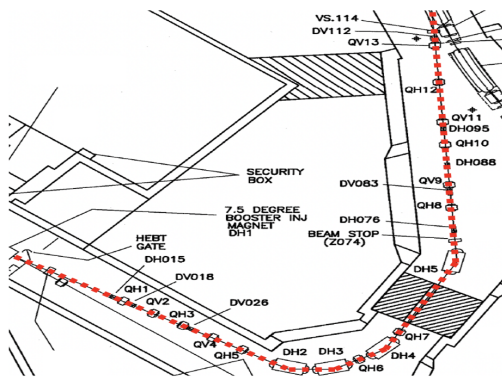


Figure 6: Layout of the Linac to Booster (LtB) transfer line (outlined with red dashed line) [10].

To streamline the Booster injection processes with ML techniques, we developed and tested a BO algorithm to automatically tune the LtB magnets to maximize beam brightness after injection into the Booster. The BO algorithm was constructed using the Xopt package [11] developed by SLAC.

This BO algorithm is set to maximize beam intensity after passing the fixed scrapers, which means the beam size going through the scrapers is minimized, also minimizing the horizontal and vertical emittances. This ultimately maximizes the luminosity in RHIC. We intentionally de-tuned the LtB line before BO process started. The BO used power supply currents of correctors and quadrupoles to maximize beam intensity after Booster injection, scraping, and acceleration. The algorithm was able to converge using four control variables, as shown in Fig. 7. Beam intensities and beam sizes, monitored in the Booster to AGS (BtA) transfer line, at least as good as the established optimum were quickly achieved.

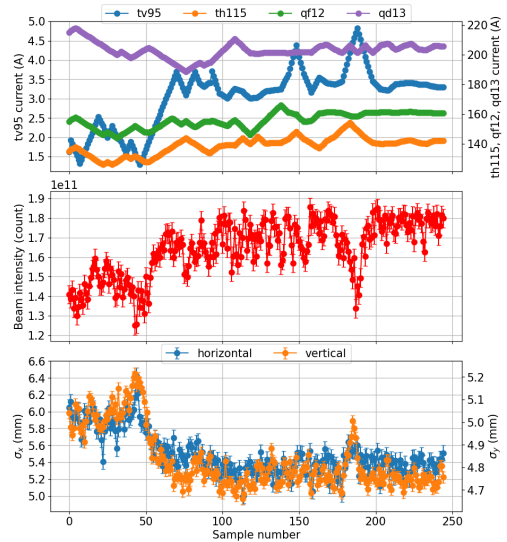


Figure 7: BO results of the Booster injection process. Top: currents of two correctors and two quadrupoles in the LtB. Middle: beam intensity after Booster injection. Bottom: Beam size in the BtA line during BO.

Booster to AGS Transfer Line

The Booster to AGS (BtA) transfer line transports beam bunches from the Booster to the AGS and also matches the beam Twiss parameters and dispersion functions to the circulating beam in the AGS at the injection point. It consists of 15 quadrupoles, two bends, a stripping foil for operations with heavy ions, and four profile monitors [12] (Fig. 8).

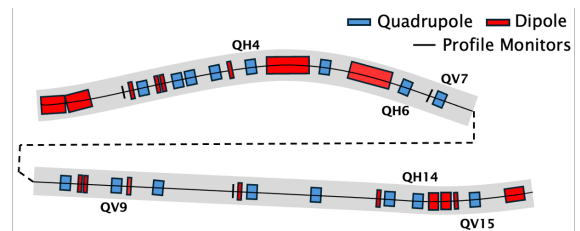


Figure 8: Layout of the Booster to AGS (BtA) transfer line [13].

We developed a BO algorithm similar to the LtB algorithm to improve the AGS injection. The algorithm aims to maximize the transmission efficiency from Booster to AGS, i.e., beam intensity at AGS injection divided by beam intensity before Booster extraction. We tested the algorithm on a untuned BtA setup, and was able to significantly improve the transmission using 4 BtA correctors, as shown in Fig. 9.

A RL algorithm was also developed with the BtA physics simulation model to minimize AGS injection mismatch. A mismatch between BtA and the AGS can be quantified by

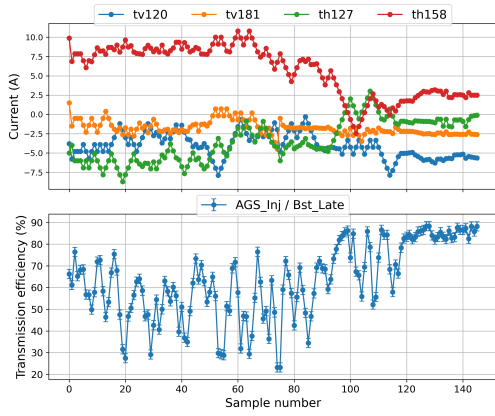


Figure 9: BO results for the AGS injection process. Top: currents of four correctors in the BtA. Bottom: transmission efficiency from Booster to AGS.

the growth in beam size (Eq. 1).

$$\frac{\sigma_x^2}{\sigma_{0x}^2} = 1 + \frac{1}{2} |\det \Delta J_x| + \frac{\Delta D_x^2 + (\beta_x \Delta D'_x + \alpha_x \Delta D_x)^2}{2 \sigma_{0x}^2} \sigma_{px}^2$$

$$\text{where } J_x = \begin{pmatrix} \alpha_x & \beta_x \\ -\gamma_x & -\alpha_x \end{pmatrix}$$

(1)

The RL environment was developed with the Gymnasium package (formerly OpenAI Gym) [14] and integrates the BtA model in Bmad [15]. Currents of six quadrupoles are chosen as control parameters. Operationally reasonable values are used for σ_{0x} and σ_{px} . The reward \mathcal{R} is defined as a function of the beam size growth ratio $\rho = \frac{\sigma}{\sigma_0}$. Ideally, we want the optimal result $\rho_* = 1$, therefore, we define a “good” ratio to be in the range $\rho \leq 1.15$. The reward function $\tilde{\mathcal{R}}$ is defined as a piecewise function of ρ (Eq. 2). The RL agent tries to minimize the mismatch effect by maximizing the award.

$$\tilde{\mathcal{R}}(\rho) = \begin{cases} -66.67(\rho - 1) + 10 & \text{if } \rho \leq 1.15 \\ -k\rho + b & \text{otherwise} \end{cases} \quad (2)$$

We employed Recurrent Proximal Policy Optimization (RPPO) from the Stable Baselines3 library [16]. The agent was trained across environments with varying measurement noise levels: 0, 5, 10, 15, 20, 25, 30%. RPPO demonstrated stable convergence for increasing levels of measurement noise [13].

Table 1 shows the the RL found currents compared to the operational values, and Fig. 10 shows the resulting beta function. The settings found by the RL agent are actually more favorable because the total current is lower and the beta function is smaller along the BtA line, which leads to smaller beam size.

BUNCH MERGING

Polarized proton beam bunches are split into two or four smaller bunches in the Booster to reduce the space-charge effect and increase polarization. Just before transferring

Table 1: BtA Magnet Currents Comparison

Magnet	Original (A)	RL Agent (A)
QV7	705.96	655.96
QV9	640.01	690.00
QV15	277.29	258.51
QH4	529.54	530.55
QH6	806.73	792.23
QH14	602.97	596.47

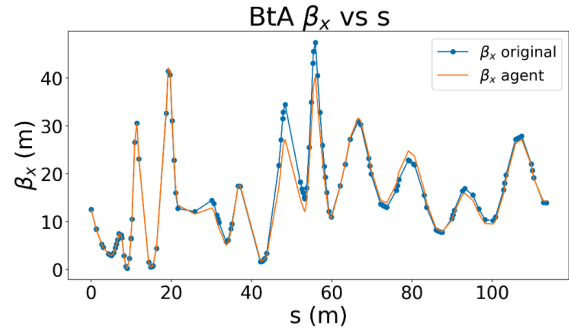


Figure 10: RL results for beta function in the BtA.

to RHIC, the smaller bunches are combined back into one bunch at the AGS extraction energy [17]. Currently, the bunch merging procedure is done by expert operators observing mountain-range displays of wall current monitor (WCM) data (Fig. 11) and tuning various control parameters empirically. With this approach, it is not only difficult and time consuming to obtain the maximal bunch merging performance, but also impractical to maintain consistently.

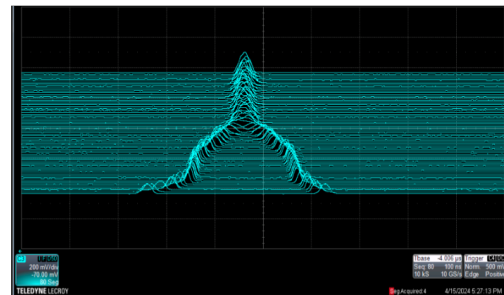


Figure 11: Mountain range display of the wall current monitor signals for a 2 to 1 merge in the AGS.

We proposed a Reinforcement Learning (RL) based approach to perform the AGS bunch merging process. The RL agent was trained on a bunch merge physics model written in Julia [18], which takes the RF cavity settings (voltages and phases) as inputs and returns information of the final merged beam profile including bunch length and bunch center. The goal of the agent is to minimize bunch length and center variation. During optimization test in the real machine, the WCM signals are processed to produce a file with beam profile information during each cycle to feed into the trained RL agent, as shown in Fig. 12.

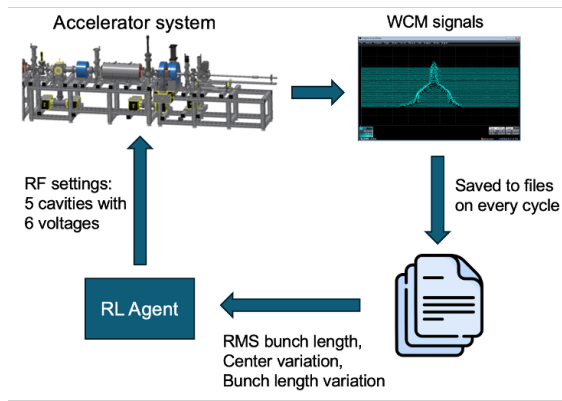


Figure 12: RL process for optimizing bunch merge process.

Figure 13 shows the results of the RL optimization test. We changed the RF settings to use a bad merge as the starting point. The RL algorithm was able to significantly improve the merge after just one step, and was able to maintain a decent merge quality with following steps.

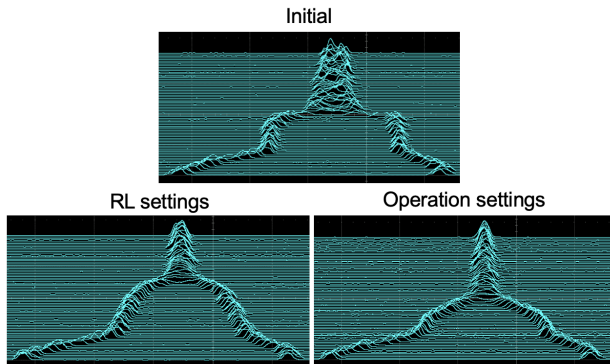


Figure 13: RL result for AGS bunch merge. Top: bad initial merge. Bottom left: merge found by RL agent. Bottom right: operational merge.

CONCLUSION

In this work, we summarized the performance of BO and RL algorithms tested on multiple experiments and accelerators at the RHIC complex. Promising results indicate that ML algorithms can be powerful tools for various optimization problems, suitable for fast and complicated tuning in real time. Beam brightness and luminosity will benefit significantly from incorporation of ML algorithms in the accelerator control system.

REFERENCES

- [1] R. Roussel *et al.*, “Bayesian optimization algorithms for accelerator physics”, *Phys. Rev. Accel. Beams*, vol. 27, no. 8, p. 084801, Aug. 2024. doi:10.1103/PhysRevAccelBeams.27.084801
- [2] C. E. Rasmussen and C. K. I. Williams, *Gaussian Processes for Machine Learning*. Cambridge, MA, United States: The MIT Press, 2006.
- [3] R. S. Sutton and A. G. Barto, *Reinforcement Learning: An Introduction*, 2nd ed.. Cambridge, MA, United States: The MIT Press, 2018.
- [4] J. Kaiser *et al.*, “Reinforcement learning-trained optimisers and Bayesian optimisation for online particle accelerator tuning”, *Sci. Rep.*, vol. 14, no. 1, p. 15733, Jul. 2024. doi:10.1038/s41598-024-66263-y
- [5] Y. S. Derbenev, “Theory of electron cooling”, arXiv:1703.09735 [physics.acc-ph], 2017. doi:10.48550/arXiv.1703.09735
- [6] Y. Gao *et al.*, “Bayesian optimization experiment for trajectory alignment at the low energy RHIC electron cooling system”, *Phys. Rev. Accel. Beams*, vol. 25, no. 1, p. 014601, Jan. 2022. doi:10.1103/physrevaccelbeams.25.014601
- [7] X. Gu *et al.*, “Enhancing beam intensity in RHIC EBIS beam-line via GPTune machine learning-driven optimization”, in *Proc. IPAC’24*, Nashville, TN, USA, May 2024, pp. 118–120. doi:10.18429/JACoW-IPAC2024-MOPC25
- [8] J. G. Alessi *et al.*, “The Brookhaven National Laboratory electron beam ion source for RHIC”, *Rev. Sci. Instrum.*, vol. 81, no. 2, p. 02A509, Feb. 2010. doi:10.1063/1.3292937
- [9] Y. Liu *et al.*, “GPTune: multitask learning for autotuning exascale applications”, *Proc. PPOPP ’21, Virtual Event Republic of Korea*, Feb. 2021, pp. 234–246. doi:10.1145/3437801.3441621
- [10] R. K. Reece *et al.*, “First Results of Proton Injection Commissioning of the AGS Booster Synchrotron”, in *Proc. PAC’91*, San Francisco, CA, USA, May 1991, pp. 839–842.
- [11] R. Roussel, C. Mayes, A. Edelen, and A. Bartnik, “Xopt: A simplified framework for optimization of accelerator problems using advanced algorithms”, in *Proc. IPAC’23*, Venice, Italy, May 2023, pp. 4847–4850. doi:10.18429/JACoW-IPAC2023-THPL164
- [12] K. A. Brown *et al.*, “The Booster to AGS Transfer Line: Comparison between Model and Measurements”, in *Proc. PAC’09*, Vancouver, Canada, May 2009, paper TH6PFP014, pp. 3726–3728.
- [13] T. Balasooriya *et al.*, “Reinforcement Learning for Charged Particle Beam Control to Minimize Injection Mismatch in Particle Accelerators”, *ICASSP 2025 - 2025 IEEE Int. Conf. on Acoustics, Speech and Signal Processing (ICASSP)*, Apr. 2025, pp. 1–5. doi:10.1109/icassp49660.2025.10889501
- [14] M. Towers *et al.*, “Gymnasium: A Standard Interface for Reinforcement Learning Environments”, arXiv:2407.17032 [cs.LG], 2024. doi:10.48550/arXiv.2407.17032
- [15] D. Sagan, “Bmad: A relativistic charged particle simulation library”, *Nucl. Instrum. Methods Phys. Res., Sect. A*, vol. 558, no. 1, pp. 356–359, Mar. 2006. doi:10.1016/j.nima.2005.11.001
- [16] A. Raffin *et al.*, “Stable-Baselines3: Reliable Reinforcement Learning Implementations,” *J. Mach. Learn. Res.*, vol. 22, no. 268, pp. 1-8, 2021.
- [17] Y. Gao *et al.*, “Optimization of AGS bunch merging with reinforcement learning”, in *Proc. IPAC’24*, Nashville, TN, USA, May 2024, pp. 1782–1785. doi:10.18429/JACoW-IPAC2024-TUPS53

- [18] J. Bezanson, A. Edelman, S. Karpinski, and V. B. Shah, “Julia: A Fresh Approach to Numerical Computing”, *SIAM Rev.*, vol. 59, no. 1, pp. 65–98, Jan. 2017. doi : 10.1137/141000671

BOOST OF ALPI SUPERCONDUCTING LINAC PERFORMANCES USING AI TECHNIQUES

L. Bellan*, I. R. Andriamaro, L. Antoniazzi, D. Bortolato, O. Carletto, L. Centofante, M. Comunian, E. Fagotti, A. Galatà, C. S. Gallo, F. Gelain, M. Giacchini, F. Grespan, D. Marcato, M. Montis, E. Munaron, Y. K. Ong¹, A. Pisent, M. Roetta, G. Savarese
INFN-LNL, Legnaro, Italy

¹also at University of Sapienza, Rome, Italy

Abstract

The heavy ion superconductive linac ALPI has been operating at the Legnaro National Laboratories since its completion in the 1990s. As the first generation in Europe, it featured several innovative techniques and design weaknesses, such as very small transverse and longitudinal acceptances. This led to long setting times and low transmission rates of 35%, compared to 93% obtained using simulations. Additionally, the machine experienced instabilities, requiring frequent accelerator retuning. From 2011 to 2024, an extensive beam dynamics studies program was conducted, culminating in the introduction of Artificial Intelligence techniques in 2022-2024. These techniques made it possible to accelerate the accelerator setup, counteract instabilities and reach the nominal transmission of the linac, about 85%, in June 2024, 32 years after its construction. This paper presents the AI techniques involved, the studies performed, and how they impact routine operations.

INTRODUCTION

ALPI (Acceleratore Lineare Per Ioni) is the last stage of acceleration of the heavy ion facility of Legnaro National Laboratories. It is CW folded independent cavities linac, equipped with 77 superconductive quarter waves (QW) cooled down at 4 K, divided in three groups (low- β 0.055 at 80 MHz, medium- β 0.11, high- β 0.13 at 160 MHz both). ALPI has three injectors: an electrostatic accelerator of Tandem type, a superconductive 80 MHz RFQ (Radio Frequency quadrupole, with an output $\beta = 0.0355$) PIAVE, which delivers the stable heavy ions and the SPES RFQ, a normalconductive 80 MHz RFQ (output $\beta = 0.0392$), which will supply the radioactive ion beams (RIB) from the SPES facility [1]. The linac was designed in the '80s and built in the '90s, and, being one of the prototype in Europe, several improvements were achieved during its commissioning and construction, especially in terms of E_0 field (accelerating field) of the QWs, allowing to reach higher energy output ($^{238}\text{U}^{32+}$ at 7.4 MeV/u). However, a low transmission with respect to the simulations expectations (35% vs 93%) and a troublesome set up have since then affected the linac, moreover there are frequent instabilities which led to beam losses. After decades of improvement in the reliability of the accelerator, both from RF, controls, cryogenics, and beam dynamics model sides, in 2023-24 we began applying artificial intel-

ligence techniques to speed up the setup of the accelerator (Fig. 1) and improve its performance.

BEAM DYNAMICS AND DIAGNOSTICS WEAK POINTS

Beam Dynamics

From the beam dynamics point of view, the main weak point is given by the ALPI lattice: as shown in Fig. 2, it is composed by 3 normal conductive quadrupoles (for transverse focusing) and by 8 QWs cavities. This very long period impacts the longitudinal phase advance, transverse RF defocusing, and the QWs magnetic steering coming from the residual magnetic field on axis. The three effects follow the Eq. (1):

$$\begin{aligned}\sigma_{0,l} &\propto E_0 \sin(-\Phi_s)/\beta^2 \\ K_{RF} &\propto E_0 \sin(-\Phi_s)/\beta^3 \\ y' &\propto B_x \sin(-\Phi_s)/\beta^2\end{aligned}\quad (1)$$

All effects are directly proportional to E_0 and to the $\sin(-\Phi_s)$. Therefore, once the accelerating fields improved of a factor of 4, we increased the effects described in Eq. (1) of the same amount. Moreover, as it is possible to see, the effects are indirectly proportional to the β^2 , β^3 of the accelerating particle. This means that the initial acceleration stage (the low- β section and initial phases of medium- β) are the most subjected to losses, and it is mandatory to increase the energy of the beam as soon as possible. However, to avoid a longitudinal phase advance > 160 deg, we had to use the alternate phase focusing techniques (differently from the initial design), introducing some de-bunching phases into the longitudinal period, to reach $\sigma_{0,l} = 65$ deg.

However, the longitudinal acceptance resulted in being greatly reduced, as shown in Fig. 3, at ALPI input. The black areas are the acceptances, while the colored areas are the particle densities. As it is possible to see, the beam is not even fully covered by the acceptances, and in particular in the longitudinal plane, the instability area intrudes deeply in the centre. Moreover, the beam distributions change during time, due to the instabilities coming from the injectors. In PIAVE-ALPI, the instabilities can come as variation of transverse first order moments (steering at input of the linac) or as a variation of the reference phase between PIAVE and ALPI, which results in an off-centering of the beam phase with respect to the longitudinal acceptance. The reason for this

* luca.bellan@lnl.infn.it

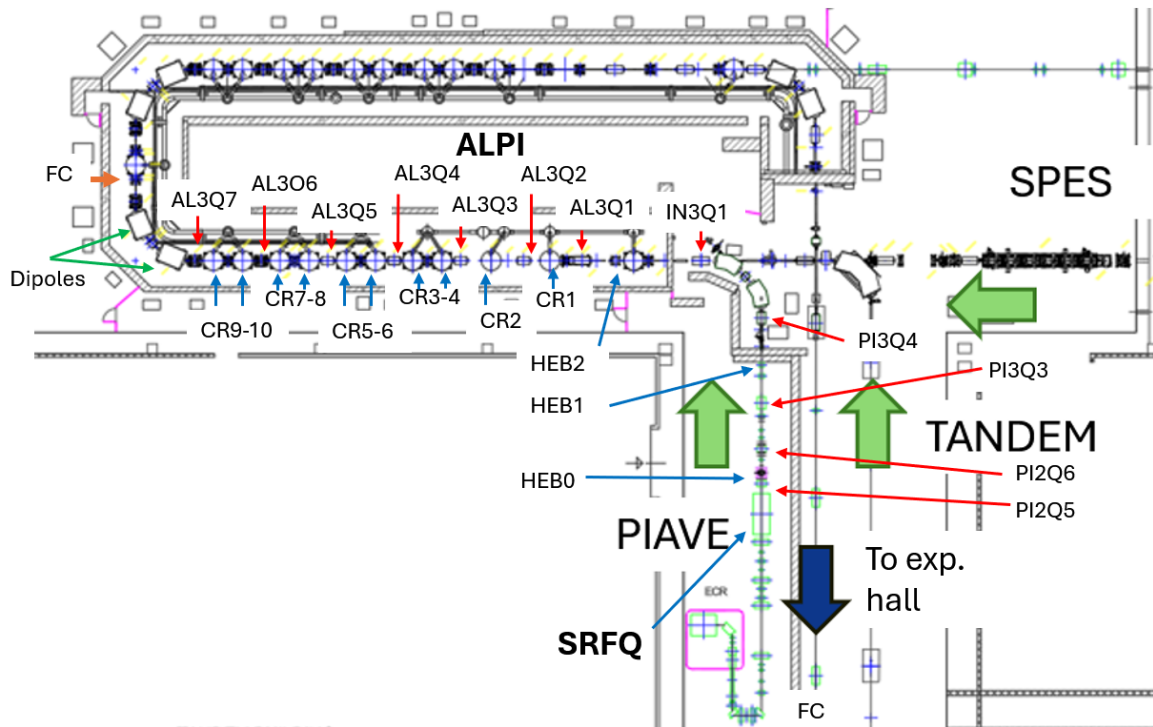


Figure 1: PIAVE TANDEM ALPI SPES accelerator. Main elements cited in the paper, such as triplets, cavities and FCs are shown.

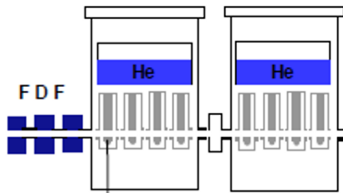


Figure 2: ALPI period: it is composed by 3 normal conductive quadrupoles and of 8 QWs cavities.

phase reference error is under study, but it may be caused by induced thermal variations of the old RF-controllers or/and of the not well isolated reference system cables. As a matter of fact, few degrees of phase difference in the baricenter of the ALPI input beam can led to losses. The results are not limited to a bad transmission 35% (with the cavities ON) with respect to the expected one 93%, but also a loss of current during the run-time due to the above mentioned instabilities. The frequency can reach of 1 per hour.

Diagnostic

ALPI is equipped with small diameter Faraday Cups (36 mm diameter) and interceptive beam profiles. The two main issues are that the FCs do not intercept the whole beam, unless a dedicated optics is set up. The beam profiles are not aligned, with a large uncertainty of their centre positions (can be high as 5 mm) and with other minor problems in the acquisition. Therefore, their usage for the steering (e.g., with the quadrupole shunting techniques) or beam character-

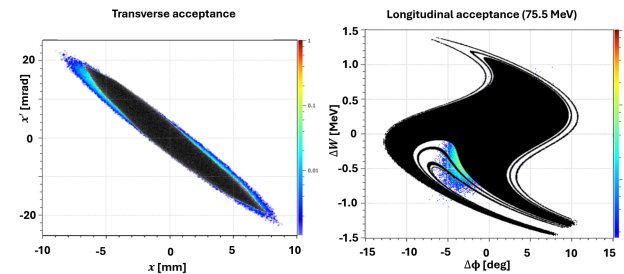


Figure 3: Transverse (left) and longitudinal (right) acceptances of the complex PIAVE-ALPI: the black areas represent the acceptances, while the colored areas are the expected input beams.

isation proved to be extremely troublesome, inefficient, and time-consuming.

AI TECHNIQUES STUDIES IN SIMULATIONS

In order to reduce the setup time of the machine (which ranges from two to three days), we decided to test artificial intelligence techniques, starting from simulations. The idea was to reduce what it is naturally a multiobjective function to a single objective function, in order to help the algorithm's convergence on the online machine. We focused the initial studies using the Particle Swarm Optimization technique [2]. We apply the technique in simulations, both onto the steering and onto the selection of synchronous phases, in both cases aiming to the FCs current after the acceleration sections. In

the case of the steering, we used a population of 25 swarm components, managing 18 steerers in 10 iterations. In the case of the longitudinal optimization, we used 3000 swarm population, 77 cavity synchronous phases, and 100 iterations, imposing not only the transmission at the FC at the end of the acceleration but also an energy constraint, to keep the wanted energy output. In both cases the techniques were successful, validating the FCs reads as an observable for transverse and longitudinal optimization [3].

MACHINE LEARNING APPLICATION ONTO THE ONLINE ACCELERATOR

In order to move from the simulations to the online machine, we had to take into account several effects not present in the simulations, such as the read-back noise, initial population/starting situation, which impact in the convergence of the algorithm. We used pyEPICS to control the PS of the magnets and SS power amplifier of the QWs from a python script, through the EPICS layer (2011) [4]. We tested two AI algorithms: the PSO (from the package pymoo [2]) and the Bayesian algorithm, from the package [5]. In this paper, we will present the online results with the Bayesian (PSO results have been presented in [3]). A key point we found was defining the interval of variation for each parameter: the main strategy is described in [3]. Practically, we built the interval of variation for each parameter starting from the best manual solution. Moreover, it proved beneficial, in our case, to start from small interval variations, allowing the algorithm to expand of 30% its variation boundaries if an optimum would have been found within 10% of the boundaries. Another beneficial strategy was to prefer a short number of iterations (but repeated) in contrast with a long, single time time-consuming one, such as the reset of the surrogate function was helpful to the convergence. One final consideration in our approach to longitudinal optimization was finding a method to eliminate all combinations that had energy levels different from the desired one. To achieve this, we drew inspiration from our cavity phasing technique, utilising dipoles positioned at the end of each acceleration section (Fig. 4). We proceed in this way:

- we switched off the quadrupole between the two dipoles after the acceleration section to set the line dispersive;
- we set the triplet which precedes the first dipole to do a waist at the beam profiler into the diagnostic box, positioned after the dipoles;
- looking at the beam centroid, changing the phase of each cavity and recording the magnetic field, we phase each cavity.

After the beam profiler, there is a small FC. The idea we had to maintain a fixed energy online was to directly observe the FC while keeping the magnetic fields of the dipoles fixed at the wanted $B\rho$. If any changes in energy occur due to specific combinations of phases, we could detect them as losses since the focusing collimator is smaller than the beam diameter.

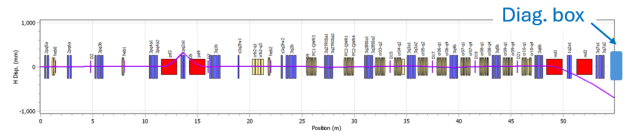


Figure 4: Simulation of D_x evolution along the linac, from the PIAVE SRFQ after the first section of acceleration. The diagnostic box position is shown.

We estimated from simulation (Fig. 4) that using this technique we can have an error of $\Delta W/W = 0.2\%$. Of course, even smaller diameter FC can further diminish the error in energy, but this quantity proved to be sufficient for the users, and it can always be corrected with the last cavity, if needed. This important result enabled us to transition from a multi-objective function to a single objective function. We considered constraints such as steering, focusing, phasing, and acceleration at frequency jumps, all while focusing on the same current of a specific FC either in the middle or at the end of the linac. Having defined the strategy, we decided to optimize the entire linac, from the PIAVE ion source optics down to the diagnostic box after the first accelerating section (half of the linac). The beam used was $^{129}\text{Xe}^{25+}$, at 4.9 MeV/u. We apply optimisations in a cycle:

- ion source optics (electrostatic quadrupoles and steerers)
- transverse optics of PIAVE LEBT (Low Energy Beam Transfer line) injection into the PIAVE SRFQ; magnetic quads, steerers. This work is described in [6]
- transverse optics of ALPI (quadrupole and steerers)
- longitudinal optics, low- β phases (absolute), MEBT bunchers fields and phases (absolute) and Three-harmonic buncher of PIAVE

The maximum number of elements tuned at the same time was 48 between quadrupoles and cavities, pointing to the FC at the end of the first acceleration section. The initial ranges for the different elements are reported in Table 1:

Table 1: Initial Boundaries

Element	Initial Range
Quadrupole average PS	$[-0.2, 0.5]\%$
Steerers PS	$\pm 2\%$
Cavities Φ_{abs}	± 2 deg
Buncher fields	± 1 kV/m

The values for the lens are in terms of PS strength, where 100% for quadrupoles indicates a strength of 30 T/m. Therefore, an average of 0.5% corresponds to a 0.15 T/m variation. It is important to remember that the algorithm can extend the boundaries if a maximum is closer to the bounds. These shorter ranges were necessary for convergence, especially when increasing the number of parameters to tune. The normal number of iterations was in the order of 100.

Results

Figure 5 shows three different set of MEBT-ALPI quadrupole average strengths (in terms of PS), starting from the exit of the RFQ. The green curve (not acc. solution) shows the values for so-called the not accelerated beam (optimization with cavities off). The low transmission (3% from the PIAVE source exit) is given by the non-adapted beam focusing to the change of the $B\rho$ given by the QWs acceleration. It is important to note that we attempted to launch the algorithm using this setup (non-accelerated optics) in order to explore the possibility of finding the correct gradients for the $B\rho$ acceleration. However, we discovered that achieving more than 10% to 30% from the optimal point (while also implementing steering) was not feasible for the Bayesian, even when we expanded the variation boundaries to $\pm 30\%$.

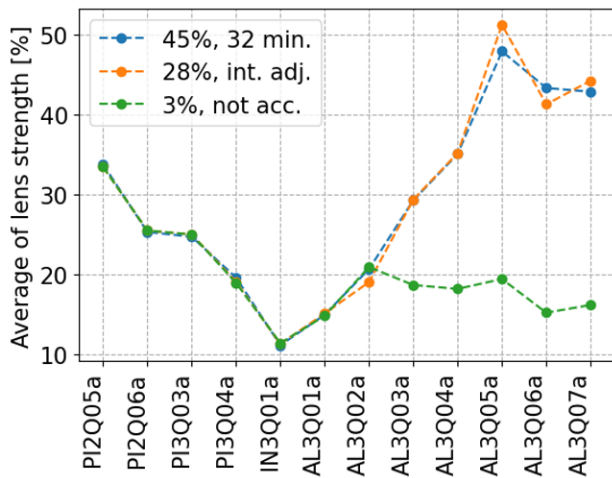


Figure 5: Average of triplet strengths with respect different set up. Green indicates not accelerated setup, orange after simulation gradient are used and bunchers optimization with ML and blu one after ALPI transverse optimization. Transmission are also indicated.

This result was significant as it highlighted the role of starting points and emphasized how these methods must integrate with standard beam dynamics knowledge. At this point, starting always from not acc. solution, we increased the gradients of the quadrupoles as expected by simulation, we optimized the longitudinal matching between PIAVE and ALPI, using the algorithm onto the bunchers of PIAVE. We reached in this way already a 28% (orange curve, ind. adj.) of transmission from the source of PIAVE, which was a record since the last decades (20%). We decided then to launch a full transverse optimization with the Bayesian, onto steerers and quadrupoles, from RFQ exit up to the FC. Because it was an overnight run, we decided to increase the number of iterations from 100 up to 1000. At iteration number 236th (32 minutes since the start) we found another maximum (45%) of PIAVE-ALPI transmission. The results is shown by the blue curve in Fig. 5. Figure 6 shows the difference with respect to the initial values of the optimum.

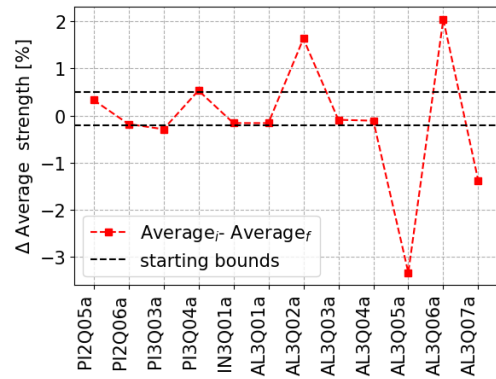


Figure 6: Average variation of the triplet strengths from PIAVE SRFQ up to the FC. Dashed lines shows the initial boundaries.

The dashed lines show the initial boundaries. As it is possible to see, the algorithm forced the boundaries, especially in the last three triplets (max variation 1 T/m). In Fig. 7 it is shown the convergence for the steering and quadrupole transverse optics optimization.

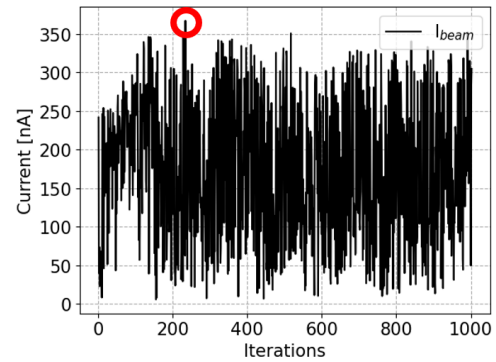


Figure 7: Current at FC with respect to iterations during transverse optimization. The best point is indicated.

It is worth noticing that we could almost double the transmission from the orange curve to the blue one, despite the small variations, another symptom of the small transverse acceptance. In the morning, aware of the frequent longitudinal instabilities that can occur during the day, we decided to initiate a longitudinal optimization of the low- β phases of the QWs, which totaled 24. We set an initial variation of ± 2 while consistently monitoring the FC. Unlike the simulation described above, we did not act on the synchronous phase directly; rather, we only operated on the phases of the SS power amplifier. This means we had an additional hidden constraint due to the synchronicity between the cavities and gaps. This second step increases the transmission of another 10-9%, reaching the record of 54.5% transmission in PIAVE-ALPI complex (typically 20% in the past decades). Results of this phasing were analyzed comparing with the initial situation Fig. 8. Plot a), shows the final synchronous phases found by the Bayesian (BO), with respect to the initial ones

ence on Heavy Ion Accelerator Technology (HIAT'25), East Lansing, MI, United States, Jun. 2025, paper MOB01, this conference.

- [2] J. Blank and K. Deb, "Pymoo: Multi-Objective Optimization in Python", *IEEE Access*, vol. 8, pp. 89497–89509, 2020. doi:10.1109/access.2020.2990567
- [3] L. Bellan *et al.*, "New techniques method for improving the performance of the ALPI Linac", *J. Instrum*, vol. 19, no. 03, p. T03005, Mar. 2024. doi:10.1088/1748-0221/19/03/t03005
- [4] M. Montis, F. Gelain, and M. G. Giacchini, "Alpi-Piave Beam Transport Control System Upgrade at Legnaro National Laboratories", in *Proc. ICALEPCS'23*, Cape Town, South Africa, Oct. 2023, pp. 1374–1376. doi:10.18429/JACoW-ICALEPCS2023-THPDP029
- [5] Bayesian Optimization: Open source constrained global optimization tool for Python, <https://github.com/bayesian-optimization/BayesianOptimization>
- [6] Y. K. Ong *et al.*, "Enhancing ALPI-PIAVE performance at INFN-LNL with advanced optimization algorithms", presented at 16th International Conference on Heavy Ion Accelerator Technology (HIAT'25), East Lansing, MI, United States, Jun. 2025, paper WEPI2, this conference.

RECIRCULATING AND ENERGY RECOVERY ION LINEAR ACCELERATORS*

J. Qiang[†], Lawrence Berkeley National Laboratory, Berkeley, CA, USA

Abstract

High-power superconducting ion linear accelerators play a vital role in both scientific research and industrial applications. However, their RF usage efficiency remains relatively low. In this paper, we review two innovative concepts: recirculating ion linear accelerators and energy recovery ion linear accelerators. These approaches significantly improve RF efficiency by enabling the ion beam to traverse the same superconducting cavity multiple times and by recovering the energy of the accelerated ion beam to return it to the RF cavities. We also propose a demonstrator for the recirculating ion linear accelerator using a scaled, low-energy electron accelerator, and discuss the potential application of the energy recovery ion accelerator in a full energy recovery electron-ion collider. These concepts offer promising avenues to substantially reduce both the construction and operational costs of superconducting linear accelerators.

INTRODUCTION

High-power superconducting ion linear accelerators (linacs) play a crucial role in both scientific research and industrial applications. They serve as drivers for spallation neutron sources, high-energy physics neutrino production, subcritical nuclear power plants, and nuclear waste transmutation. However, conventional single-pass superconducting ion linacs are less efficient in their use of RF cavities compared to circular accelerators, such as rapid cycling synchrotrons, where the beam passes through the same RF cavity multiple times. Despite their efficiency, circular accelerators suffer from slower acceleration rates and are susceptible to nonlinear resonances arising from machine imperfections.

Recirculating linacs combine the strengths of both linear and circular accelerators. They leverage the circular accelerator's ability to pass a beam through the same RF cavity repeatedly, achieving substantial energy gains, while retaining the fast acceleration characteristic of linacs. This approach significantly reduces the number of required RF cavities and cryomodules, leading to lower construction and operational costs compared to single-pass linacs.

In certain applications, such as electron-ion colliders or muon production, a portion of the ion beam retains substantial energy after interacting with a target. This high-energy portion can be redirected back into the superconducting linac and decelerated to low energy before being sent to a beam dump, thereby recovering energy and substantially reducing RF power consumption and operational costs.

Recirculating and energy recovery electron linacs have been successfully built and operated for many years [1–4], offering an optimal balance of cost and performance between straight linear and circular accelerators. These accelerators have also been proposed for next-generation light sources [5–9], and a series of dedicated workshops has explored their development [10–14].

A key distinction between ion and electron beams is the significantly greater mass of ions (for example, a proton is about 1800 times heavier than an electron), resulting in much lower velocities for ions at the same kinetic energy. In an ion linac, as the ions accelerate from MeV to GeV energies, their velocity changes considerably. Efficient acceleration under these conditions requires different types of RF cavities with varying geometric lengths or frequencies. In contrast, electrons reach velocities close to the speed of light after only a few MeV of acceleration, so their velocity changes very little. As a result, only one type of RF cavity is needed in an electron linac, making recirculating and energy recovery schemes more straightforward for electrons, without sacrificing acceleration or deceleration efficiency across a range of beam energies.

RECIRCULATING ION LINEAR ACCELERATOR

In superconducting ion linear accelerators, good acceleration efficiency is important in order to reduce the number of RF cavities needed in the accelerator. The acceleration efficiency can be measured by the transit time factor. For a given RF cavity, the energy gain ΔE_c of a charged particle through the cavity can be written as:

$$\Delta E_c = qVT \cos(\phi) \quad (1)$$

where q is the charge of the particle, $V = \int_0^L |E_z(0, z)| dz$ is the voltage across the cavity, E_z is the longitudinal accelerating electric field on axis, T is the transit time factor, ϕ is the design phase with respect to the maximum energy gain. From the above equation, we can see that for a given design phase and voltage, in order to gain more energy, the transit time factor should be as large as possible. For a periodic RF cavity with harmonic distribution of electric field along the axis, i.e. $E_z = \sin(\omega z/(\beta c)) \exp(i\omega t)$, the normalized transit time factor T_0 can be given by [15, 16]:

$$T_0(\beta) = \frac{2\beta}{\pi n} \left(\frac{\sin(\pi n(\beta - \beta_G)/(2\beta))}{\beta - \beta_G} - (-1)^n \frac{\sin(\pi n(\beta + \beta_G)/(2\beta))}{\beta + \beta_G} \right) \quad (2)$$

where n is the number of cells in the cavity operating at π -mode, $\beta = v/c$ is the normalized particle velocity, β_G is the

* Work supported by the U.S. DOE under Contract No. DE-AC02-05CH11231.

[†] jqiang@lbl.gov

geometry parameter that characterizes the synchronization between the particle and the RF field inside the cavity, and $T = \frac{\pi}{4}T_0$. For a π -mode cavity, the cell length in the cavity is $\frac{1}{2}\beta_G\lambda$, where λ is the RF wavelength of the field inside the cavity.

Figure 1 shows a plot of the transit time factor as a function of the ratio of the particle velocity β to the cavity geometric β_G with different number of cells per cavity. It is seen that as the number of cells per cavity increases, the velocity acceptance (the range of particle velocity to attain a good acceleration efficiency) decreases. A small number of cells per cavity, e.g. $n = 3$, provides large velocity acceptance. However, for a given energy range, this may require the use of a large number of RF cavities and increase the system complexity. If the number of cells per cavity is too large, besides the decrease in the velocity acceptance, the fabrication of the cavity also becomes more challenging. As a compromise, in most accelerators, a five cell ($n = 5$) per cavity structure is used to accelerate the ion beam energy from the 100 MeV level to the GeV level.

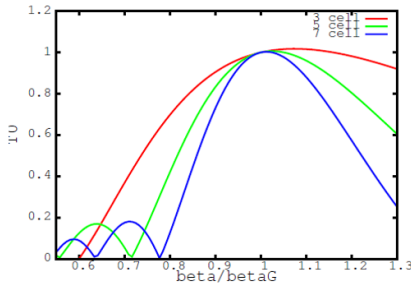


Figure 1: Normalized transit time factor as a function of the ratio of the particle beta to the geometric beta for different number of cells in a cavity.

A multi-GeV recirculating superconducting ion linac shown in Fig. 2 was proposed in reference [17]. The five-cell superconducting cavity with 650 MHz frequency was assumed in that accelerator. It can provide a high accelerating gradient (> 15 MV/m) under continuous wave (CW) operation and has also a large aperture size (~ 100 mm) for beam pass. In that proposed example, 17 superconducting cavities with 10.3 MeV energy gain per cavity were assumed to accelerate the ion beam from 150 MeV to 500 MeV in two passes, 39 cavities with 9.6 MeV energy gain per cavity to accelerate the beam from 500 MeV to 2 GeV in 4 passes, and 50 cavities with 20 MeV energy gain per cavity to accelerate the ion beam from 2 GeV to 8 GeV in six passes. This concept drastically reduces the number of superconducting cavities needed to reach the final 8 GeV beam energy from near 500 to around 100.

In the recirculating linac, an ion beam passes through the same accelerating system multiple times to reduce the number of RF cavities. Due to the fact that the ion beam is still non-relativistic, the velocity of the beam changes during acceleration and varies from pass to pass (especially in the lower energy section). This could cause a problem

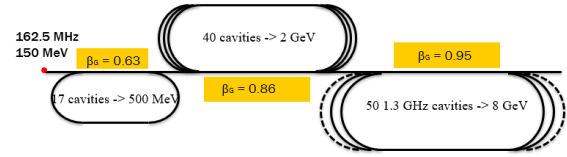


Figure 2: Schematic plot a multi-GeV recirculating ion linear accelerator.

for multi-pass acceleration. When the beam passes through the accelerator for the first time, the driven phase of each RF cavity can be tuned to achieve a design phase (e.g., -30 degrees) for the desired energy gain. When the beam passes through the accelerator for the second time, it has a higher energy and a larger velocity. Because the distance between accelerating cavities is fixed, within the same cavity, the ion will see a different RF phase from that during the first pass. This would not be a problem if the driven phase of the cavity could be quickly adjusted between each pass or between each bunch train for CW operation so that the desired energy gain and design phase for the beam can be achieved. However, such fast modulation of the RF driven phase normally cannot be easily attained for a superconducting cavity.

Let t_i^m denote the time pass between two RF cavities i and $i + 1$ during the m^{th} beam pass of the accelerator, t_i^n the time pass between the two cavities during the n^{th} beam pass. If the difference of the two time pass satisfies the condition:

$$t_i^m - t_i^n = \pm k T_{rf}, \quad k = 0, 1, 2, 3, \dots \quad (3)$$

where T_{rf} is the oscillation period of the RF field inside the cavity, the ion beam will see the same phase of the cavity during multiple passes of the accelerator.

For the first section two-pass recirculating linac proposed, the above condition can be achieved by adjusting the distance between two cavities. Here, the above condition can be rewritten as:

$$l_i \left(\frac{1}{\beta_i^1} - \frac{1}{\beta_i^2} \right) = \pm k T_{rf}, \quad k = 0, 1, 2, 3, \dots \quad (4)$$

where $\beta_i^1 = v_i^1/c$ is the normalized velocity after cavity i during the first beam pass, $\beta_i^2 = v_i^2/c$ is the normalized velocity after cavity i during the second beam pass, c is the speed of light in vacuum, and l_i is the distance between the cavity i and the cavity $i + 1$. Knowing the energy/velocity after each RF cavity during the two beam passes, one can use above equation to determine the separation distance between two cavities to maintain the same RF phase.

If we assume the same RF phase for both beam passes, using the above equation, we obtain the separation between two cavities shown in Fig. 3. It is seen that the first separation distance between cavity 1 and cavity 2 is slightly greater than the cavity length. The separation increases to about twice the cavity length at the end of the last two accelerating cavities (cavity 16 and 17). Figure 4 shows the evolution of the ion kinetic energy through the total 17 cavities during the two beam passes with a fixed driven phase of each cavity. By

appropriately arranging the separation distance between two cavities to satisfy the condition in Eq. 4, the ion beam can be correctly accelerated with the designed RF phase in both passes.

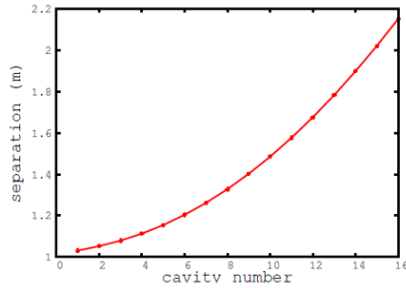


Figure 3: Separation distance between two cavities as a function of cavity number in the first section of the linac.

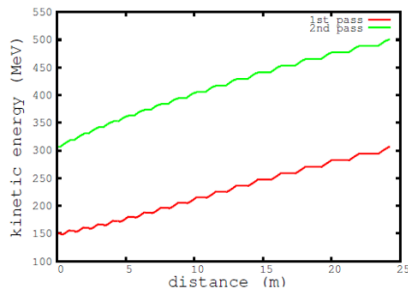


Figure 4: Two pass ion beam kinetic energy evolution through the first section of the recirculating linac.

The first section (two-pass) of the above proposed multi-GeV recirculating superconducting ion linac was studied using self-consistent macroparticle simulation with the IMPACT code [18, 19] in reference [20, 21]. Figure 5 shows the ion beam RMS transverse and longitudinal emittance evolution through the double-pass recirculating linac with 40 mA current. After careful beam dynamics optimization, the emittance can be well preserved with slight growth.

In the two-pass section of the recirculating ion linac, the separation between superconducting cavities is adjusted to satisfy the longitudinal synchronous condition so that ion beams with two different energies can be accelerated using the same RF cavity. However, for multiple passes (>2), multiple longitudinal synchronous conditions among these passes need to be satisfied for fixed design phase acceleration through the RF cavities. The phase slippage can no longer be compensated by the single control variable of spacing between cavities and requires a new approach. An energy-dependent path length change during recirculation was proposed in reference [22].

A schematic plot of this phase shifter is shown in Fig. 6. Here, an ion beam passing through the RF cavity will enter the bending magnet field region at 45 degrees with respect to the field's entrance edge. In the middle plane of the magnet,

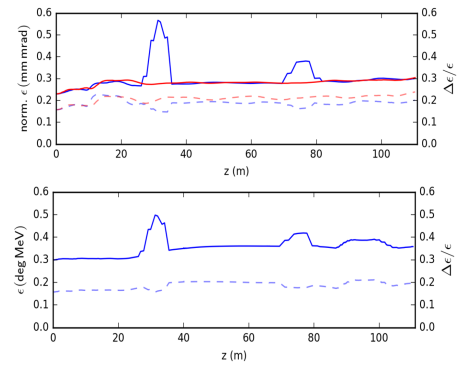


Figure 5: Proton beam RMS transverse (top) and longitudinal (bottom) emittance evolution through the double-pass recirculating linac with 40 mA current.

there is only a vertical component of the field that varies only as a function of x , the distance perpendicular to the entrance edge. With a sufficiently long magnet, the magnetic field is only a function of x and y , and there is no z component of the magnetic field in the bending magnet. Given this magnetic field distribution, an ion beam entering the bending magnet with a given angle will exit from the magnet with the same angle. In this case, with a 45 degree entry angle, the ion beam will exit the magnet at another 45 degrees with respect to the field entrance edge. The entire magnet provides 90 degree bending of the ion beam. An ion beam with different energies after the RF cavity entering the first bending magnet from the same path will be separated out inside the magnet and exit the magnet with different horizontal separations. Using the symmetry as shown in the dashed line of the above plot, those separated beams entering the second bending magnet, which has the same magnetic field distribution as the first bending magnet, will be bent for another 90 degrees and merge into a single straight path at the exit of the magnet fringe field edge due to the symmetric condition. These two 90 degree bending magnets form an achromatic system for different energy beams. By appropriately designing the field distribution along the direction perpendicular to the entrance edge, i.e., $B_y(x)$, the time differences of multiple ion beam passes through this phase shifter can be adjusted to satisfy the longitudinal synchronous conditions so that those ion beams with different energies can be accelerated by the same RF cavity multiple times.

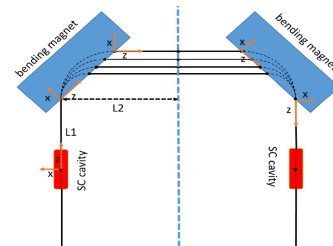


Figure 6: Schematic plot of the two fixed field bending magnet phase shifter. Here, y is the vertical direction pointing out of the plane.

Figure 7 shows a schematic plot of a multi-pass recirculating ion linear accelerator that can accelerate an ion beam energy from 150 MeV to 600 MeV.

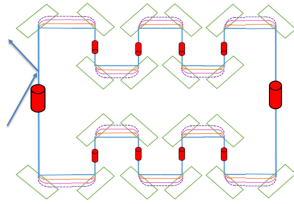


Figure 7: Schematic plot of a multi-pass recirculating ion linear accelerator.

Figure 8 show the proton beam transverse and longitudinal emittance evolutions through this phase shifter including the space-charge effects of 40 mA current for a proton beam kinetic energy of 251.25 MeV, 363.75 MeV, 476.25 MeV, and 588.75 MeV. The proton beam emittances are well preserved after the phase shifter for the four proton beam passes. A small emittance growth (about 10%) is seen in the vertical (y) dimension for the proton beam with 251.25 MeV and 363.75 MeV energy. The transverse sizes are kept within a few millimeters after this phase shifter.

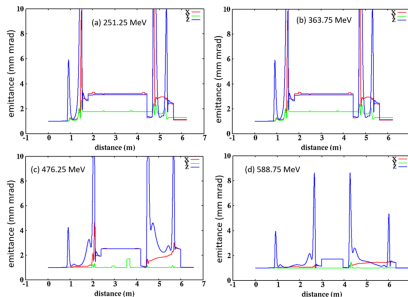


Figure 8: Proton beam transverse and longitudinal RMS size evolution through the phase shifter with 251.25 MeV (top left), 363.75 MeV (top right), 476.25 MeV (bottom left), 588.75 MeV (bottom right) kinetic energy and 40 mA current.

To test the above recirculating ion linac concept, we propose a small electron recirculating linac, i.e., an electron emulator, to demonstrate the multi-pass acceleration using the fixed field phase shifter and to ensure that there is no substantial emittance growth or beam losses. In this demonstrator, as shown in Fig. 9, a low-energy electron recirculating linac consists of two RF cavities to accelerate an electron beam from 82 keV to 272 keV in four passes to emulate the ion beam acceleration from 150 MeV to 500 MeV in the recirculating superconducting ion linac. The electron beam in this linac has the same initial and final speed but lower charge density than the ion beam in the recirculating ion linac, so that the charged particles will experience similar space-charge effects in both linacs.

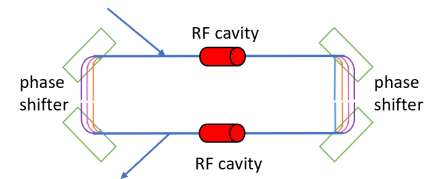


Figure 9: Schematic plot of a low-energy electron linear accelerator to demonstrate the multi-pass recirculating ion linear accelerator concept.

ENERGY RECOVERY ION LINEAR ACCELERATOR

The conventional racetrack electron energy recovery accelerator architecture is not suitable for an ion energy recovery linac, as the high-energy ion beam exiting the accelerator cannot be returned to the entrance for efficient deceleration. This is because RF cavities designed for low-energy ion beams are not effective at accelerating or decelerating high-energy ion beams.

Figure 10 presents a schematic diagram of the energy recovery ion linear accelerator proposed in reference [23]. The accelerator comprises a low-energy ion source and an RFQ (Radio Frequency Quadrupole) that accelerates the ion beam to approximately 2 MeV. Subsequently, the beam is further accelerated through a superconducting linear accelerator, which includes several types of superconducting RF cavities, reaching an energy of GeV before exiting the accelerator. After interacting with the target material, ions that have not undergone significant deflection or nuclear reactions are redirected back to the exit of the accelerator via a return loop. This ion beam is then sent backward from the end of the linear accelerator to the entrance of the superconducting linear accelerator. With an appropriately designed linear accelerator, the backward-moving ion beam will be decelerated through each RF cavity, transferring its energy back to the RF fields within the cavities. Consequently, within each cavity, the ion beam will have the correct energy and velocity corresponding to the cavity structure, ensuring effective deceleration. At the entrance of the superconducting linac, the backward-moving ion beam will have an energy of approximately 2 MeV before being directed to the beam dump. The ion beam power entering the beam dump will be significantly lower than that of the original high-energy beam, making it easier to manage. To achieve the desired energy gain for the ion beam, the RF phases within the RF cavities must be precisely set. Once established, these RF phases remain constant for all bunches, whether they are moving forward or backward. To decelerate the backward-moving ion beam using the same RF settings, the linear accelerator must be meticulously designed.

In the energy recovery ion linac design, the initial beam-line element layout and RF cavity amplitude and phase settings are chosen according to the forward-accelerating ion beam. For RF cavity i , the initial RF input phase for the forward-moving ion beam at this cavity is ϕ_i . For a

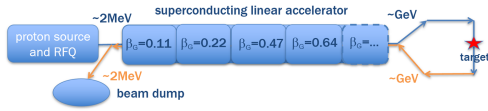


Figure 10: Schematic plot of an energy recovery ion linear accelerator.

backward-moving ion beam with the same energy as the forward-moving ion beam at the exit of RF cavity i , its initial phase has to be appropriately chosen so that the backward-moving ion beam will be decelerated to the same energy as the forward-moving ion beam at the entrance of the cavity. This initial phase for the backward-moving ion beam is denoted as φ_i . The actual phase of that backward-moving ion beam at the exit of RF cavity i from the end of the entire linear accelerator is θ_i . Normally, $\varphi_i \neq \theta_i$, the difference is given as $\delta_i = \varphi_i - \theta_i$. In order to attain the correct deceleration through RF cavity i for the backward-moving ion beam, this difference should be a multiple integer of 2π . This can be achieved by adjusting the distance between RF cavities i and $i + 1$. Assuming the velocity of the ion beam after cavity i is v_i , the change of phase $\delta\theta_i$ due to the change of the distance δl_i between cavities i and $i + 1$ is given as:

$$\delta\theta_i = \omega \frac{\delta l_i}{v_i} \quad (5)$$

where ω is the reference angular frequency. Given the initial phase difference δ_i for the backward-moving ion beam, in order to attain the correct deceleration, the change of phase should satisfy:

$$2\delta\theta_i - \delta_i = 2n\pi \quad (6)$$

where n is an integer. The resultant distance change δl_i will be:

$$\delta l_i = \frac{(\delta_i + 2n\pi)v_i}{2\omega} \quad (7)$$

After the change of separation distance between RF cavities i and $i + 1$, the new input phase for cavity $i + 1$ with angular frequency ω_{i+1} should be reset to $\phi_{i+1} - \frac{\omega_{i+1}}{\omega} \delta\theta_i$ so that the forward-moving ion beam will gain the same amount of energy through the cavity $i + 1$ as in the original setting. The initial phase of the backward-moving ion beam at the exit of RF cavity $i + 1$ will be reset to $\varphi_{i+1} + \delta\theta_i$. This process starts from the first RF cavity and repeats until the last RF cavity in the energy recovery ion linear accelerator. The initial phase θ_i for the backward-moving ion beam at the exit of RF cavity i is attained by choosing the initial phase φ_N for the last RF cavity for a given deceleration energy and running the backward ion beam through the accelerator with the original settings, i.e., initial RF cavity separation distance and RF field amplitudes and input phases.

Besides application to some muon production [24], another potential application of the ion energy recovery linac is an electron-ion collider or an ion-ion collider where the consumption of the high-energy ion beam during each collision is minimal. Nearly the entire high-energy ion beam can

be sent back to the linear accelerator for energy recovery, drastically reducing the operational costs of such colliders.

Figure 11 shows a schematic plot of an electron-ion collider based on the energy recovery electron and ion accelerators. The middle section contains a superconducting ion linear accelerator that consists of multiple types of RF cavity structures for different speeds of ions, an ion source, and a Radio Frequency Quadrupole (RFQ). This accelerator accelerates the ion beam to 20 GeV to attain relativistic speed. The ion beam exiting from this accelerator is sent upward and passes through a 180 degree right arc before entering a lower side superconducting linac that consists of a single type of RF cavity. The ion beam gains another 20 GeV kinetic energy after this linac and passes through a 180 degree left arc, now with 40 GeV ion beam energy. This ion beam is then accelerated in the upper side superconducting linac that also consists of a single type of RF cavity and attains another 20 GeV gain. After this linac, the ion beam passes through another right arc for 60 GeV beam energy. This process is repeated several times until the ion beam attains 200 GeV energy and is transported to the left arc for collision at the interaction point (IP) with a 10 GeV electron beam from the upper side superconducting linac.

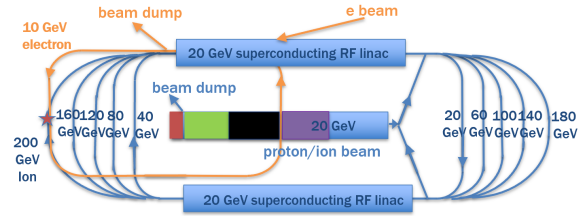


Figure 11: Schematic plot of an electron-ion collider based on energy recovery electron and ion accelerators. Here, different colors in the middle of plot represent multiple RF cavity structures for different speed of ion.

After the collision, the ion beam is sent back to the upper side linac for deceleration to 180 GeV. This ion beam passes through the right arc of 180 GeV and is decelerated by the lower side linac to 160 GeV before entering the left arc of 160 GeV. This process is repeated several times until the ion beam is decelerated to 20 GeV. This beam passes through the 20 GeV right arc and is sent back to the middle energy recovery superconducting linac proposed in this study. The beam is further decelerated in this linac until its kinetic energy is reduced to about 2 MeV before being kicked out to a beam dump.

The 10 GeV electron beam, after collision, is sent back to the upper side linac for deceleration to 2 MeV before being sent to the beam dump. If we assume that both ion beam and electron beam have 1.6 nC charges and 162.5 MHz repetition rate for $10^{34}/\text{cm}^2/\text{s}$ peak luminosity, this results in about 1 MW RF power consumption for the proposed electron-ion collider, which is an order of magnitude less than the RF power usage of the present electron-ion collider under design [25].

REFERENCES

- [1] SRF-Based Energy-Recovering Linear Accelerators (ERLs) | Jefferson Lab, <https://www.jlab.org/research/linacs>
- [2] Welcome | Cornell Laboratory for Accelerator-based ScienceS and Education (CLASSE), <https://www.classe.cornell.edu/WebHome.html>
- [3] M. Akemoto *et al.*, “Construction and commissioning of the compact energy-recovery linac at KEK”, *Nucl. Instrum. Methods Phys. Res., Sect. A*, vol. 877, pp. 197–219, Jan. 2018. doi:10.1016/j.nima.2017.08.051
- [4] M. Arnold *et al.*, “First operation of the superconducting Darmstadt linear electron accelerator as an energy recovery linac”, *Phys. Rev. Accel. Beams*, vol. 23, no. 2, p. 020101, Feb. 2020. doi:10.1103/physrevaccelbeams.23.020101
- [5] CLASSE: Energy Recovery Linac, <http://www.classe.cornell.edu/Research/ERL/>
- [6] J. N. Corlett *et al.*, “LUX - A Recirculating Linac-based Facility for Ultrafast X-ray Science”, in *Proc. EPAC'04*, Lucerne, Switzerland, Jul. 2004, paper THPKF075, pp. 2439–2441.
- [7] K. Jordan *et al.*, “JLAMP: an amplifier-based FEL in the JLab SRF ERL driver”, Jefferson Laboratory, Newport News, VA, United States, Rep. JLAB-ACT-07-621, 2007.
- [8] P. H. Williams, D. Angal-Kalinin, D. J. Dunning, J. K. Jones, and N. R. Thompson, “Recirculating linac free-electron laser driver”, *Phys. Rev. Spec. Top. Accel Beams*, vol. 14, no. 5, p. 050704, May 2011. doi:10.1103/physrevstab.14.050704
- [9] R. C. York, “5 upgradable to 25 keV free electron laser facility”, *Phys. Rev. Spec. Top. Accel. Beams*, vol. 17, no. 1, p. 010705, Jan. 2014. doi:10.1103/physrevstab.17.010705
- [10] LEPP – ERL09, <http://www.lepp.cornell.edu/Events/ERL09/>
- [11] ERL2011, <http://erl2011.kek.jp/>
- [12] 53rd ICFA Advanced Beam Dynamics Workshop on Energy Recovery Linacs (ERL-2013), <http://ssrc.inp.nsk.su/conf/ERL2013/>
- [13] CLASSE: ERL 2022, <https://www.classe.cornell.edu/NewsAndEvents/ERL2022/>
- [14] Superconducting Accelerator Center, Application and Innovation Team, <https://www2.kek.jp/casa/cERL/en/events/ERL2024/index.html>
- [15] S. Holmes *et al.*, “Project X Reference Design Report”, Fermilab, Batavia, IL, United States, Rep. FERMILAB-TM-2557, arXiv:1306.5022 [physics.acc-ph], Jun. 2013. doi:10.48550/arXiv.1306.5022
- [16] P. N. Ostroumov, “Physics design of the 8 GeV H-minus linac”, *New J. Phys.*, vol. 8, no. 11, p. 281, Nov. 2006. doi:10.1088/1367-2630/8/11/281
- [17] J. Qiang, “Wide energy bandwidth superconducting accelerating cavities”, *Nucl. Instrum. Methods Phys. Res., Sect. A*, vol. 795, pp. 77–81, Sep. 2015. doi:10.1016/j.nima.2015.05.056
- [18] J. Qiang, R. D. Ryne, S. Habib, and V. Decyk, “An Object-Oriented Parallel Particle-in-Cell Code for Beam Dynamics Simulation in Linear Accelerators”, *J. Comput. Phys.*, vol. 163, no. 2, pp. 434–451, Sep. 2000. doi:10.1006/jcph.2000.6570
- [19] J. Qiang, S. Lidia, R. D. Ryne, and C. Limborg-Deprey, “Three-dimensional quasistatic model for high brightness beam dynamics simulation”, *Phys. Rev. Spec. Top. Accel Beams*, vol. 9, no. 4, p. 044204, Apr. 2006. doi:10.1103/physrevstab.9.044204
- [20] K. Hwang and J. Qiang, “Beam dynamics simulation of a double pass proton linear accelerator”, *Phys. Rev. Accel. Beams*, vol. 20, no. 4, p. 040401, Apr. 2017. doi:10.1103/physrevaccelbeams.20.040401
- [21] Y. Tao, J. Qiang, and K. Hwang, “Overtaking collision effects in a cw double-pass proton linac”, *Phys. Rev. Accel. Beams*, vol. 20, no. 12, p. 124202, Dec. 2017. doi:10.1103/physrevaccelbeams.20.124202
- [22] J. Qiang, L. Brouwer, and R. Teyber, “Fixed field phase shifters for a multipass recirculating superconducting proton linac”, *Phys. Rev. Accel. Beams*, vol. 24, no. 3, p. 030101, Mar. 2021. doi:10.1103/physrevaccelbeams.24.030101
- [23] J. Qiang, “An energy recovery proton linear accelerator for muon production”, presented at the IPAC'25, Taipei, Taiwan, Jun. 2025, paper TUPM090, unpublished.
- [24] A. Bungau, R. Cywinski, C. Bungau, P. King, and J. Lord, “Simulations of surface muon production in graphite targets”, *Phys. Rev. Spec. Top. Accel Beams*, vol. 16, no. 1, p. 014701, Jan. 2013. doi:10.1103/physrevstab.16.014701
- [25] F. Willeke and J. Beebe-Wang, “Electron Ion Collider Conceptual Design Report 2021”, Office of Scientific and Technical Information (OSTI), Feb. 2021. doi:10.2172/1765663

A SINGLE-SLICE ROTATING GRAPHITE TARGET AT FRIB*

J. Song[†], N. Bultman, D. Cole, N. Jockheck, T. Kanemura, M. Larmann, D. Lee, G. Lee, S. Miller, M. Patil, M. Portillo, R. Quispe-Abad, M. Reaume, J. Simon, M. Steiner, J. Wei
Facility for Rare Isotope Beams, Michigan State University, East Lansing, MI, USA

Abstract

The FRIB accelerator, constructed and commissioned in 2022, serves as a leading facility for producing rare isotope beams and exploring elements beyond the limits of stability. These beams are produced by reactions between stable primary beams and a graphite production target. Meanwhile, approximately 20–40% of the primary beam power is deposited in the target, necessitating efficient heat dissipation. Currently, FRIB operates at a primary beam power of 20 kW. To enhance thermal dissipation efficiency, a single-slice rotating graphite target with a diameter of approximately 30 cm is employed. This paper presents an overview of the current status of the production target system and ongoing R&D efforts to enhance its performance and durability under high-power beam conditions.

INTRODUCTION

The Facility for Rare Isotope Beams (FRIB), a leading facility for rare isotope science, is undergoing a staged power ramp-up toward its ultimate goal of operating at 400 kW of primary beam power. FRIB currently delivers high-intensity stable ion beams ranging from oxygen to uranium and has been progressively increasing its operational beam power from 1 kW to 20 kW [1, 2] since commissioning in 2022 [3, 4]. This capability enables a wide range of nuclear science experiments, including studies of nuclear structure, reactions, and astrophysical processes. To address the intense thermal loads associated with rare isotope production, FRIB employs a single-slice rotating graphite target system [5]. This target is designed to withstand beam powers up to 50 kW, with thermal mitigation achieved by distributing the deposited energy over a larger surface area through disc rotation. This reduces surface power density and enhances thermal performance. The current system utilizes a disc approximately 30 cm in diameter, operating at moderate rotational speeds (500 rpm). The rotation speed is planned to increase to 2000 rpm in future operation to reduce both the peak temperature and the temperature gradient across the irradiated beam spot on the graphite disc. In addition to thermal and mechanical factors, radiation-induced degradation strongly influences the operational durability of the target. Radiation transport simulations indicate that radiation damage to the graphite remains relatively low on the order of 0.4 displacements per atom (DPA) even under worst-case uranium irradiation scenarios. This low damage level allows for multiple reuses of a single disc, with the operational plan

calling for retirement after approximately ten irradiation cycles. The structural configuration of the target assembly is illustrated in Fig. 1. Since the initial operation in 2022, several key hardware improvements have been implemented, including the adoption of high-temperature bearings and the application of a high-emissivity internal coating ($\epsilon \approx 0.9$) to enhance radiative heat transfer.

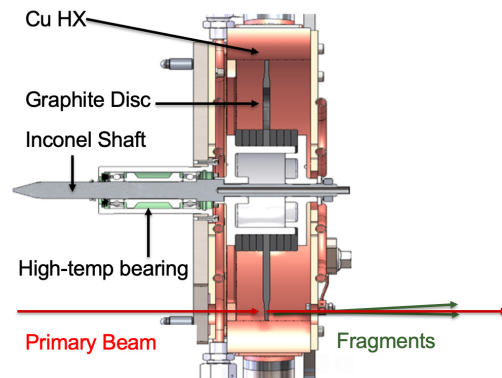


Figure 1: FRIB target assembly.

PRODUCTION TARGET

The production target system illustrated in Fig. 1 consists of a 30 cm diameter graphite disc (Mersen grade 2360), spacers made of the same graphite grade, a YSZ ceramic hub, high-temperature bearings (NSK), an Inconel shaft, and a copper heat exchanger. The interior surface of the heat exchanger was coated with a high-emissivity paint (Aremco 840-MS). Between 20–40 % of the primary beam power is deposited in production targets of varying thickness. The primary cooling mechanism is radiative heat transfer from the rotating graphite disc, with the emitted heat absorbed by side-mounted heat exchangers and water-cooled front and rear doors.

To accommodate various primary beams, eight production targets with different thicknesses are provided to optimize secondary beam yields. The configurations are summarized in Table 1. To achieve efficient secondary beam delivery, the most critical requirement is to maintain the target defect within ± 2 %, which accounts for machining tolerances, material inhomogeneities, and mechanical deformations. Recent measurements using a wedge view with beam data from ARIS indicate that the total defect is approximately 1.6 % [6]. To support consistent quality in spare targets, a system [7] capable of directly measuring the physical thickness has been developed, it was confirmed that for targets with thicknesses ranging from 2.1 mm to 5 mm, the machining precision

* Work supported by the U.S. Department of Energy Office of Science under Cooperative Agreement DE-SC0023633, the State of Michigan, and Michigan State University.

[†] songj@frib.msu.edu

Table 1: Summary of Graphite Target Thicknesses, Corresponding Areal Densities, and Associated Primary Beams Used in Operation

Target thick. (mm)	Areal density (g/cm ²)	Primary Beam
1.2	0.23	²³⁸ U
2.1	0.39	¹²⁴ Xe, ¹⁹⁸ Pt, ²³⁸ U
3.5	0.65	¹²⁴ Xe, ⁹² Mo
5.0	0.95	⁴⁸ Ca, ⁵⁸ Ni
8.0	1.54	¹⁸ O, ⁴⁸ Ca, ⁷⁰ Ge, ⁸² Se
10.0	1.86	⁴⁰ Ar, ⁴⁸ Ca
15.0	2.79	-
18.0	3.35	²⁸ Si

results in thickness variations that are, at minimum, within $\approx 1\%$ at the 2σ confidence level. Accurate implementation of temperature-dependent material properties and thermal contact conductance (TCC) is essential for reliable thermal simulations, as well as for establishing beam power limits and ensuring safe operating conditions. Surface emissivities of key components in the target system, including the graphite disc, high-emissivity-coated copper heat exchanger, Inconel shaft, and aluminum wing, were measured using the custom-built setup [8]. The measured emissivity values as a function of temperature are presented in Fig. 2. In addition, the TCCs for the spindle assembly were evaluated using the dedicated vacuum-based measurement system [9].

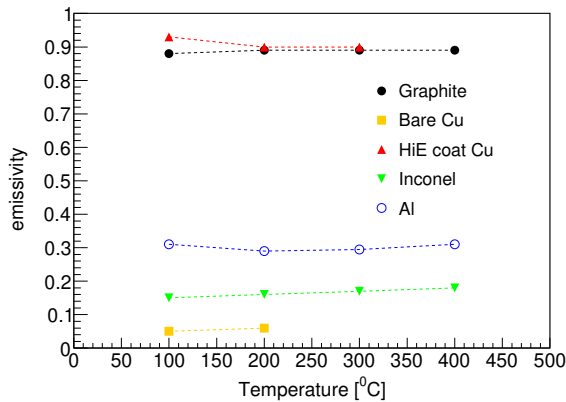


Figure 2: Surface emissivity measurements of target system materials, graphite, bare copper, high emissivity coated copper, Inconel, and aluminum, are shown as a function of temperature.

THERMAL BEHAVIOR OF THE PRODUCTION TARGET

Approximately 20–40 % of the primary beam power is deposited in the target, delivered by a Gaussian beam with a 1σ beam size of 0.25 mm, regardless of the primary beam species. For the thermal analysis based on the deposited power, the entire target assembly was modeled using ANSYS [10]. In the simulation, surface emissivities and the

TCC for the spindle were taken from our measurements. Other physical properties, such as thermal conductivity, were adopted from known reference values. The TCC for the graphite was estimated based on literature data [11]. A validation test of the TCC using the full disc module assembly is planned, and the validated values will be incorporated into the thermal analysis model. The majority of the heat is absorbed by the graphite disc, which subsequently radiates to the heat exchanger. The exchanger removes over 99 % of the deposited power via water cooling through the front and rear doors and the side section. Only a small fraction ($<1\%$) is conducted into the spindle; however, even this small amount of power can raise the bearing temperature beyond its operational limit.

To validate our thermal analysis of the graphite target, we compared the maximum temperature on the 8 mm-thick rotating graphite disc as measured by a thermal imaging system (TIS) [12, 13], at various levels of deposited power. The maximum temperatures resulting from irradiation with ⁴⁸Ca and ⁸²Se beams on an 8 mm-thick graphite disc rotating at 500 rpm were recorded during beam operations over the past two years, with primary beam powers ranging from 5 to 20 kW. Representative thermal images at ≈ 20 kW are shown in the top panels of Fig. 3. In the images, the disc rotates counterclockwise, as evidenced by the trailing edge of the beam spot. The observed maximum temperatures for ⁴⁸Ca and ⁸²Se beams were 917°C and 1146°C, respectively. These measurements are subject to a few percent uncertainty due to variations in emissivity, calibration accuracy, and beam current fluctuations. Measured and simulated maximum temperatures as a function of deposited beam power are compared in Fig. 3, using 13 recorded data points. Since the front door of the heat exchanger is only partially coated ($\approx 1/4$ remains coated), thermal simulations were conducted for two boundary conditions: fully coated and uncoated. In the model, beam power was deposited uniformly across the graphite disc thickness. The comparison between measured and simulated maximum temperatures shows good agreement within 4 %.

BEAM POWER CONSTRAINTS

Beam power constraints are determined based on the thermal limits of key components in the target system. These include the maximum allowable temperatures for the graphite disc ($<1900^\circ\text{C}$), target bearing ($<250^\circ\text{C}$), Inconel shaft ($<650^\circ\text{C}$), and ceramic hub ($<1000^\circ\text{C}$). Thermal simulations and operational planning ensure that all components remain within these limits under specified beam power conditions. Based on thermal simulation results using the complete target assembly model, beam power constraints were evaluated for both the most frequently used 2.1 mm and 8.0 mm-thick graphite discs. For both 2.1 mm and 8.0 mm-thick graphite discs, the predicted maximum temperature are shown in Fig. 4 a), and the corresponding maximum allowable deposited powers as a function of rotational speed are presented in Fig. 4 b). The temperature limits of other com-

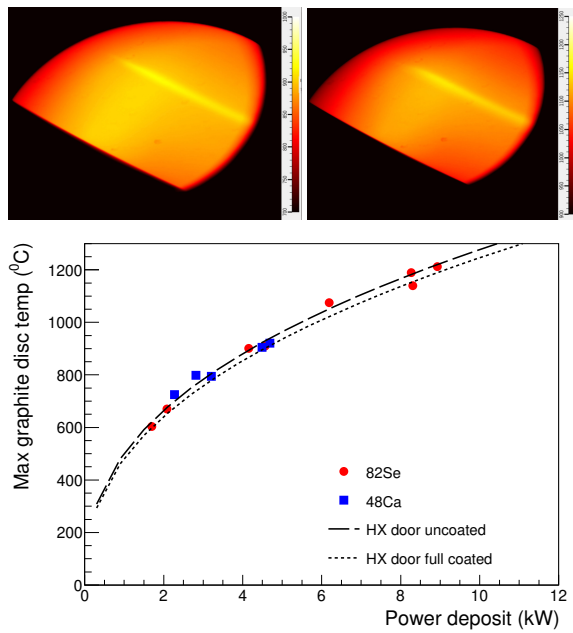


Figure 3: Thermal images for a 19 kW, 215 MeV/u ^{48}Ca beam (top left) and a 20 kW, 225 MeV/u ^{82}Se beam (top right) incident on a rotating graphite disc. Bottom: Comparison between measured and simulated maximum temperatures of the graphite disc as a function of deposited beam power for ^{48}Ca (blue squares) beams and ^{82}Se (red circles). The data correspond to an 8 mm-thick graphite disc rotating at 500 rpm. Simulated results are shown for two thermal boundary conditions at the heat exchanger: uncoated (solid line) and fully coated with a high-emissivity surface (dashed line).

ponents are primarily proportional to the deposited power in the target, with negligible dependence on target thickness and rotational speed. The maximum temperatures of each component as a function of deposited power are illustrated in Fig. 4 c). Operation appears feasible up to ≈ 25 kW of deposited power. As examples, for a 177 MeV/u ^{238}U beam incident on a 2.1 mm-thick target, operation is feasible with up to 21 kW of deposited power (equivalent to 57 kW of primary beam power) at a rotational speed of 2000 rpm. Similarly, for a 225 MeV/u ^{82}Se beam on an 8 mm-thick target, up to 37 kW of deposited power (equivalent to 88 kW of primary beam power) can be accommodated at 2000 rpm.

CONCLUSION

The single-slice rotating graphite target system at FRIB has demonstrated stable and reliable performance under primary beam powers of up to 20 kW. Design improvements such as the integration of high-temperature bearings, application of high-emissivity coatings inside heat exchanger have significantly improved thermal performance of the system. Comprehensive R&D activities have supported the development and validation of a predictive thermal model. These efforts include experimental measurements of key thermal

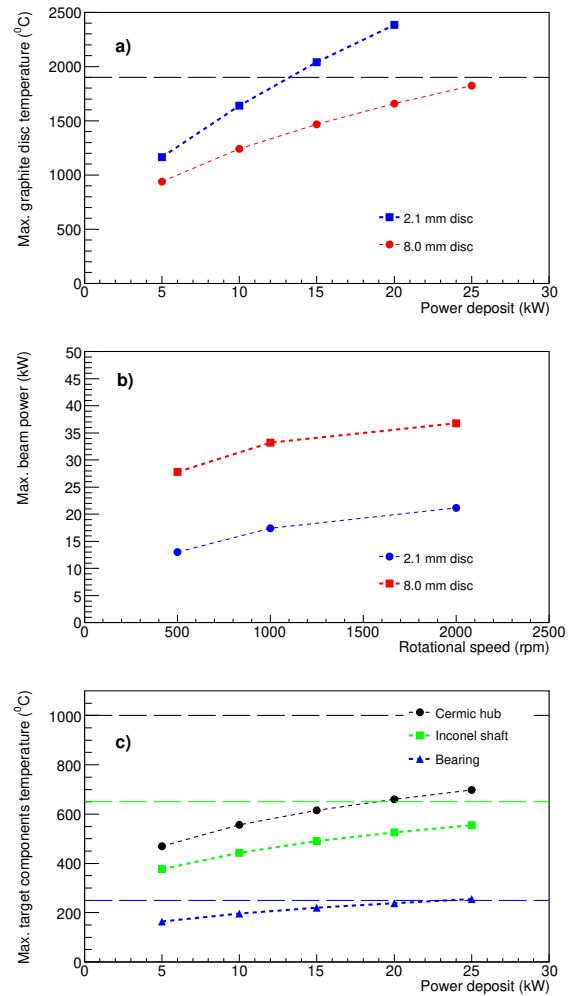


Figure 4: a) Simulated maximum temperature of graphite discs as a function of deposited power for 2.1 mm and 8.0 mm-thick targets. The dashed horizontal line indicates the graphite temperature limit of 1900°C. b) Maximum allowable deposited beam power into the target as a function of rotational speed for both disc thicknesses. c) Simulated maximum temperatures of other critical components, ceramic hub, Inconel shaft, and bearing, as a function of deposited power, along with their respective temperature limits (dashed lines).

properties such as surface emissivity and the TCC, and validation of simulated temperatures using beam-induced thermal imaging data. The comparison between measurements and simulations shows agreement within 4 %, supporting the accuracy of the model. Thermal simulations further demonstrate that all critical components including the graphite disc, Inconel shaft, ceramic hub, and bearings, remain within safe temperature limits for both 2.1 mm and 8.0 mm-thick targets, operated at 2000 rpm and 1000 rpm, respectively, for primary beam powers up to at least 50 kW. These results confirm that the current system configuration is suitable for continued operation during the transitional power ramp-up phase.

REFERENCES

- [1] J. Wei *et al.*, “Technological developments and accelerator improvements for the FRIB beam power ramp-up”, *J. Instrum.*, vol. 19, no. 05, p. T05011, May 2024.
doi:10.1088/1748-0221/19/05/t05011
- [2] P. N. Ostroumov *et al.*, “Acceleration of uranium beam to record power of 10.4 kW and observation of new isotopes at Facility for Rare Isotope Beams”, *Phys. Rev. Accel. Beams*, vol. 27, no. 6, p. 060101, Jun. 2024.
doi:10.1103/physrevaccelbeams.27.060101
- [3] J. Wei *et al.*, “Accelerator commissioning and rare isotope identification at the Facility for Rare Isotope Beams”, *Mod. Phys. Lett. A*, vol. 37, no. 09, p. 2230006, Mar. 2022.
doi:10.1142/s0217732322300063
- [4] M. Portillo *et al.*, “Commissioning of the Advanced Rare Isotope Separator ARIS at FRIB”, *Nucl. Instrum. Methods Phys. Res., Sect. B*, vol. 540, pp. 151–157, Jul. 2023.
doi:10.1016/j.nimb.2023.04.025
- [5] F. Pellemoine *et al.*, “Thermo-mechanical behaviour of a single slice test device for the FRIB high power target”, *Nucl. Instrum. Methods Phys. Res., Sect. A*, vol. 655, no. 1, pp. 3–9, Nov. 2011. doi:10.1016/j.nima.2011.06.010
- [6] M. Portillo and M. Steiner, private communication.
- [7] D. Lee *et al.*, “Physical Thickness Characterization of the FRIB Production Targets”, unpublished.
- [8] S. Yoon *et al.*, “Emissivities of the FRIB Production Target Components”, unpublished.
- [9] G. Lee *et al.*, “Thermal simulation validation for the rotating single-slice graphite target system”, unpublished.
- [10] M. Patil, J. Song, M. Reaume, M. Larmann, N. Bultman, and R. Quispe-Abad, “Thermal analysis of rotating single slice graphite target system for FRIB”, in *Proc. IPAC’24*, Nashville, TN, USA, May 2024, pp. 3827–3829.
doi:10.18429/JACoW-IPAC2024-THPS41
- [11] K. Ioki, M. Nishikawa, I. Tatsumi, T. Uchikawa, and M. Fujiwara, “Measurement of Contact Resistance and Heat Load Test on Graphite Limiter”, *J. Nucl. Sci. Technol.*, vol. 22, no. 7, pp. 529–537, Jul. 1985.
doi:10.1080/18811248.1985.9735694
- [12] I. N. Nesterenko, G. Bollen, M. Hausmann, A. Hussain, S. M. Lidia, and S. Rodriguez Esparza, “Optical System for Observation of FRIB Target”, in *Proc. NAPAC’19*, Lansing, MI, USA, Sep. 2019, pp. 570–572.
doi:10.18429/JACoW-NAPAC2019-TUPLE05
- [13] D. McNanney, S. Cogan, I. Nesterenko, S. Lidia, J. Song, and E. Daykin, “FRIB target thermal image processing for accurate temperature mapping”, in *Proc. IPAC’24*, Nashville, TN, USA, May 2024, pp. 3409–3412.
doi:10.18429/JACoW-IPAC2024-THPG62

INNOVATION FOR SUSTAINABLE ACCELERATING SYSTEMS: THE EUROPEAN iSAS PROJECT*

M. Baylac^{1,†}, J. D'Hondt², J. Knobloch^{3,4}, C. Pira⁵, A. Stocchi⁶

¹Laboratoire de Physique Subatomique et de Cosmologie (LPSC), Univ. Grenoble Alpes, CNRS, Grenoble INP, LPSC - IN2P3, Grenoble, France

²NIKHEF, Amsterdam, Netherlands

³Helmholtz-Zentrum Berlin (HZB), Berlin, Germany

⁴Universität Siegen, Siegen, Germany

⁵Istituto Nazionale di Fisica Nucleare (INFN), Laboratori Nazionali di Legnaro (LNL), Legnaro, Italy

⁶IJCLab Orsay, Université Paris-Saclay, CNRS/IN2P3, Orsay, France

Abstract

If particle accelerators have largely proven their value to society, they must now meet the challenge of energy sustainability. The European project to *Innovate for Sustainable Accelerating Systems* (iSAS) is dedicated to energy-saving of superconducting radiofrequency (SRF) accelerating systems. iSAS will develop, prototype and validate new impactful energy-saving technologies so that SRF accelerators can operate with the same or improved performance with significantly less energy.

INTRODUCTION

Particle accelerators are essential instruments for research infrastructures and for a variety of applications, accounting for 40,000 machines worldwide. In a context of sustainability, minimizing the energy consumption of accelerators is an unavoidable challenge. Funded by the EU (HORIZON-INFRA-2023-TECH-01-01), the project to *Innovate for Sustainable Accelerating Systems* (iSAS) was launched in 2024 to develop core technologies of SRF accelerating systems to minimize energy consumption [1]. It is complementary to other programs developing energy-efficient magnets or RF sources.

This project gathers 12 research laboratories or institutes (CEA, CERN, CNRS, DESY, EPFL, ESS, HZB, INFN, NIKHEF, UKRI, univ. Brussels, univ. Lancaster) as well as 6 industrial companies (ACS, Cryoelectra, Euclid Tech labs, Research Instruments, Thin Film Equipment, Zanon) over a 4-year duration. The iSAS project addresses 3 key Technology Areas with substantial potential to reduce the energy consumption of accelerators:

- energy-saving from RF power, through coherent integration of the RF power source with smart digital control systems and with novel tuners that compensate rapidly cavity detuning from mechanical vibrations,
- energy-saving from cryogenics to develop superconducting cavities with high performance at 4.2 K instead

of 2 K, thereby reducing the grid-power to operate the cryogenic system,

- energy-saving from the beam power, to enable efficient energy recovery of recirculating beams in superconducting cavities with couplers to damp the Higher-Order Modes (HOMs) excited by the passage of high-current beams in the cavities.

Enabled by its large consortium and the joint investment between research institutions and industry, iSAS envisages three Integration Activities to introduce these energy-saving Technology Areas into research facilities:

- integration into a sustainable cryomodule design, by addressing common engineering challenges to use the technologies on a parametric cryomodule design,
- integration into existing research infrastructures, by retrofitting existing accelerating systems. A cryomodule will be adapted, ready to demonstrate energy recovery of high-power recirculating beams in the PERLE research facility,
- integration into industrial solutions, with concrete co-developments with industry to expedite high Technological Readiness Level (TRL) for large-scale deployment of the new energy-saving solutions at current, future infrastructures and towards industrial applications.

The iSAS project concentrates on SRF accelerating systems with the largest leverage for energy savings. The developed technologies aim to optimize:

- ferro-electric fast reactive tuners,
- low-level radio frequency control system,
- coatings of Nb₃Sn on Cu cavities,
- couplers (fundamental, higher-order modes) and beam line absorbers.

iSAS aims to perform R&D on these technologies and to promote their implementation towards industry, by raising their TRL. Three main accelerator-driven ESFRI RIs are at the core of iSAS: ESS, EuXFEL and HL-LHC.

This paper presents the main technologies under development and the description of the work to be performed by the different laboratories within the work packages (WPs) of iSAS. The focus is set on the metric to evaluate the expected energy saving for each of these devices.

* Work supported by funding from the European Union's program Horizon-INFRA-2023-TECH-01 under GA No 101131435 – iSAS

† baylac@lpsc.in2p3.fr

ENERGY SAVING METRIC

At the beginning of the project, a metric for energy saving performances of the different technologies was defined. This metric will be filled in at the end of the project, with the equipment available and operational at that time. For this metric, the selected approach is focused on the power required for operation. We will evaluate and compare the electrical power consumption with and without the iSAS technology under similar conditions. The comparison will be performed for different use cases (specific to each technology), but always under similar conditions for each technology to ensure a fair comparison [2]. In addition, a consumption model of the PERLE ERL will be developed to evaluate the accelerator efficiency.

FERRO-ELECTRIC FAST REACTIVE TUNER

In WP1 led by HZB, a fast-tuning system is developed to compensate detuning due to mechanical vibrations or beam induced transients, which are both usually compensated by adding a significant power overhead. Ferro-Electric Fast Reactive Tuners (FE-FRTs) are an alternative to classic mechanical cavity tuners (piezo). They form a coupled system of cavity and a typically coaxial line with ferro-electric material. The permittivity of this material is changed by applying high voltage, thus generating a change of impedance allowing to control the resonance frequency of the coupled system on a very fast time scale (~ 100 ns with a tuning range in the tens of kHz) [3, 4]. FE-FRTs require an additional RF port to install on the cavity, but avoid complex control algorithms needed to take into account the highly resonant mechanical-RF cavity-tuner system. FE-FRTs should of course not compromise stability or reliability of operation, but could even better improve it beyond current state-of-the-art.

FE-FRT will be tested with a 2-cell 1.3 GHz cavity and a fully equipped nine-cell TESLA/XFEL cavity, including a tunable high-power coupler and classic mechanical tuning system. The metric to estimate the savings is the invested RF power to drive the cavity at a given field (peak and average power) for microphonics compensation, which will be converted to wall-plug power. It will be determined by comparing the RF power invest with the FE-FRT and without the FE-FRT (with the piezo control) at identical values of loaded quality factor Q .

Expected savings in RF power should be significant. The required power to operate a cavity at voltage scales with the square of the cavity bandwidth in low beam loading machines (microphonics case). For an EU-XFEL cavity operated at 25 MV/m (CW mode), a factor of 10 reduction in RF power is expected when reducing the cavity detuning from 40 Hz half-bandwidth (typical with piezo tuners) down to 5 Hz, which is reachable with a FE-FRT.

SMART LLRF

In WP2 led by DESY, an optimized Low-Level Radio Frequency (LLRF) system is developed in order to reduce the RF power required to drive the cavities, thanks to an efficient control of cavity field and detuning. To minimize the RF power, cavities must operate at a quality factor Q_{ext} as high as possible, at a narrower bandwidth. But these conditions make resonance control extremely challenging and will only reduce the RF power needs if the resonance can be properly guaranteed. So, the challenge is to find the highest Q_{ext} ($\sim Q_L$) while meeting resonance control goals and without compromising operability or reliability. AI will be integrated in this smart LLRF. Moreover, FE-FRT will also help to reach high values of Q_{ext} .

Since a LLRF system is constantly required for cavity field control, the system cannot be switched OFF for comparison purposes. Yet, options of the optimized LLRF can be switched ON/OFF or adjusted to evaluate their impact on power consumption. Several factors of the LLRF tuning system impact the consumption of the accelerator (value of coupling, shape of the modulator pulse, efficiency of the frequency control, type of amplifier, drain voltage) so several metrics will be used: instantaneous AC consumption, RF power usage, AC-to-RF efficiency, accelerator up time. Measurements will be performed at different facilities (DESY, HZB and CNRS) offering different test options (CW, pulsed, presence of beam, narrow bandwidth cavities, etc.) to cover multiple operational cases.

Optimization using the LLRF system can lead to significant savings in the electrical power of an accelerator. For example, the step-wise optimization of the modulator pulse shape at the EU-XFEL led to a significant reduction in accelerator power consumption by more than 1 MW (Fig. 1). This improvement translates into cost savings of several million euros on the yearly electrical bill [5].

Significant savings in RF power are expected for the smart LLRF system developed within iSAS. For example, optimizing the working point of a GaN solid-state power amplifier with the LLRF can boost its efficiency from 55% to 65%. Increasing the external quality factor (Q_{ext}) of a cavity operating at 20 MV/m from $Q_{\text{ext}} = 1e7$ to $Q_{\text{ext}} = 4e7$ can reduce the required power from 10 kW to 4 kW.

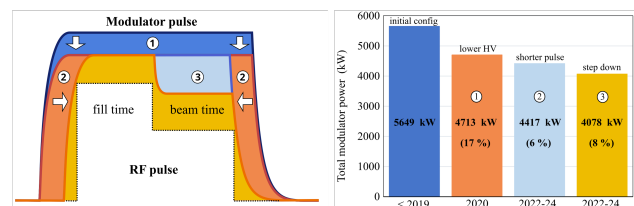


Figure 1: Left: optimization steps of the modulator pulse at EU-XFEL; right: corresponding power savings [5].

COATINGS ON COPPER CAVITIES

In WP3 led by INFN, iSAS will explore coatings of Nb_3Sn thin films on copper substrate aiming to operate RF cavities

at a temperature higher than 2 K, thus reducing dramatically the required cryogenics power [6]. To match the excellent performances obtained with cavities made of bulk Nb at operated 2 K, thin film coatings must minimize flux trapping and ensure sufficient mechanical strength to allow for cavity tunability. These R&D topics will be studied on different types of samples and eventually with a cavity operating at 4.2 K developed within iSAS.

A cavity in operation generates losses ($\propto 1/Q_0$) which must be dissipated by the cryogenic circuit. Given the coefficient of performances (COP) of the cryogenic system, dissipating these losses requires a large amount of power: about 800 W of power at room temperature is needed to account for 1 W of power dissipated at 2 K (Fig. 2). The efficiency, or quality factor, of the cavity is driven by its surface resistance R_s via $Q_0 = G/R_s$ (G is the cavity geometry factor). The surface resistance depends on several parameters (sputtering coating parameters, copper substrate surface treatments, interlayer, post-coating treatments). It comprises a temperature-dependent term (BCS) and the residual resistance: $R_s = R_{BCS}(T) + R_{res}$. The BCS term can be calculated as a function of temperature, therefore the residual resistance R_{res} can be deduced from a usual measurement of Q_0 at a given temperature.

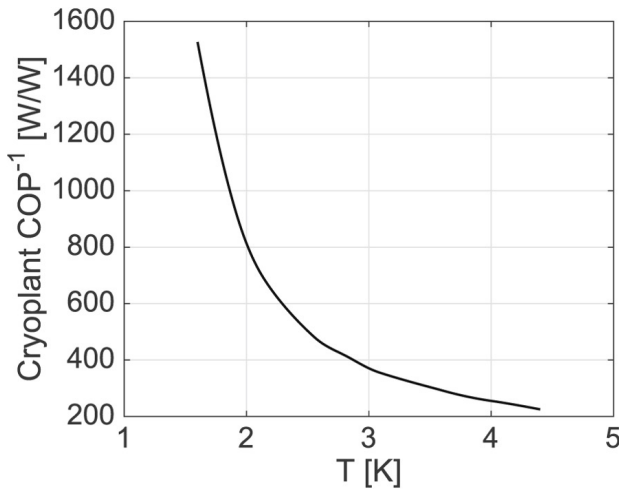


Figure 2: Typical cryogenic plant efficiency (watts of wall power to remove one watt of heat) as a function of temperature, accounting for Carnot efficiency and deviation of a realistic plant from Carnot [6].

The energy required to operate a multi-cell cavity can be characterized by the power dissipation of the cavity cell at a given accelerating field: P_{acc} per cell. This parameter accounts for both performance of the material (R_s) and the cryogenics system (COP). To estimate energy performance, we will determine the dissipated power for a Nb_3Sn coated cavity P_{acc} per cell at 1 MV/m as follows:

- Measure Q_0 versus E_{acc} , via an RF test, to deduce the surface resistance R_s at the given gradient,
- From this surface resistance evaluation of Nb_3Sn , estimate the power dissipation at 4.2 K,

- Comparison with bulk Nb at 2 K at same gradient by estimating the power dissipation at 2 K.

Three cases will be studied: quadrupole resonators QPR (400 MHz, 800 MHz), 1.3 GHz cavity (baseline of the I.FAST project [7]) and a new cavity optimized in iSAS.

With material having a higher critical temperature, it is envisaged that SRF cavities be cooled at 4.2 K while maintaining high quality factor Q_0 and accelerating field E_{acc} . Given the efficiency of the cryogenics system (≈ 240 at 4.2 K versus ≈ 800 at 2 K), running at 4.2 K instead of 2 K would reduce the power consumption by a factor of 3. The expected grid power ranges between 1-3.5 W per cell at 1 MV/m for $R_{res} = 5-30$ n Ω (Fig. 3). Thus, a Nb_3Sn cavity operated at 4.2 K outperforms a Nb cavity at 2 K, even at a residual resistance up to 5-6 times higher.

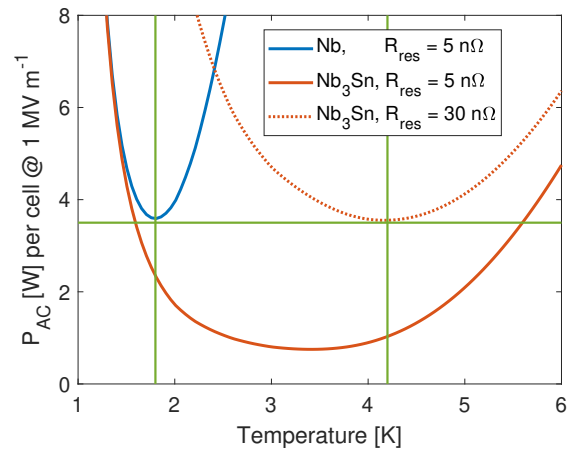


Figure 3: Calculated AC power of Nb and Nb_3Sn cavity cells versus temperature at 1.3 GHz [8].

COUPLERS

In WP4 led by CNRS dedicated to couplers, different technologies and devices are developed, mainly at 800 MHz. They will be designed, integrated and tested in accelerator-like conditions in a cryomodule capable of energy-recovery operation at the PERLE facility (Fig. 4):

- Fundamental Power Coupler (FPC) to introduce the power to excite the fundamental mode of the cavity via an antenna, in order to accelerate the beam,
- Higher Order Modes (HOM) coupler to damp the HOMs trapped in the cavity and deposit them into loads at higher temperatures.
- Beam Line Absorber (BLA) to damp HOM propagating out of the cavity, through the beam pipes by absorbing directly their power.

The cooling strategies for these components aims at reducing the heat loads to the cryogenic bath, while preserving the functional RF requirements. Even a moderate fraction of HOMs dissipated in the cryomodule's cold mass, will increase significantly the grid power for cryogenics. Optimizing the design of RF couplers is of particular importance

as FPCs and HOMs can account for half of the cryogenic load on a linac, as estimated on the Cornell CBETA ERL linac [9].

Optimization of the electric consumption for cryogenic process mainly depends on heat loads and temperatures involved. It requires fine thermal simulations and selection of the optimized cooling processes. When additional components are required, the complexity of this new component must also be considered. For example, introducing BLA may induce a potential risk of particle contamination in the cavities due to the vicinity of the BLA material and may impose specific venting precautions for this material. For the metric, we propose to calculate the electrical power consumption of the cryogenic system for different cases. The final estimation of the plug power will use the overall real efficiency of the actual cryoplant of PERLE.

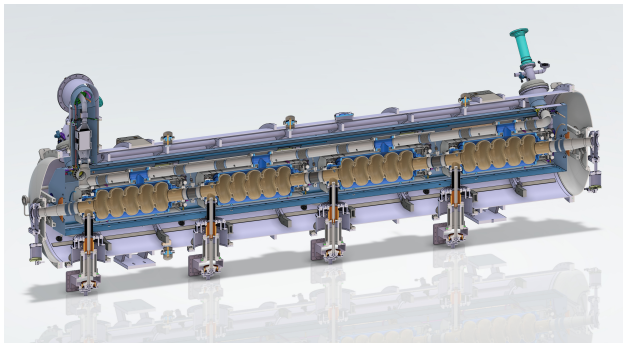


Figure 4: Cryomodule design of the energy recovery linac project PERLE with FPC, HOM coupler and BLA [10].

Fundamental Power Coupler

At 800 MHz, the power coupler uses the design of the SPL coupler considering its high RF power range and high efficiency of the heat exchanger [11]. The comparison between turbulent and laminar regimes was evaluated to select the best cooling regime. Furthermore, two cooling schemes are studied and their cooling-power consumption compared. For these two schemes, we consider, as a first approximation, that the solid conduction heat from the cold part of the FPC external conductor to the 2K bath is equal in both cases:

- Two-loop coupler (heat exchangers at 50 K and 5 K),
- One-loop coupler (heat exchanger from 5 K to 300 K).

With a given RF design, cooling scheme optimizations include materials to reduce the solid conduction (stainless steel body) and RF losses (copper coating). The one-loop cooling scheme is selected as it is about 2.5 times energetically more efficient than the two-loop scheme. It is important to note that the energy saving obtainable with the one-loop cooling scheme with helium is strictly connected with the helium inlet temperature in the double-walled tube, which should be as close as possible to the design value of 5 K.

To complete the design work performed on the FPC itself, analyzing the data from the ESS cryomodule provides valuable feedback to further optimize the FPC system by

improving the thermal insulation of the cryogenic line to the FPC.

Higher Order Modes Couplers

Higher order modes can be excited in cavities by the high-power beams. They must be handled with care as improper extraction of HOMs can strongly limit the beam intensity due to beam instabilities. Energy-recovery linacs (ERLs) are particularly subject to HOMs excitations due to recirculation of high-current beams in the superconducting cavities.

At 800 MHz, the HOM studies have been made for three different designs: hook, probe and double quarter-wave [12]. The selected scheme uses 2 hook HOM couplers per cavity. For the metric, two cooling schemes will be studied and their cooling power consumption compared:

- HOM coupler cooled at 2 K,
- HOM coupler cooled at 5 K.

HOM optimizations include geometrical design: RF optimization (to reduce the RF losses) and thermal design, flange type and material, heat interception on the RF wire as well as materials to reduce the surface resistance and consequently the RF losses. For high RRR Nb, the surface resistance is several orders of magnitude higher at 5 K than 2 K. Thus, a cooling at 5 K could be energetically efficient only with superconducting materials other than Nb, for instance Nb₃Sn which would require dedicated R&D.

It is important to mention that cooling at 5 K can compromise the functionality of the HOMs. In case of unexpected heat loads, the antenna could quench. Therefore, even if a cooling at 5 K is more efficient, the 2 K option may still be preferred because of a higher reliability against unexpected loads.

Beam Line Absorbers

Beam Line Absorber are used to damp the higher order modes propagating out of the cavity, through the beam pipes. The BLAs are designed to absorb directly the power generated by the HOMs.

At 800 MHz, the BLA studies are underway to define the optimum design to integrate in the cryomodule to be tested at the PERLE facility. For the metric, three cooling schemes will be studied and their cooling power consumption compared:

- Without BLA inside the cryomodule (BLA at 300 K),
- With BLA inside the cryomodule (BLA at 50 K),
- With BLA inside the cryomodule with an intermediate thermal intercept at 5 K (BLA at 50 K).

In the first scheme, the maximum possible dissipation could be too high for the cryoplant to withstand.

In the second scheme, the power dissipated in BLAs by the HOMs is high (~50W between each cavity) but controlled. The BLAs are placed in between each cavity. Some absorber materials have a good efficiency when cooled at 50 K (temperature loop provided by the cryoplant), but require R&D. When cooling the inter-cavity space at 50 K, residual solid conduction heat is evacuated at 2 K.

In the third scheme, an intermediate 5 K interception loop is added to the previous option. BLA optimizations include the geometrical design and R&D on microwave absorbing material cooled at 50 K. BLAs will be placed in the cryomodule. Depending on the final inter-cavity and the BLA mechanical integration, the 5 K interception could be avoided to thus circumventing the complexity and the heat losses due to an additional transfer line at 5 K.

ENERGY RECOVERY LINAC

Energy-recovery linacs are a promising technology and accelerator concepts to provide high current, high brightness and high-quality beam by minimizing the accelerator power consumption and footprint [13]. One key aspect is that the ERL concept enables to recover the beam power of the accelerated beam after the interaction point (IP), thus reducing the RF requirements compared to classical acceleration with single-pass linacs. To provide an order of magnitude of this power saving, one can consider the ERL of the PERLE project as a reference example. PERLE aims to provide a CW 20 mA electron beam at 250 MeV at the IP (5 MW) [14] with one cryomodule composed of 4 cavities.

A consumption model of the PERLE ERL will be developed to determine the accelerator efficiency. The goal is to evaluate this beam power at the IP as a fraction of total electricity consumption. This efficiency will be calculated with the best accuracy considering all the elements of the machine and impacts of errors due to perturbations (i.e. microphonics) or synchronization (path length adjustment). The same exercise will be applied to a classical linac solution and compared to the ERL efficiency.

CONCLUSION

With the European project iSAS (2024-2028), impactful energy-saving technologies will be developed, validated and integrated with a direct impact on current research infrastructures, their upgrades as well as future industrial solutions. The project concentrates on SRF accelerating systems with the largest leverage for energy savings.

The devices under optimization by the participating institutions include ferro-electric fast reactive tuners, AI-driven low level radio frequency control system, coatings of Nb₃Sn on Cu cavities, couplers (fundamental, higher order modes) and beam line absorbers. Moreover, iSAS will provide a complete accelerating structure capable of accelerating high-power beams in an energy-sustainable way: a cryomodule at 800 MHz to be tested at the ERL PERLE facility.

A detailed and concrete plan to evaluate the energy-saving metric of all the technologies developed is defined. It is the long-term ambition of iSAS to reduce the energy footprint of future SRF accelerators by half.

REFERENCES

- [1] iSAS, <https://isas.ijclab.in2p3.fr/>
- [2] M. Baylac, F. Bouly, J. Branlard, K. Canderan, P. Duchesne, Y. Gómez Martínez, A. Neuman, V. Parma, C. Pira, H. Saugnac, C. Schmidt, “iSAS WP9 - task 9.5 - Milestone 32: verifiable metric for energy-saving performances”, internal report, 2025.
- [3] N. C. Shipman *et al.*, “A Ferroelectric Fast Reactive Tuner for Superconducting Cavities”, in *Proc. SRF'19*, Dresden, Germany, Jun.-Jul. 2019, pp. 781–788. doi:10.18429/JACoW-SRF2019-WETEB7
- [4] I. Ben-Zvi, G. Burt, A. Castilla, A. Macpherson, and N. Shipman, “Conceptual design of a high reactive-power ferroelectric fast reactive tuner”, *Phys. Rev. Accel. Beams*, vol. 27, no. 5, p. 052001, May 2024. doi:10.1103/physrevaccelbeams.27.052001
- [5] J. Branlard *et al.*, “RF-based energy savings at the FLASH and European XFEL linacs”, in *Proc. LINAC'24*, Chicago, IL, USA, Aug. 2024, pp. 591–595. doi:10.18429/JACoW-LINAC2024-THZA003
- [6] S. Posen and D. L. Hall, “Nb₃Sn superconducting radiofrequency cavities: fabrication, results, properties, and prospects”, *Supercond. Sci. Technol.*, vol. 30, no. 3, p. 033004, Jan. 2017. doi:10.1088/1361-6668/30/3/033004
- [7] IFAST website: <https://ifast-project.eu>.
- [8] C. Antoine *et al.*, “Thin-film SRF roadmap”, IFAST deliverable report D9.1, 2025. doi:10.5281/zenodo.14731411.
- [9] G. Hoffstatter *et al.*, “Cornell Energy Recovery LINAC Project Definition Design Report”, 2013.
- [10] Courtesy of S. Blivet, IJCLab.
- [11] E. Montesinos *et al.*, “Conceptual SPL RF Main Power Coupler design”, CERN report, LHC Project Report-0052, 2011.
- [12] C. Barbagallo *et al.*, “First coaxial HOM coupler prototypes and RF measurements on a copper cavity for the PERLE project”, in *Proc. IPAC'23*, Venice, Italy, May 2023, pp. 89–92. doi:10.18429/JACoW-IPAC2023-MOPA025
- [13] A. Hutton, “Energy-recovery linacs for energy-efficient particle acceleration”, *Nat. Rev. Phys.*, vol. 5, no. 12, pp. 708–716, Oct. 2023. doi:10.1038/s42254-023-00644-6
- [14] S. A. Bogacz *et al.*, “Beam dynamics driven design of powerful energy recovery linac for experiments”, *Phys. Rev. Accel. Beams*, vol. 27, no. 3, p. 031603, Mar. 2024. doi:10.1103/physrevaccelbeams.27.031603

PRIMARY BEAM DEVELOPMENT FOR FRIB EXPERIMENTS*

T. Maruta[†], K. Fukushima, A. Gonzalez, K. Hwang, P.N. Ostroumov, A.C. Plastun, T. Zhang, Q. Zhao, Facility for Rare Isotope Beams, Michigan State University, East Lansing, USA

Abstract

Since starting the user operation of Facility for Rare Isotope Beams (FRIB) at Michigan State University in May 2022, the driver linac has provided more than a dozen ion beam species from Oxygen to Uranium to the production target. FRIB routinely provided 20 kW primary beams on target since March 2025, which is a factor of 20 higher than at the beginning of the scientific user operation. In this presentation, the recent progress of FRIB driver linac beam development, a discussion of efficient primary beam tuning procedures based on physics applications, and accelerator improvement projects for low-loss accelerator will be discussed.

INTRODUCTION

FRIB is a heavy ion accelerator facility constructed at Michigan State University under the corporate agreement with the U.S. Department of Energy Office of Science to support the Office of Nuclear Physics mission. The facility is comprised of the driver linac, fragment separator, and experimental area including 6 MeV/u reaccelerator. Construction was completed in January 2022, and user operation started in May 2022.

The driver linac is designed to provide a 400 kW continuous wave beam to the production target [1]. The required primary ions are generated in the Electron Cyclotron Resonance (ECR) source, selected after a 90° bend, and transported to the accelerator tunnel through 24-meter-long Low Energy Beam Transport (LEBT). The beam is accelerated by Radio Frequency Quadrupole (RFQ) and the following three linac segments (LS1, LS2 and LS3). The beam acceleration is provided by four types of Superconducting (SC) RF cavities with optimal β from 0.041 to 0.54. For the beam focusing in the cryomodules, we use SC solenoids equipped with horizontal and vertical steering coils. The layout of the linac is shown in Fig. 1. For a detailed description of the linac structure, we refer to earlier publications, for example, [2]. The beam accelerated by the LS1 interacts with the charge stripper, which is a highly beneficial technique for heavy ion accelerators. The electrons are stripped off the ions while passing through a thin material, which boosts the charge-to-mass ratio (q/A) of beams for efficient acceleration. FRIB has developed 20 – 30 μm thick liquid lithium film as the stripper (LLCS) [3] because of its high capability of thermal load and radiation resistance. Due to the stochastic nature of the stripping process, the output beam is distributed to several charge states.

In most cases, the charge state distribution is a Gaussian function, and the fraction of beam intensity in a single charge state is low. Table 1 shows recently operated beams, including the stripping efficiencies measured in FRIB. The yield of the central charge state of the ^{238}U beam is only 21% of the initial intensity.

Table 1: Beam parameters during the recent beam operations. The stripping efficiencies were measured at 17 MeV/u for ^{124}Xe and ^{238}U , and 20 MeV/u for the rest of ions.

Ion	Charge states after stripper	Energy at the target [MeV/u]	Stripping efficiency 1q / Multi-q
^{48}Ca	19+, 20+	225	72% / 98%
^{58}Ni	26+, 27+	250	66% / 94%
^{64}Zn	28+, 29+	240	71% / 88%
^{82}Se	32+, 33+	200	74% / 88%
^{124}Xe	48+ ~ 50+	240	30% / 76%
^{238}U	73+ ~ 77+	177	21% / 83%

To provide higher stripping efficiency, the FRIB linac has been designed to accelerate multiple charge states simultaneously. To avoid the growth of the effective emittance due to trajectories' displacement, the bending systems in FS1, FS2 and BDS have been designed to satisfy achromat conditions and merge all charge states' central trajectories after the bends [4]. The aperture in the dispersive plane is sufficient to accept five charge states of the uranium beam with charge state spread $\Delta q/q_{\text{cen}}$, equal to 5.3%. The multi-charge acceleration substantially reduces the deposited power of unwanted charge states on the Charge Selection Slits (CSS) installed after the first bending dipole in the FS1 and reduces required radiation shielding. In the present CSS, absorbed beam power at the single spot is limited to 500 W. For example, after the stripping, the $^{48}\text{Ca}^{19+}$ fraction is 26% and the 500 W limit corresponds to approximately 13 kW of $^{48}\text{Ca}^{20+}$ only delivered to the target.

The beam time of most experiments is less than a week. Each experiment requires different primary ion species and energy on the target. Therefore, shortening the primary beam tuning time through efficient procedures is essential to provide more time for science.

* Work supported by the U.S. Department of Energy Office of Science under Cooperative Agreement DE-SC0023633, the State of Michigan, and Michigan State University. Also, part of this work is supported by the U.S. Department of Energy Office of Nuclear Physics under Award Number DE-SC0025531.

[†] maruta@frib.msu.edu

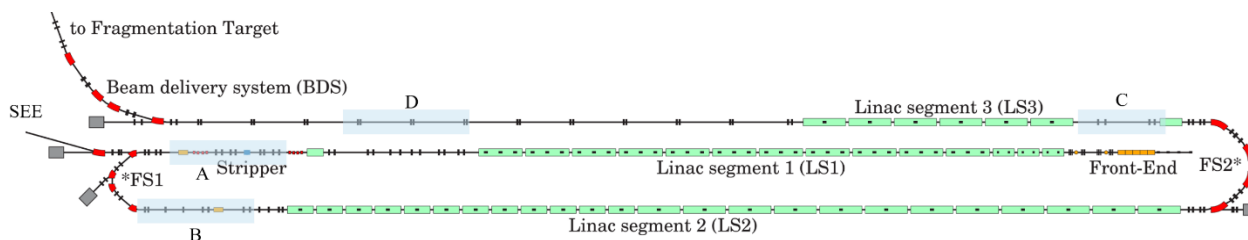


Figure 1: Layout of the FRIB driver linac.

NEW BEAM DEVELOPMENT

The development of a new primary beam starts with a pre-calculation of the accelerator setting by simulation tools. The RF cavities' from MEBT to the target are calculated by a model-based Instant Phase Setting (IPS) application [5]. The amplitude and synchronous phase of each cavity are optimized to meet the energy requirement and provide sufficient stability area in the longitudinal phase space. The calculated RF cavities' settings are loaded to 3D beam envelope code FLAME to calculate required focusing fields. The solenoids in the acceleration segments LS1 and LS2 are set to provide the transverse phase advance per period below 90° . Then, five sections of quadrupoles (upstream of the LS1, upstream of the LS2, upstream of the stripper, FS2 and BDS sections) are optimized to match Courant-Snyder (CS) parameters of all charge states simultaneously to the following beam optics. The magnets' setting is registered to the application "Settings Manager" [6] and matched CS parameters are registered to the beam envelope tuning application in the accelerator control network.

The calculated setting is applied to beamline devices at the beginning of Primary beam Development Time (PDT). The latter includes beam central trajectory tuning and envelope matching along the linac. We typically conduct matching in 5 sections of the accelerator. RMS beam size is measured in each location by varying quadrupole settings to calculate the RMS CS parameters and calculate the optimum quadrupole setting to match all charge states simultaneously.

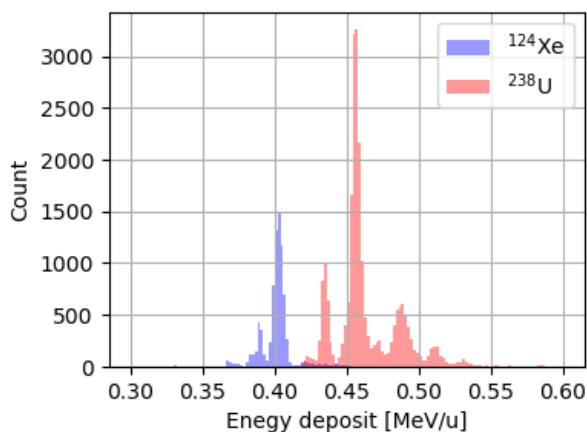
RECENT PROGRESS WITH LINAC TUNING

Since the start of the scientific user operation in May 2022, the beam power of the driver linac has gradually increased to 20 kW. Up to now, 13 stable isotope (^{18}O , ^{22}Ne , ^{28}Si , ^{36}Ar , ^{40}Ar , ^{48}Ca , ^{58}Ni , ^{64}Zn , ^{70}Zn , ^{82}Se , ^{124}Xe , ^{198}Pt , and ^{238}U) beams have been accelerated up to 300 MeV/u and delivered to the production target. In addition, seven isotope (^{16}O , ^{40}Ar , ^{86}Kr , ^{107}Ag , ^{129}Xe , ^{169}Tm , and ^{209}Bi) beams have been provided to the test station in the Single Event Experiment (SEE) beamline with energies ranging from 10 to 40 MeV/u.

Lithium Film Stage Feedback in Operation

We have observed the energy loss fluctuation at LLCS from the beginning of its operation. Figure 2 shows energy

loss distribution for ^{124}Xe and ^{238}U beams. There are 3 ~ 5 meta-stable states of the lithium film thickness quickly jumping from one to another in a 0.1 s time scale. The energy feedback system has been developed, and it is in operation to stabilize the post-stripper energy and bunch timing by automatically adjusting the driven phase of the last cavity in LS1 with 0.1 s response time [7]. This feedback system helps us to control the longitudinal emittance growth due to longitudinal tails folded by non-linear fields in FS1 buncher cavities and minimize the beam losses in the LS2 cryomodules. The latter results in the temperature increase of cold beam pipes in the cryomodules. In the absence of the feedback, the beam losses in LS2 are increased, especially for the uranium beam, if the stripper film suddenly jumps to another meta-stable state of the lithium flow.

Figure 2: Distribution of energy loss at LLCS for ^{124}Xe (pale blue) and ^{238}U (pale red) beams without LLCS stage feedback.

Another feedback system has been implemented recently to stabilize the beam energy loss in the stripper. The feedback automatically moves the LLCS stage vertically, i.e. the beam spot on the film to correct the energy loss on the film once the energy loss varies more than 5% from the reference value which is set by an accelerator physicist during the PDT. The feedback response time is approximately tens of seconds. These two kinds of feedback systems stabilize the output beam energy, arrival timing, and stripper energy loss with two orders of different time scales. Figure 3 shows how the feedback worked in a recent operation. The energy loss (red) suddenly increased from 0.43 to 0.49 MeV/u at (a). The post stripper energy (green) changes accordingly but immediately returns to the original energy by adjusting the LS1 cavity's phase (blue). The

stage feedback recognized the change of energy loss at (b) and started moving the stage (purple). The motion of the stage continued for ~ 45 sec, and the LS1 cavity phase continuously changed during the stage to keep the post-stripper energy through the end of motion at (c). Note that the energies on this plot are average for the last one second, so the energy feedback response is quicker than the plot. By activating these feedbacks simultaneously, the temperature increase in LS2 crymodules is reduced to nearly half, which unleashes 50 kW operation for ^{238}U and even higher for lighter ions.

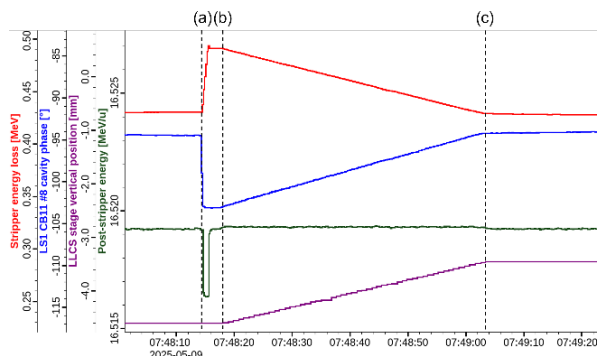


Figure 3: The post-stripper energy and energy loss at LLCS are controlled by energy and LLCS stage feedbacks. The energies (red and green) on this plot are averages for the last 1 sec, so the actual energy change is quicker than this plot.

Acceleration of Five Charge States of Uranium Beam

The world record of 10.4 kW was demonstrated in December 2023 by accelerating three charge states (3-q , $74+$, $75+$, $76+$) [8] to 177 MeV/u, resulting in 58% stripping efficiency. While a 10 kW beam has been stably delivered to the target for new isotope search, there were relatively high beam losses in the FS2 and BDS, and temperature sensors in the LS2 showed a 0.4 K increase. Note that at that time, the stripper stage feedback was not available.

Further improvements of the ^{238}U beam optics was conducted in June 2024. The RF cavities' setting was optimized to provide stability for five charge states of uranium. The differences between the central trajectories of all charge states are mitigated to be within 1.5 mm in non-dispersive sections by carefully tuning dipoles, quadrupoles and sextupoles in the bending systems. Also, the simultaneous 5-q transverse matchings were performed upstream of the LS2, LS3, and BDS sections. This tune accepts 5-q ($73+$ to $77+$), and stripping efficiency was increased to 83%. During the ramping up of the beam power to the target, the beam image of 5-q on the 2.1 mm thick static carbon target was taken at 500 W as shown in Fig. 4. No beam-lets were observed on the image, and RMS beam size on both horizontal and vertical directions is below 0.5 mm. This optics is our current reference setting and has been employed for the recent 20 kW operations with trajectories' corrections and some tunings in the front end to compensate for the beam profile variation from the ECR ion source.

The ICs, Neutron Detectors (NDs) and thermal sensor signals during the recent 20 kW operation are shown in Fig. 5 (top). Their signals from 220 to 240 meters come from the stripper and CSS. ICs in FS2 and BDS detect signals below 20 mR/hr, which is less by a factor of 5 compared to 3-q operation in 2023.

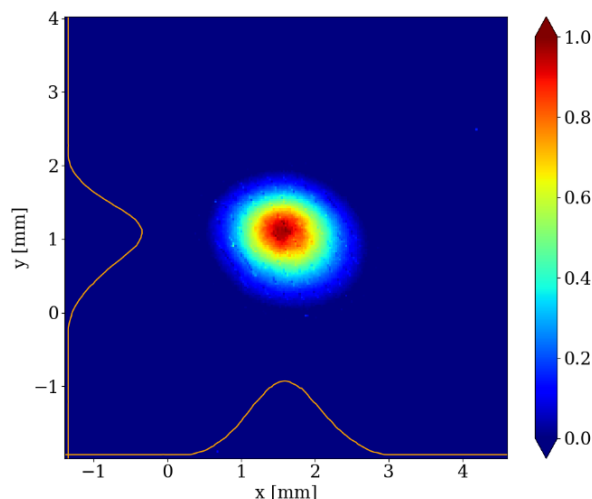


Figure 4: Thermal image of 5-q ^{238}U beam image on the static fragmentation target. The temperature range is scaled from 0 to 1.

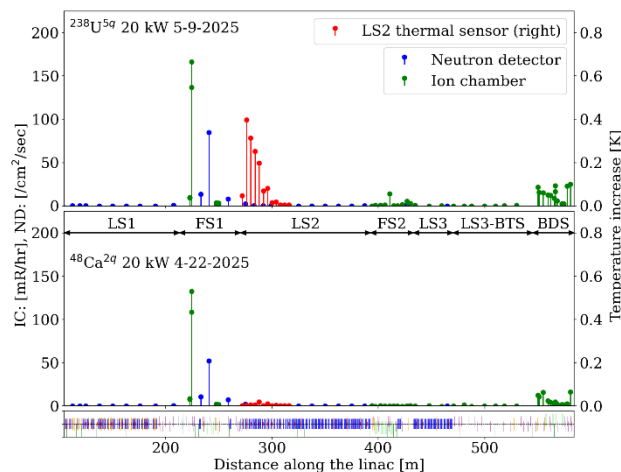


Figure 5: Beam loss signals during 20 kW $^{238}\text{U}^{5\text{q}}$ (top) and $^{48}\text{Ca}^{2\text{q}}$ (bottom). The Neutron Detectors (NDs, blue), ion chambers (ICs, green), and thermal sensors in LS2 crymodules (red) are shown. The signals from 220 to 240 m come from the stripper and the CSS.

Although the beam losses have been successfully mitigated, significant emittance growth was observed during the transverse beam tunings. Figure 6 shows the measured normalized emittance of each charge state. The emittance of $73+$ is approximately doubled at LS3 entrance and further increased by ~ 3.5 times at BDS upstream. $74+$ also shows a factor of two growth from LS3 to BDS but much less than $73+$. The emittances of other charge states remain nearly constant. The SC solenoids are installed for LSs transverse focusing, which can mix up the horizontal and

vertical emittance in 4D phase space if the beam is mismatched. The number of quadrupoles available for the matching is ten for the section upstream of the LS2 and eight for LS3, which is less than a number of quadrupoles available in the BDS. This has motivated us to plan the installation of additional quadrupoles in these areas to better match multi-q beams.

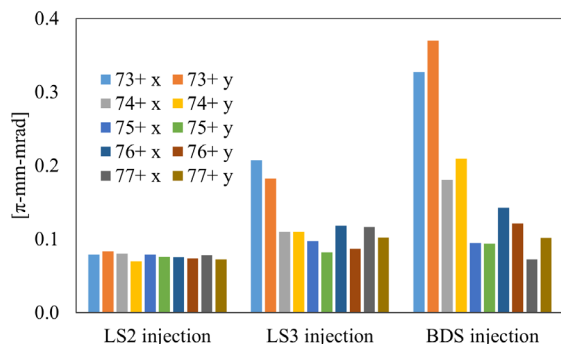


Figure 6: Normalized transverse RMS emittances for each charge state of $^{238}\text{U}^{5q}$ beam measured by quadrupole scans.

Acceleration of Two Charge States of Calcium Beam

As mentioned, 2-q acceleration is essential for the Ca beam to deliver 20 kW or higher to the target while adhering to the single spot power limit of 500 W at the CSS. 2-q beam development started from ^{82}Se beam, which is the least $\Delta q/q_{ave}$ in our beam list, and then gradually extended to the Ca beam with the highest charge spread, 5.1%, close to the design limit of the bending systems.

In the initial Ca beam development, substantial emittance growth has been observed for 20+ through LS2 and LS3. The solenoid setting in LSs was originally developed for 20+ acceleration, and increased by 2.6% for 2-q acceleration. This setting has been kept even when cavity settings were changed for different velocity profiles in LS2, which resulted in high transverse phase advance per period and irregular descent along the LS2, as shown with the blue line in Fig. 7. Currently, we speculate that the higher solenoid fields negatively impact the emittance projections into x-x' and y-y' phase spaces for the magnetized beam produced in the ECR. The solenoid setting was re-calculated so that the phase advance starts at 90° and adiabatically changes to ~35° as the green line in Fig. 7. After the beam development with the new solenoid setting, the emittance growth is mitigated, and beam losses at 20 kW are below 20 mR/hr in BDS.

ACCELERATOR IMPROVEMENT PROJECTS

Recent 20 kW operations with Ca, Ni, Zn, Se, Xe, and U beams show that the linac's beam losses are tolerable for > 50 kW if they increase linearly with the beam intensity. FS1 upgrade projects are underway to further reduce the beam losses, especially those related to the lithium stripper, and prepare the linac for acceleration of beams above 50 kW.

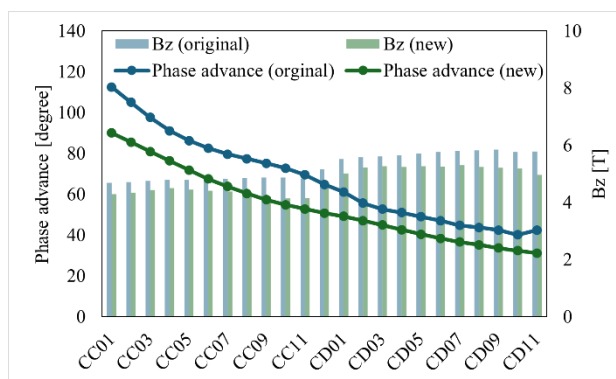


Figure 7: LS2 Transverse phase advance per period and solenoids' field in each cryomodule in original (blue) and new optics (green).

Large Bore Quadrupoles around the Stripper

The thin liquid lithium film has limited thickness uniformity. Because beam energy loss is proportional to the thickness of the film, beam energy spread increases with larger thickness nonuniformity, resulting in higher longitudinal emittance growth. Consequently, the longitudinal halo causes beam losses in the LS2.

Improving the film thickness uniformity is essential for reducing the beam losses in the cryomodules. To mitigate the nonuniformity on the beam spot, we have tuned quadrupoles upstream of the stripper in every PDT so that the beam size on the stripper is as small as possible with RMS beam size in quadrupoles below $\frac{1}{4}$ of aperture to avoid any beam losses. The black line in Fig. 8 shows the correlation between beam size and the standard deviation of the thickness of the beam spot when the average thickness on the beam spot is 1.0 mg/cm², which is evaluated using the thickness distribution measurements [3]. The RMS beam size on the stripper film has typically been 0.5 mm in recent operations, and the thickness nonuniformity is 0.12 mg/cm². The nonuniformity exponentially increases as a function of the beam size, so it is crucial to maintain beam rms size on the stripper 0.5 mm or less.

As the beam intensity increases for higher power operation, the beam emittance from the ECR ion source is possibly larger. In preparation for the larger emittance, we are planning to replace the 9 quadrupoles around the stripper (section "A" in Fig. 1) to allow the beam size to be maintained to a similar level or to enable further focusing of the beam with smaller emittances. The beam dynamics simulation shows that a larger aperture and stronger focusing quadrupoles are necessary to keep the beam size small at the stripper without beam loss on the quadrupoles. The currently installed 50-mm-bore quadrupoles (Q1-type) will be replaced with 75-mm-bore quadrupoles (Q2-type). The beam size was calculated by FLAME with various normalized emittance from 0.1 to 0.3 π -mm-mrad and turned out that we can keep same beam size even if the emittance increases by 50% or reduce beam size by 30% at same emittance as shown in Fig. 8. At the same time, we will also install a 15-mm-radius collimator just after the stripper module to eliminate large-scattered particles produced by the stripper.

After the replacement is completed, two replaced Q1-type quadrupoles will be installed upstream of the LS2 (section “B” in Fig. 1) and four will be upstream of the LS3 (section “C” in Fig. 1) to obtain additional knobs for transverse matching of multi-q beams. The placement of new quadrupoles has already been optimized by FLAME simulations for measured $^{238}\text{U}^{5q}$ CS parameters.

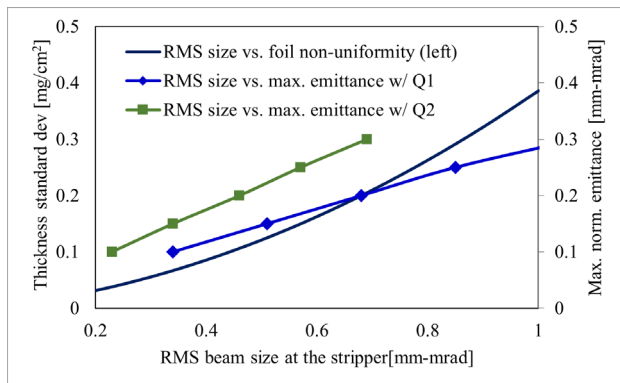


Figure 8: Li film thickness nonuniformity as a function of RMS beam size (black). Maximum normalized emittance allowing to reach the beam size on the stripper with current quadrupoles (blue) and larger aperture quadrupoles (green).

Installation of Second Harmonic Cavities

The feedback systems to compensate for post-stripper energy and energy loss at LLCS are beneficial in reducing the beam losses in LS2 cryomodules, but further mitigation is required to deliver 100 kW-level beams to the target.

After the beam passes through the LLCS, the so-called Landau tail describes its low energy distribution due to significant energy transfer by a single collision. The left side plot of Fig. 9 is the longitudinal acceptance for the $^{124}\text{Xe}^{3q}$ beam at the LLCS. The ions are lost in the LS2 if not in the white area after the stripper. The black points are simulated ^{124}Xe beam particles. These particles are simulated from the LEBT through the stripper. Then the energy loss of each particle is calculated by SRIM [9] using a measured lithium film thickness distribution. The low energy side of the acceptance is close to the beam, and possibly the Landau tail is out of the acceptance. The right plot in Fig. 9 is the acceptance with 2nd harmonics bunchers installed behind each of the current 161 MHz bunchers. The energy acceptance is significantly expanded.

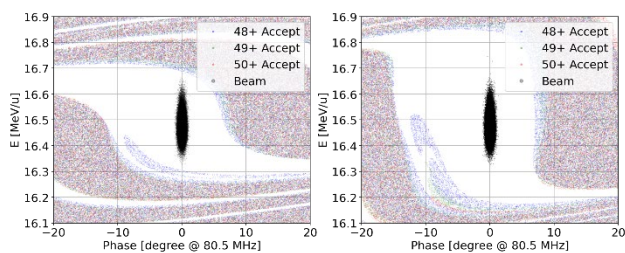


Figure 9: Simulated longitudinal phase-space acceptance at the stripper for $^{124}\text{Xe}^{3q}$ without (left) and with (right) second-harmonic cavities and beam (black).

Installation of New Wire Profile Monitors

Profile monitor scans for CS parameters calculation are one of the most time-consuming procedures during a PDT. The profile monitor at the matching sections is scanned with at least six different quadrupole settings for each charge state to calculate the CS parameters on x-x' and y-y' phase spaces. The measurement time is linearly proportional to the number of charge states. To make this procedure faster, we plan to install three profile monitors in the LS3 BTS (section “D” in Fig. 1). This section is a periodic FODO lattice with a 60° transverse phase advance per period. These profile monitors will be installed in the middle between the quadrupole doublets. Figure 10 shows the simulated rms beam ellipses on x-x' (top) and y-y' (bottom) with constraints imposed by the profile monitor measurements for $^{238}\text{U}^{5q}$.

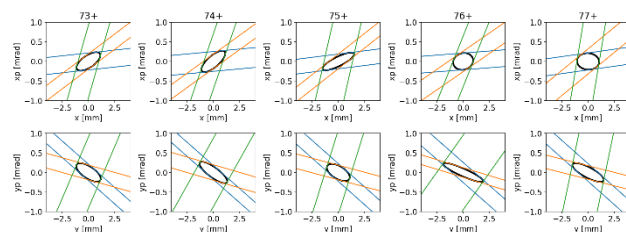


Figure 10: RMS beam ellipse on x-x' (top) and y-y' (bottom) for each of $^{238}\text{U}^{5q}$ beam and constraints imposed by three profile monitor measurements in LS3 BTS.

SUMMARY

FRIB linac routinely delivers 20 kW ion beams to the target from oxygen to uranium. We maintain uncontrolled beam losses at the level of 10^{-4} . At the current beam power level, these losses are well below 1 W/m which is an acceptable value for high power proton linacs. There is a hypothesis that the beam losses in the superconducting cavities can cause field emissions. Therefore, we keep the beam losses in the post-stripper linac about two orders of magnitude lower than 1 W/m. Recently, accelerator tunes have been developed for $^{238}\text{U}^{5q}$ and $^{48}\text{Ca}^{2q}$ beams characterized by low beam losses and suitable for higher beam power. The recent implementation of fast energy feedback and slow LLCS stage feedback reduced the beam losses in the LS2 cryomodules, which is good progress toward the next beam power level of 50 kW. Accelerator improvement projects are ongoing to mitigate further beam losses related to the LLCS, shorten the PDT, and increase science time.

REFERENCES

- [1] J. Wei *et al.*, “Accelerator commissioning and rare isotope identification at the Facility for Rare Isotope Beams,” *Mod. Phys. Lett. A*, vol. 37, no. 09, p. 2230006, Mar. 2022. doi:10.1142/s0217732322300063
- [2] P. N. Ostroumov *et al.*, “Heavy ion beam physics at Facility for Rare Isotope Beams,” *IEEE Open J. Instrum. Meas.*, vol. 15, no. 12, pp. P12034, Dec. 2020. doi:10.1088/1748-0221/15/12/p12034
- [3] T. Kanemura *et al.*, “Experimental demonstration of the thin-film liquid-metal jet as a charge stripper,” *Phys. Rev. Lett.*,

- vol. 128, no. 21, p. 212301, May 2022.
doi:[10.1103/physrevlett.128.212301](https://doi.org/10.1103/physrevlett.128.212301)
- [4] P. N. Ostroumov *et al.*, “First simultaneous acceleration of multiple charge states of heavy ion beams in a large-scale superconducting linear accelerator,” *Phys. Rev. Lett.*, vol. 126, no. 11, p. 114801, Mar. 2021.
doi:[10.1103/physrevlett.126.114801](https://doi.org/10.1103/physrevlett.126.114801)
- [5] A. S. Plastun and P. N. Ostroumov, “Instant phase setting in a large superconducting linac”, in *Proc. NAPAC'22*, Albuquerque, NM, USA, Aug. 2022, pp. 885-890.
doi:[10.18429/JACoW-NAPAC2022-THZD1](https://doi.org/10.18429/JACoW-NAPAC2022-THZD1)
- [6] T. Zhang *et al.*, “Physics Applications in Support of FRIB Beam Tuning and Operations”, presented at HIAT'25, East Lansing, MI, USA, Jun. 2025, paper MOP21, this conference.
- [7] Zhao *et al.*, “BPM feedback for LLRF energy and phase regulation in charge stripping beamlines”, in *Proc. IPAC'24*, Nashville, TN, USA, May 2024, pp. 3326-3328.
doi:[10.18429/JACoW-IPAC2024-THPG32](https://doi.org/10.18429/JACoW-IPAC2024-THPG32)
- [8] P. N. Ostroumov *et al.*, “Acceleration of uranium beam to record power of 10.4 kW and observation of new isotopes at Facility for Rare Isotope Beams,” *Phys. Rev. Accel. Beams*, vol. 27, no. 6, p. 060101, Jun. 2024.
doi:[10.1103/physrevaccelbeams.27.060101](https://doi.org/10.1103/physrevaccelbeams.27.060101)
- [9] J. F. Ziegler, M. D. Ziegler, and J. P. Biersack, “SRIM – The stopping and range of ions in matter (2010),” *Nucl. Instrum. Methods Phys. Res., Sect. B*, vol. 268, no. 11–12, pp. 1818–1823, Jun. 2010. doi:[10.1016/j.nimb.2010.02.091](https://doi.org/10.1016/j.nimb.2010.02.091)

DEVELOPMENT OF THE FIRST 1 GHz NIOBIUM-TIN QUARTER-WAVE CAVITY*

Y. Zhou^{1,†}, R. Agustsson³, P. Davis¹, G. Ereemeev², B. Guilfoyle¹, M. Kedzie¹, M.P. Kelly¹,
T. Petersen¹, S. Posen², T. Reid¹, E. Spranza³, B. Tennis²

¹Argonne National Laboratory, Lemont, IL, USA

²Fermi National Accelerator Laboratory, Batavia, IL, USA

³Radiabeam Technologies LLC, Santa Monica, CA, USA

Abstract

This work aims to demonstrate the feasibility of coating a high-frequency 1 GHz, compact niobium-3 tin (Nb₃Sn) coated quarter-wave cavity for future ion accelerators. Nb₃Sn has a BCS surface resistance up to 2 orders of magnitude lower than pure niobium widely used for SRF, which implies Nb₃Sn cavities' better performance at much higher frequencies than for niobium. This presents an opportunity for transformative size reductions in accelerating cavities. Here, we have designed, built and tested a 1 GHz quarter-wave cavity sized similarly to a soda can. Cold tests have shown a critical temperatures of $14.5 \text{ K} \pm 0.1 \text{ K}$, which might be due to the coating layer damage or tin depletion. Notably, we observed an average quality factor $\sim 8\text{E}8$ at low accelerating electric fields, ~ 7 times higher than the theoretical limit for pure niobium at this frequency.

INTRODUCTION

Niobium-3 Tin (Nb₃Sn) is a promising alternative to pure niobium for low-beta ion accelerators due to its higher superconducting transition temperature of $\sim 18 \text{ K}$ and higher superheating field, and much lower RF losses even at high frequencies. At 4.5 K, the expected Bardeen-Cooper-Schrieffer resistance (BCS resistance) of Nb₃Sn is a few nano-Ohms at 1 GHz, with two orders of magnitude improvement compared to pure niobium (see Fig. 1). The low Nb₃Sn RF losses together with 18 K critical temperature allow the use of higher frequency, much smaller cavities while maintaining 4.5 K operation that is compatible with cryocoolers. This work aims to demonstrate the feasibility of coating a high-frequency 1 GHz, compact quarter-wave niobium cavity with Nb₃Sn. The development of this cavity has the potential to transform low-beta ion accelerators through size reductions and by enabling the replacement of large helium cryoplants with small plug-in cryocoolers.

We have designed, built, and tested a 1 GHz Nb₃Sn coated quarter-wave cavity. Nb₃Sn coating has been performed by vapor diffusion in a high vacuum furnace at Fermilab. Cryogenic cold tests show a quality factor of $\sim 8\text{E}8$ at low accelerating electric fields, or ~ 7 times higher than

the theoretical limit for pure niobium at 1 GHz. This first coating does not yet meet our quality factor or gradient goals. We have stripped the coating layer and electropolished the cavity ($\sim 70 \text{ }\mu\text{m}$ removal) and have the cavity re-coated at Fermilab. Cold tests for the second coating will take place shortly.

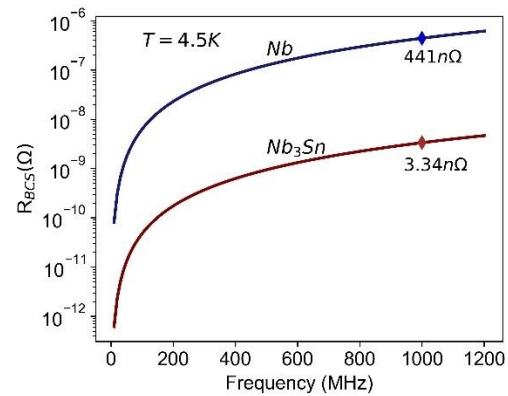


Figure 1: SRIMP calculated BCS resistance of Nb₃Sn and Niobium vs frequency at 4.5 K with material parameters from [1].

PROTOTYPE DESIGN AND FABRICATION

The cavity design was aimed to demonstrate the performance of Nb₃Sn coated low-beta quarter-wave cavity at $\sim 1 \text{ GHz}$ using the simplest possible design in this first study. The dimensions of the cavity are shown in Fig. 2(a). For simplicity, beam ports are neglected. A stainless-steel flange with RF drive and pick-up probes close the bottom of the cavity. RF losses in the stainless steel are minimized by extending the single port at the bottom of the cavity. EM simulation (Fig. 2(b)) gives a geometry factor of 49.8, peak electric field and peak magnetic field of 147 MV/m and 308 mT, respectively, for a stored energy of 1 J.

The 1 GHz prototype cavity was machined at Radiabeam from two high purity (RRR ~ 300) niobium cylindrical ingots (2.5" OD, one 3" long and the other 4.5" long). The two parts (Fig. 2(c)) were electron beam welded (Fig. 2(d)) after buffered chemical processing. The finished cavity is roughly the size of a soda can.

* Work supported by Argonne LDRD seed funding award under the LDRD number 2024-0374 and the U.S. Department of Energy, Office of Science, Office of Nuclear Physics, under Contract No. DE-AC02-06CH11357. This research used resources of ANL's ATLAS facility, which is a DOE Office of Science User Facility

† Email address: yang.zhou@anl.gov

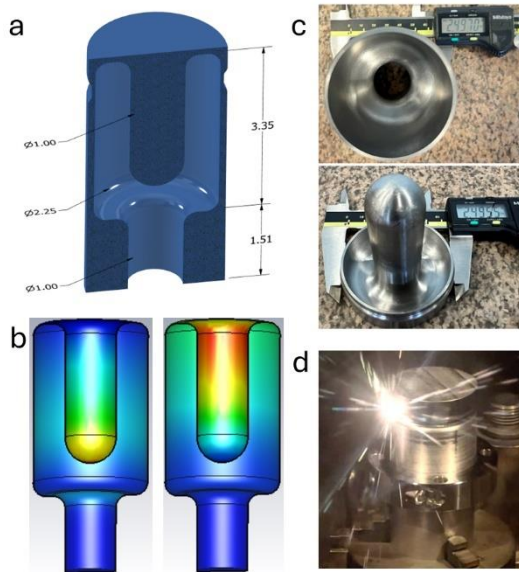


Figure 2: Cavity (a) dimensions, (b) EM simulation, and (c)-(d) fabrication.

Nb₃Sn COATING

The cavity received bulk electropolishing process to remove more than 100 μm of the niobium inside the cavity. The mirror finish is shown in Fig. 3(a). It was then anodized with a 30 V DC power supply, creating a niobium-oxide layer that appears blue. The cavity was ultrasonic cleaned and high-pressure rinsed to remove particulates, as for standard niobium.

The Nb₃Sn coating was performed by vapor diffusion in a small vacuum furnace at Fermilab. The tin sources are heated in a crucible near the cavity port. A detailed vapor diffusion Nb₃Sn coating procedure can be found in [2]. The coating inside the cavity is shown in Fig. 3(b).

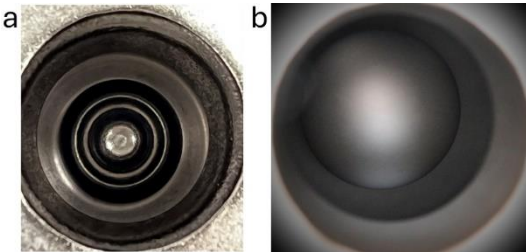


Figure 3: (a) Post-electropolishing cavity surface finish; (b) Post-coating cavity surface.

COATED CAVITY COLD TESTING

After coating the cavity, it was again high pressure rinsed and assembled in the clean room with the stainless-steel flange using indium seals. Four cold tests have been done. After the first cold test in October 2024, it was disassembled and high pressure rinsed. We re-assembled the cavity and performed another three cold tests in January and February 2025.

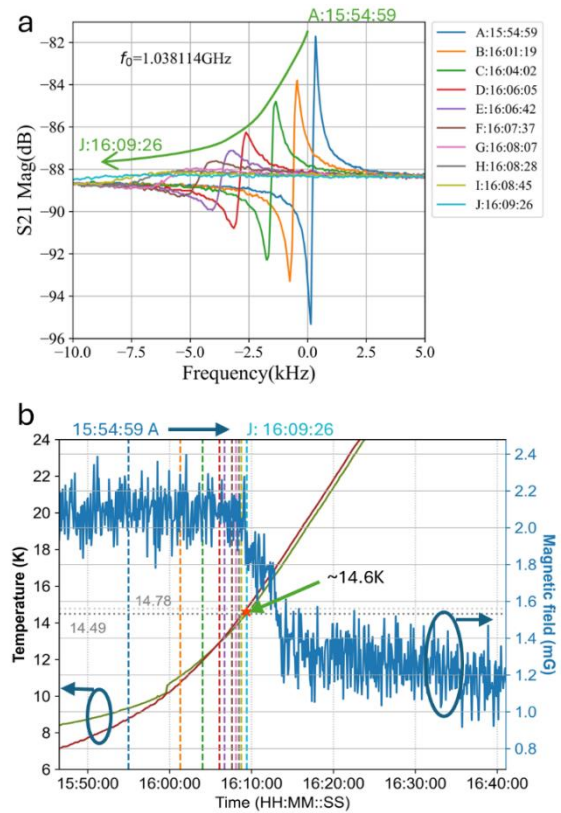


Figure 4: (a) S21 spectrum by VNA, and (b) temperature (left) and magnetic field (right) temporal profiles during the superconducting transition for the cold test in February 2025.

Superconducting Transition Temperature

Superconducting transition temperature has been diagnosed by silicon diode thermometers, together with magnetic fluxgate and S21 spectrum from vector network analyzer, during the cold tests. The temperature and magnetic field temporal profile in Fig. 4(b) shows a transition temperature of 14.5 ± 0.1 K, as indicated by the magnetic field jump due to the Meissner effect and by the smeared resonance peak on the S21 spectrum in Fig. 4(a). The observed critical temperature is lower than 18 K. One possible reason for the temperature difference could be the damage of the coating layer during cleaning. The other possible reason could be the lower atomic tin content. Figure 7 in ref. [3] shows that a lower atomic tin content results in a lower superconducting transition temperature.

Q_0 vs E_{acc} Curve

Measured Q_0 vs E_{acc} curves for this coating are presented in Fig. 5. The best Q_0 observed from those tests is around 1.5×10^9 at fields < 0.3 MV/m. The sharp Q_0 drop is around 0.75 MV/m for the cold test in October 2024, while it is around 0.4 MV/m for the other three cold tests in January and February 2025.

The Q_0 obtained at low fields, although ~ 10 times lower than the theoretical limit of Nb₃Sn (upper black dashed line in Fig. 5), is still ~ 7 times higher than would be expected from a bare niobium cavity (lower grey dashed line in Fig. 5).

We also point out that there are interference effects between the two RF probes located on the single cavity port and the Q shown in Fig. 5 is really a lower limit due to loading from the probes. The actual Q_0 is higher, and corrections will be done in the near future.

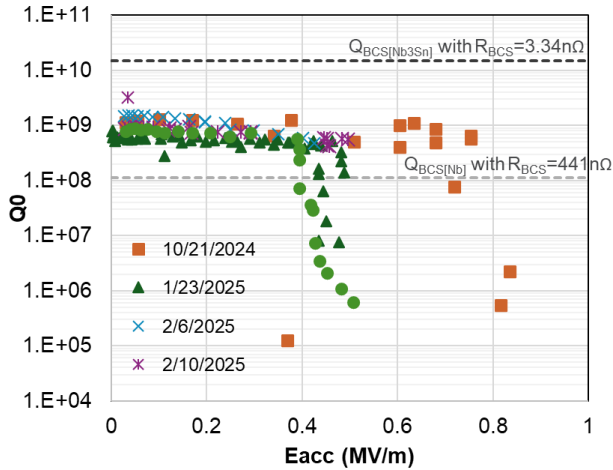


Figure 5: Q_0 vs E_{acc} curve for the coated 1 GHz cavity.

FUTURE WORK

We stripped and re-electropolished the cavity and re-coated it already at Fermilab. Cold test will follow up in the near future.

We envision a future green-field accelerator where many of these small cavities are fastened together into a multi-cavity low-beta superstructure driven by a single radiofrequency power source and cooled by stand-alone cryocoolers rather than today's large helium cryoplants. Many challenges will need to be overcome to realize this vision, especially for example, the matching and transport of beams through these smaller aperture high frequency cavities and the need for a high-frequency injector.

CONCLUSION

Here, we designed, built and tested a 1 GHz quarter-wave niobium cavity coated with Nb₃Sn by vapor diffusion. Several cryogenic cold tests were performed at Argonne. The measured superconducting transition temperature was $14.5 \text{ K} \pm 0.1 \text{ K}$, which is lower than 18 K. Notably, we also observed an average quality factor $\sim 8\text{E}8$ at low accelerating electric fields ($<0.3 \text{ MV/m}$), ~ 7 times of the theoretical limit for pure niobium at 1 GHz. The cavity has been stripped and recoated with the aim of improving both the Q and the accelerating gradient, with cold tests coming shortly. The development of this high-frequency compact cavity has the potential to transform low-beta ion accelerators, through dramatic size reductions and by enabling the replacement of large helium cryoplants with a distributed set of small plug-in cryocoolers, lowering overall costs and removing one of the major single point failures in modern superconducting linacs.

REFERENCES

- [1] H. Padamsee *et al.*, *RF Superconductivity for Accelerators*. John Wiley & Sons, 2008, p. 87.
- [2] S. Posen *et al.*, "Advances in Nb₃Sn superconducting radiofrequency cavities towards first practical accelerator applications," *Supercond. Sci. Technol.*, vol. 34, no. 2, p. 025007, Jan. 2021. doi:10.1088/1361-6668/abc7f7
- [3] A. Godeke, "A review of the properties of Nb₃Sn and their variation with A15 composition, morphology and strain state," *Supercond. Sci. Technol.*, vol. 19, no. 8, pp. R68–R80, Jun. 2006. doi:10.1088/0953-2048/19/8/r02

OPTIMIZATION OF A MINI-CHANNEL BEAM DUMP FOR FRIB OPERATION*

S. Miller[†], N. Bultman, T. Kanemura, M. Patil, R. Quispe-Abad, M. Reaume, J. Song
Facility for Rare Isotope Beams, Michigan State University, East Lansing, MI, USA
D. Winder, Oak Ridge National Laboratory, Oak Ridge, TN, USA

Abstract

The Facility for Rare Isotope Beams (FRIB) is a high-power heavy ion accelerator facility at Michigan State University began operations in 2022. Its driver linac is designed to accelerate all stable ions to energies greater than 200 MeV/u with primary beam power of up to 400 kW. Currently, FRIB is operating between 10 to 20 kW, delivering multiple primary beam species. The beam dump absorbs approximately 75% of the primary beam power. The existing beam dump head can accommodate up to 20 kW operation, with a planned upgrade to an optimized static mini-channel beam dump design with capability of 30 kW and beyond. Presented here is an overview of the mini-channel beam dump head design optimization and supporting analysis.

INTRODUCTION

The Facility for Rare Isotope Beams (FRIB) is a major nuclear physics facility for research with fast, stopped, and reaccelerated rare isotope beams. FRIB will provide access to 80% of all isotopes predicted to exist in nature. FRIB construction started in 2013 and began operations in 2022. The FRIB facility is based on a heavy-ion continuous wave (CW) superconducting driver linac, capable of accelerating uranium ions to 200 MeV/u and higher energies for lighter ions with 400 kW power striking a target to produce rare isotope beams. FRIB has adopted an incremental approach toward the ultimate design beam power of 400 kW by prioritizing safe operation and to avoid any damage to the machine. In the delivery beam system, the beam dump is designed to absorb approximately 75% of the primary beam power. Currently, FRIB routinely delivers 20 kW primary beams on target, producing rare isotopes that are separated and analysed in the Advanced Rare Isotope Separator (ARIS). The beam dump location and ARIS are shown in Fig. 1 [1-4].

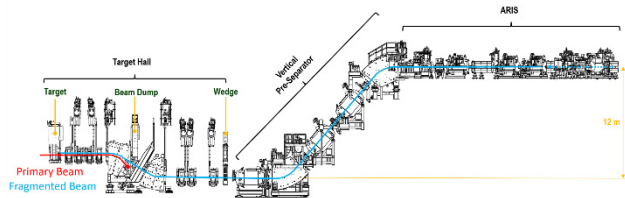


Figure 1: FRIB target hall and ARIS.

* Work supported by the Department of Energy Contract DE-SC0023633
#millers@frib.msu.edu

BEAM DUMP DESIGN

Figure 2 shows the development of the beam dump technology for FRIB. FRIB's power ramp up after initial operation is defined by specific Epochs: Epoch 1: 10 kW, Epoch 2: 20 kW, and Epoch 3: 50 kW.

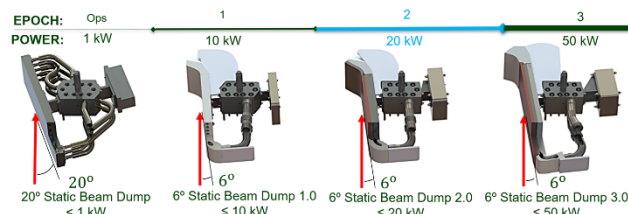


Figure 2: Beam dump design by Epoch.

20-degree Static Beam Dump: 1 kW

The 20-degree (with respect to the beamline) beam dump shown in Fig. 3, was used for FRIB initial operation, was constructed of aluminium alloys. This beam dump utilized a beam stopper (absorber) made of machined Aluminium 2219 with internal cooling passages with water flow. This beam dump design was limited to 1 kW of beam power. Copper alloys were excluded to avoid oxidation that is enhanced by chemical reactions with oxygen produced by secondary particles interactions with the cooling water [3].

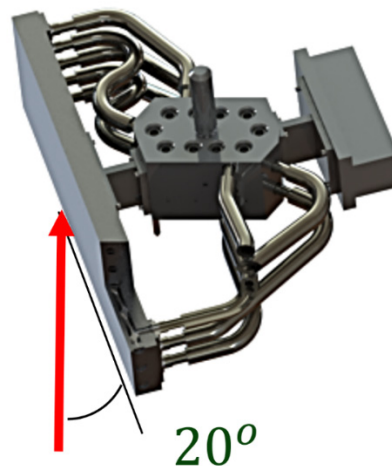


Figure 3: 20-degree beam dump design for 1 kW.

6-degree Static Beam Dump: 10 kW

The 6-degree (with respect to the beamline) beam dump, which was used for FRIB Epoch 1 of the power ramp up, as shown in Fig. 4, was also constructed of aluminium alloys. The beam dump consists of the beam stopper (absorber) made of machined Aluminium 2219 and 3D-

printed inlet and outlet parts made of Aluminium 6061 with cooling water [3]. By reducing the incident angle of the absorber surface (increasing the beam depositional footprint), the 6-degree beam dump was designed to absorb up to 10 kW of beam power.

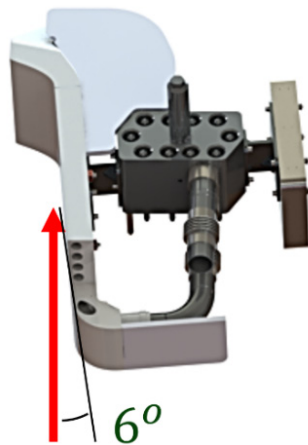


Figure 4: 6-degree beam dump design for 10 kW.

BEAM DUMP OPTIMIZATION

The introduction of the 6-degree Mini-Channel Beam Dump (MCBD) (Fig. 5) for Epoch 2 afforded an opportunity to further the development of the 6-degree absorber design. This optimization focused on material selection and cooling area geometry.

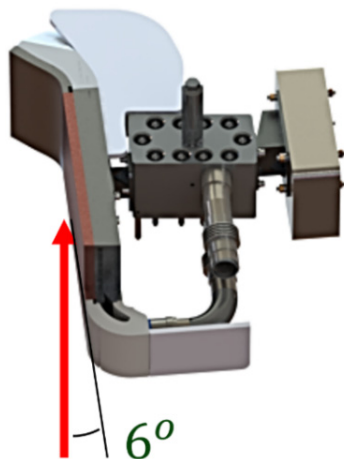


Figure 5: 6-degree mini-channel beam dump design for 20 kW.

Mini-Channel Beam Dump: Design Choices

The copper-chromium-zirconium (C18150) material selection used in the manufacture of the bi-metal absorber plates was chosen for its high thermal conductivity, yield strength, radiation resistance and use in similar applications. The thermal conductivity of the absorber plate was enhanced by machining cooling channels into the aluminium layer of the bi-metal absorber plate. An aluminium backing plate was electron beam welded to the bi-metal absorber plate establishing a vacuum tight pressure boundary. The bi-metal absorber assembly also prevents copper alloys from coming into direct contact with the cooling

water. Figure 6 illustrates the mini-channel design and the cross-section of the waterflow in the absorber plate.

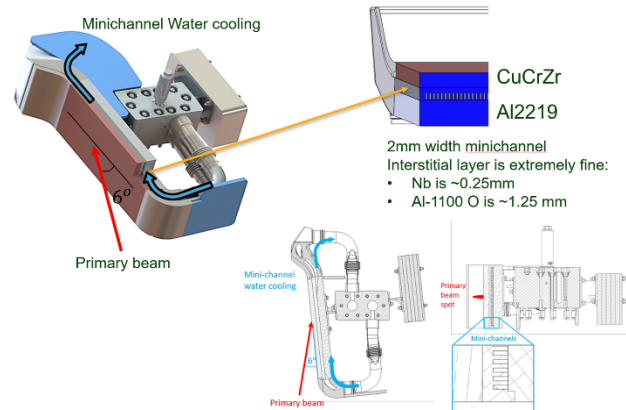


Figure 6: Mini-channel beam dump design details.

6-degree Static Mini-Channel Beam Dump: 20 kW

The 6-degree (with respect to the beamline) MCB D which was used for Epoch 2, as shown in Fig 5, was constructed of the bi-metal absorber assembly and 3D-printed inlet and outlet parts made of Aluminium 6061 with cooling water. This beam dump was designed to absorb up to 20 kW of beam power.

Mini-Channel Beam Dump: Analysis

The MCB D was assessed using the Boiler and Pressure Vessel Code (BPVC). This afforded an objective, comprehensive, code-based approach to design and qualify the beam dump. Further, by using a code-based approach, repeatability in analysis is established. Specifically, the BPVC, Division 2, Alternate Rules, Part 5: Design Analysis Requirement is applied to the MCB D structural validation. Both normal and off normal cases were considered for the beam operations. Since the MCB D is constructed from non-code materials, material properties were compiled through material testing, material property databases, and engineering literature. Prior to application of the code, a thermal fluid-solid analysis was performed on the MCB D to establish static pressures, flow rates, and maximum fluid and material temperatures [5].

Applying the BPVC considered protection against plastic collapse via the Limit Load Analysis method. This method provides a binary pass/fail criterion and therefore an extremely objective assessment. Protection against local failure was assessed by Elastic Plastic analysis. Also considered, was the protection against the collapse from buckling and protection from cyclic loading - which includes fatigue and ratcheting analysis [6]. The 6-degree MCB D successfully passed the BPVC application and analysis indicated areas for future improvement.

6-degree Optimized Mini-Channel Static Beam Dump: 30 kW and Beyond

The 6-degree MCB D was further optimized in support of Epoch 3 as shown in Fig. 7. Fabrication of the bi-metal MCB D absorber assembly utilized several enhancements.

To reduce the power onto the aluminium inlet and outlet parts, the central absorber plate (C18150) was increased by approximately 6.5 inches (16.5 cm) in length. Figure 8 displays an overlay of the previous design with the optimized design.

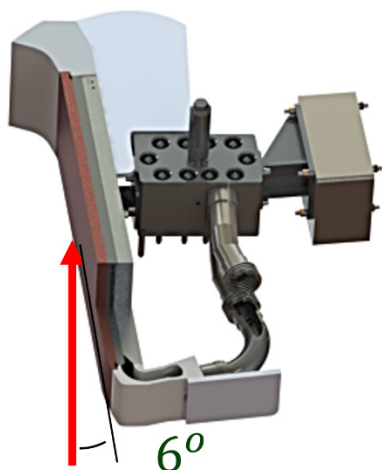


Figure 7: 6-degree optimized mini-channel beam dump design for 30 kW.

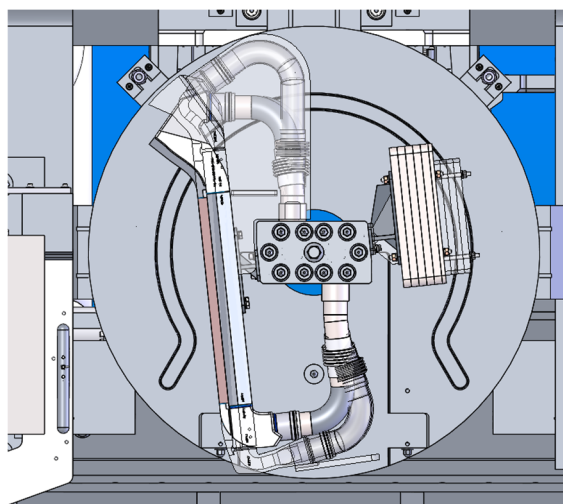


Figure 8: 6-degree optimized mini-channel beam dump overlay with the previous design.

The previous MCBBD design performance was also limited by the power deposition onto the 3D printed aluminum inlet and outlet. Consequently, analysis optimization efforts were focused on subtle geometric improvements across the absorbing surface. In addition to the temperature limitations, these components had a complex fabrication sequence, using plug welds to provide the necessary thermal contact. These complexities lead to excessive weld distortion and stress cracking on several instances during fabrication.

The inlet and outlet profile are optimized to reduce temperature hot spots and provide more gradual beam spread on the absorbing surface. Additionally, the weld design of the inlet and outlet has been improved by eliminating the need for plug welding and extending C18150 central

absorber plate to provide additional coverage of these components.

Additional capability is also recognized by further examining the temperature limitation of the central absorber plate made of C18150. The previous design of the MCBBD restricted the maximum temperature on the absorber to 250 degrees Celsius. This limitation was imposed by literature research and to establish a conservative threshold until further operational experience was gained. By performing representative electron-beam tests on the absorber plate with a cycle count that represents the operational beam on the MCBBD; it was established that C18150 absorber plate could sustain 350 degrees Celsius without failure. Further tests are planned to find the upper bound of the temperature to determine the ultimate performance of the material and consequently the beam power limitation of the device. Figure 9 shows the test article that underwent electron-beam testing [7].

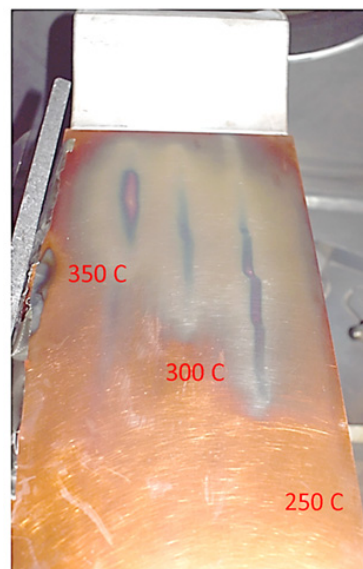


Figure 9: Electron-beam testing of mini-channel beam dump C18150 absorber plate.

CONCLUSION

The static beam dump design has served FRIB well through Epoch 2 of the power ramp up: 20 kW. The design has gradually improved with operational experience and lessons learned. The mini-channel beam dump design utilized a BPVC based approach to objectively qualify the device acceptability for use. Code application to the initial design revealed several optimizations that could be made to the initial mini-channel beam dump design. These optimizations are introduced into the current design and will be further validated by e-beam testing. The current design will be used in Epoch 3 with beam power expected up to 50 kW. This device will be installed for operation in the second half of 2025.

REFERENCES

- [1] J. Wei *et al.*, "FRIB transition to user operations, power ramp up, and upgrade perspectives", in *Proc. 21th Int. Conf. RF*

- Supercond. (SRF'23)*, Grand Rapids, MI, USA, Jun. 2023, pp. 1-8. doi:10.18429/JACoW-SRF2023-MOIAA01
- [2] P.N. Ostroumov *et al.*, “FRIB commissioning”, in *Proc. HI-AT'22*, Darmstadt, Germany, Jun.-Jul. 2022, pp. 118-123. doi:10.18429/JACoW-HIAT2022-WE1I3
- [3] R. Quispe-Abad *et al.*, “Thermal-fluid analysis and operation of a low power water-cooled tilted beam dump at Facility for Rare Isotope Beams”, in *Proc. IPAC'24*, Nashville, TN, USA, May 2024, pp. 3823-3826. doi:10.18429/JACoW-IPAC2024-THPS40
- [4] M. Patil, J. Song, M. Reaume, M. Larmann, N. Bultman, and R. Quispe-Abad, “Thermal analysis of rotating single slice graphite target system for FRIB”, in *Proc. IPAC'24*, Nashville, TN, USA, May 2024, pp. 3827-3829. doi:10.18429/JACoW-IPAC2024-THPS41
- [5] R. Quispe-Abad *et al.*, “thermal hydraulic analysis of a 20 kw beam power water cooled mini-channel beam dump at the Facility of Rare Isotope Beams”, presented at HIAT25, East Lansing, MI, Jun. 2025, paper MOP05, this conference.
- [6] M. Patil *et al.*, “Application of ASME BPVC Section VIII, Division-2, design by analysis requirement to FRIB static beam dump”, presented at HIAT25, East Lansing, MI, Jun. 2025, paper TUP05, this conference.
- [7] Song et al., “Design and experimental thermal validation of the mini-channel beam dump for FRIB”, presented at HIAT25, East Lansing, MI, Jun. 2025, paper TUP04, this conference.

STUDY ON SYNERGISTIC IRRADIATION EFFECTS OF NUCLEAR MATERIALS BASED ON COCKTAIL ION BEAM TECHNOLOGY

Y. H. Zhai^{1,2†}, L. Sun¹, Y. Yang¹, B. Zhang¹, H. Zhao¹

¹ Institute of Modern Physics, Chinese Academy of Sciences, Lanzhou, China

² University of Chinese Academy of Sciences, Beijing, China

Abstract

Cocktail ion beams, composed of multiple ion species with independently adjustable energies and charge states, have emerged as a powerful tool for simulating the complex synergistic irradiation environments encountered by structural materials in advanced nuclear systems. In this study, we report the development and application of cocktail ion beams at the Low Energy high-intensity heavy ion Accelerator Facility (LEAF), where a superconducting Electron Cyclotron Resonance (ECR) ion source and a dedicated energy modulation system enable the generation of high-intensity beams with low energy spread. The integration of a drift tube linac (DTL) and rebunching cavities allows precise energy tuning of each ion species, facilitating control over their respective penetration depths to simulate localized and overlapping damage regions. To evaluate the irradiation-induced microstructural changes, single-crystal copper samples were subjected to various irradiation schemes. Post-irradiation analyses revealed that simultaneous multi-ion exposure leads to distinct damage patterns and defect evolution compared to sequential or single-ion irradiation, highlighting the critical role of dynamic ion-ion interactions and concurrent damage processes. Furthermore, recent advancements in LEAF have enabled the development of a three-ion cocktail beam configuration (e.g., $^4\text{He}^+ + ^{16}\text{O}^{4+} + ^{131}\text{Xe}^{33+}$), which offers enhanced flexibility for simulating broader irradiation environments. This capability allows for more realistic reproduction of fusion and fission reactor conditions, providing a robust experimental foundation for exploring the coupled effects of hydrogen, helium, and heavy ions on nuclear materials.

INTRODUCTION

The LEAF [1] platform is an integrated experimental platform independently developed by the Institute of Modern Physics, Chinese Academy of Sciences (IMP-CAS). Its core objective is to deliver high-quality ion beams with variable energy ranging from 0.1 to 100 MeV, beam intensities reaching the milliampere level, and charge states spanning the full spectrum—from light ions (e.g., H_2^+ , $^4\text{He}^{2+}$) to highly charged super-heavy ions (e.g., $^{238}\text{U}^{50+}$, $^{209}\text{Bi}^{55+}$).

As illustrated in Fig. 1, the LEAF facility consists of a 45 GHz fourth-generation superconducting ECR ion source (FECR) [2], a 100 kV high-voltage platform, a low-energy beam transport line (LEBT), an 81.25 MHz radio-

frequency quadrupole accelerator (RFQ), a medium-energy beam transport line (MEBT), and several experimental terminals.

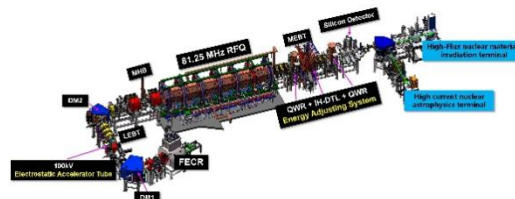


Figure 1: Layout of the LEAF platform.

Table 1: The Main Design Parameters of FECR

Spec.	Para.
ω_{rf}	28~45 GHz
RF power	≥ 20 kW
Conductor	Nb_3Sn
Mirror Fields	~ 6.4 T
Brad	~ 3.2 T
Chamber ID	$\sim \text{Ø}140$ mm
Lmirror	~ 500 mm

The design parameters of FECR are summarized in Table 1, and it is capable of efficiently generating high charge state beams such as $^{129}\text{Xe}^{40+}$ and $^{209}\text{Bi}^{55+}$. More importantly, it enables the production of multi-species cocktail beams, which provide unique irradiation conditions for studying synergistic damage effects in nuclear materials.

The LEAF-RFQ employs a four-vane structure, and in continuous wave (CW) mode, it stably accelerates particles with a charge-to-mass ratio (Q/A) between 1/2 and 1/7 from an injection energy of 14 keV/u to an output energy of 0.5 MeV/u. Given the fixed output energy of the RFQ, a dedicated energy modulation system has been integrated at the RFQ exit to broaden the range of beam conditions. This system includes an interdigital H-type drift tube linac which enables continuous modulation of the beam energy within 0.3–0.7 MeV/u [3]. To preserve beam quality during energy variation, a pair of quarter-wave resonator-based rebunchers are placed on either side of the DTL section to optimize longitudinal beam dynamics and compress energy spread [4].

COCKTAILED ION BEAM ACCELERATION

Cocktail ion beams, consisting of multiple ion species with precisely tailored mass-to-charge ratios (M/q), play a

[†]zhaiyuhan16@impcas.ac.cn.

critical role in replicating the complex irradiation environments encountered in nuclear materials research. The LEAF platform, equipped with a high-performance ECR ion source and a high-intensity heavy-ion linear accelerator, has developed advanced methodologies for producing both “time-sharing” and “simultaneous” multi-species cocktail beams. These capabilities facilitate the investigation of synergistic interactions between displacement damage and transmutation products (such as hydrogen and helium), thereby providing reactor-relevant experimental conditions for evaluating the radiation tolerance of structural materials [4].

Time-Sharing Cocktail Beams

For ion species with significantly different mass-to-charge ratios (e.g., $^{58}\text{Ni}^{15+}$ and $^4\text{He}^+$), rapid beam switching is achieved by alternately modulating the dipole magnet currents. The timing system controls the magnet power supplies at frequencies up to 0.25 Hz, enabling beam trajectory switching within 300 to 700 ms. A Multi-Harmonic Buncher (MHB) is employed upstream of the RFQ to enhance bunching efficiency and improve injection into the phase-stable region. However, this modulation introduces observable velocity differences between ion species, leading to phase mismatches at the RFQ entrance and causing a decrease in efficiency. To compensate for these mismatches, dynamic phase adjustments are applied via the low-level radio frequency (LLRF) control system, for instance, a correction of approximately $\Delta\theta \approx 6.9$ degrees is required between $^{58}\text{Ni}^{15+}$ and $^4\text{He}^+$ (see Fig. 2).

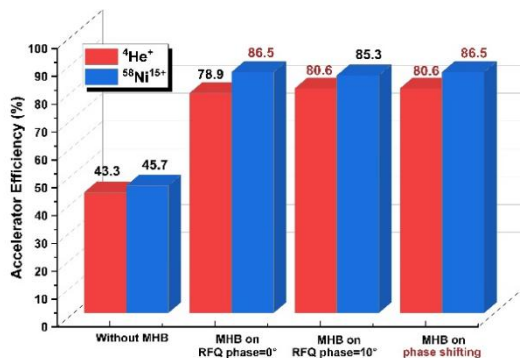


Figure 2: RFQ efficiency in different cases.

Simultaneous Cocktail Beams

For ion species with nearly identical mass-to-charge ratios—such as H_2^+ and $^4\text{He}^{2+}$ —simultaneous extraction and acceleration are feasible. The ECR ion source employs optimized gas mixing (hydrogen + helium) to stabilize the charge-state distribution and ensure beam consistency. Beam composition is analyzed via Rutherford backscattering using a silicon detector [5] and a gold foil target. The significant energy difference between the ion species (e.g., 1 MeV for H_2^+ vs. 2 MeV for $^4\text{He}^{2+}$) allows for clear spectral separation, enabling accurate quantification of each component, as shown in Fig. 3. In principle, the relative intensities of the two incident ion species can be inferred from the approximate peak values.

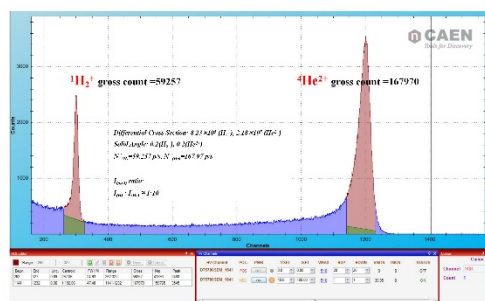


Figure 3: H_2^+ and $^4\text{He}^{2+}$ beam resolution by silicon detector.

Variable-Energy Cocktail Beams

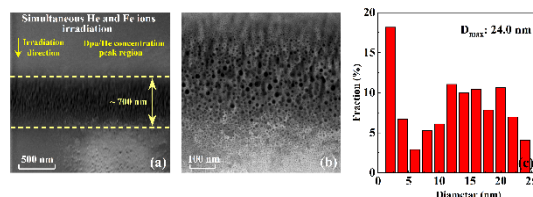


Figure 4: Cross-sectional TEM images of Dpa/He concentration peak region at different magnifications for Cu sample irradiated by simultaneous Fe and He ions irradiation.

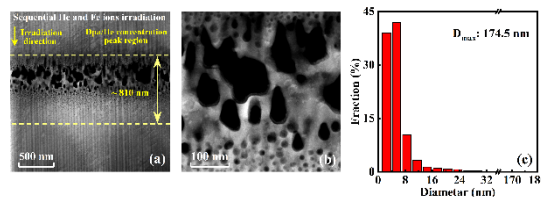


Figure 5: Cross-sectional TEM images of Dpa/He concentration peak region at different magnifications for Cu sample irradiated by He ions first, followed by Fe ions.

Leveraging the energy modulation system at LEAF, we successfully tuned the energies of individual ions within the cocktail beam to simulate differential penetration depths in target materials. For instance, setting the energies of $^4\text{He}^+$ and $^{56}\text{Fe}^{14+}$ to 0.60 MeV/u and 0.57 MeV/u respectively results in a penetration depth difference of less than 10 nm in FeCrAl alloy. Comparative irradiation experiments on monocrystalline copper revealed pronounced differences in microstructural evolution under simultaneous variable-energy irradiation, including suppressed helium bubble growth relative to sequential irradiation, as illustrated in Fig. 4 and Fig. 5 [6].

Triple-Ion Cocktail Beam Development

The LEAF platform has successfully developed high-intensity triple-ion cocktail beams such as $^{131}\text{Xe}^{33+} + ^{16}\text{O}^{4+} + ^4\text{He}^+$, achieving total beam currents exceeding 400 μA under CW-mode operation. This capability is enabled by the FEER ion source, which utilizes dual-frequency heating and enhanced magnetic confinement to stably extract multiple ion species through precise gas mixing (xenon, oxygen, helium) and plasma parameter optimization.

Based on measurements from the silicon detector, the individual ion species within the mixed beam were successfully identified. Distinct energy peaks—65.88 MeV for ^{131}Xe , 8.05 MeV for ^{16}O , and 2.01 MeV for ^4He —enable determination of beam composition, yielding a current ratio of $\text{Xe}:\text{O}:\text{He} \approx 1:1.5:7$, as shown in Fig. 6. This diagnostic method leverages total energy differences and elastic scattering characteristics to resolve individual components in the mixed beam, even when ions share similar mass-to-charge ratios.

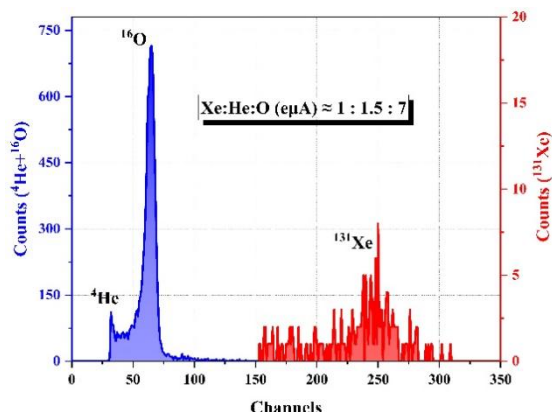


Figure 6: $^{131}\text{Xe}^{33+} + ^{16}\text{O}^{4+} + ^4\text{He}^+$ beam resolution by silicon detector.

CONCLUSION

This work demonstrates the LEAF platform's capability to deliver variable-energy multi-ion cocktail beams, including dual-ion and triple-ion modes, for simulating syn-

ergistic irradiation in nuclear materials. By combining precise energy modulation and composition control, LEAF enables reactor-relevant damage studies with improved fidelity. These advances support the development of radiation-tolerant materials for advanced nuclear systems.

REFERENCES

- [1] Y. Yang *et al.*, “Heavy ion accelerator facility front end design and commissioning”, *Phys. Rev. Spec. Top. Accel Beams*, vol. 22, p. 110101, Nov. 2019
doi:10.1103/PhysRevAccelBeams.22.110101
- [2] L. Sun *et al.*, “Progress on the development of key technologies for the fourth generation ECR ion source FECR”, *J. Phys. Conf. Ser.*, vol. 2244, no. 1, p. 012021, Apr. 2022.
doi:10.1088/1742-6596/2244/1/012021
- [3] Y. Yang *et al.*, “Development of a beam energy adjustment system after a Radio-Frequency-Quadrupole”, *Nucl. Instrum. Methods Phys. Res. A*, vol. 1039, p. 167095, Sep. 2022.
doi:10.1016/j.nima.2022.167095
- [4] Y. H. Zhai *et al.*, “Production of high intensity high charged cocktail beams at LEAF”, *Nucl. Instrum. Methods Phys. Res. A*, vol. 1027, p. 166157, Mar. 2022.
doi:10.1016/j.nima.2021.166157
- [5] G. Perdikakis, D. Bazin, J. Browne, D. Leitner, L. Y. Lin, and W. Wittmer, “Instrumentation at the low intensity frontier: diagnostics for the stopped and reaccelerated beams of NSCL and FRIB”, in *Proc. BIW'12*, Newport News, VA, USA, Apr. 2012, paper MOPG038, pp. 113-115.
- [6] Y. H. Zhai *et al.*, “Variable-energy cocktail beam technology for investigating synergistic damage in nuclear materials on LEAF platform”, *Nucl. Instrum. Methods Phys. Res. A*, vol. 1069, p. 169987, Dec. 2024.
doi: 10.1016/j.nima.2024.169987

DESIGN AND EXPERIMENTAL THERMAL VALIDATION OF THE MINI-CHANNEL BEAM DUMP FOR FRIB *

J. Song[†], N. Bultman, T. Kanemura, G. Lee,
S. Miller, M. Patil, R. Quispe-Abad, M. Reaume, J. Wei

Facility for Rare Isotope Beams, Michigan State University, East Lansing, MI, USA

Abstract

The FRIB, a leading experimental nuclear physics facility, produces high-intensity beams of proton- and neutron-rich nuclei. FRIB provides high-yield, high-purity rare isotope beams via primary beams interactions with a graphite target. After the target, the unreacted primary beam should be absorbed by a beam dump. To support operations at 20 kW, an intermediate beam dump system, called the mini-channel beam dump (MCBD), has been developed and implemented. This system features a static structure oriented at a 6° angle, reducing power density by 10 times. The MCBD is fabricated as a bimetal using an Al-Cu alloy, with a high-thermal-conductivity copper absorber for enhanced heat dissipation and 2 mm \times 7 mm aluminum cooling channels that prevent copper oxidation and significantly improve cooling efficiency. The thermal performance of the MCBD was validated through experimental testing using a 17 keV e-beam at the Applied Research Laboratory, showing measured temperatures matching ANSYS simulation within 5 % uncertainty. These results indicate that the MCBD can reliably support FRIB operations at 20 kW or higher, ensuring effective heat dissipation under high-power conditions.

INTRODUCTION

FRIB is a major nuclear physics facility dedicated to rare isotope science and is progressing toward its ultimate goal of 400 kW primary beam operation. FRIB currently provides stable heavy ion beams ranging from oxygen to uranium and has been progressively increasing its operational beam power from 1 kW to 20 kW [1,2]. Following commissioning [3,4], a static aluminum beam dump was used for primary beam powers ranging from 1 to 10 kW [5]. Approximately 20–40 % of the primary beam power is absorbed by the graphite production target, while the remaining 60–80 % must be absorbed by the downstream beam dump system. Due to the limited thermal performance of the static dump beyond 10 W, the need for an intermediate beam dump, referred to as the mini-channel beam dump (MCBD) [6], was established. Key changes compared to the previous beam dump include the use of 2 mm-wide mini-channels on the water-cooling side, increasing the average convective heat transfer coefficient (CHTC) by more than a factor of 3 [7]. The design also adopts a CuCrZr/Al2219 bimetal structure, with a Cu alloy used as the beam absorber and Al2219 form-

ing the cooling channels. The copper alloy offers ≈ 2.5 times higher thermal conductivity than Al2219, which was used in the previous design. Concepts for this system have been introduced in earlier studies [8,9]. The prototype of the MCBD was fabricated in early 2024. To validate its thermal performance via comparison with simulations, a thermal test was conducted using a 17 keV electron beam at the Applied Research Laboratory of Penn State University. The test results are under analysis, and a portion of the preliminary results is presented in the following section.

MINI-CHANNEL BEAM DUMP

The main design considerations were to enhance thermal performance and minimize the operational impact of radiation damage on the beam dump. To improve thermal performance, a copper alloy was introduced, offering ≈ 2.5 times higher thermal conductivity than Al2219. This material change allowed an increase in the maximum allowable temperature from 200 $^\circ\text{C}$ to 250 $^\circ\text{C}$, based on thermal stress analysis results. A 2 mm-wide mini-channel design was selected to achieve a CHTC approximately 3 times higher than the previous design, while maintaining a reasonable pressure drop (≈ 1 bar). Radiation damage is a critical concern, especially near the surface, as the FRIB primary beam stops within less than 1 mm from the surface. Since beam dump is not a beam window, and some surface damage may occur, the system is expected to remain fully functional under operational conditions. Additional structural analyses were performed to ensure safe operation under expected thermal loads [10].

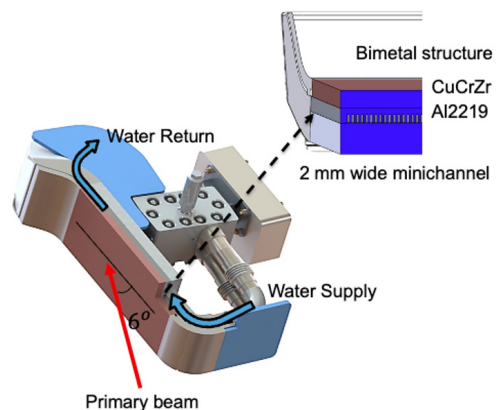


Figure 1: Schematic of the mini-channel beam dump (MCBD).

* Work supported by the U.S. Department of Energy Office of Science under Cooperative Agreement DE-SC0023633, the State of Michigan, and Michigan State University.

[†] songj@frib.msu.edu

The MCBBD designed for 20 kW operation at FRIB, as illustrated in Fig. 1, consists of a beam absorber made of a CuCrZr/Al2219 bimetal structure with 2 mm-wide water-cooling mini-channels, along with 3d printed Al alloy entrance and exit wings. The water-cooling section was made of Al alloy to prevent oxidation of the copper alloy, which could occur through chemical reaction with oxygen produced by secondary beam interactions in the water if the structure were made entirely of copper alloy. The thickness of the Cu and Al layers in the bimetal structure, fabricated using explosion bonding, are 15 mm and 5 mm, respectively. These thicknesses were selected through an optimization process aimed at reducing the temperature at the bimetal joint, thereby minimizing thermally induced stress and limiting the water temperature rise. The primary objective was to ensure the lowest possible surface temperature of the absorber.

EXPERIMENTAL VALIDATION WITH E-BEAM

This experiment aims to demonstrate the thermal performance of the mini-channel beam dump (MCBD) prototype under operational conditions. Validation of the MCBBD design is achieved by comparing measured temperatures with simulation results. A thermal analysis model using ANSYS was developed [7], and modified the average CHTC for the experimental validation test because the cooling water flow rate is fixed at 40 gpm. MCBBD was installed inside the e-beam chamber shown in Fig. 2, where the vacuum level was maintained below 1×10^{-4} torr. A 17 keV electron beam was used to irradiate the MCBBD at various power levels and beam sizes. The cooling water flow rate was maintained at 40 gpm, with an inlet temperature of 30 °C. The pressure drop across the MCBBD was ≈ 17 psi. An IR camera was installed above the chamber to measure the surface temperature through an IR window with a transmission coefficient of 0.78 at the operating spectral wavelength. The emissivity of the MCBBD surface was measured prior to installation using a reference sample and determined to be 0.05. In addition, 12 thermocouples were installed inside the MCBBD, 4 at the center and 4 on each side spaced 10 cm from the center, to monitor internal temperature for comparison thermal simulations.

In the calibration run, the vertical beam size (σ_x) was determined by a Gaussian fit from the thermal image to be 12 mm. During the test, the beam size (σ_x) was fixed at 12 mm, while the horizontal beam size (σ_y) was varied to evaluate different operational beam scenarios. The initial conservative operation temperature limit for the absorber was set at 250 °C. Assuming 75 % of a 20 kW e beam is deposited in the absorber, a beam with $\sigma_y = 56$ mm and fixed $\sigma_x = 12$ mm can reach the maximum allowable temperature of 250 °C. Surface temperature measurements were performed using an IR camera. The measurement uncertainties arise from the emissivity uncertainty of the MCBBD surface and temperature fluctuations caused by 60 Hz e-beam rastering used to achieve the desired beam size. The total

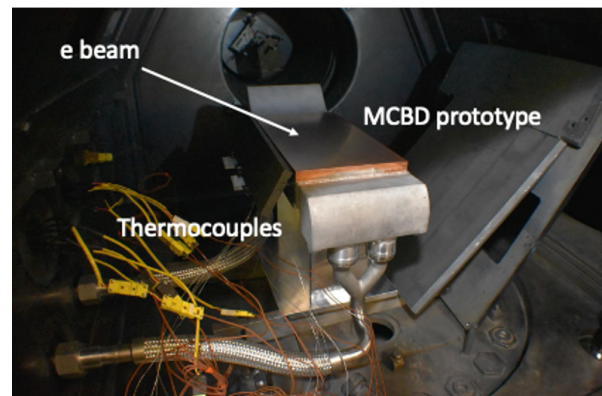


Figure 2: MCBBD test setup inside the vacuum chamber at ARL. Surface temperatures of the MCBBD were measured using an IR camera (FLIR) positioned above the chamber. Thermocouples were installed 1 inch deep inside the MCBBD to monitor internal temperatures.

uncertainty is conservatively estimated to be approximately 5 %.

Here, surface thermal data from a 17 keV, 15 kW electron beam incident on the MCBBD were compared at two different locations. Thermal images shown in panels a) and b) of Fig. 3 were used to extract temperature profiles along the x and y axes. The measured temperatures along the x and y direction for a beam centered on the absorber are plotted in panels c) and d), respectively. The black dotted circles with 5 % error bars present the measured temperature distributions, while the red lines indicate the simulation results. Similarly, the measured temperatures along the x and y directions for a beam positioned at the right edge of the absorber are compared in panels e) and f). The center profiles show excellent agreement with the simulations, however, at the right edge, the simulations tend to underestimate the measured temperature. These deviations are likely due to the lower detection threshold of the IR camera, which operates within optimized spectral ranges. Improved agreement might be achieved with a lower temperature sensitivity range.

To validate the thermal performance of the MCBBD beyond surface temperatures, internal temperature measurements were compared with simulation results. Measured temperature using 4 thermocouples embedded in the side of the MCBBD for the right edge run were used. Figure 4 presents the temperature profile along the z-direction, from the absorber surface to the joint area at a depth of 15 mm. The 2 dashed vertical lines indicate the MCBBD surface and the bimetal joint interface. Measured temperatures (black circles assuming 5 % uncertainty) are compared with simulation results (red line). Overall, the measurements show reasonable agreement with the simulations; however, a 10–20 % discrepancy is observed in the middle region. This deviation may be partly due to uncertainties in the actual depth of thermocouple implantation, which was set to 1 inch but not precisely controlled. In addition, slight improvements in beam position calibration may further reduce this difference.

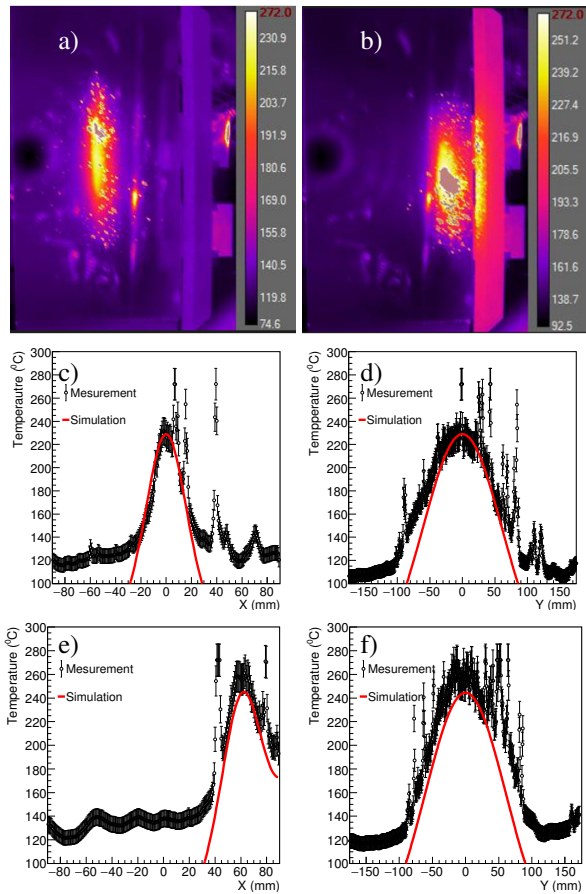


Figure 3: Surface temperature comparison between measurements and simulations for two beam test locations: center (a) and right edge (b). a) and b) show thermal images of the MCBD surface under e beam irradiation. c) and e) present vertical (X-axis) temperature profiles, and d) and f) show horizontal (Y-axis) profiles at the respective positions. Measured temperatures (black circles with 5 % error bars) are compared with thermal simulation results (red lines).

These comparisons served as an important validation step in evaluating the accuracy of the thermal model not only at the surface but also within the internal structure, particularly at the Cu/Al interface. In addition, they help to estimate the cooling water temperature rise and the effective CHTC under operational conditions.

CONCLUSION

The experimental results demonstrate that the mini-channel beam dump (MCBD) prototype performs reliably under simulated operational conditions. Surface temperature measurements at two different locations on the MCBD showed good agreement with thermal simulations, with discrepancies within $\pm 5\%$. Internal temperature measurements using embedded thermocouples also showed reasonable agreement, with deviations of 10-20 % attributed to uncertainties in thermocouple placement depth. Additional tests were conducted with various beam sizes and power

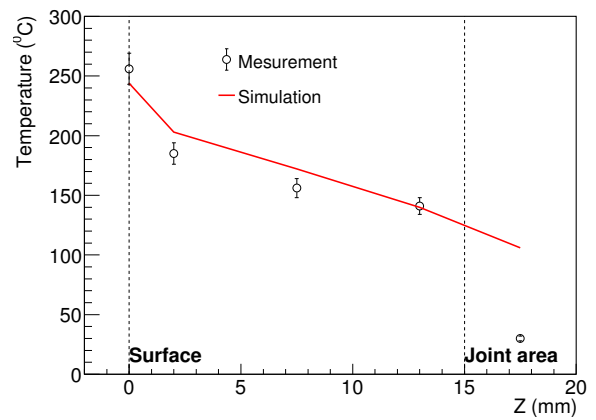


Figure 4: Temperature profiles measured within the MCBD during e beam irradiations at the right edge. The two dashed lines indicate the MCBD surface and the joint area (bimetal interface), with a total distance of 15 mm from surface to joint. Measured data (black circles), are compared with simulations results (red lines). The final thermocouple lost signal during the test.

levels, including elevated temperature conditions and CHTC measurements. Detailed results from these tests will be presented in a future publication. These results validate the thermal performance of the MCBD design and support its implementation for intermediate beam power operations at FRIB.

REFERENCES

- [1] J. Wei *et al.*, “Technological developments and accelerator improvements for the FRIB beam power ramp-up”, *J. Instrum.*, vol. 19, no. 05, p. T05011, May 2024. doi:10.1088/1748-0221/19/05/t05011
- [2] P. N. Ostroumov *et al.*, “Acceleration of uranium beam to record power of 10.4 kW and observation of new isotopes at Facility for Rare Isotope Beams”, *Phys. Rev. Accel. Beams*, vol. 27, no. 6, p. 089901, Jun. 2024. doi:10.1103/physrevaccelbeams.27.060101
- [3] J. Wei *et al.*, “Accelerator commissioning and rare isotope identification at the Facility for Rare Isotope Beams”, *Mod. Phys. Lett. A*, vol. 37, no. 09, p. 2230006, Mar. 2022. doi:10.1142/s0217732322300063
- [4] M. Portillo *et al.*, “Commissioning of the Advanced Rare Isotope Separator ARIS at FRIB”, *Nucl. Instrum. Methods Phys. Res. B*, vol. 540, pp. 151–157, Jul. 2023. doi:10.1016/j.nimb.2023.04.025
- [5] R. Quispe-Abad *et al.*, “Thermal-fluid analysis and operation of a low power water-cooled tilted beam dump at Facility for Rare Isotope Beams”, in *Proc. IPAC’24*, Nashville, TN, USA, May 2024, pp. 3823–3826. doi:10.18429/JACoW-IPAC2024-THPS40
- [6] J. Song *et al.*, “Status and R&D of the target and beam dump at FRIB”, Presented at the 8th High Power Targetry Workshop, Wako, Japan, Nov. 6-10, 2023.
- [7] R. Quispe-Abad *et al.*, “Thermal-hydraulic analysis of a 20kW beam power water-cooled mini-channel beam dump at the

- Facility for Rare Isotope Beams”, presented at HIAT25, East Lansing, MI, Jun. 2025, Paper MOP05, this conference.
- [8] D. B. Tuckerman and R. F. W. Pease, “High-performance heat sinking for VLSI”, *IEEE Electron Device Lett.*, vol. 2, no. 5, pp. 126–129, May 1981.
doi:10.1109/edl.1981.25367
- [9] J. Song *et al.*, “The nuCARIBU target system”, unpublished.
- [10] M. Patil *et al.*, “Application of ASME BPVC Section VIII, Division 2, design by analysis requirement to FRIB static beam dump”, presented at HIAT25, East Lansing, MI, Jun. 2025, Paper TUP05, this conference.

APPLICATION OF ASME BPVC SECTION VIII, DIVISION-2, DESIGN BY ANALYSIS REQUIREMENT TO FRIB STATIC BEAM DUMP*

M. Patil^{†,1}, N. Bultman¹, T. Kanemura¹, S. Miller¹, R. Quispe-Abad¹, M. Reaume¹, J. Song¹, D. Winder²

¹Facility for Rare Isotope Beams, Michigan State University, East Lansing, MI, USA

²Oak Ridge National Laboratory, Oak Ridge, TN, USA

Abstract

The Facility for Rare Isotope Beams (FRIB) at Michigan State University is a high-power heavy-ion accelerator, and began operation in 2022. Its driver linac is designed to accelerate all stable ions to energies exceeding 200 MeV/u, with a maximum beam power of 400 kW. Currently, FRIB operates at beam powers between 10 and 20 kW, delivering multiple primary beam species. Approximately 75% of the primary beam power is absorbed by the beam dump. The existing mini-channel beam dump (MCBD) absorber is designed to handle up to 20 kW, with plans for an optimized beam dump capable of supporting 30 kW and beyond. This paper presents the design-by-analysis procedures outlined in ASME Boiler and Pressure Vessel Code [1] that have been applied to the MCBD design.

INTRODUCTION

The Facility for Rare Isotope Beams (FRIB), a major nuclear physics facility for research with fast, stopped, and reaccelerated rare isotope beams, has adopted an incremental approach toward the ultimate design beam power of 400 kW prioritizing safe operation and avoiding any possible damage to the machine. Currently, FRIB routinely delivers 10-20 kW primary beams on target and beam dump, producing rare isotopes that are separated and analyzed in the Advanced Rare Isotope Separator (ARIS) [2].

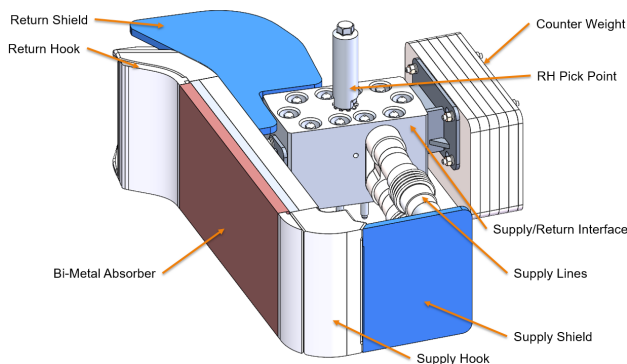


Figure 1: Details of the MCBD with key components as labelled.

The FRIB beam dump system (20kW operations) is shown in Fig 1. The primary components of the Mini-Channel Beam Dump (MCBD) consist of a C18150 copper alloy absorber plate explosion bonded to aluminum 2219

which has cooling channels. The higher thermal conductivity of the copper alloy will help to reduce the temperature increase due to beam heating. However, precautions are needed to ensure that the beam dump cooling water does not encounter the copper alloy, as copper is vulnerable to oxidation that is enhanced by chemical reactions with oxygen produced by secondary particles interacting with the water (oxidation may result in pitting of the material). Hence the cooling channels are made from aluminum alloy. The design is shown in Fig 2. This bi-metal absorber plate is welded to return and supply hooks (3D printed AlSi10Mg) that connect to the cooling water lines. An optimized version of this MCBD for 30 kW beam operation is currently being manufactured and will be installed in summer of 2025 [3]. This paper describes in brief the application of ASME BPVC Sec VIII, Div2 to the 20 kW beam dump. More detailed analysis with results can be found in the FRIB reports [4, 5]

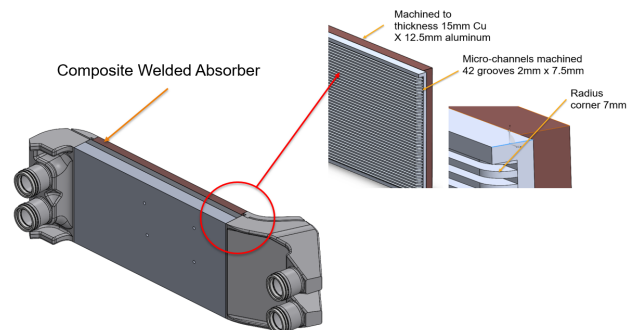


Figure 2: FRIB MCBD showing the mini channels used for cooling.

MATERIALS AND WELDS

Temperature dependent material properties are used as the input for the non-linear analysis. Material properties used for this analysis have been gathered from a mixture of in-house testing, material properties database (MPDB software) [6] and literature [7, 8]. Plasticity is modelled using a *Bilinear Isotropic Hardening* material model.

Welds are produced by the electron beam process (Al-2219 back plate to Al-2219 on the absorber plate with mini channels), and the TIG (GTAW) process for the Al-2219 to the 3D printed AlSi10Mg hooks. The welds are not modelled in the finite element model. All the weld joints are assumed bonded for the contact conditions. Our e-beam welding development and testing for AL-2219 T851 shows about 50% reduction in room temperature yield properties in the weld zone. So, the weld strength of Al 2219 has been derated by 50% in the analysis

*Work supported by the Department of Energy Contract DE-SC0023633
[†]patil@frib.msu.edu

LOAD CASES

To explain the various load cases and the pressure zone, a cut section is shown in Fig 3. There are three volumes which encounter pressurized water:

1. The 3-D printed water supply hook
2. The Al-2219 mini-channel
3. The 3-D printed water return hook

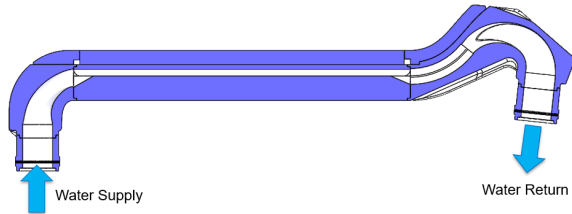


Figure 3: Cross section of the MCBD showing the water pressure volume.

The pressures in these volumes are denoted as P (65 psia). The MCBD is subjected to three basic loads. Gravity, thermal load and pressure. Gravity load is not considered in this stress analysis because the effect is negligible.

For 20 kW operations, U238 beam with $\sigma_1 = 9.77$ mm and $\sigma_2 = 2.32$ mm was identified as one of the worst-case beam loads for the C18150 absorber plate. This beam will deposit 15 kW of power in the dump. From here on this beam case loading will be referred to as the thermal load, T.

The MCBD Load cases analyzed are:

1. Beam is at the center of the absorber plate during normal operation
2. 30% decrease in thermal conductivity assumed only in a top thin layer of 0.85 mm
3. 3 water channels (in the middle) are considered as blocked
4. X direction beam offset: Max offset 72 mm
5. Y direction beam offset: Max offset 30 mm

DESIGN BY ANALYSIS

Design by analysis section of the BPVC Section VIII, Div.2: Part 5 lays down certain requirements and rules which have been followed for the numerical (FEA) analysis presented here. The analysis types are further elaborated in sections ahead.

Protection against Plastic Collapse

Section 5.2 of the code provides three alternative analysis methods for evaluating protection against plastic collapse. *Limit Load Analysis Method* (Section 5.2.3) has been used here for the analysis and results presented. Limit-load analysis addresses the failure modes of ductile rupture and the onset of gross plastic deformation (plastic collapse) of a structure.

The load case combinations and load factors are as per Table 5.4 of the code. The assessment procedure is followed as outlined in section 5.2.3.5. Elastic perfectly plastic material models have been used in ANSYS with tangent modulus set to zero. Large displacements have been turned

off in ANSYS as per the code. Since this is a pass/fail criteria, the actual results like displacements and strains indicated by the solution have no physical meaning

Table 1 shows the analysis results for all the load case combinations analyzed. The FEA model solutions for all cases converged, hence meeting the criteria.

Table 1: Limit load analysis. Load case, design loads combinations and model convergence results.

Load Case	Design Load Combination	Convergence
LC1	1.3(P + T)	Yes
LC2	1.3(P + T)	Yes
LC5	1.3(P + T)	Yes
LC4	1.3(P + T)	Yes
LC5	1.3(P + T)	Yes

Protection against Local Failure

In addition to the stress-based failure criteria, ASME BPVC also considers criteria based on local strain limits, particularly those related to the triaxial state of stress. These criteria are important for assessing the ductile behavior of materials, especially in regions where stress states are complex and may lead to localized plastic deformation.

As per section 5.3.3 of The Code, the requirements are met when the combination of the limiting triaxial strain, ϵ_L , and forming strain, ϵ_{cf} , are less than the strain that occurs because of an elastic-plastic simulation at the required load factors as per table 5.5 of Code. The limiting triaxial strain is given by the equation:

$$\epsilon_L = \epsilon_{Lu} \cdot \exp \left[-\left(\frac{\alpha_{sl}}{1+m_2} \right) \left(\frac{\sigma_1 + \sigma_2 + \sigma_3}{3\sigma_e} - \frac{1}{3} \right) \right]$$

σ_1 , σ_2 , and σ_3 are the principal stresses

σ_e is the equivalent (von Mises) stress

ϵ_{Lu} , m_2 , and α_{sl} are material constants defined as per Table 5.7 of the code

The limiting triaxial strain is used to calculate the Strain Limit Damage Ratio (SLDR). The local failure requirements are considered met if the SLDR is less than 1. The SLDR is given by:

$$SLDR = \frac{\epsilon_{peq}}{\epsilon_L}$$

ϵ_{peq} is the plastic strain.

Table 2: Protection Against Local Failure Results

Load Case	Design Load Combination	SLDR<1
LC1	1.7(P + T)	Yes
LC2	1.7(P + T)	Yes
LC5	1.7(P + T)	Yes
LC4	1.7(P + T)	Yes
LC5	1.7(P + T)	Yes

This ratio is calculated in ANSYS using a user defined expression in results. The SLDR calculated from ANSYS models was found to be lower than 1 for each node on the MCB model. Results are shown in Table 2. The SLDR was calculated for all materials: C18150, Al2219, and AlSi10Mg.

Protection against Collapse from Buckling

Buckling was not identified as concern for the MCB setup.

Protection against Collapse from Cyclic Load

To show protection against failure from cyclic loading, a fatigue screening analysis and a ratcheting assessment is needed.

Fatigue Assessment The fatigue screening analysis is performed to check if additional fatigue analysis is needed. Two methods are provided in section 5.5.2 of the code, Method A and Method B. Method A has been used here for this case. The number of cycles in Method A are limited based on the criteria provided in Table 5.9 of the code.

$$N_{AFP} + N_{APO} + N_{ATE} + N_{ATa} \leq 1000$$

Total number of beam trips as estimated from FRIB data is around 1500-2000. Majority of the beam trips are very short duration and the change in power level and hence ΔT for beam dump absorber face would be very small. This would not count as a complete cycle as per the code but to be conservative all beam trips are assumed as complete cycle. Since the total cycles $1500 > 1000$, per Method A, a fatigue analysis is required.

As seen from Fig 4, a total strain of 1% would cause fatigue failure at around 1500 cycles (Violet line with $T = 250^\circ\text{C}$). For the current uranium beam case presented here (normal operations) the total strain is of the order of 0.29%. with max surface temperature around 250°C . This is lower than the 1% limit for 1500 cycles. Note that this does not include the effects of radiation damage on the material.

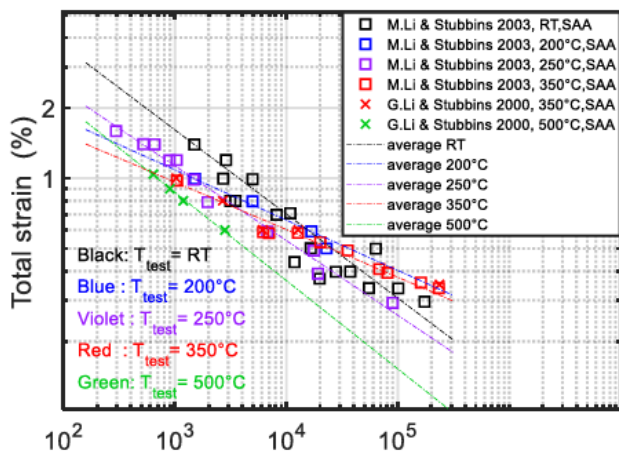


Figure 4: Total strain versus number of cycles to failure [7].

Ratcheting Assessment For MCB, an elastic-plastic stress analysis (Part 5.5.7) was used since a model for the

analysis that accurately represents the component geometry, boundary conditions, applied loads, and material properties was already developed for previous analyses.

The analysis for protection against ratcheting is performed by application, removal and re-application of the applied loadings to show that the structure eventually shakes down to elastic action, i.e., that the incremental increases in plastic deformations from each cycle are small and diminishing as the number of cycles increases. The finite element model was subjected to 7 beam load cycles as shown in Fig 5. Water pressure remains constant for the life of the beam dump. According to the code, if any one of the following conditions is met, the ratcheting criteria are satisfied

- Structure should have an elastic core
- Repeated cycles result in no change in geometry
- There is no plastic action

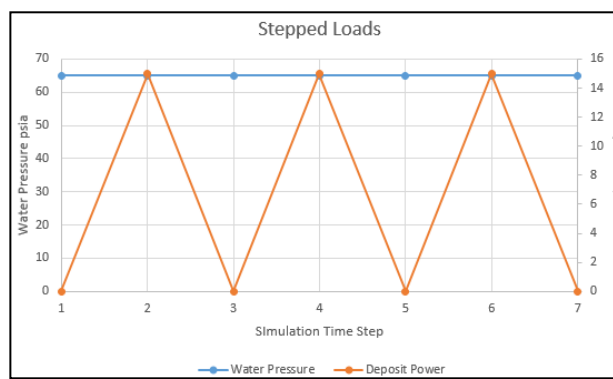


Figure 5: Load case showing constant pressure and beam power cycling.

Analysis shows that there is no change in dimension between the last and next to last cycles (load cycle 5 and 7), demonstrating convergence. This indicates that the structure passes the ratcheting assessment.

CONCLUSION

Structural analysis of the MCB for 20kW operations shows that it meets the ASME BPVC, Section VIII, Div. 2, Part 5 by satisfying the following requirements:

Protection against plastic collapse, local failure, buckling, and cyclic loading are as follows:

1. Plastic collapse – satisfied by a limit load analysis according to 5.2.3.
2. Local failure – satisfied by an elastic plastic stress analysis performed according to 5.3.2.
3. Buckling – NA
4. Fatigue assessment – the need for a fatigue analysis is assessed according to 5.5.2.3.
5. Ratcheting assessment – satisfied by elastic plastic stress analysis as per 5.5.7

The effect of thermal creep has not been studied in detail. Ref [7] has some creep data for C18150 but concludes that additional testing is required. As we ramp up our beam power more creep related data would be valuable. E-beam testing of this beam dump has been done and more ongoing to validate our thermal analysis and assumptions [9].

REFERENCES

- [1] *2021 ASME Boiler and Pressure Vessel Code*, The American Society of Mechanical Engineers, Sec VIII, Division 2.
- [2] M. Hausmann *et al.*, “Design of the Advanced Rare Isotope Separator ARIS at FRIB”, *Nucl. Instrum. Methods Phys. Res., Sect. B*, vol. 317, pp. 349–353, Dec. 2013.
[doi:10.1016/j.nimb.2013.06.042](https://doi.org/10.1016/j.nimb.2013.06.042)
- [3] S. Miller *et al.*, “Optimization of a mini-channel beam dump for FRIB operations”, presented at HIAT25, East Lansing, MI, Jun. 2025, paper TUP01, this conference.
- [4] “BPVC Pressure Analysis applied to Mini-Channel Beam Dump (MCBD)”, Facility for Rare Isotope Beams (FRIB), Michigan State University (MSU), East Lansing, MI, USA, Report FRIB-T40510-TD-001717-R001.
- [5] “Thermal Fluid-Solid Analysis of the Mini-Channel Beam Dump”, Facility for Rare Isotope Beams (FRIB), Michigan State University (MSU), East Lansing, MI, USA, Report FRIB-T40510-TD-001718-R001.
- [6] JAHM Software,
<https://www.jahm.com/>.
- [7] K. Zhang, E. Gaganidze, and M. Gorley, “Development of the material property handbook and database of CuCrZr”, *Fusion Eng. Des.*, vol. 144, pp. 148–153, Jul. 2019.
[doi:10.1016/j.fusengdes.2019.04.094](https://doi.org/10.1016/j.fusengdes.2019.04.094)
- [8] N. E. Uzan, R. Shneck, O. Yeheskel, and N. Frage, “High-temperature mechanical properties of AlSi10Mg specimens fabricated by additive manufacturing using selective laser melting technologies (AM-SLM)”, *3D Print. Addit. Manuf.*, vol. 24, pp. 257–263, Dec. 2018.
[doi:10.1016/j.addma.2018.09.033](https://doi.org/10.1016/j.addma.2018.09.033)
- [9] Song *et al.*, “Design and Experimental Thermal Validation of the Mini-Channel Beam Dump for FRIB”, presented at HIAT25, East Lansing, MI, Jun. 2025, paper TUP04, this conference.

DEVELOPMENT OF AUTOMATIC BEAM TUNING SYSTEM USING BAYESIAN OPTIMIZATION FOR HIGH INTENSITY HEAVY ION BEAMS AT RIBF

T. Nishi*, H. Fujii, N. Fukuda, Y. Morita, Y. Shimizu, T. Sumikama, A. Uchiyama
RIKEN Nishina Center, Wako, Saitama, Japan

Abstract

In general, accelerator facilities are controlled by a huge number of parameters. To optimize these parameters more efficiently and accurately, we are attempting to implement Bayesian optimization (BO). Given the importance of space charge effects and beam loading, it is desirable to adjust parameters at high beam intensity, making it crucial to develop an optimization system capable of handling high-intensity heavy ion beams. We have been working on developing indices suitable for high-intensity beams and exploring methods for optimization while maintaining operational safety. Currently, we are preparing for simulations and tests using beam line.

BAYESIAN OPTIMIZATION FOR HIGH-INTENSITY ACCELERATOR FACILITIES

The RIKEN RI Beam Factory (RIBF) [1, 2], a heavy-ion accelerator complex consisting of several cyclotrons and Linacs, is controlled or influenced by more than 600 parameters, including environmental factors. So far we developed a technique that enables the simultaneous measurement of beam transmission and spot shape on the target by tracking charge-converted particles after passing through the target. Additionally, we are investigating the use of line BO with a safety function [3, 4] to ensure safe beam optimization. We employed an automatic beam tuning program based on Bayesian optimization using Gaussian Process Regression (GPR), originally developed at SACLA, SPring-8 [5]. This program estimates the objective function for unknown parameter sets from acquired data using GPR, including predictive uncertainties. Based on this estimation, the next set of beam parameters is determined by maximizing an acquisition function. By applying this new parameter set and re-evaluating the objective function, the program continues to learn and iteratively updates the beam parameters through sequential learning.

When adapting this program to RIBF, we identified the following two key development requirements.

1. Development of beam quality indicators applicable to high-intensity beams. At high-intensity beam facilities such as RIBF, space-charge effects and beam loading in RF cavities cause the optimal tuning parameters to vary with beam intensity. Therefore, it is essential to establish indicators that can appropriately represent both beam intensity and beam quality under such conditions.

2. Implementation of a safety system to prevent excessive beam loss during tuning. Even if the algorithm ultimately converges to optimal parameters, excessive beam losses during the optimization process could lead to equipment damage or operational risks. It is thus crucial to develop a safety scheme that monitors and limits beam loss during the tuning process to ensure safe operation.

In this paper, we first present the results of beam tuning in the low-energy section to investigate the basic characteristics of Bayesian optimization. We then explain the development of evaluation metrics suitable for high-intensity beams, followed by our ongoing efforts toward implementing a practical safety scheme.

APPLICATION FOR LOW ENERGY SECTION

We applied the developed optimization program to the low-energy section, where the ion beam from the 28 GHz ECR ion source is accelerated by RILAC-II and injected into the RIKEN Ring Cyclotron (RRC). The optimization targeted quadrupole, steerer, and dipole magnets located between the ion source and the RRC injection system, using Bayesian optimization to maximize the beam current at the cyclotron extraction point.

Prior to the optimization, the RRC tuning parameters were manually adjusted by experienced operators. The objective was to increase the beam current at the RRC exit by improving upstream beam transport and better matching the beam envelope to the cyclotron acceptance. Over 70 parameters were divided into 10 groups, with each group limited to no more than 10 parameters to maintain the efficiency of the Bayesian optimization process. For the steerer magnets, groupings were arranged to include at least two steerers in both the horizontal and vertical planes, in order to avoid convergence to local minima.

To reduce noise in the objective function, the value was averaged over five consecutive measurements taken at 0.2 second intervals, achieving precision at the few enA level for beam currents around 500 enA.

The optimization result is shown in Fig. 1. After tuning the parameter ranges through preliminary tests, the full optimization was performed over 40 minutes, with each iteration taking approximately 7 seconds, resulting in around 350 trials. As a result, the beam current at the RRC exit increased from 520–530 enA to 570–580 enA, representing an improvement of approximately 10%.

* takahiro.nishi@riken.jp

It is worth noting that when the beam current was decreased to about 80 enA using an upstream attenuator, the optimization failed. This suggests that a sufficiently sensitive and reliable objective function is essential for successful optimization.

However, the optimization process occasionally caused significant drops in transmission; in the worst case, the transmission fell to just 10% of its initial value. These results highlight the importance of implementing an appropriate safety scheme, particularly when working with high-intensity and high-energy beams.

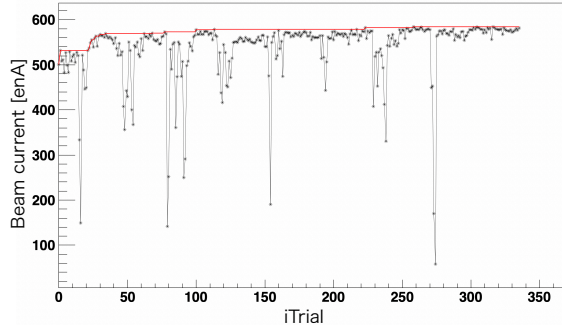


Figure 1: Beam current at the RRC exit for each trial of Bayesian optimization. The red line indicates the best result obtained up to that point.

DEVELOPMENT OF BEAM DIAGNOSTICS USING CHARGE-CONVERTED PARTICLES FOR HIGH-INTENSITY HEAVY-ION BEAMS

In order to develop diagnostics indicators applicable to high-intensity beams, we conducted a test experiment at the T-course beamline, which is located just upstream of the production target for secondary beams (see Fig. 2) [6]. The experiment was performed using a Kr^{36+} beam accelerated to 345 MeV/nucleon. The goal was to develop a novel method capable of simultaneously measuring the beam intensity and spot size under high-intensity beam conditions.

In this method, we employed a Parallel Plate Avalanche Counter (PPAC) [7] and a plastic scintillation detector, both located at the downstream focal plane F3 of the BigRIPS fragment separator, to evaluate the phase-space ellipse and the intensity of the primary beam. However, due to limitations in detector counting capability, direct measurement of the primary beam is restricted to intensities of approximately 10 kcps. To circumvent this limitation, a 1-mm-thick Be target was placed at the target to create charge-converted particles. By selecting only the charge-converted particles using a combination of bending magnets and slits, we enabled to detect the particles under significantly attenuated beam rates. For example, when injecting a 30 enA Kr^{36+} beam and configuring the system to detect Kr^{34+} , the beam

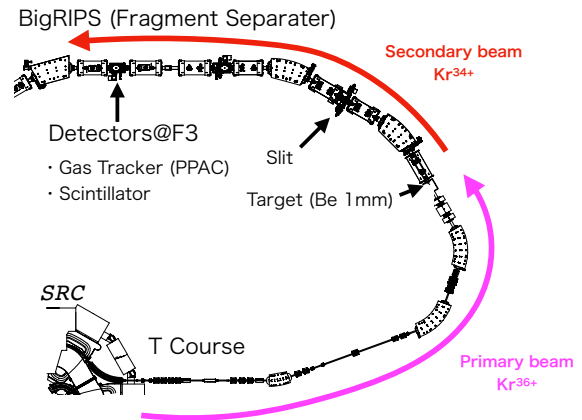


Figure 2: Schematic diagram of the measurement method for high-intensity beams using charge-converted particles with the BigRIPS separator.

rate at the detectors was reduced to approximately 10 kcps, making measurements feasible.

To validate this method, we first compared the beam spot size of Kr^{34+} obtained with the downstream PPAC against the Kr^{36+} spot observed on a fluorescent screen, while varying both beam intensity and optics settings. A good qualitative agreement between the two measurements was observed, confirming the viability of the charge-converted approach.

Following this, the method was applied to automatic ion-optics tuning using Bayesian optimization. Given the sequential nature of the method, which requires iterative evaluations, it is crucial to complete each trial within a few to 10 seconds to ensure sufficient optimization cycles. The newly developed BYACO system [8] was employed to rapidly process PPAC and scintillator data into beam spot and intensity information, which were then transmitted via EPICS to the optimization algorithm in real time.

The beam profiles at F3 before and after optimization are shown in Fig.3, which corresponds to the beam spot at the target position. The optimization resulted in a reduction of the horizontal beam width from 1.5mm to 1.1 mm (rms), while maintaining the beam transmission efficiency, as confirmed by Faraday cup measurements within the experimental uncertainty.

In summary, this study demonstrated a practical method for simultaneous measurement of beam profile and intensity using charge-converted particles. The method not only enabled the reduction of the beam spot size but also maintained transport efficiency. The flexibility of this framework is further enhanced by the integration of the BYACO system, which allows a wide range of downstream detector information—such as signal-to-noise ratios of secondary particles—to be used as objective functions in optimization processes.

In this experiment, the beam intensity was limited to approximately 30 enA due to safety considerations. However, by appropriately selecting the charge states, this technique

can be extended to higher-intensity beams. As such, the development of a safety-aware optimization algorithm represents the next essential step toward fully autonomous tuning of high-intensity beams.

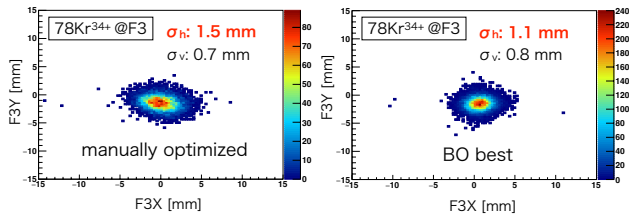


Figure 3: Beam spot of charge-converted particles (Kr^{34+}) measured by the F3 PPAC before and after Bayesian optimization.

SAFETY SCHEME: SAFE LINE-BO

To extend the optimization framework to high-intensity beams, an integrated safety mechanism is essential. Although the existing beam interlock system can shut off the beam in the event of excessive losses, this safeguard alone is insufficient for automatic tuning. Instead, an optimization algorithm that inherently avoids unsafe parameter regions is required.

To this end, we aim to implement the Safe Line Bayesian Optimization (Safe LineBO) framework [3, 4], which incorporates a separate safety function in addition to the primary objective function. The optimization process is restricted to parameter regions where the safety function exceeds a predefined threshold, taking into account both its expected value and associated uncertainty. As more data are acquired, the feasible parameter space gradually expands.

To reduce computational costs and effective optimization with high-dimensional parameters, LineBO restricts the parameter search to one-dimensional subspaces (lines), along which optimization is conducted using GPR. When an improved solution is found, a new search direction is selected, and the optimization process resumes.

We evaluated this approach via simulation using a model of the T-course beamline. Transfer matrices corresponding to different magnet settings were calculated using GICOSY, and transmission efficiencies were estimated using MOCADI [9]. The objective function was defined as the transmission efficiency to the target, while seven safety constraints were imposed, including beam losses at dipole magnet entrances and exits ($<5\%$) and a minimum transmission threshold ($>40\%$).

Figure 4 illustrates the optimization process obtained using Safe LineBO and standard Bayesian optimization for the upstream seven out of seventeen quadrupole magnets in the beamline. Each case involved approximately 300 optimization trials.

Initially, the transmission was set to 74%. After 300 trials, both methods achieved comparable final transmission values

of around 92%. However, when focusing on the number of trials required to exceed 85% transmission, Safe LineBO showed slightly faster convergence.

More importantly, with Safe LineBO, the transmission remained consistently above 75% throughout the optimization process. In contrast, standard BO led to a significant temporary drop, with the transmission falling as low as 30%.

These results suggest that Safe LineBO offers advantages in both optimization efficiency and safety, particularly when dealing with high-dimensional parameter spaces. As a next step, we plan to integrate this algorithm into our BO framework and apply it to the optimization of the actual beamline.

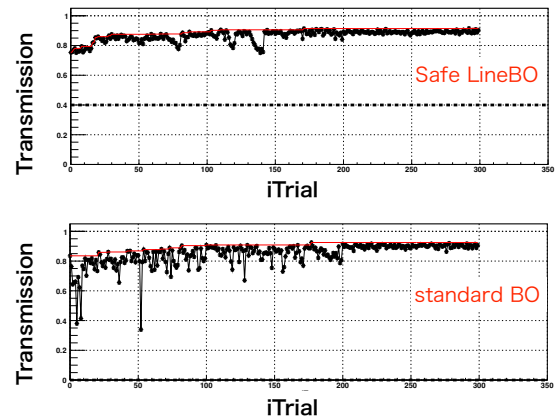


Figure 4: Simulation results of transmission optimization in the T course using Safe LineBO and standard BO. The red line indicates the best result obtained up to that point. The dashed line indicates the threshold applied to the transmission as the representative safety constraint. For standard BO, the threshold is set to zero since no safety constraint is imposed.

CONCLUSION AND FUTURE PERSPECTIVES

In this study, we presented the current progress in the development of automatic beam tuning at RIBF, with a particular focus on the use of charge-converted particles to establish reliable indicators for high-intensity beams, as well as the introduction of Safe Line Bayesian Optimization (Safe LineBO) as a safety-aware optimization framework. Looking ahead, we aim to implement these algorithms in the actual system and further enhance the optimization process by incorporating techniques such as variational autoencoders [10], toward efficient and safe high-dimensional parameter optimization for high-intensity heavy ion beams.

REFERENCES

- [1] Y. Yano, “The RIKEN RI Beam Factory Project: A status report”, *Nucl. Instrum. Methods Phys. Res., Sect. B*, vol. 261, no. 1–2, pp. 1009–1013, Aug. 2007.
doi:10.1016/j.nimb.2007.04.174

- [2] H. Okuno, N. Fukunishi, and O. Kamigaito, “Progress of RIBF accelerators”, *Prog. Theor. Exp. Phys.*, vol. 2012, no. 1, pp. 3C002-0, Dec. 2012.
doi:10.1093/ptep/pts046
- [3] F. Berkenkamp, A. Krause, and A. P. Schoellig, “Bayesian optimization with safety constraints: safe and automatic parameter tuning in robotics”, *Mach. Learn.*, vol. 112, no. 10, pp. 3713–3747, 2023.
doi:10.1007/s10994-021-06019-1
- [4] J. Kirschner *et al.*, “Adaptive and safe Bayesian optimization in high dimensions via one-dimensional subspaces”, *Proc. of the 36th International Conference on Machine Learning (PMLR)*, vol. 97, pp. 3429–3438, 2019.
doi:10.48550/arXiv.1902.03229
- [5] E. Iwai *et al.*, “Spectral-brightness optimization of an X-ray free-electron laser by machine-learning-based tuning”, *J. Synchrotron Radiat.*, vol. 30, no. 6, pp. 1048–1053, Oct. 2023. doi:10.1107/s1600577523007737
- [6] T. Nishi *et al.*, “Development of auto tuning system using Bayesian optimization for ion optics in primary beam line with 26 enA Kr beam”, *RIKEN Accel. Prog. Rep.*, vol. 56, p. 71, 2022.
- [7] H. Kumagai *et al.*, “Development of Parallel Plate Avalanche Counter (PPAC) for BigRIPS fragment separator”, *Nucl. Instrum. Methods Phys. Res. B*, vol. 317, pp. 717–727, Dec. 2013. doi:10.1016/j.nimb.2013.08.050
- [8] T. Sumikama, Y. Shimizu, and H. Haba, “BYACO ecosystem for innovative online operation of BigRIPS experiments with seamless connection to comprehensive analysis”, *RIKEN Accel. Prog. Rep.* vol. 54, p. 82, 2020.
- [9] N. Iwasa, H. Weick, and H. Geissel, “New features of the Monte-Carlo code MOCADI”, *Nucl. Instrum. Methods Phys. Res. B*, vol. 269, no. 8, pp. 752–758, Apr. 2011.
doi:10.1016/j.nimb.2011.02.007
- [10] Y. Morita, T. Washio, and Y. Nakashima, “Accelerator tuning method using autoencoder and Bayesian optimization”, *Nucl. Instrum. Methods Phys. Res. A*, vol. 1057, p. 168730, Dec. 2023. doi:10.1016/j.nima.2023.168730

APPLICATION OF ML TOOLS FOR EXTRACTION OF BPM-Q AND TRANSVERSE BEAM MATCHING *

K. Hwang[†], K. Fukushima, T. Maruta, P. Ostroumov, A. Plastun, T. Zhang, Q. Zhao
Facility for Rare Isotope Beams, Michigan State University, East Lansing, MI, USA

Abstract

Training an accurate Beam Quadrupole Moment at BPM (BPMQ) model is challenging due to data inaccuracies. Similarly, reconstructing Courant-Snyder (CS) parameters from BPMQ predictions is difficult due to the limitations of the BPMQ model. Increasing the number of BPMQ predictions helps mitigate overfitting in CS inference caused by inaccurate BPMQ predictions. We present Bayesian Active Learning (BAL) to strategically acquire measurements, improving the inference of the CS parameters despite the limitations of the model.

QUADRUPOLE MOMENTS OF THE BEAM AT BEAM POSITION MONITOR (BPMQ)

The beam quadrupole moment (BPMQ), defined by the difference in the transverse variances of the beam: $\sigma_x^2 - \sigma_y^2$, can be estimated using Beam Position Monitor (BPM) signals. For a circular cross section BPM with four pickups positioned at the top, left, right, and bottom, the BPMQ is given by [1]:

$$\text{BPMQ} = G \frac{U_R + U_L - (U_T + U_B)}{U_R + U_L + U_T + U_B} - (x^2 - y^2) \approx \sigma_x^2 - \sigma_y^2 \quad (1)$$

where G is a geometric factor that depends on the BPM cross-section geometry, U_T , U_L , U_R and U_B are the induced signal strength at the top, left, right, and bottom pickups, and x and y represent the horizontal and vertical beam centroids which are also a function of the 4 pickup signals. To minimize signal cross talk caused by prevalent sources of error throughout the linac, the induced signal strength U_i is defined as the amplitude of the 161 MHz component of the pickup signal.

VIRTUAL DIAGNOSTICS (VD) FOR BPMQ

As primary role of BPM is to measure the position of the beam, the BPMQ signal is significantly weaker compared to the centroid signal of the beam. Consequently, small errors, such as calibration inaccuracies, can lead to substantial errors in the BPMQ measurements.

We address the calibration of BPMQ using a Supervised Machine Learning (ML) approach. It is important to remark that the accuracy of the calibration model depends on the quality of the data.

* Work supported by the U.S. Department of Energy, Office of Science, Office of Nuclear Physics, under Award Number DE-SC0024707 and used resources of the FRIB Operations, which is a DOE Office of Science User Facility under Award Number DE-SC0023633

[†] hwang@frib.msu.edu

Dataset

The dataset consists of four induced signals from four BPM pickups, which serve as input features. The target output (label) for the machine learning (ML) model is the BPMQ value. The collection of training data including the BPMQ labeling involves the following steps:

- Perform a quadrupole magnet scan (q-scan). At each q-scan step, measure the root-mean-square (RMS) beam size from the beam profile using a wire scanner, referred to as the Profile Monitor (PM).
- Reconstruct the Courant-Snyder (CS) parameters by fitting the measured beam sizes. This is achieved by minimizing the difference between the measured and simulated beam sizes using the beam envelope simulation code FLAME [2].
- With the reconstructed CS parameters, simulate the beam envelope at the BPM locations (for given quadrupole settings) using FLAME to compute the corresponding BPMQ values.

The reliability of the data depends on the accuracy of PM measurement, accuracy of the lattice model and quadrupole magnet strength calibration used in FLAME simulation, beam and machine stability during measurements, BPM signal noise. To reflect the quality of the data, the dataset is categorized into two fidelity levels:

High-fidelity data: This set includes samples collected through a structured q-scan procedure, where each step is paired with a PM measurement. These data points are the same ones used for CS parameter reconstruction. After the reconstruction, samples with high reconstruction loss are excluded to further improve quality. As a result, this dataset contains only well-matched measurements and simulations.

Low-fidelity data: This set includes two types of samples: (1) data collected during the q-scan procedure but rejected due to high reconstruction loss, and (2) data collected after the CS reconstruction process, using random quadrupole magnet settings without accompanying PM scans. In the second case, BPMQ values are labeled by simulating the beam envelope using the previously reconstructed CS parameters.

BPMQ Model

We explored two Artificial Neural Network (ANN) architectures for modeling BPMQ. This model will serve as virtual diagnostics (VD). First, we designed a model structure that incorporates physical constraints to improve interpretability and generalization. The model enforces the following form for BPMQ prediction:

$$M1_{BPMQ} = g \frac{u_R + u_L - (u_T + u_B)}{u_R + u_L + u_T + u_B} - (x^2 - y^2) + FCNN(u, u^2) \quad (2)$$

where x and y are beam centroid at BPM, $g = (1 + \theta_G)G$ is the linearly calibrated geometric factor, and $u_i = (1 + \theta_i)U_i$ are the 161 MHz component of the linearly calibrated induced signals, with θ representing the model parameters. $FCNN(u, u^2)$ represents a Fully Connected Neural Network that takes as input both the induced signals u and their squared terms u^2 . The quadratic terms u^2 is chosen as an engineered feature set to capture small nonlinear responses while keeping the model compact. This helps avoid overfitting and enhances the model's ability to generalize from limited and noisy data.

The second model architecture exploits the raw time-domain data of the induced signal. This approach was motivated by the speculation that the 161 MHz component may not fully capture the transverse quadrupole moments of the beam across the entire longitudinal bunch. The architecture uses 1D convolutional layers to extract relevant features directly from the raw BPM signals, as shown in Fig. 1. Although this model performed well on the validation dataset, its ability to generalize is questionable, as the signal shape is strongly dependent on the longitudinal beam profile. Acquiring sufficient training data that encompasses the full range of longitudinal profiles would be challenging.

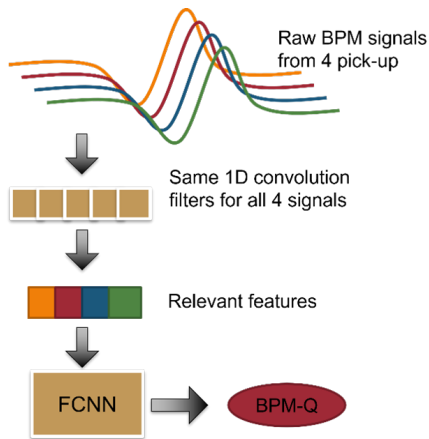


Figure 1: Model architecture of raw BPM signal input for supervised BPMQ prediction as well as relevant feature extraction.

We first train the neural network models using low-fidelity data and then apply transfer learning [3, 4] to fine-tune them with high-fidelity data. After training, relevant features are extracted from the neural network models and used as input to a Gaussian Process (GP) layer. This final GP stage predicts both BPMQ and associated model uncertainty, enabling a more reliable loss function in downstream Courant–Snyder parameter reconstruction. Figure 2 shows that the GP model uncertainty is generally higher than the prediction error, indicating a conservative uncertainty estimate that helps safeguard against overconfident predictions.

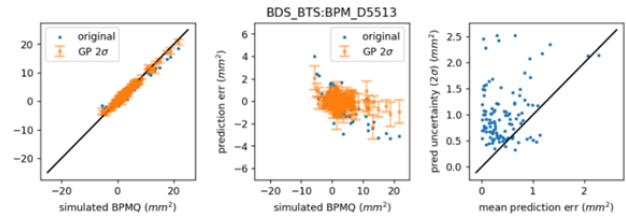


Figure 2: GP prediction of BPMQ of a BPM on validation data. Original represent the calculated BPMQ using the formula Eq. 1. Middle: prediction error with error bar. Right: prediction error versus model uncertainty. It shows that model uncertainty generally is higher than prediction error.

BAYESIAN ACTIVE LEARNING

Although the BPMQ models were well trained, their accuracy is ultimately limited by the quality of the training data labels. We also observed that even small BPMQ errors can lead to significant errors in the reconstructed Courant–Snyder (CS) parameters. Overfitting CS parameters to BPMQ errors can be mitigated by acquiring a large volume of BPMQ VD data, which can be obtained through scans of quadrupole magnets. Accurate reconstruction of CS parameters from beam quadrupole moments at a limited number of BPMs requires an efficient quadrupole magnet scan (q-scan) that maximizes information gain. To achieve this, we implement Bayesian active learning for optimal q-scan design.

Unlike passive learning, where the model is trained on a fixed, given dataset, active learning actively selects the most informative data points to query during the training process to improve model performance more efficiently. Bayesian active learning (BAL) exploits probabilistic models to determine the most efficient queries for data acquisition, often by querying data points where the model uncertainty is highest. Bayesian Optimization can also be considered a form of BAL, as it actively queries candidate points to improve the model.

Specifically, we use an ensemble of beam envelope simulations implemented in PyTorch as a surrogate model. The simulation is vectorized [5, 6] to simultaneously process many Courant–Snyder (CS) parameter sets at once to boost computational speed. Each CS parameter set and its corresponding simulated beam envelope represent a sample from a probabilistic distribution. Unlike black-box probabilistic models like GP, this approach directly incorporates physics constraints, making it highly sample-efficient and interpretable enabling the implementation of various physics-informed considerations. For example, when the quadrupole magnet setting is queried we can impose penalty on large beam size at quadrupole magnet locations to avoid beam loss.

In each iteration of Bayesian Active Learning (BAL), the ensemble of Courant–Snyder (CS) parameters is updated based on BPMQ data measured up to that point. A new quadrupole magnet setting is then queried by selecting the one that maximizes the variation in the simulated BPMQ

values produced by the surrogate model. A large variation in BPMQ implies that the CS parameters are not uniquely determined. Therefore, by measuring BPMQ at the quadrupole setting that yields the highest uncertainty in predicted BPMQ values, we can most efficiently constrain the CS parameter space.

IMPROVING CS RECONSTRUCTION ACCURACY

Among the CS parameters, we empirically found that the emittance is the most sensitive to BPMQ errors, as shown in Fig. 3. Therefore, regularizing the emittance fitting based on a prior belief of the emittance can help mitigate unrealistically large inference errors.

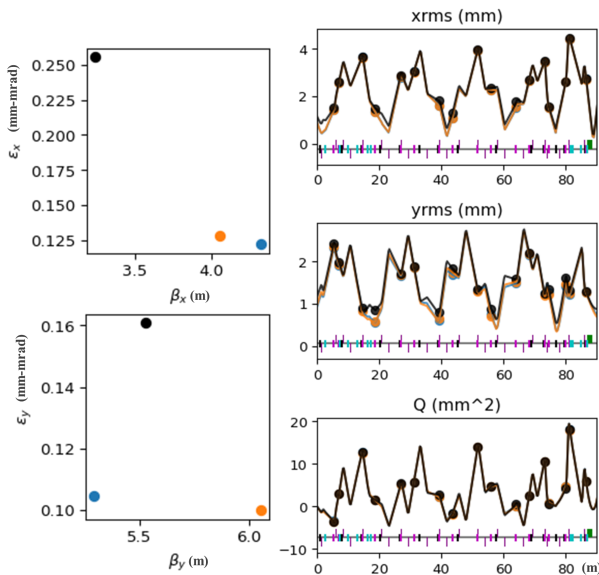


Figure 3: Degeneracy of CS solutions based on BPMQ measurements from the LS3 exit to the BDS entrance segment. The three colors represent different CS solutions at the LS3 exit, all producing nearly identical BPMQ values (average deviation $< 0.5 \text{ mm}^2$) at BPMs, while the differences in RMS beam sizes are noticeable and measurable using the profile monitor (resolution $< 0.1 \text{ mm}$). Notably, the emittance difference between solutions can be as much as a factor of two. Incorporating a prior on emittance can help resolve such ambiguities in CS reconstruction.

Further improvements to CS reconstruction can be achieved by incorporating a few profile monitor (PM) scans, which are slower but more accurate. We also apply BAL to query the quadrupole magnet settings that are expected to yield the most informative PM scan data.

BEAM TEST

Recent beam tests have shown promising results. To reduce computation time, the surrogate model for BAL was initialized after conducting 8 random quadrupole scans (q-scans). In each q-scan, BPMQ values were recorded from

16 BPMs using BPMQ VD. Although only six parameters are fitted during CS reconstruction, measurement errors can introduce uncertainty into the reconstructed CS parameters. This uncertainty is leveraged when selecting q-scans to query. Using BAL, we queried 2 additional q-scans for BPMQ measurements and 1 additional q-scan for a PM measurement.

Figure 4 shows the final CS solutions, where all ensemble members have converged to a unique solution with a mismatch factor of approximately 0.2 compared to the reference solution. The reference solution was obtained using a separate q-scan procedure with PM measurements, which is the standard method traditionally used for CS reconstruction.

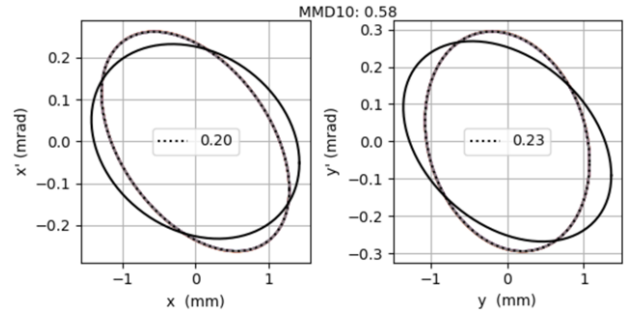


Figure 4: Final ensemble of BPMQ based CS solution. The black ellipse correspond to the reference solution.

We also performed transverse envelope matching downstream of the beamline using the BPMQ-based CS solution. It resulted in significantly lower readings from the beam loss monitors compared to envelope matching based on the PM-derived CS solution, as shown in Fig. 5.

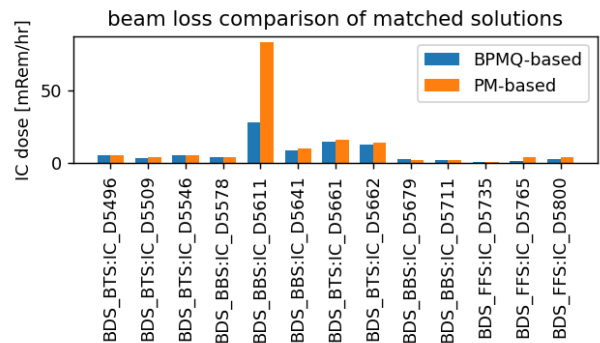


Figure 5: Comparison of Ion Chamber (IC) readings for beam loss detection using two optics solutions. Residual beam loss, even after matching with either solution, can be attributed to error of lattice model that is used for transverse envelope matching.

REFERENCES

- [1] B. E. Carlsten and S. J. Russell, "Measuring Emittance Using Beam Position Monitors", in *Proc. PAC'93*, Washington D.C., USA, Mar. 1993, pp. 2537–2540.

- [2] Z. He, M. Davidsaver, K. Fukushima, G. Shen, M. Ikegami, and J. Bengtsson, “The fast linear accelerator modeling engine for FRIB online model service”, *Comput. Phys. Commun.*, vol. 234, pp. 167–178, Jan. 2019.
doi:10.1016/j.cpc.2018.07.013
- [3] K. Hwang *et al.*, “Prior-mean-assisted Bayesian optimization application on FRIB Front-End tuning”, *arXiv:2211.06400 [physics.acc-ph]*, Nov. 2022.
doi:10.48550/arXiv.2211.06400
- [4] T. Boltz *et al.*, “Leveraging Prior Mean Models for Faster Bayesian Optimization of Particle Accelerators”, *arXiv:2403.03225 [physics.acc-ph]*, 2024.
doi:10.48550/arXiv.2403.03225
- [5] B. Wang, C. Rosales-Fernandez, W. Tang, “Improve Performance by Vectorizing Particle-in-Cell Codes: A Guide”, May 2019, <https://www.intel.com/content/www/us/en/developer/articles/technical/improve-performance-vectorizing-particle-in-cell.html>
- [6] J.-L. Vay, D. P. Grote, R. H. Cohen, and A. Friedman, “Novel methods in the Particle-In-Cell accelerator Code-Framework Warp”, *Comput. Sci. Discov.*, vol. 5, no. 1, p. 014019, Dec. 2012. doi:10.1088/1749-4699/5/1/014019

FRIB MULTI-GAP BUNCHER CONDITIONING UP TO 30 KW*

H. Ao[†], E. Gutierrez, D. Morris, X. Rao, S. Zhao

Facility for Rare Isotope Beams, Michigan State University, East Lansing, MI USA

Abstract

The Facility for Rare Isotope Beams commenced operations for scientific users in May 2022, and the driver linac currently operates at beam powers of up to 20 kW. To reduce beam loss in the linac, we plan to operate two multi-gap bunchers (MGBs) at higher accelerating voltages. This paper presents lessons learned from the initial stages of MGB operations and summarizes the phased high-power conditioning, which progressed from 18 kW to 26.5 kW, and then to 30 kW of continuous wave RF power. Both MGBs were successfully conditioned during maintenance periods. After approximately 100 hours of conditioning, MGB1 operated without tripping in the last 12 hours, and MGB2 experienced only three trips during the same period.

INTRODUCTION

The Facility for Rare Isotope Beams (FRIB) at Michigan State University (MSU) is a scientific user facility for the U.S. Department of Energy Office of Science (DOE-SC), with financial support from and furthering the mission of the DOE-SC Office of Nuclear Physics. The FRIB driver linac was designed to accelerate stable ion beams exceeding 200 MeV/u with superconducting cavities and provide a beam power up to 400 kW. User operations commenced in May 2022, and the linac currently operates at beam powers of up to 20 kW [1].

Reducing beam losses is one of the biggest challenges as beam power increases. A recent beam study observed the beam loss in Linac Segment 2 (LS2, Fig. 1) due to an energy spread increase caused by the lithium stripper [2]. To increase the longitudinal acceptance, we plan to operate two 161-MHz normal conducting multigap bunchers (MGBs, Fig. 1) at higher voltages and introduce new second harmonic RF cavities [3].

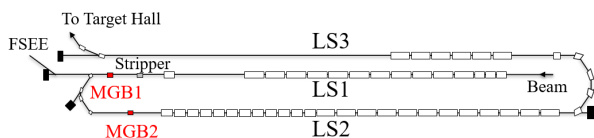


Figure 1: Layout of FRIB driver linac.

This paper provides lessons learned from the initial stages of MGB operations and summarizes the phased high-power conditioning of MGB1 and MGB2, conducted following the upgrade of the continuous wave RF amplifiers from 18 kW to 30 kW by adding two amplifier drawers

in addition to the existing four drawers to each rack of the two-rack system, with each drawer operating at 2.5 kW.

COMMISSIONING GOALS

The primary goal was to verify that both MGBs operated stably. Secondary goals included evaluating interlock settings, assessing the accuracy of RF power readbacks, monitoring long-term stability, and investigating other factors relevant to user operation. Major criteria were as follows:

- Stable cavity operation for over one hour without trips at the highest operating voltages
- Vacuum pressure rise less than 1×10^{-6} Torr and as low as reasonably achievable during startup

The second one was defined to prevent the issue encountered during the initial stages of operation. Multiple startup failures occurred due to vacuum spikes in the MGB1 at 900 kV (Fig. 2, top). Although MGB1 had previously operated at voltages higher than 900 kV for approximately 100 hours, it had been turned off for about three months. After an additional 30 hours of conditioning, no vacuum spikes were observed (Fig. 2, bottom). However, the vacuum pressure still reached approximately 1×10^{-6} Torr during startup.

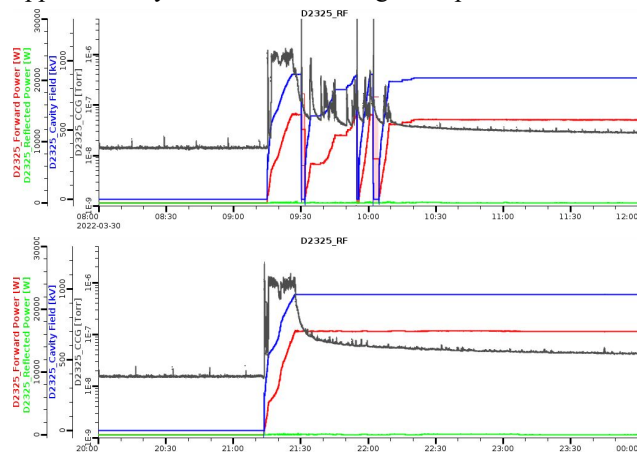


Figure 2: Pressure rise during cavity startup in the initial stages of MGB operations. Colors are consistent across all figures: red for forward power, blue for cavity voltage, and gray for vacuum pressure. (Top) Multiple trips occurred due to vacuum spikes following a three-month shutdown. (Bottom) After an additional 30 hours of conditioning, no further vacuum spikes were observed.

This result indicates that the MGBs need degassing before operating at higher voltages at which they have not been operated recently. This is primarily because higher power increases the temperature on the inner surface, which in turn generates more outgassing. The inner surface may capture residual gases during low-power operation, which are then released at higher power.

*This material is based upon work supported by the U.S. Department of Energy, Office of Science, Office of Nuclear Physics and used resources of the Facility for Rare Isotope Beams (FRIB) Operations, which is a DOE Office of Science User Facility under Award Number DE-SC0023633

[†]ao@frib.msu.edu

CONDITIONING UP TO 26.5 kW

Immediately after the RF amplifier upgrade, the overall combined power was limited to 26.5 kW due to a hardware power limit at the pallet level, set by the vendor and unchangeable without a firmware update.

For this reason, the threshold for average forward power was set to 27 kW at the directional coupler located immediately before the cavity in both systems. The maximum conditioning power reached up to 26.5 kW. The corresponding Kilpatrick factors were 0.73 for MGB1 and 0.65 for MGB2.

The initial conditioning took less than six hours to reach 26.5 kW. MGB1 tripped three times due to the reflected power interlock caused by the cavity itself before reaching 26.5 kW (Fig. 3). All other trips were related to LLRF and amplifier interlocks associated with the forward power limit settings. MGB2 tripped nine times due to reflected power, but only at the initial phase (Fig. 4).

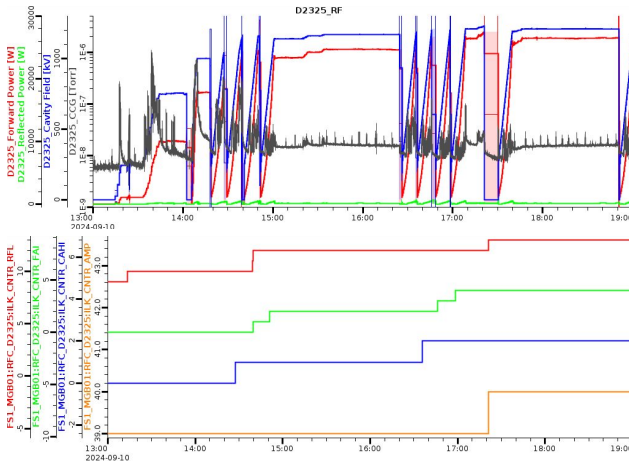


Figure 3: Initial conditioning of MGB1 up to 26.5 kW. (Top) RF and vacuum signals. (Bottom) Interlock counters for reflected power, forward power, excessive cavity field, and amplifier fault. The reflected power interlock was caused by the cavity itself.

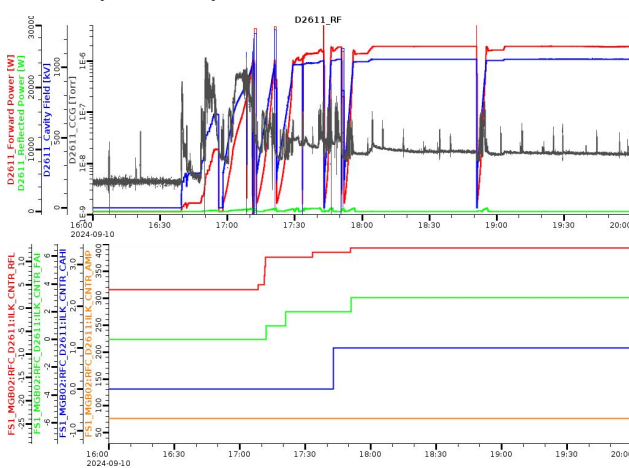


Figure 4: Initial conditioning of MGB2 up to 26.5 kW. (Top) RF and vacuum signals. (Bottom) Interlock counters.

Figure 5 shows the pressure rise during startup. A turbo pump was turned off to maintain the same conditions as in

Fig. 2. The pressure increases were less than 2×10^{-7} Torr (MGB1) and 4×10^{-7} Torr (MGB2). Both values are less than half of those observed in 2022 (Fig. 2) and are sufficient for stable operation. As noted in the commissioning goals, degassing may be required after a long shutdown or an extended period of low-power operation.

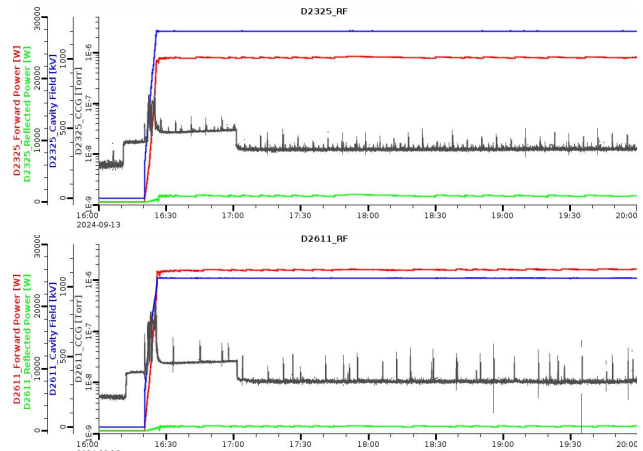


Figure 5: Pressure rise during cavity startup up to 26.5 kW. (Top) MGB1. (Bottom) MGB2. The pressure increase is less than half of the value observed in 2022.

Figure 6 shows the RF and vacuum signals at the latest stage of the conditioning. Both cavities operated stably at 26.5 kW. Note that the RF signal readings were slightly altered due to changes in cable re-calibration and frequency tuning adjustment.

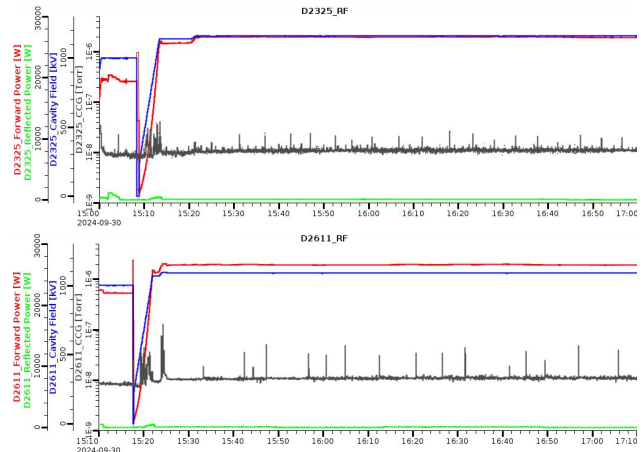


Figure 6: Latest stage of conditioning at 26.5 kW. (Top) MGB1. (Bottom) MGB2. Both systems operated stably.

CONDITIONING UP TO 30 kW

Following the firmware update of the RF amplifiers, the interlock threshold for average forward power was increased to 30.5 kW at the directional couplers for both systems. The corresponding Kilpatrick factors were 0.79 for MGB1 and 0.70 for MGB2.

The conditioning took less than three hours to increase the power from 26.5 kW to 30 kW. MGB1 tripped one time due to reflected power. Five continuous trips during the startup (around 20:30 in Fig. 7) were caused by LLRF interlock settings, not by the cavity itself.

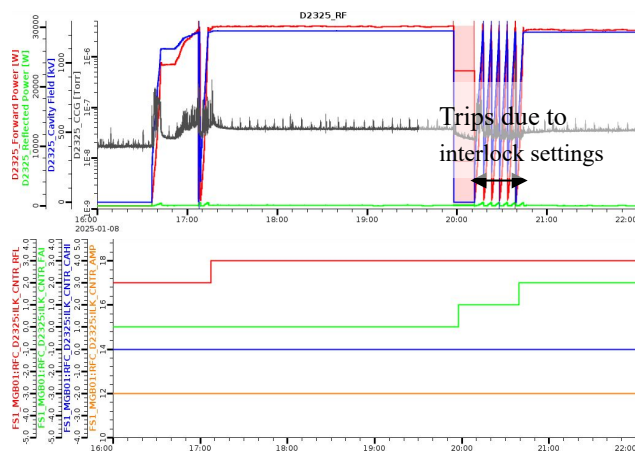


Figure 7: Initial conditioning of MGB1 from 26.5 up to 30 kW. (Top) RF and vacuum signals. (Bottom) Interlock counters.

MGB2 tripped nine times mainly due to reflected power. Since it was not very stable after reaching 30 kW, the power was slightly reduced to 29.6 kW, and then the conditioning continued for 10 hours (Fig. 8).

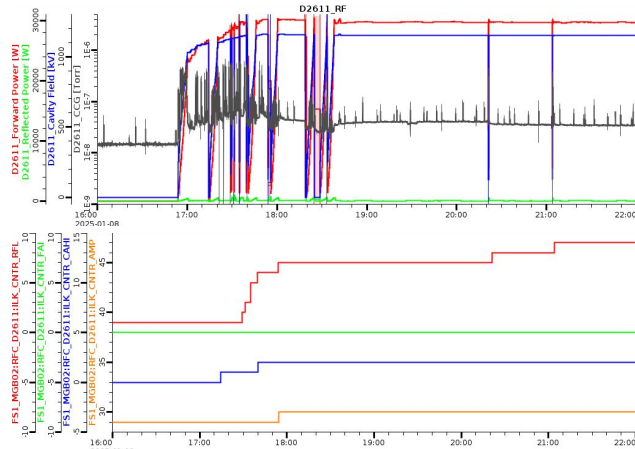


Figure 8: Initial conditioning of MGB2 from 26.5 up to 30 kW. (Top) RF and vacuum signals. (Bottom) Interlock counters.

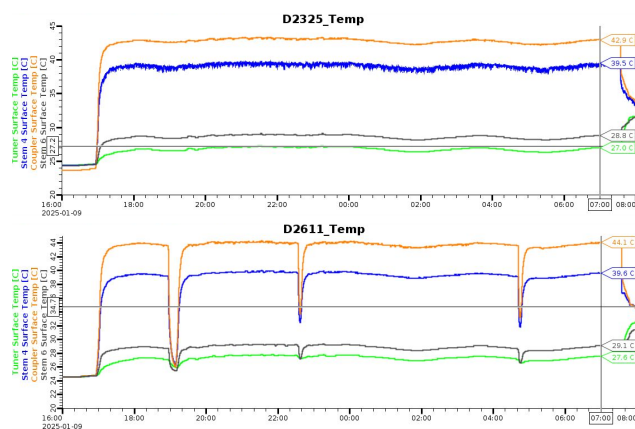


Figure 9: Surface temperatures. (Top) MGB1 at 30.0 kW. (Bottom) MGB2 at 30.2 kW.

Figure 9 shows the surface temperature changes during conditioning. The slow temperature fluctuation of

approximately $\pm 1^\circ\text{C}$ was attributed to variations in the supply water temperature. Table 1 compares measured and calculated temperatures. The calculated values were estimated by scaling the temperature changes observed at 16–17 kW operation. All measured values are lower than the estimations, indicating no unexpected rise in temperature.

Table 1: Measured and Calculated Temperatures on the Outer Surfaces of Cavities (Unit: $^\circ\text{C}$)

MGB1 (30.0 kW)	Coupler	Stem 4	Stem 6	Tuner
Calc.	48.0	44.7	34.0	31.7
Meas.	42.9	39.5	28.8	27.0

MGB2 (30.2 kW)	Coupler	Stem 4	Stem 6	Tuner
Calc.	48.6	45.0	34.2	32.3
Meas.	44.1	39.6	29.1	27.6

SUMMARY AND FINDING

Both MGB1 and MGB2 were conditioned from 18 kW up to 26.5 kW, and then to 30 kW during the maintenance periods. During the initial conditioning up to 26.5 kW, MGB1 experienced several excessive reflected power and solid-state amplifier fault interlocks particularly during startup. A few excessive reflected power interlocks were also observed later, possibly due to MGB1 operating at a higher cavity voltage than MGB2. In contrast, the excessive reflected power interlocks in MGB2 were rare after the initial conditioning.

Both MGBs took less than three hours to increase from 26.5 kW to 30 kW. In the latest stage of the conditioning, MGB1 operated for more than 12 hours without tripping. MGB2, however, tripped every 3–4 hours, so it still requires additional conditioning for more stable operation. The total conditioning times of MGB1 and MGB2 were 84.6 and 86.5 hours at 26.5 kW, and 23.2 and 25.0 hours at 30 kW, respectively.

The current operational limits are set at 5% below the highest applied voltages for a safety margin. Further conditioning will be conducted as opportunities arise to enhance operational stability.

REFERENCES

- [1] J. Wei *et al.*, “FRIB Operations First Three Years”, presented at HIAT’25, East Lansing, MI, USA, Jun. 2025, paper MOX01, this conference.
- [2] P. Ostroumov *et al.*, “Acceleration of uranium beam to record power of 10.4 kW and observation of new isotopes at Facility for Rare Isotope Beams”, *Phys. Rev. Accel. Beams*, vol. 27, p. 060101, Jun. 2024.
doi:10.1103/PhysRevAccelBeams.27.060101
- [3] A. Gonzalez *et al.*, “Mitigation of Longitudinal Beam Losses in the FRIB Linac”, in *Proc. 32nd Linac Accelerator Conf. (LINAC’24)*, Chicago, IL, USA, Aug. 2024, pp. 13-16.
doi:10.18429/JACoW-LINAC2024-MOAA002

AVOIDING BEAM INSTABILITIES AND RESONANCES WITH CIRCULAR MODES*

O. Gilanliogullari[†], Illinois Institute of Technology, Chicago, IL, USA
B. Mustapha, Argonne National Laboratory, Lemont, IL, USA
P. Snopok, Illinois Institute of Technology, Chicago, IL, USA

Abstract

Beam instabilities and resonances affect the transverse dynamics in particle accelerators and, when encountered, can trigger emittance growth and beam loss. Resonance lines originate from non-linear elements and effects in the lattice, imposing strict constraints on the choice of working points and narrowing the available tune space. Circular modes are round coupled beams with non-zero angular momentum, provide an alternative beam motion and dynamics. In this study, we derive the third-order sextupole resonance conditions in the coupled (normal-mode) parametrization and show that, with circular-mode lattice design and beam operation, most of these resonance lines are naturally suppressed due to the inherent flatness of the mode.

INTRODUCTION

Accelerators aim to deliver high-quality beams depending on the objectives to be accomplished. The design of an accelerator depends on the beam species to be accelerated and the desired energy and intensity. An accelerator lattice design incorporates both linear and non-linear elements and collective effects. Linear elements are responsible for the total number of betatron oscillations, known as the tunes of the system in orthogonal planes. The inclusion of non-linear elements introduces systematic resonances within the lattice, as discussed in many textbooks [1]. The Courant-Snyder parameterization of the betatron motion [2] shed light on the periodic behavior of the beam and the resonance conditions. Uncontrolled resonances may lead to particle loss; therefore, resonance conditions constrain the selection of tune. Collective effects, such as space charge, also produce resonance conditions [3]. Non-linear static magnetic elements are used for corrections in accelerators. For example, sextupole magnets are used for correcting chromaticity. However, the addition of sextupole elements to the lattice introduces third-order resonances. The resonance diagram shows all possible resonances within a lattice, allowing us to visualize the tune space. In the case of chromatic or collective effects, the tune-shift value is constrained based on the resonance conditions.

Conventional accelerators are designed using the uncoupled Courant-Snyder parameterization [2]. Coupling is typically treated as an error or well-controlled by design. There exist three well-known coupling parameterizations: Edwards-Teng [4], Mais-Ripken [5], and Lebedev-

Bogacz [6]. A circular mode beam is a unique type of beam that is inherently flat and has non-zero angular momentum. The dominance of angular momentum in circular modes results in strong coupling within the beam. The intrinsic flatness of the circular mode can be easily converted to real-space flatness, highly desirable for specific applications, by decoupling the beam. However, the early stages of acceleration in rings are affected by space-charge effects in the low-energy region, where flat beams are not preferred. The use of circular modes with round beams at low energy is an attractive solution, enabling flat beams at higher energies through decoupling.

In this paper, we introduce coupling and circular modes expressed using the coupled beam optics formalism. We use both Mais-Ripken and Lebedev-Bogacz parametrizations for coupled beams. We also discuss the resonances arising from the use of high order magnets, such as sextupoles in coupled dynamics and the circular modes case.

COUPLED BEAM PARAMETRIZATION AND CIRCULAR MODES

The description of a single particle in a coupled system can be expressed in terms of the Lebedev-Bogacz parameterization. This parameterization introduces the eigenvectors of the system and expresses the single-particle coordinates as a combination of projections of eigenmodes. The phase space vector $\vec{z} = [x, x', y, y']^T$ is given by:

$$\vec{z} = \frac{1}{2}\sqrt{2J_1}(\vec{v}_1 e^{-i\psi_1} + \vec{v}_1^* e^{i\psi_1}) + \frac{1}{2}\sqrt{2J_2}(\vec{v}_2 e^{-i\psi_2} + \vec{v}_2^* e^{i\psi_2}), \quad (1)$$

where $J_{1,2}$ are the modes' amplitudes, $\psi_{1,2}$ are the initial eigenmode betatron phases, and $\vec{v}_{1,2}$ are the eigenvectors given as:

$$\vec{v}_1 = \begin{pmatrix} \frac{\sqrt{\beta_{1x}}}{-i(1-u)+\alpha_{1x}} \\ \frac{\sqrt{\beta_{1x}}}{\sqrt{\beta_{1y}}e^{i\nu_1}} \\ -\frac{i u + \alpha_{1y}}{\sqrt{\beta_{1y}}}e^{i\nu_1} \end{pmatrix}, \quad \vec{v}_2 = \begin{pmatrix} \frac{\sqrt{\beta_{2x}}e^{i\nu_2}}{-i u + \alpha_{2x}} \\ \frac{\sqrt{\beta_{2x}}}{\sqrt{\beta_{2y}}} \\ -\frac{i(1-u)+\alpha_{2y}}{\sqrt{\beta_{2y}}} \end{pmatrix}, \quad (2)$$

where $\beta_{1x}, \beta_{2x}, \beta_{1y}, \beta_{2y}$ are the four betatron functions, $\alpha_{1x}, \alpha_{2x}, \alpha_{1y}, \alpha_{2y}$ are the alpha or slope functions, $\nu_{1,2}$ are the phases of coupling, and u is the strength of coupling. The phases of coupling determine how eigenmodes project onto the real phase planes, and the coupling strength measures how dominant the coupling is in the lattice. The search for matched solutions for coupled optics is described in detail in [7].

* This work was supported by the U.S. Department of Energy, under Contract No. DE-AC02-06CH11357.

[†] ogilanli@hawk.iit.edu

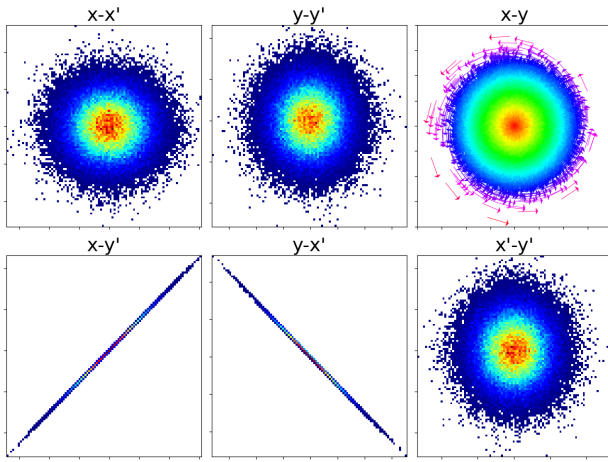


Figure 1: Circular mode beam phase spaces.

The circular mode idea was originally proposed by Y. Derbenev [8] for flat-to-round beam transformers and vortex conditions. The flat-to-round transformer uses three skew quadrupoles to project the real-space flatness onto the $y - x'$ and $x - y'$ phase planes. This transformation and the resulting coupling become clear when one examines the vortex condition. The vortex condition relates the vertical plane (y, y') to the horizontal plane (x, x') as follows:

$$\begin{pmatrix} y \\ y' \end{pmatrix} = \begin{pmatrix} 0 & \beta_c \\ -\frac{1}{\beta_c} & 0 \end{pmatrix} \begin{pmatrix} x \\ x' \end{pmatrix}. \quad (3)$$

Here, β_c is the circular mode beta function. The vortex relation suggests that the system is one-dimensional because the y plane is dependent on the x plane. The one-dimensional behavior is projected onto the eigenmode emittances, $\epsilon_2 \ll \epsilon_1$. The dynamics of the system are dominated by eigenmode 1. The phase space coordinates can be written as:

$$\begin{aligned} x &= \sqrt{\epsilon_1 \beta_0} \cos \psi_1, & y &= \sqrt{\epsilon_1 \beta_0} \sin \psi_1, \\ x' &= -\frac{1}{2} \sqrt{\frac{\epsilon_1}{\beta_0}} \sin \psi_1, & y' &= \frac{1}{2} \sqrt{\frac{\epsilon_1}{\beta_0}} \cos \psi_1. \end{aligned} \quad (4)$$

The alpha functions are zero, confining the particle to the same path in the transverse plane $x - y$, and using the normalization conditions and projection equations, the phases of couplings $\nu_{1,2} = \pi/2$ and the strength of coupling $u = 1/2$. Circular mode properties also introduce the angular momentum relation to the eigenmode emittances, $L_z = \epsilon_1 - \epsilon_2$. If there is no difference between the eigenmode emittances, then there is no angular momentum. The phase space diagrams for circular modes are shown in Fig. 1. The phase plots of $x - y'$ and $y - x'$ show intrinsic flatness, and the $x - y$ phase space plot shows the transverse momenta of the particles with the direction of motion in the transverse plane. Preservation of circular mode properties, such as angular momentum and roundness, is essential in a design. We have demonstrated in other works [9] that conservation of angular momentum has a direct relation to design phase advances and phases of coupling. The requirement for the conservation of the circular mode is having equal phase advances in

both planes. However, this requirement leads to Montague resonance at low energies due to space-charge dominance. To avoid this resonance, solenoids are commonly used for tune splitting and selecting the appropriate tune locations for modes 1 and 2.

3RD ORDER RESONANCE

Sextupole magnets are used to correct the unwanted chromatic effects in rings. Due to the non-linearity of the potential, non-linear systematic resonances exist in the ring. The normal sextupole potential is given by

$$V_s = \frac{S}{3} (x^3 - 3xy^2), \quad (5)$$

where S is the sextupole focusing strength. The Lebedev-Bogacz parametrization dictates the coordinates to be expressed as:

$$\begin{aligned} x &= \sqrt{2J_1\beta_{1x}} \cos \psi_1 + \sqrt{2J_2\beta_{2x}} \cos(\psi_2 - \nu_2), \\ y &= \sqrt{2J_1\beta_{1y}} \cos(\psi_1 - \nu_1) + \sqrt{2J_2\beta_{2y}} \cos \psi_2. \end{aligned} \quad (6)$$

Here, $2J_1 = \epsilon_1$ is used. The normal sextupole potential is added to the Hamiltonian written in terms of action-angle variables, and the analysis can be treated as perturbative. Normal-form analysis can also be carried out using Lie algebra methods; for this study, it is not necessary. We assume circular mode optics with phases of coupling $\nu_{1,2} = \pi/2$ that are periodic like the optics functions. Substituting the coordinate parametrization into the sextupole potential yields:

$$\begin{aligned} V_s(\Psi_1, J_1, \Psi_2, J_2) &= A \cos \Psi_1 + B \cos 3\Psi_1 + C \cos(\Psi_1 - 2\Psi_2) \\ &\quad + D \cos(\Psi_1 + 2\Psi_2) + E \sin(2\Psi_1 - \Psi_2) + F \sin(\Psi_2) \\ &\quad + G \sin(3\Psi_2) + H \sin(2\Psi_1 + \Psi_2). \end{aligned} \quad (7)$$

Here, $\Psi = \psi - Q\theta$, $\theta = s/R$, and Q is the tune. The amplitudes of the potential are given by

$$\begin{aligned} A &= \frac{S}{\sqrt{2}} (J_1^{3/2} \beta_{1x}^{3/2} - J_1^{3/2} \beta_{1x}^{1/2} \beta_{1y} + 2J_2 J_1^{1/2} \beta_{2x} \beta_{1x}^{1/2} - 2J_2 J_1^{1/2} \beta_{1x}^{1/2} \beta_{2y}), \\ B &= \frac{S}{3\sqrt{2}} (J_1^{3/2} \beta_{1x}^{3/2} + J_1^{3/2} \beta_{1x}^{1/2} \beta_{1y}), \\ C &= -\frac{S}{\sqrt{2}} (J_2 J_1^{1/2} \beta_{1x}^{1/2} \beta_{2x} + J_2 J_1^{1/2} \beta_{1x}^{1/2} \beta_{2y} - 2J_1^{1/2} J_2 \beta_{1y}^{1/2} \beta_{2x}^{1/2} \beta_{2y}^{1/2}), \\ D &= -\frac{S}{\sqrt{2}} (J_2 J_1^{1/2} \beta_{1x}^{1/2} \beta_{2x} + J_2 J_1^{1/2} \beta_{1x}^{1/2} \beta_{2y} - 2J_1^{1/2} J_2 \beta_{1y}^{1/2} \beta_{2x}^{1/2} \beta_{2y}^{1/2}), \\ E &= -\frac{S}{\sqrt{2}} (J_1 J_2^{1/2} \beta_{1x} \beta_{2x}^{1/2} + J_1 J_2^{1/2} \beta_{1y} \beta_{2x}^{1/2} + 2J_1 J_2^{1/2} \beta_{1x}^{1/2} \beta_{1y}^{1/2} \beta_{2y}^{1/2}), \\ F &= \frac{S}{\sqrt{2}} (2J_1 J_2^{1/2} \beta_{1x} \beta_{2x}^{1/2} - 2J_1 J_2^{1/2} \beta_{1y} \beta_{2x}^{1/2} + J_2^{3/2} \beta_{2x}^{3/2} - J_2^{3/2} \beta_{2x}^{1/2} \beta_{2y}^{1/2}), \\ G &= -\frac{S}{3\sqrt{2}} (J_2^{3/2} \beta_{2x}^{3/2} + 3J_2^{3/2} \beta_{2y} \beta_{2x}^{1/2}), \\ H &= \frac{S}{\sqrt{2}} (J_1 J_2^{1/2} \beta_{1x} \beta_{2x}^{1/2} + J_1 J_2^{1/2} \beta_{1y} \beta_{2x}^{1/2} - 2J_1 J_2^{1/2} \beta_{1x}^{1/2} \beta_{1y}^{1/2} \beta_{2y}^{1/2}). \end{aligned} \quad (8)$$

Table 1 shows the resonances from the sextupole perturbation. Interestingly, there are eight resonance conditions from coupled parametrization, whereas uncoupled dynamics have

only four. Setting off-mode functions, $\beta_{2x} = \beta_{1y} = 0$, recovers the uncoupled dynamics resonances. The comparison of the resonance diagrams between the coupled and uncoupled cases is shown in Fig. 2.

Table 1: Resonances Due to Sextupoles ($\nu_{1,2} = \pi/2$)

Resonance	Driving Term	Amplitude
$Q_1 = n$	$\cos(\Psi_1)$	$A(J_1, J_2)$
$3Q_1 = n$	$\cos(3\Psi_1)$	$B(J_1, J_2)$
$Q_2 = n$	$\sin(\Psi_2)$	$F(J_1, J_2)$
$3Q_2 = n$	$\sin(3\Psi_2)$	$G(J_1, J_2)$
$Q_1 - 2Q_2 = n$	$\cos(\Psi_1 - 2\Psi_2)$	$C(J_1, J_2)$
$Q_1 + 2Q_2 = n$	$\cos(\Psi_1 + 2\Psi_2)$	$D(J_1, J_2)$
$2Q_1 - Q_2 = n$	$\sin(2\Psi_1 - \Psi_2)$	$E(J_1, J_2)$
$2Q_1 + Q_2 = n$	$\sin(2\Psi_1 + \Psi_2)$	$H(J_1, J_2)$

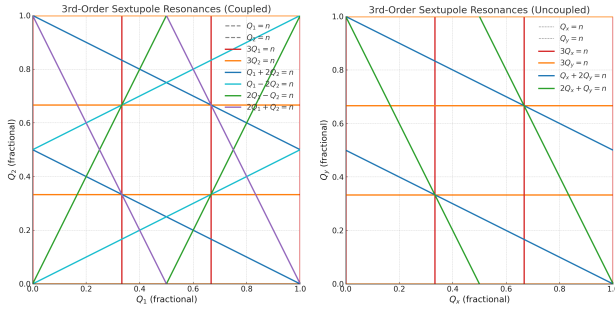


Figure 2: Tune diagrams showing sextupole resonances: Coupled parametrization (left), Uncoupled parametrization (right).

The amplitudes of the sextupole potential depend on both actions, J_1 and J_2 . The main property of circular modes is intrinsic flatness, $J_2 \ll J_1$. Ideally, mode 2 eigenmode emittance is much smaller than that of mode 1. This suggests that, for circular modes, mode 2 does not contribute to the dynamics. Setting $J_2 = 0$ removes many of the amplitudes and yields the terms A and B , which are associated with integer and third integer resonances.

Using the formalism described in [7], we designed a small ring that puts one of the tunes on resonance, as shown in Fig. 3. The tune splitting is controlled by the solenoids in the straight sections. Detailed beam simulations were performed for a 0.3 MeV/u gold ions with $\epsilon_1 = 1.0$ mm-mrad and $\epsilon_2 = 0.1$ μ m-mrad beam. The tunes are controlled using solenoids, and $Q_1 = 3.945$ and $Q_2 = 3.333$. Reversing solenoid polarity puts the dominant mode 1 on resonance. Switching solenoid polarity allows us to switch between two resonance modes. The gold ions are tracked in this storage ring using ImpacT-X tracking simulation [10]. Tracking particles through a round circular aperture with a 3-cm radius for beam stability effects.

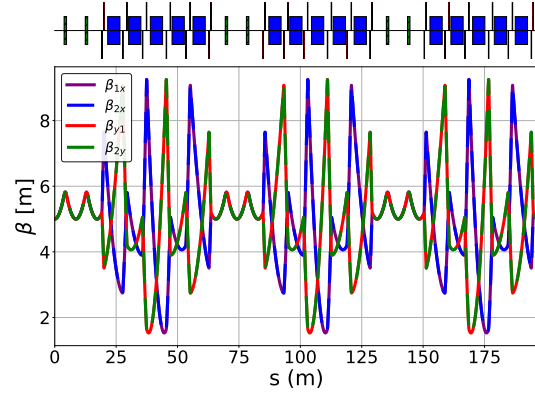


Figure 3: Lattice design with mode 2 on tune.

The operating points of the lattice are shown in Fig. 4. The red star corresponds to mode 1 being on resonance, while the green cross corresponds to mode 2 being on resonance. The number of particles that survived through ten thousand turns is shown in Fig. 5. Surviving particles indicate that even if mode 2 is on resonance, the beam does not experience the resonance due to its intrinsic flatness, which is an interesting phenomenon and confirms that circular modes behave like one-dimensional beams.

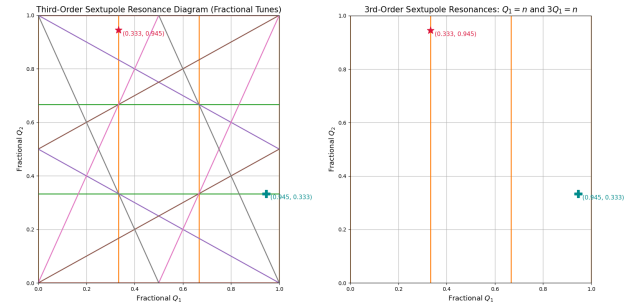


Figure 4: Working points of the lattice.

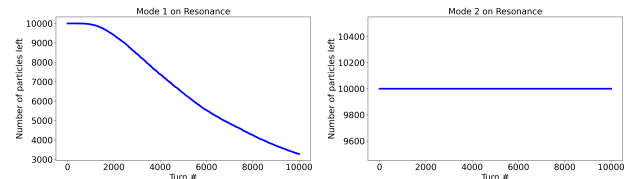


Figure 5: Number of particles survived within aperture of 3 cm. Mode 1 on resonance (left). Mode 2 on resonance (right).

CONCLUSION

In conclusion, we have shown that in coupled dynamics for third-order resonance, there exist twice as many resonance conditions as in the uncoupled case. Circular mode beams reduce the eight resonance conditions to two. We also show that putting a less dominant mode on resonance does not trigger particle loss as it does for the dominant mode.

REFERENCES

- [1] S. Y. Lee, *Accelerator Physics*, 3rd ed., World Scientific Publishing, 2018. doi:10.1142/11111
- [2] E. D. Courant and H. S. Snyder, “Theory of the alternating-gradient synchrotron”, *Ann. Phys.*, vol. 3, no. 1, pp. 1–48, 1958. doi:10.1016/0003-4916(58)90012-5
- [3] I. Hofmann and G. Franchetti, “Self-consistent study of space-charge-driven coupling resonances”, *Phys. Rev. Spec. Top. Accel Beams*, vol. 9, no. 5, p. 054202, 2006. doi:10.1103/PhysRevSTAB.9.054202
- [4] D. A. Edwards and L. C. Teng, “Parametrization of linear coupled motion in periodic systems”, *IEEE Trans. Nucl. Sci.*, vol. 20, no. 3, pp. 885–888, 1973. doi:10.1109/TNS.1973.4327279
- [5] F. Willeke and G. Ripken, “Methods of beam optics”, in *AIP Conf. Proc.*, vol. 184, pp. 758–819, 1989. doi:10.1063/1.38050
- [6] V. A. Lebedev and S. A. Bogacz, “Betatron motion with coupling of horizontal and vertical degrees of freedom”, *J. Instrum.*, vol. 5, no. 10, p. P10010, 2010. doi:10.1088/1748-0221/5/10/p10010
- [7] O. Gilanliogullari, B. Mustapha, and P. Snopok, “A Formalism for the Transport and Matching of Coupled Beams in Accelerators”, *arXiv:2505.08987*, 2025. doi:10.48550/arXiv.2505.08987
- [8] Ya. Derbenev, “Adapting optics for high energy electron cooling”, University of Michigan, Report UM-HE-98-04, 1998.
- [9] O. Gilanliogullari, B. Mustapha, and P. Snopok, “Circular modes for linacs”, *arXiv:2410.11593*, 2024. doi:10.48550/arXiv.2410.11593
- [10] A. Huebl, R. Lehe, C. E. Mitchell, J. Qiang, R. D. Ryne, R. T. Sandberg, and J.-L. Vay, “Next generation computational tools for the modeling and design of particle accelerators at exascale”, *arXiv:2208.02382*, 2022. doi:10.48550/arXiv.2208.02382

DEVELOPMENT OF HIGH TEMPERATURE OVENS FOR SOLID ION BEAM PRODUCTION AT FACILITY FOR RARE ISOTOPE BEAMS (FRIB)*

H. Cheng[†], J. Guo, G. Machicoane, X. Rao, M. Hu, A. Plastun, L. Tobos, R. Rencsok, J. Backlas
Facility for Rare Isotope Beams, East Lansing, MI, United States

Abstract

Inductive ovens are integral to Electron Cyclotron Resonance Ion Source (ECRIS), facilitating the generation of high-intensity solid ion beams. At the Facility for Rare Isotope Beams (FRIB), specialized inductive High Temperature Oven (HTO) has been developed to ensure the stable, consistent, and reliable production of solid ion beams for the High-Power ECR (HPECr) ion source. These HTOs have successfully supported the operation of various solid ion beams, including Silicon, Nickel, and Uranium. In alignment with the FRIB beam power ramp-up objectives, future requirements will include increased beam currents and prolonged operational durations for more species. To optimize HTO performance in response to these evolving demands, a series of design improvements have been implemented, drawing on insights from previous operational experience. These improvements, which address the susceptor's thickness, length, and positioning, are intended to enhance both operational stability and beam consistency. The detailed improved design, ANSYS® simulation results, and testing results will be presented and discussed.

INTRODUCTION

With the ongoing advancement of modern heavy-ion accelerator systems, there is an increasing demand for ion sources capable of delivering high-intensity, high-quality, and high-charge-state ion beams to ensure the production of accelerated ion beams with sufficiently high energy. These beams are increasingly pivotal in various scientific domains, including nuclear physics, atomic physics, and other interdisciplinary applications [1–4].

A primary method for producing such high-quality ion beams is through superconducting Electron Cyclotron Resonance Ion Sources (ECRIS). To achieve stable and intense beam production, ECRIS systems require a metal vapor pressure of approximately 10^{-3} torr. This vapor pressure is contingent upon the temperature of the evaporant material, with specific temperatures necessary to attain the desired vapor pressures for various metals, 586 °C for Bismuth, 616 °C for Lead, 1371 °C for Nickel, 1896 °C for Platinum, and 2258 °C for Molybdenum [5]. To meet these stringent temperature requirements, inductively heated ovens have been employed to ensure the stable and high-intensity production of ion beams.

While previous studies have demonstrated the efficacy of inductively heated HTOs in the production of ^{238}U beams with UO_2 at approximately 2000 °C [6–10], it is necessary to extend this technology to support the production of a diverse array of solid ion beams. In this paper, key considerations in this development include the selection of appropriate susceptor materials, the optimization of susceptor thickness, and the determination of susceptor length. These factors are critical in achieving a wide range of temperatures and ensuring a uniform temperature distribution within the susceptor, thereby enhancing stability and intensity of ion beam production and enabling the production of various solid ion beams using a single inductively heated HTO.

OVEN DEVELOPMENT

The HTO comprises several integral components, including induction coils, a susceptor (crucible), thermal insulation, a water-cooling system, a heating station, and an alternating current (AC) power supply. Prior research has demonstrated the successful production of approximately 52 eμA $^{238}\text{U}^{35+}$ ion beams with UO_2 at an oven temperature of 2000 °C [6].

To ensure the stable generation of vapor from the HTO, maintaining a uniform temperature distribution inside the susceptor is essential. During a one-week test at 2000 °C with uranium dioxide contained in the oven susceptor, partial blockage of the susceptor's front nozzle was observed. This was attributed to the condensation of uranium vapor, which originated from within the susceptor. In the initial oven design, the temperature peaked at the center of the susceptor, leading to preferential vaporization of the material in this region. The resulting vapor flux was directed toward both ends of the susceptor, where it ultimately condensed and accumulated, particularly at the front nozzle. This accumulation caused nozzle obstruction, adversely affecting the stability of the ion beam produced by the source. To address this issue, a more uniform temperature distribution within the susceptor was deemed necessary. Design modifications were implemented in a revised version of the HTO, including adjustments to the susceptor length and the addition of ceramic rings to better secure the susceptor's position.

In addition to achieving a uniform temperature distribution in the oven susceptor, to achieve the objective of utilizing the inductively heated HTO for the production of various solid ion beams, it is imperative to attain a broad temperature range and precise temperature control within the desired operating region. This necessitates the exploration of different susceptor materials, such as tungsten, in addition to the original tantalum susceptor. Due to the inherent variations in electrical resistivity and magnetic permeability among

* Work supported by the U.S. Department of Energy, Office of Science, under Cooperative Agreement DE-SC0023633, the State of Michigan, and Michigan State University.

[†] cheng@frib.msu.edu

different materials, both the skin depth and the inductive power density exhibit material-dependent behavior. As a result, the internal temperature distribution within the oven is expected to vary accordingly.

Beyond selecting appropriate susceptor materials, the influence of susceptor wall thickness on induction heating efficiency has been extensively investigated. For a given susceptor material, the skin depth is determined by the operating frequency and the material's electromagnetic properties. Using Tungsten as an example, giving the electrical resistivity of tungsten at 2200 °C is around $68 \mu\Omega \cdot m$ [11], the skin depth of tungsten at a frequency of 185 kHz, which corresponds to the test conditions, is calculated to be approximately 0.98 mm. When the thickness of the susceptor wall exceeds the skin depth, the inductively generated power remains relatively uniform throughout the wall. In contrast, if the susceptor wall is thinner than the skin depth, the skin effect becomes more pronounced, leading to a greater concentration of current near the conductor's surface. This phenomenon effectively reduces the cross-sectional area available for current conduction, thereby increasing the AC resistance of the inductor. Consequently, the quality factor of the system decreases, resulting in enhanced heat generation. This relationship underscores the importance of optimizing susceptor thickness to ensure efficient energy coupling and uniform heating within the susceptor.

ANSYS SIMULATIONS

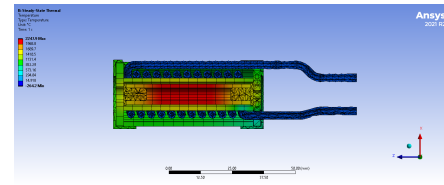
Multiple ANSYS simulations were performed with the objectives of (a) optimizing the temperature distribution to ensure uniformity throughout the susceptor interior, and (b) achieving a wide range of attainable temperatures within the oven susceptor. In these ANSYS simulations, the water-cooled copper coils are consistently maintained at ambient temperature. Heat generation within the susceptor arises from the power induced by these coils. Radiative and conductive heat losses are considered significant in the thermal analysis, while convective losses are deemed negligible due to the HTO operating under high-vacuum conditions, typically in the range of 10^{-9} to 10^{-6} torr.

Thermal Distribution

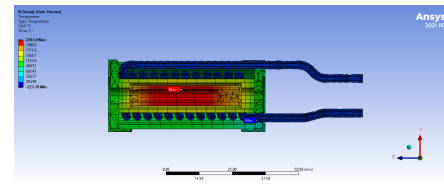
Compared to the original HTO design, the susceptor length has been reduced, and an additional ceramic ring has been installed on each side of the susceptor to enhance its positional stability in the updated configuration. Figure 1 presents the ANSYS simulation results, illustrating the temperature distribution along the HTO for both the original and modified designs.

With identical AC current applied to the induction coils and using the same oven components and materials, the original design, featuring a longer susceptor, achieves a coupled power of 681 W and a peak temperature of 2248 °C at the susceptor center. In comparison, the revised design with a shorter susceptor allows for a coupled power of 609 W and reaches a slightly higher peak temperature of 2266 °C at

the center. Regarding thermal distribution, the temperature at the susceptor's front nozzle is calculated to be approximately 1584 °C in the original configuration, whereas the shorter susceptor design yields a significantly higher front nozzle temperature of approximately 1806 °C. These results demonstrate a substantial improvement in thermal uniformity along the susceptor axis resulting from the shorter susceptor design.



(a) Original long susceptor.



(b) Modified shorter susceptor.

Figure 1: Thermal distribution in HTO with susceptor in different lengths.

Thermal Range

To extend the thermal operating range of the oven susceptor, variations in susceptor wall thickness have been systematically investigated. In particular, a series of simulations was conducted to evaluate the effect of susceptor thickness on achieving higher peak temperatures within the susceptor.

Figure 2 presents the simulated temperature distributions within the oven for susceptor wall thicknesses of 1.5 mm, 1.0 mm, and 0.5 mm, respectively. As previously discussed, the theoretical skin depth for tungsten under an AC frequency of 185 kHz at a temperature of 2200 °C is approximately 0.98 mm. When the susceptor wall thickness is less than this skin depth, the skin effect becomes more pronounced, resulting in greater current concentration near the surface and consequently increased heat generation. The simulation results corroborate this theoretical expectation.

For the 1.5 mm thick susceptor, greater than the skin depth, the calculated power density is 1.15 W m^{-3} , with a total of 681 W of power coupled into the tungsten susceptor, producing a peak internal temperature of 2248 °C. When the wall thickness is reduced to 1.0 mm, approximately equal to the skin depth, the power density slightly increases to 1.17 W m^{-3} , with 639 W of coupled power, resulting in a peak temperature of 2382 °C. For the thinnest susceptor, with a wall thickness of 0.5 mm, significantly below the skin depth, the power density rises notably to 2.4 W m^{-3} , and 643 W of power is coupled into the susceptor, leading to a peak temperature of 2638 °C.

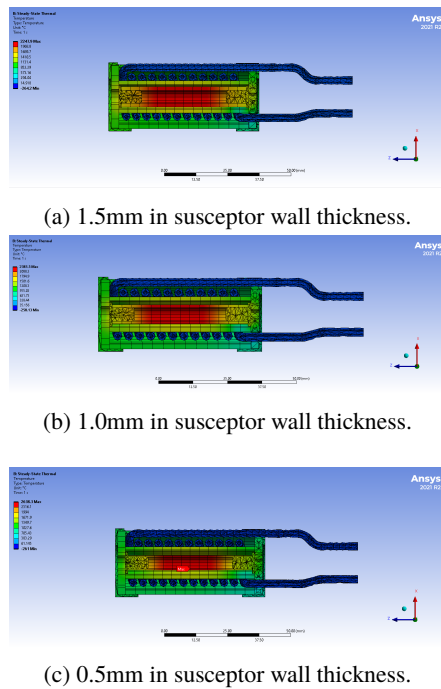


Figure 2: Thermal distribution in HTO with different susceptor wall thickness.

TEST RESULTS AND DISCUSSION

The inductively heated HTO was subjected to a series of rigorous offline evaluations using a controlled test bench to investigate two key aspects: (a) whether a shortened susceptor configuration enhances thermal uniformity within the oven susceptor, and (b) whether variations in susceptor wall thickness facilitates a broader operational temperature range. The empirical results obtained from these experiments demonstrated strong agreement with the predictive models generated through ANSYS simulations, with deviations falling within an acceptable margin of error.

Thermal Distribution

Temperature profiling of the HTO was conducted under two distinct configurations on an offline test bench. The first configuration employed the original HTO design featuring a full-length tungsten susceptor, while the second utilized a modified setup incorporating a shortened tungsten susceptor stabilized by ceramic support rings at both ends, as previously described.

During the thermal distribution assessment, the HTO was ramped to a target temperature of 2000 °C. A Type-C thermocouple was employed to record axial temperature variations along the length of the susceptor. As illustrated in Fig. 3, the red markers denote the measurement points extending from the bottom of the susceptor to its exit at the front end. In the original design, when the central region of the susceptor reached a peak temperature of 2000 °C, the temperature at the front nozzle was recorded at approximately 1421 °C. In contrast, the modified configuration with

the shortened susceptor exhibited a significantly improved thermal distribution, with the front nozzle temperature reaching approximately 1820 °C under the same central peak condition. This enhancement indicates a marked improvement in axial temperature uniformity within the susceptor.

This observed temperature gradient aligns closely with the results obtained from ANSYS simulations, thereby affirming the accuracy and predictive capability of the computational models in replicating the thermal behavior under operational conditions.

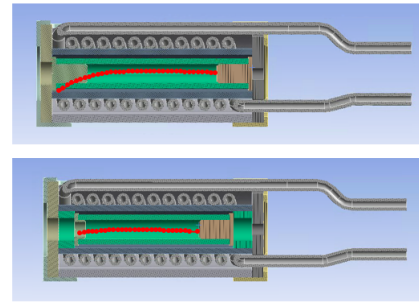


Figure 3: Thermal profiles in HTOs with original and modified susceptor designs.

Thermal Range

Furthermore, an extended range of peak temperatures within the susceptor was investigated by modifying the HTO configuration, as mentioned. Consistent with ANSYS simulation results, the configuration employing a thin-walled susceptor with a thickness of 0.5 mm achieved the highest temperature recorded among all tested setups, reaching an internal susceptor temperature of 2353 °C, as shown in Fig. 4. Additionally, multiple thermal cycling tests were conducted at peak temperatures up to 2300 °C, with the system maintained at this temperature for approximately 10 hours per cycle. No visible structural degradation or component failure was observed in the HTO, indicating robust thermal and mechanical stability under this extreme operating condition.



Figure 4: The maximum temperature ever reached in HTO at 2353 °C.

Discussion and Conclusion

Through iterative design improvements, the High-Temperature Oven (HTO) has demonstrated significantly enhanced thermal uniformity compared to the original configuration. In earlier implementations, prolonged operation with uranium, typically around one week, resulted in front nozzle clogging, which led to instability in beam output from the ion source. Following the redesign of the susceptor, this issue has been effectively resolved. The improved configuration now supports continuous uranium operation at approximately 2000 °C for durations exceeding two weeks, delivering a stable, high-intensity ion beam without interruption or performance degradation.

Furthermore, the HTO has exhibited substantial versatility across a broader temperature spectrum, enabling support for a wider range of beam species.

ACKNOWLEDGMENTS

This work was supported by the U.S. Department of Energy, Office of Science, under Cooperative Agreement DE-SC0023633, the State of Michigan, and Michigan State University.

REFERENCES

- [1] J. Wei *et al.*, “FRIB Transition to User Operations, Power Ramp Up, and Upgrade Perspectives”, in *Proc. SRF’23*, Grand Rapids, MI, USA, Jun. 2023, pp. 1–8. doi:10.18429/JACoW-SRF2023-M0IAA01
- [2] J. Wei *et al.*, “FRIB Beam Power Ramp-up: Status and Plans”, in *Proc. HB’23*, Geneva, Switzerland, Oct. 2023, pp. 351–357. doi:10.18429/JACoW-HB2023-THC1I2
- [3] W. Lu *et al.*, “Production of metallic ion beams by electron cyclotron resonance ion sources equipped with inductive heating ovens at the Institute of Modern Physics”, *Rev. Sci. Instrum.*, vol. 92, no. 3, p. 033302, Mar. 2021. doi:10.1063/5.0041671
- [4] M. Guillaume *et al.*, “Operation and development of the 28 GHz electron cyclotron resonance (ECR) ion source at the facility for Rare Isotope Beams”, presented at ECRIS2024, Darmstadt, Germany, Sep. 2024, paper MOA2, unpublished.
- [5] Vapor Pressure Data, <https://www.mbe-komponenten.de/selection-guide/vapor-pressure/>.
- [6] H. Cheng *et al.*, “Development of inductive high temperature oven (HTO) at the facility for Rare Isotope Beams”, in *Proc. IPAC’24*, Nashville, TN, USA, May 2024, pp. 602–605. doi:10.18429/JACoW-IPAC2024-MOPR70
- [7] D. Leitner, M. L. Galloway, T. J. Loew, C. M. Lyneis, I. Castro Rodriguez, and D. S. Todd, “High intensity production of high and medium charge state uranium and other heavy ion beams with VENUS”, *Rev. Sci. Instrum.*, vol. 79, no. 2, p. 02C710, Feb. 2008. doi:10.1063/1.2816790
- [8] W. Huang, D. Z. Xie, and L. T. Sun, “Development of a new high temperature oven for the production of intense metal ion beams with ECR ion sources”, *Rev. Sci. Instrum.*, vol. 90, no. 12, p. 123301, Dec. 2019. doi:10.1063/1.5127518
- [9] R. W. Ohse, “High-Temperature Vapor-Pressure Studies of UO₂ by the Effusion Method and Its Thermodynamic Interpretation”, *J. Chem. Phys.*, vol. 44, no. 4, pp. 1375–1378, Feb. 1966. doi:10.1063/1.1726869
- [10] J. K. Fink, M. G. Chasanov, and L. Leibowitz, “Thermophysical properties of uranium dioxide”, *J. Nucl. Mater.*, vol. 102, no. 1–2, pp. 17–25, Nov. 1981. doi:10.1016/0022-3115(81)90541-9
- [11] P. D. Desai, T. K. Chu, H. M. James, and C. Y. Ho, “Electrical Resistivity of Selected Elements”, *J. Phys. Chem. Ref. Data*, vol. 13, no. 4, pp. 1069–1096, Oct. 1984. doi:10.1063/1.555723

COMPUTATIONAL ANALYSIS OF MULTIPACTING ACTIVATION AND SUPPRESSION IN 325 MHz FPC *

H. Do ^{1,†}

¹Institute for Basic Science, Daejeon, Korea

Abstract

A 325 MHz RF Fundamental Power Coupler (FPC) designed to operate under 20 kW CW in the high energy Superconducting Linac (SCL) of the RAON. One of the most important consideration in the FPC EM design is to reduce and eliminate a multipacting (MP) activation in both TW mode and SW mode. Prior to the MP reduction design, the MP bands of the FPC was computed with CST Particle Studio. It was confirmed that third or higher order of MP bands were activated within the operating range on the surface condition of the coupler. Therefore, designs to suppress MP are needed. To eliminate MP, a DC voltage was applied to centre conductor of the FPC. Detailed the simulation modelling and computational analysis results where MP was effectively suppressed for both modes are presented.

INTRODUCTION

Rare isotope Accelerator complex for ON-line experiments (RAON) is a heavy ion accelerator for basic science is under development in Daejeon, Korea [1, 2]. Three SCLs of the RAON are composed of three kinds of Superconducting Radio-Frequency (SRF) cavities. One of them is the Single Spoke cavity is operating at frequency of 325 MHz in the high energy SCL. The high energy SCL is comprised of two cavity variants, SSR type I and SSR type II. SSR type I has an optimum $\beta=0.3$ and 8.5 MV/m of high accelerating gradient (E_{acc}) in CW mode. SSR type II is an optimum $\beta=0.51$ and 8.7 MV/m of E_{acc} . SSR type I and type II are required operating power the under 7 kW and 20 kW, respectively when the RF power is fully reflected.

Generally, the RF coupler is extremely over coupled (coupling $\beta > 1000$) with the SC cavity for stable RF control. However, when the high-intensity beams are accelerated in the SC cavity, load impedance varies widely from the matched to the fully reflected as the beam is loaded and unloaded. The coupler for superconducting cavities has to be tested in both TW mode and SW mode.

One of the most important consideration in the RF coupler design is to reduce and eliminate MP [3] activation. MP is an RF resonant discharge that produces in vacuum RF structure due to the secondary electron emission. The electron multiplication, MP is mainly enhanced by the combination of the RF field and the surface of the high Secondary Emission Yield (SEY) metal. When MP is activated on the inner surface of the coupler, the residual gas on the surface of the coupler is desorbed. This desorbed gas

can be attached to the surface of the cavity, the cavity performance may be degraded.

When the RF power was applied to prototype RF coupler, the MP was observed to become active in the SSR type I operating range. A setup and these results of the high-power experiment are presented. Computational research was conducted to apply a DC offset to the FPC to reduce or eliminate the MP. Detailed simulation results using various DC offsets are provided. And also, a summary and future work are described.

RF EXPERIMENT ON TEST BENCH

A high-power experimental setup for 325 MHz RF FPC is shown as Fig. 1. A test bench consists of two couplers and a test chamber as shown in Fig. 2. One of the ends of the test bench (the 1st coupler side) was connected with a Solid State Power Amplifier (SSPA). A water cooled dummy load was installed for TW mode testing or a short circuit was installed for SW mode testing on the other side of the test bench (the 2nd coupler side). In addition, the RF length of the short was changed so that the amplitude of electric field could be the maximum and the minimum at the RF window.

RF power was immediately cut off even during continuous operation when the RF power cut-off criterion was met. The vacuum level ($> 1E-6$ mbar), the signal level of electron pickup probes, the signal of arc detector and temperature level (> 330 K) were used as interlock signals for RF trips. A vacuum gauge was mounted to between the two couplers. The electron pickup probe and the arc detector were installed in near the RF window. Figure 2 shows eight temperature sensors were installed on the test bench to measure the temperature increase with applied input RF power: RF windows, test chamber, 4K intercepts, 40K intercepts. During these experiments, the cavity tripped several times due to the rise of the pressure and temperature in the RF coupler. The MP activation was observed, which was figured out by the signal measured in the electron pickup probe, the rapid increase of the vacuum level and the temperature level. Additionally, additional RF loss at the high-power dual directional coupler was measured. However, the arc signal was not detected during the experiment.

Figure 3(a) shows the temperature change at each point on the test bench measured with increasing the applied RF power at SW mode. In the 1st RF window, constructive interference occurred and the field value was maximized. And the field null with destructive interference was positioned in the 2nd RF window. The change in temperature rise generally increased with increasing input RF power. However, when the MP was activated, the temperature increased more than expected.

* Work supported by the National Research Foundation of Korea(NRF) funded by Ministry of Science and ICT (RS-2022-00214790)

† email address: hdo@ibs.re.kr

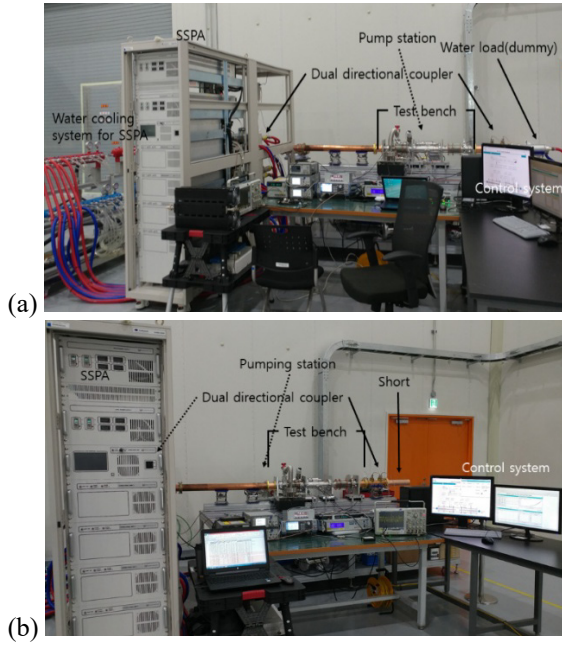


Figure 1: Setup for high power RF test: (a) TW mode; (b) SW mode.

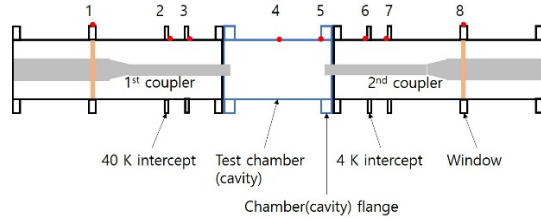


Figure 2: Location of temperature sensors in the test bench.

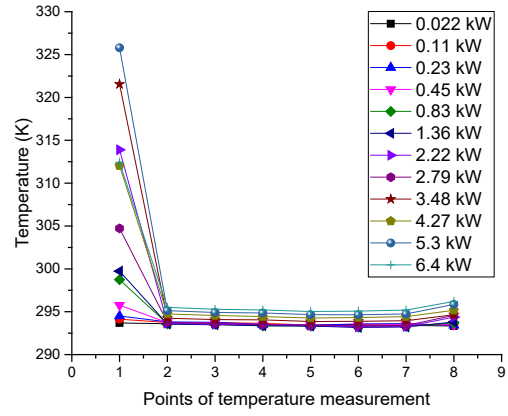
The temperature increase was noticeably larger in the RF window of the first coupler than in the other points. During this experiment, the vacuum pressure of the test bench was maintained in the middle of $1\text{E-}7$ mbar, but increased to more than $1\text{E-}6$ mbar when the MP was occurred (Fig. 3(b)).

When the MP occurs, the emitted current was measured by the electron pickup probe installed in the 1st coupler, but the current was not measured by the probe installed in the 2nd coupler since the MP activated locally.

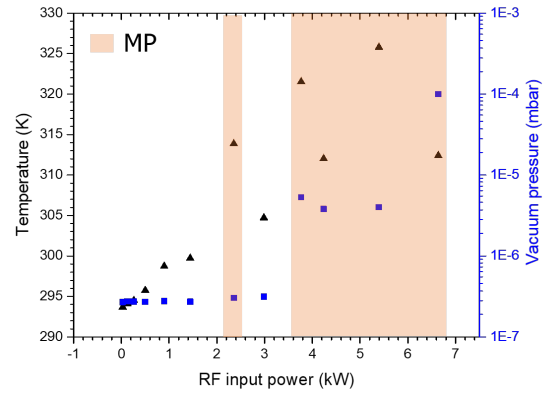
The MP bands was checked within the SSR operating range. The MP was activated when around 2.6 kW and more than 3.8 kW RF power was applied in SW mode. Depending on the reflection phase, the MP is activated at different locations, but the activated MP band is the same. In TW mode, the MP was activated above 2.8 kW. In TW mode, the Secondary Emission Yield (SEY) curve is changed according to the surface condition, so that the MP is activated irregularly.

MULTIPACTING SUPPRESSION WITH DC OFFSET

The MP power in a coaxial structure is commonly calculated with a line impedance [4, 5]. The input RF power of



(a)



(b)

Figure 3: Test results according to RF power (SW mode): (a) Temperature variations at eight points; (b) Variation of maximum temperature (at point #1) and vacuum pressure.

coaxial line for one-point MP is:

$$P_{one-point} \sim \frac{A f^4 (r_2 - r_1)^4}{(n+1)^2} Z \quad (1)$$

The input RF power of coaxial line for two-point MP is:

$$P_{two-point} \sim \frac{A f^4 (r_2 - r_1)^4}{(2n-1)^2} Z^2 \quad (2)$$

where, A is 1 for TW mode and 0.25 for SW mode, f is the frequency, n is the order of multipacting, r_1 and r_2 are the radius of the inner and outer conductors, Z is the line impedance. The line impedance of the coaxial coupler is:

$$Z = \frac{\eta_0}{2\pi} \ln \left(\frac{r_2}{r_1} \right) \quad (3)$$

where η_0 is wave impedance in vacuum. According to numerical calculation, it is figured out that higher order mode MP can be activated in both TW and SW modes in the operation range of the 325 MHz coupler (< 20 kW). Computational analysis [6] was performed with CST Particle Studio [7] to validate the MP activation bands.

As shown in Fig. 4, simple modeling that can implement both TW mode and SW mode was performed. The SEY curves of copper and wet niobium was used to obtain MP simulation results conservatively.

Emitted electrons are exponentially increased by the multipacting. Therefore, the total number of emitted electron is:

$$N(t) = N_0 e^{at} \quad (4)$$

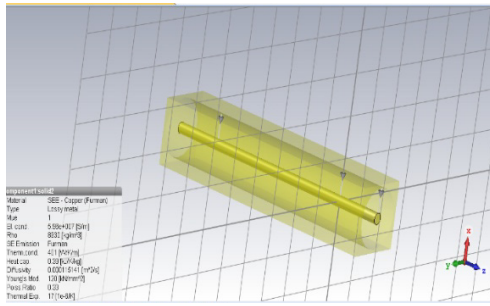


Figure 4: Modeling for MP simulation.

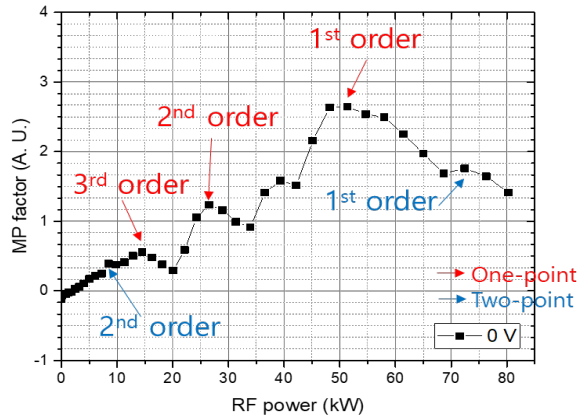


Figure 5: Simulation results of MP factor without DC offset.

where, N_0 is initial number of electrons, α is multipacting factor. The MP can be activated when the value of MP factor is greater than 0.

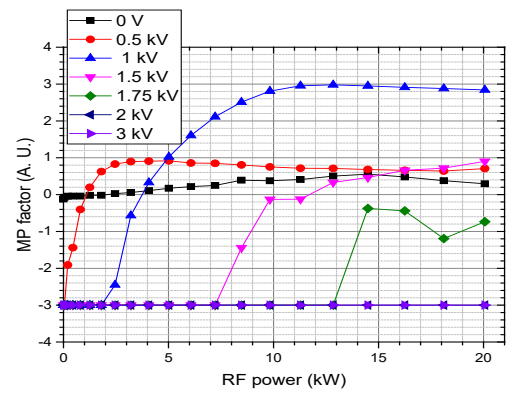
Figure 5 shows the MP simulation results using the modelling in Fig. 4. As a result of the simulation, 3rd or higher order of one-point multipacting can be activated in operation range of the 325 MHz FPC. 2nd or higher order of two-point multipacting can be activated also.

Significant performance degradation of the cavity is expected due to the MP activation if the current prototype coupler operated as-is without a complementary design of MP suppression.

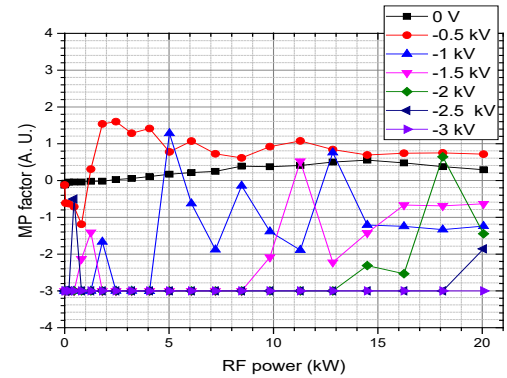
DC voltage offset was applied to the simulation model to eliminate or reduce the MP of the FPC [8]. By applying a DC bias voltage from -3 kV to 3 kV to between the inner conductor and the outer conductor of the modeling, the variations of the MP factor were calculated with respect to the RF power. When the DC offset of more than +1.75 kV or less than -2.5 kV was applied, the MP inside the FPC completely eliminate in the high energy SCL operating range of below 20 kW (Fig. 6).

SUMMARY

A prototype RF FPC operating at 325 MHz has been recently developed to transmit RF power for SSR type I cavity. The coupler was tested in high-power experiment. The activated MP bands was checked in this experiment and confirmed with numerical and computational analysis. The MP can be eliminated or reduced by applying DC voltage to the inner conductor. MP suppression is expected when



(a)



(b)

Figure 6: Simulation results of MP factor with DC offset (SW mode): (a) positive DC voltage; (b) negative DC voltage.

applying proper DC voltage ($> +1.75$ kV or < -2.5 kV). The suppression of the MP using a DC bias will be confirmed experimentally in the near future.

REFERENCES

- [1] D. Jeon *et al.*, "Design of the RAON accelerator systems", *J. Korean Phys. Soc.*, vol. 65, pp. 1010–1019, Oct. 2014. doi:10.3938/jkps.65.1010
- [2] H. J. Kim, H. C. Jung, and W. K. Kim, "Progress on superconducting linac for the RAON heavy ion accelerator", in *Proc. IPAC'16*, Busan, Korea, May 2016, pp. 935–937. doi:10.18429/JACoW-IPAC2016-M0P0Y03
- [3] R. Kishek *et al.*, "Multipactor discharge on metal and dielectrics: Historical review and recent theories", *Phys. Plasma*, vol. 5, no. 5, pp. 2120–2126, 1998. doi:10.1063/1.872883
- [4] E. Somersalo *et al.*, "Computational methods for analyzing electron multipacting in RF structures", *Particle Accelerators*, vol. 59, pp. 107–141, 1998.
- [5] Z. Zheng *et al.*, "Prediction and suppression of two-point 1st order multipacting", *Nucl. Instrum. Methods Phys. Res. A*, vol. 735, pp. 596–601, Jan. 2014. doi:10.1016/j.nima.2013.09.052
- [6] S. V. Langellotti *et al.*, "CST Particle Studio simulations of coaxial multipactor and comparison with experiments", *IEEE Trans. Plasma*, vol. 48, no. 6, pp. 1942–1949, Jun. 2020. doi:10.1109/TPS.2020.2981257
- [7] <http://www.cati.com/software/cat-studio-suite/>

- [8] P. N. Ostroumov *et al.*, “Suppression of multipacting in high power RF couplers operating with superconducting cavities”, *Nucl. Instrum. Methods Phys. Res. A*, vol. 856, pp. 77-80, 2017. doi:10.1016/j.nima.2017.02.081

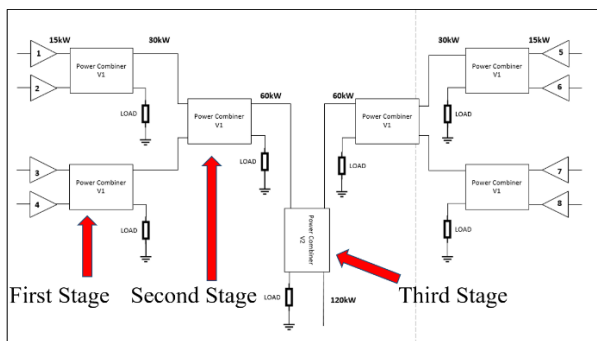


Figure 2: Schematic of cascaded power combiners.

The hybrid couplers have water-cooled loads on the isolation ports that are rated for the maximum output power in case phase settings are set incorrectly. Typically, the power to the isolation loads is up to one-quarter of the maximum output power for that stage (occurs if one input fails). Shown below is a 3-D rendering of the system (Fig. 3).

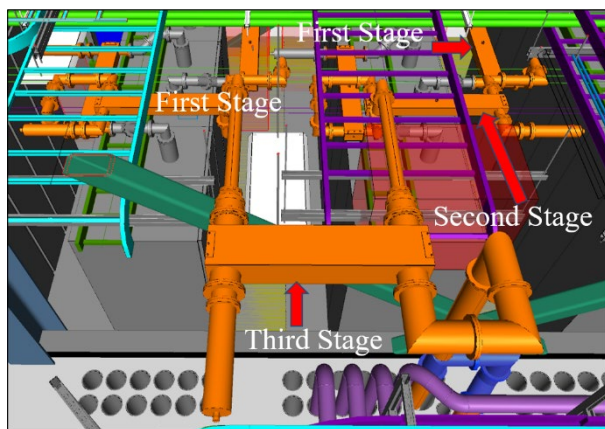


Figure 3: Hybrid combiners.

The water cooled loads are connected to an eight leg water manifold (Fig. 4). Seven of the legs are used continuously for the isolation loads and one branch is for the test load.

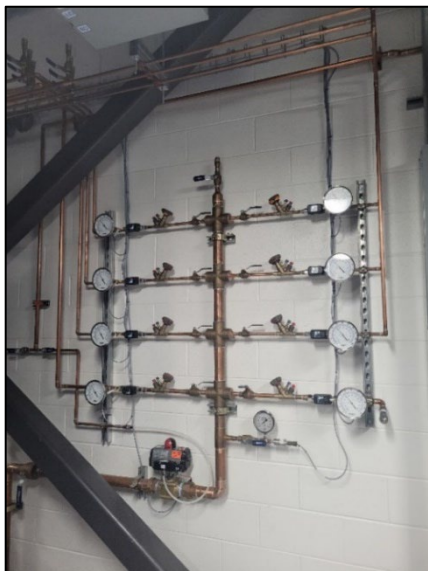


Figure 4: Water manifold design.

The amplifier system is driven by a Low Level RF (LLRF) controller through an 8-way splitter. Each output of the splitter has a 1 dB step attenuator (0.1 dB steps) to evenly balance the output power of each rack. The RF cables are phase matched to make it easier to set the correct phase delay for the each amplifier rack, which is done using internal phase shifters in the DCUs.

The LLRF controller handles the run permit for the entire system. This run permit signal is in series through all of the driver-control units, so a fault in one of the racks will cause the entire system to interlock off.

A Programmable Logic Controller (PLC) is used to calorimetrically calculate the power being sent to the isolated loads. Interlock thresholds are set to trip if too much power is being dumped into any of the loads. The PLC also monitors water flow in the loads and supply pressure in the manifold. Additionally, the PLC can close automated water valves if a major leak is detected.

TESTING RESULTS

The racks were each individually tested into an RF short prior to combining the racks. At full reflection each rack system can only handle 12 kW. Several parameters are monitored including drain current, voltage and S11. Non-ionizing radiation surveys were conducted for personnel safety at this time. Figure 5 and Figure 6 show the results of single rack testing. All 8 racks were able to reach 12 kW of output power without any issues.

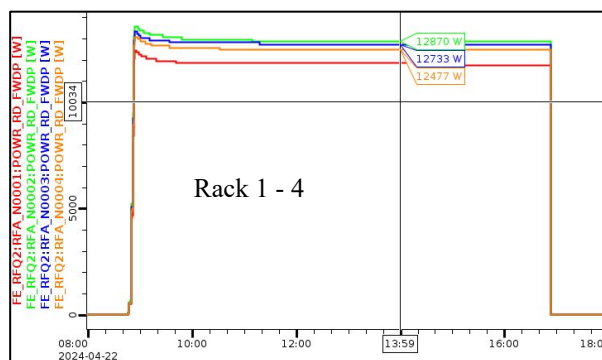


Figure 5: Power Output rack 1 through 4.

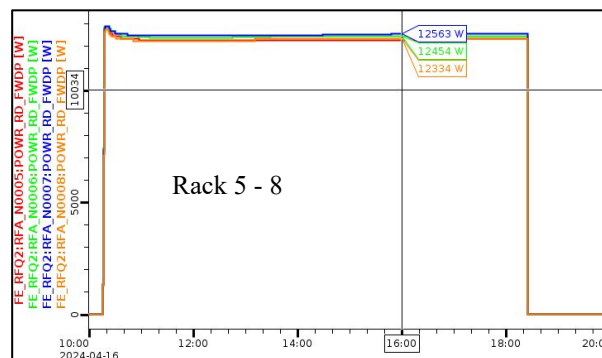


Figure 6: Power Output rack 5 through 8.

To verify performance of each 4-rack sub-subsystem, the system was initially tested with the stage 1 and stage 2 power combiners only. Due to water flow issues, the output

power was limited to 40 kW. The attenuators were adjusted to get similar output power from each rack. Using a CS-Phoebus GUI, the phase delay settings were adjusted to maximize the combined output power. Figure 7 shows the results of this testing. The output power was confirmed by comparing the sum of the rack power (measured by RF directional couplers) to the calorimetric measurement of the test load.

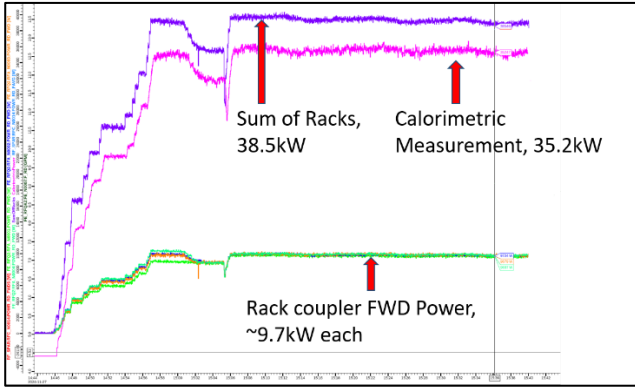


Figure 7: 40 kW testing results.

Lastly, the overall system was connected to the Stage 3 power combiner. Figure 8 shows the results of the final testing up to 120 kW. In-rack power combining efficiency, accounting for circulator and internal power combiner losses, is greater than 88.5%. The combining efficiency of the three stages of external hybrid couplers is ~98%, resulting in an overall efficiency of 86.7% at 120 kW output power.

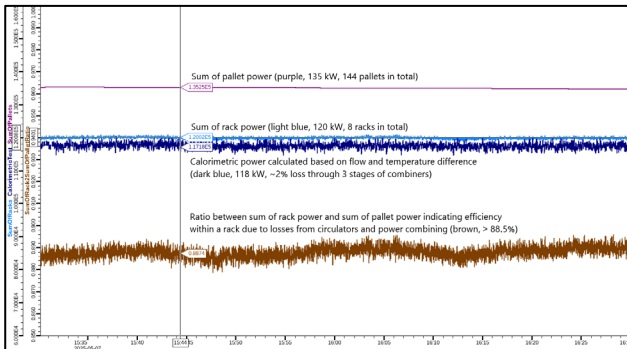


Figure 8: 120 kW testing results.

CONCLUSION

The 120 kW RFQ solid-state amplifier system is ready for commissioning with the RFQ during the FRIB 2025 summer maintenance shutdown. The existing tetrode amplifier will be kept in place as a ready spare for up to one year, and then relocated to an offline RFQ test area.

ACKNOWLEDGMENTS

The RF group thanks our colleagues and industrial partners that provided technical support and guidance, including J. Curtin, J. Bodell, R. Tatroe, C. Williams, and suppliers TRUMPF Hüttinger GmbH + Co. KG and Myat, Inc.

REFERENCES

- [1] J. Wei *et al.*, “FRIB Operations: First Three Years,” presented at. HIAT’25, East Lansing, MI, Jun. 2025, paper MOX01, this conference.
- [2] H. Ao *et al.*, “FRIB Multi-Gap Buncher Conditioning up to 30 kW,” presented at. HIAT’25, East Lansing, MI, Jun. 2025, paper TUP13, this conference.

STUDY ON PROPERTIES OF NEG DEPOSITED ON THE TITANIUM ALLOY LINED VACUUM CHAMBER

C.C. Li, J. Meng[†], C. Luo

Institute of Modern Physics, Chinese Academy of Sciences, Lanzhou, China

Abstract

A ramping rate of 12 T/s is designed for the dipole magnet of BRing at HIAF. To reduce eddy current effects, a titanium alloy lined chamber with a titanium alloy inner liner by 3D printing and an 0.3 mm ultra-thin stainless steel outer wall has been adopted. To reduce the internal pressure and enhance the beam lifetime, a film of TiZrV is coated on the chamber. The ultimate vacuum of the titanium alloy-lined vacuum chamber is tested, which indicates that after coating with TiZrV, the pressure at the middle of the chamber reduced, effectively reducing the pressure in the central region. The life of the TiZrV film was studied by repeated venting and activation cycles under two conditions of N₂ or air filling. With N₂ filling, after 15 activation cycles, the pressure in the middle of the chamber showed no significant change. However, with air filling, after 7 activation cycles, the pressure in the middle degraded, indicating a decline in the pumping performance of the TiZrV film. Air exposure significantly impacts the life of the film, necessitating that TiZrV films should be protected with N₂ in applications and minimizing exposure time.

INTRODUCTION

In order to reduce gas desorption caused by particle bombardment to vacuum chamber, generate uniform pumping effect inside the slender and long vacuum chamber, and suppress dynamic vacuum effects, the method of coating the inner surface of the vacuum chamber with NEG film is widely used internationally. Among them, TiZrV film can be fully activated by vacuum baking at 180 °C for 24 hours, and the activation temperature meets the maximum baking temperature allowed by the vacuum chamber made of common accelerator materials [1, 2]. It is widely used in accelerator at home and abroad. The ramping rate of the dipole magnet of BRing in the new generation particle accelerator named HIAF is 12 T/s [3]. To reduce eddy current effects, IMP adopts a new structure of 0.3mm titanium alloy lined thin-walled ultra high vacuum chamber as the dipole vacuum chamber (see Fig. 1). The total length of the vacuum chamber is about 3.3 meters, consisting of some titanium alloy rings and a stainless steel thin-walled shell. The titanium alloy ring is made by 3D printing.

The conventional pumping scheme is installing sputtering ion pumps and titanium sublimation pumps on both sides of the dipole vacuum chamber. The pumps are far away from the middle of the dipole vacuum chamber, resulting in poor pressure in the middle and unable to meet the beam life requirements. By using magnetron sputtering coating technology with solenoid, TiZrV films are

deposited onto the surface of a titanium alloy lined vacuum chamber to generate uniform pumping effect, reduce pressure gradient, and improve beam quality and life.

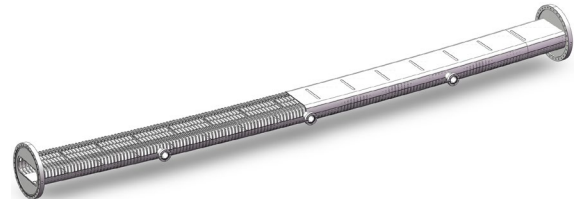


Figure 1: The model of titanium alloy lined vacuum chamber.

EXPERIMENTS AND RESULTS

Build a coating platform with solenoid to deposit TiZrV film on the surface inside the vacuum chamber [4]. The coating parameters are: discharge current of 0.2 A, discharge voltage of 500 V, working pressure of 1Pa, magnetic field intensity of 220 Gauss, and coating duration of 10 hours. Figure 2 is a image of glow discharge.

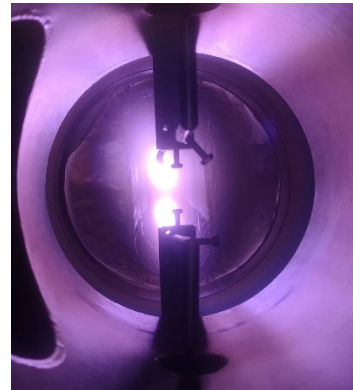


Figure 2: Glow discharge.

The surface morphology of TiZrV film was analyzed by SEM (see Fig. 3), and the results showed that the film morphology is located in the T zone (transition zone) [5], which is a dense and highly anisotropic columnar structure with good pumping performance. EDS was used to analyze the composition of TiZrV film (see Fig. 4), and the results showed that the prepared film had a Ti, Zr and V composition ratio (Ti:Zr:V=33.68%:21.24%:45.08%) located in the "low activation temperature zone" [6], with a low activation temperature and can be activated at 180 °C.

[†]mengjun@impcas.ac.cn

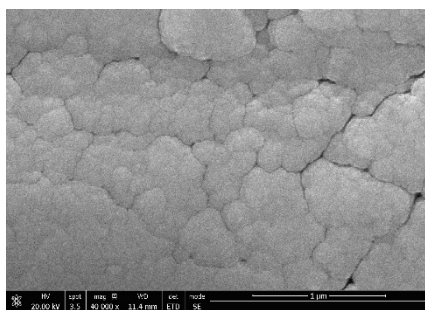


Figure 3: SEM analysis image of TiZrV film.

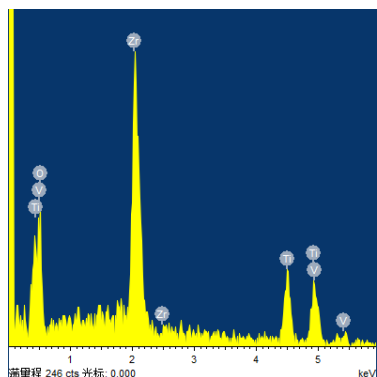


Figure 4: EDS analysis image of TiZrV film.

The ultimate vacuum before and after TiZrV film coating in a titanium alloy dipole vacuum chamber was experimentally studied, and the life of TiZrV film was evaluated under multiple activation cycles of N₂ or air filling. The test data has certain significance for protecting TiZrV film, extending its life, and reducing the number of maintenance in engineering applications.

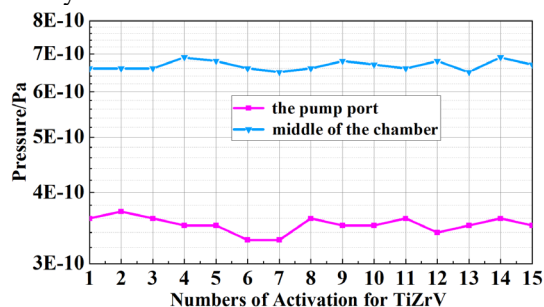
Build an ultimate vacuum testing platform (see Fig. 5), installing one sputtering ion pump and one titanium sublimation pump on each side of the titanium alloy vacuum chamber as the main pumps, to test the ultimate vacuum of the titanium alloy lining vacuum chamber before and after TiZrV coating by baking at 230 °C for 48 hours. For TiZrV coated chambers, sufficient activation with 230°C for 24 hours should be carried out during the baking process.



Figure 5: Ultimate vacuum and life testing device for titanium alloy lined vacuum chamber.

The test results show that after TiZrV coating, the pressure in the middle of the thin-walled vacuum chamber lined with titanium alloy optimized from 1.62×10^{-9} Pa to 6.6×10^{-10} Pa. The TiZrV film effectively reduced the pressure gradient.

At the same time, the life of TiZrV film on the surface of titanium alloy lined vacuum chamber was tested by N₂ or air venting and activation cycles. Fill N₂ and perform 15 rounds of activation cycle. In the first round of testing, the ultimate pressure in the middle of the titanium alloy lined vacuum chamber was 6.6×10^{-9} Pa, and the pressure at the pump port was 3.6×10^{-10} Pa. After 15 cycles of activation, the pressure in the middle was 6.7×10^{-10} Pa, and the pressure at the pump port was 3.5×10^{-10} Pa (see Fig. 6). There was no significant decrease in pressure, indicating that the pumping speed of TiZrV during N₂ cycling was basically not lost.

Figure 6: Ultimate vacuum of activation cycles with N₂ filling for titanium alloy lined vacuum chamber.

After 7 rounds of activation cycles with air, the pressure in the middle of chamber coated by TiZrV was 1.1×10^{-9} Pa (see Fig. 7), which is worse to 1.67 times compared to the first activation, and the pumping performance of TiZrV film decreased.

When TiZrV works, it adsorbs oxygen-containing components such as CO, CO₂, O₂, etc of the air to form oxides. When activated, oxygen element diffuses into the interior of the film. As the number of activations increases, the content of dissolved oxygen elements inside the film increases, resulting in a decrease in pumping speed for H₂, which is the main components in extremely high vacuum. Air has a significant impact on the life of TiZrV films. Therefore, in engineering applications, the chamber coated by TiZrV films must be filled with N₂ for protection and the exposure time should be minimized as much as possible.

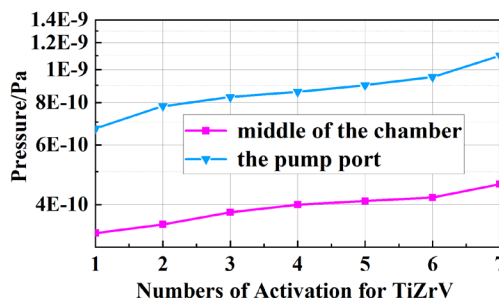


Figure 7: Ultimate vacuum of activation cycles with air filling for titanium alloy lined vacuum chamber.

CONCLUSION

By depositing TiZrV film on the thin-walled vacuum chamber lined with titanium alloy, the pressure gradient inside the vacuum chamber was effectively reduced. The ultimate vacuum in the middle of the chamber after TiZrV

coating is 6.6×10^{-10} Pa. There is no attenuation for the pumping speed of TiZrV after 15 rounds of activation cycles with N₂ filling, while there is a significant decrease for the pumping speed of TiZrV after 7 rounds of activation cycles with air filling. During the preservation process of TiZrV film, N₂ protection is required to reduce the damage of oxygen components in the air to the film and extend its life.

REFERENCES

- [1] C. Benvenuti, P. Chiggiato, P. Costa-Pinto *et al.*, *Vacuum properties of Ti Zr V non-evaporable getter films*, European Organization for Nuclear Research, Geneva, Switzerland, CERN EST/99-007 (SM), 1999.
- [2] C. Benvenuti, P. Chiggiato, F. Cicoira, and V. Ruzinov, “Decreasing surface outgassing by thin film getter coatings”, *Bull. Soc. Vac. Coaters*, vol. 50, no. 1–2, pp. 57–63, May 1998. doi:10.1016/s0042-207x(98)00017-7
- [3] J. C. Yang *et al.*, “High Intensity heavy ion Accelerator Facility (HIAF) in China”, *Nucl. Instrum. Methods Phys. Res., Sect. B*, vol. 317, pp. 263–265, Dec. 2013. doi:10.1016/j.nimb.2013.08.046
- [4] Changchun Li, “Study on properties of TiZrV film deposited on the dipole XHV vacuum chamber in HIAF-Bring”, Ph.D. thesis, University of Chinese Academy of Sciences, 2024.
- [5] A. Prodromides, “Non-Evaporable Getter Thin Film Coatings for Vacuum Applications”, Ph.D. thesis, Ecole Polytechnique, Lausanne, Geneva, CERN, 2002.
- [6] B. Window and N. Savvides, “Unbalanced dc magnetrons as sources of high ion fluxes”, *J. Vac. Sci. Technol., A*, vol. 4, no. 3, pp. 453–456, May 1986. doi:10.1116/1.573904

DESIGN AND OPERATIONAL EXPERIENCE OF FRIB MAGNET AND ELECTROSTATIC POWER SUPPLIES*

K. Holland†, R. Bliton, A. Kohler, L. Nguyen

Facility for Rare Isotope Beams, Michigan State University, East Lansing, MI, USA

Abstract

This paper will present design principles, procurement strategies, installation and testing plans, and availability data from commissioning and operation of over 1500 magnet and electrostatic power supplies at the Facility of Rare Isotope Beams (FRIB). This paper introduces the types of power supplies required for the FRIB which range in size from electrostatic high voltage power supplies less than 1 Watt to 150 kW magnet power supplies. The power supplies range in complexity from simple single quadrant units to four-quadrant pulsed electrostatic high voltage units to units requiring complex auxiliary equipment. Stability requirements of these power supplies range from 10 ppm for some sensitive experimental equipment to 3000 ppm for some multipole magnets.

INTRODUCTION

The Facility for Rare Isotope Beams (FRIB) is a heavy ion linear accelerator (linac) nuclear physics research facility with fast, stopped, and reaccelerated rare isotope beams. The facility has been performing user experiments since May, 2022 [1], prior to this, staged beam commissioning started in 2017 and continued until January 2022 [2].

In total there are over 1500 power supplies (PS) in operations at FRIB. Based on experience from commissioning and the first years of operations, this paper consists of five sections describing (i) design principles, (ii) procurement strategies, (iii) PS testing, (iv) availability, and (v) ongoing tasks.

DESIGN PRINCIPLES

The FRIB PS design is based on the flow down of functional requirements. To ensure high availability, while not arbitrarily driving up costs, the FRIB requirements include the flow down of field margin from Beam Physics, to Magnets, and finally to PS. This is important as adding margin to the current requirement for a magnet that is operating in saturation could result in much lower magnetic field margin. To further ensure high reliability, operational margin is added to the PS voltage and current for commercial off the shelf (COTS) PS (minimum 10% each for 5 year warranty), or included in specification for build to spec PS.

To ensure the best overall value for the magnet and PS systems, the PS requirements were optimized with stakeholders from Accelerator Physics, Magnet Engineering, and PS Engineering. The number of different types of mag-

nets and power supplies was minimized, allowing for common spare parts, minimizing technical risk, labor risks, and life-cycle costs. PS types were further reduced by using modular topology, as shown in Fig. 1, with different numbers of modules in series or parallel, and different auxiliary equipment required to meet the requirements of each specific magnet. When compared to large standalone units that require repair in place, the modular PS reduces the mean-time-to-repair (MTTR) during failures as the faulted module can be swapped out fairly quickly, then repaired and tested off-line.



Figure 1: Modular type SCM PS.

The room temperature dipole magnet (RTDM) PS in Folding Segment 1 (FS1) and the Beam Delivery System (BDS) were optimized by serial magnet connection with higher voltage PS. This relaxed the ripple, stability, and machine protection system (MPS) threshold requirements by an order of magnitude. Trim coil magnets PS were installed, to provide some adjustment to compensate for alignment.

The four FS1 dipoles require a switch to allow 3 operating modes: (i) With the PS off, pass straight through to the first beam dump. (ii) With the first dipole energized to allow beam to bend and the second dipole off to allow beam to pass through to the second beam dump. (iii) With all four dipoles energized to pass beam to Linac segment 2 (LS2).

The FE electrostatic (e)-dipoles interface with both PPS (Personnel Protection System) and MPS, to prevent beam from entering the linac tunnel. PPS is done through redundant AC contactors, and high voltage (HV) grounding relay. The e-dipoles interface to MPS through 30 kV 200 A-peak solid state HV push-pull half-bridge switches that disconnects the HV PS from the e-dipole, and discharges the

* Work supported by the U.S. Department of Energy Office of Science under Cooperative Agreement DE-SC0023633, the State of Michigan, and Michigan State University.

† holland@frib.msu.edu

e-dipole capacitance threw a current limiting resistor with a 1 micro second time constant, as shown in Fig. 2.

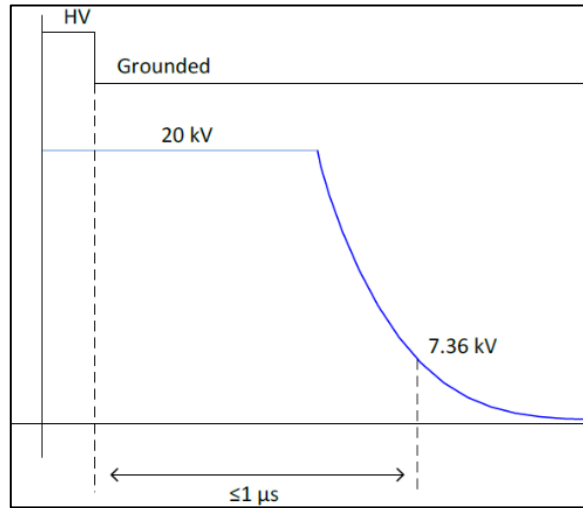


Figure 2: Electrostatic-dipole switch timing.

Many FRIB Linac PS tie into the MPS system through Direct-Current Current Transducers (DCCTs) which mitigate PS current fluctuations causing miss-steering or focusing of beam. Dipole DCCTs are in the MPS Fast Protection System (FPS). Measuring the FPS DCCTs current, comparing to the threshold, and sending a trigger signal, must be accomplished within 10 μ s. This is done with electronics that digitize and process the DCCT analog signal. Additionally MPS DCCTs are used on some multipole magnets, analog signals are digitized and processed through a PLC, as the 150 ms required response time is much slower.

The FRIB PS design benefited from a thorough design review process, with highly experienced PS engineers from other labs, and incorporating lessons learned by collaborations with other labs. The design addresses recommendations and lessons learned such as margin requirements, factory testing, and required PS responses to utilities and external controls abnormal conditions.

PROCUREMENT STRATEGIES

The procurement requirements were to obtain best value and on-time delivery of PS that fulfill the technical specifications, while considering total cost of ownership by minimizing life cycle costs.

The general PS procurement strategy was to buy COTS PS wherever possible, if not then build to specification. Where the build-to-spec procurement strategy was used, first article and pre-production rounds of procurements were held to ensure the requirements were met prior to allowing the supplier to move to full scale production.

728 PS were required for the FRIB linac through the vertical pre-separator. They were divided into the following 5 procurement families:

Cryomodule Heater PS, Quantity 60. 1000 ppm stability class allowed COTS PS. The heater resistance was optimized to use one of the room temperature magnet (RTM) PS models, minimizing the number of types of PS.

RTM PS, quantity 312. 500 ppm stability class or higher allowed the use of COTS PS. A parallel modular configuration was selected to meet the magnet requirements where higher power was needed. Additionally, the supplier designed a custom module to add the required free-wheeling diode and ground fault detection to the COTS PS.

RTDM PS, quantity 9. 100 ppm stability class requirement, auxiliary components, and low quantity led to build-to-spec. A modular series configuration was chosen to meet the higher power magnet requirements and higher voltage where magnets are connected in series.

HV PS, quantity 74. COTS and build-to-spec with one supplier. The majority of the HV PS required 2-quadrant operation for the electrostatic (e)-quads and e-dipoles, which were built-to-spec. FRIB ion sources required several 1-quadrant HV PS in the 1 to 100 kV range, with up to 2 kW power, these were achieved with COTS HV PS.

Superconducting magnet (SCM) PS, quantity 273. Build-to-spec procurement strategy due to: (i) stability classes from 20 ppm class dipoles to 1000 ppm for solenoids, (ii) 4-quadrant operation requirement for most magnets, and (iii) complex energy extraction circuits.

After the SCM PS supplier was selected, a detailed design process was followed, further optimization was achieved by using 4-quadrant for all types, and building to the tightest stability required in each current range:

20 A - \leq 500 ppm stability using a shunt current feedback device. Identical internal dump resistors.

100 A - \leq 100 ppm stability using a DCCT. Identical external dump resistor modules.

\geq 250 A - \leq 20 ppm stability using a DCCT. Dump resistors in several sizes, each for a range of magnet stored energy ratings. PS designed in 250 A modules, with the capability to operate in parallel. All designed to be used with fast dump switch modules.

PS TEST RESULTS

The FRIB PS testing strategy was developed to eliminate technical risks as efficiently as possible. The strategy required several rounds of testing:

First article and pre-production factory acceptance testing (FAT), rigorous test plans were developed to ensure that not only the specifications were met, but also to validate the component margin and thermal calculations. SCM PS dump resistors were verified to prove the temperature simulation was valid. Capacitor and IGBT temperatures were verified, ensuring high availability of those components. Voltage and current measurements of the AC/DC bulk PS, chopper resistor, and output filters verified the PS operation was in-line with the simulation. Several issues were identified during the first article and pre-production FAT which was an ideal time to mitigate those issues.

When the pre-production PS passed FAT, they were delivered to FRIB where rigorous acceptance criteria list (ACL) testing was completed successfully. Several PS were installed immediately and run long term as part of operations, further validating their designs.

During production the supplier completed FAT of each PS and provided FRIB FAT reports for each prior to delivery. Once received at FRIB, production ACL testing of a sample of 5 to 10%, or at least 1 PS of each model was completed. Examples of FAT and ACL tests are shown in Fig. 3 and Fig. 4, respectively.

Initial test of each PS in-situ into dummy load was then completed where the PS functionality of each PS and its supporting systems were validated, and magnet interlock testing was completed.

Final integrated testing, including magnet polarity testing and thermal imaging, was completed when installation of the magnet and all supporting systems were complete.

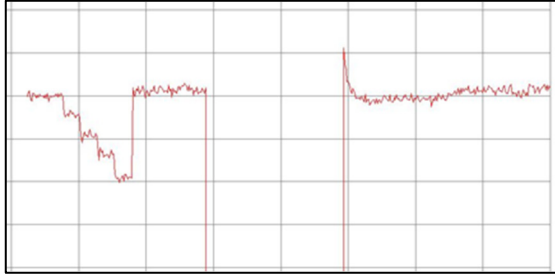


Figure 3: FAT PS current resolution and reproducibility examples, scale is 10 ppm/div, 2 min/div.

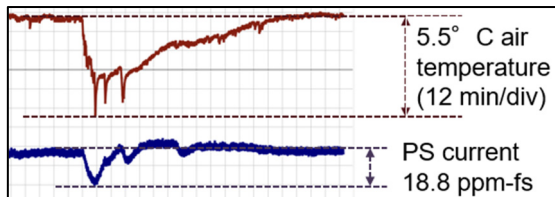


Figure 4: ACL temperature coefficient test example.

AVAILABILITY DATA

Following standard availability calculations, the expected availability of over 1500 FRIB PS is ~99%. With data from several years of commissioning and operations of FRIB PS, we see that FRIB modular PS availability has exceeded the calculations. Table 1 summarizes the availability of the FRIB PS by fiscal year. During the first 4 years the number of PS in operations grew exponentially during staged commissioning. The transition to operations in 2022 and beyond shows the typical ‘bathtub’ curve with infant mortalities and software bugs explaining the higher number of PS incidents in 2022.

It is difficult to pinpoint the reason that the higher availability has been achieved. Many aspects of the overall approach to FRIB PS availability have been presented: The design principles included margin, optimization, and design reviews. The FRIB approach to procurement led to partnering with successful suppliers. The tiered testing approach mitigated technical risks.

The FRIB approach to availability also included detailed PS and DC cable installation, testing, and maintenance procedures with layered quality assurance (QA) steps. For example, lug crimping and bolted connection installation and testing are performed with calibrated tools, following train-

ing with QA steps, and periodic inspections are done during operations, resulting in highly reliable connections, greatly reducing risk of connection failures.

Cooling of power electronics can also greatly improve reliability. Many build-to-spec FRIB PS are water cooled, with component temperatures verified during FAT, and flow rate set with alarms and redundant interlocks. The majority of the FRIB PS are installed on a server room type raised floor with air vents strategically located to direct cold air directly to high-power air-cooled racks.

Additional steps to reduce MTTR have been taken: using modular PS, training, ensuring tested spare PS availability, and PS replacements in legacy areas with FRIB types where possible.

Table 1: FRIB PS Availability

FY	Ops. Hours	Incidents	Downtime Hours	Avail.
2019	788.8	9	3.8	99.5%
2020	929.9	3	4.9	99.5%
2021	1815	6	6.8	99.6%
2022	3846	20	24.6	99.4%
2023	5901	8	8.1	99.9%
2024	6081	6	11.9	99.8%

ONGOING TASKS

As FRIB transitioned to operations, effort has been devoted to supporting FRIB operations and bringing legacy area power supplies to FRIB standards. Using FRIB PS types where possible to improve availability, lower cost of ownership, improve digital hygiene, etc. Additionally, periodic routine maintenance activities such as inspections and cleaning have been started.

With NRTL listed Absence of Voltage testers (AVT) now on the market, multiple options exist for engineered solutions to improve Lock-out-tag-out (LOTO) safety and reduce complexity. AVTs are now used on new PS installations, and are being retrofitted into existing systems.

SUMMARY

In this paper, we briefly shared our experience of PS design, procurement, testing, and operation at FRIB. Many strategies were provided such as design optimization, navigating major procurements, a method of layered testing, and the FRIB approach to improving PS availability and safety. We hope this provides some useful information for future accelerator projects.

REFERENCES

- [1] J. Wei *et al.*, “FRIB transition to user operations, power ramp up, and upgrade perspectives”, in *Proc. SRF’23*, Grand Rapids, MI, USA, Jun. 2023, pp. 1-8.
doi:10.18429/JACoW-SRF2023-M0IAA01
- [2] P. N. Ostroumov *et al.*, “FRIB commissioning”, in *Proc. HIAT’22*, Darmstadt, Germany, Jun.-Jul. 2022, pp. 118-123.
doi:10.18429/JACoW-HIAT2022-WE1I3

oxygen gas mixture. The vacuum system included a scroll pump to establish a pressure in the range of 10 to 300 mTorr. A residual gas analyzer (RGA) was used to sample and monitor gases pumped out during plasma processing. Viewports on both beam port flanges allowed us to see the cavity interior and identify the location of the plasma.

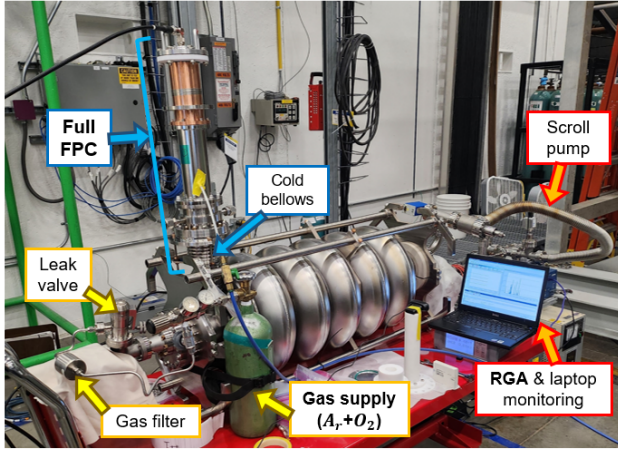


Figure 2: FRIB400 cavity with full FPC and gas supply, and pumping.

Cavity Plasma

We were able to generate plasma in each of the 5 cells in turn, as shown in Fig. 3, by driving a combination of TE_{111} passband modes. We used 4 out of 5 modes ($2\pi/5$ to π) to drive the plasma.

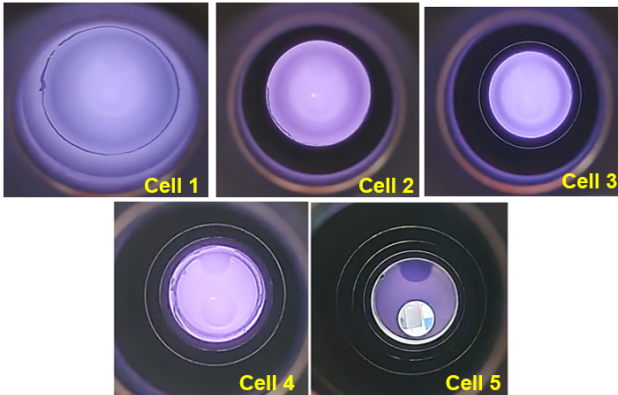


Figure 3: Light from the plasma glow discharge in each cell, as seen through the viewport on the FPC side.

The unperturbed drive frequency (equal to the resonant frequency before plasma ignition) and the input RF power for initial plasma ignition are shown in Table 1 for each mode. For cells 1, 3, and 4, we could ignite the plasma using only one mode ($4\pi/5$, $3\pi/5$ and π mode, respectively). For cells 2 and 5, we had to generate plasma in an adjacent cell first and then transfer the plasma by driving another mode, superposing the RF fields; “dual-tone” control of

the plasma. For example, to transfer the plasma from Cell 1 to Cell 2, we drove the $4\pi/5$ mode, increased the input power, and ignited Cell 1, producing a reduction in the RF field amplitude. Then we drove the $2\pi/5$ mode, gradually increasing the input power to increase the field in Cell 2 until the plasma moved from Cell 1 to Cell 2. A similar method was used to move the plasma from Cell 4 to Cell 5.

Table 1: Plasma Drive Parameters for Each Cell

Drive mode (TE_{111})	P_f [W]	Drive Frequency [GHz]	Cell number
$4\pi/5$	6.5	1.286	1
$4\pi/5 + 2\pi/5$	8.5	1.286, 1.344	$1 \rightarrow 2$
$3\pi/5$	13	1.316	3
π	4.4	1.278	4
$\pi + 3\pi/5$	5.8	1.278, 1.316	$4 \rightarrow 5$

Parameter Scans

When the plasma ignites, it absorbs RF power, leading to a drop in the cavity quality factor, and the resonant frequencies shift up (Δf_{res}) [8, 9]. A larger plasma density will produce a larger Δf_{res} . We can then shift the drive frequency up (Δf_{drive}) to be closer to the resonant frequency, which in turn can cause an additional shift in the resonant frequency. This process can continue until the plasma is no longer sustained or the coupler ignites.

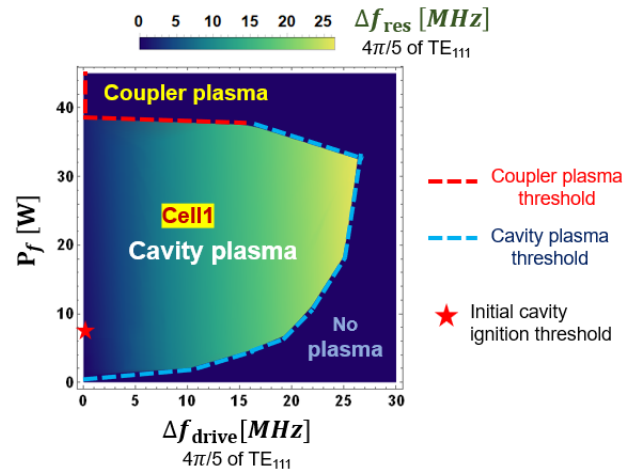


Figure 4: Parametric scan for plasma in Cell 1 driven by the TE_{111} $4\pi/5$ mode.

Figure 4 shows an intensity map of the measured resonance frequency shift Δf_{res} (from which we can infer the plasma density), as a function of the drive frequency shift Δf_{drive} and the input RF power (P_f) when driving the $4\pi/5$ mode and generating plasma in Cell 1. In general, we observe a brighter plasma glow with higher Δf_{drive} and higher P_f . If Δf_{drive} is too high, the plasma cannot be sustained

(dashed blue line in Fig. 4). On the other hand, if P_f is too high, the plasma can move to the FPC region (dashed red line in Fig. 4). The red star in Fig. 4 shows the P_f value for initial cavity plasma ignition; note that plasma can still be sustained at a lower P_f after ignition, showing a “hysteresis” behaviour. Parametric scans of the type shown in Fig. 4 allow us to identify the optimum condition for high cavity plasma density without coupler ignition.

PLASMA CLEANING TRIAL

We drew rings on 8 of the irises of a 5-cell cavity with a permanent marker; irises being a region of high surface electric field for the FM. We then attempted to remove the rings with an argon-oxygen plasma. If the oxygen reacts with the hydrocarbons from the permanent marker, gaseous by-products such as CO, CO₂, and H₂O may be produced and pumped out of the cavity.

As shown in Fig. 5, we saw an increase in the partial pressures of these gases in the RGA signal after turning on the plasma. Almost all rings were removed after approximately 10 hours of cleaning in each cell. As the TE₁₁₁ is a dipole passband, the field distribution is not axisymmetric, given that we drive only 1 polarization. However, as seen in Fig. 6, we observe an azimuthally-symmetric removal of the rings, which indicates that the field distribution does not impair the uniformity of cleaning.

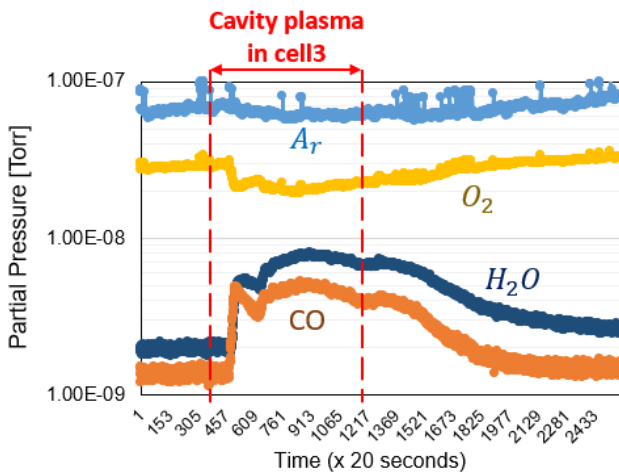


Figure 5: Selected RGA signals during plasma cleaning of Cell 3. The signal from by-products (CO, H₂O) increases with plasma on, while the O₂ signal decreases.

SUMMARY AND FUTURE PLANS

A feasibility study for plasma processing of the FRIB energy upgrade 5-cell cavity has been completed. We could ignite plasma in each cell via the full FPC using the TE₁₁₁ passband with a maximum input power of 13 W. We measured used parametric scans to find the drive power and drive frequency shift to maximize the plasma density for each cell. Finally, we verified the plasma cleaning efficiency

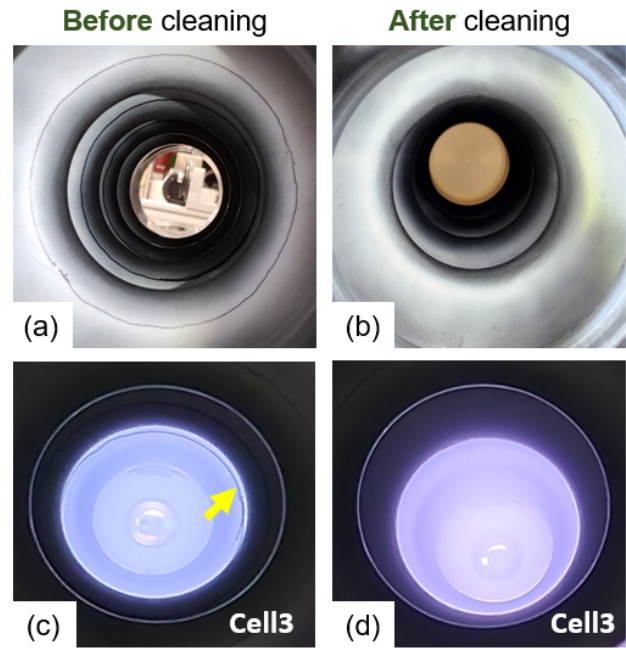


Figure 6: Photos of irises before and after plasma cleaning. The permanent rings are visible before plasma cleaning (a, c) and are removed by the plasma (b, d). (a) and (b) are with the plasma off; (c) and (d) are with the plasma on.

by removing hydrocarbon contamination from each cell. Our results indicate that plasma processing with the FPC using the TE₁₁₁ HOM is a suitable approach.

The next step planned for our development effort is a plasma processing trial on a jacketed FRIB400 cavity that showed field emission in several cold tests. We will investigate whether our plasma processing procedure can reduce the field emission.

REFERENCES

- [1] P. V. Tyagi *et al.*, “Improving the work function of the niobium surface of SRF cavities by plasma processing”, *Appl. Surf. Sci.*, vol. 369, pp. 29–35, Apr. 2016. doi:10.1016/j.apsusc.2016.02.030
- [2] K. E. Tippey *et al.*, “Improving the Work Function of Nitrogen-Doped Niobium Surfaces for SRF Cavities by Plasma Processing”, *J. Phys. Conf. Ser.*, vol. 1067, p. 082010, Sep. 2018. doi:10.1088/1742-6596/1067/8/082010
- [3] M. Doleans *et al.*, “Plasma Processing R&D for the SNS Superconducting Linac RF Cavities”, in *Proc. SRF’13*, Paris, France, Sep. 2013, paper TUP057, pp. 551–557.
- [4] M. Doleans *et al.*, “In-situ plasma processing to increase the accelerating gradients of superconducting radio-frequency cavities”, *Nucl. Instrum. Methods Phys. Res., Sect. A*, vol. 812, pp. 50–59, Mar. 2016. doi:10.1016/j.nima.2015.12.043
- [5] P. Berrutti *et al.*, “Plasma ignition and detection for in-situ cleaning of 1.3 GHz 9-cell cavities”, *J. Appl. Phys.*, vol. 126, no. 2, p. 023302, Jul. 2019. doi:10.1063/1.5092235
- [6] B. Giaccone *et al.*, “Plasma cleaning of the SLAC Linac Coherent Light Source II high energy verification cryomodule

- cavities”, *Phys. Rev. Accel. Beams*, vol. 25, no. 10, p. 102001, Oct. 2022.
doi:10.1103/physrevaccelbeams.25.102001
- [7] T. Powers, I. Senevirathne, N. Raut, and T. Ganey, “An overview of plasma processing of SRF cavities at JLAB”, in *Proc. LINAC’24*, Chicago, IL, USA, Aug. 2024, pp. 577–582.
doi:10.18429/JACoW-LINAC2024-THXA005
- [8] J. C. Slater, “Microwave Electronics”, *Rev. Mod. Phys.*, vol. 18, no. 4, pp. 441–512, Oct. 1946.
doi:10.1103/revmodphys.18.441
- [9] M. Doleans *et al.*, “Ignition and monitoring technique for plasma processing of multicell superconducting radio-frequency cavities”, *J. Appl. Phys.*, vol. 120, no. 24, Dec. 2016.
doi:10.1063/1.4972838

HIGH RESOLUTION CURRENT CONTROL FROM SWITCHED MODE POWER SUPPLY*

D. Novak[†], K. Bunnell, C. Dickerson, S. Klohe, S. Kumar, D. Santiago-Gonzalez, D. Stanton
Argonne National Laboratory, Lemont IL, USA

Abstract

The Argonne Tandem Linac Accelerator System (ATLAS) has been a National User Facility since 1985. Since the commissioning of the Californium Rare Isotope Breeder Unit (CARIBU) in 2012, it has used 2 bespoke water-cooled linear power supplies to allow for milliamp control of the isobar separator magnets, which allows for milligauss control of the magnets. During the upgrade to nuCARIBU, the aging linear power supplies were replaced with off-the-shelf (OTS) switched mode power supplies (SMPS). The benefit of the SMPS is higher efficiency, lower cost, and since they are air-cooled, no load on the water cooling infrastructure. The limitation of the SMPS is a decrease in resolution in current control. To overcome this limitation, a device was constructed that allows control of a sub-milliamp constant current sink, which is placed in parallel to the magnet. This arrangement allows the control system to “leak” a precise amount of current away from the magnet, effectively giving sub-milliamp control of the current going into the magnet.

INTRODUCTION

The CARIBU, Californium Rare Isotope Breeding Unit, facility at Argonne ATLAS was commissioned in 2012, and has been providing low intensity, high purity, and neutron-rich beams for re-acceleration through ATLAS. Due to issues with the procurement of Californium, it was decided to replace the Californium source and cask with a compact proton cyclotron. As a proton source, the cyclotron has the advantage of being a more reliable source of fission products, a higher overall fission rate, and easier to maintain and operate since it can be shut off [1].

BACKGROUND

CARIBU was designed with a compact high-resolution isobar separator [2, 3], which requires precise control of the magnetic field. This was previously achieved with a pair of bespoke linear power supplies, which operated with 6-digit current resolution, between 0 and 335 Amps in constant-current mode. As these power supplies aged, they began to require more and more maintenance, until they got to the point where they could no longer be controlled remotely. The original manufacture had been sold, and the new owner no longer supported the power supplies. When it came time for the nuCARIBU upgrade, it was decided to

replace the power supplies for the isobar separator magnets [4].

Off-the-shelf SMPS were deemed an acceptable replacement for the bespoke supplies. SMPS power supplies have a number of benefits when compared to linear power supplies. SMPS power supplies operate at a much higher efficiency, requiring only air cooling, where as the linear supplies required water cooling. This reduces stress on the cooling systems in ATLAS, as well as reducing maintenance of the power supplies. The SMPS are off-the-shelf components from TDK-Lambda that are still in production and are well supported. The SMPS supplies operate at a much lower temperature, extending their useful lifespan. Due to the low cost from the economies-of-scale, it is economical to have spare supplies on-hand.

The downside of off-the-shelf SMPS is the finite output resolution across the product range. In basic SMPS designs, the output is controlled by the switching frequency and/or duty cycle of the switched element, but generally it is the duty cycle that controls the output. The duty cycle is digitally controlled by a Pulse Width Modulator, PWM, controller which is a peripheral of a micro-controller. Being digitally controlled, the PWM has a finite number of steps between minimum and maximum pulse-width. This finite number of steps defines the resolution of the power supply. To achieve economies of scale as well as the re-use of the control interface software, power supply makers will tend to re-use the digital part of the design across a broad range of power supplies. So power supplies capable of 50 Amps, will have the same number of output steps as supplies capable of 250 Amps. In other words, as voltage and current output increases, accuracy decreases due to the fixed number of steps in digital sub-system. Similar to the output, the read back channels also suffer from a fixed number of steps in the Analog to Digital Converter, ADC, used in the measurement side of the power supply. This means that the accuracy of voltage and current measurement goes down as output capability increases.

ISSUE

The magnetic field produced must be controlled to account for variations in the conditions of the CARIBU hall. The largest single influence on the magnets, and thus the field, is the water cooling system used by the magnets. The temperature of the cooling system water fluctuates, which affects the field. To account for these changes, a control loop is used within the control system to keep the field strength as constant as possible. As a result of the limitations of the SMPS supply, the algorithm to control the magnetic field had to be adjusted. This was mainly due to the current control resolution. The SMPS power supply is

* This work was supported by the U.S. Department of Energy, Office of Nuclear Physics, under Contract No. DE-AC02-06CH11357. This research used resources of ANL's ATLAS facility, which is a DOE Office of Science User Facility.

[†] dnovak@anl.gov

said to only have the resolution as shown on the front panel display. This display is only 5 digits, but we found that the actual resolution was closer to 5.5-digits. This means that the power supply could be controlled down to around 0.005 Amps, over a range of 0-250 Amps. In the magnets being used, that 5 mA step equates to roughly 0.015 Gauss. In order to avoid over-controlling the measured Gauss value, and oscillating between control values, a fairly wide band of ± 0.60 Gauss from the set point was used as the minimum delta to begin changing current on the power supply by the control algorithm. While workable, this made for a less than ideal solution.

SOLUTION

To be able to precisely control the current going to the magnet, and thus control the magnetic field, a method was needed to bleed small amounts of current away from the magnet. A potentiometer of appropriated size was placed in parallel to the magnet and was tested in the arrangement as seen in Fig. 1.

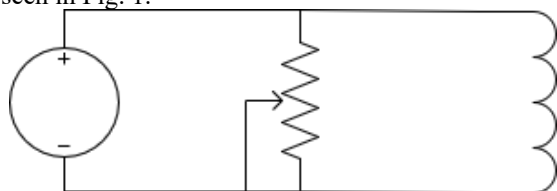


Figure 1: Simplified model.

Testing this arrangement proved that the concept was sound. Current was bled through the potentiometer in a very controllable manner.

In the next step, the potentiometer was replaced with a digital potentiometer which was control by a networked micro-controller. See Fig. 2. This arrangement allowed the digital potentiometer to be controlled remotely by the control system. The bleed circuit was tuned to be able to bleed around 5mA, which was chosen to coincide with the power supplies minimum steps size. The effectively gives 256 additional steps within the power supplies minimum step, for a new minimum step size of about 19.5 nA.

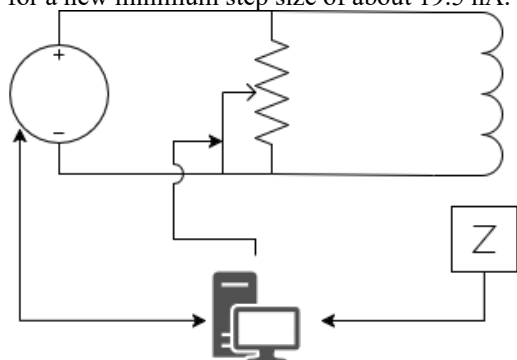


Figure 2: Device in control system.

New software was written to be able to control this new device and testing of the new system began. Initial testing showed good results, however as the potentiometer was moved to the extreme edges of available control values, non-linear current values were noted. This is due to the voltage changes in the power supply as the load changes.

In the final iteration of the system, the digital potentiometer was integrated as part of a programmable constant-current sink. This alleviated the problem of non-linear current values, and allowed for basic PID control of the bleed circuit to achieve requested Gauss value within the magnet.

The PID control of the circuit was integrated within the original control algorithm used for the magnets, which would only start its control loop when the original algorithm was within the boundaries that indicate that control had been achieved. This prevents the two algorithms from competing against each other, and makes integration with existing control software throughout ATLAS easier. The two control algorithms can then be thought of as two completely separate control algorithms, a gross control algorithm and a fine control algorithm.

FINDINGS

With the hardware and the software in place, we were able to do A/B comparison testing with the two isobar separator magnets in CARIBU. This proved very advantageous, as the two magnets are in close physical proximity and connected to the same cooling water system. This means that both magnets are seeing approximately the same external influences, and thus make it easier to validate the effectiveness of the system in real time.

In Fig. 3 we see a comparison of the Gauss versus time output of the 2 magnets over approximately 6.4 hours. The line labeled "114" shows the Gauss value from magnet using the device and running the gross control loop as well as the PID/fine control loop. The line labeled "115" is the identical magnet running only the gross control loop. Both magnets have a set-point of 3000.000 Gauss.

Initial testing showed that when the fine control loop handed control over to the gross control loop, there were temporary jumps in the Gauss value. See Fig. 4. These jumps seemed to be partially caused by trying to aggressively compensate the device during the handover from the fine loop, to the gross loop. This was mostly resolved by doing no compensation during the handover. The handover from fine to gross control still shows some jumps, but the jump is on the order of 0.020 Gauss, and is brief. This performance is much better than the gross loop alone, and deemed sufficient for nuCARIBU.

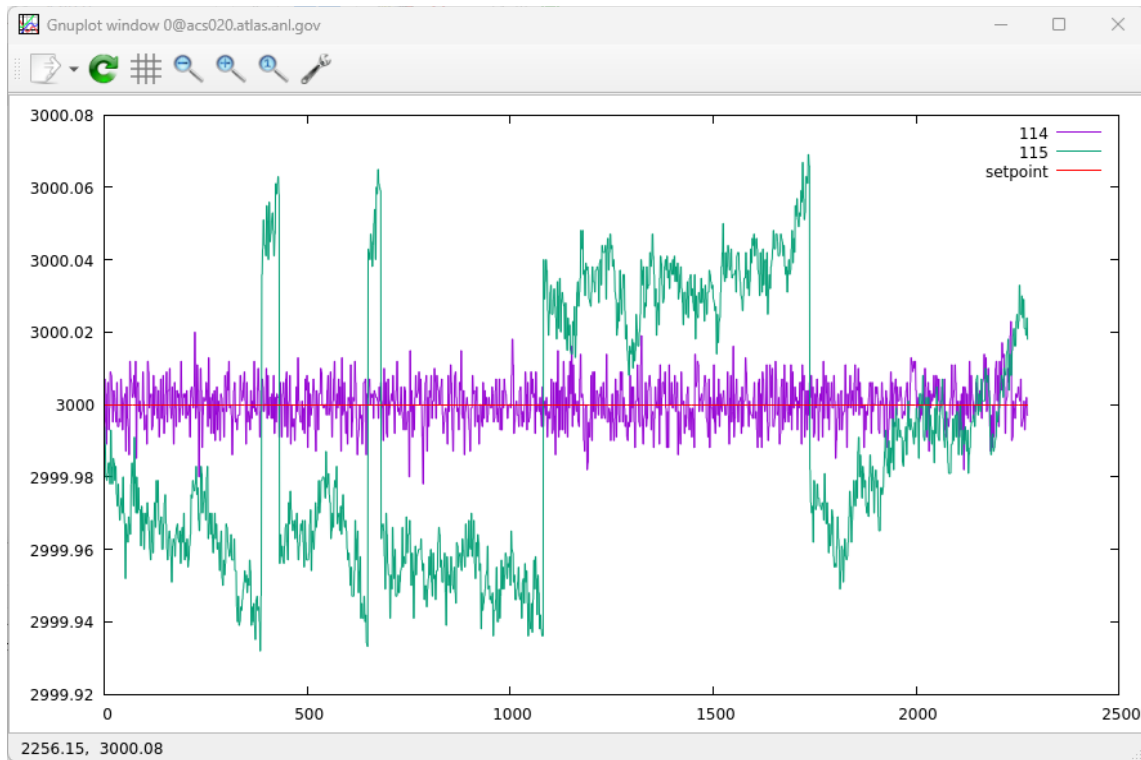


Figure 3: Example of magnetic field, in Gauss, versus time for isobar separator magnets trying to maintain a set point of 3000 Gauss. Line 114 shows fine control, while the 115 line shows gross control.

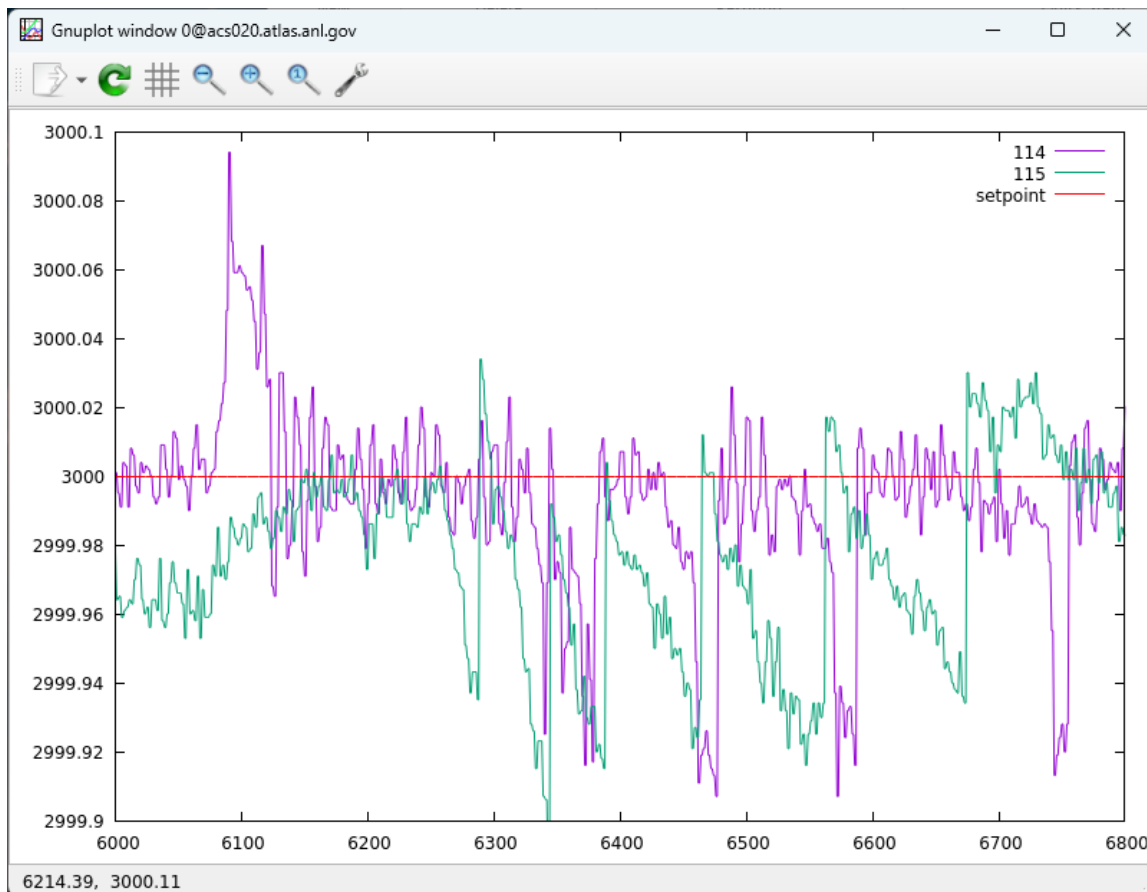


Figure 4: Showing magnetic field, in Gauss, versus time for the isobar separator magnets. This shows over compensating when handing over from fine control to gross control.

More tuning of the fine control PID loop could be done, as there is still some oscillation in the system. However, tuning the PID is a very slow process, due to the unpredictable nature of the changes in Gauss readings, due to cooling water temperature fluctuations. In addition, the feedback sensor is noisy, the cost for adjusting the fine control is very low, and the current system is 3-4x better than previously, there isn't a large incentive to further optimize the PID of the fine control loop at this time.

In a run of 3179 samples, over about 8.8 hours, the system without the fine control loop showed a standard deviation of the Gauss measurement of 0.0386. The same run on the other magnet with the fine control loop, showed a standard deviation of the Gauss value of 0.0102. This is an improvement of over 3 times better Gauss control. This could probably be improved with more PID tuning, but the limitations of the Gauss meter would begin limit the ability to measure those changes.

Templates are provided for recommended software and authors are advised to use them. Please consult the individual conference help pages if questions arise.

CONCLUSIONS

With the addition of the parallel circuit to bleed current away from the magnet, we were able to effectively take an inexpensive SMPS capable of approximately 5 mA of resolution, and give it approximately 19 nA resolution.

This allowed for our control algorithm to improve regulation from ± 0.060 Gauss, to less than ± 0.020 Gauss, with room for further improvement. This has allowed for the creation of a much more stable magnetic field for the isobar separator than was previously available.

This process could be applied to other loads that require sub-milliamp current control.

REFERENCES

- [1] G. Savard, "nuCARIBU: Upgrade of the CARIBU facility at Argonne", presented at HIAT'22, Darmstadt, Germany, Jun-Jul. 2022, paper TH1I1, unpublished. https://accelconf.web.cern.ch/hiat2022/talks/th1i1_talk.pdf
- [2] C. N. Davids and D. Peterson, "A compact high-resolution isobar separator for the CARIBU Project", in *Proc. PAC'09*, Vancouver, Canada, May 2009, paper FR5REP116, pp. 5050-5052.
- [3] M. Portillo, T. A. Barlow, J. A. Nolen, "Design layout of an isobar separator based on 5th order calculations", in *Proc. PAC'01*, Chicago, IL, USA, Jun. 2001, paper RPAH073, pp. 3015-3017.
- [4] G. Savard *et al.*, "Radioactive beams from gas catchers: The CARIBU facility", *Nucl. Instrum. Methods Phys. Res. B*, vol. 266, no. 19–20, pp. 4086–4091, Oct. 2008. [doi:10.1016/j.nimb.2008.05.091](https://doi.org/10.1016/j.nimb.2008.05.091)

ASSESSMENT OF MAGNETIC QUADRUPOLE PICK-UP STRUCTURE AT FRIB*

C.A. Sarabia-Cardenas[†], S.M. Lidia, P.N. Ostroumov,

Facility for Rare Isotope Beams, Michigan State University, East Lansing, MI, USA

Abstract

A magnetic quadrupole pick-up structure is being assessed for creation and future use at The Facility for Rare Isotope Beams (FRIB) at Michigan State University (MSU). The geometric design makes use of magnetic loops that couple with the radial magnetic field of a beam, allowing for rejection of the beam intensity signal of the beam, while leaving the dipole signal as the dominant signal and enhancing the quadrupole signal. Of interest is examining the response due to the multiple charge state heavy ion beams that FRIB produces and the ability to resolve the differing charge states. Presented here is the optimization of the device for the FRIB beamline.

INTRODUCTION

The Facility for Rare Isotope Beams (FRIB) produces high intensity heavy ion beams of varied species and charge states [1]. Measurement of the beam's quadrupole moment is being investigated to characterize the transverse rms beam sizes and evaluate Courant Snyder parameters for proper matching in critical sections in the linac. There are a number of interceptive methods to capture the quadrupole moment, like wire scanners or viewers, but interceptive methods take a long time to evaluate the beam parameters in the phase space. In addition, non-destructive methods can be used during high-beam-power operations to assess beam envelopes in real time.

Non-destructive methods for estimating the quadrupole moment of the transverse beam distribution have existed since 1966 [2] using beam position monitors (BPMs), a standard diagnostic device of which there are many placed all throughout the LINAC sections in the FRIB beamline [3]. However, the usual design of an electrostatic position pick-up as a BPM generates very low signal corresponding to a quadrupole moment measurement. Electrostatic BPMs are largely optimized for linear response to beam displacement, while the quadrupole moment is measured from the quadratic term in beam displacement, leading to small signals. There have been efforts to make significant changes to BPM geometry and increase sensitivity to quadrupole components [4], but complicated electrode geometries pose their own challenges.

The method presented here instead is a magnetic quadrupole pick-up, which boasts a simpler geometry and the ability to suppress the common mode of the beam, making

the dipole and quadrupole signals of the beam much stronger and more easily measurable.

Preliminary work is being done to develop this device for FRIB based on the success that similar pick-ups have enjoyed at facilities like the CERN PS [5], though this device will be distinct and differently optimized, based on the needs of FRIB.

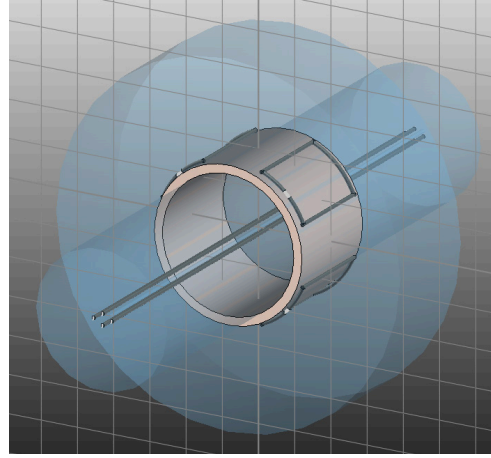


Figure 1: A 3D model of the magnetic quadrupole pick-up structure modelled in CST Studio Suite. The four wires at the center are a simple beam model.

PICK-UP DESIGN

The magnetic quadrupole pick-up structure, shown in Fig. 1, is designed with four wire loops at 45° angle to the horizontal plane. These loops are placed just outside a ceramic vacuum tube to interact with the beam's magnetic fields while avoiding issues of the loops being vacuum compatible or needing feedthroughs. The entire structure is placed inside a pillbox cavity to maintain the continuation of wall currents through the structure. Additionally, the radius of the pillbox should be at least twice that of the beam pipe so that the conducting walls of the pillbox do not interfere with the magnetic flux through the wire loops. The wire loops are oriented as shown in Fig. 1 to couple only with the radial component of the beam's magnetic field. To see this, the magnetic field of the beam is expressed in cylindrical coordinates as [5]:

$$\vec{B}(\rho, \theta) = -I \frac{\mu_0}{2\pi} \left[\frac{1}{\rho} \hat{\theta} + \bar{x} \left(\frac{\cos \theta}{\rho^2} \hat{\theta} - \frac{\sin \theta}{\rho^2} \hat{\rho} \right) + \bar{y} \left(\frac{\sin \theta}{\rho^2} \hat{\theta} + \frac{\cos \theta}{\rho^2} \hat{\rho} \right) + \kappa \left(\frac{\cos 2\theta}{\rho^3} \hat{\theta} - \frac{\sin 2\theta}{\rho^3} \hat{\rho} \right) + \dots \right], \quad (1)$$

where κ is itself the quadrupole moment that is of interest to measure and is given by:

$$\kappa = \sigma_x^2 - \sigma_y^2 + \bar{x}^2 - \bar{y}^2, \quad (2)$$

*This material is based upon work supported by the U.S. Department of Energy, Office of Science, Office of Nuclear Physics, under Award Number DE-SC0025531 and Office of High Energy Physics, under Award Number DE-SC0018362

[†]sarabiac@frib.msu.edu

where \bar{x} and \bar{y} are beam position relative to the beam centre while σ_x and σ_y are the RMS beam size. Longitudinally, the beam is assumed to be highly bunched at the linac RF frequency.

It becomes clear from Eq. 1 that coupling to the radial component of the magnetic term cancels the common mode term, giving only the dipole and quadrupole terms. The quadrupole moment itself is extracted from the pick-up signal combinations [6]:

$$D_x = TR + BR - BL - TL. \quad (3)$$

$$D_y = TR - BR - BL + TL. \quad (4)$$

$$Q = TR - BR + BL - TL. \quad (5)$$

Where TR is the voltage signal from the top right loop, BL from the bottom left, etc. They are noticeably similar to the signals from standard BPMs, simply twisted by 45° and missing the sum (common mode) signal, which is made 0 by deliberate design. To extract the quadrupole moment, κ is related to Eq. 5 is given by (to first order):

$$Q = Z_Q I \kappa. \quad (6)$$

Where I is the beam current and we define Z_Q as the transfer impedance (in units of V/A/m²) which is dependent on pick-up geometry. Perhaps the clearest example of this is as the opening angle of the wire loops increase so does Z_Q , but this is not a linear effect as the impedance levels off [5]. The opening angle of 45° is seen to maximize the quadrupole signal in comparison to the dipole signal.

It's important to note that a separate current measurement of the beam is needed in order to extract the quadrupole moment from the quadrupole signal, since the instrument cannot measure the current. However, due to the prevalence of BPMs and wall current monitors, measuring the current near the quadrupole pick-up should not be an issue.

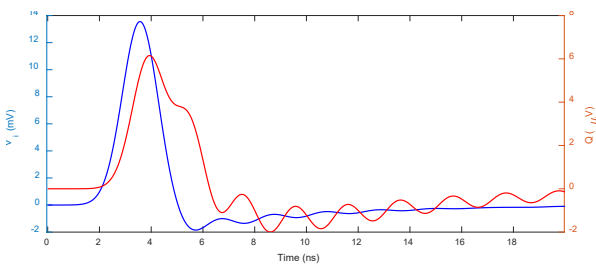


Figure 2: Quadrupole signal and beam voltage profile from CST for a 40 μ A and 40.25 MHz modelled beam.

MODELLING RESULTS

Modelling was performed in CST [7], as shown in Fig. 1. Here the structure was set to a longitudinal length of 50 mm, with a ceramic radius of 40.75 mm and an outer cavity radius of 95 mm, exceeding the requirement that the cavity radius be twice the radius of the ceramic. The lowest resonant frequencies of the outer cavity structure are 921 MHz [TM00] and 1324 MHz [TM01]. These are well above our operating frequency of 40.25 MHz, so they will not be an issue.

Beams themselves were modelled as 4 wires with a signal travelling in-phase down the wires. The beams were modelled in this fashion because any future test-stand measurements would be performed with a four wire configuration.

Beam currents less than 650 μ A (the eventual current of FRIB) and at 50 MHz were modelled like this, as shown in Fig. 2. CST was able to faithfully reproduce the quadrupole moment of beam sizes up to 10 mm and over a similarly large range of beam displacement as well.

This beam was modelled at a group velocity of $\beta = 0.18$, and future simulation work will focus on detailed modelling of group velocities. Further work will focus on precisely optimizing the longitudinal length of the cavity for maximum signal strength.

CONCLUSION

The goal of this project will be to develop a magnetic quadrupole pick-up structure that can be used with high-intensity heavy ion beams. An overview of the device was presented, as well as some preliminary work on expected results from the instrument.

ACKNOWLEDGEMENTS

Michigan State University operates the Facility for Rare Isotope Beams as a user facility for the U.S. Department of Energy Office of Science (DOE-SC), supporting the mission of the DOE-SC Office of Nuclear Physics

REFERENCES

- [1] P. N. Ostroumov *et al.*, “Acceleration of uranium beam to record power of 10.4 kW and observation of new isotopes at Facility for Rare Isotope Beams”, *Phys. Rev. Accel. Beams*, vol. 27, no. 6, pp. 060101, 2024. doi:10.1103/PhysRevAccelBeams.27.060101
- [2] L.L. Gol'din, “Investigation of Charged Particles Beams by Means of Signal Electrodes”, *Instruments and Experimental Techniques*, pp. 780–784, 1966. Translation of Pribory i Tekhnika Eksperimenta, vol. 4, pp. 18–21, Jul.–Aug. 1966.
- [3] S. M. Lidia *et al.*, “Overview of Beam Diagnostic Systems for FRIB”, in *Proc. IBIC'15*, Melbourne, Australia, Sep. 2015, pp. 226–230. doi:10.18429/JACoW-IBIC2015-MOPB071
- [4] T. Watanabe *et al.*, “Commissioning of the beam energy position monitor system for the superconducting RIKEN heavy ion linac”, in *Proc. IBIC'20*, Santos, Brazil, Sep. 2020, pp. 295–302. doi:10.18429/JACoW-IBIC2020-FRA004
- [5] A. Jansson and D. J. Williams, “A new optimised quadrupole pick-up design using magnetic coupling”, *Nucl. Instrum. Methods Phys. Res., Sect. A*, vol. 479, no. 2–3, pp. 233–242, Mar. 2002. doi:10.1016/s0168-9002(01)00899-3
- [6] A. Jansson, “The Measurement of higher order moments of beam transverse distribution using a magnetic pick-up”, CERN, Geneva, Switzerland, Rep. CERN Internal Note, PS/OP/Note 98-27, 1998.
- [7] CST Studio Suite, <https://www.cst.com>

CALIBRATING THE FRIB CHOPPER MONITOR*

J. Hartford[†], E. Bernal Ruiz, M. Ikegami, Z. Li
Facility for Rare Isotope Beams, East Lansing, MI, USA

Abstract

At FRIB, a chopper in the low energy beamline is used for beam duty factor control as well as beam mitigation for machine protection. The chopper requires power to be applied to stop beam, which makes it non-failsafe. As such, monitoring the health of the entire chopper system is paramount, ensuring that: the chopper is functioning properly, undesired high-power beam will not be delivered downstream, and high-speed beam mitigation is available when requested. To ensure the functioning of the chopper system, a chopper monitor has been developed and has been in use to support operation in FRIB. In supporting its operation, it has been identified that particular attention must be paid to the calibration of the chopper monitor system. In this paper, we present the established calibration methodology for the chopper monitor system together with the associated analytical processes.

INTRODUCTION

The FRIB linac has a chopper in its low-energy beam transport [1] to generate a pulse structure in the heavy ion beam by deflecting a temporal portion of it with a transverse electric field. The deflected beam is intercepted with a downstream beam absorber. The chopper is used to 1) generate a regular notch (beam-off period) for beam diagnostics systems, 2) generate pulsed beams for beam tuning, and 3) mitigate the beam at an interlocked event for machine protection.

The chopper system has two deflecting plates to which the high voltage (HV) is applied by HV power supplies through HV switches. The FRIB Global Timing System (GTS) provides a beam pulse structure signal to the chopper monitor. The chopper monitor receives feedback signals from the HV switches representing the connected voltage level and the outgoing/incoming electric charge flow rate (current) (see Fig. 1).

The GTS signal, voltage levels, and outgoing/incoming charge flows are all compared to their expected values to ensure that the process is proceeding properly. Charge flow monitoring is seen as the primary indicator of system health due to it being a variable related to both voltage applied and load connected, informing the monitor that the chopper is connected and functioning. The chopper monitor, should it detect an issue with any of the monitored parameters or receive a beam mitigation request from the FRIB Machine Protection System (MPS) [2], quickly latches the chopper in the beam blocked state until operators intervene.

* Work supporting the U.S. Department of Energy Office of Science under Cooperative Agreement DE-SC0023633, the State of Michigan and Michigan State University.
[†] hartforj@frib.msu.edu

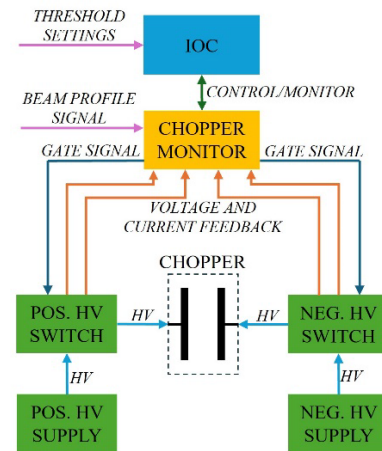


Figure 1: The basic chopper system.

The chopper monitor is a field programmable gate array (FPGA)-based system interfaced with the MPS, and utilizing an input/output controller (IOC) for the operator interface [3]. The IOC displays GTS signal parameters, HV level readings, and outgoing/incoming charge readings from the chopper monitor and sends to it trip thresholds. Due to the reality of integrating between the different components of the chopper system, data is represented in varying ways, requiring that a careful calibration be conducted to translate between these representations.

DATA TRANSLATION

The readback and threshold data are represented in three different ways as they move through the system (see Fig. 2).

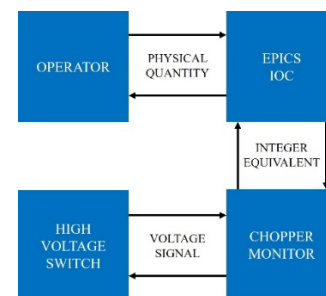


Figure 2: Varying data representations.

At the lowest level, between HV switch and chopper monitor, the data takes the form of a variable voltage. This voltage is received into the chopper monitor by way of analog-to-digital converters (ADCs). The low voltage signal representing HV level is received directly by an ADC while the low voltage signal representing current is first passed through an integrator circuit before being received by the ADC so that the ADC outputs a measurement of charge rather than current [3]. This conversion, from voltage level to its integer equivalent, is fixed and based on the ADCs.

Between the field programable gate array (FPGA) of the chopper monitor [3] and the IOC the data exists as a unitless integer. These integers, however, are not readily useable by the operator and must be converted into a physical quantity with unit. Likewise, threshold settings are input by the user as a physical quantity and must be converted into an integer to be made useable by the hardware. This conversion factor is determined through a curve fitting which we refer to as a calibration.

Over time, the circuitries of the chopper monitor age, and their output changes. As this happens, the monitored values may no longer be accurate, which may mean the thresholds are no longer appropriate. This necessitates regular checking and recalibrating of the chopper monitor system to keep it functioning as intended.

TESTING OF INTEGRATOR CIRCUIT

Before fitting a curve, the chopper monitor's ADC inputs for current, which utilize integrator circuits, were checked for proper functioning and linearity. This test was conducted by connecting the current monitor output of the HV switch to the proper chopper monitor input and to a high-impedance input of an oscilloscope which was used to verify that charge was as expected. Three different capacitive loads were tested. The first was using only the internal capacitance of the switch (no connected load), the second was with a 6 ft RG-59 cable with safe high voltage (SHV) connectors on either side, and the third was with a load capacitor added onto the end of the cable; these amounted to capacitive loads of 39 pF, 173 pF, and 240 pF, respectively, and were checked using an inductance, capacitance, and resistance (LCR) meter. Each load was tested at six different voltage levels: 1 kV, 1.5 kV, 2 kV, 2.5 kV, 3 kV, and 3.5 kV. The results showed good linearity of the ADC output with respect to charge (see Fig. 3).

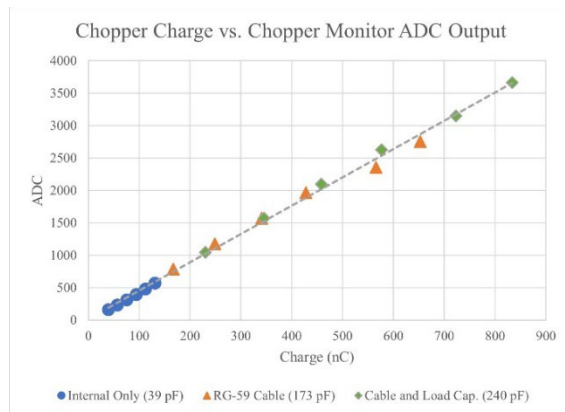


Figure 3: Charge Vs. ADC.

CALIBRATING IN THE LAB

Prior to placing the chopper monitor into production, a calibration is conducted in the test lab. Figure 1 shows what is essentially the same setup but instead of the chopper, load capacitors were connected to each switch. This gave each HV switch a load of 240 pF: the sum of the internal load, the 6 ft RG-59 cable, and load capacitor. The HV

switches were then configured such that they would pulse the HV off with a pulse width of 0.6 μ s and frequency of 100 Hz. The HV power supplies were set, and ADC measurements were taken, at seven different HV level settings: 1 kV, 1.5 kV, 2 kV, 2.5 kV, 2.8 kV, 3 kV, and 3.5 kV (the negative of these values is used for the negative HV switch).

Calibration of Charge ADCs

The chopper monitor's charge ADCs, one for the positive HV switch and one for the negative, record and display the live, high, and low charge values for the charge (outgoing charge) and discharge (incoming charge) cycles separately. Once the first HV level is set, the HV switches are allowed to pulse for at least one minute while high and low charge values are captured. Once an adequate amount of time has passed and the high and low values are stable, their average is calculated and recorded (see Table 1).

Table 1: ADC Reading at HV Level

HV Level (kV)	+HV Charge	+HV Dis-charge	-HV Charge	-HV Dis-charge
1.0	1031	1103.5	1102	996
1.5	1561	1620.5	1616.5	1518
2.0	2093.5	2129	2126	2029
2.5	2628	2644	2623	2541
2.8	2940.5	2943.5	2921.5	2862.5
3.0	3148.5	3149.5	3126.5	3067
3.5	3662	3644.5	3613	3560.5

A first-order polynomial was then fit to each set of data, as shown in Eq. (1), using MATLAB and holding the power supply voltage level V_{PS} in kV as the independent variable and the ADC reading as the dependent. Results of the four curve fittings are found in Table 2.

$$ADC = aV_{PS} + b \quad (1)$$

Table 2: Charge Curve Fitting

Measure	a	b
+HV Charge	1055	-19.02
+HV Discharge	1018	92.17
-HV Charge	1005	107.2
-HV Discharge	1029	-27.39

Equation (1) is then rearranged to solve for V_{PS} , which will be in kV (see Eq. (2)), and inserted into the capacitance formula, arranged to solve for charge q (see Eq. (3, 4)).

$$V_{PS} = \frac{1}{a}ADC - \frac{b}{a} \quad (2)$$

$$q = CV \quad (3)$$

$$q = C \left(\frac{1}{a}ADC - \frac{b}{a} \right) \quad (4)$$

When C is held equal to the capacitive load (in pF) used during the calibration, in our case 240 pF, and a and b are

set equal to the values in Table 2 for the appropriate input channel, a charge (in nC) can be determined.

Calibration of Voltage ADCs

The chopper monitor's voltage input ADCs, also with one for the positive HV switch and one for the negative, are calibrated in the same fashion. There is no differentiation between charge and discharge as voltage level is constant throughout.

Voltage input ADC readings are taken with the HV power supplies set at the same voltage levels used for charge calibration. A first order polynomial (identical to eq. (1)) was then fit to that data using MATLAB, holding the voltage level in V as the dependent variable and the ADC reading as the dependent (see results in Table 3).

Table 3: Voltage Curve Fitting

Measure	a	b
+HV Voltage	1.005	7814
-HV Voltage	1.013	7772

The equation is then rearranged to solve for V_{PS} (as in Eq. (2)), which will be in V.

IN PRODUCTION

IOC Implementation

The readback and threshold settings for the four charge measurements (+HV charge, +HV discharge, -HV charge, -HV discharge) are implemented as calculation records in the IOC. These records use Eq. (3) and (4) with C held to be the capacitive load used during the calibration (in the earlier example: 240 pF) and a and b are held to be the appropriate values from Table 2. Calculated charge is in nC.

The readback and threshold settings for the two voltage measurements (+HV level, -HV level) are implemented as analog records in the IOC. These records have a slope and offset function built in. Slope is set equal to $1/a$, and offset is set equal to $-b/a$ (see Eq. (2)) using the appropriate values for a and b from Table 3. Calculated voltage is in V.

In both cases, readbacks in physical terms are calculated from ADC integer values while threshold settings in integer values for the FPGA are calculated from user settings input in physical terms.

Functional Checks

Once the chopper monitor is placed in production, with the chopper connected to the HV switches (see Fig. 1) and the calibration constants have been implemented in the IOC the system can be validated. After verifying correct install of the hardware, the HV power supplies are switched on and the chopper is started with a pulse width of 0.6 μ s and frequency of 100 Hz. The positive and negative high voltage, charge, and discharge values are checked with the HV power supplies set at the same seven levels used for calibration (1 kV, 1.5 kV, 2 kV, 2.5 kV, 2.8 kV, 3 kV, and 3.5 kV). Voltage readings should be within 5% of the voltage setting. Charge readings should be within 5% of the calculated charge for the chopper system which

can be calculated using Eq. (3), where C is set equal to the chopper system capacitance of 198 pF and V is set equal to the HV setting in kV.

Calibrating While in Production

If the readings are found to be outside of the 5% allowable deviation the calibration process previously described can be completed with the in-production system. The process is the same with the only major difference being the capacitive load of 198 pF due to the use of the chopper itself during an in-production calibration. ADC readings are taken at the previously mentioned HV levels and new curves are fit. The new calibration values are then input into the IOC along with the calibration capacitance of 198 pF. After the IOC is updated, it is verified by again running the chopper and checking the charge and voltage readings.

CONCLUSION

The methodology for calibration and verification of the chopper monitor has been established to ensure proper functioning of the chopper of the FRIB linac.

Prior to conducting an initial calibration, the integrator circuits of the charge input ADCs were checked for linearity. With them found to be linear, ADC readings are then taken at different points for all input channels and first order polynomials are fit to the six different sets of data. Once those polynomials are implemented on the IOC, monitor data can be read out, and trip thresholds can be input, as physical quantities, which are necessary for error-free and efficient operation.

Once placed in production, the calibration is checked and confirmed to provide readings within 5% of expected value. If they are, sufficiently tight thresholds can be set for detection of chopper disconnect and its inability to function. With the calibration and verification complete, the chopper and chopper monitor are now ready to perform their function as beam duty factor controller beam mitigation device. Regular checks of the chopper monitor calibration with in-production re-calibration when found to be out of range ensure that the chopper monitor voltage and charge readings are accurate, trip thresholds are appropriate, and the chopper can continue to function as needed for the operation of the FRIB.

REFERENCES

- [1] E. Pozdeyev *et al*, "FRIB Front End Construction and Commissioning", in *Proc. IPAC'18*, Vancouver, BC, Canada, Apr. 2018, pp. 58-62.
doi:10.18429/JACoW-IPAC2018-MOZGBF1
- [2] Z. Li *et al*, "FRIB Fast Machine Protection System: Engineering for Distributed Fault Monitoring System and Light Speed Response", in *Proc. LINAC'16*, East Lansing, MI, USA, Sep. 2016, pp. 959-961.
doi:10.18429/JACoW-LINAC2016-THPLR046
- [3] Z. Li *et al*, "FRIB Fast Machine Protection System: Chopper Monitor System Design", in *Proc. LINAC'18*, Beijing, China, Sep. 2018, pp. 336-338.
doi:10.18429/JACoW-LINAC2018-TUP0007

SUPERCONDUCTING MULTIPOLE TRIPLETS MAGNETS COMMISSIONING FOR THE S³ SPECTROMETER AT GANIL / SPIRAL2

M. Aburas^{1,2}, M. Authier², G. Brunet^{1,3}, F. Carville^{1,2}, G. Dillasser², F. Esnault^{1,2}, B. Haize^{1,3}, T. Lefrou^{1,3}, F. Lutton^{1,3}, H. Savajols^{1,3}, M-H. Stodel^{1,3}, G. Tocabens³, A. Wagret-Quatromme^{1,3}

¹Grand Accélérateur National d'Ions Lourds (GANIL), Caen, France

²Commissariat à l'énergie atomique et aux énergies alternatives (CEA-IRFU), Gif-sur-Yvette, France

³Centre National de la Recherche Scientifique (CNRS-IN2P3), Orsay, France

Abstract

The “Super Separator Spectrometer” project S³ is under technical commissioning at the GANIL facility (Caen-France). It is a new research installation designed for fundamental physics experiments with high intensity heavy ions beams produced from the SPIRAL2 linear accelerator. This spectrometer will open new horizons for nuclear physics. The S³ spectrometer is made of seven Superconducting Multipole Triplets (SMT) to guide and focalize the beam and select the particles of interest.

This paper presents SMTs technology and their magnetic, electrical and cryogenic operating characteristics as well as their technical commissioning for the S³ project.

S³ SUPER SEPARATOR SPECTROMETER

S³ Project aims to push the boundaries of nuclear physics by enabling the study of unstable nuclei and super heavy elements, particularly those beyond 104 in the periodic table [1]. The design of the primary target is optimized for fusion-evaporation production. S³ is a two-stage optical structure combining a large acceptance momentum achromat and a high-resolution mass separator (Fig. 1). Each stage includes 2 dipoles and 4 multipoles triplets. These multipoles are superimposed superconducting quadrupoles, sextupoles, octupoles and steerers mounted by 3 singlets in a SMT.

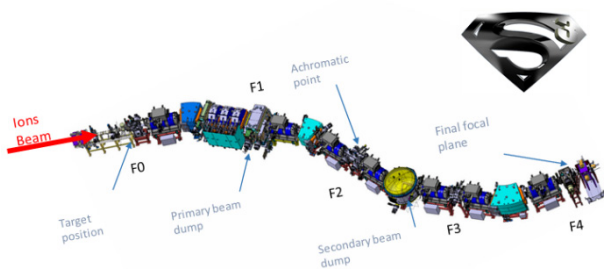


Figure 1: S3 Spectrometer.

Seven SMTs, 3 room temperature Dipoles, 3 open quadrupoles and 1 electric field dipole will allow S³ to achieve high transmission and high resolution in mass to charge ratio for scientists. SMTs (Fig. 2) are superconducting iron-free magnets designed to generate high-purity multipolar magnetic fields [2]. Each triplet is composed of three sets of independent singlets of multipoles assembly: quadrupoles, sextupoles, octupoles and steerers, allowing precise control of the magnetic field (Fig. 3).

SMT



Figure 2: SMT (CMI).

The multipole magnets were developed by AML [3] and their integration into the cryostat was performed by CMI [4].

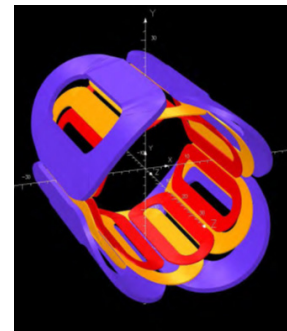


Figure 3: Coils of a singlet.

All the coils are made from NbTi superconducting wire with 5.6 K critical temperature at 2,65 T peak and a critical current of 597 A at 4.2 K. The winding technique is based on Walstrom type coils and all high order harmonics are near zero. The maximum total energy stored in an SMT is 165 kJ (mainly in quads) and the system is designed to discharge quickly and safely in the event of a quench. The top current leads are high-temperature conduction-cooled superconductors with LN₂ (top) and LHe (bottom). These HTS are made with BSCCO (Bi2223) and YBCO tapes for flexibility.

Each SMT is powered by a Power Supply System. A PSS consists of 8 power supplies (PS), a Magnet Safety System and a computer-based control system. There are 8 PS (one 100 A, three 600 A and four 400 A) for the 11 magnet

coils. A wired electrical cabinet ensures adaptation of the load's configuration.

A dedicated HMI enables the user to check the loads configuration, adjust the quench detection parameters and control each Ps of a PSS. A standalone FPGA-based system provides quench detection and triggers rapid load dumping in less than a second

One of the key components for quench protection are the SMT voltage measurement and protection system. This system is referred to as the **ISDAQ** and is located near the SMT. It measures all voltages generated (Copper current leads, HTS current leads and coil voltages) in real time and transmits these informations to the PSS FPGA system.

CRYOGENIC QUALIFICATION

The seven cryostats of S3 use liquid helium (LHe) for superconducting coils and liquid nitrogen (LN₂) for the thermal shield.

These two cryogenic fluids are provided by a cryogenic installation consisting of a Cold Box (Fig. 4), compressor, ORS, atmospheric heater, Dewar of liquid helium, Dewar of liquid nitrogen and a cryogenic transfer line (CTL).



Figure 4: S3 Cold Box (Helial SF from ALAT).

Each SMT has a set of instrumentation—including temperature sensors, liquid helium (LHe) and liquid nitrogen (LN₂) level sensors, pressure transmitters, vacuum gauges, and cryogenic valves—enables the monitoring and supervision of the cryostat's proper operation.

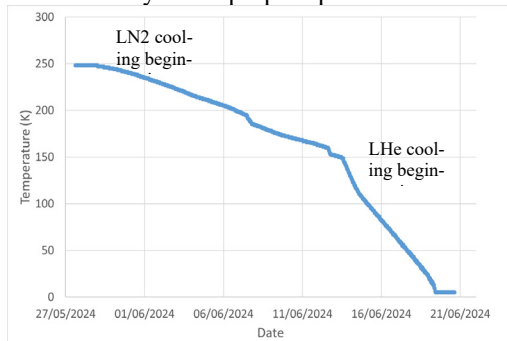


Figure 5: Magnet temperature during the cooling down.

In 2024, a significant milestone was achieved with the successful cool down of six out of the seven SMT (Fig. 5). This operation validated the full functionality of the cryogenic system. (Refrigerator, cryogenic distribution line, cryostats). The cooling down of each SMT consists of two

phases, thermal shield cooling using LN₂ and then the coils cooling with LHe.

To validate the security system, we did a fast dump at nominal current (360 A) (Fig. 6).

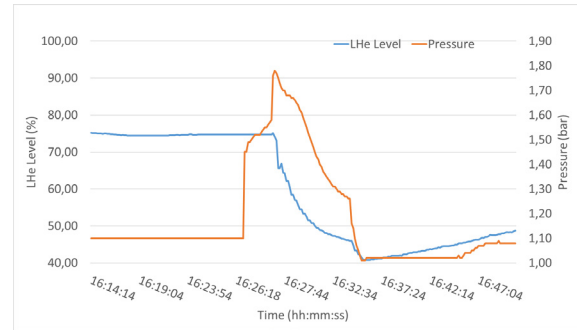


Figure 6: LHe level and tank pressure variations during a fast dump

ELECTRICAL QUALIFICATION

All singlet magnets were independently tested at maximum current by the manufacturer (AML) during manufacture. The tests following their integration into the SMT could not be done out in the factory (CMI) and must therefore be carried out by the S3 project on site. Once cooled to 4 K with liquid helium, each magnet is tested one by one at the maximum current planned by the project. These currents are nearly 70% of the factory maximum tested current (Q @ 350 A; S @ 280 A and O @ 160 A).

During this test, the voltages are measured during linear current ramps in order to check the self-inductors of the coils. The quadrupoles have each a total inductance of 430mH and store each more than 46 kJ. Sextupole and Octupole have respectively 110 mH and 28 mH each for less than 7 kJ and 1 kJ stored energy.

Then, each magnet is electrically tested to verify the proper functioning of the high temperature superconducting (HTS.70 K) current leads and the low temperature superconducting (LTS at 4 K) coils. The current is increased in steps to the maximum value and the voltages across the HTS and the coils as well as the temperature and pressures in the cryostat are measured.

Finally, a dump test is performed on each SMT with all magnets at nominal value to verify proper functioning of all electric parts. The electrical insulation is rechecked following this test to ensure that the dump and the overvoltage have not damaged the SMT.

Electrical tests highlighted current limitations at the LTS wires interconnections between coils at around 300 A. This is due to inadequate cooling at the top of the cryostat. This issue can be resolved by improving the LHe level regulation and modifying the HTS design.

MAGNETIC QUALIFICATION

A characterization of the magnetic field of one SMT magnets was carried out using a specific designed 3D measuring bench (Fig. 7) [5].

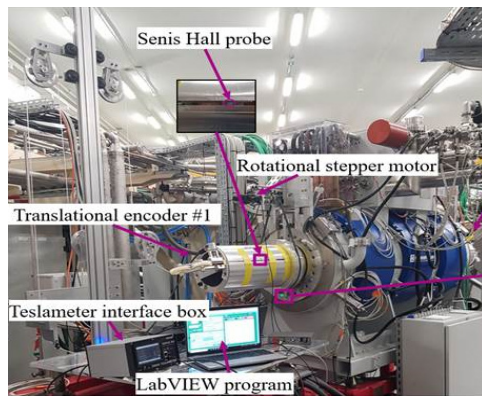


Figure 7: 3D Magnetic bench in S3 room.

These measurements validate the magnetic specifications, the effective magnetic length (Fig. 8), the magnetic field linearity, the field gradient and the real magnetic effect of each magnet to anticipate the polarity wiring of each power supplies for the expected beam optics (Fig. 9).

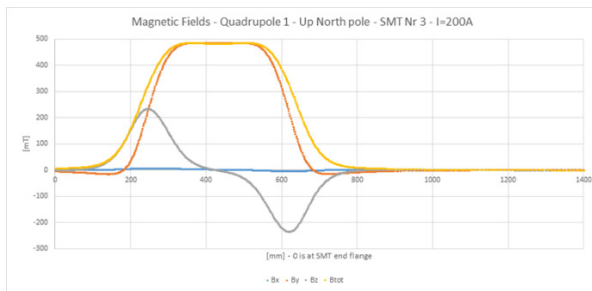


Figure 8: Magnetic length of one quadrupole (x: blue, y: orange, z: grey, total: yellow).

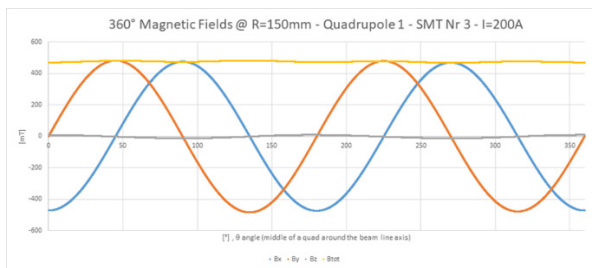


Figure 9: 360° fields of a quadrupole (x: blue, y: orange, z: grey, total: yellow).

The next step will be to achieve the alignment of the **SMTs** by measuring the magnetic field outside the quadrupoles in order to determine their magnetic center. This innovative method will enable the optical adjustment of the SMT installed in S³ to be carried out without opening the vacuum beam line.

IMPROVEMENTS

Following the tests carried out in the first commissioning phase, the following points are or will be subject to modifications:

- Removal of iron yokes to be able to align properly the cold mass.

- New HTS current leads design (CEA IRFU and GANIL), to improve mechanical and temperature behavior (ReBCO only).
- Repair of a low temperature superconducting (LTS) wire inside a SMT, which broke between two quadrupoles (Fig. 10).



Figure 10: Inside the helium enclosure, a view of a singlet wiring.

- Addition of a level gauge and LHe level regulation at the top of cryostat to improve LTS wire cooling and maximum operating current.
- Modification of the voltage tap wiring to make IS-DAQ detect quench of the LTS wire between coils.
- External magnetic mapper being developed for the SMTs alignment (Fig. 11). The magnetic alignment of the SMTs will be carried out directly on site in their final position with the entire spectrometer installed.

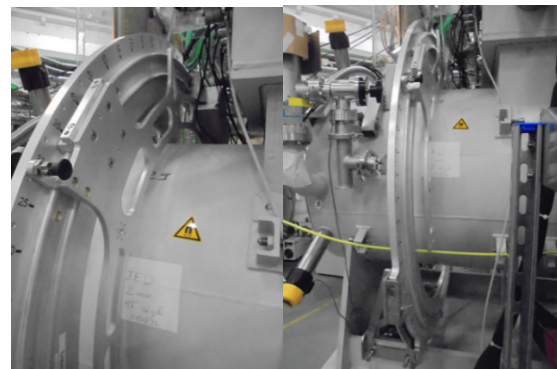


Figure 11: External magnetic mapper.

CONCLUSION

SMTs are very compact superconducting magnets, which has generated strong constraints on manufacturing processes and technical choices. Their design will allow them to achieve high optical beam performance.

The testing phase showed encouraging results and some problems which are being corrected in order to begin the optical commissioning phase with beam of S3 at the end of 2025.

REFERENCES

- [1] F. Déchery *et al.*, "The Super Separator Spectrometer S3 and the associated detection systems: SIRIUS & LEB-REGLIS3," *Nucl. Instrum. Methods Phys. Res. B*, vol. 376, pp. 125–130, Jun. 2016.
doi: 10.1016/j.nimb.2016.02.036

- [2] M. Aburas *et al.*, “Superconducting multipole triplets for the Super Separator Spectrometer,” *IEEE Trans. Appl. Supercond.*, vol. 34, no. 3, pp. 1–4, May 2024.
doi:10.1109/tasc.2024.3356434
- [3] AML, Advanced Magnet Lab,
https://mitusmagnets.com/.
- [4] CI. Cryomagnetics, Inc, https://cryomagnetics.com
- [5] A. Esper *et al.*, “Superconducting multipole triplet field measurements,” *J. Phys. Conf. Ser.*, vol. 2687, no. 7, p. 072027, Jan. 2024.
doi:10.1088/1742-6596/2687/7/072027

STATUS OF HIGH PERFORMANCE ECR ION SOURCES: ACHIEVEMENTS AND PERSPECTIVES

L. Sun^{1, 2†}, H. W. Zhao^{1, 2}

¹State Key Laboratory of Heavy Ion Science and Technology, Institute of Modern Physics,
Chinese Academy of Sciences, Lanzhou, China

²School of Nuclear Science and Technology, University of Chinese Academy of Sciences,
Beijing, China

Abstract

The demand for high-intensity (0.5–1.0 emA) highly charged heavy ion beams continues to grow among next-generation heavy ion accelerator facilities worldwide, yet their production remains a significant challenge in the field. Electron Cyclotron Resonance (ECR) ion sources, recognized as the most powerful technology for generating such beams, have been widely adopted by major heavy ion accelerator facilities globally, driving continuous advancements in this domain. Despite more than five decades of development since the first ECR ion source prototype was introduced, these sources remain at the forefront of high-charge-state and high-intensity ion beam production. This paper reviews the latest advancements in high-performance ECR ion sources, focusing on four key areas: (1) the development of new ion source designs, (2) high-performance operational achievements, (3) emerging technologies in the field, and (4) future prospects for delivering high-intensity beams for heavy ion accelerators.

INTRODUCTION

Heavy ion science plays an indispensable role in both fundamental research and societal applications. Heavy ion beams have served as essential tools for advancing our understanding of nuclear structure, synthesizing over a thousand new isotopes, and discovering dozens of new elements. Beyond fundamental science, heavy ion technology has significantly impacted industry and medicine. For instance, heavy-ion therapy systems worldwide have demonstrated remarkable efficacy in treating cancer, while nuclear track membrane [1] production—a rapidly growing industry—relies heavily on heavy ion accelerators. Additionally, single-event effect (SEE) studies enable critical advancements in space exploration [2]. To generate energetic heavy ion beams, heavy ion accelerators have undergone continuous development over the past 80 years. Among the key requirements for efficient acceleration is the production of highly charged ion beams. This demand has driven the invention of various ion sources, including Electron Cyclotron Resonance (ECR) ion sources, Electron Beam Ion Sources (EBIS), and Laser Ion Sources (LIS). Notably, ECR ion sources have proven unparalleled in delivering high-current, high-charge-state ion beams, solidifying their dominance in the field.

The ECR ion source was first proposed and prototyped by Richard Geller in the 1970s [3]. Over the past five

decades, hundreds of such devices have been deployed worldwide, serving both scientific facilities and practical applications. The growing demand for high-performance heavy ion beams—particularly in power frontier projects like superconducting radiofrequency (SRF) linacs (e.g., FRIB) and intensity frontier programs such as synchrotrons (e.g., HIAF)—has driven the need for more advanced ECR ion sources. An ECR ion source operates by generating plasma through microwave heating within a min-B magnetic confinement structure. The interaction between microwave radiation and the magnetic field configuration critically determines the source's performance. Over the years, empirical scaling laws have been established to summarize the fundamental principles governing ECR ion sources, providing essential guidance for their continued development.

Guided by scaling laws, achieving high-performance ECR ion sources necessitates operation in high magnetic field (high-B) and high microwave frequency regimes. Superconducting ECR ion sources, which leverage the strong magnetic fields generated by highly excited superconducting coils, have emerged as the most promising solution for producing high-performance, highly charged ion beams. The first prototype of such a system, the SERSE ion source [4], was jointly developed by LNS-INFN and CEA-Grenoble in the late 1990s. Subsequently, modern high-performance superconducting ECR ion sources optimized for 24–28 GHz microwave frequencies were pioneered—most notably by the VENUS source (LBNL, 2002) [5], and the SECAL source (IMP, 2005) that introduced a novel reserved magnetic configuration [6]. Further advancements were achieved with the SuSI source (MSU) [7] and the SCECRIS source (RIKEN) [8], diversifying the landscape of high-performance ECR ion sources. Despite these successes, challenges persist in extending ECR ion sources to high-power, high-current heavy-ion beam applications. This paper reports recent progress in addressing these challenges and discusses future perspectives for ECR ion source development.

NEW HIGH PERFORMANCE ECR ION SOURCES

In recent years, numerous high-performance ECR ion sources have been proposed, developed, or commissioned for routine operation. These ion sources—primarily designed for new heavy-ion accelerator facilities or upgrades of existing accelerator systems—are universally optimized to deliver high-charge-state heavy-ion beams with exceptional intensity. Their development has become critical to

[†]sunlt@impcas.ac.cn

advancing the capabilities of modern accelerator facilities, where they serve as indispensable workhorses for beam production.

The HPECR (High-Power Electron Cyclotron Resonance) ion source [9] for the FRIB was commissioned to deliver highly charged heavy-ion beams for the SRF linac. Based on the VENUS ion source design, the HPECR is also a superconducting ECR ion source optimized for operation at 28 GHz. Installed at the FRIB front end in 2023, this ion source, when integrated with an inductive heating oven, has demonstrated the capability to produce ~ 100 eμA of U^{35+} beam current, with 30 eμA routinely delivered for stable operation. This performance enabled FRIB's recent world record in uranium beam acceleration, achieving 20 kW beam power. The synthesis of superheavy elements (SHE)—particularly new elements in the 8th period of the periodic table—has become a major focus in nuclear physics, with leading laboratories such as RIKEN (Japan), IMP (China), LBNL (USA), and FLNR (Russia) engaged in a highly competitive research effort. RIKEN has successfully deployed a 28 GHz superconducting ECR ion source (SECRIS), a duplicate of their existing system, which now operates routinely, delivering over 150 eμA of $^{51}V^{13+}$ for SHE experiments [10]. Similarly, at IMP, SECRAL-III—a successor to SECRAL-II—has recently been installed for the CAFE2 SHE facility [11]. Additionally, FLNR is developing a 28 GHz superconducting ECR ion source for the DC-280 cyclotron upgrade, intended to serve as a second injector for uranium beam acceleration. In parallel, the NEWGAIN project [12] at GANIL aims to enhance SPIRAL2's capability in accelerating heavy-ion beams up to uranium. A key component of this initiative is the ASTERICS ion source, currently under development. Designed with a 180-mm-diameter plasma chamber and optimized for high magnetic fields, ASTERICS is expected to support routine 28 GHz operation [13], further advancing SPIRAL2 heavy-ion beam performance.

At JYFL, an 18 GHz ECR ion source HIISI [14] has been developed, utilizing high mirror fields and strong radial fields, demonstrating the capability to deliver >10 nA of Xe^{44+} for the K130 cyclotron. Owing to its high magnetic fields, large-diameter ($\varnothing 100$ mm) plasma chamber, and multi-frequency microwave heating, this source achieves performance comparable to state-of-the-art superconducting ECR ion sources operating at the same frequency. The hybrid superconducting ECR ion sources, which combine superconducting mirror coils and a permanent magnet hexapole, represent an advanced approach to generating high magnetic fields. Recent implementations of this technology include the AISHa source at INFN-LNS [15] and HECRAL-C at IMP. Both sources employ an LHe-free superconducting magnet design, enhancing their practicality for long-term operation. HECRAL-C, recently commissioned as a linac injector for a heavy-ion therapy facility, has demonstrated stable performance, delivering >1.3 eμA of dc C^{4+} ion beams for medical applications.

RESEARCH TOWARDS CHALLENGES

When operating at higher frequencies, ECR ion sources require stronger magnetic fields, increased microwave power, and larger plasma chamber volumes to achieve high-density, stable plasma and superior beam performance. However, these advancements introduce new technical challenges, as highlighted in the review talk at HIAT25 [16]. A decade later, many of these challenges remain unresolved. Nevertheless, the most critical issues have made good progresses that include:

- Efficient microwave heating
- Localized overheating of the plasma chamber due to plasma losses under high microwave power.
- The production of ion beams from refractory metals, such as uranium, which presents significant material and operational difficulties.

Microwave Heating Study

The issue of microwave heating efficiency was first highlighted by D. Hitz in 2006 when comparing the O^{6+} beam current dependence on microwave power injection at 18 GHz and 28 GHz [17]. This question remained unresolved until 2013, when C. Lyneis conducted an experiment using a snake-mode converter for HE_{11} -mode microwave injection, evaluating its effectiveness against the conventional over-sized TE_{01} mode. However, this study did not yield conclusive results [18]. A year later, a similar experiment was performed at IMP using a tapered waveguide. Initial findings demonstrated that the method of microwave introduction into the plasma chamber significantly influences plasma behaviour, particularly in high-power ECR plasma heating [19]. This discovery led to the development of the Vlasov microwave launcher for ECR ion sources [20]. Although the first Vlasov launcher lacks axial position adjustability, it exhibits a clear impact on highly charged ion production. Subsequent validation with an online movable Vlasov launcher confirmed that microwave heating efficiency strongly depends on the launching scheme, and optimized highly charged ion yields can be achieved through adjustable launcher positioning [21].

These results provide new insights into the plasma heating mechanisms in highly charged ECR ion sources potentially guiding future research directions.

High Power Plasma Chamber

In a traditional ECR ion source plasma chamber, the primary concern is to manage the heat transferred from the plasma to the inner wall. This is crucial to prevent the demagnetization of the permanent magnet (in 2nd ECR ion sources) or to avoid strong instability and outgassing caused by temperature rise. Before the 3rd generation ion source reached its performance limit, the typical microwave power during routine operation was around 3-5 kW. As a result, there were very few reports of plasma chamber damage caused by hot plasma. In an ECR ion source, the hot electrons in the plasma are strongly magnetized and confined. The mechanism of ECR plasma confinement and the min - B structure of the three - dimensional magnetic

field can lead to localized overheating on the plasma chamber surface [22]. Once the plasma conditions exceed a certain threshold, this overheating can cause a tiny hole and subsequent water leakage. In practice, the six sextupole coils are not perfectly aligned, and there are obvious concentricity errors between the plasma chamber and the sextupole fields, which exacerbate the situation. Localized overheating can boil the cooling water flowing through the plasma chamber. When stationary bubbles form, the wall dries out, and the heat - exchange coefficient decreases (since there is no direct cooling from the water). This causes the wall temperature to rise rapidly, potentially leading to melting. Subsequently, under the high pressure of the cooling water, a hole can form. A rough estimate shows that for a third - generation ECR ion source, the localized heat flux onto the chamber surface can reach 1 MW/m² per kW of microwave heating. The damage to the plasma chamber due to localized overheating is not a long - term process but occurs almost instantaneously.

Recently, a novel plasma chamber has been designed, fabricated, and used in routine high - power operations. Based on the concept of a micro - channel structure, by optimizing the local structure where a burnt hole is likely to occur, a good balance is achieved among the water flow rate, heat - exchange efficiency, and water flow distribution. This has enabled the SECRAI-II ion source to operate safely at a peak microwave power of 12 kW during performance tests and routinely at 8 kW for the production of intense highly charged ion beams for accelerators. With this issue resolved, the third - generation ECR ion source can be safely operated at power levels up to 10 kW, which is sufficient for most applications.

High Temperature Oven

The production of intense ion beams using an ECR ion source requires a reliable and stable gas-feeding system. Since most elements in nature exist in solid states, it is essential to evaporate the material and introduce it into the plasma. Traditionally, resistor ovens, sputtering, and MIVOC methods are commonly employed for the production of metallic ion beams. However, for refractory materials, especially those required for SHE research or large-scale facilities, such as vanadium, titanium, chromium, and uranium, high - temperature ovens are needed. These ovens must be durable at operating temperatures up to 2000°C. Given that the oven is exposed to complex operating conditions involving high magnetic fields, high operating temperatures, and high electrical currents, traditional resistor ovens are often damaged by strong Lorentz forces.

At IMP, a high-temperature oven based on the inductive heating concept has been developed and is now in routine operation for producing refractory metallic ion beams. Since its validation in 2019 [23], the total operating time of these inductive heating ovens at IMP have exceeded 20,000 beam hours. This technology has proven to be reliable and easy to handle when used with the 3rd generation ECR ion source for the production of intense refractory ion beams. Recently, a similar oven design has been adopted for the routine operation of the HPECR ion source to

produce intense U³⁵⁺ beam. This has enabled the high-power acceleration of uranium beams in FRIB SRF linac. At LBNL, a vertically-positioned susceptor inductive heating oven has also been successfully developed [24]. Its long - term operation to deliver a >100 eμA ⁵⁰Ti¹²⁺ beam for SHE exploration using the 88-inch cyclotron has verified its durability. At RIKEN, through careful structural design and refinement of the oven's structural materials, an oven based on the traditional resistor heating design has also been shown to be durable for high - temperature operation [25]. This oven design has been routinely used with RIKEN's ion sources to deliver >110 eμA U³⁵⁺ and ~150 eμA ⁵¹V¹³⁺ beams for their heavy-ion beam accelerators.

In general, the challenge of producing intense refractory ion beams using the third-generation ECR ion source is no longer pressing today. The ECR ion source community has found solutions to produce 500 eμA U³⁵⁺ beams.

4TH GENERATION ECR ION SOURCE

In the development of (ECR) ion sources, the frequency-scaling principle remains applicable. To develop high-performance ECR ion sources that outperform the current state-of-the-art high-charge-state machines, the development of next-generation machines is imperative. 3rd generation ECR ion sources typically operate at frequencies ranging from 18 to 28 GHz. Consequently, the 4th generation ECR ion sources are anticipated to operate at frequencies approximately twice that of the existing ones, specifically in the range of 40 to 56 GHz. Correspondingly, the peak magnetic fields inside the plasma chamber should reach as high as B_{inj}>5.0 T and B_r>2.8 T. These field strengths are unattainable with the conventional magnets used in 3rd generation ECR ion sources. There are two viable approaches (Fig. 1) for designing the magnets of the fourth - generation ECR ion sources. One is the conventional structure with solenoids on the outside and a sextupole on the inside, which employs Nb₃Sn superconductors. The other is an unconventional structure using NbTi superconductors that can fully utilize the generated magnetic flux. In this non-conventional design, the sextupole coil generates a solenoid moment inside the plasma chamber.

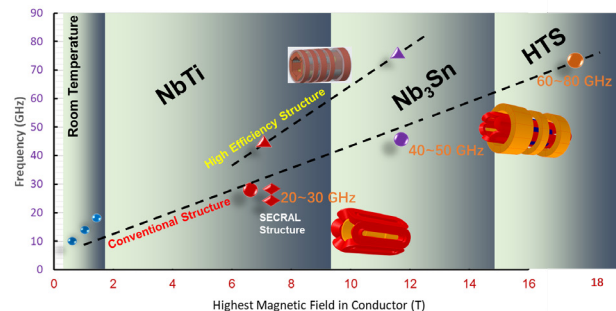


Figure 1: The viable approaches towards next generation ECR ion source magnet.

At IMP, the prototype ion source FEER has recently been developed [26]. It is equipped with a NbTi sextupole and four Nb₃Sn solenoids, achieving a B_{inj} of approximately 4.5 T and a B_r of approximately 2.7 T. The first

plasma, heated by 28+45 GHz microwaves, has successfully produced intense ion beams, such as 360 eμA of Bi³⁵⁺. The development of a full Nb₃Sn magnet is still in progress. As a backup ion source for FRIB, a hybrid superconducting ECR ion source magnet using a Nb₃Sn sextupole and NbTi solenoids is under development at LBNL [27]. Meanwhile, LBNL is fabricating a novel-structured magnet that uses only NbTi superconductors to reach the magnetic fields required for 45 GHz operation of an ion source called MARS-D [28]

We can anticipate that there will be at least two 4th generation ECR ion sources available in the laboratory for the production of highly charged ion beams in 5 years. However, more challenges may be encountered during the performance optimization process.

PERSPECTIVES

In recent years, with the advancement of research on ECR ion sources, researchers have gained new insights and made novel discoveries. These aspects were either not addressed or overlooked during low-power operation previously.

Quench Protection and Operation Safety

The existing high-performance ECR ion sources predominantly employ high - field superconducting magnets. The typical stored energy of the cold mass ranges from 0.6 to 0.9 MJ, presenting relatively few challenges in quench protection. However, the next-generation ECR ion sources utilizing Nb₃Sn magnets face severe challenges in quench protection. One crucial issue is the high stored energy. For example, the 45 GHz FEER has a total stored energy of 1.6 MJ. Moreover, the quench propagation speed of the Nb₃Sn superconductor is ten times slower than that of the NbTi superconductor. This slow propagation speed makes it extremely challenging to mitigate the risk of excessively high temperatures at the quench point. Furthermore, the intense flux jump observed in the FEER magnet indicates that this problem may occur throughout the entire magnet energizing process [29]. It can interfere with the quench detection system and may trigger either false or real quenches during the ion source tuning process aimed at performance optimization.

Transient Instability with Intense Beams

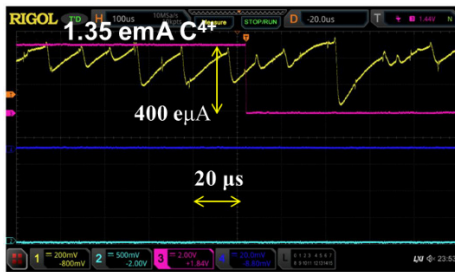


Figure 2: Transient instability with ECR ion source.

Intense heavy-ion beams are predominantly generated for injection into high - current linacs or synchrotron ring accelerators. We have detected strong transient instability

in the delivered high - intensity ion beams. The typical duration of this instability ranges from 10 to 100 μs, which lies outside the well-known kinetic instability domain. This type of instability shows no obvious periodic characteristics (Fig. 2). However, we have observed a maximum transient drop of up to 50% in the beam intensity, followed by a recovery within a time frame of 10 to 100 μs. This phenomenon may have an impact on the operating current load effect of the linac and the bunch - to - bunch stability of the synchrotron. Further investigation is still required to fully understand this instability.

Beam Quality of Intense Beams

Accelerating a CW heavy-ion beam of high charge states at the 1 emA level remains a global challenge. The ion source must be able to generate a high-intensity heavy-ion beam reaching several emA, and the beam quality must be precisely controlled for injection into downstream accelerators. In recent high-intensity acceleration experiments using LEAF [30] and the warm front-end of HIAF, we discovered that the transmission efficiency of a high-intensity O⁶⁺ beam drops rapidly when the current exceeds 500 eμA. This decline is attributed to the space-charge effect and the degradation of beam quality during transmission. The acceleration of a CW proton beam up to 10 emA has already been achieved. However, the injected proton beam is carefully controlled to ensure excellent beam quality. In contrast, for heavy-ion beams produced by ECR ion sources, the ion distribution in the phase space is dispersed. This makes it difficult to achieve a good match for downstream acceleration and transmission, necessitating novel concepts and innovative solutions.

Before this issue can be resolved, to achieve the acceleration of a 1 emA U³⁵⁺ beam, the ion source is expected to produce approximately 2.0 emA of U³⁵⁺. To meet the 400 kW power goal of FRIB, the ion source may need to extract more than 600 eμA, or even up to 1 emA, of a CW U³⁵⁺ beam.

New Techniques for ECR Ion Sources

It should be noted that, considering the existing techniques associated with 3rd generation ECR ion sources, there remains room for further performance enhancement. However, this will require innovative concepts and novel techniques. With a deeper understanding of ECR plasma sustained by microwave heating, breakthroughs may be achieved in the fine-tuning or manipulation of the interaction between microwaves and the plasma. These breakthroughs could lead to the optimization of the control of the Electron Energy Distribution Function (EEDF) to generate a greater quantity of the desired ions.

In recent years, AI for science has been advancing at a rapid pace. ECR researchers are leveraging machine learning to enable ECR ion sources to operate more intelligently [31, 32]. Although it will take some time for exploration before it can be put into practical operation, it is certain that this approach will enhance the online operation efficiency and quality for heavy ion accelerators. Nevertheless, a long-term development plan needs to be formulated.

CONCLUSION

This paper offers a concise overview of the recent advancements in ECR ion sources, specifically focusing on their high-performance operation for accelerators. It encompasses the development of new ion sources, as well as novel technologies and discoveries. However, it should be noted that some significant progress, particularly in the areas of ion source experiments and theoretical studies, has not been covered in this paper. In recent years, the ECR ion source community has made remarkable headway in the field of high-performance ECR ion sources. Their contributions have been fundamental to the progress of heavy-ion accelerator science and the associated physics research. These achievements not only lay a solid foundation for future research but also open up new possibilities for the development of more advanced accelerator technologies and applications. Overall, while this paper provides a useful starting point for understanding the current state of ECR ion sources, further in-depth research and exploration are needed to fully exploit the potential of these sources in the context of accelerator-based applications.

ACKNOWLEDGEMENT

This work was supported by the National Natural Science Foundation of China (Grant Nos. 11427904, 12025506), and the Scientific Instrument Developing Project of the Chinese Academy of Sciences, Grant No. GJJSTD20210007.

REFERENCES

- [1] V. I. Kuznetsov, A. Yu. Didyk, and P. Yu. Apel, "Production and investigation of nuclear track membranes at JINR", *Int. J. Radiat. Appl. Instrum. Part D*, vol. 19, no. 1–4, pp. 919–924, Jan. 1991. doi:10.1016/1359-0189(91)90342-f
- [2] A. Dufour *et al.*, "Heavy-ion and proton Single Event Effect (SEE) characterization of 7nm FinFET AMD Versal™", in *2023 23rd European Conf. on Radiation and Its Effects on Components and Systems (RADECS)*, Sep. 2023, pp. 1–8. doi:10.1109/radecs59069.2023.10767067
- [3] R. Geller, "Highly charged ECR ion sources: Summary and comments (invited)", *Rev. Sci. Instrum.*, vol. 61, no. 1, pp. 659–661, Jan. 1990. doi:10.1063/1.1141898
- [4] G. Ciavola, S. Gammino, P. Briand, G. Melin, and P. Seyfert, "The SERSE project", *Rev. Sci. Instrum.*, vol. 65, no. 4, pp. 1057–1059, Apr. 1994. doi:10.1063/1.1145060
- [5] D. Leitner, "First results of the superconducting ECR ion source VENUS with 28 GHz", in *Electron Cyclotron Resonance Ion Sources: 16th Int. Workshop on ECR Ion Sources (ECRIS'04)*, 2005, pp. 3–9. doi:10.1063/1.1893356
- [6] H. W. Zhao *et al.*, "Advanced superconducting electron cyclotron resonance ion source SECRAL: Design, construction, and the first test result", *Rev. Sci. Instrum.*, vol. 77, no. 3, Mar. 2006. doi:10.1063/1.2149307
- [7] G. Machicoane, D. Cole and P. Zavodszky, "Commissioning results of the 18GHz fully superconducting ECR ion source SUSI", in *Proc. of ECRIS08*, Chicago, IL USA Sept. 2008.
- [8] T. Nakagawa, "28 GHz SC-ECRIS at RIBF", in *Proc. Cyclotrons'10*, Lanzhou, China, Sep. 2010, paper WEM1C1002, pp. 321–326.
- [9] H. Ren *et al.*, "Development and status of the FRIB 28 GHz SC ECRIS", *J. Phys. Conf. Ser.*, vol. 2244, no. 1, p. 012008, Apr. 2022. doi:10.1088/1742-6596/2244/1/012008
- [10] T. Nakagawa *et al.*, "Development of RIKEN 28 GHz SC-ECRISs for synthesizing super-heavy elements", in *Proc. HIAT'18*, Lanzhou, China, Oct. 2018, pp. 77–81. doi:10.18429/JACoW-HIAT2018-TUZA01
- [11] W. Lu *et al.*, "Production of highly charged metallic ion beams with a room temperature ECR ion source-LECR5 for the CAFE2 facility at IMP", *Nucl. Instrum. Methods Phys. Res., Sect. A*, vol. 1062, p. 169207, May 2024. doi:10.1016/j.nima.2024.169207
- [12] M. Moscatello *et al.*, "NEWGAIN project at GANIL-SPIRAL 2: design of the new heavy ion injector for the superconducting linac", in *Proc. IPAC'23*, Venice, Italy, May 2023, pp. 1765–1767. doi:10.18429/JACoW-IPAC2023-TUPA193
- [13] T. Thuillier *et al.*, "ASTERICS, a new 28 GHz electron cyclotron resonance ion source for the SPIRAL2 accelerator", *J. Phys. Conf. Ser.*, vol. 2743, no. 1, p. 012059, May 2024. doi:10.1088/1742-6596/2743/1/012059
- [14] H. Koivisto *et al.*, "A new 18 GHz room temperature electron cyclotron resonance ion source for highly charged ion beams", *Rev. Sci. Instrum.*, vol. 91, no. 2, Feb. 2020. doi:10.1063/1.5128860
- [15] G. Castro *et al.*, "The AISHa ion source at INFN-LNS", *J. Phys. Conf. Ser.*, vol. 2244, no. 1, p. 012025, Apr. 2022. doi:10.1088/1742-6596/2244/1/012025
- [16] L. T. Sun *et al.*, "Challenges for the Next Generation ECRIS", in *Proc. HIAT'15*, Yokohama, Japan, Sep. 2015, paper THM1101, pp. 268–273
- [17] D. Hitz, "Recent Progress in High Frequency Electron Cyclotron Resonance Ion Sources," in *Advances in Imaging and Electron Physics*, 2006, pp. 1–164. doi:10.1016/s1076-5670(06)44001-5
- [18] C. Lynceis *et al.*, "A mode converter to generate a Gaussian-like mode for injection into the VENUS electron cyclotron resonance ion source", *Rev. Sci. Instrum.*, vol. 85, no. 2, Dec. 2013. doi:10.1063/1.4832064
- [19] L. Sun *et al.*, "Advancement of highly charged ion beam production by superconducting ECR ion source SECRAL (invited)", *Rev. Sci. Instrum.*, vol. 87, no. 2, Oct. 2015. doi:10.1063/1.4933123
- [20] J. W. Guo *et al.*, "A new microwave coupling scheme for high intensity highly charged ion beam production by high power 24–28 GHz SECRAL ion source", *Rev. Sci. Instrum.*, vol. 91, no. 1, Jan. 2020. doi:10.1063/1.5131101
- [21] X. Wang *et al.*, "Demonstration of high-efficiency microwave heating producing record highly charged xenon ion beams with superconducting electron cyclotron resonance ion sources", *Phys. Rev. Accel. Beams*, vol. 27, no. 8, Aug.

2024.

[doi:10.1103/physrevaccelbeams.27.083401](https://doi.org/10.1103/physrevaccelbeams.27.083401)

- [22] T. Thuillier *et al.*, “Investigation on the electron flux to the wall in the VENUS ion source”, *Rev. Sci. Instrum.*, vol. 87, no. 2, Dec. 2015. [doi:10.1063/1.4935989](https://doi.org/10.1063/1.4935989)
- [23] W. Lu *et al.*, “Production of intense uranium beams with inductive heating oven at Institute of Modern Physics”, *Rev. Sci. Instrum.*, vol. 90, no. 11, Nov. 2019. [doi:10.1063/1.5128419](https://doi.org/10.1063/1.5128419)
- [24] D. Todd, J. Benitez, and L. Phair, “A novel inductive oven design to produce high-current, moderate mass ion beams for superheavy element searches”, *Nucl. Instrum. Methods Phys. Res., Sect. A*, vol. 1072, p. 170183, Mar. 2025. [doi:10.1016/j.nima.2024.170183](https://doi.org/10.1016/j.nima.2024.170183)
- [25] J. Ohnishi, Y. Higurashi, and T. Nakagawa, “Progress in high-temperature oven development for 28 GHz electron cyclotron resonance ion source”, *Rev. Sci. Instrum.*, vol. 87, no. 2, Oct. 2015. [doi:10.1063/1.4933030](https://doi.org/10.1063/1.4933030)
- [26] L. Sun *et al.*, “The superconducting magnet development for the next generation ECR ion source on LEAF”, *Appl. Supercond.*, vol. 13, p. 100151, Mar. 2025. [doi:10.1016/j.supcon.2025.100151](https://doi.org/10.1016/j.supcon.2025.100151)
- [27] T. Shen *et al.*, “Design and development of a 28 GHz Nb₃Sn ECR ion source superconducting magnet”, *IEEE Trans. Appl. Supercond.*, vol. 34, no. 5, pp. 1–5, Aug. 2024. [doi:10.1109/tasc.2024.3358767](https://doi.org/10.1109/tasc.2024.3358767)
- [28] M. Juchno *et al.*, “Shell-based support structure for the 45 GHz ECR ion source MARS-D”, *IEEE Trans. Appl. Supercond.*, vol. 32, no. 6, pp. 1–5, Sep. 2022. [doi:10.1109/tasc.2022.3158375](https://doi.org/10.1109/tasc.2022.3158375)
- [29] L. Sun *et al.*, “Development of a 1/2-length prototype high field Nb₃Sn magnet for the 4th generation ECR ion source”, *Acta Mech. Sin.*, vol. 40, no. 4, Dec. 2023. [doi:10.1007/s10409-023-23376-x](https://doi.org/10.1007/s10409-023-23376-x)
- [30] Y. Yang *et al.*, “Commissioning and operation of LEAF with high intensity heavy ion beams”, presented at HIAT25, East Lansing, Michigan, United States, Jun. 2025, paper TUC01, this conference.
- [31] A. Kireeff, L. Phair, M. J. Regis, M. Salathe, and D. S. Todd, “Utilizing python to prepare the VENUS ion source for machine learning”, in *Proc. NAPAC'22*, Albuquerque, NM, USA, Aug. 2022, pp. 151-153. [doi:10.18429/JACoW-NAPAC2022-MOPA44](https://doi.org/10.18429/JACoW-NAPAC2022-MOPA44)
- [32] Y. Morita *et al.*, “Developments of control system for ion source using machine learning”, *J. Phys. Conf. Ser.*, vol. 2244, no. 1, p. 012105, Apr. 2022. [doi:10.1088/1742-6596/2244/1/012105](https://doi.org/10.1088/1742-6596/2244/1/012105)

MEASUREMENT OF FORWARD-DIRECTED NEUTRONS GENERATED BY AN INVERSE KINEMATIC REACTION USING INCIDENT ${}^7\text{Li}^{3+}$ BEAM

T. Sakabe^{1,†}, A. Cannavo¹, G. Ceccio⁵, M. H. Gamage², S. Ikeda¹, T. Kanesue¹, J. Kohl⁶,
M. Okamura^{1,3}, B. Schmitz⁶, A. Smushkin⁶, K. Takahashi⁴, P. Zitzmann⁶

¹Brookhaven National Laboratory, Upton, New York, USA

²Columbia University, New York City, New York, USA

³Institute of Science Tokyo, Tokyo, Japan

⁴Nagaoka University of Technology, Niigata, Japan

⁵Nuclear Physics Institute of the Czech Academy of Science, Husinec, Czech Republic

⁶Technische Universität Darmstadt, Darmstadt, Germany

Abstract

We are developing an accelerator-based neutron source using the inverse kinematic reaction between an energetic lithium-ion and a proton target. This reaction can achieve a naturally collimated neutron beam. Our group has proposed a compact neutron source with an intense lithium-ion beam, which can supply a converged neutron flux. The present study aims to investigate the angular distribution of neutrons produced by the inverse kinematic reaction. The neutron measurement experiment was conducted by making a collision between a lithium-ion and a polypropylene target at the Tandem Van de Graaf accelerator at BNL. Throughout the experiment, a large concentration of neutrons was observed in the forward direction, which agrees well with the feature of the inverse kinematic reaction.

INTRODUCTION

Neutron techniques are used in many fields due to their unique properties. They support non-destructive tests for the structure [1], composition [2], and imaging [3]. Neutrons also help produce isotopes by activating some elements [4, 5]. Various neutron sources are used depending on neutron beam requirements. Examples include radioactive isotopes, reactors, and accelerators. Each neutron method is designed to fit its specific application. Compact accelerator sources are gaining attention these days because they are easier to use and cheaper than large-scale facilities. Most traditional sources use proton beams with lithium or beryllium targets. However, such reactions emit neutrons in all directions. Many neutrons are wasted, and unwanted radiation occurs near the target. To resolve this issue, a neutron source using the inverse kinematic reactions was proposed [6, 7].

In the inverse kinematic scheme, a lithium beam is used instead of a proton beam. Neutrons can be focused in the forward direction thanks to the momentum of the heavier lithium beam compared to the proton target. This forward beam forms a narrow cone of neutrons. The cone becomes sharper near the reaction threshold energy (13.098 MeV [7]). It also increases neutron flux in the forward direction. As a result, radiation in other directions is reduced. This can lower the shielding needs of the facility. Hydrogen-rich targets like plastics or metal hydrides are suitable. One major limitation of the inverse kinematic scheme is the lithium

ion beam current. Conventional accelerators typically reach peak currents of up to 100 μA , limiting neutron applications. Due to this limitation, prior studies on the inverse kinematic scheme are limited.

A compact accelerator-based neutron source utilizing an intense lithium-ion beam has been developed by our group at Brookhaven National Laboratory (BNL) to overcome conventional limitations. A peak pulsed current of 35 mA for the ${}^7\text{Li}^{3+}$ ion current was achieved using a laser ion source [8]. This advancement offers the potential for broadening the scope of neutron applications with a lithium-beam-driven neutron source. As the achieved beam energy is 1.43 MeV and remains below the reaction threshold, further post-acceleration is required. The system development is currently underway.

This study aims to experimentally characterize the angular distribution of neutrons from the inverse kinematic reaction over a range of 0 to 135 degrees for future applications. For this purpose, the Tandem Van de Graaf accelerator at BNL [9] was used to utilize an energetic lithium-ion beam. The accelerator system realized collisions between lithium ions and protons in a polypropylene target that was installed at the end of the beam line. The liquid scintillators were placed around the target chamber to investigate the angular distribution of neutrons. A shadow cone [10, 11], which was made of a low-carbon steel and borated polyethylene, was used to evaluate the contribution of scattering neutrons to the liquid scintillator measurement. The present paper reports the angular distribution of neutrons from the inverse kinematic reaction based on the measurement data by the liquid scintillators.

METHODOLOGY

Table 1 shows the experimental conditions. An incident ${}^7\text{Li}^{3+}$ ion beam was provided by the Tandem Van de Graaf accelerator at BNL. A polypropylene target was installed at the end of the beam line. A belt-conveyor-type of polypropylene target was adopted for the present experiment, as shown in Fig.1. The polypropylene roll was rotated during the beam operation to use the fresh surface of the target continuously for the collision.

The liquid scintillators (BC-501) were located around the target chamber as shown in Fig. 2. The angles of the scintillators were 0, 20, 40, 90, and 135 degrees, respectively. The top surface of the scintillator faced the target

perpendicularly. Table 1 shows the experimental conditions. A digitizer (SIS3316, struck innovative system) was used for the data acquisition. For data analysis, the pulse shape discrimination method was adopted to extract neutron signals from the entire data set.

Table 1: Experimental Conditions

Target material	C_3H_6
Target thickness (μm)	12
$^7Li^{3+}$ energy (MeV)	15
$^7Li^{3+}$ beam current (nA)	60
Neutron production reaction	$p(^7Li,n)^7Be$
Distance between the target and the scintillator (cm)	90
Measurement time for each shadow cone condition (min)	15



Figure 1: The belt-conveyor-type target.

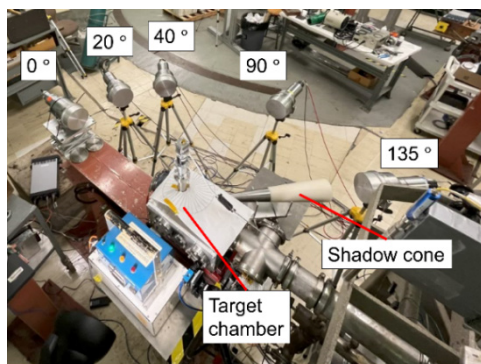


Figure 2: Experimental setup around the target chamber.

The shadow cone was employed to evaluate the influence of scattering neutrons in the experimental setup. Fig.3 shows the geometrical setting of the shadow cone. The front side of the shadow cone was made of low-carbon steel, which is equivalent to 1018 steel, and served as a fast neutron filter. The back side of the shadow cone was made of a borated polyethylene, of which the weight percentage of boron is 5.0 %, and served as a neutron absorber. The shadow cone was located between the target and the liquid scintillator, as shown in Fig. 2 and Fig.3. The shadow cone can cut off neutrons from the target position since it covers the solid angle from the target to the scintillator surface. The experimental system can measure only neutrons

coming from points other than the target when using the shadow cone. By comparing the neutron signals with and without the shadow cone, the neutron signals from the target side and other sides can be obtained separately. The position of the cone was changed at every measurement to evaluate the scattering neutrons at each scintillator position.

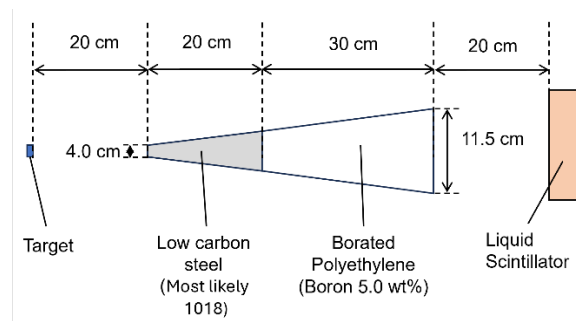


Figure 3: Geometrical setting of the shadow cone.

RESULTS AND DISCUSSION

Figure 4 shows the angular distribution of neutron signals measured by the liquid scintillators. The plots are normalized by one nano-ampere. In the legend, “SC” stands for the shadow cone. Data corresponding to different angles are plotted using distinct marker shapes. The Li-beam direction is defined as 0 degrees. Please note that the graph scale adapts to a log scale for the neutron signals of the liquid scintillators in Fig. 4. These data are the raw data of the liquid scintillator after the neutron and gamma discrimination, which are not compensated by the detector efficiency. The data at the 20-degree position was not obtained.

Neutron signals showed the highest values at 0-degree positions without the shadow cone. This result reflects neutron convergence in the forward direction, which is the feature of the inverse kinematic reaction. Based on the two-body collision kinematics [12], the half-vertex angle of the neutron emission cone is calculated to be 21 degrees for the 15 MeV lithium beam. Accordingly, all detectors, except the one placed at 0 degrees, were located outside the emission cone. Therefore, a large difference in the neutron signals was observed between the detector at 0 degrees and the other detectors.

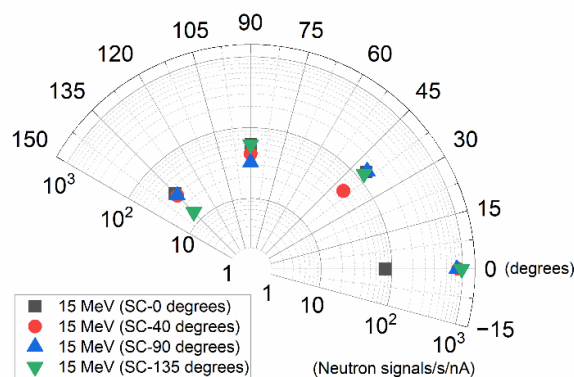


Figure 4: Angular distribution of neutron signals measured by the liquid scintillators.

The shadow cone significantly reduced the neutron signal. By comparing the radiation signals with and without the shadow cone, the ratio of the scattering neutrons to the total neutrons is obtained (Table 2). The “scattering neutrons” in Table 2 means neutrons coming from the floor, the wall, the ceiling, and the experimental setups. These data are also based on the raw data of the liquid scintillator.

At 0-degree position, approximately 92 % of neutrons came from the target side. On the other hand, at the other positions, the ratio of the scattering neutrons was higher than that at the 0-degree position. These results support the existence of the neutron convergence in the forward direction.

Although the detectors at 40, 90, and 135 degrees were located outside the theoretical neutron emission cone, the ratios of scattering neutrons at these angles were only about 42% to 55%. Some neutrons may have been scattered and reflected inside the target chamber and, as a result, entered the detector from the same direction as the target position. Table 2: Ratio of the Scattering Neutrons to the Total Neutrons

Angle	Scattering neutrons / Total neutrons (%)
0	8.3
40	43.3
90	55.4
135	42.5

CONCLUSION

The angular distribution of neutrons produced via the inverse kinematic reaction, $p(^7\text{Li},n)^7\text{Be}$, was investigated at the Tandem Van de Graaf accelerator facility in BNL. The angular distribution was measured using the liquid scintillators (BC-501). The large neutron concentration in the forward direction was observed throughout the experiment. The result agrees with the theoretical characteristics of the inverse kinematic reaction. Further analysis and investigation, including the estimation of the actual neutron flux by considering the detector efficiency, are required for the design of future neutron applications.

REFERENCES

- [1] International Atomic Energy Agency, “Neutron Scattering with Low and Medium Flux Neutron Sources Processes,” IAEA-TECDOC-1961, <https://www.iaea.org/publications/14884/neutron-scattering-with-low-and-medium-flux-neutron-sources>
- [2] K. Sueki, K. Kobayashi, W. Sato, H. Nakahara, and T. Tomizawa, “Nondestructive Determination of Major Elements in a Large Sample by Prompt γ Ray Neutron Activation Analysis,” *Anal. Bioanal. Chem.*, vol. 68, no. 13, pp. 2203–2209, Jul. 1996. doi:10.1021/ac9511051
- [3] N. Kardjilov, I. Manke, A. Hilger, M. Strobl, and J. Banhart, “Neutron imaging in materials science,” *Appl. Mater. Today*, vol. 14, no. 6, pp. 248–256, Jun. 2011. doi:10.1016/s1369-7021(11)70139-0
- [4] K.-N. Leung, J. K. Leung, and G. Melville, “Feasibility study on medical isotope production using a compact neutron generator,” *Appl. Radiat. Isot.*, vol. 137, pp. 23–27, Jul. 2018. doi:10.1016/j.apradiso.2018.02.026
- [5] E. J. Mausolf, E. V. Johnstone, N. Mayordomo, D. L. Williams, E. Y. Z. Guan, and C. K. Gary, “Fusion-Based Neutron Generator Production of Tc-99m and Tc-101: A Prospective Avenue to Technetium Theranostics,” *Asian J. Pharm. Sci.*, vol. 14, no. 9, p. 875, Aug. 2021. doi:10.3390/ph14090875
- [6] J. H. Dave, C. R. Gould, S. A. Wender, and S. M. Shafroth, “The $1\text{H}(^7\text{Li}, n)^7\text{Be}$ reaction as an intense MeV neutron source,” *Nucl. Instrum. Methods Phys. Res.*, vol. 200, no. 2–3, pp. 285–290, Sep. 1982. doi:10.1016/0167-5087(82)90444-6
- [7] M. Lebois *et al.*, “Development of a kinematically focused neutron source with the $p(^7\text{Li},n)^7\text{Be}$ inverse reaction,” *Nucl. Instrum. Methods Phys. Res., Sect. A*, vol. 735, pp. 145–151, Jan. 2014. doi:10.1016/j.nima.2013.07.061
- [8] M. Okamura *et al.*, “Demonstration of an intense lithium beam for forward-directed pulsed neutron generation,” *J. Manage. Sci. Rep.*, vol. 12, no. 1, Aug. 2022. doi:10.1038/s41598-022-18270-0
- [9] Brookhaven National Laboratory, “BNL Tandem Van de Graaff,” <https://www.bnl.gov/tandem/>
- [10] M. H. Obeid, A. Ismail, A. Bitar, M. Alahmad, and R. Shweikani, “Measurement of the scattered neutrons using the shadow cone methodology in a neutron calibration bunker,” *Appl. Radiat. Isot.*, vol. 177, p. 109916, Nov. 2021. doi:10.1016/j.apradiso.2021.109916
- [11] ISO, “ISO 8529-2:2000 Part 2: Calibration fundamentals of radiation protection devices related to the basic quantities characterizing the radiation field,” <https://www.iso.org/standard/25667.html>Avai
- [12] P. Liu *et al.*, “Laser-Driven Collimated Neutron Sources Based on Kinematic Focusing,” *Phys. Rev. Appl.*, vol. 18, no. 4, Oct. 2022. doi:10.1103/physrevapplied.18.044004

HIGH INTENSITY ^{50}Ti BEAM PRODUCTION FOR SUPERHEAVY ELEMENT RESEARCH*

D.S. Todd[†], J.Y. Benitez, N. Brickner, P. Coleman, N. Intwala, S. Small, D. Thatcher
Lawrence Berkeley National Laboratory, Berkeley, CA, USA

Abstract

Elements 115-118 were discovered by bombarding transuranic targets with high-current ^{48}Ca beams, but a lack of heavier targets prevents extending the periodic table using these beams. The recent production of two atoms of element 116 by LBNL researchers using ^{50}Ti opens a new pathway for the discovery of elements beyond 118. The 88-Inch Cyclotron's acceleration and delivery of the μA ^{50}Ti beams used to create these two particles are discussed. In particular, we present the novel inductive oven used to provide a stable stream of ^{50}Ti vapor to LBNL's superconducting electron cyclotron resonance ion source Venus, extract $>100\ \mu\text{A}$ Ti^{12+} , and minimize consumption of this expensive, low-abundance isotope.

INTRODUCTION

Lawrence Berkeley National Laboratory (LBNL) has a long history of involvement in the discovery of radioactive elements, having been directly involved in or been the site of the discovery of 15 such elements (and one stable element). The last element discovered at LBNL, seaborgium (element 106), was produced by bombarding a californium target with oxygen beams [1]. Since that time, a further twelve elements have been discovered at other laboratories around the world. With its upcoming search for element 120, LBNL will once again try to expand the periodic table using a californium target, this time using ^{50}Ti projectile beams.

The six most recent element discoveries, elements 113-118, were the result of experiments with ^{48}Ca beams incident upon actinide targets of increasing atomic number from 94 to 98 (Pu to Cf). A lack of sufficient material for targets with atomic number greater than 98 prevents this successful projectile from extending the periodic table further. However, a potential way to continue in the same vein is to use projectile beams with higher atomic number.

The production of element 120 using ^{50}Ti projectile beams will require beam energies in the 5-6 MeV/u range to surpass the Coulomb barrier, and high currents ($\sim\mu\text{A}$) for reasonable production rates of multiple-per-year of beam time. As a demonstration that ^{50}Ti beams can be used for superheavy (atomic number > 103) element production, high-current beams were developed by the Operations and Ion Source teams at LBNL's 88-Inch Cyclotron and used to bombard a ^{244}Pu target to produce element 116 (Lv) particles [2]. This result represents the first time that superheavy elements have been produced using titanium ion beams and paves the way for the upcoming element 120 search.

* This work was supported by the U.S. Department of Energy, Office of Science, Office of Nuclear Physics under contract number DE-AC02-05CH11231 (LBNL).

[†] email address: dstodd@lbl.gov

Based on predicted element 120 cross-sections, the 88-Inch Cyclotron staff has been charged with producing $^{50}\text{Ti}^{12+}$ beam currents in excess of $1\ \mu\text{A}$ to superheavy element experiments continually for multiple runs of ten-day-length. Additionally, as ^{50}Ti is a low-abundance, expensive isotope, we are tasked with producing these beams while maintaining a material consumption rate less than 5 mg/hour. In the following two sections we describe what this means for both the cyclotron and the source providing it beam. The difficulties titanium presents in the source are discussed and the novel inductive oven we have designed and used to demonstrate ^{50}Ti 's viability in superheavy research is presented in the subsequent section. The two final sections give results using this oven and discuss further optimizations to be made to improve performance.

ACCELERATOR

LBNL's 88-Inch Cyclotron is a flexible, K140 cyclotron originally designed as a light ion accelerator. However, with the addition of increasingly advanced electron cyclotron resonance (ECR) ion sources, this cyclotron has accelerated over half of the naturally occurring elements. The acceleration frequencies of the cyclotron's single dee are between 5.6 and 16.5 MHz with a maximum dee voltage of approximately 70 kV. In recent years, the majority of this cyclotron's accelerated beams have been used for two purposes: single event space effects testing and superheavy element research. For the former, low-current beams (typically 10s of pA to 10s of nA) with energies between 5 and 20 MeV/u and masses across the periodic table are delivered to experimenters to test radiation effects on space-bound equipment. For the latter, high-current, moderate mass beams (up to a couple μA with atomic mass in the 40-50 amu range) are delivered to heavy targets with energies in the 5-6 MeV/u range.

For the cyclotron, the production of high-current ^{50}Ti beams is an extension of well more than two decades' experience accelerating high-current beams for superheavy element production. After the completion of transmission improvements and the addition of a spiral inflector, the 88-Inch Cyclotron has demonstrated its ability to accelerate and deliver over $2\ \mu\text{A}$ $^{48}\text{Ca}^{11+}$ beams to superheavy element researchers [3]. The accelerated species for the titanium beams is $^{50}\text{Ti}^{12+}$, and since its mass-to-charge ratio is similar to the successful experiments with ^{48}Ca , transport through the injection line and spiral inflector is possible without any modifications. There is no reason to not expect similar cyclotron performance for titanium beams as was found for calcium, provided the ion source can produce the required beam currents.

ION SOURCE

The 88-Inch Cyclotron's primary injector source for high-current ion beams is the fully-superconducting ECR

ion source VENUS. The magnetic structure for VENUS is a sextupole made up of NbTi racetrack coils nestled inside three NbTi solenoid coils [4]. The combination of these coils produces a “minimum-B” configuration where the magnetic field magnitude is a minimum at the source center and increases in all directions. Two injected microwave frequencies, 28 and 18 GHz, are used to resonantly energize electrons on closed surfaces of constant magnetic fields about that minimum, and the resulting confined, energetic electrons ionize neutrals and ions to produce the highly-charged ions needed by the cyclotron. The microwaves for VENUS are produced by a gyrotron that can deliver up to 10 kW of 28 GHz power and two 18 GHz klystrons that can deliver 2 kW each.

It is generally easiest to produce high-current ion beams if that material can be delivered to the source plasma as a gas. For high-current beams from materials like calcium and titanium which are solid at room temperature, we typically use ovens to heat them to the point they outgas significantly and direct this gas toward the plasma. This aiming of ejected gas toward the plasma is extremely important for many of the beam materials used for superheavy element research. Superheavy elements typically have neutron numbers more than 50% greater than their proton numbers, so both the targets and incoming beams need to be neutron rich. The neutron-rich isotopes used, such as ^{48}Ca and ^{50}Ti , are low-abundance and are therefore expensive. Any material injected into the source that is not captured by the plasma is lost to any “cold” surface it encounters, so to improve efficiency it is best to aim the injected material at the plasma center (the center of the source) where the plasma density is highest and therefore there is the greatest chance of that material ionizing and being extracted as beam. Additionally, net cross-field diffusion is outward from the source center for ions, so starting ions as near the axis as possible improves the likelihood of these ions being converted to beam.

Because ^{50}Ti is both expensive and rare, the ion source group was tasked with producing the needed 60-100 μA of $^{50}\text{Ti}^{12+}$ beam to deliver >1 μA to the target (assuming typical 10-20% transmission through the cyclotron) while consuming 5 mg or less per hour of ^{50}Ti .

OVENS

Both high- and low-temperature ovens have been successfully used with the VENUS ion source [5, 6]. The low-temperature ovens used for calcium beam production have performed particularly well, producing beams on target with currents up to 2 μA while consuming ^{48}Ca at a rate of approximately 0.5 mg/hour. The key characteristic making this oven so efficient is the set of 10 8.5-mm-long channels with diameters of either 0.97 or 1.09 mm that direct the ^{48}Ca gas toward the plasma center. It is essential that these channels stay as hot or hotter than the crucible holding the material to prevent condensation and clogging. Maintaining this higher temperature is possible for the low-temperature oven (maximum temperature $\sim 700^\circ\text{C}$), as it relies on conduction for temperature equilibration and the body temperatures are low enough that radiative losses aren't a major issue. Titanium's required temperatures of

approximately 1600°C to outgas significantly prevent its use in this otherwise highly-effective oven.

The crucibles for the resistive, high-temperature ovens historically used in VENUS are constructed thin-walled conductors that can reach temperatures over 2000°C . However, these ovens are susceptible to damage from strong Lorentz forces during operation as these currents are nearly perpendicular to the VENUS' local 3-4 tesla magnetic fields. Additionally, at high operating temperatures the oven material is susceptible to damage from (often poorly understood) chemical reactions between the crucible and the desired beam material and/or its gas.

Rather than focusing on the chemistry difficulties, we decided to produce an inductive oven to get the material to temperature. Inductive ovens have been successfully used in high-field ECR ion sources at IMP in China and at FRIB in the United States [7, 8]. Both laboratories utilize a design where a cylindrical susceptor (the inductively-heated crucible) has its symmetry axis parallel to the long axis of the source, and material is ejected through a hole in one end. The fact that these ovens are typically required to be positioned centimeters off of the source axis, means that much of the material ejected from the oven will not pass through the heart of the source plasma and efficiency will be lower than might be possible with better aiming. Adding any sort of a channel at the exit end is made difficult as the inductive coil's highest magnetic field (and therefore highest temperature of the coaxial susceptor) is near the center of the inductive coil. Any channel in a region with lower inductive flux is susceptible to clogging if its temperature is lower than the material location, and radiative cooling of any channels at the end of the oven must be considered as it isn't easily thermally shielded.

To get around these difficulties, we have designed a novel inductive oven with its coil perpendicular to the long axis of the source [9]. The axis of the cylindrical susceptor is vertical (Fig. 1), allowing for a rotation of the susceptor opening about that symmetry axis toward the plasma to better deliver outgassed material into the source plasma. Additionally, this configuration allows for the use of the oven with materials that melt before sublimating.

In order to make the oven quickly serviceable, the oven assembly and the ~ 1.1 -meter-long shaft it is attached to has been designed to fit through a 37.1-mm-diameter port. The hollow annealed copper coil (OD: 3.97 mm, wall thickness: 0.36 mm) has five turns and is typically operated at approximately 175 kHz heating frequency, requiring ~ 800 -1000 W of operational power for titanium production.

The yttria-stabilized zirconia insulator body is nested within the coil with an outside diameter of 21.6 mm, wall thickness of 3 mm, and height of 27 mm. The coils have been designed so that a thin zirconia rod is supported by the coils and which supports the oven assembly (Fig. 1). This is perhaps the weakest aspect of the design, but the rods have not failed in any serious way while in use.

The molybdenum susceptor (OD: 12.7 mm, wall thickness: 1.2 mm) is 17.3 mm tall and has a material exit aperture machined approximately halfway up the side by sweeping a 2-mm-diameter hole perpendicular to the cylinder axis 1.9 mm.

To minimize thermal conduction between the insulator and the susceptor, angled and split molybdenum rings were constructed to maintain ~ 1 mm spacing between the susceptor and the insulator while minimize contact area between the ring and each.

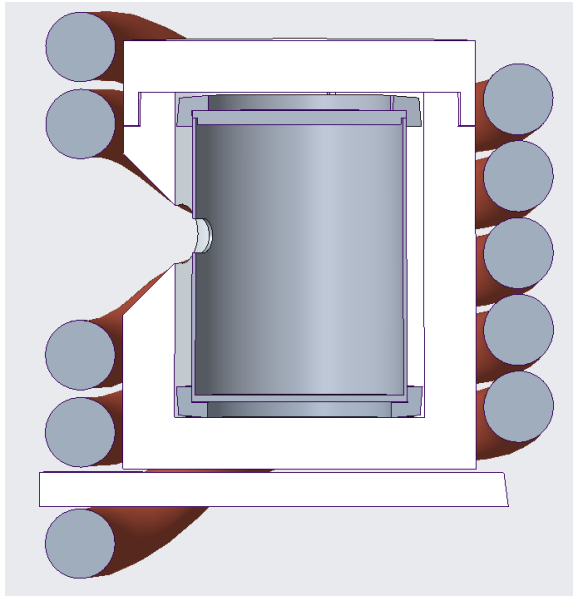


Figure 1: Cross-section of the inductive oven. A five-turn inductive coil surrounds a 3-mm-thick ytria-stabilized zirconia insulator (white) which is supported by an insulator from the same material held in place by the coils. The molybdenum susceptor is supported within the insulator by a pair of angled molybdenum rings that minimize thermal contact between susceptor and insulator.

RESULTS

As we were under time constraints to produce ^{50}Ti beams, the inductive oven only had one natural titanium test run in VENUS before being put into service with ^{50}Ti beams. As of this writing this oven has performed exceptionally well and played a central role in the first ever production of element 116 with titanium beams. The oven has been used for over ten weeks of cyclotron beam production in ten day intervals. During that time, the source would effortlessly produce $\sim 100 \mu\text{A}$ $^{50}\text{Ti}^{12+}$ beams and was able to produce over $200 \mu\text{A}$, though this is much more than the cyclotron can accelerate. Beam currents delivered to experiments were between 1 and $2 \mu\text{A}$, as can be seen in Fig. 2.

Consumption rates for experimental runs have been found to be between 2.5 and 4.5 mg/hour, and are largely dependent on the care taken when tuning the source (it is often possible, and tempting, to produce more beam by increasing the oven output rather than source optimization). To date, as the oven and source have produced sufficient beam, little time has been spent exploring the operation space. As a case in point, the oven has only been run using relatively low microwave heating power (~ 600 - 1000 W of 18 GHz) and only at magnetic fields necessary for 18 GHz operation.

It should be noted that though Fig. 2 shows long term beam variation, the source is quite stable for short term

variations. The instabilities that plagued other titanium production attempts due to titanium acting as a getter material and affecting source pressure have not been an issue with this oven. With more time and effort, we are confident we could reduce the long-term variations in beam current. It should be noted that a characteristic of these beams that we don't run into as much with our non-metal beams is the frequent (hourly at a minimum) need to provide minor adjustments to the analysing dipole immediately after the source when sending these titanium beams through the cyclotron. We have also seen considerably higher (50-100% higher) total extracted beam currents when running titanium and for an extended period after. This will be addressed in later work.

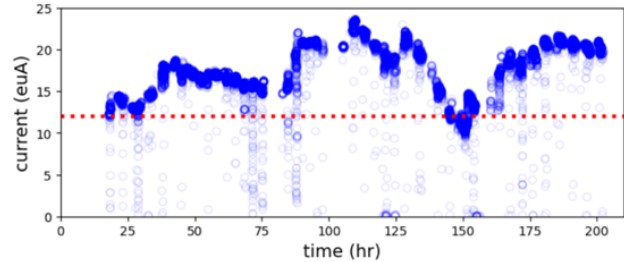


Figure 2: $^{50}\text{Ti}^{12+}$ beam current (circles) measured by inductive pickup immediately upstream of the superheavy element experiment for a recent ten-day-run, with $1 \mu\text{A}$ indicated with the horizontal dotted line. Note that slow variations in beam current are not important for these experiments, so experimenters would often prefer a slow variation of current rather than interruptions for tuning. The drops in current below $1 \mu\text{A}$ are typically for cyclotron tuning, cyclotron RF clamps, Faraday cup insertion, etc.

FURTHER OPTIMIZATION

The greatest hindrance to oven optimization is availability of the VENUS ion source. The ovens can be tested offline to ensure they don't clog, for example, but optimizing consumption rates requires the ovens be installed and operated in VENUS: a source that is in high demand and in near-continuous use. Additionally, there is a bit of recovery time needed after titanium (like many metals) has been used in the source, so testing titanium between cyclotron runs is not ideal. Making things more difficult, to accurately measure consumption rate (the primary number we are trying to optimize), we need the source to run at least a day with each configuration and it needs to be pulled and weighed between configuration changes, so this work is extremely time consuming and we have a limited schedule.

To date we have not made any changes to the oven's location relative to the plasma (closer or further), and we haven't taken great care in accurately setting its rotation angle. It is expected that both of these parameters could be optimized to improve material consumption rates.

Initial testing of the addition of aiming channels has taken place. We have added channels to a cylindrical oven (Fig. 3) and to an elongated design, and for both cases, when inductively heated, the temperatures of the channels have been found to be greater than the remainder of the visible susceptor through the insulator aperture (Fig. 4)—a necessary condition to prevent clogging. The cylindrically

symmetric design has been tested in VENUS with natural titanium, and was found to be capable of producing similar beam currents to the design discussed above, but did not demonstrate a noticeable improvement in material use efficiency. However, it is important to note that the oven was run continuously for multiple days without clogging. The alignment optimization that has not yet taken place for the oven above is much more critical when using a channelled susceptor that emits a more directed output gas, and will be crucial moving forward. Further measurements will be performed with a more dedicated effort to align the barrels and maintain that alignment upon insertion.

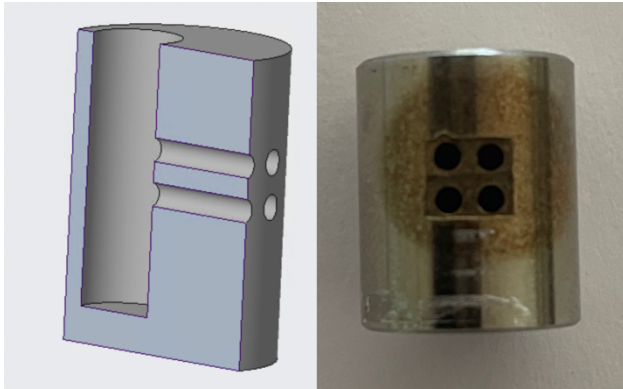


Figure 3: Cross-sectional view (left) of the cylindrical susceptor of same overall dimensions as the primary oven but with aiming channels added. The actual molybdenum susceptor is shown at right.



Figure 4: Thermal imaging of the channel holes of an elongated susceptor design looking through the aperture of the surrounding insulator, where lighter colors indicate higher temperatures. The circular holes can be seen to be hotter than the surrounding susceptor, making them less likely to clog from material condensation.

These alignment issues illustrate the shortcomings of a cylindrically symmetric barrel design: the fact that it is easily rotated about its axis and difficult to align. As mentioned, we have tested an elongated design that breaks rotational symmetry, but the initial design was too long and radiation losses prevented it from reaching outgassing temperatures (note that as temperatures approach 1780°C , the susceptor will radiate heat away at $\varepsilon \text{ W/mm}^2$, where ε is the blackbody emissivity). This susceptor was tested with silver and it produced hundreds of microamp beams, but

optimized consumption rates were not possible as the 28 GHz microwaves raised the temperature of the oven higher than desired (the inductive supply wasn't even turned on and the oven was heated by microwaves).

As mentioned above, running the titanium beams using a combination of 28 and 18 GHz power should and will be explored, and it is highly likely that this combination will lead to operation modes that provide better consumption than those found using 18 GHz only.

ACKNOWLEDGEMENTS

This work incorporated the efforts and discussions of nearly everyone from the Operations team at LBNL's 88-Inch Cyclotron facility. Special thanks go to members of the mechanical team (John Garcia, Sixuan Zhong, Nathan Seidman, and Brian Bell) for susceptor and coil construction and the electrical team (Collin Anderson, Brendan Ford, Nathaniel Bohm, and Michel Kireeff Covo).

REFERENCES

- [1] A. Ghiorso *et al.*, "Element 106", *Phys. Rev. Lett.*, vol. 33, no. 25, pp. 1490–1493, Dec. 1974.
doi:10.1103/physrevlett.33.1490
- [2] J.M. Gates, *et al.*, "Toward the discovery of new elements: production of livermorium ($Z=116$) with ^{50}Ti ", *Phys. Rev. Lett.*, vol. 133, no. 17, Oct. 2024.
doi:10.1103/physrevlett.133.172502
- [3] D.S. Todd, *et al.*, "High current beam extraction from the 88-Inch Cyclotron at LBNL", in *Proc. Cyclotrons '13*, Vancouver, Canada, paper, MO2PB02, pp. 19–21.
- [4] J. Y. Benitez *et al.*, "Recent progress on the superconducting ion source VENUS," *Rev. Sci. Instrum.*, vol. 83, no. 2, Feb. 2012. doi:10.1063/1.3662119
- [5] D.J. Clark and C.M. Lyneis, "The production of beams from solid materials at the LBL ECR source", *J. Phys. Colloques*, vol. 50, No.C1, pp. C1-759-C1-766, Jan. 1989.
doi:10.1051/jphyscol:1989180
- [6] D. Leitner, M. L. Galloway, T. J. Loew, C. M. Lyneis, I. Castro Rodriguez, and D. S. Todd, "High intensity production of high and medium charge state uranium and other heavy ion beams with VENUS," *Rev. Sci. Instrum.*, vol. 79, no. 2, p. 02C710, Feb. 2008. doi:10.1063/1.2816790
- [7] W. Lu *et al.*, "Production of metallic ion beams by electron cyclotron resonance ion sources equipped with inductive heating ovens at the Institute of Modern Physics," *Rev. Sci. Instrum.*, vol. 92, no. 3, Mar. 2021.
doi:10.1063/5.0041671
- [8] H. Ren *et al.*, "Development and status of the FRIB 28 GHz SC ECRIS," *J. Phys. Conf. Ser.*, vol. 2244, no. 1, p. 012008, Apr. 2022. doi:10.1088/1742-6596/2244/1/012008
- [9] D. Todd, J. Benitez, and L. Phair, "A novel inductive oven design to produce high-current, moderate mass ion beams for superheavy element searches," *Nucl. Instrum. Methods Phys. Res., Sect. A*, vol. 1072, p. 170183, Mar. 2025.
doi:10.1016/j.nima.2024.170183

SINGLE-BUNCH EXTRACTION AT THE 88-INCH CYCLOTRON*

M. Kireeff Covo[†], J. Benitez, D. Todd, J. Cruz Duran, S. Blim, C. Anderson, M. Johnson, J. Garcia, B. Ninemire, D. Xie, L. Phair, Lawrence Berkeley National Laboratory, Berkeley, CA, USA

Abstract

The extraction system of the 88-Inch Cyclotron at Lawrence Berkeley National Laboratory has been modified to enable single-bunch extraction. This is achieved by increasing the voltage of the first deflector to oversteer the beam, halting extraction, and then selectively switching it off using a high-voltage chopper to synchronize the deflector's operational voltage with the transit time of a single bunch, enabling its extraction. A pre-chopper positioned before the cyclotron limits the beam available for acceleration, minimizing activation and sputtering damage from discarded bunches. This cost-effective technique is crucial for time-sensitive experiments and provides precise control over dose delivery, broadening the cyclotron's range of applications. Future efforts will focus on increasing extraction frequency by optimizing the deflector electronics for faster recovery times, and exploring sequential switching of two deflectors to reduce the required oversteering voltage.

INTRODUCTION

Recent developments in pulsed power technology have led to significant enhancements in beam chopping systems for particle accelerators. High-voltage switching units composed of series and parallel arrays of modern semiconductors, such as MOSFETs, IGBTs, and SCRs, can now deliver fast switching performance with low jitter and high efficiency. These systems are capable of managing hundreds of kilovolts and tens of kiloamperes within sub-microsecond timescales, enabling precise temporal control of particle beams for high-resolution applications across various accelerator facilities [1, 2].

Tandem beam chopper systems are typically categorized as either fast and slow choppers or as pre-chopper and main chopper [3, 4]. In the first configuration, fast choppers are used in applications requiring nanosecond-scale resolution, such as precise bunch selection and timing control, while slow choppers serve broader intensity modulation purposes. In the latter configuration, the pre-chopper is generally positioned early in the acceleration stage to shape the beam before it gains significant energy, whereas the downstream main chopper further refines beam delivery by deflecting or transmitting bunches to either the target or the beam dump.

To enhance chopper system performance, researchers have explored advanced hardware and optimization techniques that improve synchronization between beam dynamics and switching events. High-speed electronics and real-time feedback loops enable precise control over bunch timing and

beam intensity, capabilities crucial for time-of-flight experiments, neutron cross-section measurements, and laser-driven fusion diagnostics.

For the 88-Inch cyclotron, this precision is especially important for time-of-flight neutron spectroscopy, where accurate timing between pulses prevents overlap from sequential broad-spectrum bunch bursts, particularly in experiments using deuteron beams striking beryllium targets to generate fast neutrons.

PRE-CHOPPER AND MAIN CHOPPER TANDEM SCHEME

The 88-Inch Cyclotron at Lawrence Berkeley National Laboratory supports research in nuclear science and radiation effects using light and heavy ions produced by three electron cyclotron resonance ion sources: ECR, AECR, and VENUS [5], Fig. 1. These sources can deliver mixed ion species ("cocktails") through an injection line equipped with attenuators for beam intensity control and a pre-chopper that limits beam power into the machine.

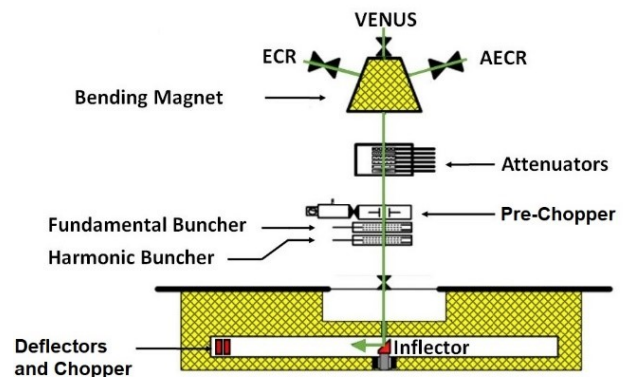


Figure 1: Layout of the extraction lines from the ion sources and the injection line into the cyclotron.

The beam is subsequently bunched by fundamental and harmonic bunchers for acceleration and extraction via three electrostatic deflectors. However, due to energy spread caused by particles arriving at different RF phases, bunches become radially dispersed, resulting in extraction across multiple RF cycles even if a single RF bucket is injected at the cyclotron [6].

Under normal conditions, injecting several consecutive RF bunches results in extraction on every RF cycle. Figure 2 shows how multiple-turn extraction arises when the chopper narrows the injection window to a single RF bunch. The remaining single bunch, after acquiring energy spread during acceleration, is extracted over multiple turns. Because

* Work supported by the Director, Office of Science, Office of Nuclear Physics, Division of Nuclear Physics, U.S. Department of Energy under Contract No. DE-AC02-05CH11231.

[†] mkireeffcovo@lbl.gov

the cyclotron operates in third harmonic mode, extraction occurs every three RF cycles, preserving the original phase relationship from injection, as confirmed by fast current transformer (FCT) measurements.

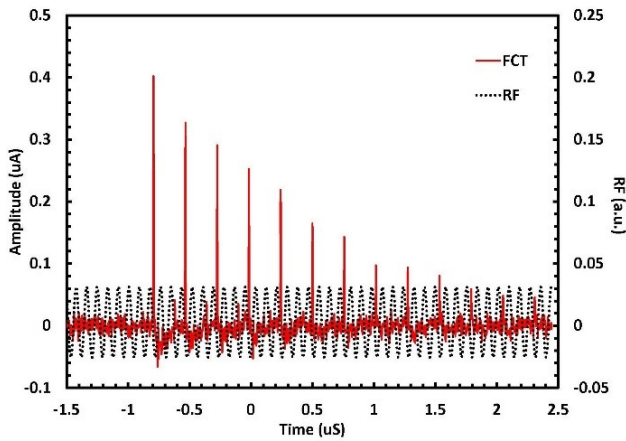


Figure 2: Extraction from a single RF bucket during the injection of a 6 MeV $^2\text{H}^+$ beam, with the cyclotron operating at 11.6 MHz in third harmonic mode.

Although single-turn extraction can be realized from a single RF-bucket injection by placing slits near the cyclotron center to restrict phase acceptance, this approach significantly reduces beam intensity.

To achieve single-bunch extraction from the cyclotron's quasi-continuous beam without compromising instantaneous beam intensity, a tandem pre-chopper and chopper configuration was implemented at the 88-Inch Cyclotron. This method repurposes the existing first deflector as a chopper using commercial components, eliminating the need for specialized hardware, concurrent with the use of the pre-chopper to limit the damage and activation from the discarded energetic bunches during extraction into the cyclotron structures.

HARDWARE

The pre-chopper system at the 88-Inch Cyclotron uses commercially available high-voltage MOSFET pulsers (Behlke FSWP 51-02 [7]) to control beam injection. Positioned before the beam enters the cyclotron, it applies up to ± 2 kV across electrostatic plates to steer the beam away from the inflector, effectively blocking injection. When the voltage is removed, the beam continues to the inflector and enters the RF acceleration process.

For safe and reliable operation, the pre-chopper is liquid-cooled with Galden HT135 PFPE fluid and includes an interlock that shuts it down if temperatures exceed 75°C . The system also incorporates ceramic capacitors for voltage buffering and series resistors to protect the pulsers from voltage reflections due to impedance mismatches.

The chopper system hardware at the 88-Inch Cyclotron shown in Fig. 3 [8]. It utilizes a fast high-voltage SCR switch (Behlke HTS 800-100-SCR [7]) integrated into the first electrostatic deflector to achieve single-bunch extraction. This

switch, capable of handling up to -80 kV, manipulates beam trajectories by oversteering or understeering them during fast voltage transitions. The deflector itself, measuring 0.52 m in length and 5 cm in width, produces about 46 pF of capacitance.

The SCR-based switch is triggered by an isolated driver circuit and sustains conduction until current drops below a threshold. While these switches are reliable and well-suited for high-voltage applications, their frequency limit is a few kilohertz, and they are protected by a thermal interlock if they overheat.

To protect the chopper system from transients and reverse voltages, three high-voltage diode assemblies (Behlke FDA 1000-150 [7]) are employed. These diodes manage flyback voltage spikes, safeguard the power supply, and assist with switching stability. Additional components, such as a 100 nF capacitor and a 200 k Ω discharge resistor, support proper SCR operation by maintaining the necessary holding current. Together, these components enable precise control over beam extraction by biasing the outer electrodes of the first electrostatic deflector, while the inner septum electrodes remain grounded.

EXPERIMENTAL RESULTS

The 88-Inch Cyclotron at LBNL was configured to accelerate 16 MeV deuteron beams using a first harmonic RF at 6.3 MHz. To reduce activation and sputtering from high beam power, the pre-chopper limited the beam duty cycle to 10^{-5} , delivering 10 μs pulses every second.

Figure 4 illustrates the effectiveness of the chopped deflector system used for beam selection at the 88-Inch Cyclotron. The x-axis represents time in microseconds. The left y-axis displays current from a FCT diagnostic, Bergoz Instrumentation model FCT-082-05:1-H [9], located after the deflectors. The right y-axis shows the chopper voltage signal.

The top trace in blue shows the pre-chopped beam, which consists of a continuous train of bunches selected by the pre-chopper without activating the chopper. The red trace beneath it represents the extracted beam after the chopper is turned on: several bunches are allowed through initially, and once the deflector is switched off, subsequent bunches are suppressed. The green dash-dotted line shows the chopper voltage for timing purposes. Before applying the trigger, the first deflector voltage is at its operational level, approximately -44.6 kV in the experiment, allowing bunches to be extracted. After the trigger arrives, the chopper shuts off the deflector field, preventing further bunches from being steered out of the cyclotron. The RF signal, shown as a continuous sinusoidal waveform at the bottom in light blue, matches the cyclotron's operating frequency.

Figure 5 demonstrates the effect of varying deflector voltages on beam suppression and single-bunch extraction at the 88-Inch Cyclotron. The x-axis shows time in nanoseconds. The left y-axis represents the beam current in arbitrary units as measured by the FCT mentioned before, and the right

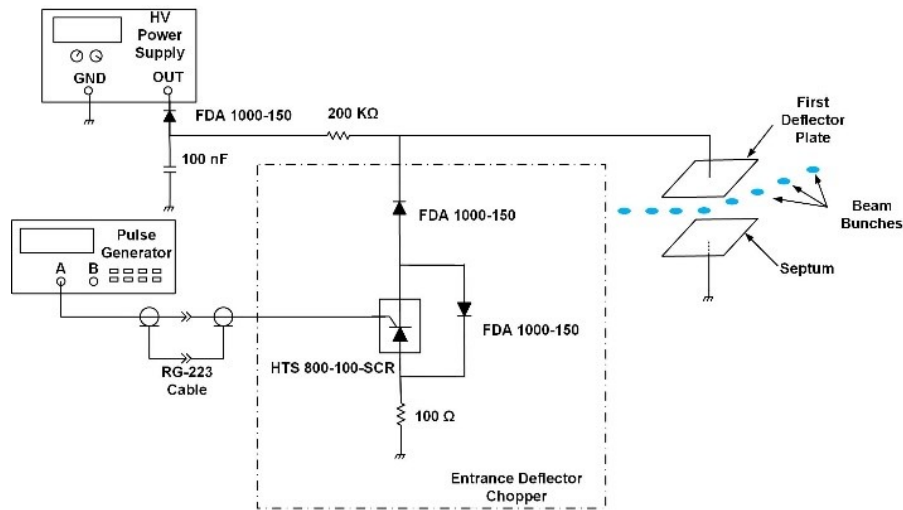


Figure 3: Deflector beam chopper. One HTS 800-100-SCR unit can switch up to -80 kV to the first deflector plates, enabling single bunch extraction from the cyclotron.

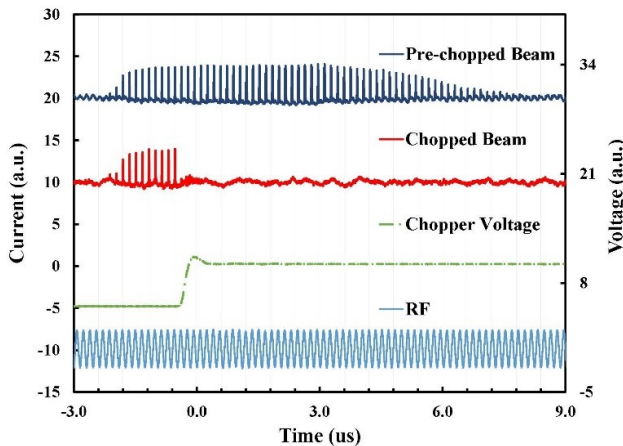


Figure 4: A deflector beam chopper suppresses 16 MeV deuterium beam bunches. The figure shows the microstructure of a $10\text{ }\mu\text{s}$ macro pulse defined by the pre-chopper, both before and after being chopped. The head and tail of the extracted beam macro pulse have different amplitudes due to the energy spread during the acceleration process.

y-axis corresponds to the voltage across the deflector, also in arbitrary units.

Four current traces labeled FCT_44.6KV, FCT_50KV, FCT_55KV, and FCT_65KV are shown, each corresponding to a different fixed voltage applied to the first deflector. The green FCT_44.6KV trace, which uses the -44.6 kV nominal deflection voltage for beam extraction, shows multiple bunches being extracted over time. As the voltage is increased to -50 kV (red), -55 kV (blue), and -65 kV (orange), beam extraction becomes increasingly suppressed. At -65 kV , only a single bunch is observed, confirming effective single-bunch extraction.

The green dash-dotted line labeled DEFL_44.6KV represents the switching of the deflector voltage from its -44.6 kV nominal value to zero, occurring just before time zero. The

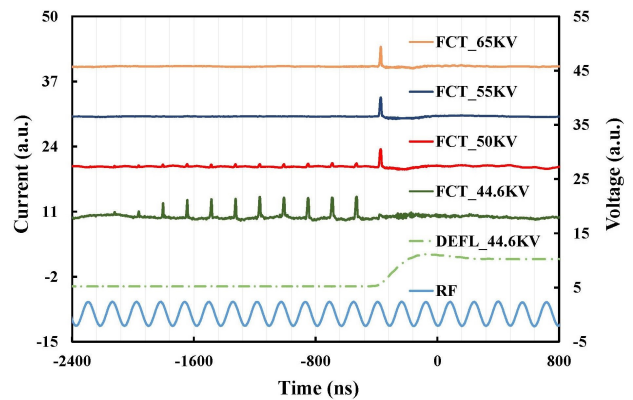


Figure 5: Single-bunch extraction with the chopped deflector technique.

bottom waveform in light blue shows the RF signal from the cyclotron, providing a phase reference synchronized with the beam bunches.

Together, these traces highlight the tuning process for achieving single-bunch extraction by adjusting the deflector's over-steering voltage. As the voltage deviates from the nominal value, only a narrow time window remains in which the beam receives the precise steering force needed for extraction, enabling the selection of a single bunch while blocking the rest. The switching occurs during bunch transit, and the optimal phase ensures consistent single-bunch delivery. This confirms precise synchronization between the RF system and deflector switching, enabling controlled extraction.

The extracted bunches showed a Gaussian profile with a 5.5 ns standard deviation, and the deflector's switching off time was about 350 ns . Subsequent phase shifts demonstrated the setup's precise timing control and reproducibility.

In the current configuration, the 100 nF buffer capacitor charges to the high-voltage level in approximately 50 ms

through the power supply's 100 k Ω output impedance. Once the SCR is triggered, the capacitor begins to discharge through the 200 k Ω resistor. This partial discharge continues for about 60 ms until the current falls below the SCR's 100 mA holding current threshold, at which point the SCR turns off. This ensures reliable SCR turn-off and allows the system to reset for the next switching cycle in approximately 110 ms, limiting the maximum achievable pulse repetition rate.

As part of future improvements, replacing the 200 k Ω resistor with a 2 M Ω resistor causes the current through the SCR to drop below its holding threshold much sooner, turning it off before the buffer capacitor is significantly discharged. In this configuration, only the first deflector plate, estimated to have a capacitance of 46 pF, is discharged with a time constant of 92 ns. The discharge is essentially complete within about 460 ns. This modification protects the power supply and enables significantly higher repetition rates.

CONCLUSION

This study introduces a cost-effective chopped deflector method for achieving a single-bunch extraction at the 88-Inch Cyclotron. The technique combines a pre-chopper to reduce power deposition from discarded beam bunches with a modified first deflector, equipped with a fast high-voltage SCR switch, to select and extract a single bunch. The method proved repeatable and is adaptable for various ion species by initially oversteering the beam with the first deflector and then switching it off to coincide with the transit time of a single bunch. Future improvements will permit higher repetition rates by maintaining the buffer capacitor's mostly charged.

ACKNOWLEDGEMENTS

The authors thank Brendan P. Ford, Nathaniel Bohm, and Erik Line for their electronics support; Alexander Donoghue, Scott M. Small, Nicholas M. Brickner, Nishi Intwala, Patrick Coleman, and Devin T. Thatcher for their operations support; and Nathan Seidman, Roman Nieto, Donald Bell, and Sixuan

Zhong for their mechanical support of the LBNL 88-Inch Cyclotron.

REFERENCES

- [1] W. Merz and M. Grimes, "Fast opening switch approach for high-voltage vacuum tube protection application", *2012 IEEE Int. Power Modulator and High Voltage Conf. (IPMHVC)*, Jun. 2012, pp. 308–311. doi:10.1109/ipmhvc.2012.6518741
- [2] T. Fowler, M. J. Barnes, T. Kramer, F. Mueller, and T. Stadlbauer, "Design and measurements of a fast high-voltage pulse generator for the MedAustron low energy transfer line fast deflector", in *Proc. IPAC'12*, New Orleans, LA, USA, May 2012, paper THPPD075, pp. 3689–3691. <https://accelconf.web.cern.ch/IPAC2012/papers/thppd075.pdf>
- [3] F. Caspers, "Review of fast beam chopping", CERN, Geneva, Switzerland, Tech. Rep. CERN-AB-2004-096-RF, Dec. 2004, pp. 578–582. <https://accelconf.web.cern.ch/104/papers/TH202.pdf>
- [4] C. Plostinar, "Design principles for high power linear accelerators", Ph.D. dissertation, Dept. Phys., Univ. Oxford, Oxford, U.K., 2015, pp. 142–188. <https://ora.ox.ac.uk/objects/uuid:c425c3c8-772c-49a0-8764-257ae6af5bd6>
- [5] M. Kireeff Covo *et al.*, "The 88-Inch Cyclotron: A one-stop facility for electronics radiation and detector testing", *Meas.*, vol. 127, pp. 580–587, Oct. 2018. doi:10.1016/j.measurement.2017.10.018
- [6] M. Kireeff Covo *et al.*, "Single radio frequency bucket injection in the 88-Inch Cyclotron using a pulsed high voltage chopper", *Rev. Sci. Instrum.*, vol. 95, no. 1, p. 015112, Jan. 2024. doi:10.1063/5.0183628
- [7] Behlke Power Electronics GmbH, <https://www.behlke.com/>.
- [8] M. Kireeff Covo *et al.*, "Chopped deflector technique for single-bunch extraction at the 88-In Cyclotron", *IEEE Trans. Nucl. Sci.*, vol. 71, no. 12, pp. 2487–2492, Dec. 2024. doi:10.1109/tns.2024.3483452
- [9] Bergoz Instrumentation, Fast Current Transformer (FCT), <https://www.bergoz.com/products/fct/>.

ADVANCES IN TRANSVERSE BEAM HALO CHARACTERIZATION AND IMPLICATIONS FOR HL-LHC*

M. Rakic^{1,†}, P. Hermes, S. Redaelli

European Organization for Nuclear Research (CERN), Geneva, Switzerland

M. Seidel, Paul Scherrer Institute (PSI), Villigen, Switzerland

¹also at École Polytechnique Fédérale de Lausanne (EPFL), Lausanne, Switzerland

Abstract

Measurements of the transverse beam halo in the LHC showed that it contains a non-negligible portion of the total stored beam energy, with potential implications for collimation system performance, machine availability and overall machine protection. In the HL-LHC era, when a significant increase in stored beam energy is planned, the understanding and modelling of the beam halo distribution becomes even more important. This applies particularly for the risk quantification in view of new failure scenarios not present in the LHC, like fast failures of the new crab-cavities or of the quench protection system of new triplet magnets. This contribution summarizes the recent progress in beam halo measurement, new findings from refined analysis methods, an overview of the employment of key measurement techniques, and advancements in experiments aiming to quantify the origin of beam halo. We describe the latest halo models and how they affect the performance of potential active halo control mechanisms in simulations. These developments form a critical input to HL-LHC machine protection strategies.

INTRODUCTION

The Large Hadron Collider (LHC) at CERN is a synchrotron designed to accelerate and collide two beams of protons or heavy ions. Its original design specified a maximum stored energy of 362 MJ per beam at 7 TeV, with intensities of 1.15×10^{11} particles per bunch (ppb) [1]. This value was exceeded during the current operational Run 3, with stored energies reaching up to 430 MJ. Following the planned Long Shutdown 3 (LS3), the LHC will be upgraded to the High-Luminosity LHC (HL-LHC), where stored energies are expected to reach 680 MJ with 2.2×10^{11} ppb [2]. Even small particle losses from such high-intensity beams can trigger quenches in the superconducting magnets, reducing operational efficiency. In worst case scenarios, uncontrolled beam losses could even induce damage to accelerator hardware components. To mitigate these risks, the LHC employs a sophisticated multi-stage collimation system, which will undergo major upgrades to prepare for the HL-LHC era [3]. The collimation system is distributed around the ring, with key installations in Insertion Region (IR) 3 for off-momentum cleaning and IR 7 for betatron cleaning. The primary collimators (TCPs) are placed closest to the beam in

normalized transverse space and intercept large-amplitude particles. Secondary (TCSG) collimators, shower absorbers (TCLA) and tertiary (TCT) collimators, are designed to absorb particles deflected from upstream collimators [4], and optimise the cleaning performance. The material and design of each collimator vary depending on its function [3, 5].

The term *transverse beam halo* refers to particles at large transverse amplitudes, arbitrarily defined beyond 3σ , where σ is the RMS betatron beam size, computed using the nominal normalized emittance: $\epsilon_{\text{LHC}}^n = 3.5 \mu\text{m rad}$ for the LHC and $\epsilon_{\text{HL}}^n = 2.5 \mu\text{m rad}$ for HL-LHC [6]. In Run 3, the measured emittance ϵ_M^n is often lower, around $2 \mu\text{m rad}$ [7]. The most reliable method to characterize the transverse halo is collimator scraping, described in the following chapter. Measurements from LHC Run 1 and 2 indicated that up to 5 % of the beam could lie beyond $3\sigma_{\text{LHC}}$ [8, 9], close to the TCP collimators. Assuming linear scaling with beam intensity, this corresponds to a potential 35 MJ of stored halo energy in HL-LHC [9], though this extrapolation is subject to uncertainties due to changes in beam parameters and machine configuration. In scenarios involving sudden orbit changes—such as those triggered by a crab cavity failure, this halo energy could cause risk to collimators or operational efficiency due to frequent beam dumps [10]. Mitigation hardware (Hollow Electron Lenses [11, 12]) that was initially foreseen to be installed in HL-LHC, is not going to be available at the start of HL-LHC operation. A detailed understanding of the transverse distribution is therefore essential for realistic failure scenario modelling and effective mitigation [13]. This article provides a comprehensive overview of current methods for measuring and quantifying the beam halo, reviews existing analytical approaches, and introduces recent developments in halo distribution modelling. It concludes by discussing the implications of the updated models for halo depletion, supported by numerical simulations evaluating their impact on HL-LHC operation.

METHOD OF HALO MEASUREMENT

Collimator Scraping

The primary collimators in the LHC consist of two movable jaws positioned symmetrically around the circulating beam, at an amplitude of $5\sigma_{\text{LHC}}$ at the top energy of 6.8 TeV in Run 3. These jaws can be independently moved toward the beam core in increments as small as $5 \mu\text{m}$, thereby reducing the effective betatron cut. In IR 7, three primary collimators are installed per beam, enabling halo scraping in

* Research supported by the HL-LHC project.

† milica.rakic@cern.ch

the horizontal (H), vertical (V), and skew (S) planes. During the halo scraping procedure, the other collimation stages remain at their nominal operational settings.

Before starting the halo scraping, the TCP jaws are aligned using beam-based alignment techniques [14], ensuring an accurate centring of the jaws and clearly define the initial betatron cut. As one or both jaws are incrementally moved inward, an increasing fraction of the beam halo is progressively intercepted, and the associated particle losses are monitored using the Beam Current Transformer (BCT) [15]. Two BCT devices provide measurements of both the total (DC) and bunch-resolved (FR) beam currents. The Beam Loss Monitors (BLMs) [16] can also be used for this purpose. They are located downstream of each TCP and provide higher dynamic range. A more detailed discussion of the BCT and BLM-based diagnostic methods can be found in [17, 18]. The inward movements are stopped once a predefined target amplitude is reached (typically $3\sigma_{\text{LHC}}$) or until beam losses approach the beam abort threshold levels. As an outcome, a fraction of the beam current stored in the transverse beam halo is measured as a function of the collimator amplitude.

Scraping measurements are inherently destructive, which precludes repeated measurements on the same beam. Continuous halo monitoring in operation therefore requires alternative approaches, which are currently being developed. As potential techniques, measurements based on Synchrotron Radiation Halo telescopes, Beam Gas Curtain, and Beam Gas Ionization monitors [19] are considered. In this work, the authors present their results based on the scraping measurements using BCT data.

Post-processing

A dataset comprising over ten scraping measurements, taken at the end of physics fills during Run 2 (6.5 TeV) and Run 3 (6.8 TeV), has been analysed to provide insights into the transverse beam halo under operational conditions. The transverse halo profile was reconstructed as a function of betatron amplitude for each beam and for both the horizontal (H) and vertical (V) transverse plane. To account for variations in beam emittance across measurements (ranging from 1.2 to 3.1 $\mu\text{m rad}$), determined using the Beam Synchrotron Radiation Telescope (BSRT) [20], the betatron cut was re-scaled according to the measured emittance ϵ_M . This re-normalisation is essential for mitigating biases introduced by fluctuations in beam size.

We conduct two complementary analyses: the first utilizes BCT-DC signal which provides a measurement of the total beam intensity. In this approach, data were aggregated over a common amplitude range to estimate the mean halo content, with corresponding 95 % confidence intervals computed to quantify statistical uncertainty. The second analysis employs a BCT-FR approach, capable of resolving individual bunch currents, from which summary statistics can be derived. The distribution of halo content across all bunches

is visualized as a two-dimensional histogram. The increased volume of data in this per-bunch analysis facilitates a more precise estimation of the average halo content.

BEAM HALO MODELS

Generalised Gaussian Models

The characterisation of the analytical form of the transverse beam halo has been the focus of extensive research efforts, with Gaussian (G), q-Gaussian (qG), and double-Gaussian (dG) distributions being among the most frequently employed models [8, 9]. Let us model collimator scraping in normalised transverse phase space, defined by coordinates (U, U') , where $U = \{X, Y\}$. The generalized particle amplitude in this space is expressed as $r = \sqrt{U^2 + U'^2}$. Consequently, halo profiles derived from collimator scrapings are naturally represented in radial space, incorporating both canonical variables. Standard analytical distributions are typically defined in projection space, with their probability density functions depending solely on a single normalized coordinate U .

To compare scraping-derived halo profiles to analytical models, it is imperative that both be expressed within a common coordinate framework—either in projection space or radial space. Although these representations are, in principle, mathematically interchangeable, the present study adopts the radial space formulation as the reference framework. The above-mentioned analytical distributions are transformed into radial space using the inverse Abel transformation [21], following the methodology detailed in [6]. The final forms of the corresponding probability density functions (PDFs) are presented below without derivation:

$$f_G(r) = \frac{r}{\sigma^2} \cdot e^{-\frac{r^2}{2\sigma^2}}, \quad (1)$$

$$f_{dG}(r) = w_1 \cdot f_{G1}(r) + (1 - w_1) \cdot f_{G2}(r), \quad (2)$$

$$f_{qG}(r) = \frac{\beta(3-q)}{2\pi} r \left(1 + \beta(q-1)r^2\right)^{\frac{q+1}{2(1-q)}}. \quad (3)$$

Here, r denotes the particle amplitude; σ is the standard deviation, w_1 and $1 - w_1$ represent the normalized weights of the two Gaussian components $f_{G1}(r)$ and $f_{G2}(r)$, respectively; and β and q are parameters¹ governing the width and tail population of the q-Gaussian distribution. Notably, the special case where $w_1 = 1$, $\sigma_1 = 1$ for the double-Gaussian or $q = 1$, and $\beta = 0.5$ for the q-Gaussian, results in a distribution that equals the Gaussian form.

To compare these models with experimental data, the cumulative distribution functions (CDFs) corresponding to the aforementioned PDFs are fitted to the measured profiles using a least-squares optimization. To preserve the physical validity of the modelled beam, the second-order moment (i.e., the beam size and thereby the emittance) is constrained to remain constant throughout the fitting procedure.

¹ Note that β is not the betatron function

Results Based on BCT-DC Analysis

Figures 1 and 2 present the halo content, expressed as estimated stored halo intensity in the HL-LHC, as a function of the collimator amplitude r , expressed in units of the measured beam size σ_M . The mean estimates obtained from Run 2 and Run 3 are indicated by red and blue markers, respectively, with corresponding 95% confidence intervals. In all cases the starting TCP position was at $5\sigma_{\text{LHC}}$. Following the LHC Injectors Upgrade [22], the smaller emittance delivered in Run 3 causes the measured halo at a given amplitude in σ_{LHC} to correspond to larger amplitudes in σ_M compared to Run 2. The mean halo profiles have been fitted to the modelled CDFs corresponding to the Gaussian, double-Gaussian, and q-Gaussian distributions.

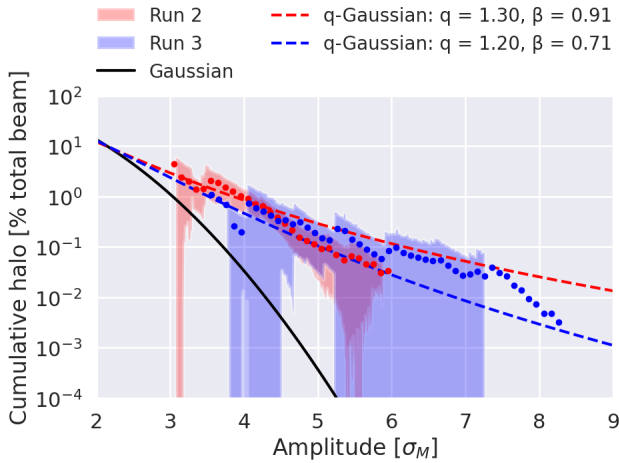


Figure 1: Estimated total stored HL-LHC halo intensity as a function of amplitude, fitted using q-Gaussian distributions for Run 2 (red line) and Run 3 (blue line) measurements. For comparison, a standard Gaussian distribution is also shown (black line).

These results indicate that the measured halo distribution exhibits significantly higher population levels compared to the standard Gaussian distribution, as illustrated by the black line in Fig. 1. This observation aligns qualitatively to previously reported findings [18]. Moreover, the measured data are well represented by q-Gaussian models, specifically with parameters $q = 1.3$, $\beta = 0.91$ for Run 2 (red dashed line), and $q = 1.2$, $\beta = 0.71$ for Run 3 (blue dashed line).

The best-fit double-Gaussian models—defined by $w_1 = 0.15$, $\sigma_1 = 1.7$, $\sigma_2 = 0.8$ for Run 2 (red dash-dot line), and $w_1 = 0.05$, $\sigma_1 = 1.9$, $\sigma_2 = 0.9$ for Run 3 (blue dash-dot line) shown in Fig. 2—adequately capture the halo structure near the beam core. However, they fail to accurately represent the high-amplitude tail of the distribution, which is critical for halo characterization. For reference, a previously adopted double-Gaussian model with parameters $w_1 = 0.65$, $\sigma_1 = 1.0$, and $\sigma_2 = 2.0$ (black dash-dot line in Fig. 2) is also included. Although this model adopts a conservative approach, it clearly demonstrates its limitations in accurately capturing the characteristics of the measured data.

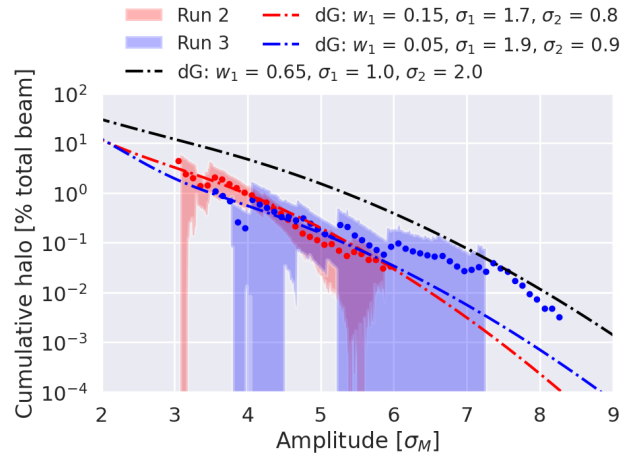


Figure 2: Estimated total stored HL-LHC halo intensity as a function of amplitude, fitted using double-Gaussian distributions for Run 2 (red line) and Run 3 (blue line) measurements. For comparison, the previously used double-Gaussian halo model is shown as a black dash-dot line.

Results Based on BCT-FR Analysis

A procedure similar to the one described above was applied to bunch-resolved beam current measurements. In this case, the scaling was performed using the emittance σ_M of each individual bunch, rather than an averaged beam emittance, thereby eliminating uncertainties associated with the averaging process. The influence of the bunch-by-bunch orbit shifts induced by the beam-beam interaction are not considered.

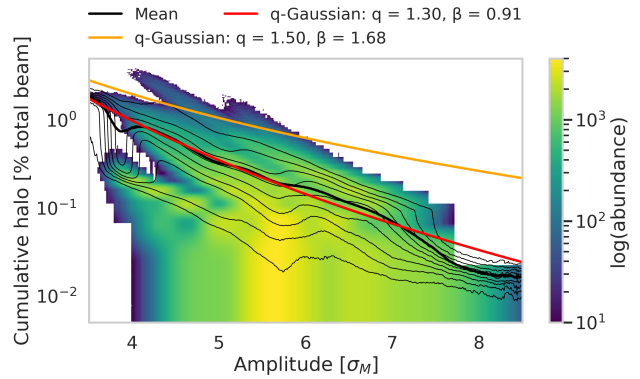


Figure 3: Estimate of the stored HL-LHC halo intensity as a function of amplitude, based on bunch-resolved current measurements. The bunch population is represented as a logarithmic heatmap, with q-Gaussian fits overlaid: $q = 1.3$, $\beta = 0.91$ (red line), and $q = 1.5$, $\beta = 1.68$ (orange line).

Figure 3 presents a two-dimensional histogram compiled from four Run 3 measurements, encompassing data from over 42 000 bunches. The colour map represents the abundance of bunches at each combination of amplitude and halo content. Thin black lines indicate the 10th to 90th percentiles, while the thick black line denotes the mean values across the data. The q-Gaussian model, characterized

by parameters $q = 1.3$ and $\beta = 0.91$ (red line), shows an excellent agreement with the mean of the bunch-resolved data. It is clearly visible that this q-Gaussian model provides an accurate representation of the halo measured across bunches. It is not far from the full-beam measurements, with the difference possibly driven by the different re-scaling to the measured emittances.

For machine protection simulations, more conservative models can be employed, such as a q-Gaussian distribution with parameters $q = 1.5$ and $\beta = 1.68$ (orange line), selected to lie above the 90th percentile. Given the uncertainty in individual bunch trajectories under failure conditions, this model is based on the most highly populated bunches to ensure relevance for worst-case scenarios. These updated profiles serve as the reference for halo mitigation and depletion studies, and are intended to replace the previously used double-Gaussian model in upcoming numerical investigations of HL-LHC failure scenarios.

HALO DEPLETION STUDIES

HEL Concept Overview

Various halo control and depletion techniques have been explored over the years [23]. These include active halo control using the Hollow Electron Lenses (HEL) [11, 12], which are unavailable at least until the start of LHC Run 5 [3]. The HEL generates a circularly symmetric hollow electron beam between an inner (r_i) and an outer (r_o) radius that propagates co-axially with the circulating proton beam, but in the opposite direction. This electron beam interacts electromagnetically with the proton beam in a manner that preserves the integrity of the beam core, which experiences a nominally null field, while imparting small transverse kicks $\theta(r)$ to halo particles:

$$\theta(r) \sim \frac{f(r)}{r}, \quad f(r) = \begin{cases} 0, & \text{if } r < r_i, \\ \frac{r^2 - r_i^2}{r_o^2 - r_i^2}, & \text{if } r_i < r < r_o, \\ 1, & \text{if } r > r_o. \end{cases} \quad (4)$$

where r is the particle amplitude. These kicks increase the particle action of the halo particles, thereby enhancing their controlled diffusion towards the collimation system, where they are absorbed. Among the various possible operational modes [12], the *random turn-by-turn pulsing mode*—in which the HEL current is switched randomly on or off each turn has been shown to be the most efficient. When switched on, the electron current is fixed [24]. We will therefore focus on this operational mode for this study.

The performance of the HEL in halo depletion is quantified using the depletion efficiency, denoted as \mathcal{R} :

$$\mathcal{R} = 1 - \frac{n_{\text{halo}}^{\text{HEL}}}{n_{\text{halo}}^0}. \quad (5)$$

where $n_{\text{halo}}^{\text{HEL}}$ denotes the number of halo particles in the halo if the HEL is used, while n_{halo}^0 corresponds to the number of halo particles in the absence of HEL operation. Both figures are computed at amplitudes affected by the hollow electron beam. In the context of HL-LHC there are two primary collimator settings currently being considered: the nominal IR 7 TCP half-gap of $r_{\text{TCP}} = 6.7 \sigma_{\text{HL}}$ and relaxed half-gap of $8.5 \sigma_{\text{HL}}$ at HL-LHC top-energy – introduced to reduce the impact of the impedance on the circulating beam.

Simulation Setup and Machine Settings

The HEL is set up using an electron current of 5 A, electron energy of 10 keV and a length of 3 m. The electron beam radii are $r_i = r_{\text{TCP}} - 2 \sigma_{\text{HL}}$ and $r_o = 2 r_i$. The HL-LHC V1.6 optics after energy-ramp at 7 TeV and $\beta^* = 15$ cm are used, without considering the beam-beam effects. The main machine optics parameters are shown in Tab. 1. At the position of the HEL the local optics are round (same in both planes) with $\beta_x = \beta_y = 280$ m.

Table 1: HL-LHC Optics Parameters Used in Numerical Simulations Where $Q_{x,y}$ are the Tunes in Transverse Planes, Q' is the Chromaticity, I_{MO} is the Landau Octupole Current, and r_{TCP} is the TCP Half-Gap of the Primary Collimators

Parameter	Value
Beam	B1
β^* (IR1 / IR5)	15 cm
Q_x, Q_y	62.305, 60.311
Q'	15
I_{MO}	380 A
r_{TCP}	$(6.7 - 8.5) \sigma_{\text{HL}}$
r_i^{HEL}	$(4.7 - 6.5) \sigma_{\text{HL}}$

The initial distributions used in all simulations are $q = 1.3$ and $\beta = 0.91$ (qG-1.3) which is the most realistic representation of the halo, and the q-Gaussian of $q = 1.5$ and $\beta = 1.68$ (qG-1.5) as a worst case scenario for conservative simulations, and as a comparison to the previously used double-Gaussian of $w_1 = 0.65$, $\sigma_1 = 1.0$ and $\sigma_2 = 2.0$ (dG-0.65). Each simulation considers 100 000 initial particles, with no momentum spread $\delta = 0$.

Results of HEL Cleaning Performance

The simulated HEL depletion efficiency in the random pulsing mode, with collimators in nominal position at $r_{\text{TCP}} = 6.7 \sigma_{\text{HL}}$ is presented in Fig. 4. For both q-Gaussian distributions, a depletion efficiency of more than 90 % can be achieved within one minute of HEL operation at maximum current. In contrast, the double-Gaussian model with $w_1 = 0.65$ attains a DE of only 66 % over the same duration. These results are consistent with previous studies [24] and can be explained by the interplay of the different cumulative halo distributions and the non-linear scattering angle

as a function of amplitude, exerted by the HEL beam. Particles from distributions with larger halo population near the TCPs (q-Gaussian) are depleted faster than those from distributions with a smaller halo population in this region (double-Gaussian).

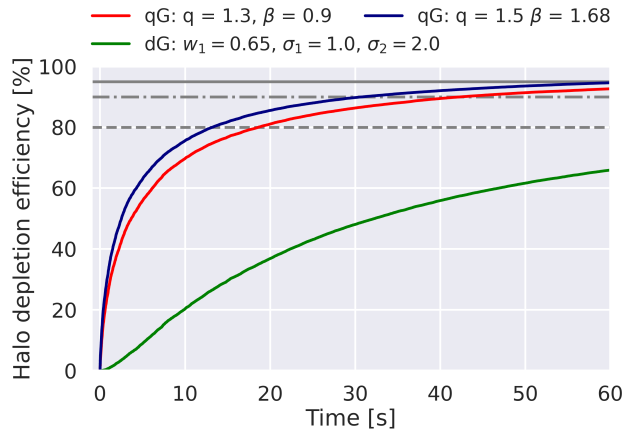


Figure 4: Simulation of halo depletion efficiency (DE) with the HL-LHC TCP set to 6.7σ for three different initial distributions: qG-1.3 (red), qG-1.5 (blue), and dG-0.65 (green). Depletion efficiency thresholds of 80 % (dashed line), 90 % (dash-dot line), and 95 % (solid line) are indicated by gray horizontal lines.

The same procedure is applied to an alternative scenario in which the collimators are at relaxed settings, with $r_{\text{TCP}} = 8.5 \sigma_{\text{HL}}$ and the HEL inner radius at $r_i = 6.5 \sigma_{\text{HL}}$, with remaining HEL parameters unchanged, as illustrated in Fig. 5. In this configuration, the achievable depletion efficiency (DE) within one minute is significantly reduced for both q-Gaussian distributions. After two minutes of HEL operation, the depletion efficiency reaches only 18 % for the $q = 1.3$ model and 27 % for the $q = 1.5$ model. Note that a likely contributing factor to this difference is that increasing the HEL inner radius r_i reduces the deliverable kick strength, making the HEL less effective in this configuration. Nonetheless, both cases demonstrate the continued effectiveness of the HEL, reinforcing its importance as a key instrument to be considered for halo control in HL-LHC Run 5, independent of the actual distribution of beam halo particles.

OUTLOOK AND CONCLUSIONS

The presented study offers a detailed characterization of the transverse beam halo expected at the HL-LHC, using collimator scraping as the primary diagnostic technique. The analysis of measured data – both for the total beam and bunch-resolved measurements – revealed consistent and complementary results. Several analytical distributions were investigated for halo modelling, including Gaussian, q-Gaussian, and double-Gaussian profiles, using a fitting algorithm that conserves the measured beam size. Among these, the q-Gaussian distribution, with parameters $q = 1.3$

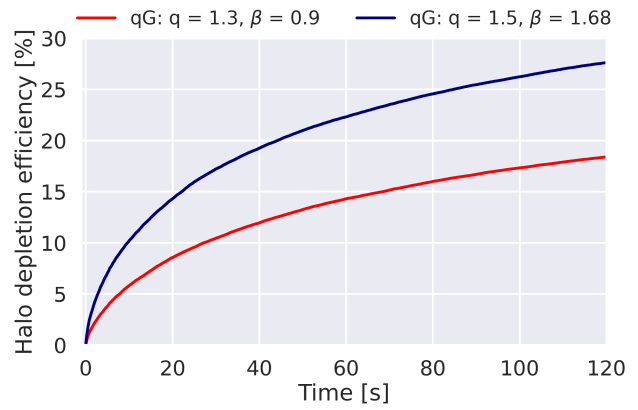


Figure 5: Simulation of halo depletion efficiency with TCP set to 8.5σ for two different initial distributions: qG-1.3 (red) and qG-1.5 (blue).

and $\beta = 0.91$, provided the best fit to the data, especially in the high-amplitude regions that are critical for machine protection. Additionally, an alternative q-Gaussian model with $q = 1.5$ and $\beta = 1.68$ is proposed for machine protection studies, as it effectively captures all measured halo profiles with content above the 90th percentile. These models will serve as baseline inputs for future HL-LHC failure scenario analyses. Extrapolation of the measured halo distributions to HL-LHC energies indicates an overpopulation in the beam halo compared to a Gaussian distribution, which must be carefully evaluated for possible impacts on machine safety.

As a case study, simulation-based analyses were performed to evaluate the sensitivity of halo depletion efficiency to the underlying beam halo model, using HEL as an active halo control mechanism. The results confirm that the HEL can effectively deplete the halo, particularly in the random pulsing mode, when operated with the HL-LHC collimation baseline settings. A moderate reduction in efficiency is observed under more relaxed collimation settings currently under consideration for Run 4. Further on, a difference between the HEL depletion efficiency is observed based on initial halo distribution. Future work will investigate alternative active halo control methods to meet HL-LHC performance and protection goals. Concurrently, updated halo models will be integrated into failure scenario simulations – such as quench protection heater and crab cavity malfunctions – and depletion strategies will be validated via tracking simulations and, where possible, experimental beam measurements.

ACKNOWLEDGMENTS

We would like to thank the BE-OP LHC shift crews for their constant support in these measurements, as well as colleagues from BE-ABP-INC for their invaluable inputs and constructive discussions.

REFERENCES

- [1] O. S. Brüning *et al.*, “LHC Design Report”, CERN, Geneva, Switzerland, Rep. CERN-2004-003-V1, 2004.
doi:10.5170/CERN-2004-003-V-1
- [2] O. Aberle *et al.*, “High-Luminosity Large Hadron Collider (HL-LHC): Technical Design Report”, CERN, Geneva, Switzerland, Rep. CERN-2020-010, 2020.
doi:10.23731/CYRM-2020-0010
- [3] S. Redaelli, R. Bruce, A. Lechner, and A. Mereghetti, “Chapter 5: Collimation system”, in *High-Luminosity Large Hadron Collider (HL-LHC): Technical Design Report*, vol. 10, Geneva, Switzerland: CERN, 2020, pp. 87–114.
doi:10.18429/JACoW-HB2023-THBP49
- [4] B. Salvachua *et al.*, “LHC collimation cleaning and operation outlook”, in *Proc. Evian Workshop on LHC beam operation*, Evian-les-Bains, France, 2012, pp. 155–160. <https://cds.cern.ch/record/2302435>
- [5] R. W. Assmann *et al.*, “The Final Collimation System for the LHC”, in *Proc. EPAC’06*, Edinburgh, UK, Jun. 2006, paper TUODFI01, pp. 986–988.
- [6] M. Rakic, P. Hermes, and S. Redaelli, “An updated HL-LHC halo population model based on recent experimental measurements”, in *Proc. IPAC’25*, Taipei, Taiwan, Jun. 2025, paper WEPS110, pp. 2396–2399.
doi:10.18429/JACoW-IPAC25-WEPS110
- [7] S. Kostoglou, H. Bartosik, I. Efthymiopoulos, and G. Sterbini, “Analysis of losses and emittance growth in the 2024 LHC run and correlation with Dynamic Aperture”, in *Proc. IPAC’25*, Taipei, Taiwan, Jun. 2025, paper WEPM044, pp. 2026–2029.
doi:10.18429/JACoW-IPAC25-WEPM044
- [8] G. Valentino *et al.*, “Beam diffusion measurements using collimator scans in the LHC”, *Phys. Rev. Spec. Top. Accel. Beams*, vol. 16, no. 2, p. 021003, Feb. 2013.
doi:10.1103/physrevstab.16.021003
- [9] A. Gorzawski *et al.*, “Probing LHC halo dynamics using collimator loss rates at 6.5 TeV”, *Phys. Rev. Accel. Beams*, vol. 23, no. 4, p. 044802, Apr. 2020.
doi:10.1103/physrevaccelbeams.23.044802
- [10] B. Lindstrom *et al.*, “Crab Cavity Failures Combined with a Loss of the Beam-Beam Kick in the High Luminosity LHC”, in *Proc. IPAC’18*, Vancouver, Canada, Apr.-May 2018, pp. 192–195. doi:10.18429/JACoW-IPAC2018-MOPMF042
- [11] S. Redaelli *et al.*, “Hollow electron lenses for beam collimation at the High-Luminosity Large Hadron Collider (HL-LHC)”, *J. Instrum.*, vol. 16, no. 03, p. P03042, Mar. 2021.
doi:10.1088/1748-0221/16/03/p03042
- [12] D. Mirarchi *et al.*, “Nonlinear dynamics of proton beams with hollow electron lens in the CERN high-luminosity LHC”, *Eur. Phys. J. Plus*, vol. 137, no. 1, p. 7, Dec. 2021.
doi:10.1140/epjp/s13360-021-02201-5
- [13] B. Lindstrom *et al.*, “Fast failures in the LHC and the future high luminosity LHC”, *Phys. Rev. Accel. Beams*, vol. 23, no. 8, p. 081001, Aug. 2020.
doi:10.1103/PhysRevAccelBeams.23.081001
- [14] G. Azzopardi, B. Salvachua, G. Valentino, S. Redaelli, and A. Muscat, “Operational results on the fully automatic LHC collimator alignment”, *Phys. Rev. Accel. Beams*, vol. 22, no. 9, p. 093001, Sep. 2019.
doi:10.1103/PhysRevAccelBeams.22.093001
- [15] P. Odier, M. Ludwig, and S. Thoulet, “The DCCT for the LHC Beam Intensity Measurement”, in *Proc. DIPAC’09*, Basel, Switzerland, May 2009, paper MOPD45, pp. 143–145. <https://jacow.org/d09/papers/MOPD45.pdf>
- [16] S. Morales Vigo *et al.*, “Beam lifetime monitoring using beam loss monitors during LHC Run 3”, in *Proc. IPAC’23*, Venice, Italy, May 2023, pp. 4645–4648.
doi:10.18429/JACoW-IPAC2023-THPL086
- [17] P. Hermes *et al.*, “Collimator Scan Based Beam Halo Measurements in LHC and HL-LHC”, in *Proc. IBIC’23*, Saskatoon, Canada, 2023, pp. 164–168.
doi:10.18429/JACoW-IBIC2023-TU3C03
- [18] M. Rakic *et al.*, “Updated analysis of beam halo measurements in LHC Run 2 and Run 3”, in *Proc. IPAC’24*, Nashville, TN, USA, May 2024, pp. 3175–3178.
doi:10.18429/JACoW-IPAC2024-THPC67
- [19] J. Pucek *et al.*, “Beam Synchrotron Radiation Halo, Beam Gas Curtain and Beam Gas Ionization monitor development”, in *HL-LHC Beam Halo Monitor Review*, Geneva, Switzerland, 2024. <https://indico.cern.ch/event/1483006/contributions/6253169/>
- [20] R. Jung, F. Méot, and L. Ponce, “LHC proton beam diagnostics using synchrotron radiation”, CERN, Geneva, Switzerland, Rep. CERN-2004-007, 2004.
doi:10.5170/CERN-2004-007
- [21] N. H. Abel, “Auflösung einer mechanischen Aufgabe”, *J. für die reine und angewandte Math.*, vol. 1826, no. 1, pp. 153–157, Jan. 1826. doi:10.1515/crll.1826.1.153
- [22] H. Damerau *et al.*, “LHC Injectors Upgrade, Technical Design Report”, CERN, Geneva, Switzerland, Rep. CERN-ACC-2014-0337, 2014. doi:10.17181/CERN.7NHR.6HGC
- [23] J. F. Wagner *et al.*, “First Attempts at using Active Halo Control at the LHC”, in *Proc. IPAC’16*, Busan, Korea, May 2016, pp. 2486–2489.
doi:10.18429/JACoW-IPAC2016-WEPMW028
- [24] P. Hermes *et al.*, “HL-LHC Beam Dynamics with Hollow Electron Lenses”, in *Proc. HB’21*, Batavia, Illinois, United States, 2022, pp. 59–64.
doi:10.18429/JACoW-HB2021-MOP09

THE BEAM DYNAMICS CASE OF BEAM-BEAM WIRE COMPENSATORS FOR THE HL-LHC ERA

P. Bélanger^{*,1}, R. Baartman, D. Kaltchev, TRIUMF, Vancouver, Canada
G. Sterbini, CERN, Geneva, Switzerland

¹ also at University of British Columbia, Vancouver, Canada

Abstract

Beam-beam long-range interactions are known to be a strong source of non-linearities in hadron colliders, undermining the performance of the Large Hadron Collider (LHC) during proton-proton collisions. In order to enhance the luminosity production of the machine and increase the tolerance of the working point after the High Luminosity upgrade of the LHC (HL-LHC), dedicated correctors such as beam-beam wire compensators can be used. In this paper, the beam dynamics of this compensation problem is studied in details, ultimately showing that the linearity of the machine can be significantly improved throughout the beam core — and up to several sigmas — leading to an improvement of the dynamic aperture. This conclusion is shown to be supported by analytic calculations, simulation studies, as well as experimental results presented in earlier work. With the proposed approach, wire compensators can be positioned according to the collimation settings, simplifying their implementation in the machine for the HL-LHC era.

INTRODUCTION

The Large Hadron Collider (LHC) is soon to be upgraded into the High-Luminosity LHC (HL-LHC) which is planned to be operational by 2030. For this new era, the focus will be to increase the luminosity production of the machine by pushing the operational scenarios into increasingly challenging regimes. As such, controlling the non-linearities of the lattice and improving the beam lifetime is critical to reach the target of the HL-LHC project. Alongside electron clouds, the main source of non-linearities in the LHC is the beam-beam (BB) effect, arising from the electromagnetic interaction between the two counter-rotating beams. In the interaction regions (IRs), the two beams share a common beam pipe and perturb one another. Head-On (HO) collisions take place at the interaction points (IPs), whereas Long-Range (LR) interactions are distributed on both sides of the IPs. These interactions, akin to strong multipolar errors, occur several times (≈ 50) per IR for the nominal bunches and contribute to the excitation of high-order resonances, eventually leading to particle diffusion, particle losses and the reduction of dynamic aperture [1–3].

To mitigate this problem, current-carrying wires have been proposed as a correction device to compensate the BBLR kicks [4–6]. As shown in Fig. 1, these so-called beam-beam wire compensators (BBWCs) need to be

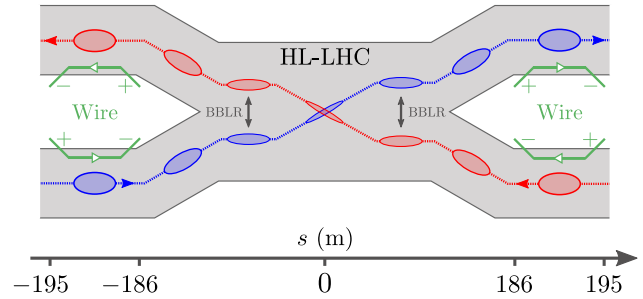


Figure 1: BBCW layout for HL-LHC around IP1 and IP5.

Table 1: HL-LHC Parameters (End of Lumi-Levelling)

Parameter		Value	Unit
Beam Energy	E	7.0	(TeV)
Bunch intensity	N_b	1.13×10^{11}	(p ⁺ /b)
Norm. Emittance	$\varepsilon_x^N, \varepsilon_y^N$	2.5	($\mu\text{m}\cdot\text{rad}$)
Beta at the IP	β^*	15	(cm)
Half-crossing	$\theta_c/2$	250	(μrad)
Crabbing angle	θ_{cc}	-190	(μrad)
Octupoles	I_{oct}	-60	(A)
Chromaticity	$\Delta Q_x, \Delta Q_y$	15	

installed after the separation dipoles in order to act separately on the two beams, which travel in opposite directions.

The Maxwellian equivalence between current-carrying wires and beams of charged particles has been well-established theoretically by several authors over the last few decades [4, 6, 7]. On the experimental front, successful beam-beam compensation was recently demonstrated in the LHC during dedicated machine development experiments [8, 9] as well as regular LHC operation [9]. However, the integration of a full-scale compensation system in the machine for the HL-LHC era — the first of its kind — requires additional considerations to optimize the effects on the beam dynamics, as discussed below.

In this paper, the linearity of the IRs is studied with and without BBWCs at various amplitudes using the non-linear residual, which will be introduced. This method complements the usual resonance driving terms (RDTs) approach, while reducing the complexity of the analysis by directly using generic tracking codes to reach its conclusions. To support the results, dynamic aperture scans are presented.

* philippe.belanger@cern.ch

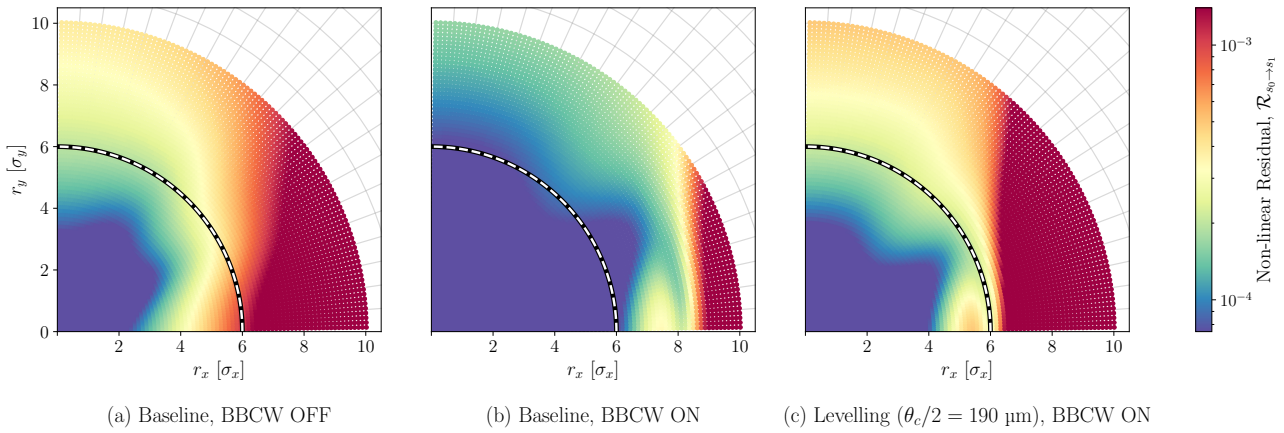


Figure 2: Non-linear residual, \mathcal{R} , through IR1 for various amplitudes, (r_x, r_y) , in HL-LHC. (a) Without BBWCs. (b) With BBWCs at 15σ and 400 A·m. (c) After reducing the crossing angle, with BBWCs at 12σ and 400 A·m.

EQUIVALENCE PRINCIPLE

In the transverse plane (4D), the beam-beam kick from a gaussian bunch of protons with size σ is purely radial and scales with the radial distance, r , following:

$$\Delta p_r = -e \frac{\mu_0}{2\pi r} (IL)_{\text{eq}} \times \left(1 - e^{-r^2/2\sigma^2}\right), \quad (1)$$

where $(IL)_{\text{eq}} = -N_b \cdot (ec) \cdot [(1 + \beta^2)/(2\beta)]$ is the equivalent current for a bunch of intensity N_b traveling with a relativistic velocity parameter β . One can see that the beam-beam *long-range* kick (a regime where $r \gg \sigma$) is equivalent to the kick of an infinite wire powered with the equivalent current $(IL)_{\text{eq}}$. In turn, it can be shown that the magnetic field of an infinite wire is the one of a pure multipole, exciting contributions from all multipolar components [10]. As such, the effect on the beam dynamics scales with the beta functions (β_x, β_y) at the location of the kick and depends on the beta ratio, $\rho = \beta_y/\beta_x$.

In principle, any single BBLR kick can be naturally compensated using a dedicated BBWC installed in phase at the appropriate beta ratio ($\rho_{\text{BBLR}} = \rho_{\text{BBWC}}$) and at the appropriate distance from the beam. That being said, the HL-LHC lattice contains many BBLRs distributed over the IRs (≈ 50 , with varying beta ratios), and only 2 BBWCs located after the separation dipoles on each sides of the IRs. This specific compensation scheme, introduced and thoroughly studied in earlier work [6], makes use of the antisymmetric optics of the IRs to reduce the number of BBWCs required. Indeed, with the phase advance between the BBLRs being negligible and the antisymmetric optics of HL-LHC (left to right, $\rho_L = 1/\rho_R$), it has been shown that the overall RDTs of the lattice could be optimally compensated using only a pair of wires. Since the beam-beam separation is symmetric on both sides of the IPs, it is moreover required that the BBWCs be placed symmetrically on both sides of the IPs to reach the optimal compensation.

This equivalence principle — reducing 50 BBLRs to 2 BBWCs — is an important feature of the problem. However, departing from the optimal compensation scheme suggested in earlier work [6], this paper is set to demonstrate that a satisfactory compensation can also be achieved over a wide range of operational parameters. In particular, it will be shown that the 2 BBWCs need not be installed symmetrically on both sides of the IPs, but can instead be installed at a similar normalized distance (in units of σ_x and σ_y). This choice of implementation could, in principle, facilitate the integration of the devices in the machine (in terms of machine protection), ensuring that the requirements of the HL-LHC collimation hierarchy are safely met.

COMPENSATION AND LINEARIZATION

Phase Space Rotation

Let's consider a general transverse Hamiltonian (4D) acting between the longitudinal locations s_0 and s_1 and written in terms of the normalized Courant-Snyder coordinates, \vec{x} , following:

$$\tilde{\mathcal{H}}_{s_0 \rightarrow s_1} = \mu_x \pi (\tilde{x}^2 + \tilde{p}_x^2) + \mu_y \pi (\tilde{y}^2 + \tilde{p}_y^2) + \tilde{\mathcal{H}}_{\text{NL}}(\vec{\tilde{x}}), \quad (2)$$

where μ_x and μ_y are the linear phase advances (in units of 2π) for both planes and $\tilde{\mathcal{H}}_{\text{NL}}(\vec{\tilde{x}})$ is a general non-linear term. As can be shown from Lie algebra [11, 12], the transformation $\exp(: -\tilde{\mathcal{H}}_{s_0 \rightarrow s_1} \Delta s :)$ corresponds to a pure rotation in both the (\tilde{x}, \tilde{p}_x) and the (\tilde{y}, \tilde{p}_y) phase spaces if the non-linear part of the Hamiltonian, $\tilde{\mathcal{H}}_{\text{NL}}(\vec{\tilde{x}})$, vanishes. On the other hand, with the non-linear term being non-zero, the corresponding transformation becomes a non-trivial deformation of the phase space. This is namely the case, *e.g.*, for the IRs of HL-LHC, when BBLR kicks are considered. It is possible, however, to combine non-linear lenses in such a way that the non-linear term vanishes or reduces to an additional linear term. Hence, we shall say that a non-linear beam line like the one of eq. (2) is *compensated* if the overall transformation

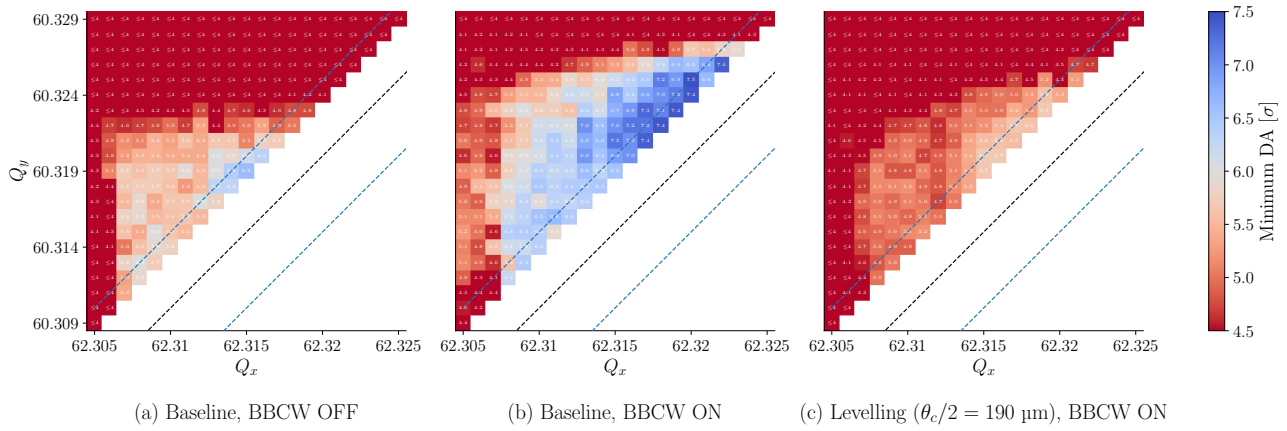


Figure 3: Dynamic aperture scans over various working points, (Q_x, Q_y) , for HL-LHC. (a) Without BBWs. (b) With BBWs at 14.75σ and 450 A-m. (c) After reducing the crossing angle, with BBWs at 13σ and 450 A-m.

takes the form of a pure rotation in the Courant-Snyder phase space with some non-trivial effective rotation numbers μ'_x and μ'_y . In other words: to compensate is to linearize, bringing the transformation back to a pure rotation.

Non-Linear Residual

This particular framing of the problem makes it clear that the linearity of a beam line can be measured by evaluating how the corresponding transformation, $\exp(-\tilde{H}_{s_0 \rightarrow s_1} \Delta s)$, departs from a pure rotation. As shown in a separate work [12], this can be achieved by comparing the Courant-Snyder linear invariant, $J_x = \frac{1}{2}(\tilde{x}^2 + \tilde{p}_x^2)$, to the Poincaré non-linear invariant [13], I_x , via the *non-linear residual*, \mathcal{R} , defined as:

$$\mathcal{R} \equiv \frac{\|\langle \vec{J} \rangle - \vec{I} \|}{\|\vec{I} \|} \quad \text{with } \vec{I} = \begin{pmatrix} I_x \\ I_y \end{pmatrix} \text{ and } \langle \vec{J} \rangle = \begin{pmatrix} \langle J_x \rangle \\ \langle J_y \rangle \end{pmatrix}, \quad (3)$$

where the average $\langle \vec{J} \rangle$ is taken over N particles uniformly distributed over 4-dimensional tori, allowing to cover all possible phases in both planes, ϕ_x and ϕ_y . This figure of merit can be evaluated directly from tracking data to quantify the non-linear deformation. To do so, particles are placed at fixed radial amplitudes (r_x, r_y) in the Courant-Snyder phase space $((\tilde{x}, \tilde{p}_x)$ and (\tilde{y}, \tilde{p}_y)) with various phases (ϕ_x, ϕ_y) and tracked through the beam line. By symplecticity, the projected areas $(I_x, I_y) = \frac{1}{2}(r_x^2, r_y^2)$ are preserved throughout the beam line but the radial excursions, $\frac{1}{2} \langle \tilde{x}^2 + \tilde{p}_x^2 \rangle$ and $\frac{1}{2} \langle \tilde{y}^2 + \tilde{p}_y^2 \rangle$ are not, due to non-linear deformations. Hence, the non-linear residual can be ultimately evaluated following:

$$\mathcal{R}_{s_0 \rightarrow s_1} = \sqrt{\frac{(\langle \tilde{x}^2 + \tilde{p}_x^2 \rangle - r_x^2)^2 + (\langle \tilde{y}^2 + \tilde{p}_y^2 \rangle - r_y^2)^2}{r_x^2 + r_y^2}}, \quad (4)$$

at various amplitudes. By definition, the residual vanishes ($\mathcal{R} = 0$) for a pure rotation and is strictly positive ($\mathcal{R} > 0$) otherwise.

BBLR COMPENSATION IN HL-LHC

In Fig. 2, the linearity of a section of the HL-LHC lattice (IR1) is evaluated for the baseline configuration of the machine at the end-of-levelling. One can see that without BBWs (Fig. 2(a)), the lattice becomes highly non-linear around the 6σ line. With compensation (Fig. 2(b)), the level of linearity originally found only in the core of the beam is pushed beyond the 6σ line, showing a successful compensation of the BBLR kicks. Finally, it is also shown that BBWs can allow to reduce the crossing angle further into the levelling process (Fig. 2(c)) while preserving a similar non-linear residual to that of the baseline configuration.

Contrarily to typical RDT-based approaches, the non-linear residual allows to visualize the effect of non-linearities at various amplitudes, while providing a comparative metric to assess the quality of the compensation. As such, one can conclude that a satisfactory compensation is obtained in IR1 — despite the non-optimal compensation scheme considered — as shown in Fig. 2(b). To validate these claims, dynamic aperture scans were performed for each configuration, as shown in Fig. 3. One can see that the DA is significantly improved (reaching the HL-LHC target of 6σ) for a wide variety of working points when powering the BBWs.

SUMMARY

This paper presents a revised compensation scheme for beam-beam wire compensators in the HL-LHC era, allowing the wires to be positioned at the same normalized distance on both sides of the IPs. By studying the non-linear residual over IR1, it is shown that BBWs can significantly improve the stability of the beam dynamics over a wide region of the transverse plane, making the machine sufficiently linear, beyond the 6σ line. To support this claim, dynamic aperture scans are provided, showing an improved range of possible working points for HL-LHC.

REFERENCES

- [1] K. Skoufaris *et al.*, “Numerical optimization of dc wire parameters for mitigation of the long range beam-beam interactions in High Luminosity Large Hadron Collider”, *Phys. Rev. Accel. Beams*, vol. 24, no. 7, p. 074001, 2021. doi:10.1103/PhysRevAccelBeams.24.074001
- [2] W. Herr, “Beam-beam effects in the LHC”, 1995. <https://inspirehep.net/literature/381737>
- [3] W. Herr *et al.*, “Long-range beam-beam effects in the LHC”, in *ICFA Mini-Workshop on Beam-Beam Effects in Hadron Colliders (BB)*, 2013. doi:10.5170/CERN-2014-004.87
- [4] J. P. Koutchouk, “Correction of the long-range beam-beam effect in LHC using electro-magnetic lenses”, in *Proc. PAC’01*, Chicago, IL, USA, Jun. 2001, pp. 1681–1683. <https://jacow.org/p01/papers/TPPH012.pdf>
- [5] F. Zimmermann, “10 years of wire excitation experiments in the CERN SPS”, in *ICFA Mini-Workshop on Beam-Beam Effects in Hadron Colliders (BB)*, 2013. doi:10.5170/CERN-2014-004.153
- [6] S. Fartoukh, A. Valishev, Y. Papaphilippou, and D. Shatilov, “Compensation of the long-range beam-beam interactions as a path towards new configurations for the high luminosity LHC”, *Phys. Rev. Accel. Beams*, vol. 18, no. 12, p. 121001, 2015. doi:10.1103/PhysRevSTAB.18.121001
- [7] Y. Papaphilippou and F. Zimmermann, “Weak-strong beam-beam simulations for the Large Hadron Collider(bb)”, *Phys. Rev. Accel. Beams*, vol. 2, no. 10, p. 104001, 1999. doi:10.1103/PhysRevSTAB.2.104001
- [8] G. Sterbini *et al.*, “First results of the compensation of the beam-beam effect with dc wires in the LHC”, in *Proc. IPAC’19*, Melbourne, Australia, May 2019, pp. 2262–2265. doi:10.18429/JACoW-IPAC2019-WEYYPLM3
- [9] P. Belanger, R. Baartman, D. Kaltchev, and G. Sterbini, “Beam-beam long-range wire compensators in LHC Run 3”, in *Proc. IPAC’23*, Venice, Italy, pp. 2789–2792, 2023. doi:10.18429/JACoW-IPAC2023-WEPA060
- [10] P. Belanger, R. Baartman, D. Kaltchev, and G. Sterbini, “A topological approach to the problem of beam-beam compensation”, in *Proc. of BB24 (in preparation)*, 2024.
- [11] A. Chao, “Special topics in accelerator physics: Lie algebra technique for nonlinear dynamics”, SLAC, Tech. Rep. SLAC-PUB, 2012. <https://www.slac.stanford.edu/~achao/lecturenotes.html>
- [12] P. Belanger and G. Sterbini, “A topological description of accelerator beam dynamics”, <https://arxiv.org/search/physics?searchtype=author&query=Belanger,+P>
- [13] P. Belanger and G. Sterbini, “Numerical evaluation of the integrals of motion in particle accelerator tracking codes”, *arXiv:2503.19122*, 2025. doi:10.48550/arXiv.2503.19122

MITIGATING THE THERMAL CHALLENGES IN CARBON STRIPPER: TEST BENCH SIMULATION TO ENHANCE DEVICE STABILITY*

B. Abdelmegied[†], T. Kanemura, F. Marti

Facility for Rare Isotope Beams, Michigan State University, East Lansing, MI, USA

Abstract

The linear accelerator of the Facility for Rare Isotope Beams (FRIB) employs both liquid lithium and carbon strippers at a location where the beam energy reaches 17–20 MeV/u to increase the mean charge state of the beam being accelerated. Effective thermal management in carbon strippers is critical for ensuring reliability and component longevity. This study simulates beam heating using a 460 nm laser to investigate the thermal response of carbon foil, guiding future design improvements for heavy-ion beam applications. Key objectives include emissivity measurement under controlled conditions—vital for understanding heat transfer—and implementing mechanical upgrades such as replacing plastic components with metal gears and bearings, applying high-emissivity coatings inside the chamber, and integrating a proximity sensor for rotation monitoring. These enhancements aim to improve thermal efficiency, measurement accuracy, and overall system durability under high-temperature conditions

INTRODUCTION

Carbon stripper foils are subjected to intense thermal loads during operation, leading to thermal stress and potential degradation. Studies have shown that the thermal behavior of these foils is influenced by factors such as emissivity, thermal conductivity, and mechanical robustness. To address these challenges, research has focused on exposing foil to different beam species to evaluate the thermal response of carbon foils. Additionally, finite element simulations have been employed to model the temperature fields induced by irradiation, providing insights into minimizing the thermal stresses of the carbon stripper components should provide guidance for the design improvements [1–4].

The carbon stripper was the main charge stripper to support FRIB user program until October 2023 when the beam power was ramped up to 10 kW at the target from the previous 5 kW. The issue that temporarily made the carbon stripper suspended from operation was frequent rotation stalls that prevented continuous beam operation. It was assumed that plastic components surrounding the hot carbon foil expanded due to the heat conducting from the foil, and increased friction, which then seized the rotation. To

investigate this behavior and test potential improvements, an identical experimental setup was made.

This study utilizes laser-induced heating, simulating beam heating, to examine thermal responses under dynamic conditions. It also explores hardware and structural modifications to improve the stripper's robustness and operational efficiency.

EXPERIMENTAL SETUP

The experimental arrangement features a vacuum chamber fitted with laser heating and thermal diagnostics. A blue laser beam, angled through an upper-right port, irradiates a carbon foil mounted inside. An infrared (IR) camera aligned with a ZnSe window on the bottom right port records real-time thermal images. A thermocouple inserted through a feedthrough port measures the wall temperature inside the vacuum chamber, whose inner surface is coated with a high-emissivity coating (Fig. 1).

Inside the chamber, the ANI carbon foil (from Applied Nanotech Inc.) is mounted on a custom-designed gear system, allowing both rotation and vertical motion. This dual-movement mechanism enables the laser beam to heat various foil segments, simulating dynamic beam-stripping conditions (Fig. 2). The diameter of the foil is 100 mm.

The current experiment utilizes adjustable rotation speeds between 100 and 500 RPM, spreading the thermal load along the foil's circumference. Vertical motion velocity was fixed at 7.5 mm/sec (this is the maximum speed in the middle of cyclic linear motion. The speed profile is sinusoidal repeating acceleration from and deceleration to zero speed at the turning points of the direction of motion), enabling the laser to sweep across a vertical span. The laser beam targeted a radial region between 20 mm and 40 mm, distributing heat more evenly and allowing analysis of radial thermal gradients.

The 460 nm laser delivers a maximum power of 55 W but is operated at 11.9 W for this test. Given the foil's 84% absorption efficiency at this wavelength, approximately 10 W is absorbed. The laser is focused on a 3 mm beam spot, producing localized, high-temperature regions on the foil. This condition represents the stripping of a ⁴⁸Ca beam being delivered to the rare isotope production target at a beam power of 10 kW.

The ZnSe viewport, with 98% IR transmission between 7–12 μm, allows thermal imaging without compromising vacuum integrity. This configuration supports non-contact, temperature diagnostics crucial for understanding the foil's response to transient heating.

* Work supported by the U.S. Department of Energy, Office of Science, Office of Nuclear Physics and used resources of the Facility for Rare Isotope Beams (FRIB) Operations, which is a DOE Office of Science User Facility under Award Number DE-SC0023633

[†]Abdelmegied@frib.msu.edu

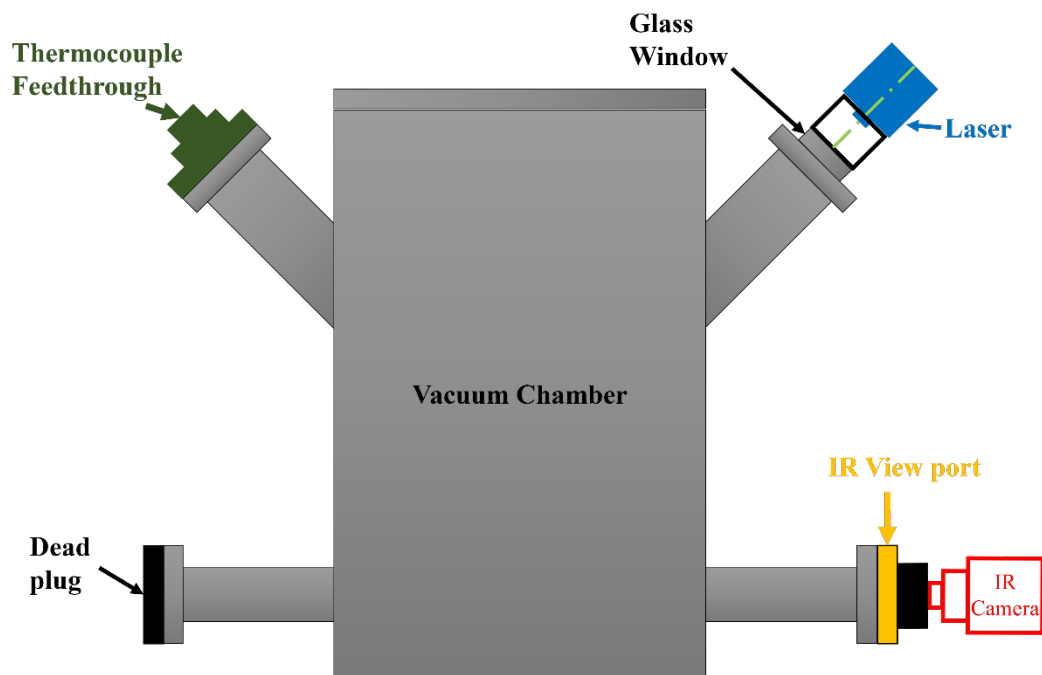


Figure 1: Experimental setup sketch.

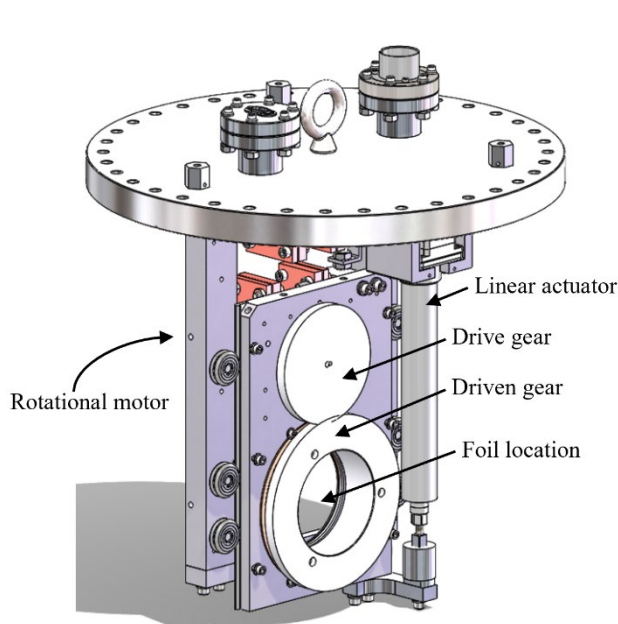


Figure 2: Experimental setup assembly.

RESULTS

Temperature Distribution from Rotating Exposure

Initial findings, pending final emissivity calibration, indicate significant localized heating of the foil under laser irradiation. Figure 3 shows a thermal image captured during simultaneous rotation and vertical translation of the foil at 100 RPM and 7.5 mm/sec respectively. A bright yellow zone represents the area directly heated by the laser. As the foil moves, the thermal trail fades, reflecting effective dissipation.

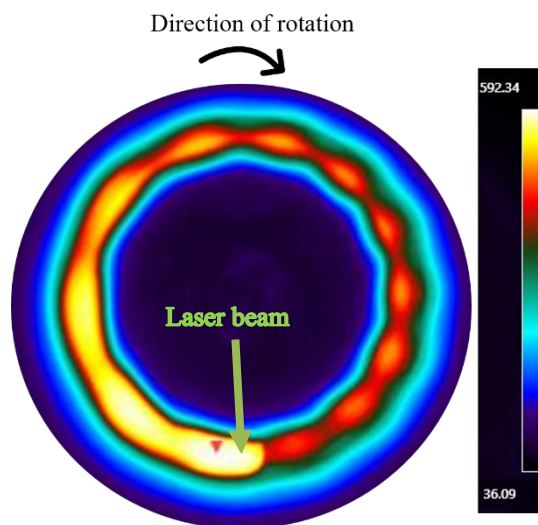


Figure 3: Thermal image example rotating at 500 RPM.

Influence of Rotational Speed on Temperature

Figure 4 presents temperature data across various vertical positions and rotational speeds. The horizontal axis represents the different vertical location as the foil moves up and down while rotating. The higher temperature at the same rotational speed occurs at the smaller radial location, while the lower temperature occurs at the larger radial location. This thermal accumulation leads to intensified heating. This happens due to the smaller circumference of the smaller radial location and the larger circumference at the larger radial location. Larger circumferences allow the temperature to drop before it comes back again to the laser beam. As RPM increases, less heat is retained due to shortened exposure time with the laser, enabling more efficient cooling.

The rotational motion promotes quicker departure from the laser's heat zone, which reduces the maximum temperature. These results emphasize that higher RPMs are more effective for reducing thermal load, although mechanical limitations at high speeds must be considered.

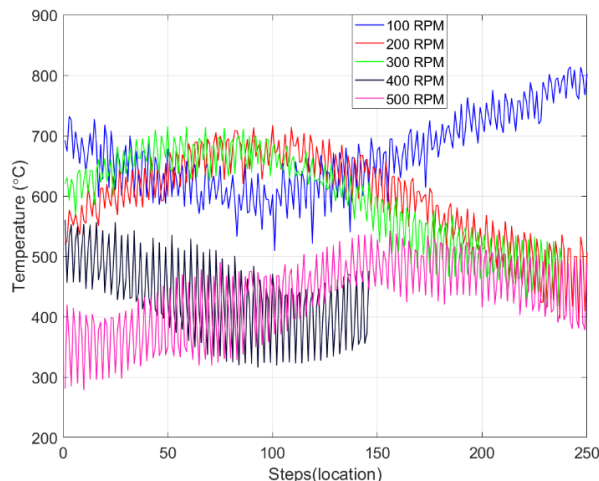


Figure 4: Mean maximum temperature at different vertical location for different RPM

Figure 5 summarizes this relationship by plotting average temperature versus RPM. The data show a steep decline in mean temperature from roughly 700°C at 100 RPM to around 430°C at 500 RPM. This nonlinear trend confirms that thermal exposure time strongly influences heating, particularly at lower RPMs. Knowing that the highest foil angular velocity during operation was 100 RPM

The trend clearly demonstrates that increasing rotational speed is a practical strategy for managing foil temperature during high-power operation. However, engineering trade-offs such as gear wear and dynamic stability must be factored into future system designs.

The localized thermal load leads to rotational stalls; this could be avoided if we can evenly distribute the thermal load to allow symmetric expansion and contraction in addition to lower maximum temperatures.

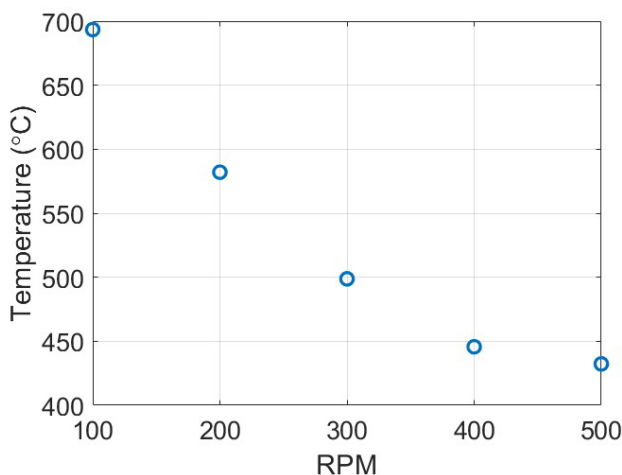


Figure 5: Mean temperature at different RPM.

CONCLUSION

This study successfully established a test bench for simulating the thermal dynamics of carbon stripper foils under conditions mimicking those in FRIB's LINAC. By using a 460 nm laser within a vacuum environment and enabling both rotational and vertical movement of the target foil, the setup allowed accurate replication and analysis of beam-induced heating.

Thermal imaging showed that heat accumulates significantly at lower rotation speeds due to prolonged exposure, while higher speeds enable efficient heat dissipation. The sharp decrease in temperature with increased RPM is confirmed by instantaneous temperature and mean temperature data, which supports the use of rapid mechanical motion to control peak temperatures.

The real-time IR diagnostics provides valuable data to validate future thermal models. Measuring emissivity under controlled conditions is essential for converting IR signals into precise temperature readings, a key requirement for accurate thermal simulation and system tuning.

To further enhance stripper performance, several design upgrades are recommended. Replacing plastic components with heat-resistant metals, applying high-emissivity coatings inside the chamber, and adding sensors to monitor rotation in real time can significantly boost system durability and diagnostic capability.

These efforts form a comprehensive strategy for mitigating thermal stress in carbon strippers. The approach outlined here not only improves heat management but also lays the groundwork for future innovations in stripper design for high-power accelerator applications.

REFERENCES

- [1] F. Marti *et al.*, "A carbon foil stripper for FRIB," in *Proc. LINAC '10*, Tsukuba, Japan, Sep. 2010, pp 659-661.
- [2] W. Barth *et al.*, "Carbon stripper foils for high current heavy ion operation," *J. Radioanal. Nucl. Chem.*, vol. 299, no. 2, pp. 1047-1053, Aug. 2013.
[doi:10.1007/s10967-013-2651-3](https://doi.org/10.1007/s10967-013-2651-3)
- [3] K. Kupka *et al.*, "Intense heavy ion beam-induced temperature effects in carbon-based stripper foils," *J. Radioanal. Nucl. Chem.*, vol. 305, no. 3, pp. 875-882, Apr. 2015.
[doi:10.1007/s10967-015-4057-x](https://doi.org/10.1007/s10967-015-4057-x)
- [4] B. Lommel *et al.*, "Preparation of different carbon stripper foils and application in beam diagnostics," EPJ Web of Conferences, vol. 285, p. 05002, 2023.
[doi:10.1051/epjconf/202328505002](https://doi.org/10.1051/epjconf/202328505002)

IMAGE MAPPING FOR MULTIPLE CHARGE STATE BEAMS USING A BEAM INDUCED FLUORESCENCE PROFILE MONITORS*

A. Lokey[†], Facility for Rare Isotope Beams, Michigan State University, East Lansing, MI, USA

Abstract

Work continues on a minimally invasive, nitrogen fluorescence gas sheet at the Facility for Rare Isotope Beams (FRIB). A low density gas sheet may be used to observe the 2D transverse beam profile of high intensity, multiple charge state beams with minimal interference. Spatially and temporally correlated profiles are of particular interest in locations where there is significant charge state spread, such as the FRIB linac folding segments. A low-density gas sheet measurement system offers advantages for gas handling in nitrogen sensitive areas, however signal intensity is significantly lower than techniques using higher density gas sheets and jets. This work discusses measurement considerations for photon distributions generated by several spatially separated interaction points and design considerations for a high-sensitivity optics system for handling the expected low signal intensity.

INTRODUCTION

Beam induced fluorescence (BIF) monitors are currently in use and under development at several facilities and offer a minimally interfering method to monitor the 2D transverse beam profile [1, 2]. In BIF devices, the beam excites a working gas which then emits photons during a de-excitation process. The gas can be shaped and positioned so that the resulting data collected correlates to the transverse beam profile.

Minimally interfering monitors are useful for high intensity beams, where component degradation with devices that intercept the beam become a concern. For example, the Facility for Rare Isotope Beams (FRIB) linac produces heavy ion beams of various species that can be selected to have multiple charge states. The linac consists of three folding sections with 60 degree bends. Achromatic optics are used to steer the beam through the turns, which causes spread in the charge states as it passes [3]. A 2D simultaneous profile in this area could give helpful insight to operators. Figure 1 shows a simulated example of this at four positions through the first folding section.

For this design, the profile will be measured by collecting photons generated by the interaction of the beam with low density nitrogen gas sheet. The beam interacts with the sheet at a 45-degree angle which encodes the x and y profile data in a coordinate transform [4]. Since relatively little gas is introduced into the system using a rarefied sheet, there are lesser requirements on gas handling and pumping

* This material is based upon work supported by the U.S Department of Energy, Office of Science, Office of Nuclear Physics and used resources of the Facility for Rare Isotope Beams (FRIB), which is a DOE Office of Science User Facility, under Award Number DE-SC0000661

[†] lokey@frib.msu.edu

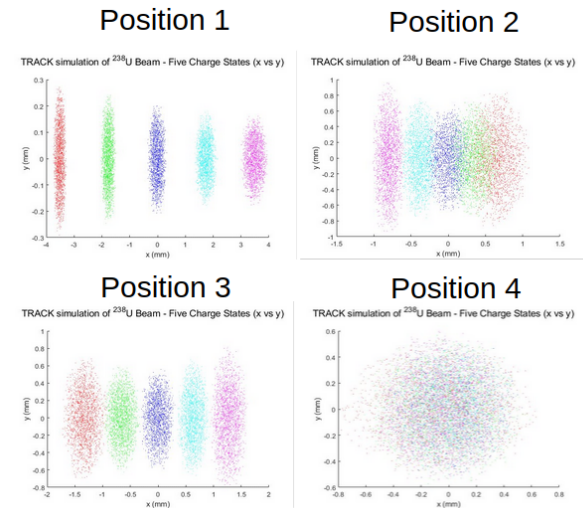


Figure 1: TRACK simulation of 5 charge state ^{238}U through the FS1 turn.

systems. This is desirable for viewing profiles in areas that have somewhat tighter space constraints due to their small relative footprint. However, signal acquisition is a concern for low density gas sheets due to fluorescence cross sections generally being lower than other processes, as well as fewer interactions with the working gas.

OPTICS AND ELECTRONICS CONSIDERATIONS

Fluorescence Process

The fluorescence cross section is proportional to the differential energy loss of the interaction and square of the charge state of the ion. This is advantageous for high charge state ions, as the photon production will be higher. During collision, the working gas undergoes both ionization and excitation, the former of which creates singly charged ions and secondary electrons. Neutral atoms are also excited by these secondary electrons, and both species de-excite releasing optical photons [5].

Photon Capture

Total photon yield is proportional to the gas pressure, the number of particles in a bunch, and the ion charge. Due to the low density of the gas molecules in the system, low fluorescence cross section even for favorable working gases, and a small solid angle of detection, the signal of the monitor is expected to be low.

Measurement and integration time is also usually long due to the fact that enough photons must be captured by the system to accurately determine the profile [6].

Some systems under development use a higher density of gas to increase signal output, the tradeoff being increased gas handling requirements and system complexity. However, integration time and resolution for these types of systems seems promising [1].

Response Functions

Yamada et. al. show that the transverse beam profile $F(x, y; z)$ can be correlated to the acquired image $g(\mu, \nu)$ by integrating over the field of view being imaged (D), as shown in Eq. 1:

$$g(\mu, \nu) = \int_D R(\mu, \nu, x, y, z) F(x, y; z) dx dy dz \quad (1)$$

In a general approximation, the measured photon distribution can be considered a good representation of the beam profile assuming the gas sheet is uniform and thin, in which case the response function R becomes 1 at the exact location of the gas sheet [2].

However, the authors found that this approximation introduces significant error and does not account for other effects in the system. This poses problems for real-time signal analysis, as the solution for the full integral becomes quite complex. Yamada et al. propose a new approximation for determining the profile which allows for faster processing once the response function of the system is determined [6].

Figure 2 shows the signal transformations and block diagram of a gas sheet monitor. The measured image is transformed by the response function R, which is found from the density of the gas sheet, the fluorescence cross section (σ), the motion of the gas molecules T_1 , the out of focus effect from the angle T_2 , resolution effects from the image intensifier T_3 , as well as the image intensifier amplification efficiency spatial distribution and detection efficiency spatial distribution of the CCD camera [6].

Expected Photon Generation

The number of emitted photons can be estimated from the effective optical cross section using the beam current and cross-sectional area, the charge of the ions, and number of target particles in the interaction volume seen by the imaging system [2].

Early estimates were found to be around 5000 photons per second [7]. This estimate assumed each ion interacted with a gas molecule and did not take into account factors such as the solid angle of detection.

A calibration simulation was first set up using a 16 x 16 grid of interaction points using Geant4 [8]. The initial transform, without including optical system considerations showed a reasonable relationship for photons generated at the given angle [4].

A second simulation using more realistic distributions is being performed to determine a more accurate photon estimate as well as how spatially separated the groupings

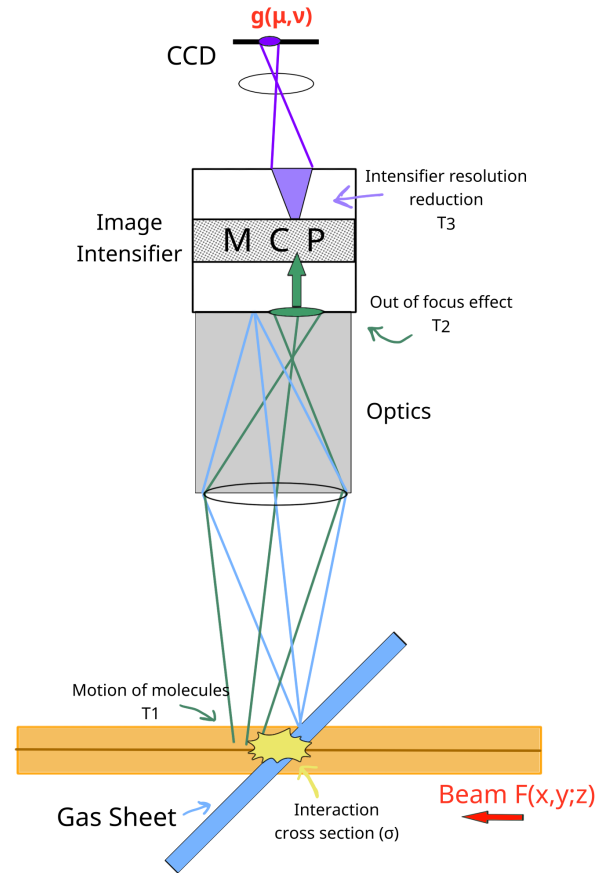


Figure 2: Typical construction and components of the response function of a molecular flow gas sheet monitor, based on [6].

must be to distinguish individual charge states. Using image processing techniques, the profile can be aligned to represent the x-y coordinate space taking into consideration general system effects, optical misalignment, and sheet thickness. For the purpose of this work, a python script was developed using a total least-squares method to estimate the transformation map between the simulated distribution and the expected x-y beam profile [9].

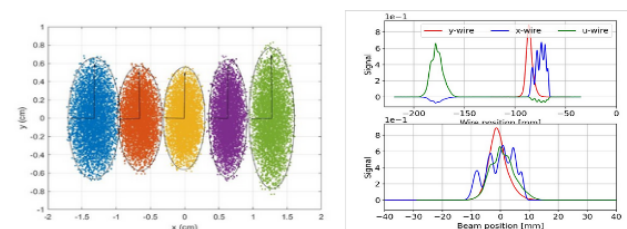


Figure 3: a) Estimated elliptical distributions to be used as a multi-charge state beam in simulation. b) Real profile monitor data taken from wire scanners at the same location of interest.

Figure 3 shows an TRACK distribution simulating a 5 charge state ^{238}U beam at the center point of the first folding

section bend. A gaussian particle distribution is then created based on the simulated dimensions. The distribution is also compared with real wire scanner data taken from the same point in the accelerator.

MECHANICAL DESIGN

Gas Sheet Generator

Design work is completed on the mechanical portion of the system. The device creates a gas sheet by leaking gas into a thin slit with large length and width dimensions compared to its depth. This gives the molecules a large mean free path, reducing intermolecular collisions in the generator and therefore narrowing the gas density distribution across the gas sheet [2]. The sheet is further collimated to remove molecules emitted at off-angles, reducing the divergence of the sheet as it passes through the interaction chamber.

Figure 4 shows a close up view of the gas sheet generating section. The width and length of the slit are 100 mm, with a channel depth of 0.1 mm, increasing to 0.3 mm at the nozzle exit and collimating slit to achieve the desired thickness. The generator is placed on a rotatable cradle, allowing for the angle of the gas sheet to be adjusted for calibration or reoriented for density measurement tests. The distance of the slit from the collimator is also adjustable to calibrate for minimal sheet divergence. The generating chamber is separately evacuated of off-angle molecules using a dedicated 750 l/s turbomolecular pump so as to minimize interference with the sheet formation before it exits the section.

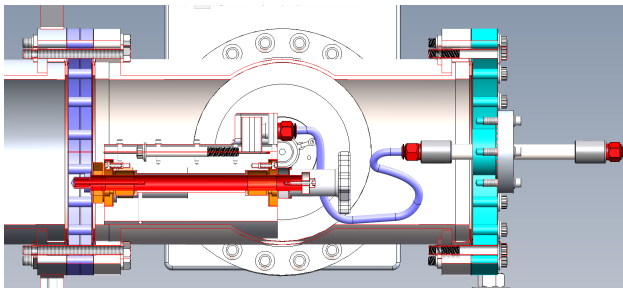


Figure 4: Mechanical design of the gas sheet generating chamber with adjustable slit-collimator distance.

The interaction chamber is an off-the-shelf 6 way cross, held at ultra high vacuum. The gas sheet is removed from the chamber by a second TMP directly across from the collimating slit.

The imaging system is attached at the top of the cross, at a distance of 160 mm from the interaction point at the center of the chamber. Additional work is being done to determine if this is acceptable for both photon collection and radiation hardness requirements.

CONCLUSION

Using a low-density gas sheet offers advantages for gas handling in nitrogen sensitive areas, however signal intensity and long integration time is a significant concern for use with real-time monitoring. Work continues on an application of image processing techniques to help determine the theoretical light output, optical transforms, and error estimation for the designed system.

REFERENCES

- [1] O. Sedláček *et al.*, “Gas jet-based fluorescence profile monitor for low energy electrons and high energy protons at LHC”, pp. 312–317, 2023.
doi:10.18429/JACoW-IBIC2023-WE3I01
- [2] I. Yamada, M. Wada, K. Moriya, J. Kamiya, P. K. Saha, and M. Kinsho, “High-intensity beam profile measurement using a gas sheet monitor by beam induced fluorescence detection”, *Phys. Rev. Accel. Beams*, vol. 24, no. 4, p. 042 801, 2021.
doi:10.1103/PhysRevAccelBeams.24.042801
- [3] P. N. Ostroumov *et al.*, “FRIB from Commissioning to Operation”, in *Proc. HB’23*, Geneva, Switzerland, pp. 9–15, 2024.
doi:10.18429/JACoW-HB2023-MOA1I2
- [4] F. Becker, “Beam induced fluorescence monitors”, in *Proc. DIPAC’11*, pp. 575–579, 2011. <https://jacow.org/DIPAC2011/papers/WEOD01.pdf>
- [5] R. Hampf, J. Wieser, and A. Ulrich, “Light emission processes in the context of optical beam profile monitors”, *Eur. Phys. J. D*, vol. 77, no. 3, p. 51, 2023.
doi:10.1140/epjd/s10053-023-00624-6
- [6] I. Yamada and J. Kamiya, “Response function measurement for a non-destructive gas-sheet beam profile monitor”, *Rev. Sci. Instrum.*, vol. 95, no. 12, p. 123 308, 2024.
doi:10.1063/5.0234781
- [7] A. Lokey and S. Lidia, “Measuring uniformity and gas density of gas sheet profile monitor for use with heavy-ion accelerators”, in *Proc. IPAC’24*, Nashville, TN, pp. 2284–2286, 2024.
doi:10.18429/JACoW-IPAC2024-WEPG35
- [8] *Geant4*. <https://geant4.web.cern.ch/>
- [9] S. Van Der Walt *et al.*, “Scikit-image: Image processing in Python”, *PeerJ*, vol. 2, p. e453, 2014.
doi:10.7717/peerj.453

BEAM LOSS DETECTION AND MITIGATION AT FRIB*

S. Cogan[†], T. Kanemura, S. Lidia, T. Maruta, D. McNamey, P. Ostroumov, A. Plastun, Q. Zhao, S. Zhao, Facility for Rare Isotope Beams, East Lansing, MI, USA

Abstract

This work presents an overview of beam loss detection and mitigation at the Facility for Rare Isotope Beams (FRIB). A diverse array of loss monitoring systems—including ion chambers, neutron detectors, halo rings, fast thermometry, and differential beam current monitors (BCM)—are deployed to detect losses ranging from large events that risk machine damage to low-level losses that result in undesirable machine activation. To ensure protection, hundreds of detector thresholds with varying time responses are precisely configured for each beam mode, ion species, and energy. The Threshold Configuration Tool (TCT), a sophisticated software solution, optimizes these thresholds to safeguard the machine while minimizing false trips. Additionally, FRIB's high-power beam employs a novel self-healing liquid lithium film charge stripper, which introduces beam energy fluctuations and occasional gaps in the film, leading to downstream losses. Fast and slow feedback systems stabilize the post-stripper beam energy, effectively reducing these losses. This work will discuss how FRIB experiences running at 10kW beam power influenced the evolution of our systems and tools.*

LINAC OVERVIEW

The FRIB linac, utilizing superconducting RF cavities and consisting of over 500 meters of beamline, is designed to eventually deliver up to 400 kW of sustained heavy ion beam power to target. FRIB first delivered 1 kW of continuous beam power on target in May 2022 [1]. Since then, the maximum beam power on target has been steadily increasing, up to 2025 where we regularly deliver 20 kW of Uranium on target. Beam loss detection and mitigation has been a requirement from the start, and we have a robust Machine Protection System (MPS) [2] with an extensive network of sensors, detectors, controllers, and data acquisition systems which contribute not only diagnostic information, but fast-acting not-OK signals that can stop the beam delivery within 15 μ s in order to protect the machine.

Machine Protection System

The Machine Protection System is one the most important and complex systems at FRIB. It directly connects to 400+ devices and controllers, with controllers interfacing with hundreds more detectors providing input. As FRIB increases the machine power, it is necessary and challenging to configure MPS appropriately to both protect the machine sufficiently and avoid frequent (unnecessary)

faults which reduce beam time for experiments. There is an array of diagnostic devices which have responsibility for fast response to MPS, capable of detecting a problem condition in as fast as a few microseconds. As of 2025, we have integrated 13 non-intercepting beam current monitors (BCMs), 27 neutron detectors (NDs), and 44 ionization chambers (ICs) distributed throughout the linac to support the fastest MPS response. Each of these devices can respond to signals averaged over multiple timeframes, from 1 sec average down to 15 μ s average. For these beam loss monitors alone, over 300 different MPS thresholds need to be managed in order to protect the machine in a wide variety of run conditions including beam development and tuning, pulsed modes with high peak power to various linac destinations, and continuous (CW) beam delivered to the production target.

Beam Stability in the Linac

As beam power is increased, not only must we protect the machine from large sudden losses, but we must limit low-level losses that arise from perturbations of our beam transport. The largest contributor of beam perturbations in our linac is our liquid lithium charge stripper (LLCS) [3] which is necessary to strip high power beam. It is comprised of a self-healing liquid lithium film, with laminar flow, in vacuum, to increase the ion charge state after the first linac segment. This film, while being remarkably stable, does experience occasional fluctuations or disruption in the flow. This can result in slow or sudden change of the post-stripper charge states, but more importantly, a different energy loss across the film, leading to different arrival times at RF accelerating cavities, and increasing beam instability and losses downstream. Several beam feedback mechanisms were introduced to mitigate these instabilities, as much as possible.

THRESHOLD CONFIGURATION TOOL FOR MPS

The FRIB linac undergoes a wide range of beam operations, each associated with varying levels of risk. At higher beam power, the tolerances for Beam Loss Monitor (BLM) Machine Protection thresholds need to be tight. At lower beam power, during beam tuning or beam development, these thresholds should be more relaxed to permit activities such as RF cavity tuning, which necessarily generate a noticeable but acceptable level of beam losses in certain locations.

With hundreds of individual thresholds to configure for a wide array of beam operating modes and a multi-dimensional problem space (ion species, beam energy, peak power, average power, pulsed modes, beam destination, etc) a highly automated tool is the only way to avoid over-

* This material is based upon work supported by the U.S. Department of Energy, Office of Science, Office of Nuclear Physics and used resources of the Facility for Rare Isotope Beams (FRIB) Operations, which is a DOE Office of Science User Facility under Award Number DE-SC0023633

[†] cogan@frib.msu.edu

whelming machine operators and achieve reliable protection. We began with a simple tool, and added complexity to handle more scenarios as our understanding and experience grew. Each iteration was informed by the advanced physics group, beam diagnostics, and operators. After several years of iteration [4], we have arrived at a highly functional automated Threshold Configuration Tool (TCT) which sufficiently protects our machine while requiring very little input from machine operators in most scenarios, and yet provides high flexibility to facilitate a quick response to unique emergent situations. The flexibility is achieved through many device-specific scale factors, overrides, and other TCT parameters which influence TCT calculations. While these may need to be tweaked on occasion by a diagnostics or advanced physics expert, these complicated TCT features are separated from the primary user interface into dedicated sections titled *AP Config* and *Diag Expert*, as seen in Fig. 1.

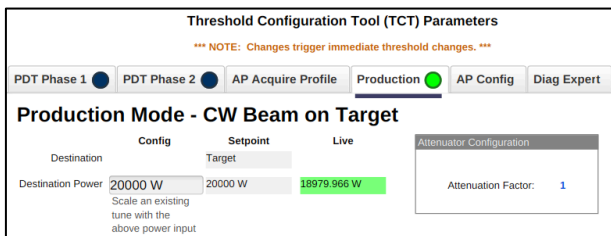


Figure 1: Operator interface for the TCT's Production Mode. Beam power on target is the single required input.

We identified three operational phases that have unique requirements for machine protection; Primary beam Development Time (PDT) Phase 1 is intended for beam tuning operations under 25 W. This mode is used for cavity phasing and other beam studies. In phase 1, the TCT enables a limited set of BLMs, permitting small losses at the beam destination and other expected loss locations. PDT Phase 2 is intended to ramp up power up to 10 kW. Many more beam loss monitors enabled, and loss thresholds are set more tightly. Expected losses or radiation profiles are modelled using historical data to set appropriate thresholds and avoid false faults. Expected losses primarily include radiation detected at the charge selector slits and the final beam destination. The intention is to not remain in PDT Phase 2 for very long, as the threshold margins in this mode are set somewhat permissively due to limitations of our simplified model and the desire to avoid frequent false MPS faults. The primary purpose of the TCT's Phase 2 is to facilitate power ramp up to 10kW where a high transmission beam delivery can be confirmed, and where our diagnostics can be used to collect a beam loss profile specific to the current ion beam and machine conditions. This loss profile snapshot is used in Production Mode, which is used for experiment production. The beam loss profile data is used to scale thresholds up or down as a function of the operational power level. The Production phase calculates tight tolerances for all loss monitors, utilizing the standard deviation measured for each detector signal to reliably achieve very low false fault rate. Operators spend the most time in this mode, and it is the most simple for them to administrate,

using the interface shown in the Fig. 1 to input a single value: beam power on target.

LIQUID LITHIUM FILM STABILITY

Fluctuations in beam energy can have a significant impact on downstream beam losses. The liquid lithium film experiences slow fluctuations due to thermal effects and other systemic drifts over time. It also experiences sudden changes in laminar flow, where the film thickness changes due to laminar flow finding a new mode. These laminar flow changes happen within microseconds and may remain stable in the new mode anywhere from seconds to hours. Fluctuations in film thickness result in changes to the post-stripper beam energy, which can result in beam losses downstream, since the beam transport was tuned for a specific energy profile. To avoid frequent MPS faults in these scenarios, it is necessary to utilize beam diagnostics as feedback to other systems which stabilize the beam energy and maintain the best possible transmission efficiency. Two independent feedback mechanisms have been developed to mitigate these instabilities.

Fast Feedback: BPM-LLRF Feedback System

The first feedback system is a fast-acting feedback which stabilizes energy and beam arrival time changes in less than 0.1 seconds. Beam Position Monitor (BPM) phase data is used to track beam velocity between two BPMs located downstream of the stripper, as well as a single BPM phase just before entering our second linac segment (LS2) which is used to monitor arrival time (or phase) for the tuned LS2 RF cavities. BPM phases are used to provide feedback for two low level RF (LLRF) cavities located upstream of the charge stripper. One RF cavity is used to stabilize the energy, the other used to stabilize arrival time [5]. The effect is that the pre-stripper energy is constantly adjusted up and down so that the post-stripper energy is extremely stable, to about 10 ppm. The graph in Fig. 2 shows the effective feedback, which drives changes to the pre-stripper energy in order to stabilize post-stripper energy.

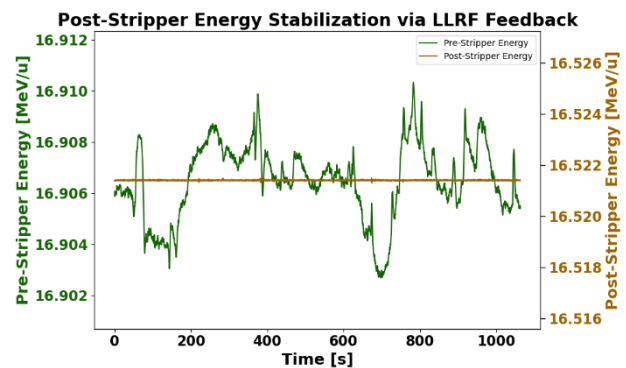


Figure 2: Downstream energy stabilization using LLRF/BPM feedback system.

Energy stabilization via the LLRF feedback system makes small energy and time of flight (TOF) corrections very quickly, utilizing a 100 Hz stream of BPM phase data during continuous (CW) operations. While this effectively

corrects for most sources of beam instability, there was yet another improvement to beam stability which was necessary.

Slow Feedback: Lithium Stage Motion

The second feedback system leverages the thickness profile of the lithium film to stabilize the energy loss in the film and maintain minimal beam halo formation in both longitudinal and transverse phase spaces due to scattering and energy straggling. Thicker film results in more energy loss, and if the thickness drifts far enough away from the nominal settings, an elevated beam halo can result in losses in the post-stripper accelerator. This is an effect that the BPM-LLRF feedback cannot mitigate. Occasionally, the beam location on the film might drift to a particularly unstable region of the film. Motion feedback is utilized to adjust the impact point of the beam on the film, up or down, in an attempt to keep the energy loss in the film constant, which corresponds to a consistent film thickness.

A nominal energy difference across the film is determined for a given beam, and the feedback software moves the film stage up and down to maintain this nominal energy difference (Fig. 3). Input filtering and hysteresis prevents excessive stage motion.

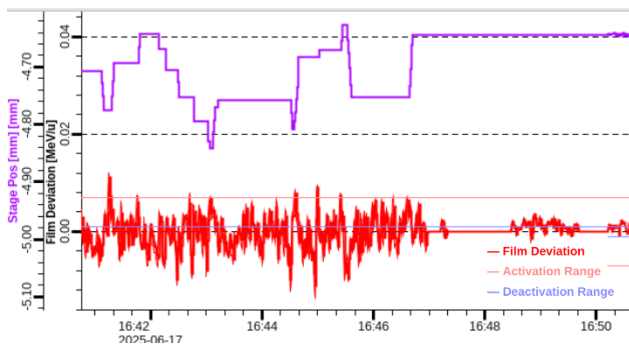


Figure 3: Stage motion feedback correcting for changes in lithium film thickness, keeping energy loss within ± 0.01 MeV/u of the nominal thickness.

CONCLUSION

At FRIB, we have developed effective systems for detecting beam losses, machine protection, and mitigation of

beam instability to enable highly-reliable and relatively uninterrupted beam delivery to experiments at up to 20 kW of continuous beam power while maintaining low residual activation of our beamline. We have effectively automated much of the machine protection configuration complexity through automated threshold configuration management with our TCT. Several sources of beam loss have been effectively reduced by utilizing both fast and slow feedback systems to stabilize beam energy, arrival time, and beam distribution in the phase space.

These systems and tools have been critical in achieving stable operations for experiments at 20 kW. As we approach the next milestone of 50kW in the coming year, the demand on these tools will only increase. We will likely need to extend these tools further, pushing them for faster response, or integrating additional fast diagnostics. Entirely new feedback systems may need to be developed in order to mitigate other sources of instability. We look forward to meeting these challenges and updating the community with our progress.

REFERENCES

- [1] J. Wei *et al.*, “FRIB operations: first three years”, presented at HIAT’25, East Lansing, MI, USA, Jun. 2025, paper MOX01, this conference.
- [2] Z. Li, D. Chabot, S. Cogan, and S. M. Lidia, “Current status and prospects of FRIB machine protection system”, in *Proc. NAPAC’19*, Lansing, MI, USA, Sep. 2019, pp. 437-439. doi:10.18429/JACoW-NAPAC2019-TUPLM29
- [3] T. Kanemura *et al.*, “Experimental demonstration of the thin-film liquid-metal jet as a charge stripper,” *Phys. Rev. Lett.*, vol. 128, no. 21, May 2022. doi:10.1103/physrevlett.128.212301
- [4] D. McNanney *et al.*, “An approachable beam loss monitor configuration and operation tool for FRIB”, in *Proc. IPAC’24*, Nashville, TN, USA, May 2024, pp. 3405-3408. doi:10.18429/JACoW-IPAC2024-THPG61
- [5] S. Zhao *et al.*, “BPM feedback for LLRF energy and phase regulation in charge stripping beamlines”, in *Proc. IPAC’24*, Nashville, TN, USA, May 2024, pp. 3326-3328. doi:10.18429/JACoW-IPAC2024-THPG32

BEAM INTENSITY PREDICTION FOR ECR ION SOURCE USING MACHINE LEARNING

Y. Morita*, RIKEN Nishina Center, Saitama, Japan

K. Kamakura, Center for Nuclear Study (CNS), the University of Tokyo, Tokyo, Japan

A. Kasagi, Graduate School of Artificial Intelligence and Science, Rikkyo University, Tokyo, Japan

T. Nish, RIKEN Nishina Center, Saitama, Japan

N. Oka, National Institute of Information and Communications Technology, Tokyo, Japan

Abstract

The Electron Cyclotron Resonance Ion Source (ECRIS) plays a vital role in generating highly charged ion beams for accelerator-based research. However, maintaining stable beam intensities remains challenging due to unmeasurable or slowly varying internal states. This study proposes a machine learning-based beam intensity prediction framework that incorporates both numerical operational data and plasma light images acquired through the extraction electrode. Experiments were conducted on two ion sources at RIKEN: the HyperECRIS and the RIKEN 28 GHz ECRIS. Predictive models with and without image data were developed and evaluated. The inclusion of plasma images led to improved prediction accuracy in both cases, indicating that such images effectively supplement hidden plasma conditions. These results demonstrate the potential of image-assisted modeling as a foundation for autonomous ECRIS control.

INTRODUCTION

The Electron Cyclotron Resonance Ion Source (ECRIS) is a powerful tool, particularly for the production of highly charged heavy ions. It is therefore widely used in accelerator facilities. However, especially in the generation of metallic ion beams, the conditions within the ion source such as plasma parameters can change rapidly, making it difficult to maintain a stable beam over extended periods. Currently, the operation relies on experienced operators performing manual optimization. Our aim is to automate this optimization process by incorporating machine learning techniques, thereby enhancing the sophistication of ECRIS operations. As a first step, we have developed a method for accurately monitoring changes in ECRIS conditions and continuously measuring beam intensity without interrupting beam delivery.

DATA COLLECTION

In machine learning, the input data is of critical importance. To effectively monitor changes in the ECRIS state, sufficient information must be supplied as model input. Operators typically monitor various parameters such as vacuum pressure and drain current, in addition to operational parameters, when tuning the ECRIS. However, changes in

some parameters? such as vacuum level or vapor from high-temperature ovens? occur gradually and with delay, making immediate assessment difficult. Since not all internal states, like oven temperature, are directly measurable, beam intensity may change gradually even when observable parameters remain constant. To capture such dynamics, we focused on acquiring information about plasma conditions. However, it is currently difficult to obtain plasma characteristics like electron density and temperature without interfering with beam delivery. As an alternative, we opted to capture plasma light images using a camera [1]. These images can be easily obtained through the beam extraction aperture, and if proven useful for beam prediction, the method could be applied to various ECRIS. Experiments were conducted on two ion sources at RIKEN's RIBF facility: the HyperECRIS [2] and the RIKEN 28GHz ECRIS [3]. For the HyperECRIS, 17 parameters were used as machine learning inputs, including mirror coil current, 14 GHz RF power, gas valve settings, vacuum level, and beamline elements such as magnets and slits. Additionally, plasma light images were captured with a handheld camera through the extraction electrode (Fig. 1).

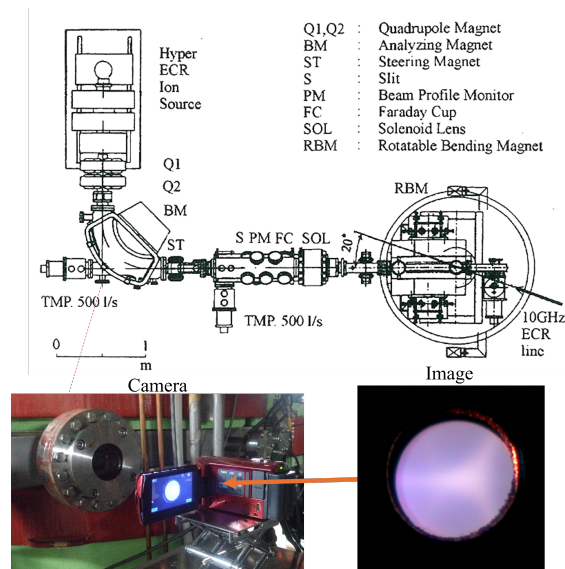


Figure 1: Plasma light imaging of HyperECRIS. Plasma light was captured with a handheld camera through a extraction electrode.

In the case of the RIKEN 28 GHz ECRIS, a similar approach was taken, but more parameters were included due

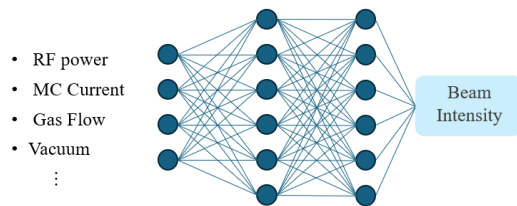
* yasuyuki.morita@riken.jp

to additional components such as high-temperature ovens, bias disks, and accel-decel electrodes. Observed parameters also expanded to include factors like cooling water temperatures in the chamber. A scientific camera (FLIR Grasshopper3 GS3-U3-41C6C-C) was used for capturing plasma light images. Although camera settings were kept constant in principle, gain and exposure time were included among the machine learning inputs. In total, 60 parameters, including operational, observational, beamline, and camera settings, were utilized.

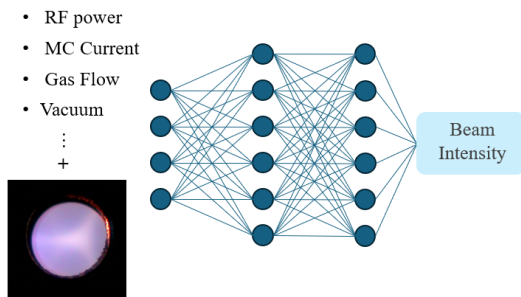
MODEL DESIGN

To differentiate the predictive value of various types of data, we constructed two types of models for both ion sources:

- A model using only numerical data such as operational parameters.
- A model using numerical data and plasma light images.



(a) Conceptual diagram of the model with only numerical values. In this model, the middle layer consists of 5 layers.



(b) Conceptual diagram of the model using both numerical and image. The images were processed using a convolutional neural network (CNN) called 'ResNET50' [4] and then combined with the numerical data in 2 fully coupled layers.

Figure 2: Conceptual illustrations of the two models used in this study: Fig. (2a) uses only numerical parameters such as operating parameters; Fig. (2b) uses the numerical parameters and also the plasma light image.

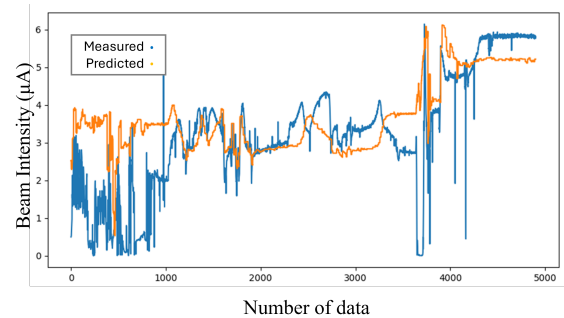
These models are shown in Fig. 2. While the size of the input layer varied according to the number of numerical parameters, the remaining components of the models were identical for both ECRIS systems. For training and validation, the ion source was started up twice on the same

day: one run provided training data, and the other served as validation data. This procedure was followed for both HyperECRIS and RIKEN 28GHz ECRIS.

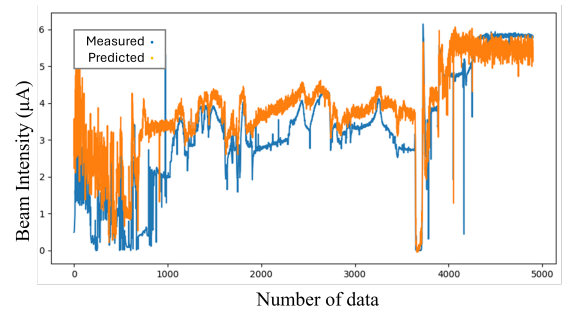
PERFORMANCE EVALUATION

HyperECRIS

Results are shown in Fig. 3. Figure (3a) displays predictions from the model using only numerical data after 100 training epochs. Figure (3b) [5] shows the results from the model using both numerical data and plasma light images after the same training. Table 1 shows the loss values calculated by mean squared error.



(a) Prediction results for the validation data in the model using only numerical data. It is possible to predict the approximate beam intensity, but not the detailed trend.



(b) Prediction results for the validation data in the model using both numerical data and plasma optical images. The accuracy of the prediction of detailed trends was improved compared to the results of only numerical data.

Figure 3: Results of beam intensity prediction in HyperECRIS, Fig. (3a) for the numerical only model and Fig. (3b) for the model with plasma light.

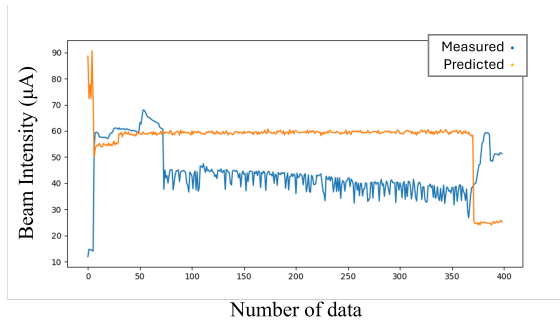
Table 1: Values of Loss Functions for Validation Data in HyperECRIS

Numerical Data Only	Both Numerical Data and Plasma Light Images
1.68	0.92

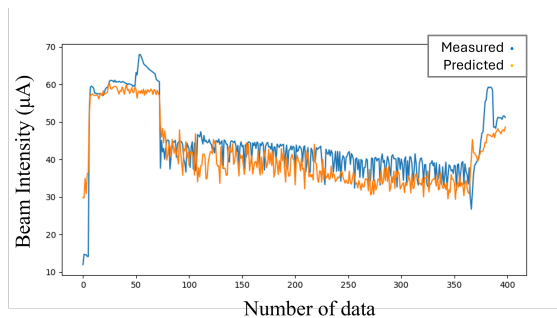
The model using plasma images better captured fine trends and yielded a lower loss, indicating improved prediction accuracy when plasma images were included.

RIKEN 28 GHz ECRIS

Results are shown in Figure 4. The model using only numerical data (Figure 4a) exhibited lower prediction accuracy, while the model incorporating plasma images (Figure 4b) more effectively captured fine patterns. Figure 5a was due to oven emission only, Figure 5b was due to plasma and oven emission. The visible light emission from the plasma was weak, and the effect of the oven emission adds to it, making it difficult to confirm by eye. This improvement is also reflected in the lower mean squared error in Table 2. The reason why the loss function was larger than that of HyperECRIS was due to the higher beam intensity. Despite weaker visual contrast in plasma images (Fig. 6) due to factors like high RF frequency and intense oven glow, the inclusion of image data led to better results, suggesting that the images contain otherwise unobservable information.



(a) Prediction results for the validation data in the model using only numerical data. This model may be able to handle large changes in conditions, such as those at the end of the data, but the results did not show a correct response to changes in beam intensity.

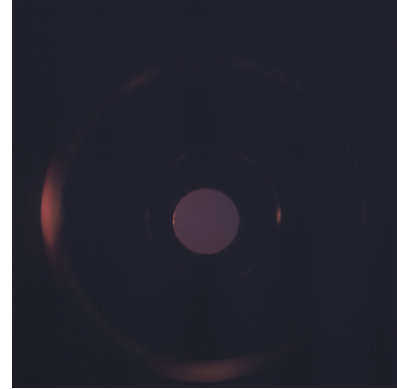


(b) Prediction results for the validation data in the model using both numerical data and plasma optical images. This model sometimes missed predictions, but the results were very well predicted compared to the model using only numerical data.

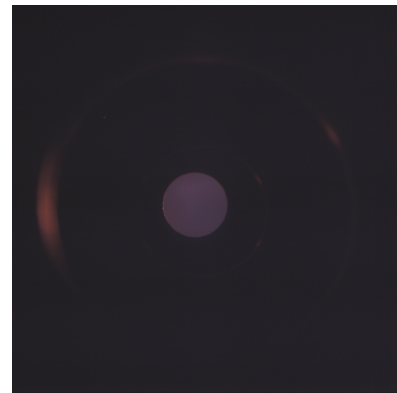
Figure 4: Results of beam intensity prediction in RIKEN 28GHz ECRIS, Fig. (4a) for the numerical only model and Fig. (4b) for the model with plasma light.

Table 2: Values of Loss Functions for Validation Data in RIKEN 28 GHz ECRIS

Numerical Data Only	Both Numerical Data and Plasma Light Images
399	32.6



(a) Image with oven heated and no RF incident.



(b) Image with the oven heated and RF also injected.

Figure 5: Image taken through an extraction electrode.

CONCLUSION

As a first step toward the autonomous control of ECR ion sources, we developed a beam intensity monitoring system using machine learning. To compensate for unobservable parameters, we captured plasma light images through the extraction electrode. We compared model performance with and without these images, finding that the inclusion of plasma images significantly improved prediction accuracy for both HyperECRIS and RIKEN 28 GHz ECRIS. These findings suggest that plasma images can supplement hidden parameters and enable better understanding of ion source conditions.

ACKNOWLEDGEMENT

This research was partially supported by the RIKEN Fellowship Program.

REFERENCES

- [1] K. Kamakura *et al.*, “Preparation for machine learning-aided control of HyperECR ion source”, in *Proc. 20th Annual Meeting of Particle Accelerator Society of Japan*, Funabashi, Japan, Aug.-Sep. 2023, pp. 769-770.
- [2] Y. Ohshiro, S. Yamaka, S. Kubono, and S. Watanabe, “Development of an ECR ion source at CNS”, in *Proc. Cyclotrons’04*, Tokyo, Japan, Oct. 2004, Oct. 2004, paper 19P20.
- [3] T. Nagatomo *et al.*, “New 28-GHz superconducting electron cyclotron resonance ion source for synthesizing super-heavy elements with $z > 118$ ”, in *Proc. ECRIS’18*, Catania, Italy, Sep. 2018, pp. 53–57.
doi:10.18429/JACoW-ECRIS2018-TUA3
- [4] R. Rácz, S. Biri, and J. Pálkás, “Electron cyclotron resonance plasma photos”, *Rev. Sci. Instrum.*, vol. 81, no. 2, 2010.
doi:10.1063/1.3267289
- [5] K. Kamakura *et al.*, “Machine learning-aided ECRIS beam current prediction”, in *Proc. 21st Annual Meeting of Particle Accelerator Society of Japan*, Yamagata, Japan, 2024, pp. 817-818.

JuTrack, A Julia-BASED TOOL FOR ACCELERATOR MODELING AND TRACKING WITH AUTO-DIFFERENTIATION *

J. Wan[†], H. Alamprese, Y. Hao, C. Ratcliff

Facility for Rare Isotope Beams, Michigan State University, East Lansing, MI, USA

J. Qiang

Lawrence Berkeley National Laboratory, One Cyclotron Road, Berkeley, CA, USA

Abstract

JuTrack is a novel accelerator modeling and tracking package developed in the Julia programming language. Taking advantage of compiler-level automatic differentiation (AD), JuTrack allows rapid and accurate derivative calculations for arbitrary differentiable functions. This paper introduces the core capabilities of JuTrack, including lattice modeling and particle tracking, and demonstrates how AD-derived derivatives enhance the efficiency of beam physics studies through several practical examples.

INTRODUCTION

Derivatives are important in scientific computing tasks, such as accelerator modeling and particle tracking simulation. Traditional approaches to calculate derivatives primarily involve numerical and symbolic methods. While numerical methods can approximate derivatives for complex systems, they often suffer from precision limitations due to truncation errors and round-off errors, especially for ill-conditioned problems. On the other hand, symbolic methods, though accurate, struggle with deriving analytical expressions for complicated systems.

To address these challenges, automatic differentiation (AD) emerges as a robust alternative [1]. AD is a kind of computational technique used to evaluate the derivatives of functions in computer programs. Unlike numerical differentiation and symbolic differentiation, AD calculates derivatives of functions by decomposing functions into elementary operations and applying the chain rule to these operations sequentially. This method not only ensures computational precision but also enhances performance by avoiding the complexity and overhead associated with symbolic methods. So far, AD has been a fundamental tool in various fields such as machine learning, optimization, and numerical simulation [2].

To integrate AD capability in traditional particle tracking works, a novel accelerator modeling package, JuTrack [3], is developed in the Julia programming language. This package is specifically designed for numerical simulation of particle tracking using symplectic integration [4]. In addition to standard particle tracking, JuTrack also supports the computation of Truncated Power Series Algebra (TPSA) [5]. A powerful LLVM-level AD tool, Enzyme [6], is implemented

in this code for swift and precise derivative computation at the compiler level.

ACCELERATOR MODELING

Figure 1 shows the structure of the JuTrack code. It includes four main parts: lattice functions, TPSA functions, tracking functions, and utility functions. As a particle tracking tool, JuTrack supports 6-D tracking of the particle coordinates $[x, p_x, y, p_y, z, \delta]$, where x and y are the transverse coordinates, p_x and p_y are the transverse momentum normalized by the reference particle momentum p_0 , z is the path lengthening with respect to the reference particle, and $\delta = \delta p/p_0$ is the momentum deviation with respect to the reference particle.

In addition to standard particle tracking, JuTrack also supports calculation of TPSA. The 6-D coordinates $[x, p_x, y, p_y, z, \delta]$ can be represented as coefficients of six polynomials and tracked as standard 6-D particle coordinates. The results of the TPSA tracking are also six polynomials representing the 6-D coordinates.

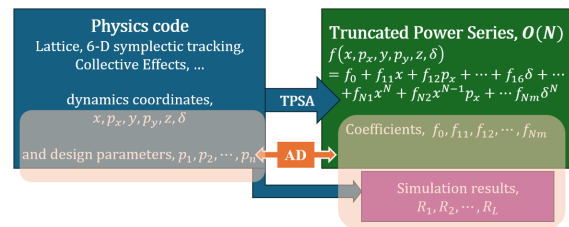


Figure 1: Overview of the JuTrack workflow. JuTrack applies AD to compute derivatives of both map coefficients and beam observables with respect to design parameters.

Taking the Hadron Storage Ring (HSR) of the Electron-Ion Collider (EIC) [7] as an example, in this section, we will demonstrate how to build such a complex accelerator lattice and how to calculate the Courant-Snyder parameters of the ring in JuTrack.

Figure 2 shows the optics of the storage ring. The periodic optics is solved based on the transfer matrix of the ring, which is calculated from the first-order TPSA tracking. Compared to the MAD-X [8], a well-known accelerator modeling tool used for the EIC design, the maximum difference of β_x and β_y is around 1% level. This error is due to the different treatment of dipole field errors in both codes. For a lattice without such dipole field error, identical optics and betatron tunes are obtained by both codes, e.g., the Electron Storage Ring (ESR) of the EIC shown in Ref. [3].

* Work supported by DOE office of science, with award number DE-SC0024170.

[†] wan@frib.msu.edu

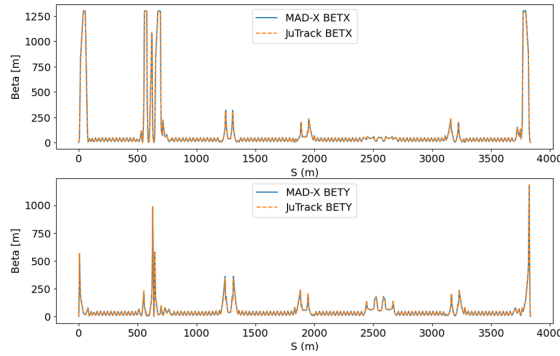


Figure 2: Comparison of beta functions of the HSR of the EIC obtained from JuTrack and MAD-X, respectively.

AUTO DIFFERENTIATION

Derivatives of Particle Tracking Results

JuTrack allows automatic calculation of derivatives for arbitrary differentiable functions. The differentiated function can be the calculation of any differentiable lattice parameters and related simulation results. The inputs of the function are usually design parameters of the accelerator, such as parameters of magnets and RF cavities.

Taking a simple beam line [Q1, D1, Q2, D2] as an example, where Q1 and Q2 represent quadrupoles, and D1 and D2 represent drift space. A particle starting with initial coordinates $[1e^{-3}, 1e^{-4}, 0, 0, 0, 0]$ is tracked through the sequence of the transport line. The strengths of the two quadrupoles, k_1 and k_2 , are used as input variables of the differentiable function. The outputs of the function are 6-D coordinates of the particle at the exit of the beam line.

Table 1 shows the automatically obtained derivatives of the final 6-D coordinates with respect to k_1 and k_2 when $k_1 = 1.0 \text{ m}^{-2}$ and $k_2 = -1.0 \text{ m}^{-2}$. The results are proven to be true by comparing them with numerical differentiation. The derivatives of vertical coordinates are zero because the particle is initially positioned at the center of the quadrupole in the vertical plane.

Table 1: Derivatives of Single Particle Tracking Results ($k_1 = 1.0 \text{ m}^{-2}$ and $k_2 = -1.0 \text{ m}^{-2}$)

	dx	dp_x	dy	dp_y	dz	$d\delta$
dk_1	$-3.1e^{-3}$	$-2.1e^{-3}$	0	0	$2.5e^{-6}$	0
dk_2	$8.4e^{-5}$	$1.5e^{-4}$	0	0	$-8.1e^{-6}$	0

Differentiation with Optics

In this section, we demonstrate how to obtain derivatives of Twiss parameters for a storage ring and how to optimize the Twiss parameters using the derivatives.

A 3-rd generation storage ring light source is chosen as an example. The ring lattice consists of 20 identical double-bend-achromatics (DBAs) where the β_x at the center of the long straight section is 10 m. The optimization task is to

optimize the β_x at the center of the long straight section to be 7 m by tuning k_1 , which is the strength of the first quadrupole in the DBA cell. The derivative of β_x with respect to k_1 can be automatically obtained with AD. See in Fig. 3, the value of k_1 is adjusted based on a simple gradient descent optimization strategy, $k_1 = k_1 - \text{step} \times d\beta_x/dk_1$, where the step size is set to be $1e^{-4}$. Within 10 steps, the β_x is optimized to the desired value.

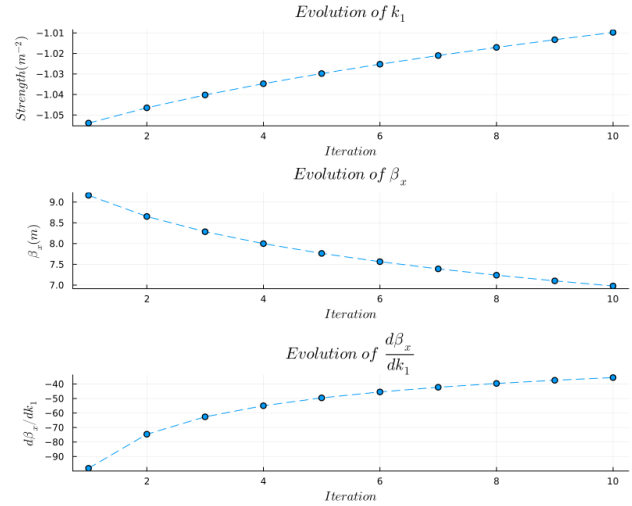


Figure 3: Optimization of β_x by tuning k_1 based on the derivative $d\beta_x/dk_1$.

Differentiation with Space-Charge Effects

The nonlinear space charge effects from the Coulomb interaction can significantly damage the beam quality in a high intensity or a high brightness accelerator by causing emittance growth, beam halo, and even particle losses. JuTrack supports the simulation of transverse space-charge effects based on a spectral method [9]. In this work, we simulate a 1 GeV proton beam with 5,000 macro particles transported through periodic FODO cells. The normalized emittance of the beam is 1 mm with a Gaussian distribution in both horizontal and vertical planes.

The final emittance (normalized by the initial emittance) is calculated using JuTrack. In the meantime, the derivatives of the final emittance with respect to the lattice parameters are automatically obtained via AD. Figure 4 presents these derivatives with respect to the lengths of the drift spaces (D1L, D2L and D3L), and the lengths (Q1L and Q2L) and strengths (Q1k and Q2k) of the quadrupoles. For validation purposes, we also compute approximate derivatives using the finite difference method. It is found that the results of the finite difference approach nearly converge when the difference is less than 10^{-4} . However, when the difference is too small, e.g., less than 10^{-9} , the round-off errors will dominate. Therefore, we choose a reasonable difference of 10^{-6} in the calculation. The close agreement between the AD results and the finite difference approximations confirms the accuracy of the AD computations. Our results show that

the emittance variation is more sensitive to the length of the first quadrupole, which is consistent with the findings reported in [8].

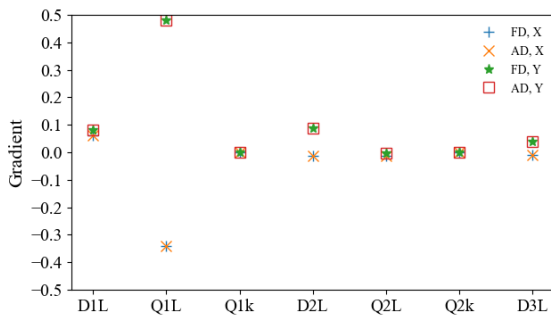


Figure 4: Derivatives of final emittance with respect to seven lattice parameters. FD and AD represent the derivatives obtained with finite difference approximation and automatic differentiation, respectively.

CONCLUSION

An AD-enabled accelerator modeling code is in development based on Julia. The capabilities of this AD code are demonstrated through its application to a single-particle tracking scenario. Furthermore, we demonstrate how to optimize Twiss parameters of a storage ring accelerator using the automatically calculated derivatives.

The package is available at <https://github.com/MSU-Beam-Dynamics/JuTrack.jl.git>. This package is still being actively improved, with the aim of delivering a comprehensive AD-enabled tool for accelerator modeling.

ACKNOWLEDGEMENTS

This work is supported by DOE office of science, with award number DE-SC0024170. J. Q.'s work was supported

by the U.S. Department of Energy under Contract No. DE-AC02-05CH11231.

REFERENCES

- [1] C. C. Margossian, "A review of automatic differentiation and its efficient implementation", *WIREs Data Min. Knowl. Discovery*, vol. 9, no. 4, p. e1305, Mar. 2019. doi:10.1002/widm.1305
- [2] A. G. Baydin, B. A. Pearlmutter, A. A. Radul and J. M. Siskind, "Automatic differentiation in machine learning: a survey", *J. Mach. Learn. Res.*, vol. 18, pp. 1–43, 2018, <https://www.jmlr.org/papers/volume18/17-468/17-468.pdf>
- [3] J. Wan, H. Alamprese, C. Ratcliff, J. Qiang, Y. Hao, "JuTrack: A Julia package for auto-differentiable accelerator modeling and particle tracking", *Comput. Phys. Commun.*, vol. 309, p. 109497, 2025. doi:10.1016/j.cpc.2024.109497
- [4] E. Forest and R. D. Ruth, "Fourth-order symplectic integration", *Physica D*, vol. 43, pp. 105–117, 1990. doi:10.1016/0167-2789(90)90019-L
- [5] M. Berz, *Modern Map Methods in Particle Beam Physics*, Academic Press, 1999.
- [6] W. Moses and V. Churavy, "Instead of rewriting foreign code for machine learning, automatically synthesize fast gradients", *Adv. Neural Inf. Process. Syst.*, vol. 33, pp. 12472–12485, 2020. doi:10.48550/arXiv.2010.01709
- [7] A. Accardi and *et al.*, "Electron-Ion Collider: The next QCD frontier: Understanding the glue that binds us all", *Eur. Phys. J. A*, vol. 52, pp. 1–100, 2016. doi:10.1140/epja/i2016-16268-9
- [8] H. Grote and F. Schmidt, "MAD-X – An upgrade from MAD8", in *Proc. PAC'03*, Portland, OR, USA, May 2003, paper FPAG014, pp. 3497–3499. doi:10.1109/PAC.2003.1289960
- [9] J. Qiang, "Differentiable self-consistent space-charge simulation for accelerator design", *Phys. Rev. Accel. Beams*, vol. 26, no. 2, p. 024601, Feb. 2023. doi:10.1103/physrevaccelbeams.26.024601

MACHINE-LEARNING-ASSISTED RAPID BEAM ENERGY CHANGE AT THE ATLAS HEAVY ION LINAC*

A. Ravichandran[†], B. Mustapha
Argonne National Laboratory, Lemont, IL, USA

Abstract

Studying nuclear reactions to develop new medical isotopes requires the measurement of production cross sections at varying beam energies. To do this efficiently without wasting beam time available for experimentation, the energy needs to be changed rapidly over a very wide range. We present recent experimental results, employing machine learning methods for rapid tuning of ^{16}O & ^{136}Xe beams following manual energy change. For the ^{16}O beam energy is changed from a base value of 106 MeV to 71 MeV and for the ^{136}Xe beam energy is changed from the base energy of 803 MeV to 671 MeV and 525 MeV. Retuning from the base energy took ~ 15 minutes compared to ~ 30 minutes for operator tuning. The collected data is then used to validate the same procedure in a virtual model of ATLAS running the TRACK simulation code with error $\sim 6\%$ across energies. Preliminary virtual model error is corrected by considering quadrupole misalignments and real values of input beam parameters obtained by Bayesian inference.

INTRODUCTION

Nuclear cross section data is critical to making informed decisions to produce isotopes. Renne et al. [1] discuss a rapid and cost-effective procedure relying on prompt gamma cascades, a short burst of high yield gamma emissions measured using the Gamma-sphere detector at the ATLAS linac in Argonne. This procedure, however, requires measurements made at a wide range of beam currents and energies that require manual operator energy change and magnet tuning that takes appreciable time. Figure 1 shows the beamline section of the Argonne linac considered here between the last accelerating cavity and the Gamma-sphere detector

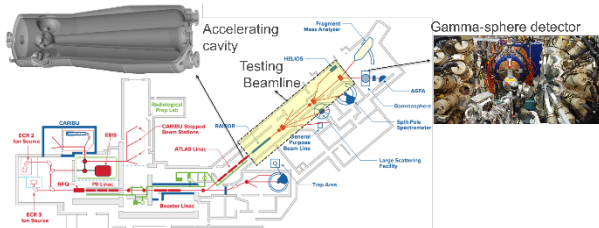


Figure 1: Testing beamline at ATLAS for ML model.

Scheinker et al. [2] discuss machine learning techniques using convolutional neural networks that do not require model retuning for complex time-varying systems.

* Work was supported by the U.S. Department of Energy, under Contract No. DE-AC02-06CH11357. This research used the ATLAS facility, which is a DOE Office of Nuclear Physics User Facility
[†] aravichandran@anl.gov

Deep reinforcement learning based methods coupled with high-fidelity physics engines have been extensively studied at Los Alamos National Laboratory by Pang et al. [3], Argonne National Laboratory by Mustapha et al. [4] and the Stanford Linear Accelerator Centre by Edelen et al. [5]. This work explores a novel new approach of real-time tuning of a linear accelerator following energy change based on prior information available from a previous tune for a different beam energy. As discussed further, an instantaneous increase to $\sim 50\%$ beam transmission was achieved by applying the proposed technique presented here. Experimental data collected during the process is further used to refine a virtual accelerator model. The goal is to use model predictions to further improve the tuning procedure of the online ML model.

EXPERIMENTAL RAPID BEAM ENERGY CHANGE RESULTS

Experimental tune following a manual energy change procedure consists of performing a primary ML tune by Bayesian optimization with initial random data sets for a base energy (106 MeV for ^{16}O Beam). Figure 2 shows variation of magnet control settings during tuning procedure.

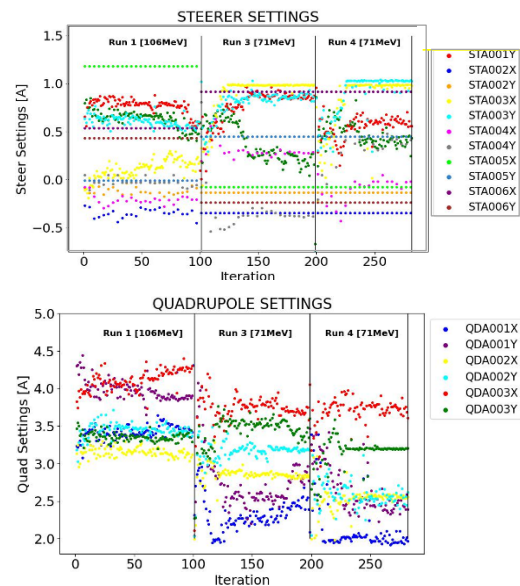


Figure 2: Element settings controlled by the ML model during the experimental tuning process for ^{16}O Beam.

Hard limits are set on magnet settings prior to performing the automatic ML tune to avoid damaging the devices. Figure 3 shows this initial ML tune (red dots) at 106 MeV clearly reaching 98% transmission. All magnet settings corresponding to this 98% transmission are stored. Next beam energy is manually changed by the operators to

71 MeV by adjusting the appropriate settings of the last accelerating cavities shown in Fig. 1. Following this, the stored magnet settings from 106 MeV corresponding to 98% transmission are scaled based on beam rigidity for the new energy (71 MeV) and applied to the complete beam-line. As noted below, this instantaneous procedure immediately increases transmission from 0% to ~60% for Run 2, 57% for Run 3 and 47% for Run 4 all at 71 MeV.

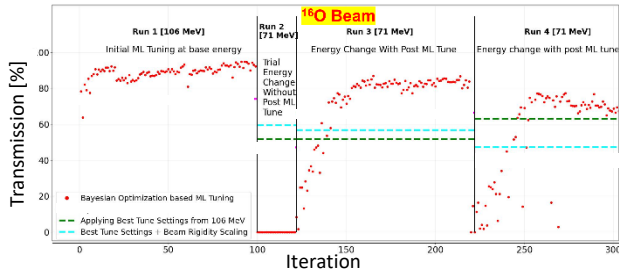


Figure 3: ^{16}O Beam rapid energy change tune without initial random data as prior to the machine learning model.

An automatic secondary ML tune without any initial data seed was performed for the previous case to estimate the best values of transmission that can be possibly achieved and further for comparison with the instantaneous rapid change procedure. Based on these results, for the ^{136}Xe beam, tuning at the base energy (525 MeV) was performed with 6 initial random data seeds. Figure 4 clearly illustrates this procedure. Applying beam rigidity-based scaling to the best magnet settings from 525 MeV results in an immediate transmission rise to 23% for 671 MeV and 6% for 803 MeV. Appreciable improvement as previously noted was not achieved for this case. Furthermore, the secondary ML tune with 6 initial random data priors resulted in equal if not higher transmission than operator tune only after a considerable number of iterations (~50) of the Bayesian procedure as shown below.

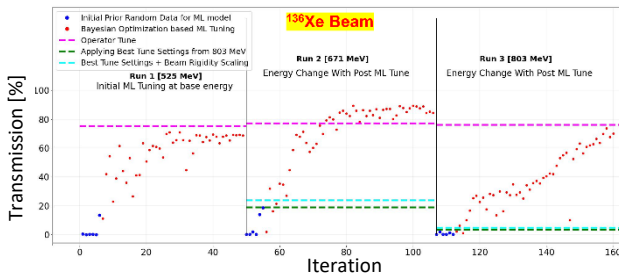


Figure 4: ^{136}Xe Beam rapid energy change procedure with 6 initial random data priors at 3 different energies.

All runs previously presented employed transmission-based Bayesian optimization procedure without accounting for beam profiles. Based on insights gained from the previously performed experimental runs, the ^{136}Xe Beam procedure is repeated but instead employing a weighted multi-objective Bayesian optimization accounting for both beam transmission and beam profile width in the tuning process. Moreover, once the scaled best magnet settings from the base energy (in the following case-803 MeV) is applied to the secondary energy, these values are also included along with the 6 random initial data seed priors of

the Bayesian optimization model. As could be noted from the following Fig. 5, an instantaneous jump in transmission from 0% to 52% for 671 MeV and to 57% for 525 MeV is noted after the inclusion of profile width in the ML model. Moreover, fewer iterations (~15) achieve higher transmission than operator values during the secondary tune when using the scaled best tune settings from 803 MeV in the initial data seed.

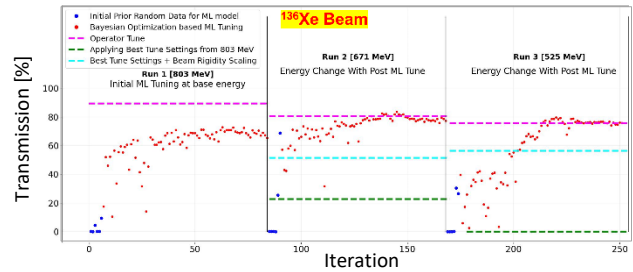


Figure 5: Transmission + Profile based combined weighted objective BO tuning.

VIRTUAL MODEL RESULTS

An accurate virtual model capable of simulating the considered beamline would be valuable to seed the initial prior data set as previously demonstrated. The TRACK particle simulation software is used to this extent. However, preliminary simulation results showed a consistent error of ~30% for a wide range of operating conditions for the considered beamline. Ravichandran et al. [6] discussed in detail the procedure for extracting critical quadrupole magnet misalignments. This procedure based on Bayesian inference is extended in this work. In addition to minimizing errors in transmission, errors in beam profile are also minimized. In addition to accounting for the influence of misalignments, the influence of real beam parameters at the inlet of the considered beamline which varies with beam energy is also considered. A weighted/scaled multi-objective Bayesian inference procedure with 33.33% (1/3rd) weight for transmission, beam profile width, profile center each is shown in Fig. 6. Gradual reduction in total virtual model error from ~50% to 5% over 100 iterations is observed. One such preliminary procedure is carried out to estimate misalignments that can be universally applied across different energies. Following this, secondary procedures unique to every beam energy are carried out to estimate real input beam parameters (ϵ, α, β) that minimize model error even further.

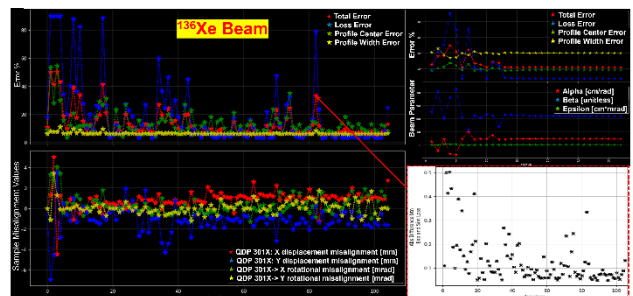


Figure 6: Weighted multi-objective optimization.

For ^{16}O , profile information was not collected. Therefore, a single objective (transmission) error minimization based on procedure previously outlined was performed. As noted in Fig. 7 below, minimal virtual model error was achieved across different energies and experimental cases corresponding to low value of beam transmission ($\sim 6\%$ mean difference between experimentally measured transmission and simulated values across all these cases).

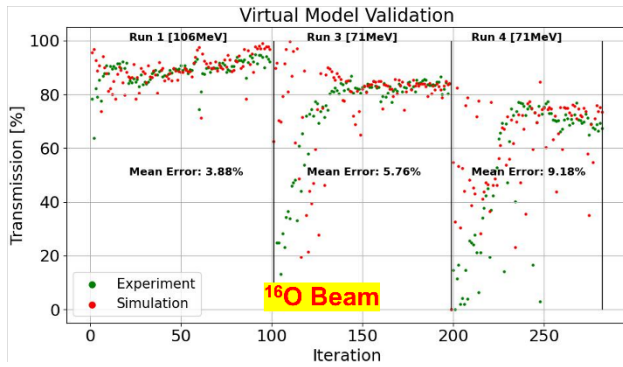


Figure 7: Virtual model simulations for ^{16}O Beam.

The weighted-multi-objective procedure previously discussed is implemented to minimize total model error for ^{136}Xe Beam simulations and shown in Fig. 8.

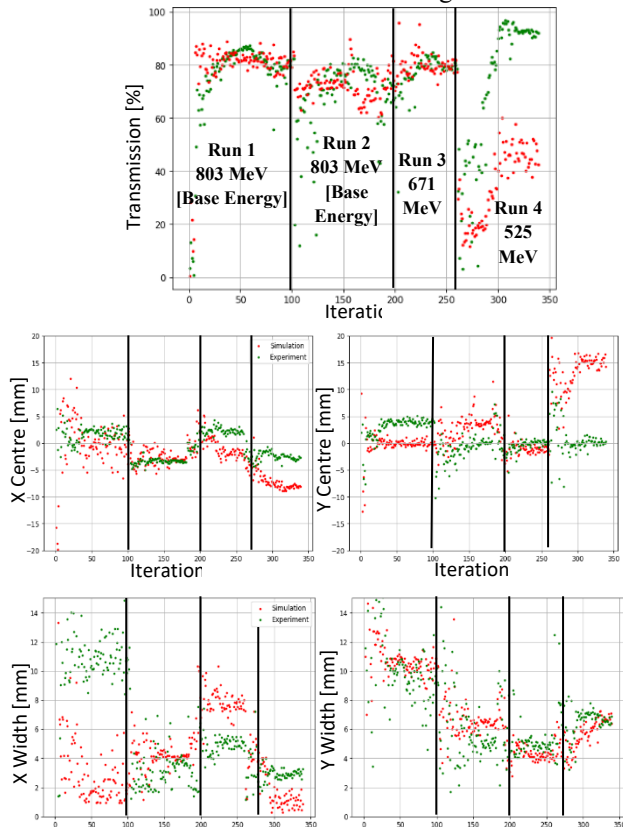


Figure 8: Virtual model simulations for ^{136}Xe Beam.

As can be observed (especially Run 1), minimizing errors in transmission leads to increase in profile width/center error and vice versa. It is evident that complete beam shape needs to be considered in the multi-objective optimization procedure. Difference in Run 4 model transmission

clearly due to incorrect input beam parameters for this energy. Table 1 summarizes magnitude of model predicted input beam parameters for different energies.

Table 1: Input Beam Parameters for Different Energies

Energy [MeV]	α [unitless]	β [cm/rad]	ϵ [cm*mrad]
Base, ^{16}O :106	0.695	638	0.0631
71	0.404	499	0.0596
Base, ^{136}Xe :803	0.940	447	0.0533
671	0.940	447	0.0533
525	1.139	452	0.0615

CONCLUSION

Current ML based experimental rapid beam tuning has been demonstrated with reasonable reproducibility following a manual operator energy change. Combined objective BO method to reduce virtual model error gaps not robust enough to minimize both beam transmission and profile errors simultaneously. Other tomography-based methods to reconstruct real input beam distribution are currently under development. Incorporating automatic energy change, adjusting accelerating cavity phase and demonstrating this by using the virtual model is also currently under development

REFERENCES

- [1] A. Renne, C. M. Gattermann, A. Korchi and J. Nolen, "A novel approach to cross section measurement: prompt gamma isotope yield reconstruction with GammaSphere", *J. Nucl. Med.*, vol. 65, p. 242560, 2024.
- [2] A. Scheinker, F. Cropp, S. Paiagua, and D. Filippetto, "An adaptive approach to machine learning for compact particle accelerators", *J. Manage. Sci. Rep.*, vol. 11, pp. 19187, Sep. 2021. doi:10.1038/s41598-021-98785-0
- [3] X. Pang, S. Thulasidasan, and L. Rybarczyk, "Autonomous control of a particle accelerator using deep reinforcement learning", *arXiv:2010.08141*, p. 7, 2020. doi:10.48550/arXiv.2010.08141
- [4] J. L. Martinez Marin *et al.*, "Reinforcement Learning and Bayesian Optimization for Ion Linac Operations", in *Proc. HIAT'22*, Darmstadt, Germany, Jun.-Jul. 2022, pp. 130-135. doi:10.18429/JACoW-HIAT2022-TH1I2
- [5] A. Edelen, C. Mayes, D. Bowring, and D. Ratner, "Opportunities in Machine Learning for Particle Accelerators", *arXiv:1811.03172*, p. 25, 2018. doi:10.48550/arXiv.1811.03172
- [6] A. Ravichandran and B. Mustapha, "Extracting critical beam-line element misalignments from data using a beam simulation model", in *Proc. LINAC'24*, Chicago, IL, USA, Aug. 2024, pp. 53-55. doi:10.18429/JACoW-LINAC2024-MOPB003

DESIGN IMPROVEMENT OF A MINICHANNEL BEAM DUMP WING THROUGH AI-DRIVEN GENETIC ALGORITHMS*

G. Lee[†], N. Bultman, T. Kanemura, M. Patil, R. Quispe-Abad, J. Song

Facility for Rare Isotope Beams, Michigan State University, East Lansing, MI, USA

Abstract

The Facility for Rare Isotope Beams (FRIB) requires its beam dump to handle an increase in primary beam power from 20 kW to 50 kW. This paper presents a hybrid optimization framework that combines a Genetic Algorithm (GA) and Soft Actor-Critic (SAC) reinforcement learning to enhance the beam dump's thermal performance for 50 kW operation. The GA conducts a global search for key geometric design variables, while a SAC agent fine-tunes the local geometry to create a uniform heat distribution. The optimized design successfully lowered the maximum temperature across a range of beam sizes, achieving a nearly uniform temperature profile and enabling safe operation at 50 kW. A 3D simulation confirmed the design's even surface temperature and an 86% increase in power-handling capability compared to the original design.

INTRODUCTION

Beam dumps are the heat removal system directing unused beam power for heat removal. FRIB's current beam dump is a static, water-cooled structure where the beam strikes at a shallow angle ($\sim 6^\circ$) to spread out the energy deposition [1]. As FRIB upgrades its beam power from 20 kW to 50 kW, the existing dump design needs to be improved to handle the greater thermal load [2]. The primary goal is to prevent excessive localized heating by optimizing the geometry. This ensures that heat is distributed more evenly across the dump's surface for various beam sizes. Traditional engineering approaches struggle to optimize this problem, as they cannot easily account for the many interconnected geometric variables and multi-condition requirements. Therefore, advanced optimization techniques are needed.

Genetic Algorithms (GAs) are well-suited for such tasks and have been widely applied to complex engineering optimization problems due to their ability to perform global searches [3]. However, in high-dimensional design spaces, GAs may struggle to find the global optimum and can instead converge to a local minimum. Reinforcement learning (RL) has shown promise in optimizing control policies and continuous parameters in complex systems by learning through trial and error. For this reason, we selected RL to fine-tune the rough, low-dimensional design initially identified by the GA. In particular, the Soft Actor-Critic (SAC) algorithm utilizes a replay buffer to achieve high sample

efficiency, making it well-suited for refining engineering designs in computationally expensive simulations [4].

Given these considerations, this work employs a hybrid GA+RL framework to redesign the FRIB beam dump for 50 kW operation. The approach first uses a GA to explore the global design space of the dump's geometry, and then an SAC agent locally refines the shape for optimal thermal performance. Our objective is to minimize the maximum temperature in the dump for several representative beam sizes, ensuring a robust design across the anticipated operating range.

METHOD

The beam dump consists of a bi-metal main plate and two 3D-printed side wings that are attached to cover multiple beam sizes. The bi-metal plate is a copper alloy (Cu-CrZr) bonded to an aluminium alloy (Al 2219) layer using explosion bonding on the beam-facing side [5-6]. This design combines high thermal conductivity with a protective aluminium layer to reduce water activation.

The optimization targeted a ^{238}U beam with a 2.1 mm thick graphite target. As shown in Fig. 1, four representative beam sizes (σ_x, σ_y) were selected to cover a wide operational range: (2.11, 7.68), (2.90, 14.20), (5.10, 19.25), and (6.97, 25.98), with units in mm.

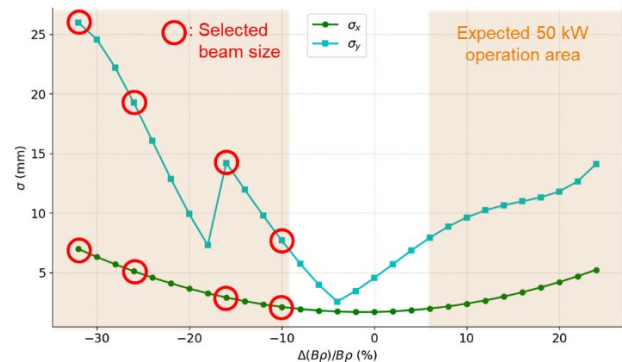


Figure 1: Variation of beam size with ^{238}U momentum deviation.

A custom 2D Finite Difference Method (FDM) thermal simulation code was developed in Python to reduce the extensive simulation time required by the GA and SAC algorithms. As shown in Fig. 2, this code divides the dump into four sections (S1–S4) corresponding to different material regions (the two wings as S1 and S4, and the bi-metal plate segments as S2 and S3). The overall design geometry was constrained to 600 mm \times 140 mm by the facility's design boundary.

* Work supported by the U.S. Department of Energy Office of Science under Cooperative Agreement DE-SC0023633, the State of Michigan, and Michigan State University.

[†] leeg@frib.msu.edu

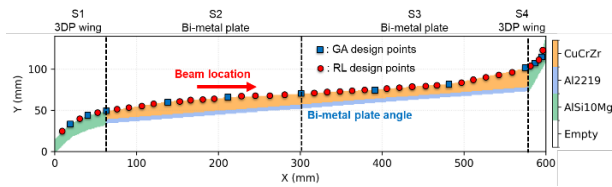


Figure 2: Schematic of the geometry used for simulation.

A two-stage optimization was used. In the first stage, a Genetic Algorithm performs a global search over coarse design variables, including section lengths, the bi-metal plate angle, beam location, and the blue rectangular design points shown in Fig. 2. In the second stage, the best solution from the GA is refined using reinforcement learning. The agent observes the environment's state through a 2D temperature grid produced by the thermal simulation. This image-like data is then processed by a Convolutional Neural Network (CNN) feature extractor, which allows the agent to learn and react to spatial thermal patterns. The agent's action is a continuous vector that applies small adjustments to the y-coordinates of the design points along the upper surface, which are indicated by red circles in Fig. 2. The reward, determined empirically, was based on the temperature difference between the GA's final result and the current RL result. If the RL agent improved upon the GA result, the reward function was $0.1 \times \Delta T + 1$; otherwise, it was $0.05 \times \Delta T$.

For the design constraints, the minimum lengths of the first (S1) and last (S4) sections in Fig. 2 were set to 50 mm and 20 mm, respectively, to ensure manufacturability. The angle of the bi-metal plate relative to the beam was set to a range of 2° – 8° . The horizontal impact position of the beam center can be offset by up to ± 30 mm. The copper plate thickness at the beam center point was set to 12 mm, and the 3D-printed wing thickness was set to 15 mm to prevent the water from reaching its boiling temperature.

For the thermal simulation, the interfaces between sections S1-S2 and S3-S4 were considered to be insulated, assuming that welding occurs only on the exterior surfaces. The convective heat transfer on the lower surface was calculated using a heat transfer coefficient derived from a COMSOL simulation. To speed up the simulation, thermal conductivity was treated as constant. To ensure correlation between the 2D Python FDM simulation and the 3D COMSOL Finite Element Method (FEM) simulation, the heat flux on each upper surface was applied using an equivalent heat transfer coefficient ($C_i k(\sigma_x)^{-p_i}$), where C_i and p_i are dimensionless coefficients for section i that scale the empirical heat conduction effect, and k is the thermal conductivity at the upper surface.

RESULTS

The hybrid optimization approach produced an improved geometry for the FRIB beam dump, leading to reductions in peak temperature and a substantial increase in operational power handling. Figure 3 illustrates the GA optimization process over 500 generations. Initially, the maximum temperatures exceeded 600°C but rapidly declined,

stabilizing at 314.5°C with consistent temperatures across all sigma cases.

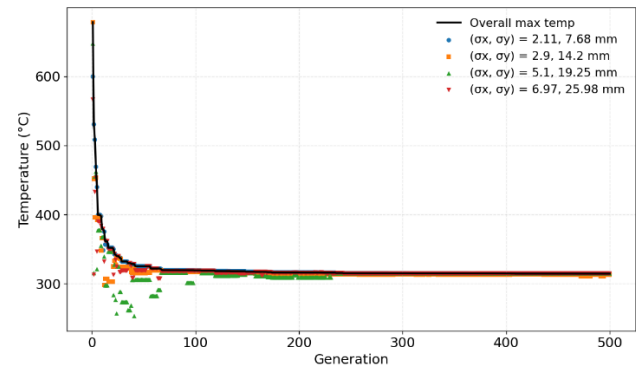


Figure 3: Genetic Algorithm temperature trend by generation.

Subsequently, the SAC reinforcement learning algorithm refined the geometry further, as shown in Fig. 4. During 500 reinforcement learning episodes, the peak temperature, which started at the 314.5°C inherited from the GA solution, progressively dropped to approximately 311°C . This was accompanied by a consistent rise in the reward, indicating effective local geometric refinement.

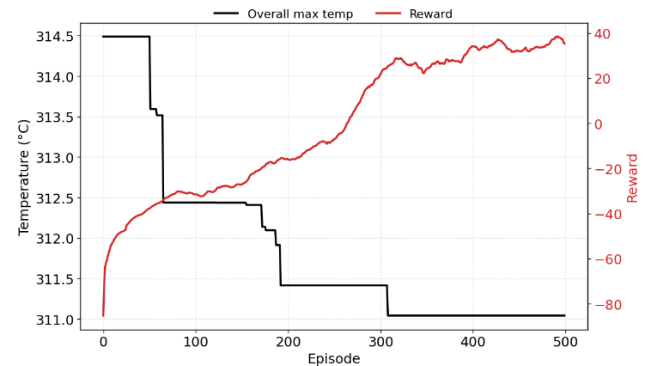


Figure 4: Reinforcement Learning temperature and reward trend by episode.

A visual comparison of the original and optimized geometries is presented in Fig. 5. The key optimized design parameters are as follows: the lengths of Section 1 and Section 4 were 60.5 mm and 26.3 mm, respectively. The tilt angle of the bi-metal main plate was determined to be 4.56° , a reduction from the original 6° , which helps minimize the temperature in scenarios with a small beam size. Additionally, the optimal beam impact position was shifted by $+15.8$ mm in the x-direction.

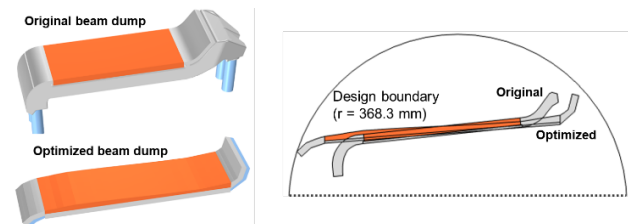


Figure 5: Comparison of the original and optimized beam dump shapes

Figure 6 demonstrates the improved thermal performance across various beam sizes, with the 3D simulation results showing substantial reductions in peak temperatures in all tested scenarios. The temperature of the optimized beam dump was compared to that of the original design for the four sigma cases. For instance, the peak temperature for the smallest beam size dropped from 603°C to 315°C. Temperatures for the intermediate beam sizes were reduced from 555°C to 309°C and 658°C to 305°C, respectively. Similarly, the largest beam scenario showed a significant reduction from 724°C to 318°C. Collectively, these results highlight the robustness of the optimized design, which maintains a low and relatively uniform surface temperature across a wide range of conditions.

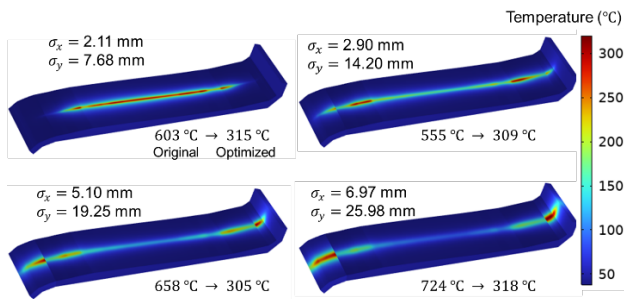


Figure 6: Temperature distribution of the optimized beam dump for the four sigma cases.

The enhanced power handling capacity of the optimized design is further illustrated in Fig. 7, which compares the beam power limitations of the optimized and original designs under variations in momentum deviation, with a material temperature limit of 350°C. The optimized design consistently outperformed the original, safely handling primary beam powers exceeding 50 kW across a large range of deviations. Overall, the optimized geometry provided an average 86% increase in operational power handling capability compared to the original design.

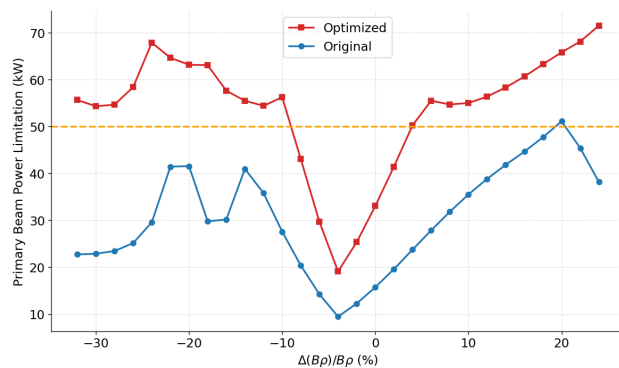


Figure 7: Primary beam power limits of the optimized and original beam dumps at 350°C material temperature limit.

CONCLUSION

This study confirms that combining a Genetic Algorithm for global exploration with reinforcement learning for local fine-tuning is an effective method for achieving significant improvements in thermal performance. The new geometry substantially reduced maximum temperatures, created a more uniform temperature distribution, and boosted power handling capability by an average of 86%. These outcomes provide a foundation for the practical implementation of the new design at FRIB and demonstrate the potential of this methodology for similar high-power accelerator components and other heat removal systems. Future work will focus on refining these optimization techniques to create even smoother geometric shapes capable of handling higher primary beam power limits.

REFERENCES

- [1] J. Wei *et al.*, “FRIB operations: first three years”, presented at HIAT’25, East Lansing, MI, USA, Jun. 2025, paper MOX01, this conference.
- [2] T. Kanemura *et al.*, “High power targetry devices at FRIB: challenges, status and plan”, presented at HIAT’25, East Lansing, MI, USA, Jun. 2025, paper MOZ03, this conference.
- [3] S. Katoch, S. S. Chauhan, and V. Kumar, “A review on genetic algorithm: past, present, and future”, *Multimedia Tools Appl.*, vol. 80, no. 5, pp. 8091–8126, Oct. 2020.
doi:10.1007/s11042-020-10139-6
- [4] T. Haarnojo, A. Zhou, P. Abbeel, and S. Levine, “Soft Actor-Critic: Off-Policy Maximum Entropy Deep Reinforcement Learning with a Stochastic Actor”, in *Proc. 35th Int. Conf. Machine Learning (ICML’18)*, Stockholm, Sweden, 2018, pp. 1861–1870.
- [5] J. Song *et al.*, “Design and experimental thermal validation of the mini-channel beam dump for FRIB”, presented at HIAT’25, East Lansing, MI, USA, Jun. 2025, paper TUP04, this conference.
- [6] R. Quispe-Abad *et al.*, “Thermal-hydraulic analysis of a 20kW beam power water-cooled mini-channel beam dump at Facility for Rare Isotope Beam”, presented at HIAT’25, East Lansing, MI, USA, Jun. 2025, paper MOP05, this conference.

ALPI-PIAVE PERFORMANCE AT INFN-LNL WITH ADVANCED OPTIMIZATION ALGORITHMS

Y. K. F. Ong^{*1}, L. Bellan, D. Bortolato, M. Montis, M. Comunian, A. Pisent, E. Fagotti
INFN-LNL, Legnaro, Italy

¹also at La Sapienza University of Rome, Rome, Italy

Abstract

The ALPI-PIAVE heavy-ion accelerator at INFN-LNL requires precise tuning due to its complex beam dynamics and high-dimensional parameter space. Although designed for a transmission efficiency of 60%, actual performance is typically limited to 15–20%, highlighting the need for more effective optimization strategies. In this work, we evaluate Bayesian Optimization (BO) and Trust Region Bayesian Optimization (TuRBO) to improve the tuning efficiency and robustness of the PIAVE injector line. To address the sensitivity of BO-based methods to parameter drifts, we incorporate Particle Swarm Optimization (PSO) and introduce controlled perturbations to assess algorithm performance under dynamic conditions. The results demonstrate the potential of these machine learning techniques for real-time accelerator optimization.

INTRODUCTION

Online accelerator optimization is a time-consuming but essential part of operating an accelerator facility, where users depend on the timely delivery of requested beams. This tuning process requires extensive manual adjustments and expert knowledge due to the large number and variety of accelerator components and parameters involved. At heavy-ion facilities like INFN-Legnaro, where a different ion beam is requested for each experiment, tuning efficiency becomes even more critical. Implementing automated optimization algorithms could streamline this process and help ensure that beam delivery remains on schedule.

Bayesian Optimization (BO) has emerged as a powerful tool for both offline and online accelerator tuning, valued for its flexibility, low initialization cost, rapid convergence, and robustness to noise [1]. BO constructs a probabilistic surrogate model, typically a Gaussian process [2] to approximate the objective function and its uncertainty. Then it uses an acquisition function to iteratively select evaluation points, effectively balancing exploration and exploitation. This strategy enables efficient identification of optimal parameters with relatively few evaluations.

This work aims to develop and evaluate advanced machine learning-based optimization techniques, including a novel Adaptive Region Bayesian Optimization (ARBO) algorithm and a hybrid BO-PSO strategy, for improving the efficiency, robustness, and scalability of online tuning in the ALPI-PIAVE accelerator complex at INFN-LNL.

THE ALPI-PIAVE HEAVY-ION ACCELERATOR

The ALPI linear accelerator consists of 20 cryostats (CR), each housing four Quarter Wave Cavities that were initially designed to operate at 3 MV/m with a 10 mm bore aperture and require independent tuning based on the ion beam type. The linac period design incorporates a triplet and two cryostats (8 cavities) to maximize space. Currently, ALPI has two injectors for stable ions: the electrostatic accelerator TANDEM, which accelerates light ions, and the PIAVE superconducting RFQ, with an output energy of 587.5 keV/u [3]. A third injector, SPES-ADIGE, is currently being installed [4]. Both active injectors suffer from low transmission to ALPI due to its aggressive transverse focusing, which makes the system highly sensitive to beam misalignments. Although the ALPI-PIAVE accelerator complex was designed for a transmission efficiency of 60%, the actual transmission is approximately 15–20%.

The PIAVE injector line, shown in Fig. 1, includes an ECR ion source, LEGIS (LEGnaro ecrIS), which produces positive heavy ions. These ions are transported and injected into a superconducting RFQ, followed by three 80 MHz bunchers for proper longitudinal matching to the ALPI linac booster. The PIAVE line also features 11 sets of quadrupoles (1 singlet, 6 doublets, and 4 triplets) for transverse focusing and 10 horizontal and vertical steerers for beam trajectory correction. Before sending the beam to ALPI, its quality is evaluated using a Faraday cup (FC) located at PM9. For the following algorithm tests, a beam of $^{129}\text{Xe}^{25+}$ was transported and accelerated through the PIAVE line. The transmission was optimized by adjusting the beam trajectory and focusing using the steerers and quadrupoles while monitoring the beam current at the PM9 FC.

Adaptive Region Bayesian Optimization (ARBO) vs. Trust Region Bayesian Optimization (TuRBO)

For the first test, we compared the Python Bayesian Optimization (BO) module developed at MIT [5] with the Trust Region Bayesian Optimization (TuRBO) implementation from BoTorch [6]. We introduced an additional feature to the BO algorithm that allows the search region (R) to expand if the current best set point (S_{best}) lies near the boundary of the defined R . This expansion can be applied to one or multiple parameters, depending on their proximity to the boundary, and is evaluated after each iteration. From this point onward, we refer to this modified version of the algorithm as Adaptive Region Bayesian Optimization (ARBO). This algorithm was also used to optimize the longitudinal

* ysaong@lnl.infn.it

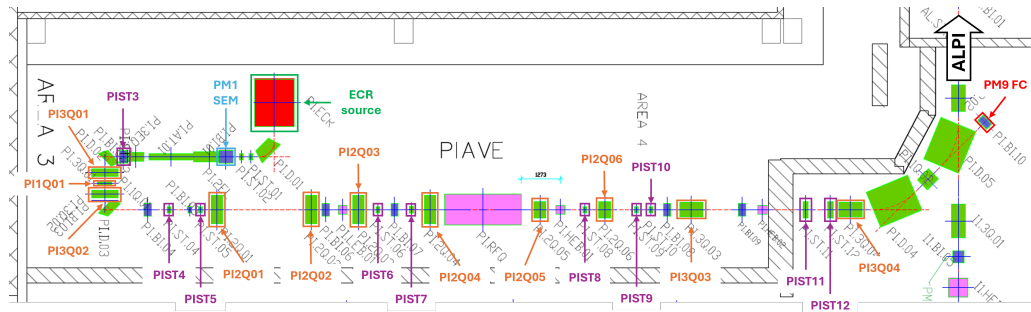


Figure 1: Schematic diagram of the PIAVE injector for the ALPI Superconducting Linac at INFN-Legnaro. Elements used in the optimization algorithm tests are enclosed in colored boxes: steerers (purple), quadrupoles (orange), the ECR ion source (green), the beam profiler (blue), and the Faraday cup (red).

acceptance of ALPI [7]. The main differences between the two algorithms as utilized in this study are highlighted in Table 1.

Table 1: Comparison Between Adaptive Region Bayesian Optimization (ARBO) and Trust Region Bayesian Optimization (TuRBO) Algorithm Parameters Utilized in This Study

Feature	ARBO	TuRBO
Search Region (R)	Starts at $\pm 2^*$ (can grow during the optimization)	Fixed at $\pm 5^*$ (does not grow)
When Region Is Checked	After every iteration (user-defined)	Every 4 iterations (depends on batch size and success/failure count)
When to Adapt Region	If the best solution is within 10% of the boundary	Requires 4 successes to grow, 10 failures to shrink
How the Region Changes	Expands lower/upper bounds by 33.33% of current region range	Doubles the size on success, halves it on failure
Exploration vs. Exploitation	Uses $\kappa = 2.4$ (more exploration); can explore further near the best point	Starts with global search trust region ($TR = 0.8$), then refines locally using TR success/failure

*with respect to the starting set point (S) of the parameter

To compare the algorithms, we used all 16 PIAVE steerers as optimization parameters, aiming to maximize the beam current measured at the PM9 FC. Figure 2 shows the relative beam transmission through the PIAVE line, compared to the initial current, along with the Δ set points of the steerers for both algorithms (highlighting the best solutions). Both algorithms successfully improved the PIAVE transmission. However, ARBO achieved the highest relative transmission of 23.1% in fewer than 20 iterations. This efficiency is attributed to ARBO's strategy of starting with a smaller R , which then expands adaptively based on the $S_{best,i}$ found. In contrast, TuRBO initially explores a larger global R before narrowing down to local optimization. Moreover, although ARBO began with a smaller R than TuRBO, its adaptive region feature allowed it to eventually explore

beyond TuRBO's fixed global bounds, giving ARBO a potential advantage in discovering better solutions.

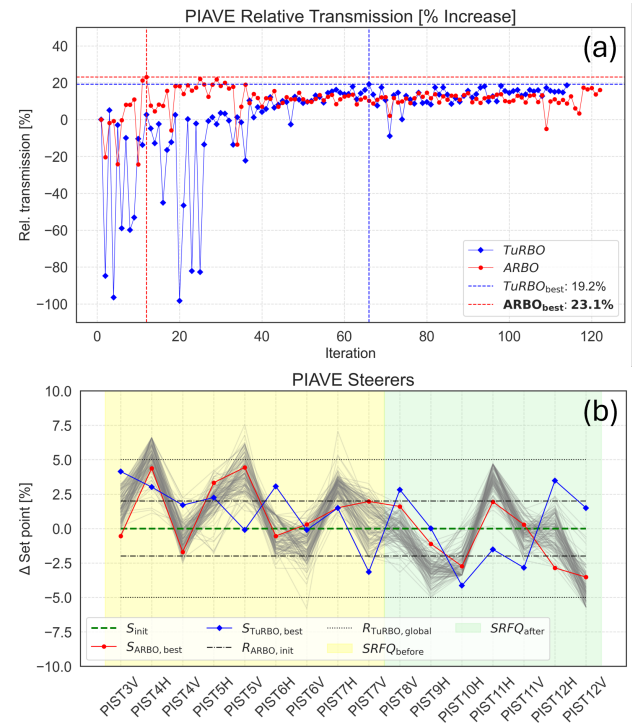


Figure 2: (a) Relative transmission increase in PIAVE and (b) Δ set points for the PIAVE steerers during the optimization process for ARBO (red) and TuRBO (blue). The gray lines represent the set points explored by the ARBO while the red and blue points indicate the best set points found by the ARBO and TuRBO, respectively.

Bayesian Optimization (BO) + Particle Swarm Optimization (PSO)

From previous accelerator tests, we observed that Particle Swarm Optimization (PSO) performs well in the presence of instabilities during optimization runs [3]. This observation motivated us to explore whether combining Bayesian Optimization (BO) with PSO could enhance BO's effectiveness

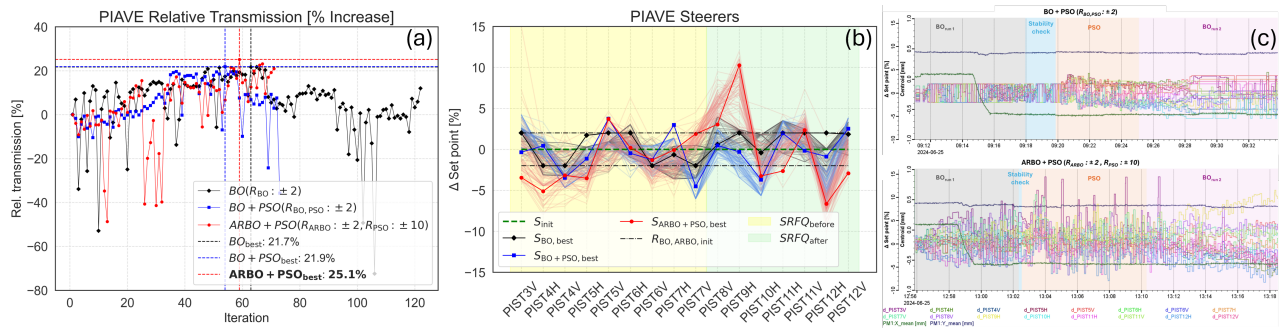


Figure 3: (a) Relative transmission improvement in PIAVE and (b) Δ steerer set points during optimization using BO (black), BO + PSO (blue), and ARBO + PSO (red). Panel (c) shows the optimization sequence for BO + PSO and ARBO + PSO, including beam centroid shifts at PM1 and Δ steerer adjustments. A perturbation was introduced during iterations 20–30 of the first BO run (BO + PSO and ARBO + PSO), while the single BO run began with the perturbation already present. This perturbation is evident in the shift of the beam's x centroid.

under unstable conditions. PSO was integrated by introducing a stability check after the initial BO run: it re-evaluates previously tested S 's and verifies whether the measured beam current remains within 10% of the previously recorded value. If the stability check fails, a short PSO run is triggered, and the resulting S_{best} 's for each parameter are used to initialize a new BO or ARBO run. To simulate controlled instability, we intentionally altered the focusing strength of the LEGIS ECR source triplet during the optimization process.

The resulting relative PIAVE transmission and steerer settings S for three cases—BO, BO + PSO, and ARBO + PSO—are shown in Fig. 3. Among the tests, ARBO + PSO achieved the highest relative transmission and continued to optimize beyond the point where BO and BO + PSO had apparently converged. This is evident from both the transmission trend after identifying S_{best} and the archiver graph (refer to Fig. 3(a) and (b)): while the BO + PSO parameters remained stable, ARBO + PSO continued to adjust its S , suggesting ongoing optimization. Furthermore, ARBO's adaptive region feature allowed the algorithm to explore a larger search space R , which proved beneficial in identifying a new S_{best} under the perturbed conditions of the line.

Adaptive Region Bayesian Optimization (ARBO) Full PIAVE Test

To evaluate the dimensional scalability of ARBO, we tested the algorithm using all available optical parameters in the PIAVE line, including steerers, quadrupole averages, and quadrupole unbalances, for a total of 37 parameters. The quadrupole average represents the overall focusing strength of a doublet or triplet, while the unbalance quantifies the difference between vertical and horizontal focusing, which can be used to control the beam's first-order moments.

Figure 4 shows the transmission through PIAVE during the optimization process. ARBO achieved a maximum transmission of 63.9%, more than doubling the initial value. The entire optimization was completed in less than 20 minutes and the result represents the highest transmission recorded

since PIAVE began operations. In particular, this is also the first time that PIAVE's transmission has approached its theoretical limit of approximately 65–70%.

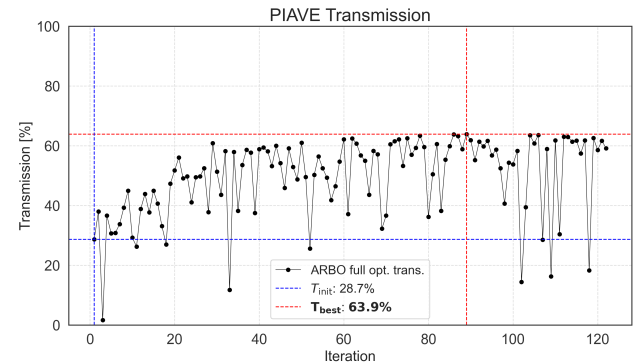


Figure 4: PIAVE transmission during ARBO using all available optical elements—steerers, and quadrupole averages and unbalances—for a total of 37 parameters.

CONCLUSION

In this paper, we introduced Adaptive Region Bayesian Optimization (ARBO), a modified version of Bayesian Optimization (BO) tailored for accelerator autotuning, and compared its performance with open-source BO modules, including standard BO and TuRBO. Additionally, we explored a hybrid approach by combining BO with Particle Swarm Optimization (PSO) to leverage the strengths of both algorithms for optimizing under unstable conditions. Although the ARBO + PSO algorithm showed promising results, further studies are required to fully assess its convergence behavior over extended runs.

We also evaluated the scalability of ARBO by optimizing 37 parameters simultaneously, achieving the highest transmission ever recorded in the PIAVE accelerator, approaching its theoretical performance limit. These results demonstrate the significant potential of machine learning-based autotuning techniques in enhancing accelerator performance and operational efficiency.

Future work will focus on applying these techniques to high-intensity machines, where constraints such as beam peak power and beam losses must be carefully managed.

REFERENCES

- [1] R. Roussel *et al.*, “Bayesian optimization algorithms for accelerator physics”, *Phys. Rev. Accel. Beams*, vol. 27, no. 8, p. 084 801, 2024.
doi:10.1103/PhysRevAccelBeams.27.084801
- [2] C. E. Rasmussen and H. Nickisch, “Gaussian processes for machine learning (gpml) toolbox”, *J. Mach. Learn. Res.*, vol. 11, pp. 3011–3015, 2010. <https://www.jmlr.org/papers/volume11/rasmussen10a/rasmussen10a.pdf>
- [3] L. Bellan *et al.*, “New techniques method for improving the performance of the ALPI Linac”, *JINST*, vol. 19, no. 03, p. T03005, 2024.
doi:10.1088/1748-0221/19/03/T03005
- [4] D. Bortolato *et al.*, “Hardware commissioning of the renovated piave injector at infn-lnl”, in *J. Phys. Conf. Ser.* p. 012 076, 2019. doi:10.1088/1742-6596/1350/1/012076
- [5] F. Nogueira, *Bayesian Optimization: Open source constrained global optimization tool for Python*, 2014, <https://github.com/bayesian-optimization/BayesianOptimization>
- [6] M. Balandat *et al.*, “BoTorch: A Framework for Efficient Monte-Carlo Bayesian Optimization”, in *Adv. Neural. Inf. Process. Syst.* 2020. doi:10.48550/arXiv.1910.06403
- [7] Y. K. Ong *et al.*, “Advanced algorithms for linear accelerator design and operation”, in *Proc. LINAC’24*, Chicago, IL, USA, pp. 484–487, 2024.
doi:10.18429/JACoW-LINAC2024-TUPB075

STUDY OF PONDEROMOTIVE INSTABILITY IN THE FRIB $\beta = 0.53$ HALF-WAVE RESONATOR*

J. Brown^{1,2†}, W. Chang¹, S. Kim¹, T. Xu^{1,2}, S. Zhao¹,
¹Facility for Rare Isotope Beams, East Lansing, MI, USA

²Department of Physics and Astronomy, Michigan State University, East Lansing, MI, USA

Abstract

Superconducting radio-frequency niobium cavities are susceptible to deformations caused by external or internal forces, leading to shifts in the cavity resonant frequency. One source of deformation comes from the radiation pressure of the cavity fields, producing the so-called Lorentz force detuning effect. This effect can couple to the cavity mechanical modes in a generator-driven mode, leading to the ponderomotive instability. In the FRIB 322 MHz, $\beta = 0.53$ Half-Wave Resonators (HWR), the instability appeared when the cavity was detuned, with thresholds depending on low-level RF control parameters, such as closed loop gain, as well as the accelerating gradient. Using a measured Lorentz transfer function, Simulink simulations were conducted to predict the instability thresholds, which were then compared with experimental results. We find good agreement for simulated and experimental thresholds on the negative side of the resonance curve and note inconsistencies with theory for proportional feedback systems and discuss paths forward for analytical studies.

INTRODUCTION

The $\beta = 0.53$ Half-Wave Resonator

The Facility for Rare Isotope Beams (FRIB) is a heavy ion, superconducting (SC), continuous wave (CW) linear accelerator capable of accelerating ^{238}U ions to 200 MeV/u [1]. The acceleration schemes employs $\beta = 0.53$, 322 MHz half-wave resonators (HWRs) as the highest beta cavity among four different types of SC cavities. The field profiles for the $\beta = 0.53$ HWR from CST Studio [2] are shown in Fig. 1.

The capacitance C is built up in the high electric field regions such as the accelerating gaps whereas the inductance L is formed in the high magnetic field regions of the cavity periphery. These two factors thus determine the resonance frequency of the cavity ω_0 via:

$$\omega_0 = \frac{1}{\sqrt{LC}}. \quad (1)$$

Since the capacitance and inductance are determined by the geometry, changes to the geometry result in a change in ω_0 , which leads to a detuning from the generator frequency. CW linac operation allows for the choice of using

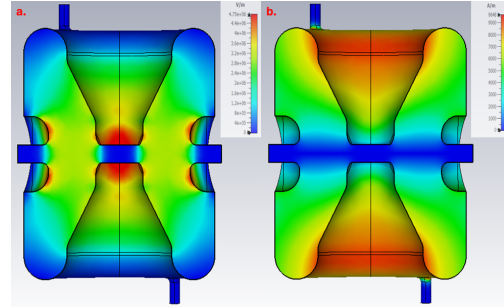


Figure 1: Fundamental electric field (left) and magnetic field(right). Internal energy normalized to 1 J .

relatively high Q_{ext} couplers, due to relatively weak beam loading effects compared to pulsed machines. This leads to reduced RF power costs with narrow bandwidths. In this case, it is necessary to maintain frequency excursions due to detuning effects at the level of the loaded bandwidth or lower. Otherwise, the RF power required for amplitudes and phase stabilities could be even higher than the case of using a lower Q_{ext} couplers (a larger bandwidth) [3].

In this work, we focus on a specific type of detuning effects: the Lorentz force detuning effect and the possible instabilities that can arise from its presence.

Lorentz Force Detuning

The RF fields in the cavity produce a radiative/Lorentz pressure on the walls of the cavity, leading to deformations. As such, this Lorentz pressure detunes the cavity. This effect can be divided into static and dynamic effects, depending on its coupling with the cavity's mechanical vibrational modes.

Static Lorentz Force Detuning In a steady-state case, as is most applicable to CW operation, the Lorentz pressure causes a static shift $\delta\omega$ in the resonance frequency. This shift is proportional to the square of the accelerating gradient E_{acc} [4]:

$$\delta\omega = -k_L E_{acc}^2, \quad (2)$$

where k_L is the so-called static Lorentz force detuning (LFD) coefficient. This coefficient is geometry dependent and relates the effect of deformation/detuning to the accelerating field.

This ponderomotive effect also creates a tilt in the resonance curve of the cavity as shown in Fig. 2, where a hysteresis region is created on the lower branch of the resonance curve. This now opens the door to the first kind of ponderomotive instability: the monotonic or jump instability.

* This material is based upon work supported by the U.S. Department of Energy, Office of Science, Office of High Energy Physics, under Award Number DE-SC0018362 and Office of Nuclear Physics and used resources of the Facility for Rare Isotope Beams (FRIB) Operations, which is a DOE Office of Science User Facility under Award Number DE-SC0023633.

† brownjac@frib.msu.edu

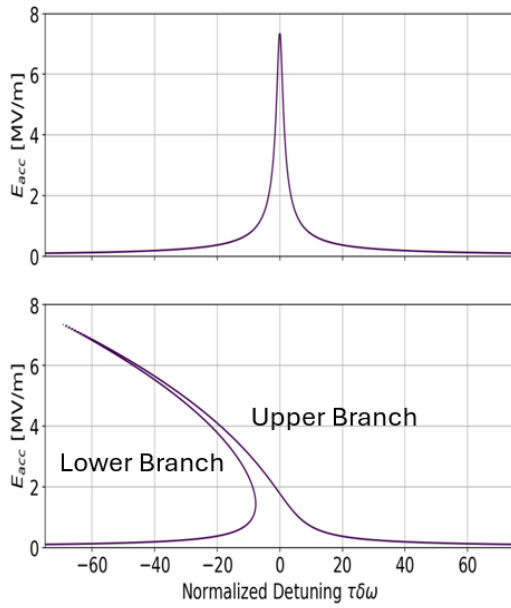


Figure 2: Normal resonance curve of the cavity (top) and resonance curve in the presence of the Lorentz pressure without amplitude feedback and/or tuning (bottom). τ is the cavity electrical decay time.

The monotonic/jump instability is characterized by a sudden drop in field level and excitation of mechanical vibrations when passing from the upper branch of the resonance to the lower branch. This can be thought of as the cavity going from a higher energy, unstable equilibrium to the lower energy, stable state. Amplitude feedback systems and in some cases, mechanical tuning of the cavity, can remove the tilting effect and thus greatly reduce the chance of this instability.

Dynamic Lorentz Force Detuning In real cryomodule operations, modulation of the cavity field can occur at various frequencies due to microphonics. If the modulation frequency is close to the resonance frequency of one of the cavity's mechanical vibrational modes (frequencies denoted by Ω_μ), the mechanical mode can couple to the modulation of the RF field, leading to an increased detuning effect. These dynamic effects can be described by the Lorentz transfer function, defined in the Laplace domain as [4]:

$$LTF(s) = -2E_{acc} \sum_{\mu} \frac{k_{\mu} \Omega_{\mu}^2}{s^2 + (2/\tau_{\mu})s + \Omega_{\mu}^2}, \quad (3)$$

where τ_{μ} is the mechanical mode decay time and k_{μ} is a LFD coefficient specific to mode μ . This function can be measured and the effects of modulation at mechanical resonance can be clearly seen, as shown in Fig. 3.

We now discuss the second kind of ponderomotive instability: the oscillatory instability. This instability appears on the positive branch of the resonance curve, and can occur when the cavity field is modulated and there is non-zero static detuning.

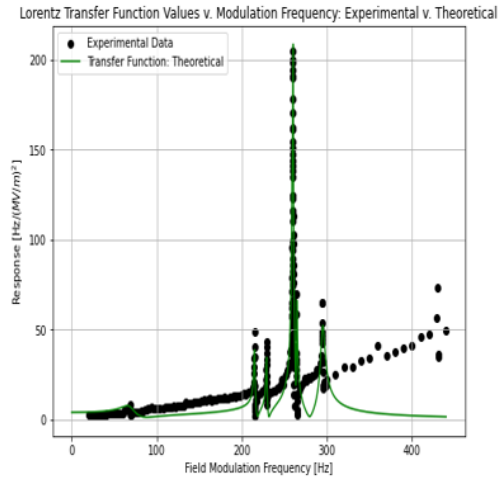


Figure 3: Lorentz transfer function measurement for $\beta = 0.53$ HWR. Y-axis is cavity response to field modulation [$\text{Hz}/(\text{MV}/\text{m})^2$] and x-axis is modulation frequency.

We describe the progression of this instability in more detail:

1. Initial modulation of E_{acc} occurs due to either mechanical or electrical noise, producing a modulation amplitude δE_{acc} .
2. The field modulation applies a pressure at the modulation frequency Ω_{mod} . If $\Omega_{mod} \approx \Omega_{\mu}$, the mechanical mode can be excited, causing displacement δx_{μ} .
3. Cavity mechanical mode excitation results in a frequency shift $\delta\omega_{\mu}$ in accordance with the Lorentz transfer function (Eq. 3), $\delta\omega_{\mu} \propto k_{\mu} Q_{\mu}$.
4. There are a few possible paths to unstable behavior from here. If the cavity is being operated in an open loop and the external modulation persists, the above steps will repeat until RF interlocks on the minimum cavity field engage or the external modulation stops. If there is phase feedback systems present with insufficient gain, the low-level RF (LLRF) controller will send more power to the cavity to keep the phase setpoint without end. The above steps can repeat until the RF interlocks on the maximum RF power engage.

The schematic of the oscillatory instability and experimental example can be seen in Fig. 4. This instability can be suppressed with additional amplitude feedback systems in the LLRF controller, a component of feedback present in all accelerator operations. Sufficient amplitude control would stop this loop at step 2, leading to no runaway effect.

GOALS AND METHODOLOGY

FRIB employs active disturbance rejection control (ADRC) algorithms [5], which use extended state observers (ESOs) for feedback on cavity amplitude and phase.

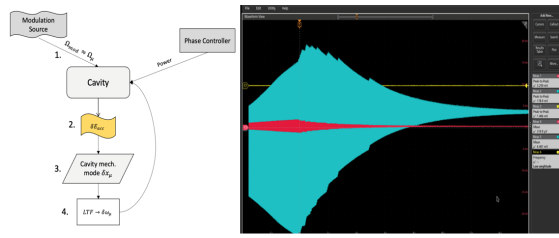


Figure 4: Schematic of oscillatory instability progression, with 1-4 corresponding to the respective bulleted items (left) and experimental example of growth in detuning (blue) and field (red) when detuned to one side of the resonance curve (right).

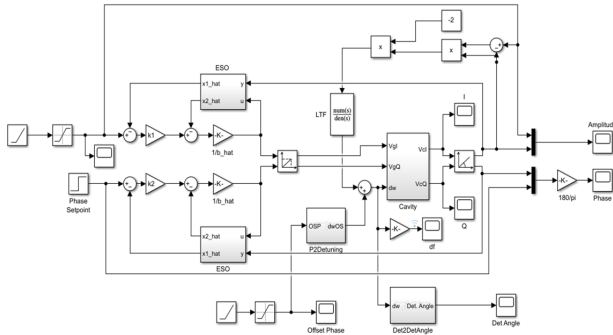


Figure 5: Simulink model of FRIB feedback+cavity code. The static offset feature can be seen in the bottom middle.

ADRC is a non-linear process unlike traditional proportional-integral-differential control. Ponderomotive instability was encountered during production for FRIB in 2020, and was then suppressed empirically using higher amplitude feedback gains. We therefore seek to better understand the behavior of these instabilities in the presence of this non-linear feedback system.

To model the cavity and feedback systems, we use a Simulink model adopted from [6]. A schematic of our system can be seen in Fig. 5. We have incorporated the measured LTF to feedback detuning values into the cavity electrical equations. A static detuning offset has been added as well to detune the cavity up to $\pm 45^\circ$ (half-bandwidth) and record instability onset to compare with experimental measurements in the linac.

RESULTS AND DISCUSSION

We present the results from our Simulink model (dots) and experimental measurements (diamonds) in Fig. 6. We swept through 4 different amplitude controller gains and 3 different E_{acc} . In general, we observed that the instability thresholds decrease with increased E_{acc} , certifying that these phenomena are related to the Lorentz pressure.

There is some inconsistent behavior seen in both experiment and simulation. On the positive side, our simulation predicts no instability within $+45^\circ$ for all choices of field and gains. We see that is not represented for measurements at $E_{acc}=7.4$ MV/m and 8.1 MV/m. Additionally we see in a

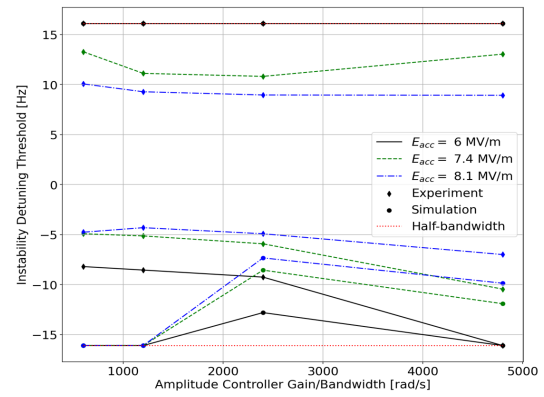


Figure 6: Plot of instability threshold in terms of static detuning versus amplitude controller gain. Results for simulation and experiment are shown for 3 different fields.

few cases that the instability threshold decreased (not all) as we moved to higher controller gains, which is not consistent with an established theory of the ponderomotive instability relating to proportional, linear feedback systems [7, 8].

We now discuss the negative side results. As we employ amplitude feedback systems to correct the static effect, we expect that the negative side to be instability free. However, we see that both simulation and measurement shows instabilities. In experiment, we see a growth in field and phase that we associate with the oscillatory instability rather than the rapid drop in field of the monotonic instability when detuned to the negative side. These two facts suggest that the instabilities we see on the negative side are in some way related to our LLRF controller.

SUMMARY AND OUTLOOK

We have presented a method to predict instability thresholds in SRF cavities and showcased preliminary results compared to experimental measurements; there is good agreement between simulation and experiment for higher amplitude controller gains on the negative side of the resonance curve. We note some inconsistencies from existing theory for proportional theory. To better understand the root cause for these phenomena, we will be conducting an analytical study of closed loop transfer functions for ADRC feedback. This will help us in understanding the connection between ADRC and the Lorentz transfer function and open up doors to further suppress these effects, as well as understand the discrepancies between simulation and measurement on the positive side.

REFERENCES

- [1] J. Wei *et al.*, “FRIB transition to user operations, power ramp up, and upgrade perspectives”, in *Proc. SRF’23*, Grand Rapids, MI, USA, Jun. 2023, pp. 1–8.
doi: 10.18429/JACoW-SRF2023-MOIAA01
- [2] U. Becker, “CST’s commercial beam-physics codes”, in *Proc. ICAP’06*, Chamonix, France, Oct. 2006, paper

- THM2IS03, pp. 308–308. https://jacow.org/icap06/TALKS/THM2IS03_TALK.PDF
- [3] T. Wangler, “RF acceleration in linacs”, in “RF Linear Accelerators”, Wiley-VCH Verlag GmbH & Co. KGaA, 2008, pp. 32–52.
- [4] J.R. Delayen, “Ponderomotive instabilities and microphonics—a tutorial”, *Physica C: Superconductivity*, Vol. 441, no. 1–2, pp. 1–6, 2006. doi:10.1016/j.physc.2006.03.050
- [5] Z. Gao, “Active disturbance rejection control: From an enduring idea to an emerging technology”, in *2015 10th Int. Workshop on Robot Motion and Control (RoMoCo)*, Jul. 2015, pp. 269–282. doi:10.1109/romoco.2015.7219747
- [6] J. Vincent *et al.*, “On active disturbance rejection based control design for superconducting RF cavities”, *Nucl. Instrum. Methods Phys. Res. A*, vol. 643, no. 1, pp. 11–16, Jul. 2011. doi:10.1016/j.nima.2011.04.033
- [7] J. R. Delayen, “Phase and amplitude stabilization of superconducting resonators”. Ph.D. Dissertation, California Institute of Technology, 1978. doi:10.7907/ZS1J-1E35
- [8] D. Schulze, “Ponderomotorische Stabilität von Hochfrequenzresonatoren und Resonatorregelungssystemen”, Dissertation Karlsruhe, KFK-1493, 1971. (“Ponderomotive Stability of R.F. Resonators and Resonator Control Systems”, Argonne National Lab, ANL-TRANS-944, 1972).

MULTI-Q BEAM STUDIES AT FRIB: SIMULATIONS AND MEASUREMENTS

A. Gonzalez*, K. Fukushima, T. Maruta, P. N. Ostroumov, A. S. Plastun
Facility for Rare Isotope Beams, Michigan State University, East Lansing, MI, USA

Abstract

The Facility for Rare Isotope Beams (FRIB) linear accelerator is capable of simultaneously transporting and accelerating multiple-charge-state heavy-ion beams. Accurate transverse and longitudinal matching of these beams is a challenging problem, particularly in achromatic bending segments of the linac. To solve it, we employ both macroparticle tracking and linear optics codes. The simulation models are being developed, cross-checked, and validated by beam measurements. The studies are focused on the beam size, envelope matching, charge state separation, and the response of the beam position. The results of the studies with the 16.5 MeV/u five-charge-state uranium beam will be presented.

INTRODUCTION

Charge stripping is essential for efficient acceleration of heavy-ion beams. When a heavy-ion beam is stripped, the resulting charge distribution is a Gaussian function centered on the mean charge state. The mean and standard deviation of this Gaussian depends on many factors like beam velocity, atomic mass of ions in the beam, stripper material and stripper thickness. For optimal placing of a 17 MeV/u uranium beam on the most uniform area of the FRIB liquid lithium stripper, a mean charge state of 75+ with 21% of initial beam intensity is produced [1]. Therefore, the post-stripper segments of the FRIB driver linac were designed to accept and simultaneously accelerate multiple charge states and deliver them to the target. In March 2025, we developed the linac tune to produce 20 kW of uranium beam on the target by accelerating five charge states after the stripper.

To support the beam dynamics optimization and simulations in the FRIB linac, two codes are used: TRACK [2] and FLAME [3]. TRACK is a 3-dimensional particle tracking code which simulates the dynamics of multi-charge-state heavy ion beams. FLAME, which stands for Fast Linear Accelerator Model Engine, is a linear optics code which uses matrices to simulate trajectories and beam envelopes. This makes it very useful for various optimization problems, such as the development of design magnet settings. After applying the FLAME-created settings to the machine, the Courant-Snyder (CS) parameters measured with profile monitors often do not match those in simulations.

In the FRIB linac, wire scanner profile monitors are used to measure the profile of a beam. To find the CS parameters, a technique known as a quadrupole scan is used. A set of 7-10 different currents in two quadrupoles close to the desired profile monitor are used and the horizontal, vertical,

and diagonal beam sizes are measured at every step. Then, horizontal emittance, vertical emittance, and CS parameters are optimized in FLAME until the simulation best fits the measurements at each step. Each step of the scan takes about two to three minutes, meaning one complete scan can take around 15 to 30 minutes. For a five-charge-state uranium beam, measuring all charge states can take over two hours.

During primary beam development, we perform quadrupole scans at the entrance of all three linac segments, upstream of the stripper, and at the entrance of the Beam Delivery System (BDS). Better simulation accuracy will reduce the amount of measurements needed, greatly reducing beam tuning time, and improve the quality of beam matching, which in turn will mitigate the beam loss. These two reasons provided motivation to investigate the simulation models and try to improve their accuracy.

TRANSVERSE BEAM MATCHING IN FS1

These studies focus on the first 180° achromatic bend in the FRIB linac, Folding Segment 1 (FS1). In FS1, for a multi-charge-state beam, we do a quadrupole scan and reconstruct the beam envelopes with FLAME for each individual charge state. Based on the reconstructed envelopes, the quadrupole fields close to the entrance to Linac Segment 2 (LS2) are adjusted to match the beam to LS2. At the location of the stripper, the transverse beam size of each charge state should be equal. However, in the reconstructions, the rms beam size of each charge state at the stripper is different, as seen in the blue bars of Fig. 1, meaning the FLAME model is not accurate. Using a five-charge-state uranium beam with an energy of 16.5 MeV/u, measurements and simulation results were compared with the goal of improving the FLAME model.

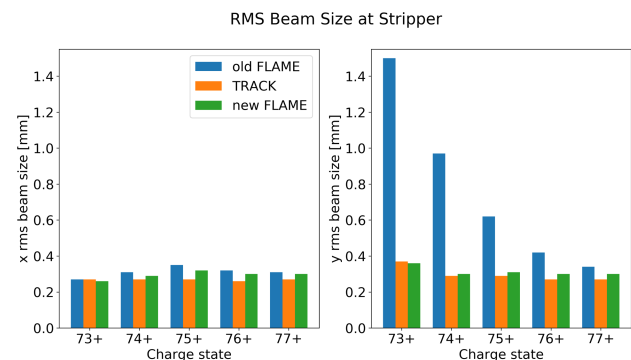


Figure 1: Comparison of rms beam sizes at lithium stripper for five-charge-state uranium beam.

* gonzalea@frib.msu.edu

Effective Lengths of Quadrupoles

We evaluated the effective length of quadrupoles using the 3D computer model. In FS1, there are two types of quadrupoles, Q1 quadrupoles are used in the straight sections and Q6 quadrupoles are used in the bending section. FLAME uses a “hard-edge” model, which ignores fringe fields by definition and models the magnetic field gradient as constant for a certain effective length in the longitudinal direction. The effective length is defined by $L_{eff} = \frac{\int_{-\infty}^{\infty} G dl}{G_0}$ where G_0 is the magnetic field gradient in the center of the magnet and $\int G(l) dl$ is the integral of the gradient in the longitudinal direction of the magnet.

Due to the lack of 3D models of the quadrupole magnets, initially we set the effective lengths equal to their geometrical lengths, and used them until recently. The 3D models of quadrupoles were created in CST Studio based on their final drawings and their magnetic fields were simulated. The 3D fieldmaps produced by these simulations were used to calculate the effective lengths displayed in Table 1 and imported into our TRACK model.

Table 1: Quadrupole Length Comparison

Quad Type	Effective Length (cm)	Geometric Length (cm)
Q1	26.1	25.0
Q4	38.1	33.5
Q5	45.1	40.5
Q6	28.9	25.0

In the FLAME model, the effective length for Q1 quadrupoles was correct, while the effective lengths for the other quadrupole types were updated to their corresponding values in Table 1.

3D TRACK Model Validation

To validate the 3D TRACK model, two dipole correctors upstream of the first 45-degree FS1 bending dipole were used to kick the central trajectory of each charge state of a five-charge-state uranium beam by ± 2 mm in the vertical direction and ± 1 mm in the horizontal direction. The trajectories of the beam charge states throughout FS1 were measured with BPMs in all four cases and compared with the reference trajectory. The measured results from the stripper to the entrance of LS2 are shown as dots in Figs. 2 and 3. The lines show the centroid trajectories simulated with the TRACK 3D model. The simulated trajectories match the BPM measurements well, thus validating the updated model.

TRACK and FLAME Comparisons

The FLAME reconstruction at the profile monitor was used to generate a particle distribution for TRACK for each charge state. These distributions were simulated backwards in TRACK from the profile monitor to the stripper. The

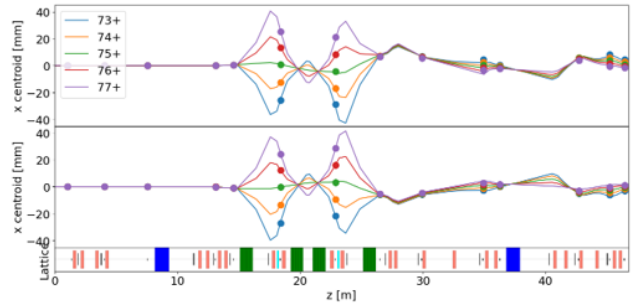


Figure 2: Comparison of horizontal central trajectory measurements (dots) and TRACK simulations (lines) for a five-charge-state uranium beam when each charge state enters the FS1 bending section with an offset of +1 mm (top) and -1 mm (middle). The FS1 lattice is shown in the bottom plot with red boxes as quadrupoles, blue as RF cavities, green as dipoles, cyan as sextupoles and thin black as correctors.

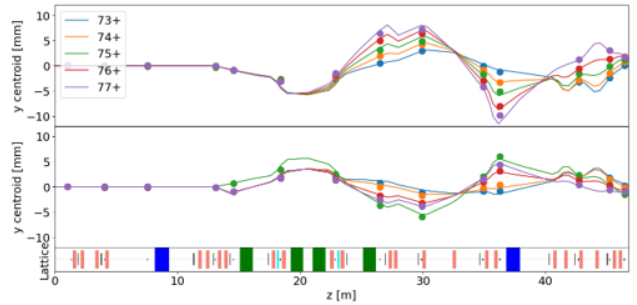


Figure 3: Comparison of vertical central trajectory measurements (dots) and TRACK simulations (lines) for a five-charge-state uranium beam when each charge state enters the FS1 bending section with an offset of +2 mm (top) and -2 mm (middle).

orange and blue bars in Fig. 1 compare the rms beam sizes for each charge state at the stripper between the backwards TRACK simulation and the FLAME reconstruction.

Next, the beam envelopes and trajectories in TRACK and FLAME were compared. The differences between the models originate in the bending section, which contains four 45-degree dipoles, four Q6 quadrupoles and two sextupoles. In both models, the sextupoles are hard-edge, so they cannot be responsible for the difference. After updating the effective length of the Q6 quadrupoles, Fig. 4 compares the rms beam envelopes in FS1 between the forward FLAME simulation and the backwards TRACK 3D simulation for the 73+ charge state. There is still a significant difference between the TRACK and FLAME simulations beginning in the bending section and propagating upstream to the stripper. Therefore, there must be a difference in the dipole models.

Linear Dipole Corrections

FLAME uses a hard-edge dipole model, whereas the 3D field model has an extended length to include fringing fields. From CST simulations, the effective length of the 45-degree FS1 bending dipole was calculated to be 5% higher than the

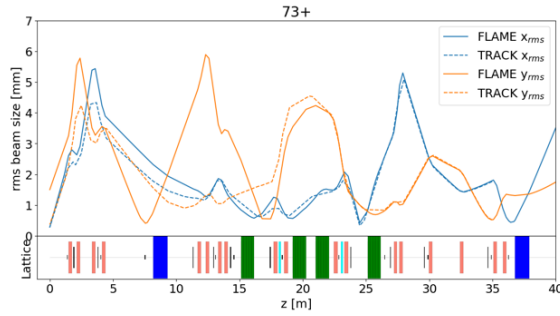


Figure 4: Comparison of rms beam envelopes beginning at the stripper between the backward TRACK simulation and the forward FLAME simulation with updated Q6 quadrupole effective lengths.

geometrical length used in the FLAME model. The FLAME FS1 dipoles were updated to this higher effective length.

FRIB dipoles bend the beam in the horizontal plane. The fringe magnetic fields of the dipole also provide linear quadrupole-like focusing in both the horizontal and vertical directions, which depend on the pole face angle of the dipole. The FLAME transverse 4×4 dipole fringe transfer matrix is:

$$\begin{bmatrix} 1 & 0 & 0 & 0 \\ \frac{\tan(\psi)}{\rho} \frac{q}{q_{ref}} & 1 & 0 & 0 \\ 0 & 0 & 1 & 0 \\ 0 & 0 & -\frac{\tan(\psi - \beta)}{\rho} \frac{q}{q_{ref}} & 1 \end{bmatrix} \quad (1)$$

where ρ is the bending radius, ψ is the pole face angle, and β is a correction to the pole face angle in the vertical direction [4, 5]. The correction angle is responsible for the variation of the pole gap height [6]. Previously, the FLAME code did not include this β term and the charge state dependence term, $\frac{q}{q_{ref}}$, where q is the ion charge state and q_{ref} is the charge state of the central or reference ion. Using a simulation with sextupoles turned off, ψ and β were optimized to best fit FLAME envelopes and trajectories of all five charge states to those from the TRACK 3D model simulations using a Nelder-Mead optimization algorithm. Figure 5 shows a comparison of the rms beam envelopes for the 73+ charge state between this updated FLAME model and the TRACK 3D model when both simulations are given the same initial CS parameters at the stripper. As shown in Fig. 5, the envelopes still do not perfectly match. There must be non-linear effects responsible for the residual mismatch.

Non-Linear Dipole Corrections

Despite being a linear optics code, FLAME contains a sextupole element that approximates the non-linear effects of a sextupole magnet on a beam. To reproduce the sextupole component present in the magnetic field of the 3D dipole, a few very thin sextupole elements were distributed inside the FLAME dipole. The strength of these sextupoles was then scaled to best fit the TRACK 3D envelopes and trajectories for a five-charge-state uranium beam. Figure 6 shows the rms envelope comparison for 73+ between this new FLAME

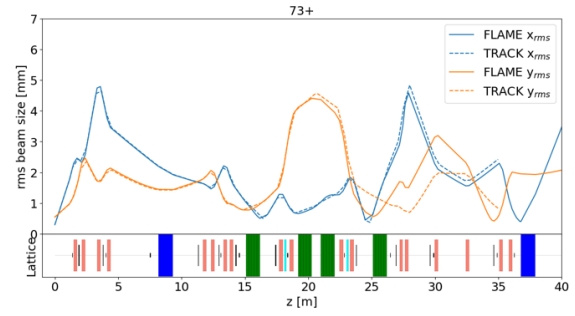


Figure 5: Comparison of rms beam envelopes beginning at the stripper between the updated FLAME simulation and a TRACK simulation with the same initial conditions.

model and the 3D TRACK model. After this fitting, the new FLAME model was used to optimize the parameters of the sigma matrix for each charge state at the stripper to best fit the measurements of the quadrupole scan, similar to the procedure used while performing beam reconstruction for matching, with results shown in the green bars in Fig. 1. The new model produces nearly equal beam sizes at the stripper for each charge state, which is expected, showing definite improvement from the original FLAME model.

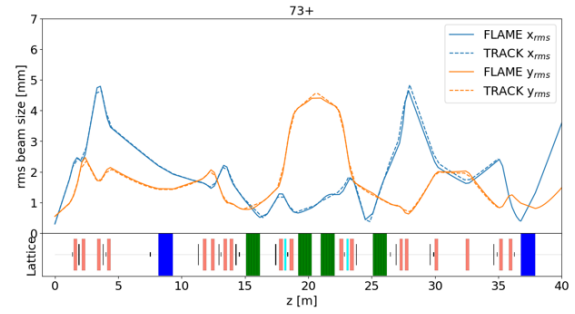


Figure 6: Comparison of rms beam envelopes beginning at the stripper between the fully updated FLAME simulation and a TRACK simulation with the same initial conditions.

CONCLUSION

Improvements were made to the FLAME model to better match simulations to the behavior of the beam in the driver linac. A TRACK model of FS1 with 3D fields for all dipole and quadrupole magnets was created and verified with BPM trajectory measurements. To fit the results of the FLAME simulation to the TRACK and BPM results, FLAME dipole fringe-field focusing and the effective lengths of FLAME quadrupoles were updated and non-linear sextupole components were added to the FLAME dipole model. As evidenced by Figs. 1 and 6, these updates produced a clear improvement in the FLAME model. Recently, we used the updated FLAME model to set up FS1 and FS2 magnets for transport of a three-charge-state xenon beam. The achromat tuning time was reduced with good results of aligned trajectories of all three charge states in LS2 and LS3.

ACKNOWLEDGEMENTS

This material is based upon work supported by the U.S. Department of Energy, Office of Science, Office of Nuclear Physics, and used resources of FRIB Operations, which is a DOE Office of Science User Facility under Award Number DE-SC0023633 and Office of High Energy Physics, under Award Number DE-SC0018362.

REFERENCES

- [1] P. N. Ostroumov *et al.*, “Acceleration of uranium beam to record power of 10.4 kW and observation of new isotopes at Facility for Rare Isotope Beams”, *Phys. Rev. Accel. Beams*, vol. 27, no. 6, p. 060101, Jun. 2024.
doi:10.1103/PhysRevAccelBeams.27.060101
- [2] P.N. Ostroumov, V. Aseev, and B. Mustapha, *TRACK—a code for beam dynamics simulation in accelerators and transport lines with 3D electric and magnetic fields*, 2006, <http://www.phy.anl.gov/atlas/TRACK>
- [3] Z. He, Y. Zhang, J. Wei, Z. Liu, and R. M. Talman, “Linear envelope model for multi-charge state linac”, *Phys. Rev. ST Accel. Beams*, vol. 17, no. 3, p. 034001, Mar. 2014.
doi:10.1103/PhysRevSTAB.17.034001
- [4] K. L. Brown, “A first and second order matrix theory for the design of beam transport systems and charged particle spectrometers”, *Adv. Part. Phys.*, vol. 1, pp. 71–134, 1968.
<https://www.osti.gov/biblio/4492169>
- [5] K. L. Brown, F. Rothacker, D. C. Carey, and F. C. Iselin, “Transport: a computer program for designing charged particle beam transport systems”, CERN-80-04, FERMILAB-NAL-091, UC-28, 1983. doi:10.5170/CERN-1980-004
- [6] A. Septier and H. Enge, “Deflecting magnets” in *Focusing of Charged Particles*, Albert Septier, Ed. Cambridge, MA, USA: Academic Press, 1967, pp. 203–264.
doi:10.1016/B978-0-12-636902-1.50012-3

VARIABLE WEDGE FOR ARIS*

Z. Wu^{1,2,†}, M. Hausmann¹, X. Rao¹, B. Sherrill¹

¹Facility for Rare Isotope Beams, East Lansing, MI, USA

²Department of Mechanical Engineering, Michigan State University, East Lansing, MI, USA

Abstract

A variable wedge degrader system has been developed at the Facility for Rare Isotope Beams (FRIB) to purify in-flight rare isotope beams. The system incorporates three independently movable wedge pairs: two with quadratic profiles for angle tuning (covering 3–20 mrad) and one with a linear profile for fine thickness adjustment. To support experiments at FRIB's DB2 location, the system maintains an approximately linear relationship between beam angle and center thickness, typically following $\text{Angle} \approx 1.2 \times \text{Thickness}$, resulting in a thickness range of 2.5 – 16.67 mm. An automated MATLAB-based controller selects the appropriate operating mode—high-angle or low-angle—and calculates wedge positions and virtual stepper motor steps accordingly. Simulations confirm the system achieves target angle-thickness combinations across most of the range, with larger deviations observed near 4–5 mrad. This paper presents the design architecture, control logic, and simulation results validating system performance.

INTRODUCTION

Wedge-shaped degraders are widely used for in-flight purification of rare isotope beams, a technique first implemented at GANIL [1]. By placing a degrader at a dispersive focal plane, energy loss becomes position-dependent, creating an achromatic focus downstream and enabling ion separation based on magnetic rigidity [2–4]. This approach has been adopted in fragment separators at RIKEN [5, 6], GSI [7, 8], NSCL [9], and the Facility for Rare Isotope Beams (FRIB) [10, 11]. At FRIB, the Advanced Rare Isotope Separator (ARIS) system utilizes degraders at multiple focal points—including the Pre-Separator and DB2 diagnostic box—to achieve beam purification through the momentum-loss achromat method [10, 12, 13]. More than 60 fixed-profile wedges have been fabricated to support over 8,000 operational hours [14], with additional applications including momentum spread reduction by a factor of three [15]. Currently, each wedge is custom-manufactured based on pre-run LISE++ simulations [16], which limits flexibility during last-minute beamline adjustments and contributes to downtime between experiments. To address these challenges, we present a variable wedge degrader system inspired by the tunable design of Hwang *et al.* [17], which demonstrated real-time angle control via symmetric motion of quadratic-profile aluminum wedges. The proposed system integrates two pairs of angle-controlling wedges—one optimized for low-angle operation

(≤ 7 mrad), the other for high-angle operation (> 7 mrad)—alongside a third linear-profile wedge pair for thickness compensation. This architecture enables simultaneous and decoupled tuning of beam angle (3–20 mrad) and center thickness (2.50–16.67 mm), covering the full operational envelope of the DB2 beamline. The following sections present the system design, operating principles, and simulation results validating its performance.

DESIGN

The 6-piece variable wedge system is designed to make each pair operate via symmetric displacement of its components to achieve the desired configuration. Based on the input angle and center thickness, the system automatically selects the appropriate mode and moves the unused pair(s) outside the effective region (beyond ± 50 mm). This design allows for continuous and decoupled adjustment of both angle and thickness across the operational range.

The general form of the thickness-versus-position function for a wedge pair under symmetric displacement is defined as follows:

$$y = f(x) = f_a \left(x - \frac{1}{2} \Delta x \right) + f_b \left(x + \frac{1}{2} \Delta x \right) \quad (1)$$

For High Angle Wedges (≥ 7 mrad),

$$f_{1,2}(x) = 2(-a_1 \Delta x + b_1)x + (c_1 + c_2) \quad (2)$$

Similarly, for Low Angle Wedges (< 7 mrad),

$$f_{3,4}(x) = 2(-a_3 \Delta x + b_3)x + (c_3 + c_4) \quad (3)$$

For Linear Shaped Wedges,

$$f_{5,6}(x) = -b_5 \Delta x + (c_5 + c_6) \quad (4)$$

Where,

- $f_i(x)$ is the stacked thickness of the i th wedge as a function of transverse position, x . x is ranging from 0 to +200 mm.
- Δx is the distance between the center positions of two wedges within one pair, to represent the distance each wedge moves away from the center please use $\frac{1}{2} \Delta x$.
- $a_1 = 0.0001$ is the component of second order term for Wedge 1, a_1 and a_2 are only different in sign, so $a_2 = -0.0001$. Wedge 1 and Wedge 2 have the same component value on linear terms, so $b_1 = b_2 = 0.01$, then $c_1 = 0.5$ and $c_2 = 2.5$, representing different constant terms.
- Similarly, for Wedge 3 and Wedge 4, $a_3 = -a_4 = 0.00014$, $b_3 = b_4 = 0.0015$, $c_3 = c_4 = 1.1$.
- For Wedge 5 and Wedge 6, $b_5 = -b_6 = 0.03925$, $c_5 = 0.5$ while $c_6 = 8.35$.

The overall layout of the wedge system is shown below (Figs. 1 and 2). With desired angle and center thickness put in, the system will decide which pairs of wedges will be in the effective range and move away the unused pair(s).

* Work supported by the U.S. Department of Energy, Office of Science, Office of Nuclear Physics and used resources of the Facility for Rare Isotope Beams (FRIB) Operations, which is a DOE Office of Science User Facility under Award Number DE-SC0023633.

†wuz@frib.msu.edu

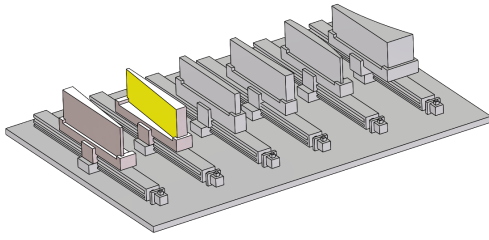


Figure 1: Overall layout of wedge system model.

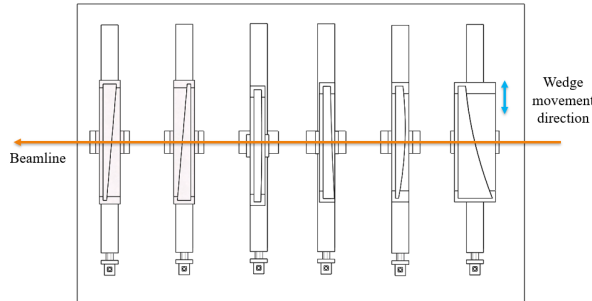


Figure 2: Top view of wedge system model with beamline direction and wedge movement direction.

SIMULATION

Method

To validate the proposed variable wedge system, a MATLAB-based graphical interface and a corresponding Simulink model were developed. The MATLAB Panel allows users to input desired angle and center thickness, automatically selects the operating mode, and visualizes wedge positions. Based on the same control logic, the Simulink model simulates motor behavior by translating wedge positions into stepper motor commands. Together, these tools provide a foundation for future hardware integration and are backed by analytical position–thickness relationships established in earlier sections.

MATLAB Panel Design

In the MATLAB Panel, users are required to input a combination of desired angle and center thickness. In principle, all combinations within the system's operating range are valid for simulation. According to the experimental requirements of FRIB's DB2 line [11], the desired relationship between angle and center thickness is approximately linear, with a typical ratio of Angle $\approx 1.2 \times$ Center Thickness. The system is designed to accommodate angle variations from 3 mrad to 20 mrad and center thickness values ranging from 2.50 mm to 16.67 mm.

The MATLAB Panel is composed of three primary sections: the Operating Section, Plot Section, and Information Section.

The **Operating Section** includes two numeric input fields for users to enter the desired angle and center thickness. A "Compute" button initiates the simulation based on the inputs. A "Mode" indicator displays the system's automatically selected mode—either *High Angle* or *Low Angle*—based on the angle input. The system switches to High Angle mode for inputs above 7 mrad and to Low

Angle mode for inputs at or below 7 mrad, reflecting the design differences in wedge geometry. This selection logic is fully integrated within the system for automatic mode switching.

The **Plot Section** includes two graphical outputs. The *Wedge Displacement Result* plot visually displays the layout and positioning of the wedges in use, with a legend identifying Wedge A, Wedge B (quadratic wedge pairs), and Wedge 5, Wedge 6 (linear wedge pairs). The *Slope Across x* plot verifies the achieved angle by showing the derivative of total thickness, ensuring simulation correctness.

The **Information Section** provides detailed output, including the calculated positions of each active wedge and the thickness contribution from each component.

Figure 3 demonstrates system behavior under both operating modes. Only the active wedge pairs are shown for clarity, while unused wedges are automatically moved outside the system's effective range (± 50 mm) in the physical implementation.

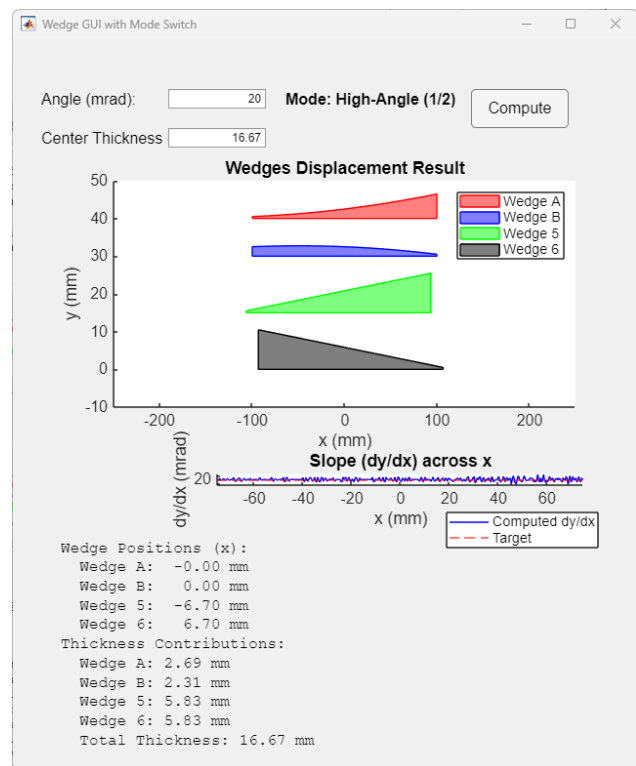


Figure 3: High angle simulation example.

Simulink Model Design

Building upon the MATLAB logic, a Simulink model was developed to emulate the real-time behavior of the wedge actuator system under stepper motor control. The model converts the computed wedge positions into discrete step counts and generates corresponding pulse signals to simulate motor operation and actuator movement.

The simulation runs on a **fixed-step discrete solver** with a **sample time of 0.0005 s**, selected to balance simulation speed and temporal resolution. The architecture consists of four main blocks: (1) Desired Value Input, (2) Mode

Selection and Wedge Position Computation, (3) Position-to-Step Conversion, and (4) Motor Pulse Generation and Monitoring.

Once the user inputs the desired angle and center thickness, the system validates feasibility, selects the appropriate operating mode (High or Low Angle), and calculates target wedge positions. These are translated into motor step counts, and pulse generators issue signals to the virtual motors. The system continuously tracks the number of steps taken by each motor; once all motors reach their targets, the process pauses to await the next command.

Figure 4 illustrates the Simulink model structure and highlights the flow of information from input parameters to simulated mechanical output.

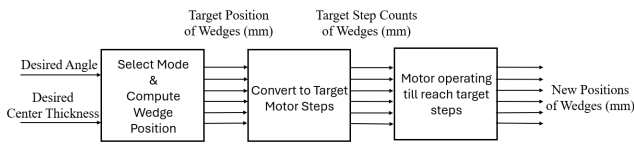


Figure 4: Model's operation principal.

RESULTS & DISCUSSION

To evaluate system performance, a representative simulation was performed with an input angle of **10 mrad** and center thickness of **8.33 mm**. The system automatically selected **High-Angle mode**, computed the center positions of active wedges, and translated these into step counts for stepper motor actuation. Unused wedge pairs were retracted beyond the effective range (± 50 mm), with their positions set to ± 200 mm. All wedges started moving at position $x = 0$. Table 1 summarizes the computed wedge positions and corresponding motor steps.

Table 1: Target Position and Motor Steps for Each Wedge (Angle = 10 mrad, Center Thickness = 8.33 mm)

Wedge number	Target Position [mm]	Target Step count
1	+25	3,150
2	-25	-3,150
3	200	25,197
4	-200	25,197
5	58	7,307
6	-58	-7,307

Figure 5 shows the wedge layout before and after motion. Only active wedge pairs are displayed for clarity.

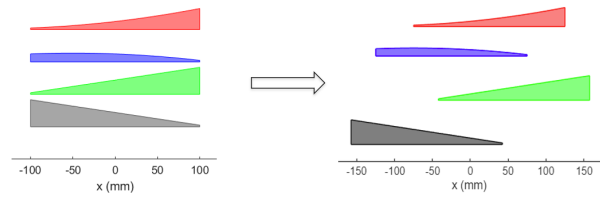


Figure 5: Initial and final layout of wedge system.

Figure 6 illustrates the step progression over time. Positive values represent clockwise motion (rightward wedge shift), and negative values represent counterclockwise motion (leftward shift). Each motor moves until reaching its target step count, then pauses for the next command. Users can update the angle or thickness at any point to adjust wedge positions live.

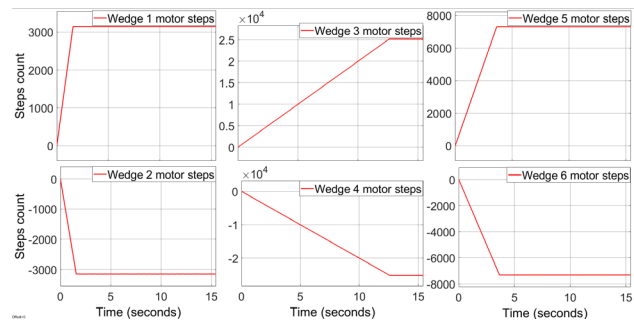


Figure 6: Step counts versus time (s) plot 10 mrad case.

The simulated motor setup assumes a 1.8° per step stepper motor combined with a 0.0625" lead screw, yielding 3,200 steps per inch or 0.0003125" per step. With a maximum speed of 2,000 steps/sec, the full motion in this case takes approximately **12.6 seconds**.

The system reliably achieves the desired wedge configuration for most input combinations. However, as discussed earlier, low-angle cases near 4–5 mrad may experience greater deviation due to limited linear wedge overlap. Further refinement may improve coverage in this region.

CONCLUSION & FUTURE WORK

The variable wedge degrader system has been successfully simulated, achieving continuous tuning from 3 mrad to 20 mrad with accurate thickness control. The Simulink-based control logic has been fully verified in simulation. Future work will focus on building a physical prototype, optimizing the quadratic wedge profile to reduce deviations observed at 4–5 mrad, and exploring material selection and fabrication methods for implementation.

ACKNOWLEDGMENT

The author would like to thank Prof. Ranjan Mukherjee and Prof. Guoming Zhu from the Department of Mechanical Engineering at Michigan State University for valuable guidance and support throughout the design and simulation of the variable wedge system.

REFERENCES

- [1] J. J. P. Dufour *et al.*, “Projectile fragments isotopic separation: Application to the lise spectrometer at GANIL,” *Nucl. Instrum. Methods Phys. Res., Sect. A*, vol. 248, no. 2–3, pp. 267–281, Aug. 1986.
doi:10.1016/0168-9002(86)91008-9
- [2] K.-H. Schmidt, E. Hanelt, H. Geissel, G. Münzenberg, and J. P. Dufour, “The momentum-loss achromat — A new method for the isotopical separation of relativistic heavy ions,” *Nucl. Instrum. Methods Phys. Res., Sect. A*, vol. 260, no. 2–3, pp. 287–303, Oct. 1987.
doi:10.1016/0168-9002(87)90092-1
- [3] H. Geissel *et al.*, “Ions penetrating through ion-optical systems and matter — non-liouvillian phase-space modelling,” *Nucl. Instrum. Methods Phys. Res., Sect. A*, vol. 282, no. 1, pp. 247–260, Oct. 1989.
doi:10.1016/0168-9002(89)90148-4
- [4] H. Folger *et al.*, “Targets and degraders for relativistic heavy ions at GSI,” *Nucl. Instrum. Methods Phys. Res., Sect. A*, vol. 303, no. 1, pp. 24–33, May 1991.
doi:10.1016/0168-9002(91)90759-j
- [5] T. Kubo *et al.*, “The RIKEN radioactive beam facility,” *Nucl. Instrum. Methods Phys. Res., Sect. B*, vol. 70, no. 1–4, pp. 309–319, Aug. 1992.
doi:10.1016/0168-583x(92)95947-p
- [6] T. Kubo, “In-flight RI beam separator BigRIPS at RIKEN and elsewhere in Japan,” *Nucl. Instrum. Methods Phys. Res., Sect. B*, vol. 204, pp. 97–113, May 2003.
doi:10.1016/S0168-583X(02)01896-7
- [7] G. Münzenberg, “The separation techniques for secondary beams,” *Nucl. Instrum. Methods Phys. Res., Sect. B*, vol. 70, no. 1–4, pp. 265–275, Aug. 1992.
doi:10.1016/0168-583x(92)95942-k
- [8] M. Winkler *et al.*, “The status of the Super-FRS in-flight facility at FAIR,” *Nucl. Instrum. Methods Phys. Res., Sect. B*, vol. 266, no. 19–20, pp. 4183–4187, Oct. 2008.
doi:10.1016/j.nimb.2008.05.073
- [9] B. M. Sherrill, D. J. Morrissey, J. A. Nolen, and J. A. Winger, “The A1200 projectile fragment separator,” *Nucl. Instrum. Methods Phys. Res., Sect. B*, vol. 56–57, pp. 1106–1110, May 1991.
doi:10.1016/0168-583x(91)95108-p
- [10] M. Hausmann *et al.*, “Design of the Advanced Rare Isotope Separator ARIS at FRIB,” *Nucl. Instrum. Methods Phys. Res., Sect. B*, vol. 317, pp. 349–353, Dec. 2013.
doi:10.1016/j.nimb.2013.06.042
- [11] X. Rao *et al.*, “Operation status of FRIB wedge systems and plan for power ramp up,” in *Proc. IPAC'24*, Nashville, TN, USA, May 2024, pp. 3545–3548.
doi:10.18429/JACoW-IPAC2024-THPR24
- [12] H. Geissel *et al.*, “The GSI projectile fragment separator (FRS): a versatile magnetic system for relativistic heavy ions,” *Nucl. Instrum. Methods Phys. Res., Sect. B*, vol. 70, no. 1–4, pp. 286–297, Aug. 1992.
doi:10.1016/0168-583x(92)95944-m
- [13] C. Scheidenberger *et al.*, “Energy and range focusing of in-flight separated exotic nuclei — A study for the energy-buncher stage of the low-energy branch of the Super-FRS,” *Nucl. Instrum. Methods Phys. Res., Sect. B*, vol. 204, pp. 119–123, May 2003.
doi:10.1016/S0168-583X(02)01898-0
- [14] B. Forgacs and X. Rao, “Design automation of pre-separator wedges for FRIB advanced rare isotope separator,” in *Proc. IPAC'24*, Nashville, TN, USA, May 2024, pp. 3549–3551.
doi:10.18429/JACoW-IPAC2024-THPR25
- [15] L. Bandura *et al.*, “Fragment separator momentum compression schemes,” *Nucl. Instrum. Methods Phys. Res., Sect. A*, vol. 645, no. 1, pp. 182–186, Jul. 2011.
doi:10.1016/j.nima.2010.12.015
- [16] O. B. Tarasov *et al.*, “LISE cute++, the latest generation of the LISE ++ package, to simulate rare isotope production with fragment-separators,” *Nucl. Instrum. Methods Phys. Res., Sect. B*, vol. 541, pp. 4–7, Aug. 2023.
doi:10.1016/j.nimb.2023.04.039
- [17] J. Hwang *et al.*, “Angle-tunable wedge degrader for an energy-degrading RI beamline,” *Prog. Theor. Exp. Phys.*, vol. 2019, no. 4, Apr. 2019. doi:10.1093/ptep/ptz028

HIGH ENERGY ION IMPLANTATION AT BNL*

D.B. Steski^{1,†}, C. Carlson¹, T. Kubley¹
¹Brookhaven National Laboratory, Upton, USA

Abstract

Silicon carbide (SiC) has several properties such as wide band gap and high voltage breakdown, that give it a significant advantage over silicon for the next generation of medium and high frequency applications. To fully realize these advantages, requires deep ion implantation ($\sim 6\text{ }\mu\text{m}$). Unfortunately, the energy of conventional ion implanters limits the implantation depth in SiC to approximately $1\text{ }\mu\text{m}$. Brookhaven National Laboratory (BNL) has developed a system that uses the 15 MV MP-class Tandem Van de Graaffs to implant ions in SiC to a depth $>15\text{ }\mu\text{m}$. By changing the ion beam energy in discrete steps, the overlapping implantations can build a uniform implantation profile from the maximum implantation depth to the surface. To implant ions near the surface of the SiC wafer requires the use of an energy absorber to degrade the ion energy from 10's of MeV to a few keV. BNL has built a system to demonstrate the feasibility of this approach. The BNL system is described, and the results of high energy implantation for high voltage SiC devices are presented. Future improvements to the system are also discussed.

INTRODUCTION

The Tandem Van de Graaff Facility [1] at Brookhaven National Laboratory (BNL) (Fig. 1) consists of two MP-class tandems (MP6 and MP7) (Fig. 2). Each tandem can be operated independently at a terminal voltage of $>14\text{ MV}$. The tandems are connected to the BNL Booster synchrotron by a 900 m long transfer line and can provide a variety of ion species (from protons to gold) for use at the Relativistic Heavy ion Collider (RHIC) and the NASA Space Radiation Laboratory (NSRL). The tandems can also supply ion beams to two local target rooms (TR2 and TR4) for space and industrial applications.

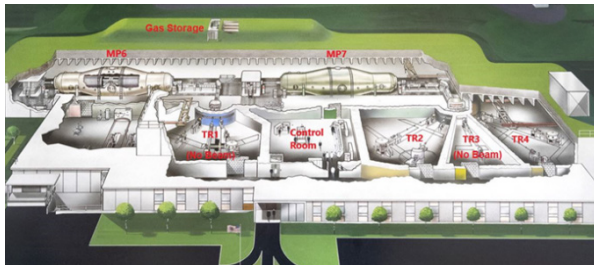


Figure 1: The BNL Tandem Van de Graaff Facility.

BNL was approached with the idea of using the Tandem Van de Graaffs to perform high energy implantations in silicon carbide (SiC).

* Work supported by Brookhaven Science Associates, LLC under Contract No. DE-SC0012704 with the US Department of Energy

† steski@bnl.gov

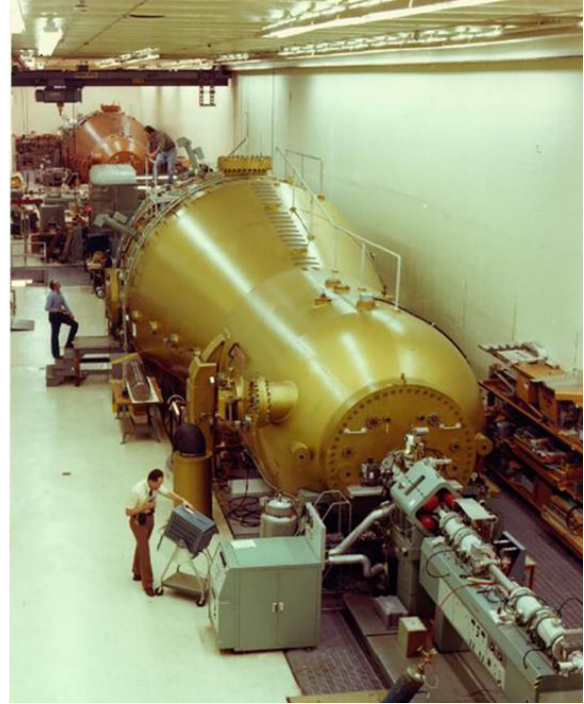


Figure 2: MP7 in foreground, MP6 in background.

The power electronics industry is very interested in the use of SiC in medium voltage and high frequency applications. Unfortunately, the low dopant diffusion constant for SiC limit the implantation depth of conventional implanters to $<1\text{ }\mu\text{m}$. To fully take advantage of SiC's properties, deep implantations ($>6\text{ }\mu\text{m}$) are required. The BNL designed system, described below, has demonstrated implantation of aluminium and nitrogen in SiC to a depth of $>12\text{ }\mu\text{m}$.

HIGH ENERGY IMPLANTER

The high energy implanter [2] at BNL, uses an existing beam line in target room 2. The beam line has the unique feature that the diameter of the beam pipe increases from 100 mm to 710 mm just before the end vacuum chamber. This feature of the beam line allows the beam to be swept horizontally over a large area.

The implanter (Fig. 3) consists of a pair of horizontal deflector plates, an aluminium foil energy absorber, a series of Faraday cups for beam diagnostics and a vertical linear stage on to which the SiC wafers are mounted. The deflector plates sweep the beam horizontally at 400 Hz while the linear stage drives the wafers vertically through the swept ion beam at 10 mm/sec. This relatively slow speed ensures that the implantation is uniform over the entire wafer.

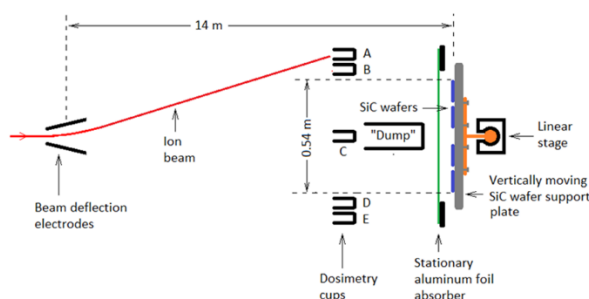


Figure 3: Overhead view of high energy implanter.

There are a total of 6 Faraday cups used in the system. The “Dump” cup is an insertable Faraday cup that gives a precise measurement of the unswept beam before the start of each implantation. Once the beam is measured the horizontal deflection plates are turned on and the “Dump” cup is removed. The dosimetry cups (A, B, C, D and E) are used to monitor the beam intensity and the sweep width during the implantation. Once the design fluence is reached the linear stage will stop with the wafers out of the path of the ion beam.

For SiC, the dopant ions of interest are aluminium and nitrogen. To create the negative ions required by the Tandem Van de Graaffs a caesium sputter source is used. Nitrogen does not form a negative ion, so a cathode was pressed with an equal mixture of graphite (C) and boron nitride (BN) [3]. This resulted in a large CN⁻ current. For the aluminium beam, a cathode of 99.999% pure Al was used to produce a large Al₂⁻ beam. In both cases, the negative molecule was stripped to a positive ion in the tandem terminal using a stripper gas before acceleration back to ground potential.

The desired implantation profile is a uniform concentration of implanted ions from the surface to the maximum depth. The beam from the tandem has a very small energy spread and results in very narrow implantation peaks. By varying the ion beam energy in discrete steps, the overlapping implantation peaks build a uniform distribution. However, this requires beam energies from 10's of MeV to a few keV's. It is challenging for any single accelerator to cover such a large energy range. To accomplish the implantation at the surface of the wafer, an aluminium energy absorber (Fig. 4) is used immediately in front of the SiC wafers. This allows a higher energy beam to be efficiently transported through the tandems before being degraded to the desired energy right before the wafers. The energy absorber has the additional advantage of broadening the implantation profile of each ion beam energy, thus reducing the number of energy steps needed to build the uniform profile.

A simulation with 24 implantations at different energies and the expected accumulated dose (Fig. 5) was generated. This is compared to the secondary-ion mass spectrometry (SIMS) analysis of an actual implantation. The SIMS analysis agrees with the simulation to within 0.87%. Other implantations showed larger discrepancies but still within the 2% accuracy of the dosimetry.

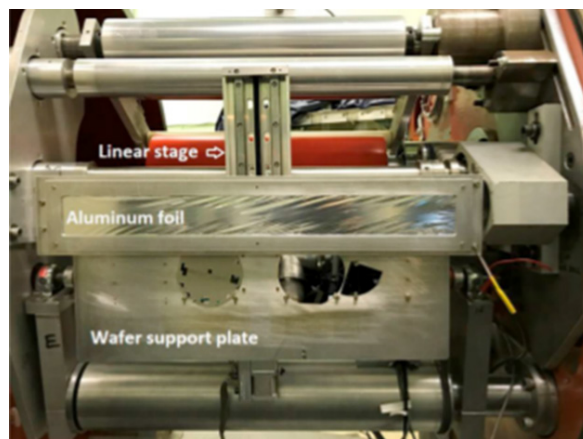


Figure 4: Photograph showing aluminium foil energy absorber, linear stage and wafer support plate.

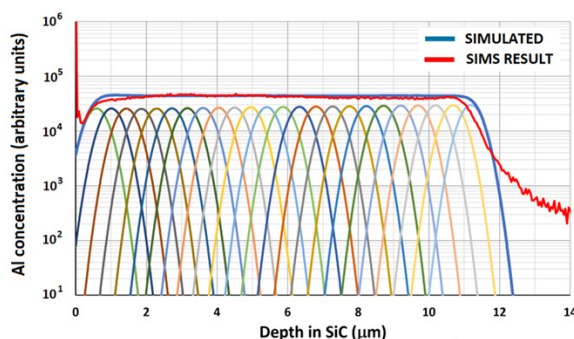


Figure 5: The simulation vs SIMS analysis of an Al implantation in SiC.

HEATED WAFER IMPLANTATION

The high energy implantation of ions into SiC may cause damage to the SiC lattice. One idea to mitigate this damage is to anneal the SiC wafers at high temperatures during the implantation process. The BNL high energy implanter has been upgraded to investigate this idea.

Because the room temperature linear stage and aluminium energy absorber are mounted on the door to the large vacuum chamber, a new door was fabricated that included a new linear stage and mounting plate supporting 4 wafer heaters capable of attaining ~1000 °C (Fig. 6). The original door is mounted on an “I” beam and can be rolled out of position while the new door can be attached using an overhead crane. This allows the beam line to be used for multiple applications.

The new wafer heaters (Fig. 7) are mounted on a 600 mm linear drive and can accept either 4 inch or 6-inch wafers. As before the wafers are driven vertically through the horizontally swept ion beam. In front of the heaters is a water-cooled heat shield with the aluminum energy absorber. An infrared camera looks through a slot in the heated shield to measure the surface temperature of the wafers during the implantation. Each heater can be controlled independently up to ~1000 °C.

The system is presently being commissioned with several test implantations.

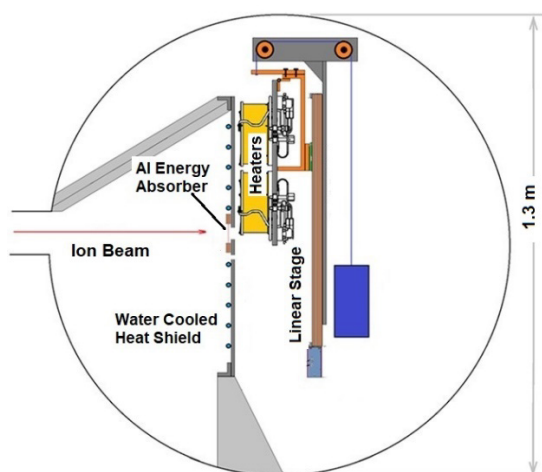


Figure 6: Schematic of heated wafer system.

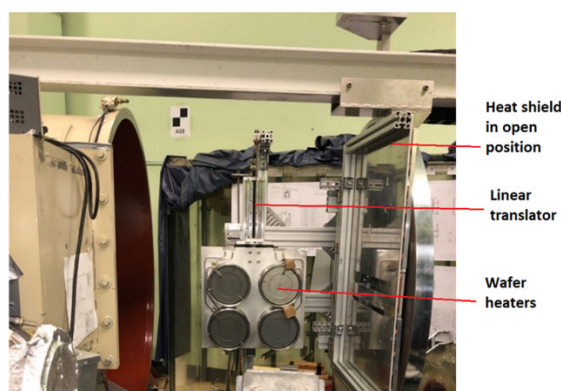


Figure 7: Photograph of wafer heaters

ENERGY FILTERED IMPLANTATION

Another idea to reduce the SiC lattice damage during the high energy implantation is to use Energy Filtered Ion Implantation (EFII) [4] technology. The energy filter (Fig.8) is a micropatterned silicon membrane that replaces the aluminum energy absorber. The energy filter converts a monoenergetic ion beam to an ion beam with a uniform energy spread.

This will reduce the dose rate at a specific depth and potentially reduce the lattice damage. It will also eliminate the need to use multiple beam energies from the tandem, potentially shortening the time required for the entire implantation.

For an initial test, a flat profile EFII was used with a 90 MeV Al beam. This was implanted into a silicon wafer. The SIMS analysis (Fig. 9) showed a flat profile from the surface to a depth of 26 μm .

Another test was conducted using both the EFFI and heated wafer system. These wafers will be sent out for SIMS analysis and lattice damage characterization.

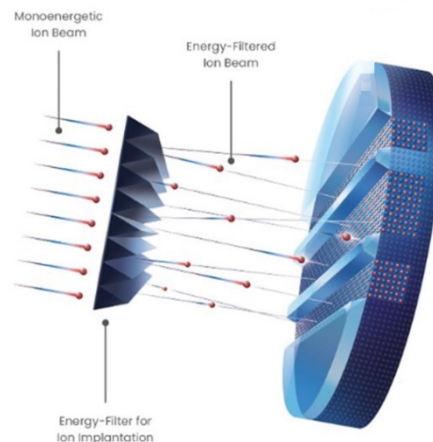


Figure 8: Energy filter converting mono energetic beam to uniform energy beam.

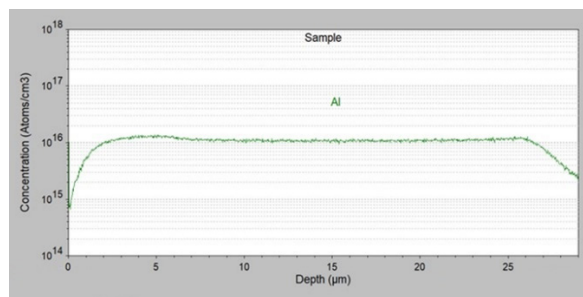


Figure 9: SIMS analysis of a 90 MeV Al beam through the energy filter implanted into silicon

CONCLUSION

Brookhaven National Laboratory has developed a high energy ion implanter capable of implanting ions in silicon carbide to a depth of $>12 \mu\text{m}$. The system has been upgraded to heating the SiC wafers during the implantation process. The use of an energy filter is also being investigated to reduce damage to the SiC lattice and to reduce the overall implantation time. Although all of the work to date has involved Al and N ions for implantation in SiC, the same principles can be extended to the implantation of gallium nitride (GaN) or any other material as long as sufficient quantities of the desired negative ion can be produced.

REFERENCES

- [1] P. Thieberger, "The Brookhaven double MP facility: Recent developments and plans for the future," *Nucl. Instrum. Methods Phys. Res.*, vol. 220, no. 1, pp. 45–53, Feb. 1984. doi:10.1016/0167-5087(84)90406-x
- [2] P. Thieberger *et al.*, "Novel high-energy ion implantation facility using a 15 MV Tandem Van de Graaff accelerator,"

Nucl. Instrum. Methods Phys. Res., Sect. B, vol. 442, pp. 36–40, Mar. 2019. doi:[10.1016/j.nimb.2019.01.016](https://doi.org/10.1016/j.nimb.2019.01.016)

[3] [3] R. Middleton. A Negative-Ion Cookbook, <https://www.c-ad.bnl.gov/TVDG/cookbook/>

[4] mi2-factory GmbH, <https://mi2-factory.com/>

SIX-DIMENSIONAL BEAM MATCHING WITH LINEAR ACCELERATOR STRUCTURES*

Y.K. Batygin[†], Los Alamos National Laboratory, Los Alamos, NM, USA

Abstract

Beam matching is a common technique routinely employed in accelerator design to minimize beam losses and preserve beam quality. A matched beam occupies the smallest volume in 6D phase space, leading to improved beam brightness, a measure of the beam's quality. Six-dimensional beam matching involves adjusting beam parameters to match the accelerator's lattice. Here we present an analytical treatment of 6D beam matching of a high-intensity beam onto an RF structure. We discuss the application of the averaging method to attain an analytical solution for a set of matched 3D beam envelope equations. We then consider the more general self-consistent approach to beam equilibrium in 6D phase space based on Hamiltonian analysis. Finally, we discuss the role of the equipartitioning concept in beam matching.

AVERAGED BEAM ENVELOPES

Beam matching is often attributed to finding a periodic solution for beam envelopes in periodic accelerator structures using state-of-the-art codes as TRACE-3D [1]. The 3D equations for beam envelopes $R_x = \sqrt{5\langle x^2 \rangle}$, $R_y = \sqrt{5\langle y^2 \rangle}$, $R_z = \sqrt{5\langle z^2 \rangle}$ can be written as

$$\frac{d^2 R_x}{dt^2} = -\frac{q\beta c}{m\gamma} G(z) R_x + f_x(R_x, R_y, R_z), \quad (1)$$

$$\frac{d^2 R_y}{dt^2} = \frac{q\beta c}{m\gamma} G(z) R_y + f_y(R_x, R_y, R_z), \quad (2)$$

$$\frac{d^2 R_z}{dt^2} = f_z(R_x, R_y, R_z), \quad (3)$$

where the functions f_x , f_y , f_z are

$$f_x(R_x, R_y, R_z) = \frac{\varepsilon_x^2 c^2}{\gamma^2 R_x^3} + \frac{\Omega^2 R_x}{2} + 3 \frac{I}{I_c} \frac{c^2 M_x \lambda}{\gamma^3 R_y R_z}, \quad (4)$$

$$f_y(R_x, R_y, R_z) = \frac{\varepsilon_y^2 c^2}{\gamma^2 R_y^3} + \frac{\Omega^2 R_y}{2} + 3 \frac{I}{I_c} \frac{c^2 M_y \lambda}{\gamma^3 R_x R_z}, \quad (5)$$

$$f_z(R_x, R_y, R_z) = -\Omega^2 R_z + \frac{\varepsilon_z^2 c^2}{\gamma^6 R_z^3} + 3 \frac{I}{I_c} \frac{M_z c^2 \lambda}{\gamma^3 R_x R_y}, \quad (6)$$

m and q are the mass and charge of particles, β and γ are beam velocity and energy, $G(z)$ is the gradient of quadrupole lenses, $\varepsilon_{x,y,z} = 5\varepsilon_{x,y,z_rms}$ are 5-rms normalized beam emittances, $\Omega = \sqrt{2\pi q E |\sin \varphi_s| / (m\beta\gamma^3 \lambda)}$ is the longitudinal oscillation frequency, $E = E_0 T$ is the amplitude of the accelerating wave, φ_s is the synchronous phase, λ is the RF wavelength, I is the beam current, $I_c = 4\pi\varepsilon_0 mc^3 / q$ is the characteristic beam current, M_g , $g = x, y, z$ are ellipsoid coefficients:

$$M_g = \frac{1}{2} \int_0^\infty \frac{R_x R_y \gamma R_z ds}{(R_g^2 + s) \sqrt{(R_x^2 + s)(R_y^2 + s)(\gamma^2 R_z^2 + s)}}, \quad (7)$$

and $R_g = R_x, R_y, \gamma R_z$. Here we consider a typical case where the longitudinal oscillation frequency is changing slowly concerning the variation of the alternative-sign gradient of quadrupole lenses. Importantly, envelope equations contain rapidly oscillating parts determined by the function $G(z)$, and weakly oscillating functions f_x , f_y , f_z due to the variation of beam sizes $R_g = R_x, R_y, R_z$. The gradient of the focusing field with the focusing period S can be expanded into a Fourier series:

$$G(z) = \sum_{n=1}^\infty g_n \sin\left(\frac{2\pi n z}{S}\right). \quad (8)$$

According to the averaging method [2], solutions of differential equations of second order, containing fast oscillating and slow variable terms, can be represented as

$$R_x(z) = \bar{R}_x(z) + \xi_x(z), \quad R_y(z) = \bar{R}_y(z) + \xi_y(z), \quad (9)$$

where $\bar{R}_x(z)$, $\bar{R}_y(z)$ are slow variable functions with respect to fast oscillation frequency determined by alternative-sign gradients, and $\xi_x(z)$, $\xi_y(z)$ are small-amplitude, rapidly oscillating functions. For the smooth part of the solution, application of the averaging method gives:

$$\frac{d^2 \bar{R}_x}{dt^2} = -\frac{1}{2} \sum_{n=1}^\infty \frac{F_n^2}{\omega_n^2} \bar{R}_x + f_x(\bar{R}_x, \bar{R}_y, R_z), \quad (10)$$

$$\frac{d^2 \bar{R}_y}{dt^2} = -\frac{1}{2} \sum_{n=1}^\infty \frac{F_n^2}{\omega_n^2} \bar{R}_y + f_y(\bar{R}_x, \bar{R}_y, R_z), \quad (11)$$

[†] batygin@lanl.gov

where the harmonics of the expansion of the quadrupole field are $F_n = g_n q \beta c / (m\gamma)$, $\omega_n = 2\pi n \beta c / S$.

The envelope equations for smoothed 3D beam envelopes \bar{R}_x , \bar{R}_y , R_z can be written as

$$\frac{d^2 \bar{R}_x}{dz^2} - \frac{\varepsilon_x^2}{(\beta\gamma)^2 \bar{R}_x^3} + \frac{\mu_s^2}{S^2} \bar{R}_x - 3 \frac{I}{I_c} \frac{M_x \lambda}{\beta^2 \gamma^3 \bar{R}_y R_z} = 0, \quad (12)$$

$$\frac{d^2 \bar{R}_y}{dz^2} - \frac{\varepsilon_y^2}{(\beta\gamma)^2 \bar{R}_y^3} + \frac{\mu_s^2}{S^2} \bar{R}_y - 3 \frac{I}{I_c} \frac{M_y \lambda}{\beta^2 \gamma^3 \bar{R}_x R_z} = 0, \quad (13)$$

$$\frac{d^2 R_z}{dz^2} - \frac{\varepsilon_z^2}{(\beta\gamma^3)^2 R_z^3} + \frac{\mu_{oz}^2}{S^2} R_z - 3 \frac{I}{I_c} \frac{M_z \lambda}{\beta^2 \gamma^3 \bar{R}_x \bar{R}_y} = 0, \quad (14)$$

where $\mu_s = \mu_o \sqrt{1 - \mu_{oz}^2 / (2\mu_o^2)}$ is the phase advance of transverse oscillations of a synchronous particle at the period of the focusing structure S in the presence of an RF field, μ_{oz} is the phase advance of longitudinal oscillations:

$$\mu_{oz} = \sqrt{2\pi q E \lambda |\sin \phi_s| / (mc^2 \beta \gamma^3)} (S / \beta \lambda), \quad (15)$$

and μ_o is the phase advance of transverse oscillations in the focusing structure only per focusing period

$$\mu_o = \frac{qS}{m\gamma} \sqrt{\frac{1}{2} \sum_{n=1}^{\infty} \frac{g_n^2}{\omega_n^2}}. \quad (16)$$

Small-amplitude fast components $\xi_x(z)$, $\xi_y(z)$ are determined by quickly oscillating terms:

$$\xi_x = \sum_{n=1}^{\infty} \frac{F_n \sin \omega_n t}{\omega_n^2} \bar{R}_x, \quad \xi_y = -\sum_{n=1}^{\infty} \frac{F_n \sin \omega_n t}{\omega_n^2} \bar{R}_y. \quad (17)$$

Taking only the first terms in Eqs. (17), the solutions to the envelope equations in smooth approximation can be written as

$$R_x(z) = \bar{R}_x(z)[1 + v_{\max} \sin(2\pi z / S)], \quad (18)$$

$$R_y(z) = \bar{R}_y(z)[1 - v_{\max} \sin(2\pi z / S)], \quad (19)$$

where the amplitude of variation of envelopes is

$$v_{\max} = g_1 q S^2 / (4\pi^2 mc \beta \gamma). \quad (20)$$

Twiss parameters of the beam $\alpha_{x,y}$, $\beta_{x,y}$ are related to envelope parameters through well-known expressions

$$\beta_{x,y} = \beta \gamma R_{x,y}^2 / \varepsilon_{x,y}, \quad \alpha_{x,y} = -R'_{x,y} \sqrt{(\beta \gamma) \beta_{x,y} / \varepsilon_{x,y}}. \quad (21)$$

In general, Equations (9) describe envelope oscillations of an unmatched beam, with slow variation of average radius $\bar{R}_x(z)$, $\bar{R}_y(z)$, $R_z(z)$, superimposed onto fast oscillations, Eqs. (17), with the period of the focusing structure. For a FODO focusing structure with a length of quadrupole D and period S , the phase advance of transverse oscillations, μ_o , and amplitude of fast oscillations, v_{\max} , are [3]

$$\mu_o = (S / 2D) \sqrt{1 - (4/3)(D/S)} (qG_o D^2) / (m\gamma \beta c), \quad (22)$$

$$v_{\max} = \mu_o \frac{(2/\pi^2)}{\sqrt{1 - (4/3)(D/S)}} \frac{\sin(\pi D / S)}{(\pi D / S)}. \quad (23)$$

Furthermore, in the thin lens approximation, $D \ll S$, Eq. (23) gives the amplitude of small oscillations $v_{\max} \approx (2/\pi^2) \mu_o = 0.2026 \mu_o$, and for $D = 0.5S$ (FD structure) $v_{\max} = (4\sqrt{3}/\pi^3) \mu_o \approx 0.223 \mu_o$.

In the case of beam focusing by a periodic sequence of solenoids with period S , length D , and magnetic field B_o , the phase advance of transverse oscillations per focusing period and ripple amplitude are given by [4]

$$\mu_o = \theta \sqrt{S/D} \sqrt{1 - (\theta^2/6)} [1 - 0.5(D/S) - 0.5(S/D)], \quad (24)$$

$$v_{\max} = (\theta^2 / 2\pi^3) (S/D)^2 \sin(\pi D / S), \quad (25)$$

where $\theta = qB_o D / (2mc \beta \gamma)$ is the rotational angle of particle trajectory in a solenoid.

SIX-DIMENSIONAL MATCHED BEAM

For the typical beam with equal transverse emittances $\varepsilon_x = \varepsilon_y = \varepsilon$, the averaged matched transverse beam sizes are equal to each other, $\bar{R}_x = \bar{R}_y = R$. The equilibrium beam sizes, determined by conditions $\bar{R}_x'' = \bar{R}_y'' = R_z'' = 0$, are defined from the coincident solution of Eqs. (12), (13), and (14):

$$\left(\frac{R}{R_{ot}}\right)^4 - 2b_t \left(\frac{R}{R_{ot}}\right)^2 - 1 = 0, \quad \left(\frac{R_z}{R_{oz}}\right)^4 - b_z \left(\frac{R_z}{R_{oz}}\right)^3 - 1 = 0, \quad (26)$$

where we have introduced equilibrium beam sizes with vanishing current $I = 0$

$$R_{ot} = \sqrt{\varepsilon S / (\beta \gamma \mu_s)}, \quad R_{oz} = \sqrt{\varepsilon_z S / (\beta \gamma^3 \mu_{oz})}, \quad (27)$$

and transverse, b_t , and longitudinal, b_z , space charge parameters

$$b_t = \frac{3}{2} \frac{I}{I_c} \frac{1}{\beta \gamma} \left(\frac{R_{ot}}{\varepsilon}\right)^2 \left(\frac{\beta \lambda}{2R_z}\right) (1 - M_z), \quad b_z = 3\gamma^3 M_z \frac{I}{I_c} \frac{\lambda R_{oz}^3}{R^2 \varepsilon_z^2}. \quad (28)$$

The search for a solution is performed until the sum of squares of equations (26)

$$\chi = \left(\frac{R}{R_{ot}} - \sqrt{b_i + \sqrt{1 + b_i^2}} \right)^2 + \left[\left(\frac{R_z}{R_{oz}} \right)^4 - b_z \left(\frac{R_z}{R_{oz}} \right)^3 - 1 \right]^2 \quad (29)$$

reaches a small value, typically $\chi \approx 10^{-4}$. Upon finding equilibrium beam sizes, R , R_z , Equations (9), (17), (26) provide matched conditions for beam envelopes.

SELF-CONSISTENT BEAM EQUILIBRIUM

Analysis of 6D beam matching based on 3D envelope equations is limited by the approximation of the bunch as a 3D uniformly charged ellipsoid. More general self-consistent treatment of beam dynamics assumes simultaneous solution of Vlasov's equation for the beam distribution function of canonical-conjugate variables $f(\vec{x}, \vec{P}, t)$

$$\frac{df}{dt} = \frac{\partial f}{\partial t} + \frac{\partial f}{\partial \vec{x}} \frac{d\vec{x}}{dt} + \frac{\partial f}{\partial \vec{P}} \frac{d\vec{P}}{dt} = 0, \quad (30)$$

and Poisson's equation for the scalar beam potential

$$\frac{\partial^2 U_b}{\partial x^2} + \frac{\partial^2 U_b}{\partial y^2} + \frac{\partial^2 U_b}{\partial \zeta^2} = -\frac{q}{\epsilon_0} \int_{-\infty}^{\infty} f d\vec{P}. \quad (31)$$

The general approach to finding a stationary, self-consistent beam distribution function is to represent it as a function of the constant of motion, $f = f(H)$, and then to solve Poisson's equation for the unknown space charge potential of the beam [5]. In Ref. [6], the self-consistent problem for a high-brightness beam in an RF field was solved assuming 6D beam distribution function is an exponential function of the Hamiltonian, $f = f_0 \exp(-H/H_0)$, where H is the Hamiltonian of averaged particle motion,

$$f = f_0 \exp\left(-\frac{p_x^2 + p_y^2}{2m\gamma H_0} - \frac{p_z^2}{2m\gamma^3 H_0} - q \frac{U_{ext} + U_b \gamma^{-2}}{H_0}\right). \quad (32)$$

In Eq. (32), p_x , p_y , p_z are the momentum components of a particle, oscillating around a synchronous particle, U_{ext} is the potential of the external field, and U_b is the space charge potential. From Eq. (32), the transverse rms momentum spread of the beam is $\langle p_x^2 \rangle = \langle p_y^2 \rangle = m\gamma H_0$, while longitudinal rms momentum spread is $\langle p_z^2 \rangle = m\gamma^3 H_0$. Transverse, $\epsilon_{rms} = \epsilon_{x-rms} = \epsilon_{y-rms}$, and longitudinal, ϵ_{z-rms} , rms beam emittances are:

$$\epsilon_{rms} = \frac{\sqrt{\langle x^2 \rangle \langle p_x^2 \rangle}}{mc}, \quad \epsilon_{z-rms} = \frac{\sqrt{\langle \zeta^2 \rangle \langle p_z^2 \rangle}}{mc}. \quad (33)$$

Putting together Eqs. (32), (33), the value of H_0 can be expressed as a function of the beam parameters:

$$H_0 = \frac{mc^2}{\gamma} \frac{\epsilon_{rms}^2}{\langle x^2 \rangle} = \frac{mc^2}{\gamma} \frac{\epsilon_{rms}^2}{\langle y^2 \rangle} = \frac{mc^2}{\gamma^3} \frac{\epsilon_{z-rms}^2}{\langle \zeta^2 \rangle}. \quad (34)$$

Equation (34) can be rewritten as

$$\frac{\epsilon}{R} = \frac{\epsilon_z}{\gamma R_z}, \quad (35)$$

which expresses the equipartitioning condition for the beam in an RF field [7]. From the above derivations, it is clear that the equipartitioning is a consequence of the stationary nature of the beam distribution function, Eq. (32), and, therefore, is the necessary condition for beam equilibrium. If the distribution function of averaged motion is stationary (time-independent), equipartitioning is fulfilled. The opposite statement is not valid in the general case: there are infinitely many distribution functions that obey condition (35), but which are not necessarily stationary.

To find the stationary beam distribution, it is necessary to solve Poisson's equation for the unknown self-consistent space charge potential of the beam, Eq. (31). In Refs. [6, 8] it was shown that, to the first approximation, the self-consistent space charge potential of an intense beam is opposite to the external potential, and the particle distribution in real space is close to uniform within the bunch which boundary determined by the nonlinear equation:

$$I_0 \left(\frac{k_z r}{\gamma} \right) \sin(\varphi_s - k_z \zeta) + k_z \zeta \cos \varphi_s + C (k_z r)^2 - \sin(\varphi_s - k_z R_z) - k_z R_z \cos \varphi_s = 0, \quad (36)$$

where $k_z = 2\pi / (\beta\lambda)$, and the constant C is

$$C = \frac{\sin(\varphi_s - k_z R_z) + k_z R_z \cos \varphi_s - I_0 (k_z R / \gamma) \sin \varphi_s}{(k_z R)^2}. \quad (37)$$

The shape of a matched bunch with a constant particle density is transformed in real space (r, ζ) from an ellipsoidal shape to a "separatrix"-type when the longitudinal beam size becomes comparable to the separatrix size.

ACKNOWLEDGEMENT

The research presented in this paper was supported by the Laboratory Directed Research and Development program of Los Alamos National Laboratory under project number 20240177ER.

REFERENCES

- [1] K.R. Crandall, D.P. Rusthoi, “TRACE 3D Documentation”, Los Alamos National Laboratory, Los Alamos, NM, USA, Report LA-UR -97-886, 1997.
- [2] L.D. Landau, E.M. Lifshitz, *Mechanics*, Amsterdam: Elsevier, 1974.
- [3] Y. K. Batygin, A. Scheinker, S. Kurennoy, and C. Li, “Suppression of space charge induced beam halo in nonlinear focusing channel”, *Nucl. Instrum. Methods Phys. Res., Sect. A*, vol. 816, pp. 78–86, Apr. 2016.
[doi:10.1016/j.nima.2016.01.045](https://doi.org/10.1016/j.nima.2016.01.045)
- [4] Y. K. Batygin, “Dynamics of intense particle beam in axial-symmetric magnetic field”, *Nucl. Instrum. Methods Phys. Res., Sect. A*, vol. 772, pp. 93–102, Feb. 2015.
[doi:10.1016/j.nima.2014.10.034](https://doi.org/10.1016/j.nima.2014.10.034)
- [5] I.M. Kapchinskiy, *Theory of Resonance Linear Accelerators*, Harwood, 1985.
- [6] Y. K. Batygin, “Self-consistent particle distribution of a bunched beam in RF field”, *Nucl. Instrum. Methods Phys. Res., Sect. A*, vol. 483, no. 3, pp. 611–628, May 2002.
[doi:10.1016/S0168-9002\(01\)01943-X](https://doi.org/10.1016/S0168-9002(01)01943-X)
- [7] R. A. Jameson, “Beam-intensity limitations in linear accelerators”, *IEEE Trans. Nucl. Sci.*, vol. 28, no. 3, pp. 2408–2412, 1981. [doi:10.1109/tns.1981.4331708](https://doi.org/10.1109/tns.1981.4331708)
- [8] Y. K. Batygin, “Six-dimensional matching of intense beam with linear accelerating structure,” *Nucl. Instrum. Methods Phys. Res., Sect. A*, vol. 995, p. 165074, Apr. 2021.
[doi:10.1016/j.nima.2021.165074](https://doi.org/10.1016/j.nima.2021.165074)

NEWGAIN PROJECT AT GANIL: CONSTRUCTION OF THE NEW HEAVY ION INJECTOR FOR SPIRAL2*

F. Chautard^{1,†}, D. Ackermann¹, J. Dumas⁵, M. Di Giacomo¹, A. Fournier², F. Hanchin¹, C. Haquin¹, C. Jamet¹, J. Karam¹, C. Lesigne¹, M. Michel¹, G. Normand¹, Ph. Robillard¹, C. Peaucelle³, O. Piquet⁵, P. Sénécal¹, D. Simon⁵, I. Stephan⁴, T. Thuillier³, Y. Trehudic¹

¹GANIL, Caen, France

²Université de Bordeaux, CNRS-LP2I, Bordeaux, France

³Université Grenoble Alpes, CNRS-LPSC, Grenoble, France

⁴Université Paris-Saclay, CNRS-IJCLAB, Orsay, France

⁵CEA/IRFU, Saclay, France

Abstract

The NEWGAIN (NEW GANil INjector) project is now in the construction phase at GANIL. The goal is to accelerate heavier ions with the SPIRAL2 accelerator, ions with an A/q ratio of up to 7. With this upgrade, SPIRAL2 will provide high-intensity beams, from protons to uranium, strengthening GANIL international competitiveness, both in fundamental sciences and related applications. The paper will provide an update on the progress of the construction phase and the main milestones achieved and to come. The layout and the main technical components of the new injector, based on 2 ECR ion sources (one of them existing), two LEBT, one RFQ and a MEBT section to transport the beam into the present MEBT connected to the SPIRAL2 LINAC are presented.

INTRODUCTION

The NEWGAIN project aims to build a second injector designed for A/q = 3 to 7 ions, to produce very intense heavy ion beams up to uranium, far exceeding the performance of the existing injector. Thus, a new superconducting source will be developed to complement the existing sources and achieve high-intensity uranium beams.

Thanks to this improvement, the SPIRAL2 LINAC [1] will deliver, within the limits of its operating energy, the most intense beams in the world (Table 1) on a wide variety of ions ranging from protons to uranium, and will strengthen GANIL's international competitiveness, both in fundamental sciences and in associated applications.

The project is organized within a large technical collaboration framework, composed of the following French accelerator laboratories from CEA/DRF/IRFU and CNRS/IN2P3: GANIL, IRFU/DACM and DIS, LPSC, LPCCaen, IPHC, LP2iB, IJCLab. These different partners are already used to collaborate in different projects with GANIL, the latest example to date being the construction of the SPIRAL2 facility. The NEWGAIN project is coordinated by GANIL.

*This work benefited from state aid managed by the French National Research Agency under the Future Investment Program bearing the reference ANR-21-ESRE-0018

†chautard@ganil.fr

Table 1: Ion Beam Intensities in SPIRAL2 Actual Beam-line and with the NEWGAIN Injector

Ions	Intensity [pμA]		
	SPIRAL2	NEWGAIN	
	Phoenix V3 A/Q≤3	Phoenix V3 A/Q≤6	SC Ion Source A/Q≤7
18O	80*	-	375
19F	>15	>40	>40
36Ar	16*	70	45
40Ar	3.6	70	45
36S	2.3	-	-
40Ca	2.9*	10	20
48Ca	1.2	10	20
58Ni	1.1*	4	8
84Kr	0.1	10	20
139Xe	0.001	7	>10
238U	<<0.001	0.1	10

*Measured, Foreseen

GENERAL LAYOUT

This second injector is designed to be fully compatible with the existing facility (Fig. 1) and to further enhance its 'multi-user' capabilities. It is composed of the following (Fig. 2):

- A high-performance superconducting ion source (Source 1/7) called ASTERICS [2],
- A low energy beam transport allowing the connection of both ion sources (superconducting ion source and existing room temperature ion source) to the RFQ (LBE3). The mass separation at the exit of the ion sources can be tuned up to 150, depending on the ion choices and the experiment needs,
- A RFQ that will accelerate heavy ions with minimal beam losses up to the injection energy for the superconducting LINAC (RFQ2),
- A medium energy beam transport to the LINAC (LME2), giving also the possibility to send the beam into an experimental area (to be built) in the future.

The injector will be installed in an existing cave built 15 years ago in the SPIRAL2 building. The view of the injector inside the existing facility is shown on Fig. 3.

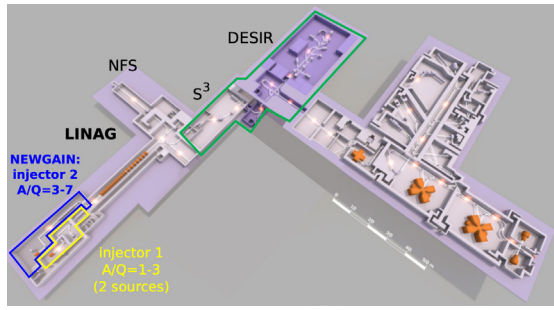


Figure 1: General layout of the NEWGAIN injector.

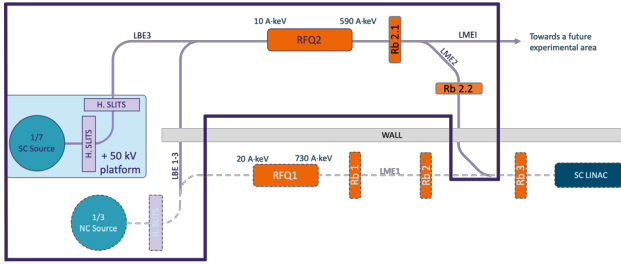


Figure 2: NEWGAIN principle layout (in dotted lines are the existing elements of SPIRAL2).

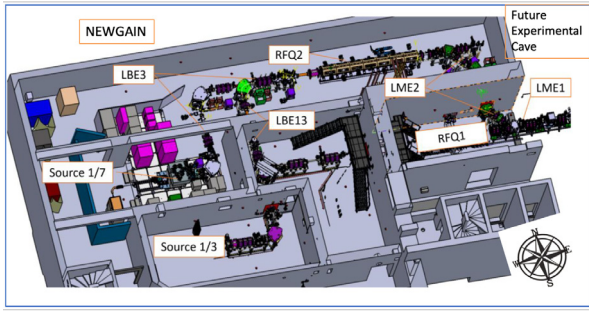


Figure 3: General 3D layout of the NEWGAIN injector inserted in the SPIRAL2 building (preliminary design).

The main injector parameters and reference beams considered for the design are listed in Table 2. The beam coming from the existing source will be limited to $A/q=6$, the current maximum source extraction voltage being fixed at 60 kV.

Table 2: NEWGAIN Main Parameters

Main Frequency	88.0525	MHz	
LEBT Input energy	10	keV/A	
RFQ Input energy	10	keV/A	
MEBT Input energy	0.590	MeV/A	
HEBT Input energy for A/q=7	7	MeV/A	
Reference beams	⁴⁸ Ca	¹¹⁺ ²³⁸ U	³⁴⁺
Normalized RMS emittance	0.2	0.15	π .mm.mrad
Beam intensity	220	340	μ A
LEBT beam power	10	24	W
MEBT beam power	0.54	1.4	kW
HEBT beam power	6.9	16.7	kW

PROJECT STATUS

Since May 2023, part of the project has entered into the construction phase. Then, the general configuration for the beam lines is fixed. Only the superconducting source and its platform are still in the detailed design phase.

The project is divided into two phases. The first phase will take place both at GANIL, with the installation of the injector linking the existing Phoenix V3 source to SPIRAL2 LINAC via the new RFQ2 (adapted to heavy ions), and at LPSC (Grenoble, France), where the ASTERICS source will be installed for its uranium beam commissioning. Once the ASTERICS source has been commissioned, it will be integrated into GANIL NEWGAIN line to transport uranium beams to the experimental room of GANIL.

As the period of tests and commissioning of the ASTERICS source might be long due to the state of the art design of this source, it is planned to proceed these tests at the LPSC laboratory (Grenoble) by the source experts. Meanwhile, the transport lines of NEWGAIN and the RFQ will be tested at GANIL with the PHOENIX V3 beams.

Schedule

One of the most difficult challenges to manage is the project interaction with the operation of the existing machine. SPIRAL2 has numerous operating periods and the schedule must take this major constraint (common to all existing installations) into account. The risk is that it will not be possible to take advantage of the machine downtime due to the unavailability of NEWGAIN equipment for installation. The project team must anticipate these periods in an agile manner. Thus, the first ongoing difficulty is the drilling of the emergency exit in the SPIRAL2 building. With authorizations from the technical controller running late, a six-month slippage has already impacted the project. The phases and order of equipment installation are then called into question to meet the project milestones.

Figure 4 shows the project roadmap based on work packages.

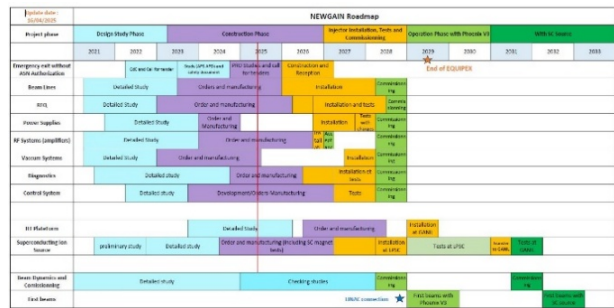


Figure 4: NEWGAIN roadmap.

INSTALLATION PROGRESS

Due to the short duration of the project, the strategy was to use as much as possible the design of the equipment already existing on SPIRAL2 to reduce the development study time. Nevertheless, some equipment have benefited benefit from necessary improvements identified during the operation of SPIRAL2. The year 2025 (Fig. 4) marks the

end of the main equipment order period. Vacuum equipment, power supplies and automatism devices have already been received and stored. The major equipment such as the RFQ, the ASTERICS superconducting coil, the quadrupoles, solenoids and RF amplifiers have been ordered and under construction.

Superconducting Ion Source

One of the main critical items of the source is its superconducting magnet constituted of one NbTi superconducting sextupole inside three NbTi superconducting solenoids. The preliminary design was first described in [2], and the detailed design of the magnet and its cryogenic satellite is in progress. The SC ion source is placed on a 50 kV platform. It was then decided to design an enlarged version of the VENUS ion source [3], called ASTERICS for Advanced Spiral Two Electron cyclotron Resonance Ion source at Caen with Superconducting magnet. The design [4] keeps the same magnetic system as VENUS ion source but increases the overall plasma chamber dimensions: the cylindrical chamber has a 600 mm length (~500 mm for VENUS) and 181 mm diameter (141 mm for VENUS). The aim is to enhance significantly the magnetic intensity of the last closed magnetic surface (which mitigates the risk to burn the plasma chamber), and to let room to develop and install dedicated hardware to enhance the conversion yield of metallic atoms into ion beam (new ovens, hot temperature controlled liners) [5]. The mechanical global view of the ion source is presented in Fig. 5.

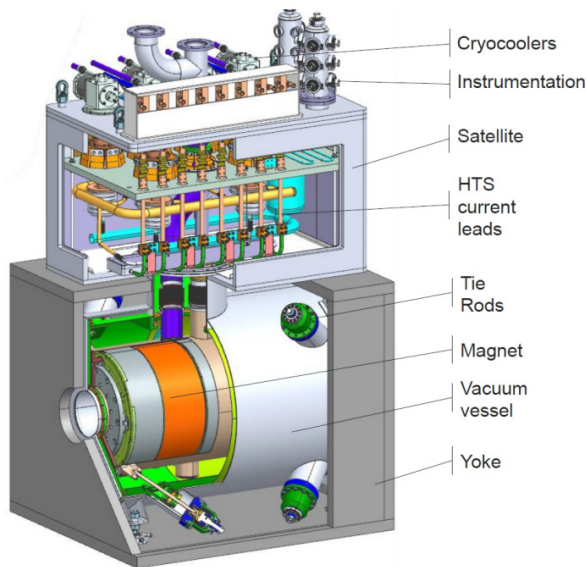


Figure 5: Skinned view of the ASTERICS cryostat ion source, its magnet and the surrounding iron yoke.

In September 2024, the validation of the ground platform layout with the operator was completed. This step marked the convergence of a complex iterative process involving multiple conflicting constraints in April 2025. The kick-off meeting for the ASTERICS superconducting magnet manufacturing contract took place. An international review of

the source mechanics was held in May 2025. It allowed experts to evaluate both the source design and the construction strategies. The resulting report helped us to consolidate our implementation choices.

Beam Transport

The Low Energy Beam transport (LBE3-Fig. 6) connects the superconducting source to the RFQ. The possibility to use the beams from the existing Phoenix V3 source with higher mass-to-charge ratio than with the RFQ1, is added through a second dedicated low-energy transport (LBE13), connected to LBE3 upstream the RFQ. The Line Medium Energy (LME2) then injects the beam into the superconducting LINAC. The design has been optimized through beam dynamics calculation whose results are presented in [6].

The LBE3, whose optical functions are shown in Fig. 7, is composed of 2 solenoids after the ion source extraction, 2 sets of horizontal slits for q/A selection, an accelerating tube at the platform exit, 10 quadrupoles equipped with a vertical or horizontal steerer, two 90° dipoles, 6 profilers, 6 slits including 3 vertical and horizontal sets, 1 Pepper pot, 2 Faraday cups, one 100 kHz chopper, 1 Emittance meter in the 2 planes, 2 safety beam stops. 1 double solenoid at RFQ entrance and 1 ACCT in flange.

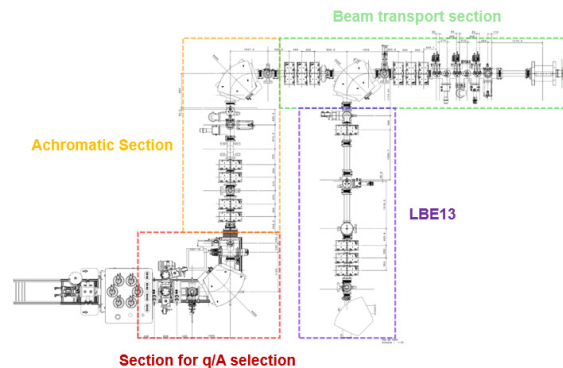


Figure 6: Optical functions of the LBE3.

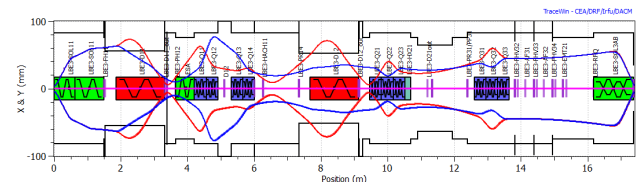


Figure 7: Nominal beam envelope for NEWGAIN up to the entrance of the RFQ1 of SPIRAL2.

The medium energy transport to the LINAC (LME2) is approximately 10 meters long and is composed of 4 triplets of quadrupoles including steering coils, 4 dipoles (3 identical and one insertion dipole in the LME1), 2 rebunchers, identical to those of the existing in SPIRAL2, 1 ACCT in flange at RFQ output, 1 Faraday cup, 5 profilers, 1 phase probe.

An additional section (LMEI) is added at the 0° RFQ exit, towards a future experimental area. It already integrates a permanent “tuning” bench containing some diagnostics that could not be mechanically placed in the main MEBT. The LMEI is composed of a triplet of quadrupoles, two phase probes, and a diagnostic chamber containing an emittance meter, a profiler, and fast and slow faraday cups.

The beam envelopes (Fig. 7) allow to survey the high intensity beam produced by the sources along the injector and extensive beam dynamics calculation have been done to first dimension the interceptive equipment such as Faraday cup, slits, dipoles, vacuum chambers. The various simulations allow to consolidate the mechanical design of the injector.

RFQ

The RFQ is a standard four-vane bulk copper cavity, composed of 7 segments. Mechanical studies are based on the first SPIRAL2 RFQ, for which operation experience is very positive [7]. Only the vacuum ports were changed to have a more uniform and performant pumping along the cavity. 4 smaller circular openings per section have been preferred to the 4 large racetrack ones of RFQ1. The RF design was simplified by using a constant voltage profile and aimed at reducing the cavity loss to fit the surface available for the installation of the amplifiers, and to maintain the Kilpatrick factor below 1.65. The main RFQ parameters are presented in Table 3.

The RFQ cavity in Fig. 8 is composed of 7 sections and is currently under construction. The 2 first sections should be pre-assembled in CEA/IRFU laboratory end of 2025 and Delivery of all other sections to GANIL is expected from February 2026 to June 2026.

Table 3: RFQ Main Parameters

Frequency	88,0525	MHz
Accelerating Voltage	70	kV
Surface Electric Field	1,65	Kilpatrick
Cavity loss	92	kW
Length	7	m
Vane Modulation	1 to 2,7	
Power coupling ports	4	
Tuning plungers/segment	4x2	

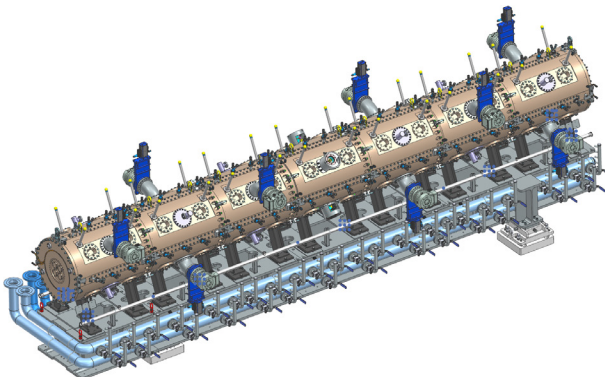


Figure 8: NEWGAIN RFQ2.

RF Systems

The RF systems for NEWGAIN is composed of rebunchers, amplifiers and transmission lines. It will be based on the LLRF designed for SPIRAL2 [8] and on new solid-state amplifiers.

The driving scheme for the 4-port RFQ will be simplified by using only one LLRF (instead of four in master/slave configuration) as shown in Fig. 9. Since the installation of the phase locked loop mode to turn on RFQ1, the reflected power to be managed has strongly decreased (< 12%) and the cost, dimensions and running constraints of circulators are probably no more justified. Then, the possibility not to use these devices has been investigated on a low power 4-port resonant combiner. An isolated first splitter will be used, as well as amplifiers equipped with gain and phase control, and transmission lines of equal phase lengths, to have similar gain variations of the amplifiers when the cavity is detuned. The first prototype of a solid-state amplifier withstanding 15% mismatch, was produced by an industrial company and was successfully tested at the factory. It is now at GANIL for final acceptance tests before the launch of series production. The prototype meets the specifications and the option for the optional tranches should be finalized before the summer.

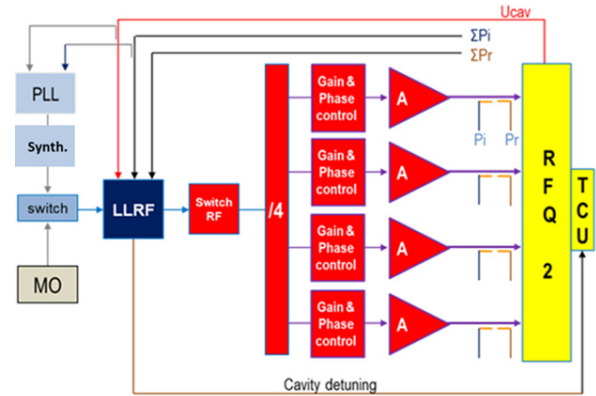


Figure 9: RFQ2 driving principle.

The 3D integration of the RF power distribution, including the option with circulators, was completed in May 2025. The specifications are finalized and ready for the consultation, which is scheduled for the end of 2025 and will concern the supply and installation of the equipment. The installation phase is estimated to arrive about six months after the consultation. Partial dismantling will be required for the installation of the RFQ.

Diagnostics

Diagnostics that will be used for beam tuning and survey are identical to those installed on SPIRAL2 [9] except for the AC-Current Transformers (ACCT), placed at RFQ entrance and exit. The modifications and developments primarily focus on sensitivity for low beam intensities. This work also concerns all SPIRAL2 diagnostics for future S3 beams. The current measurement range for the CF and ACCT is 1 mA to achieve sufficient accuracy for low in-

tensities. The diagnostics pool will be composed of 4 Faraday cups, 15 profilers, 2 AC-Current Transformers, 3 phase probes, 2 emittance-meters. In addition, an upgrade of the existing SPIRAL2 beam survey systems has to be completed to take into account the new beams from NEWGAIN. The existing ECSF (Electronic for Beam Structure Control) must be modified and upgrade in order to integrate NEWGAIN injector as well as the SPMT (Thermal Machine Protection System).

CONCLUSION

The NEWGAIN project is progressing well in its construction phase started on May 2023. In May 2025 the first symbolic modification of the existing SPIRAL2 line has been made, i.e. the installation of a new vacuum chamber in the common dipole LBE12 with a new exit to NEWGAIN. The next main milestones will be the drilling of the emergency exit in the existing building. This civil engineering operation is a prerequisite for any installation to establish the geodetic network of the room after construction. The main difficulty is the availability of technical human resources and a strict workload plan for the project but also for the entire GANIL projects is being consolidated to ensure the milestones are met. GANIL is a Basic Nuclear Installation (INB) and the project must request start-up authorization via safety files submitted to the French Nuclear Safety and Radiation Protection Authority (ASNR). 2029 should be the year of production of the first beams in NEWGAIN and see the first start-up of the ASTERICS superconducting source.

ACKNOWLEDGEMENTS

This work is supported by Agence Nationale de la Recherche, with the contract # 21-ESRE-0018 EQUIPEX+ NEWGAIN.

REFERENCES

- [1] A. Orduz *et al.*, “Commissioning and operation of the SPIRAL2 SC linac”, in *Proc. IPAC’23*, Venice, Italy, May 2023, pp. 5187-5192. doi:10.18429/JACoW-IPAC2023-FRDX3
- [2] D. Xie, J. Y. Benitez, C. M. Lyneis, D. S. Todd, and W. Lu, “Recent production of intense high charge ion beams with VENUS”, in *Proc. ECRIS’16*, Busan, Korea, Aug.-Sep. 2016, pp. 141-145. doi:10.18429/JACoW-ECRIS2016-THA001
- [3] D. Simon *et al.*, “Progress in the design of the ASTERICS 28 GHz ECR ion source superconducting magnet for the NEWGAIN project at GANIL”, *IEEE Trans. Appl. Supercond.*, vol. 34, no. 5, pp. 1–5, Aug. 2024. doi:10.1109/tasc.2023.3341913
- [4] T. Cadoux *et al.*, “Mechanical design of the superconducting magnet for the 28 GHz ECR ion source ASTERICS”, *IEEE Trans. Appl. Supercond.*, vol. 34, no. 5, pp. 1–6, Aug. 2024. doi:10.1109/tasc.2024.3355351
- [5] T. Thuillier *et al.*, “ASTERICS, a new 28 GHz electron cyclotron resonance ion source for the SPIRAL2 accelerator”, *J. Phys. Conf. Ser.*, vol. 2743, no. 1, p. 012059, May 2024. doi:10.1088/1742-6596/2743/1/012059
- [6] J. Dumas, O. Kamalou, A. Orduz, and E. Traykov, “Beam dynamics in the NEWGAIN project at GANIL-SPIRAL2”, in *Proc. IPAC’23*, Venice, Italy, May 2023, pp. 3192-3195. doi:10.18429/JACoW-IPAC2023-WEPL035
- [7] P. Hamel, M. J. Desmons, O. Piquet, B. Prevet, and N. Sellami, “RFQ NEWGAIN: RF and thermomechanical design”, in *Proc. IPAC’22*, Bangkok, Thailand, Jun. 2022, pp. 1510-1512. doi:10.18429/JACoW-IPAC2022-TUPOMS038
- [8] P. De Antoni *et al.*, “The architecture of the low level RF electronics for Spiral2”, presented at LLRF Workshop, Knoxville, TN, USA, Oct. 2007, unpublished.
- [9] C. Jamet *et al.*, “SPIRAL2 diagnostic qualifications with RFQ beams”, in *Proc. IBIC’19*, Malmö, Sweden, Sep. 2019, pp. 188-192. doi:10.18429/JACoW-IBIC2019-MOPP036

DEMONSTRATION OF CAVITY FIELD MAPPING BY FALLING DROPS OF LIQUID*

X. Du, L. Groening

GSI Helmholtzzentrum für Schwerionenforschung GmbH, Darmstadt, Germany

Abstract

This paper presents a novel bead-falling method for precise mapping of electromagnetic fields in radio-frequency (RF) cavities, critical for accelerator design. Unlike the traditional bead-pull method, which relies on a wire-pulley system prone to mechanical errors, this technique uses free-falling beads to eliminate perturbations from wires. A compact, portable device integrates a bead release system, detection mechanism and a mini-computer for rapid and accurate field measurements. Tested on a three-gap buncher cavity and a scaled Alvarez-type cavity, the method demonstrates high precision even under low signal-to-noise ratios and environmental vibrations. This approach simplifies setup, enhances measurement speed, and offers potential as a new standard for RF cavity diagnostics.

INTRODUCTION

Radio-frequency (RF) cavities are fundamental components in particle accelerators, shaping electromagnetic fields to accelerate charged particles. Precise field measurements are essential for ensuring cavity performance aligns with design specifications, particularly for applications in high-energy physics and medical accelerators. The bead-pull method, rooted in Slater's perturbation theory [1], has been the standard for mapping field distributions by measuring frequency shifts induced by a bead moved through the cavity via a wire-pulley system. However, this method faces challenges, including mechanical complexities, wire-induced perturbations (especially for higher-order modes), and time-consuming setup processes.

To address these limitations, we developed a bead-falling measurement method, as detailed in [2], which eliminates the wire-pulley system by using free-falling beads or droplets to perturb the cavity field. This technique simplifies the experimental setup, reduces mechanical errors, and enables rapid measurements suitable for real-time monitoring. The method's versatility allows it to be applied to various cavity types, such as Radio-Frequency Quadrupoles (RFQs) and Drift Tube Linacs (DTLs), enhancing the efficiency of cavity tuning and diagnostics. This paper elaborates on the method's design, hardware, software, and experimental validation, demonstrating its potential to redefine RF cavity field measurements.

CONCEPTUAL DESIGN AND ADVANTAGES

The bead-falling method induces perturbations by releasing a bead or droplet to fall freely through the RF cavity along the beam axis, with a VNA capturing resulting phase or frequency shifts (Fig. 1). The bead's position is correlated with time using kinematic equations, accounting for gravitational acceleration, to map the field distribution accurately.

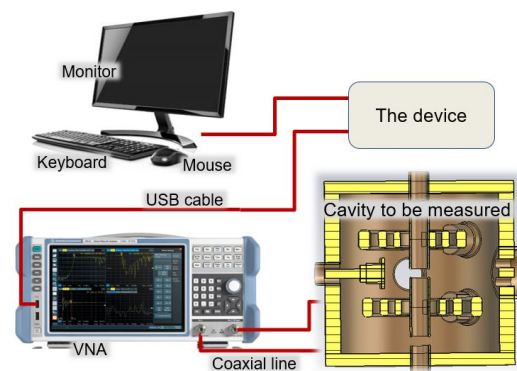


Figure 1: Scheme of bead-fall RF-measurements. The cavity is connected to two of the VNA ports. The device includes the bead/droplet release system and the bead detector. It is positioned such that the falling bead is aligned to the beam axis of the cavity. Beads are released from the top and fall freely through the bead-detector and subsequently through the cavity.

Compared to the bead-pull method, this approach offers several advantages:

- **enhanced precision:** small beads (0.5–1 mm) minimize field variations across their volume, and the absence of a wire eliminates perturbations, particularly for dipole modes.
- **rapid measurements:** free-fall durations of less than 0.5 s enable measurements at 2 Hz, supporting real-time field monitoring during tuning.
- **simplified setup:** eliminating the wire-pulley system reduces setup time and mechanical complexity, making the method adaptable to various cavity geometries.
- **material flexibility:** the use of liquid droplets (e.g., water) allows for rapid, iterative measurements, enhancing experimental efficiency.
- **robustness:** the method performs reliably under challenging conditions, such as low signal-to-noise ratios

* Work supported by GSI Helmholtzzentrum für Schwerionenforschung GmbH

or environmental vibrations, as demonstrated in our experiments.

These advantages make the bead-falling method particularly suited for tuning multi-gap cavities like RFQs and DTLs, where iterative field measurements are critical to correct machining-induced deviations [3].

HARDWARE AND SOFTWARE

Hardware Design

The measurement device (Fig. 2) is a compact, portable unit integrating a bead release system, detection mechanism, and control system, costing less than \$300. A medical drip infuser generates water droplets, with a valve controlling droplet size and release rate to ensure consistent measure iterations. A laser diode and light sensor form a photoelectric barrier, triggering the VNA (Rohde & Schwarz ZNB-4, 10 kHz IF bandwidth) when the bead passes a predefined point. A Raspberry Pi 4B serves as the control and computing unit, enabling data acquisition and processing. A 3D-printed cap aligns the bead with the cavity's beam axis.

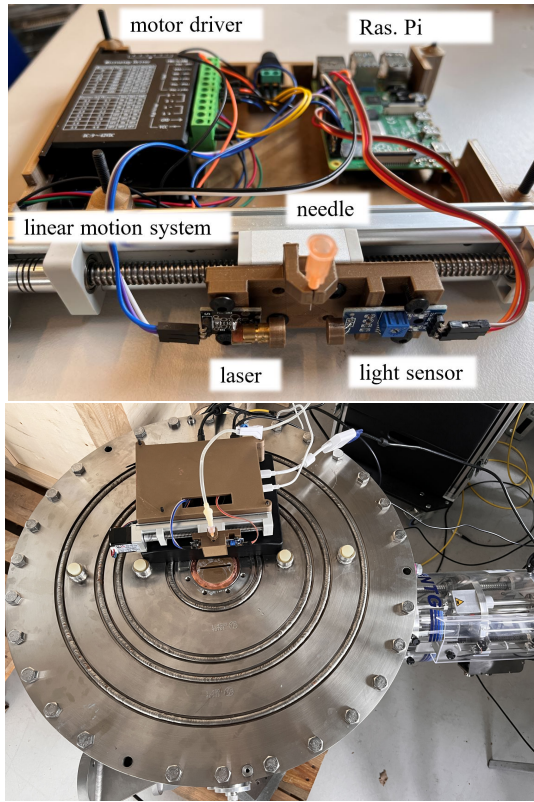


Figure 2: All components are fixed to the 3D printed case (a). Measurement device installed on top of the cavity to be measured (b).

For cavities requiring off-axis measurements (e.g., RFQ quadrants), a linear motion system adjusts the release position, though this was not needed for the experiments described here. The entire device's volume is only half the

size of a letter-sized sheet of paper, making it portable and lightweight compared to the traditional wire-pulley system, and it is universal for all kinds of cavities, except the cavity is not suitable for vertical standing.

Software Implementation

The software, with an intuitive user interface (Fig. 3), is pivotal in orchestrating the device's operations, offering several key functionalities that enhance the measurement capabilities and data processing efficiency.

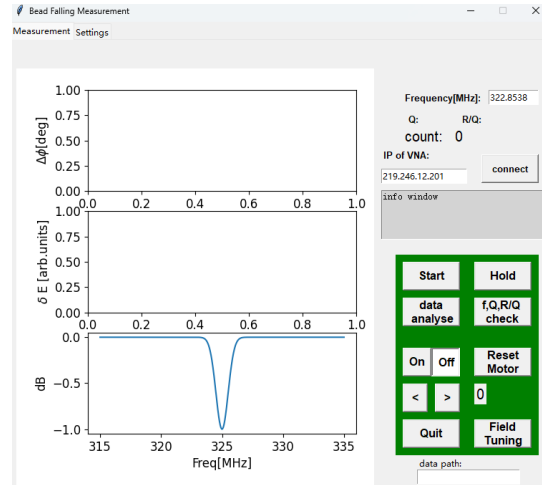


Figure 3: User interface for measurement control and visualization.

The programme converts measured phase-time curves to field-position curves using kinematic models and applies Singular Value Decomposition (SVD) to filter noise from repeated measurements. The software automates iterative measurements, enabling real-time field updates at 2 Hz, and includes features to mitigate frequency drift by re-measuring resonance frequency every 120 s.

Field Tuning Program

The tuning algorithm uses a response matrix to model the effect of each tuner on field components at various longitudinal positions [3]. The field distribution is measured using the perturbation technique, represented as a vector $[\delta E_1, \delta E_2, \dots, \delta E_M]$, where δE_m is the gap voltage (for DTL cavities) or magnetic field (for RFQs) at the m_{th} position.

Adjusting a tuner changes the field distribution. The initial tuner setting is zero, and the required tuner adjustments, δT , are found by solving:

$$\begin{pmatrix} \delta E_1 \\ \delta E_2 \\ \vdots \\ \delta E_M \end{pmatrix} = \begin{pmatrix} \frac{\partial E_1}{\partial T_1} & \frac{\partial E_1}{\partial T_2} & \dots & \frac{\partial E_1}{\partial T_N} \\ \frac{\partial E_2}{\partial T_1} & \frac{\partial E_2}{\partial T_2} & \dots & \frac{\partial E_2}{\partial T_N} \\ \vdots & \vdots & \ddots & \vdots \\ \frac{\partial E_M}{\partial T_1} & \frac{\partial E_M}{\partial T_2} & \dots & \frac{\partial E_M}{\partial T_N} \end{pmatrix} \begin{pmatrix} \delta T_1 \\ \delta T_2 \\ \vdots \\ \delta T_N \end{pmatrix}. \quad (1)$$

This overdetermined system is solved to minimize the difference between measured field distributions respect to the

desired one. For RFQ tuning with four quadrants, the field distributions of 4 quadare concatenated, increasing M to $4M$. The tuning program's user interface is shown in Fig. 4. Due to non-linear tuner effects and adjustment errors, the process is iterative to achieve the desired field distribution.

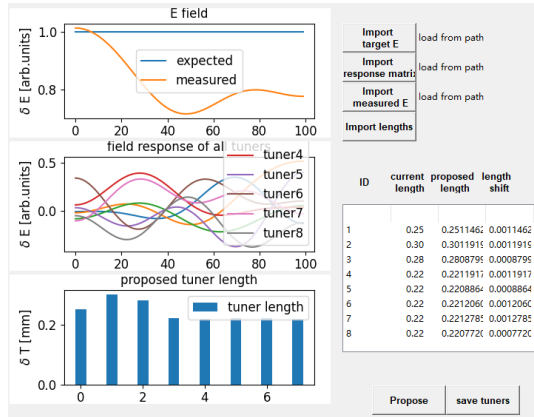


Figure 4: The user interface of the tuning program.

MEASUREMENTS

Three-Gap Buncher Cavity

A three-gap buncher cavity (36.136 MHz, $Q=1000$, Fig. 5) was tested, its parameters are listed in Table 1. The cavity was aligned vertically using a plumb line and adjustable legs, with a 3D-printed cap ensuring droplet alignment. Calibration involved dropping beads from various heights to determine the system delay (78.32 ± 0.85 ms) and initial velocity, using phase shift data from three equidistant gaps.

Table 1: Parameters of the Buncher BB3

Parameter	Unit	Value
RF-frequency	MHz	36.136
Gaps	#	3
Gap length	mm	12.7–13.5
Drift tubes	#	2
Drift tube length	mm	38.1–40.8
Aperture	mm	100
Tank diameter	mm	420
Tank length	mm	525.7
Q-factor		1000

Despite a low Q-factor, SVD processed 500 iterations of 3000-point data, yielding clear field distributions (Fig. 7). Comparisons with simulations showed minor deviations due to machining inaccuracies (Fig. 6).

Two-dimensional field measurements, facilitated by a slit in the 3D-printed cap, provided detailed field maps, confirming the method's ability is not limited to on-axis field measurement. With proper translation and scaling, the measured field (denoted by \hat{E}_{abs}) can be compared with the

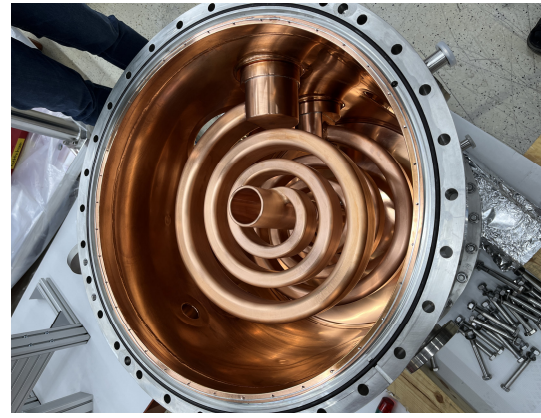


Figure 5: Three-gap buncher cavity (36 MHz).

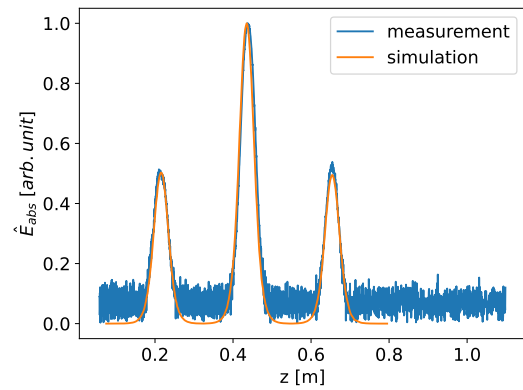


Figure 6: Measured vs. simulated electric field in the buncher cavity.

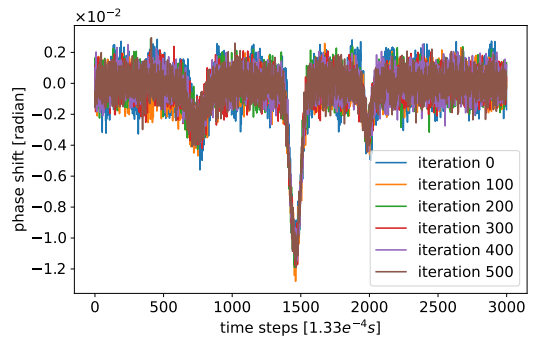


Figure 7: Measured data taken with the buncher cavity with 3000 discrete time points within 0.4 second each, corresponding to a length of about 1.2 m along the cavity axis.

corresponding field obtained from simulation (denoted by E_{abs}), as shown in Fig. 8. The rapid measurement capability allowed real-time monitoring during tuning, enabling iterative adjustments to achieve the desired field flatness, being critical for buncher cavities in accelerator systems.

Alvarez-Type Cavity Model

A 1:3 scale aluminum Alvarez-type cavity [4,5] was tested under challenging conditions (low Q, environmental noise). It is depicted in Fig. 9 and its parameters are listed in Table 2.

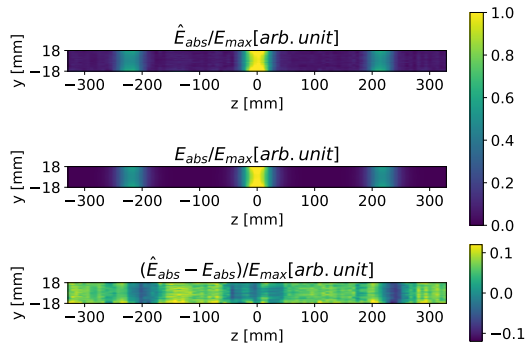


Figure 8: The distribution \hat{E}_{abs} represents the experimentally measured two-dimensional field, while E_{abs} denotes the corresponding field obtained from simulations. Both fields are normalized to their respective maxima, specifically the peak value observed at the middle gap. The term $\hat{E}_{abs} - E_{abs}$ quantifies the deviation of the measured values from the simulated ones.

Despite a 2:1 signal-to-noise ratio, rapid iterative measurements and SVD analysis extracted clear field distributions (Fig. 10).

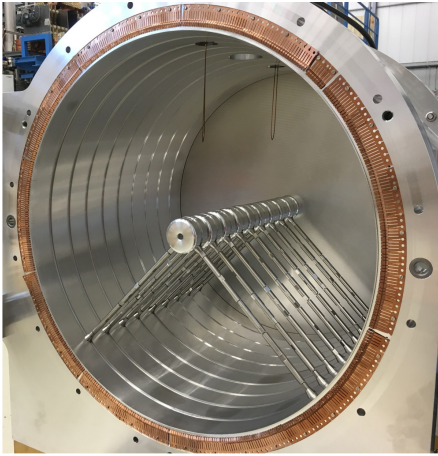


Figure 9: 1:3 scale Alvarez-type cavity model.

Table 2: Parameters of the Alvarez-Type DTL Cavity

Parameter	Unit	Value
RF-frequency	MHz	325.224
Gaps	#	10
Gap length	mm	12.7–13.5
Drift tubes	#	9
Drift tube length	mm	38.1–40.8
Drift tube diameter	mm	60.0
Aperture	mm	10.0
Tank diameter	mm	634.5
Tank length	mm	525.7
Q-factor		500

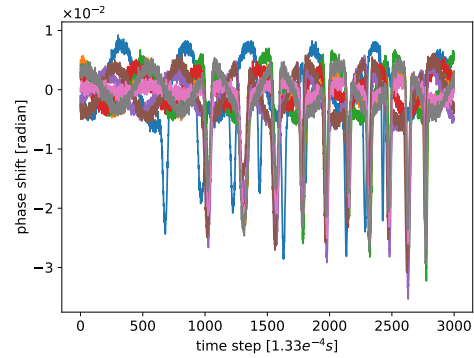


Figure 10: Measured phase shift data from the Alvarez-type DTL, with a signal-to-noise ratio of approximately 2. Different colors represent multiple phase shift measurements conducted using the DTL. Only five representative results from thousands are presented.

In the measurement results for the buncher cavity, the field distribution overwhelmingly dominates relative to the noise, allowing the first singular vector to be approximately regarded as the field distribution. However, The measurement data for the aluminium cavity is more complex, with the magnitude of background noise being on the same order as the field distribution. Results from Singular Value Decomposition (SVD) indicate a clear periodic oscillation within the background, which is not orthogonal to the real field distribution. Since the singular vectors obtained from SVD must be orthogonal, the primary singular vector does not represent the actual field distribution. To address this, the real field distribution is considered as a linear combination of the first four singular vectors with specific weights. By using a small segment (0-900 out of 3000) of the measurement data without gaps as a reference, the four weights can be solved, thus yielding the final measurement field distribution (Fig. 11).

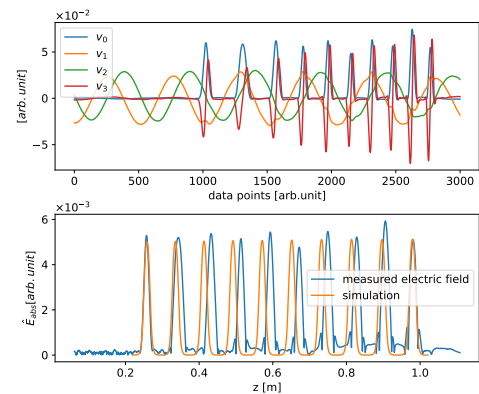


Figure 11: Upper: the first four singular vectors. Lower: measured electric field along the beam axis of the DTL model cavity.

LIMITATIONS

The method is limited to cavities shorter than 3.5 m due to sampling rate constraints and Coriolis force effects (0.22 mm deflection at 3.5 m). It is unsuitable for cavities with significant gravity-induced deformation, such as Alvarez resonators with slender support rods, as observed in the model cavity measurements.

CONCLUSION

The bead-falling measurement method, as detailed in [2], offers a transformative approach to RF cavity field mapping, combining precision, speed, and simplicity. Its compact, low-cost device and noise-resilient measurements make it a versatile tool for accelerator diagnostics. Future developments will focus on enhancing its applicability to diverse cavity types and integrating advanced tuning algorithms to further streamline the tuning process, potentially impacting the design and optimization of next-generation accelerators.

REFERENCES

- [1] L. C. Maier and J. C. Slater, “Field strength measurements in resonant cavities”, *J. Appl. Phys.*, vol. 23, no. 1, pp. 68–77, 1952. doi:10.1063/1.1701980
- [2] X. Du and L. Groening, “Radio-frequency cavity field measurements through free falling bead”, *Phys. Rev. Accel. Beams*, vol. 28, no. 1, p. 012001, 2025. doi:10.1103/PhysRevAccelBeams.28.012001
- [3] B. Koubek, A. Grudiev, and M. Timmins, “RF measurements and tuning of the 750 MHz radio frequency quadrupole”, *Phys. Rev. Accel. Beams*, vol. 20, no. 8, p. 080102, 2017. doi:10.1103/PhysRevAccelBeams.20.080102
- [4] A Seibel, O. K. Kester, X. Du, L. Groening, and S. Mickat, “Ten gap model of a new Alvarez DTL cavity at GSI”, in *Proc. IPAC’15*, Richmond, VA, USA, May 2015, pp. 3748–3750. doi:10.18429/JACoW-IPAC2015-THPF027
- [5] M. Heilmann *et al.*, “Scaled Alvarez-cavity model investigations for the UNILAC upgrade”, in *Proc. IPAC’18*, Vancouver, Canada, Apr.-May 2018, pp. 916–919. doi:10.18429/JACoW-IPAC2018-TUPAF079

OPERATION OF A PULSED GAS STRIPPER DURING REGULAR USER BEAM TIME AT GSI

P. Gerhard* and M. Maier

GSI Helmholtzzentrum für Schwerionenforschung GmbH, Darmstadt, Germany

Abstract

The charge state spectrum of heavy ions like uranium stripped at 1.4 MeV/u using nitrogen as stripping target can be narrowed significantly by applying pulsed injection of hydrogen into a dedicated interaction chamber. Pulsing reduces the gas load of the pumping system to an acceptable amount. Such a setup is under construction at GSI. Time-resolved investigations of the build-up of the stripping target have been carried out. A prototype setup has been operated during six months of user beam time in 2024 and is currently again in operation for the user beam time 2025, mainly with nitrogen but also with hydrogen. A number of ion species has been stripped in the course of the beam times, and a considerable amount of data on stripping efficiencies have been measured using both gases. The contribution summarizes the challenges related to establishing such a setup, the results being obtained so far and lessons learned.

INTRODUCTION

The GSI accelerator facility, in particular the UNILAC (UNiversal Linear ACcelerator) and the heavy ion synchrotron SIS18, serve as injector for the upcoming Facility for Antiproton and Ion Research (FAIR), the commissioning of which will start in 2026. High intensity ion beams are provided by dedicated high current sources and pre-accelerated by the high current injector (HSI). The HSI is designed for handling ions with a mass-to-charge-ratio of up to $A/q = 65$, since the ions delivered by the high current sources have inherently low charge states [1]. A gas stripper is necessary to increase the charge state to enable efficient acceleration in the subsequent Alvarez drift tube linac. Stripping is applied at 1.4 MeV/u after acceleration in the HSI. Until recently, a continuous nitrogen gas jet was employed as stripping target [2]. Out of the charge state spectrum resulting from the stripping process, one charge state has to be separated for further acceleration. For heavy ions like uranium, this results in the loss of up to $\approx 87\%$ of the beam.

In order to increase the yield into the desired charge state, introducing hydrogen and other gases as stripping targets was investigated [3]. With H_2 , the width of the charge state distribution of heavy ions is significantly reduced and the stripping efficiency increased accordingly, e. g. by approximately 50% for $^{238}U^{28+}$. Additionally, an increase of the mean charge state can be achieved for all ions. The proof-of-principle was demonstrated successfully in 2016 [4–6].

The decision to introduce H_2 into regular operation induced several challenges. Since hydrogen is highly combustible, comprehensive safety measures have to be imple-

mented. H_2 is also much more difficult to pump. It soon became clear that the gas load had to be reduced, which lead to the pulsed operation of the gas target. It exploits the low duty factor of the UNILAC by delivering only short pulses of high gas density synchronized with the beam pulse. This was realized via commercially available, fast injection valves. Together with the demand to have different gases (H_2 and N_2) and target densities available in parallel, the now pulsed gas stripper became a much more complex system than the jet stripper was. Therefore, a fully automated setup suitable for safe and regular operation has to be developed [7, 8].

In late 2023, it was decided to utilize the development setup for the user beam time 2024, putting the pulsed stripper into regular operation ahead of schedule. This was repeated for the beam time 2025. Several improvements were implemented to minimize the restrictions on operation given by the developmental status of the setup. The still incomplete implementation of the safety concept meant that only N_2 operation was possible for user operation.

DEVELOPMENT SETUP AND RECENT UPGRADES

A second generation stripper setup (Fig. 1) was designed after it was found during the proof-of-principle that the original valves would break down after only a few hours of operation [7]. It contains two fast injection valves of a new

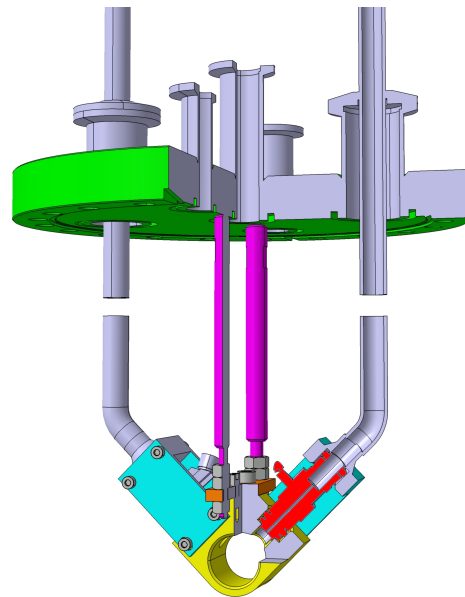


Figure 1: Sketch of the current pulsed stripper setup. The fast injection valve is indicated in red. More details in [7, 8].

* p.gerhard@gsi.de

type designed for gas injection and was intended for further system development and experimental H_2 operation. The two valves allow for independent operation of two different stripping targets. Time-resolved measurements of the build-up and evolution of the gas target had been carried out with this setup using the ion beam to probe the target in order to qualify the new valve type [8].

The development gas control is shown in Fig. 2. Its main purpose is to control the gas pressure supplied to the injection valves and thereby the target density. It allows for providing H_2 and N_2 to two injection valves at the same time. To facilitate long-term operation during beam time, the gas control was connected to the central N_2 supply, while H_2 is supplied from gas cylinders. Each gas line is equipped with a pneumatically driven safety cut-off valve, which is controlled by a simple interlock system. In the event of a safety-relevant failure, the gas supply is cut-off quickly, providing enough safety for short-term experimental hydrogen operation and machine safety for long-term unattended operation with nitrogen during beam times. Both supply lines are equipped with a flow meter, which proved essential in the early detection of valve failures.

Stripping with N_2 requires gas pressures well below 1 bar(a), especially for light and intermediate ions. This was rarely done before and rather challenging with the cylinder pressure reducers used so far. To improve operation at low pressures, two dedicated, mechanical low-pressure regulators were added to the gas control setup before the beam time 2024. The operational flexibility was enhanced by adding a high-pressure bypass line and extending the corresponding purge lines.

A major step forward in terms of safety was achieved by the installation of a new, large, explosion safe roots pump station in 2023. Another upgrade of the vacuum system was the exchange of the four turbo-molecular pumps situated at the differential pumping sections of the gas stripper chamber

[7]. The new pumps were selected to achieve maximum throughput for hydrogen at high vacuum pressures, allowing for higher gas loads.

MODUS OPERANDI

Since the current development stripper setup was never intended to be used for regular long-term operation, there was no automation or remote operation and monitoring foreseen. Partial remote control of the stripper was enabled by simply using remote access to a PC, which was used to control the setup locally. By this, the valve controller and later also the electronic pressure controller (see below) as well as monitoring of the gas flow was remotely accessible. Still, many settings and the daily inspections and manual logging have to be done locally. This is especially true for the gas handling, because all valves and pressure gauges are manually operated only, as were the two mechanical low-pressure regulators used during beam time 2024. The only valves automated are the two safety cut-off valves.

Despite the improvements done, the stripper remained being an expert system. Unlike the jet stripper, there was no control and, due also to technical limitations, no monitoring of the stripper available for the operators from the main control room. This was even more serious, because the pulsed stripper relies on the correct timing to trigger the valve opening and closing, which still needs to be adjusted manually by the stripper team on-site because the integration of the pulsed stripper into the accelerator control and timing system is still missing. An on-call service by the team was established to support the accelerator operating crews properly.

LESSONS LEARNED

During the first user beam time it quickly became evident that, due to the restrictions mentioned above, a simple operating scheme had to be devised in order to minimize the

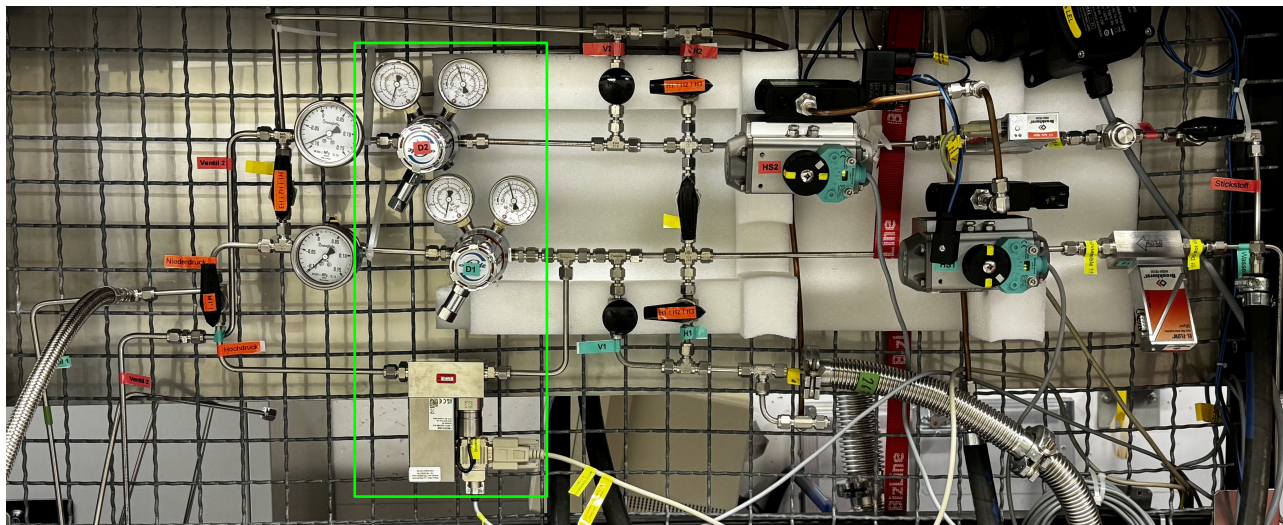


Figure 2: Foto of the gas control for the pulsed gas stripper. In the green frame are the two manual low-pressure regulators added early in 2024 (top and center) and the electronic pressure controller installed later (bottom).

need for adaptations to the stripper settings and to allow the operators to keep track of it. Therefore, parallel operation with both injection valves at different pressures for different beams was rarely used. Most of the time, the stripper was set up to serve all beams with one valve set to one pressure and timing, reproducing the jet operation. The settings were usually only revised when a new ion species was accelerated. In 2025, two valve operation was tried again successfully thanks to the experience gained in the meantime, when the trade-off using only one pressure setting was not acceptable. This finally leads to the conclusion, that the pulsed stripper system is rightly intended to be fully automated and integrated into the accelerator control system.

In terms of stripping results, the pulsed stripper performed well, as was expected from the knowledge gained in previous machine beam times. No significant differences or drawbacks compared to the jet stripper were observed as long as the correct timing was applied.

The large variety of ion species operated gave a valuable overview of the pressure range needed, which was not known before. Especially the very low pressures needed for some ions turned out to be very demanding. In general, the mechanical pressure controllers added in preparation of the beam time proved to be essential, although achieving a desired low pressure setting precisely needed painstaking fine-tuning. They also turned out to be unstable under changing operating conditions, because of the lack of a strong, adjustable feedback. In the event, manual re-tuning was applied.

The main lesson learned was about the service life of the injection valves. Operation along the whole beam time offered the opportunity to collect long-term statistics, which would otherwise have been impossible. With the very short service life of the original valves in mind, a detailed book keeping of the operational parameters was established to be able to reconstruct the operational demands put on the individual valve in case it would fail. The results were alarming: two valves failed after $\approx 20\%$ of their expected service life of $380 \cdot 10^6$ cycles as given by the manufacturer, a third valve showed irregularities after $\approx 14\%$. This corresponds to only a few weeks of high duty operation at cycle frequencies of 25–50 Hz. All valves that failed did so during or shortly after high duty operation by getting in open position. The cause for the failure and whether it is strictly linked to the high duty operation is unknown. None of the other valves that did not fail achieved anywhere near the number of cycles of the failed ones. This kind of failure was anticipated in the risk assessment as the worst case scenario for the hydrogen operation, because the maximum amount of H_2 would be released into the vacuum system, exposing the pumps and vacuum exhaust to the risk of overloading.

OPERATIONAL IMPROVEMENTS

In preparation for the beam time 2025, improvements based on the lessons learned were implemented. In addition

to the mechanical pressure regulators, an electronic pressure controller was installed, offering several advantages:

- the connection to the local PC enabling remote setting and read out of the gas pressure;
- the integrated, configurable PID controller provided a precise feedback, mitigating the instability of the mechanical pressure regulators under changing operational conditions;
- any pressure within the range of the controller was easily achievable.

The only drawback observed so far were the comparatively coarse settings at very low pressures, while the stability and precision of the controller was flawless even at the very low settings, which are outside the recommended operating range. At the same time, this was used to test the electronic pressure controller extensively before its implementation in the fully automated gas control station.

The very short service life of the valves under high duty operation gave rise to additional modifications. With the cause of the failure still being unknown, it is obvious that the valves are operated at gas pressures far below their intended use. The gas also serves as a coolant. In order to bring the operating pressures into the recommended range, a valve was fitted with an orifice of 0.6 mm at the outlet, reducing the original opening by a factor of four (Fig. 3 right).



Figure 3: Injection valves used for the pulsed gas stripper. The valve on the right is modified by an orifice with a diameter of 0.6 mm placed in the outlet tube. On the left, an unmodified valve is shown for comparison. In front of the valves are an O-ring and another orifice with O-ring mounted.

With this modification, the same flow through the valve, which determines the target density, should be achieved at a pressure about four times higher than without the orifice. Comparison of stripping data acquired with and without orifice (see next section) showed that the increase in pressure was about a factor of 4.5. This should enhance the cooling and the damping of the impact of the valve tappet on the seat during the fast opening and closing. Further optimization could be achieved by slightly changing the diameter of the orifice. Additionally, the voltage and current profiles

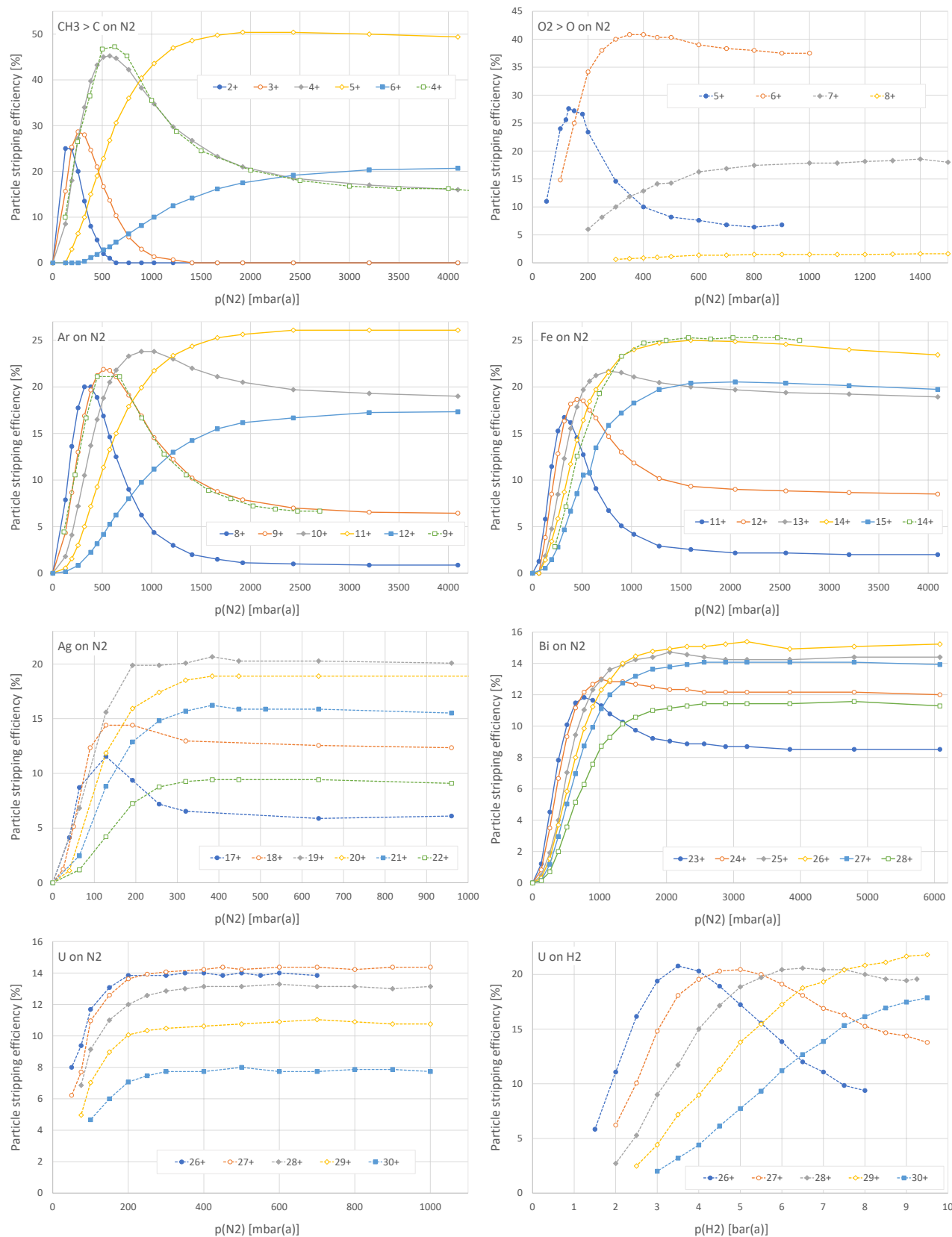


Figure 4: Particle stripping efficiencies measured for different ions and molecules, charge states and stripping gases. Dashed and solid lines indicate data taken with a standard or modified injection valve respectively, refer to the text for details.

for driving the valves were adapted in order to reduce the mechanical stress on the valves.

STRIPPING DATA

The beam time operation permitted the acquisition of stripping data for a large number of ion species. This is difficult to achieve during dedicated machine development beam times, because every change of the ion species requires an exchange of the ion source and a complete setup of the beam up to the gas stripper, which takes up a lot of time. With a new ion species set up during user beam time routinely every few weeks, this now comes for free. The drawback is, that the time for data taking is extremely limited because it requires exclusive operation of the accelerator while the users are already waiting for the beam. To support this, during beam time 2025 the data taking was approved as an official accompanying machine experiment, allowing for ≈ 1 h of beam time per ion species.

The graphs in Fig. 4 show exemplary stripping data for light, intermediate and heavy ions and the molecule CH_3 stripped by H_2 or N_2 as indicated in the upper left corner of each graph. The plotted data are particle stripping efficiencies as a function of the applied system pressure for several charge states per ion species. They were taken using valves without and with the added orifice, indicated by dashed and solid lines respectively. For CH_3 , Ar and Fe, a single curve measured without orifice is plotted together with several curves measured with orifice in the same graph for comparison, with the single curve's pressure being scaled by a factor of 5 for CH_3 and 4.5 for Ar and Fe, respectively. It has to be mentioned, that all data were taken manually during the user beam time. Due to various reasons, significant systematic and random errors should be considered, as is obvious for some data points.

During both beam times, similar data were also taken for O_2 , Ar, Ti, Cr, Fe, Ni, Kr, Mo, Ag, Er, Au, Pb, Bi, and U. All species were exclusively stripped by N_2 except uranium, which was also stripped by H_2 .

CONCLUSIONS AND OUTLOOK

The opportunity to extensively test the pulsed gas stripper before the system is completed and ready for regular operation was unexpected and on short notice. Nevertheless, after a short preparation period, about one year of successful operation during two user beam times was achieved and yielded results, which could not have been gained otherwise. Several issues have been identified or confirmed, some of them being anticipated. Some improvements have already been implemented and tested, others are planned to be realized soon. The latest status report of the pulsed hydrogen gas stripper project with more details is available in [9]. Valuable experiences and a significant amount of stripping data was acquired for a broad range of ion species, demonstrating that the performance of the pulsed gas stripper covers all operational expectations.

The main parts remaining for the completion of the pulsed stripper are the automated gas control station and the integration into the accelerator control system, a dilution device for the safe disposal of the hydrogen, a fully-fledged interlock system and the production version of the stripper setup. The call for tenders for the gas control station was recently published, installation and commissioning are planned for 2026. The dilution device is currently in development, simulations for a proof-of-concept are in progress. The design of the interlock system is in an early planning stage, while the design of the production stripper is in a final stage (Fig. 5). It will contain four valves, two for each gas type with one for operation at high and low pressure each.

ACKNOWLEDGMENTS

The authors would like to thank all the colleagues who provided immediate, straightforward help and constant assistance during beam time operation and for the whole project. Special thanks go to the vacuum department as well as the operating crew for their patience, and to the beam diagnostics.

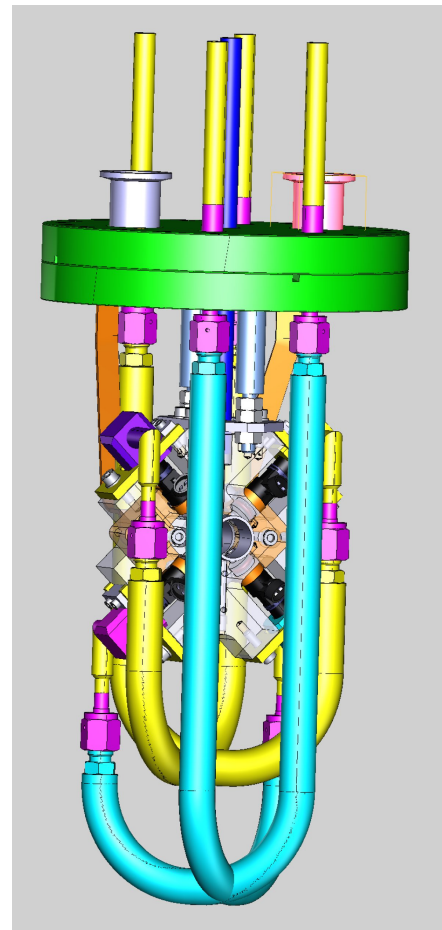


Figure 5: Sketch showing the current design status of the production stripper, containing four injection valves in an X-configuration.

REFERENCES

- [1] U. Ratzinger, “The New GSI Prestripper Linac for High Current Heavy Ion Beams”, in *Proc. LINAC’96*, Geneva, Switzerland, Aug. 1996, paper TU202, pp. 288–292.
- [2] W. Barth and P. Forck, “The New Gas Stripper and Charge State Separator of the GSI High Current Injector”, in *Proc. LINAC’00*, Monterey, CA, USA, Aug. 2000, paper MOD13, pp. 235–237.
- [3] B. Schlitt *et al.*, “Charge Stripping Tests of High Current Uranium Ion Beams with Methane and Hydrogen Gas Strippers and Carbon Foils at the GSI UNILAC”, in *Proc. IPAC’13*, Shanghai, China, May 2013, paper THPWO010, pp. 3779–3781.
- [4] P. Scharrer *et al.*, “Stripping of High Intensity Heavy-Ion Beams in a Pulsed Gas Stripper Device at 1.4 MeV/u”, in *Proc. IPAC’15*, Richmond, VA, USA, May 2015, pp. 3773–3775. doi:10.18429/JACoW-IPAC2015-THPF035
- [5] P. Scharrer *et al.*, “A Pulsed Gas Stripper for Stripping of High-Intensity, Heavy-Ion Beams at 1.4 MeV/u at the GSI UNILAC”, in *Proc. HIAT’15*, Yokohama, Japan, Sep. 2015, paper TUA1C01, pp. 144–147.
- [6] P. Scharrer *et al.*, “Developments on the 1.4 MeV/u Pulsed Gas Stripper Cell”, in *Proc. LINAC’16*, East Lansing, MI, USA, Sep. 2016, pp. 387–389. doi:10.18429/JACoW-LINAC2016-TUOP03
- [7] P. Gerhard *et al.*, “Development of Pulsed Gas Strippers for Intense Beams of Heavy and Intermediate Mass Ions”, in *Proc. LINAC’18*, Beijing, China, Sep. 2018, pp. 982–987. doi:10.18429/JACoW-LINAC2018-FR1A05
- [8] P. Gerhard and M. T. Maier, “On the UNILAC Pulsed Gas Stripper at GSI”, in *Proc. LINAC’22*, Liverpool, UK, Aug.-Sep. 2022, pp. 258–261. doi:10.18429/JACoW-LINAC2022-MOPORI13
- [9] M. Maier, P. Gerhard, and L. Groening, “Status of the pulsed hydrogen gas stripper project at GSI”, presented at the IPAC’25, Taipei, Taiwan, Jun. 2025, paper TUPB034, unpublished.

RF POWER LIMITS OF 4-ROD RFQS*

H. Podlech^{†1,2}, P. Braun, H. Hähnel, K. Kümpel, U. Ratzinger², J. Storch, S. Wagner, C. Zhang^{1,3}

Institute for Applied Physics, Goethe University, Frankfurt, Germany

¹also at Helmholtz Research Academy Hesse for FAIR (HFHF),
GSI Helmholtzzentrum für Schwerionenforschung, Frankfurt, Germany

²also at Bevatech GmbH, Walldorf-Mörfelden, Germany

³also at GSI Helmholtzzentrum für Schwerionenforschung, Darmstadt, Germany

Abstract

Radio Frequency Quadrupoles (RFQ) are today the standard structures for focusing, bunching and accelerating a DC beam delivered by an ion source. Regardless of the used RF structure, 4 electrodes (rods, vanes) are periodically charged by RF fields and generate a time varying electric quadrupole field. The two most common RF structures are the 4-Vane RFQ and the 4-Rod RFQ. While the 4-Vane RFQ is a cavity operated in the TE_{211} -mode, the 4-Rod RFQ is a transmission line resonator consisting of a chain of strongly coupled RF cells. The 4-Rod RFQ is the most frequently used structure for frequencies below 250 MHz. In the past, the 4-Rod RFQ had problems with high power operation and high average thermal load. In the last years, a vigorous R&D program has been performed to make the 4-Rod RFQ suitable for such applications. The progress of the development of high power 4-Rod RFQs with associated projects are presented.

INTRODUCTION

RFQ accelerators operated with high power and high duty factor up to cw facing in general many challenges. The most common problems are local excessive heating due to high power densities and thermal instabilities resulting in significant frequency shifts. The most prominent example of a 4-Rod high power RFQ developed in the past is the SARAF RFQ. This 3.9 m long RFQ has been designed to accelerate a 4 mAduteron beam to 1.5 AMeV with 100% duty factor. The required total RF power of 250 kW resulted in a thermal load of more than 60 kW/m. Although the SARAF RFQ could successfully accelerate protons (cw) and deuterons (50%), it was not possible to reach the full power level. Finally, it was required to re-design the electrodes with lower beam energy (1.27 AMeV) to limit the RF power to 200 kW [1]. Based on this experience, an R&D program has been initiated to optimize the 4-Rod structure, especially with respect to high power operation.

176 MHZ RFQ PROTOTYPE

As part of the R&D program, the cooling of stems, electrodes, and tuning plates was optimized in particular. A new manufacturing method using thick-film copper plating was established. For this purpose, the cooling channels were

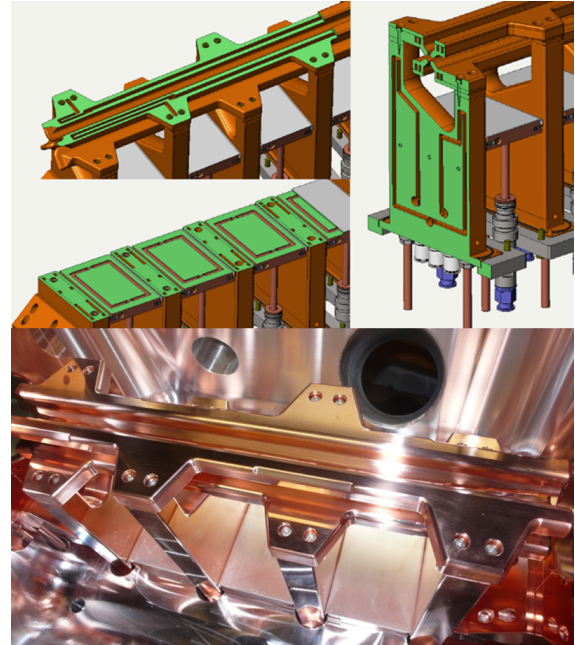


Figure 1: Cooling channels of the 176 MHz RFQ prototype (top), fabricated prototype (bottom).

milled into the individual blanks (electrodes, stems, tuning plates), filled with conductive wax, and then copper plated several millimeter thick. This was followed by final machining to the required dimensions and removal of the wax. Figure 1 shows the cooling channels of the 176 MHz proto-

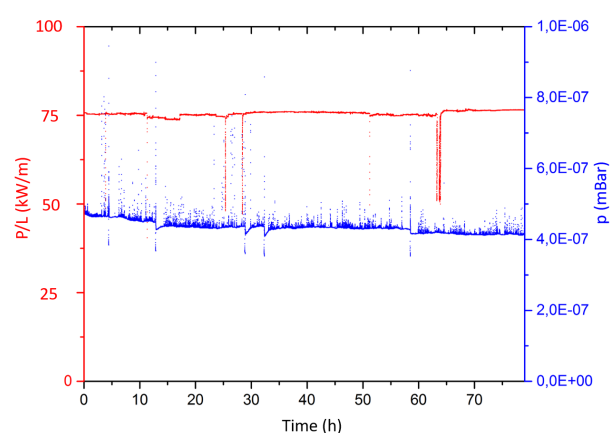


Figure 2: Prototype long run test with 30 kW (75 kW/m).

* BMBF Project No. 05P15RFRBA, HFHF, LOEWE No. HA1575/23-128

[†] h.podlech@iap.uni-frankfurt.de

type and the manufactured 40 cm long RFQ prototype. Since there are essentially no tank wall losses, it has been decided to use an aluminum tank without copper plating. Low-level RF measurements showed a Q_0 value of 4300 and a shunt impedance of 73 k Ω m, respectively. This is approximately 75% of the value given by simulations. In recent years, several test campaigns have been conducted with the RFQ prototype. Figure 2 shows the result of a long run test at a specific power of 75 kW/m. Finally, the prototype could be operated stably with an RF power of 50 kW, which corresponds to a thermal load of 125 kW/m. The maximum power was 60 kW cw or 150 kW/m. At this power level, the limit was exceeded and there was a damage to the transition between a tuning plate and stem (Fig. 3).



Figure 3: Damage at the transition between tuning plates and stems after operation with 150 kW/m.

PROJECTS

The success of these developments paved the road for the use of the 4-Rod RFQ in different projects that asked for high-power and high-duty factors up to cw operation.

MYRRHA

MYRRHA is an European project that aims to demonstrate the large-scale feasibility of nuclear waste transmutation based on a spallation source and a subcritical reactor. The proton Linac delivers a 600 MeV, 4 mA cw beam, resulting in a beam power of 2.4 MW [2]. The MYRRHA RFQ operates at 176.1 MHz and accelerates the beam from 30 keV to 1.5 MeV within a length of 4 m. Due to the challenging reliability requirements of the MYRRHA project, the RFQ design is very conservative with respect to electrode voltage (44 kV) and beam dynamics. In addition, it is the first 4-Rod RFQ with full dipole compensation [3]. The RFQ has been conditioned up to a cw power of 145 kW without any issue. Beam tests showed a very high transmission of 98% without any measurable emittance growth [4]. Figure 4 shows operational RFQ and the RF commissioning to 145 kW. The total commissioning time was about 9 days.

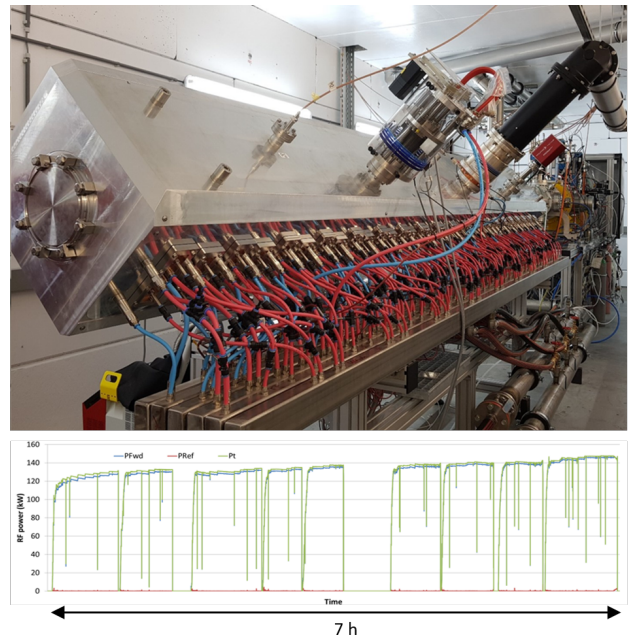


Figure 4: Operational MYRRHA RFQ (top), RF conditioning from 120 kW to 145 kW (bottom).

FRANZ

The Frankfurt neutron source FRANZ is a small-scale compact accelerator-based neutron source. It can deliver a 30 mA proton beam with an energy of 2 MeV to a lithium target. The RFQ accelerates protons from 60 keV to 700 keV within 1.7 m (Fig. 5). A short IH-cavity directly coupled to the RFQ provides 1.3 MV of additional voltage. The Linac can provide almost any beam pulse scheme but can also be operated in cw mode. The RFQ has been commissioned up to 85 kW cw RF power. The beam tests showed a very high transmission close to 100% [5].

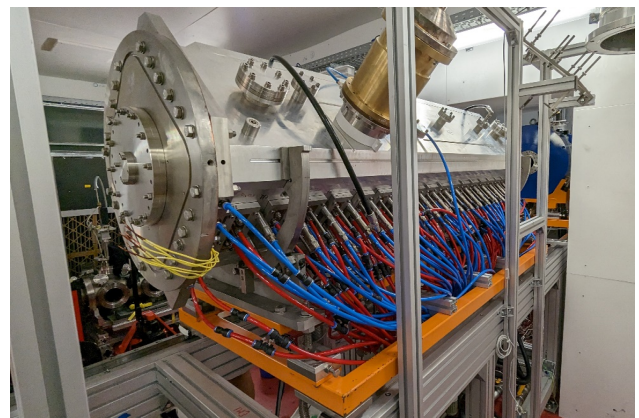


Figure 5: RFQ of the Frankfurt Neutron Source FRANZ.

GSI High Charge Injector

The High Charge Injector (HLI) at GSI/Darmstadt was originally designed to accelerate ions with a maximum A/q

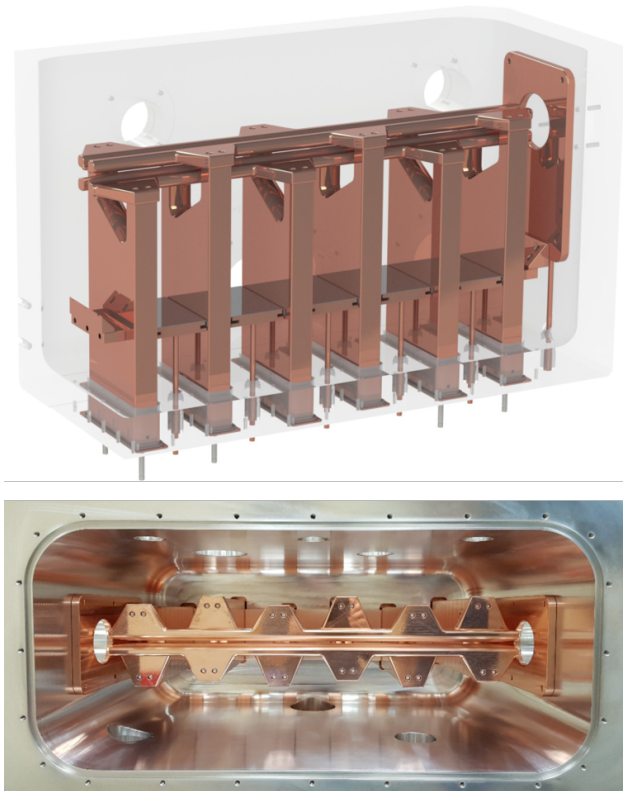


Figure 6: Rendered 3D-Model of the new HLI-Prototype (top) and the realized RF structure (bottom).

of 8.5 with a duty factor of 25%. Since the HLI will serve as the injector for the superconducting cw heavy ion Linac HELIAC in the future, a new RFQ was developed that was to be operated for an A/q ratio of 6 with 100% duty factor. However, it turned out that the RFQ suffers from barely controllable mechanical oscillations and thermal instabilities [6]. Therefore, it was decided to develop another RFQ with optimized properties. Figure 6 schematically shows the 108 MHz prototype and the realized RF structure. Performance tests confirmed (up to 30 kW/m that the prototype meets the requirements in terms of both mechanical stability and cooling [7]. It is planned to start construction in 2026.

High Brilliance Neutron Source

The High Brilliance Neutron Source (HBS) [8] currently under development at Forschungszentrum Jülich is scalable in terms of beam energy and power due to its modular design. The driver Linac will accelerate a 100 mA proton beam to 70 MeV. The Linac can be operated with a duty factor of up to 25%. The technology of the Linac is based on the MYRRHA injector design. The pulsed operation allows it to increase the specific RF power by a factor of 4 keeping the thermal load in the same range as MYRRHA (up to 30 kW/m). The high beam current is challenging with respect to beam dynamics asking for a rather high electrode voltage in the RFQ of 85 kV. In addition, the transition energy into the CH-DTL should be around 2.5 MeV. Because of the frequency of 176 MHz, the resulting RFQ would have

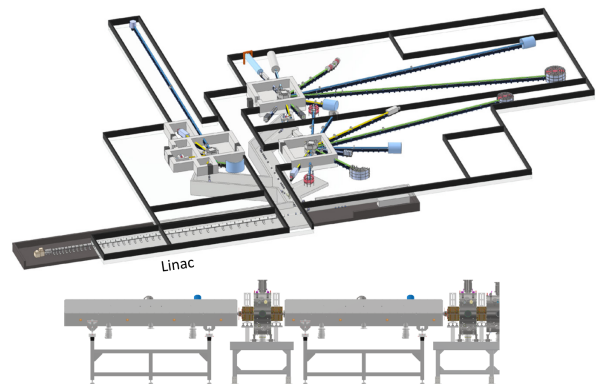


Figure 7: Overview of the HBS project(top) and double-RFQ (bottom).

a length exceeding 6 m. Therefore, it has been decided to use two RFQs with a short matching-section between them at an energy of 1.25 MeV (Fig. 7). The required peak power of both RFQs is 100 kW/m [9].

FURTHER IMPROVEMENTS

Despite the significant progress made, further improvements are planned. Conventional production methods have the disadvantage that optimum cooling channels cannot be realized. This is where additive manufacturing (“3D-printing”) can be helpful. Therefore, it is planned to realize the inner structure of the prototype using additive manufacturing, in particular to improve cooling in areas with very high power density. The outer geometry of the resonance structure is to be retained so that the results can be better compared with the existing prototype. In parallel, several issues as thermal conductivity, surface properties, erosion corrosion and dimensional stability are being addressed [10]. Figure 8 shows the present cooling channels (left) and the cooling based on additive manufacturing. In addition, a new RFQ

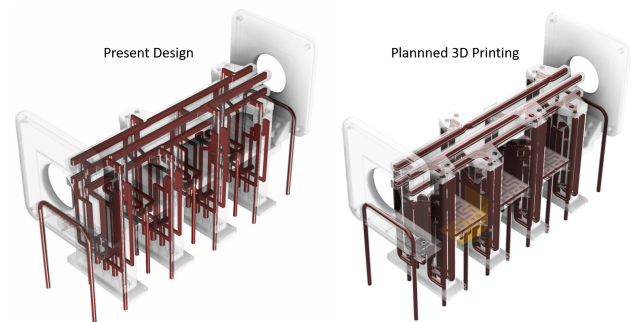


Figure 8: Cooling channels with conventional manufacturing (left) and with additive manufacturing (right).

demonstrator is being under construction in close cooperation between IAP and Bevatech GmbH. It aims for about 10% higher shunt impedance (improved RF contacts), better vacuum by using metal seals and higher alignment. In addition, a new RFQ demonstrator is being under construction

in close cooperation between IAP and Bevatech GmbH. It aims for about 10% higher shunt impedance (improved RF contacts), better vacuum by using metal seals and higher alignment accuracy. The main idea is the use of massive tuning block instead of tuning plates. Tension rods will be used to realize a press fitting and excellent RF and thermal contact between the tuning blocks and stems [11] (Fig. 9). RF power tests are foreseen in 2025.

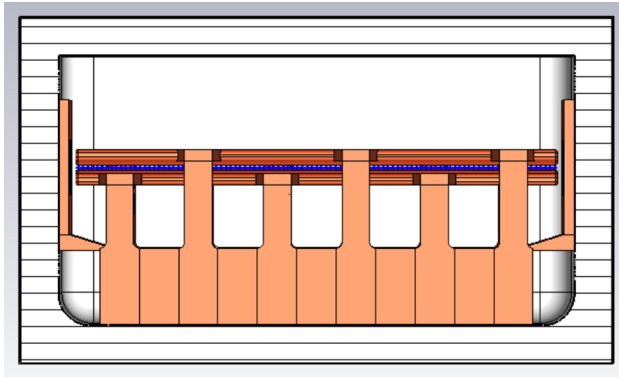


Figure 9: Model of the LOEWE-3 RFQ demonstrator.

CONCLUSIONS

The R&D program has produced impressive results in the operation of high power 4-Rod RFQs and in the power levels that can be achieved stably. In addition, a series of measures not mentioned here in the area of beam dynamics and end-field optimization have now led to extremely high transmissions in operation.

This makes the 4-Rod RFQ an attractive alternative to the 4-Vane RFQ for frequencies below 250 MHz not only for heavy ions but also for protons and deuterons in the context of high current accelerator based neutron sources.

ACKNOWLEDGEMENTS

The authors would like thank the technical staff at IAP and all collaborators at FZ Jülich, GSI, SCK•CEN and Bevatech GmbH.

REFERENCES

- [1] L. Weissman *et al.*, “Installation, high-power conditioning and beam commissioning of the upgraded SARAF 4-rods RFQ”, *J. Instrum.*, vol. 13, no. 05, p. T05004, May 2018. doi:10.1088/1748-0221/13/05/t05004
- [2] D. Vandeplasse, J.-L. Biarrotte, H. Klein, and H. Podlech, “The Myrrha Linear Accelerator”, in *Proc. IPAC’11*, San Sebastian, Spain, Sep. 2011, paper WEPS090, pp. 2718–2720. <https://jacow.org/IPAC2011/papers/WEPS090.pdf>
- [3] K. Kümpel, H. C. Lenz, N. F. Petry, H. Podlech, A. Bechtold, and C. Zhang, “Dipole Compensation of the 176 MHz MYRRHA RFQ”, in *Proc. IPAC’17*, Copenhagen, Denmark, May 2017, pp. 2240–2242. doi:10.18429/JACoW-IPAC2017-TUPVA070
- [4] A. Gatera *et al.*, “Minerva (MYRRHA Phase 1) RFQ Beam Commissioning”, in *Proc. IPAC’21*, Campinas, Brazil, May 2021, pp. 675–678. doi:10.18429/JACoW-IPAC2021-MOPAB205
- [5] H. Hähnel *et al.*, “High-power RF conditioning and 700 keV beam commissioning of the revised RFQ for the Frankfurt Neutron Source”, in *Proc. IPAC’24*, Nashville, TN, USA, May 2024, pp. 3497–3500. doi:10.18429/JACoW-IPAC2024-THPR09
- [6] P. Gerhard *et al.*, “Experience with a 4-Rod CW Radio Frequency Quadrupole”, in *Proc. LINAC’12*, Tel Aviv, Israel, Sep. 2012, paper THPLB07, pp. 825–827.
- [7] S. R. Wagner, M. Basten, D. Koser, and H. Podlech, “High Power Tests of a New 4-Rod RFQ with Focus on Thermal Stability”, in *Proc. HIAT’22*, Darmstadt, Germany, Jun.-Jul. 2022, pp. 93–95. doi:10.18429/JACoW-HIAT2022-TUP10
- [8] T. Gutberlet *et al.*, “High Current Accelerator-driven Neutron Sources - The HBS project for a next generation neutron facility” *Nucl. Sci. Technol. Open Res.*, vol. 3, p. 10, Feb. 2025. doi:10.12688/nucleartechopenres.17606.1
- [9] J. Baggemann *et al.*, R. Gebel, A. Lehrach, H. Podlech, “Technical Design Report HBS Volume 1 – Accelerator”, R. Gebel, A. Lehrach, H. Podlech, Eds., Forschungszentrum Jülich GmbH, Jülich, Germany, ISBN 978-3-95806-709-7, 2023.
- [10] J.-S. Storch, E. Boos, H. Hähnel, H. Podlech, K. Kümpel, and P. Braun, “Improvements to 4-rod RFQs with additive manufacturing processes”, in *Proc. IPAC’24*, Nashville, TN, USA, May 2024, pp. 3494–3496. doi:10.18429/JACoW-IPAC2024-THPR08
- [11] K. Kümpel, H. Hoeltermann, H. Podlech, J. Storch, S. Altürk, and U. Ratzinger, “The LOEWE-3 RFQ project”, in *Proc. IPAC’24*, Nashville, TN, USA, May 2024, pp. 3485–3487. doi:10.18429/JACoW-IPAC2024-THPR05

A CHARGE STRIPPER RING FOR RIKEN RI BEAM FACTORY

H. Imao*

RIKEN Nishina Center, Wako, Japan

Abstract

The Charge Stripper Ring (CSR), developed at RIKEN RI Beam Factory (RIBF), is designed to enhance the intensity of uranium heavy-ion beams. CSR features a structure in which multiple charge states of the beam are simultaneously circulated while undergoing repeated charge exchange with an internal target, enabling both high-efficiency charge conversion and continuous-wave operation. To address the complexity arising from stochastic charge-state transitions, a dedicated simulator based on linear beam dynamics was developed. Using this tool, tuning strategies and tolerance evaluations were performed, yielding favorable results. Furthermore, the CSR concept is extended to propose a new class of ring accelerator, termed “Chreostron,” which recycles heavy-ion beams through internal targets with charge exchange. Its potential applications and associated theoretical challenges are discussed.

INTRODUCTION

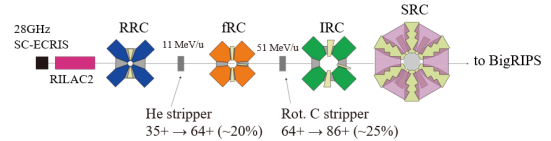
The RIKEN Radioactive Isotope (RI) Beam Factory (RIBF) [1] is a major heavy-ion accelerator facility that has enabled extensive research on unstable nuclei. A key achievement of RIBF is the production of rare neutron-rich RI beams via in-flight fission of high-intensity uranium beams. These rare isotopes have been essential for experimental studies related to the astrophysical r-process, establishing RIBF as a central facility in the field. The scientific output from RIBF has significantly advanced low-energy nuclear physics and has promoted the development of next-generation RI beam facilities worldwide. The FRIB in the United States began operation in 2022, while RAON (Korea), HIAF (China), and FAIR (Germany) are under construction.

To further expand its scientific reach, an upgrade to RIBF is proposed to access proton-rich and heavy nuclei with atomic numbers greater than ~ 50 . These nuclei are expected to exhibit complex and rich nuclear phenomena such as alpha clustering and fission. The production of rare RI beams in the region will be achieved via projectile fragmentation using more intense uranium beams.

A key technical limitation at RIBF is the low charge-state conversion efficiency at the charge strippers, which restricts further enhancement of uranium beam intensity. Addressing this issue is critical for realizing the full potential of the proposed upgrade and for accessing previously unexplored regions of the nuclear chart. Currently, two types of charge strippers are employed: a helium gas stripper [2–4] and a rotating graphite disk stripper [5, 6]. The combined conversion efficiency for uranium beams is approximately 5%, which imposes a significant constraint on the achievable beam intensity. This limitation directly

impacts the overall performance of the RIBF accelerator complex. To overcome this limitation, a novel ring-based system known as the Charge Stripper Ring (CSR) [7, 8] has been proposed to significantly enhance charge conversion efficiency (Fig. 1).

(A) Present acceleration scheme for uranium ions



(B) New acceleration scheme with CSR1 and CSR2

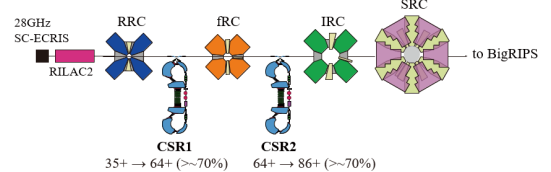


Figure 1: Comparison between the current acceleration scheme for uranium ions and the proposed new scheme utilizing CSR1 and CSR2. The new approach aims to enhance charge state conversion efficiency by a factor of ten, offering significant improvements in beam quality and overall acceleration performance.

CSR is a dedicated ring that incorporates an internal target (stripper), allowing the beam to repeatedly pass through the stripper and thereby increase the likelihood of charge-state conversion. The ring is designed to be isochronous, enabling ions of different charge states to circulate along paths of equal length, and supports continuous-wave (CW) operation similar to that of a cyclotron. It also includes energy-recovery cavities and charge-independent beam focusing elements to maintain stable and efficient beam transport.

Currently, RIBF is advancing the design works of CSR1, intended for use as the first stripper for uranium beams. The CSR1 operates at a circulation energy of 10.8 MeV/u, injecting uranium ions in the 35+ charge state and extracting ions in the 64+ state with an efficiency exceeding 60% (more than three times the current performance). This represents a promising technological advancement for increasing uranium beam intensity.

This report presents the principles, design, and beam tuning methodology of CSR, and introduces the conceptual framework of Chreostron, a generalized extension of CSR with broad potential applications.

BASICS OF CSR1

The CSR1 is employed as the first stripper for uranium beams at RIBF (Fig. 2). It operates with an initial injection

*imaoh@riken.jp

of U^{35+} beam bunches at a kinetic energy of 10.8 MeV per nucleon and a frequency of 18.25 MHz. Upon entering the ring, the U^{35+} ions pass through a two-stage gas stripper composed of nitrogen and helium, where they undergo stochastic charge state transitions. Among the resulting charge states, eight dominant components (U^{59+} to U^{66+}) are continuously introduced into the ring orbit via charge exchange injection from U^{35+} and circulate along orbits with identical circumference for all charge states. The energy loss during each passage through the stripper is approximately 2 percent of the initial kinetic energy, and is compensated by built-in RF acceleration cavities. As a result, the eight charge states are simultaneously transported within the CSR1 at equal energy. Of these, U^{64+} ions are continuously extracted from the CSR1 using a static magnetic kicker. This process selectively extracts particles that have stochastically transitioned to the U^{64+} charge state after passing through the stripper, and can be regarded as a form of charge-exchange extraction. The remaining seven charge states continue to circulate within the ring and are repeatedly injected into the stripper along with newly injected U^{35+} bunches, thereby undergoing successive charge-state conversion cycles.

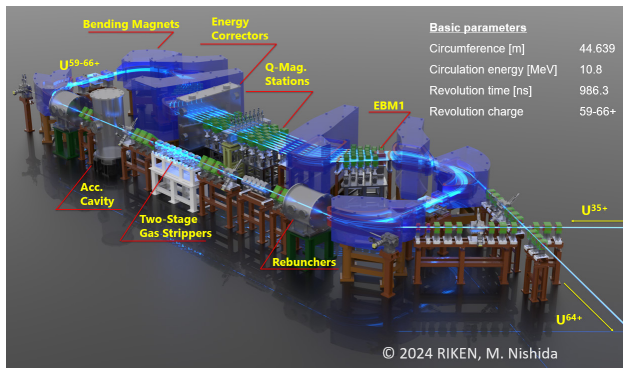


Figure 2: Realistic 3D representation of CSR1, including key structural components and fundamental design parameters.

During the charge-state conversion process in the stripper, the charge states of ions within the beam bunch change randomly, resulting in mixing among beams of different charge states. If the phase-space alignment among the injected beams of different charge states is not properly matched, this mixing can lead to emittance growth in the resulting combined beam. To prevent this in CSR1, the phase-space ellipses in all three dimensions at the stripper location are carefully matched to be similar and upright for all charge states. Additionally, the zero-dispersion condition is satisfied at the stripper. Moreover, the isochronous condition, which is nearly equivalent to the equal path length condition, is fulfilled for the circulating orbits of all charge states, ensuring temporal synchronization at the stripper location. In other words, the bunch structure is preserved. These design features collectively enable the maintenance of beam quality and stable operation in CW mode.

CSR1 consists of the following key components. First, a two-stage gas stripper using helium (He) and nitrogen (N_2)

is employed for charge-state conversion. This configuration is designed to suppress charge-state drift during circulation within CSR, thereby preventing the beam from deviating from the eight charge states that are capable of stable circulation. To establish isochronous orbits for all circulating charge states, eight main bending magnets (BM1–BM8) are arranged around the ring. These magnets are designed to ensure that beams of different charge states circulate with the same orbit length. To compensate for the energy loss of approximately 2% caused by passage through the stripper, an accelerating cavity is installed within the ring. Additionally, independently configured energy correctors for each charge state provide fine energy tuning, ensuring energy consistency among the simultaneously circulating multi-charge-state beams. A rebuncher is installed to support longitudinal focusing and matching of the beam. For transverse focusing and matching, four quadrupole magnet stations (QS1–QS4) are employed, consisting of a total of 63 charge-state-independent quadrupole magnets. This configuration allows independent and flexible focusing for beams of different charge states. Beam injection and extraction are handled by dedicated bending magnets (e.g., EBM1), with U^{64+} ions selectively extracted using the static magnetic kicker EBM1. In addition, several steerers are installed to correct closed orbit distortions (COD), along with diagnostic vacuum chambers for monitoring the beam conditions. These components are essential for enabling CSR1 to achieve simultaneous multi-charge-state transport, CW operation, and precise matching among beams of different charge states.

LATTICE DESIGN

In CSR1, eight equilibrium orbits corresponding to eight charge states (U^{59+} to U^{66+}) are considered, although U^{64+} is extracted midway and does not actually circulate. The lattice is a mirror-symmetric achromatic system. (Here, the circulating energy is assumed to be constant, and details related to energy loss and recovery are neglected.) The helium stripper is placed at the symmetry plane of the achromatic section.

Each time the beam passes through the stripper, the charge state changes. Ideally, the ions continue to circulate while stochastically transitioning between charge states until they reach U^{64+} and are extracted. To avoid emittance growth due to mismatches among the eight optics configurations, the lattice is designed so that the phase-space ellipses in all three dimensions at the stripper location (eigenellipse) are identical for all charge states. The injected U^{35+} beam is matched to this common eigenellipse.

To achieve transverse matching of the eigenellipse, charge-state-independent quadrupole magnets are arranged in four quadrupole magnet stations (QS1–QS4). For longitudinal matching, two rebunchers (Reb1 and Reb2) are placed in the achromatic section. All focusing elements are arranged symmetrically to preserve mirror symmetry.

Let $R'(q)$ be the 6×6 one-turn transfer matrix for charge state q . Using the half-cell matrix $M'(q)$ and its mirror-symmetric counterpart $M'_R(q)$, we can write as $R' = M'_R M'$. Let $A(q)$ be the transfer matrix from the stripper to

the rebuncher, $B(q)$ the matrix from the rebuncher to the midpoint (endpoint of half-lattice), and $K(q)$ the linear kick matrix at the rebuncher, with $K_{56} = -k$. The half-lattice transfer matrix is then written as $M' = BKA$. If we define the matrix without the kick as $M = BA$, then the full one-turn matrix R' can be simplified using the elements of M as:

$$R' = \begin{pmatrix} 2M_{11}M_{22} - 1 & 2M_{12}M_{22} & 0 & 0 & 0 & 0 \\ 2M_{21}M_{22} & 2M_{11}M_{22} - 1 & 0 & 0 & 0 & 0 \\ 0 & 0 & 2M_{33}M_{44} - 1 & 2M_{34}M_{44} & 0 & 0 \\ 0 & 0 & 2M_{43}M_{33} & 2M_{33}M_{44} - 1 & 0 & 0 \\ 0 & 0 & 0 & 0 & \frac{2ab-1}{a+b-2}M_{56} & 0 \\ 0 & 0 & 0 & 0 & \frac{2b(a+b-2)}{M_{56}} & 2ab-1 \end{pmatrix}.$$

Here, the condition $M_{26} = 0$ is required, and the parameters are defined as $a = (K \cdot A)_{66} = 1 - k \cdot A_{56}$, and $b = 1 - k \cdot B_{56}$. In CSR, the lattice described above is applied to all circulating charge states.

The components of the one-turn matrix R' are decoupled in all directions and can be treated independently. The conditions $R'_{16} = R'_{26} = 0$ confirm that the system is achromatic. The symplectic condition $R'_{51} = R'_{52} = 0$ ensures that the orbit length is independent of the ion's position and angle at the stripper. Due to symmetry, it is evident that $R'_{11} = R'_{22}$, $R'_{33} = R'_{44}$, and $R'_{55} = R'_{66}$, indicating that the phase-space ellipses in all three dimensions are upright. In this case, the Twiss parameter $\alpha = 0$, since α is antisymmetric with respect to the symmetry point, resulting in a beam waist at the center of the stripper. This is advantageous for minimizing emittance growth and facilitating passage through the stripper orifice. To ensure matching of the eigenellipses for all eight charge states under the condition $M_{26} = 0$, the beta functions β_x , β_y , and β_z at the center of the stripper must be identical, with their values determined by considering the sources of emittance growth during CSR1 circulation.

A linear optics calculation was performed to determine whether a solution exists under realistic conditions for CSR1 that ensures the matching of eigen-ellipses in all three phase space directions. Based on the quadrupole magnet configuration shown in Fig. 3, the focusing strengths of the quadrupoles were optimized to achieve matched eigen-ellipses. The optimization targeted transverse beta functions of $\beta_x = \beta_y = 3.33$ m and a longitudinal beta function of $\beta_z = 2.40$ m.

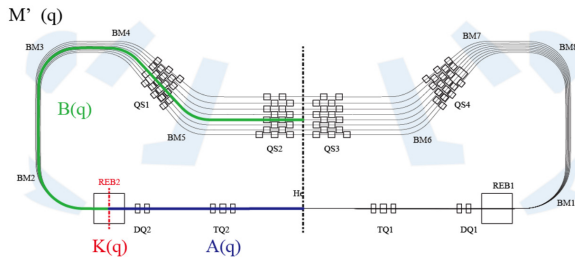


Figure 3: Schematic layout of the optical system in CSR1, including quadrupole magnet stations (QS1–QS4) and rebunchers (REB1–REB2).

During this process, the focusing strength of the charge-independent quadrupole magnets was constrained to be

below 20 T/m. Careful attention was paid to ensure that the transverse beam envelopes in the X and Y directions remained within the physical aperture, and that the momentum dispersion in dispersive regions such as the quadrupole stations did not become excessively large.

Figure 4 illustrates the beam envelopes and bunch lengths for eight charge states. The design assumes transverse emittances of $\epsilon_x = 5$ mm·mrad and $\epsilon_y = 5$ mm·mrad, and a longitudinal emittance of $\epsilon_z = 0.32$ cm·%. Under these conditions, the beta functions for all eight charge states were found to agree within 5% in all three directions.

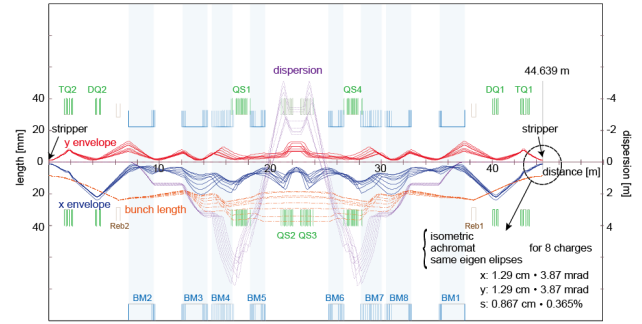


Figure 4: Example of matched beam envelopes, bunch lengths, and dispersion functions for eight charge states circulating in CSR1. All profiles coincide at the stripper location, demonstrating simultaneous matching of beam parameters under a partially shared lattice configuration.

The magnetic field gradients of the quadrupole magnets used in the optimization satisfy the constraint of being below 20 T/m, confirming that the solution is physically feasible and realistic for implementation in CSR1.

CHARGE-STATE CONVERSION COMPLEXITY AND VERIFICATION OF TUNABILITY VIA SIMULATION

One of the defining features of CSR is the inherent complexity of charge-state evolution resulting from repeated charge-exchange processes. For a beam comprising N distinct charge states circulating M times, the number of possible charge-state trajectories, i.e., lattice histories, can reach a maximum of $I + N + N^2 + \dots + N^M = (N^{M+1} - I)/(N - I)$.

In the case of CSR1, where seven charge states circulate within the ring, even at the fifth circulation stage, the number of possible lattice histories can exceed 20,000. A simplified simulation involving the injection of 10^5 beam bunches into CSR1 revealed that approximately 5×10^5 bunches circulated within the ring, resulting in the formation of over 55,000 distinct charge-state trajectories. The Simpson diversity index calculated for this distribution was 0.95, indicating an exceptionally high degree of charge-state diversity.

Such a high degree of charge-state diversity implies that the influence of resonance phenomena, typically a concern in synchrotron rings operating with a single charge state, is effectively mitigated. On the other hand, effects such as magnetic field imperfections caused by alignment errors in magnet assemblies and space-charge interactions are

expected to exhibit complex, charge-history-dependent responses. In particular, in CSR, where beam separation and recombination occur repeatedly and the beam intensity varies during circulation, evaluating the impact of space-charge effects becomes significantly more challenging than in conventional accelerators. Compensation for closed-orbit distortion (COD) and space-charge effects in circulating beam bunches with diverse charge-state trajectories represents a novel issue that has rarely been addressed in accelerator ring designs based on single-charge-state beams. These are unique challenges inherent to multi-charge-state transport rings such as CSR.

To demonstrate the principle-based tunability of CSR under various operational conditions, a dedicated simulation framework for CSR1 was developed, focusing on linear beam dynamics. The simulation was designed to be computationally lightweight while maintaining sufficient responsiveness to parameter variations. Magnet alignment errors were modeled using Brown's method [9], incorporating perturbation terms into the transfer matrices of each lattice section. Space-charge effects were evaluated using envelope equations under the assumption of elliptical beam symmetry, with divergence forces computed iteratively [10]. Furthermore, the simulator is capable of generating realistic mock signals from more than 50 beam position monitors (BPMs) distributed throughout CSR1. These signals include beam centroid positions, quadrupole moments, and timing information. By observing these simulated signals, it is possible to perform magnet tuning operations within CSR1 in a manner that closely approximates real-time adjustments in an actual machine.

In this study, various tuning parameters were systematically varied, including the trim coil strengths of quadrupole and steering magnets, the orbit correction settings of the main bending magnets, and the aperture states of beam slits and beam stoppers. Through analysis of the resulting changes in beam trajectory and emittance, a fundamental understanding of CSR1's tunability and operational stability was achieved.

Studies conducted using the CSR1 simulator have demonstrated that satisfactory tuning results can be achieved under a wide range of operational conditions (Fig. 5). It was confirmed that beam divergence caused by space-charge effects can be largely compensated using only the quadrupole magnets located in the straight section containing the stripper (Fig. 6). This result indicates that even in a multi-charge-state transport ring such as CSR, where complex physical effects differ significantly from those in conventional accelerator designs, appropriate tuning strategies can be successfully established. Furthermore, the simulator is being utilized to optimize tuning procedures and to quantitatively evaluate tolerance ranges for various error sources. These efforts are expected to enhance operational stability in the actual machine and improve the efficiency of tuning operations.

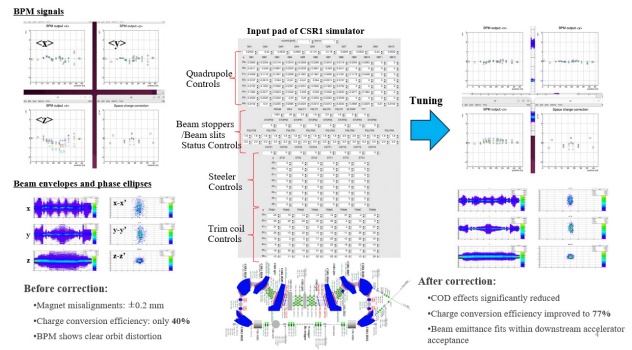


Figure 5: COD correction using the CSR simulator. Realistic BPM signals were generated by introducing random magnet misalignments. Key beamline parameters, including quadrupole strengths and steering elements, were iteratively adjusted. Effective orbit correction was achieved with acceptable alignment tolerances.

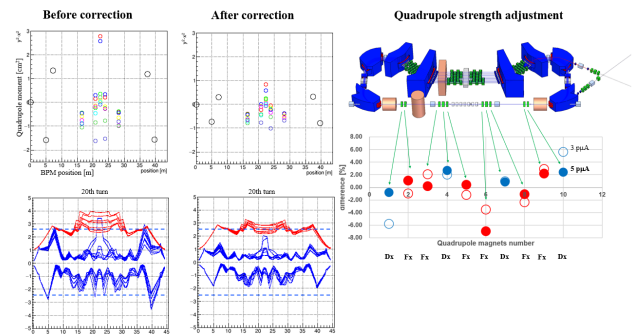


Figure 6: Figure illustrating space-charge correction via quadrupole tuning. Left: BPM signals at the 20th turn before correction, showing betatron oscillations exceeding the aperture (dotted lines). Center: corrected signals confined within the target aperture. Right: quadrupole adjustment below 7%, demonstrating effective compensation with minimal tuning.

As part of future developments, we are exploring the implementation of AI-assisted beam tuning techniques by utilizing the CSR1 simulator to train AI models across a wide range of operational scenarios. In beam systems characterized by multiple charge states and complex charge-state histories, AI can learn the beam's response to parameter variations under diverse conditions. Through this learning process, AI has the potential to offer rapid and highly accurate solutions to this novel and complex optimization problem that has traditionally been difficult to address through manual tuning alone.

CHREOSTRON: CONCEPTUAL EXTENSION OF CSR AND A NEW FRAMEWORK FOR ACCELERATORS

Based on the insights gained from the CSR design, we propose a generalized accelerator concept, termed the Chreostron (Fig. 7). The Chreostron is defined as a ring structure that incorporates an internal target and enables the simultaneous recycling of multiple charge states of a CW heavy-ion beam, with charge conversion occurring

during circulation. The Chreostron is designed to operate under complex conditions in which charge-state transitions and distributions occur, allowing for repeated and efficient interactions between the heavy-ion beam and the internal target. As demonstrated in the CSR, heavy ions undergo charge-state changes through interactions with the internal target and circulate along distinct orbits corresponding to their respective charge states. Consequently, it is essential to ensure the consistency of beam parameters at the location of the internal target, where charge conversion takes place, for all circulating charge states.

This expanded concept is not limited to the application of CSR as an efficient charge stripper. It also envisions a wide range of advanced functionalities, including various beam manipulations, efficient nuclear transmutation using internal targets, the effective generation and observation of rare nuclear events, and the production and utilization of secondary particles with high efficiency (Fig. 7). At the same time, the Chreostron architecture introduces new types of challenges that have not been encountered in conventional accelerators. These include the complexity of beam trajectories resulting from probabilistic charge-state transitions and the need to manage repeated interactions with internal targets. Such challenges must be generalized and formalized within the Chreostron framework, which calls for the development of new theoretical foundations in accelerator physics. Our current focus is on addressing specific technical issues within CSR. However, in the future, we aim to identify and systematize the universal principles underlying these challenges within the broader framework of Chreostron.

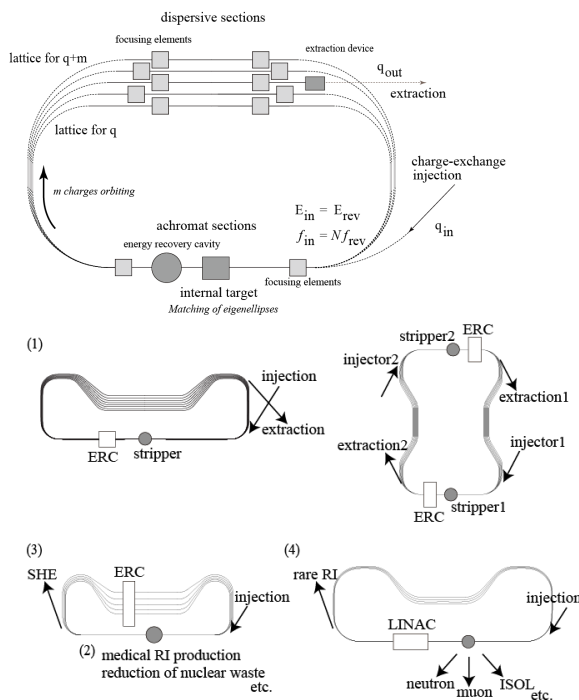


Figure 7: Conceptual illustration of Chreostron and their potential applications, including: (1) modification of heavy-ion beam characteristics, (2) transmutation of internal targets, (3) generation of rare events induced by nuclear reactions, and (4) production of secondary particles.

SUMMARY

This report presents the development of the CSR1 at RIBF, designed to enhance the intensity of uranium beams. The system architecture, operational principles, tuning strategies, and future prospects, including the Chreostron concept, are discussed. CSR1 aims to improve charge-exchange efficiency by simultaneously circulating multiple charge states of uranium ions, generated from an initially injected U^{35+} beam via an internal stripper. U^{64+} ions are selectively extracted based on probabilistic charge conversion, while other charge states are recirculated to the stripper, enabling repeated charge-exchange cycles. Due to the coexistence of multiple charge states, precise matching of beam parameters at the stripper location is essential to mitigate emittance growth and ensure stable CW operation. Dedicated simulation studies incorporating magnetic field imperfections and space-charge effects have demonstrated effective beam control through quadrupole magnet tuning. Future work includes the application of AI-based optimization using the CSR1 simulator to explore automated beam tuning.

The CSR concept has also been extended to propose a new accelerator framework, termed Chreostron, which incorporates internal targets and enables recycling of heavy-ion beams undergoing charge-state transitions. This approach is expected to support a broad range of applications, including advanced beam manipulation, nuclear transmutation, rare-event generation, and efficient production of secondary particles. However, it also introduces new challenges associated with the control of beams with complex charge-state histories and repeated interactions with high-power internal targets, requiring further theoretical and experimental investigation.

ACKNOWLEDGEMENTS

The author would like to thank the staff at the Nishina Center for Accelerator Science for their valuable support and contributions throughout this work. The author acknowledges Y. Yano and M. Wakasugi for stimulative discussions on key ideas of the CSR.

REFERENCES

- [1] Y. Yano, "The RIKEN RI Beam Factory Project: A status report," *Nucl. Instrum. Methods Phys. Res., Sect. B*, vol. 261, no. 1–2, pp. 1009–1013, Aug. 2007. doi:10.1016/j.nimb.2007.04.174
- [2] H. Okuno *et al.*, "Low-Z gas stripper as an alternative to carbon foils for the acceleration of high-power uranium beams," *Phys. Rev. Spec. Top. Accel. Beams*, vol. 14, no. 3, Mar. 2011. doi:10.1103/physrevstab.14.033503
- [3] H. Imao *et al.*, "Charge stripping of ^{238}U ion beam by helium gas stripper," *Phys. Rev. Spec. Top. Accel. Beams*, vol. 15, no. 12, Dec. 2012. doi:10.1103/physrevstab.15.123501
- [4] H. Imao *et al.*, "R&D of Helium Gas Stripper for Intense Uranium Beams," in *Proc. Cyclotrons 2013*, Vancouver BC, Canada, Sep. 2013, pp. 265–268.

- [5] H. Hasebe *et al.*, “Development of a rotating graphite carbon disk stripper,” *AIP Conf. Proc.* 1962, p. 030004, 2018.
[doi:10.1063/1.5035521](https://doi.org/10.1063/1.5035521)
- [6] H. Hasebe *et al.*, “Development of a high-density highly oriented graphite stripper,” *EPJ Web of Conferences*, vol. 229, p. 01004, 2020. [doi:10.1051/epjconf/202022901004](https://doi.org/10.1051/epjconf/202022901004)
- [7] H. Imao, “Charge Stripper Ring for RIKEN RI Beam Factory,” *IEEE Open J. Instrum. Meas.*, vol. 15, no. 12, pp. P12036–P12036, Dec. 2020.
[doi:10.1088/1748-0221/15/12/p12036](https://doi.org/10.1088/1748-0221/15/12/p12036)
- [8] H. Imao, “Status update of the Charge Stripper Rings project,” *IEEE Open J. Instrum. Meas.*, vol. 18, no. 03, p. P03028, Mar. 2023.
[doi:10.1088/1748-0221/18/03/p03028](https://doi.org/10.1088/1748-0221/18/03/p03028)
- [9] K. L. Brown, F. Rothacker, D. C. Carey, and C. Iselin, “The effect of beam line magnet misalignments,” *Nucl. Instrum. Methods*, vol. 141, no. 3, pp. 393–399, Mar. 1977.
[doi:10.1016/0029-554x\(77\)90628-0](https://doi.org/10.1016/0029-554x(77)90628-0)
- [10] F. J. Sacherer and T. R. Sherwood, “The Effect of Space Charge in Beam Transport Lines,” in *Proc. PAC’71*, Chicago, IL, USA, Mar. 1971, pp. 1066-1068.
[doi:10.1109/TNS.1971.4326279](https://doi.org/10.1109/TNS.1971.4326279)

RARE ISOTOPE BEAM TUNING IN FRIB *

K. Fukushima[†], A. C. Dombos, M. Hausmann, D. Kahl, E. Kwan,
P. N. Ostroumov, M. Portillo, B. M. Sherrill, M.K. Smith, M. Steiner
Facility for Rare Isotope Beams, Michigan State University, East Lansing, MI, USA

Abstract

The Facility for Rare Isotope Beams (FRIB) provides rare-isotope beams for user experiments in nuclear physics, nuclear astrophysics, fundamental symmetries, etc. A superconducting driver-linac accelerates heavy-ion beams onto the production target, and the Advanced Rare Isotope Separator (ARIS) collects and purifies the rare isotope fragments of interest. Subsequently, the transfer hall beamlines deliver isotopes to user setups at experiment stations. The isotope beam condition from ARIS strongly depends on the fragment of interest. Therefore, the beamline settings are optimized for each experiment based on various users' requirements on the fly. Two new beamlines in the transfer hall were commissioned in 2025, bringing the total number of available end stations to five. Since the first user experiments in 2022, ongoing beam tests and operations have continued to improve operational efficiency for users. Results and findings of beam tuning obtained from the commissioning and recent operations are reported in this paper.

INTRODUCTION

The Facility for Rare Isotope Beams (FRIB) started the scientific user program in May 2022 [1, 2]. The driver linac accelerates all stable ions above 200 MeV/u onto the production target, and the Advanced Rare Isotope Separator (ARIS) [3, 4] provides in-flight separation of projectile fragments and fission fragments. Subsequently, the transfer hall beamlines deliver isotopes to user setups at experiment stations. The transfer hall setting is optimized for each experiment to satisfy various users' requirements. We commissioned the S1 and S2 beamlines in 2025 and started user experiments. Five experiment stations are currently in operation. To optimize the performance of the transfer hall beamline, we prepare and utilize a secondary beam from the production target dedicated to tuning, the so-called pilot beam.

In the following sections, we report on the beam tuning method to deliver the separated fragment beam to the user stations.

BEAMLINE LAYOUT

Figure 1 and Fig. 2 show the beam transmission and layout of the transfer hall beamlines, respectively. The transfer hall is located downstream of ARIS and connected at Diagnostics Box 5 (DB5). There are 5 destinations in the transfer

hall: S1, S2, S3, N4S, N4N. The S1 to S3 lines are utilized for the in-flight experiments with different detectors at the end. The N4 lines are utilized for the gas-cell beam stopper and connected to the low-energy experimental area and the Re-accelerator beamline downstream. These beamlines consist of quadrupoles and switching dipoles, and both are superconducting. Typically, the transmission of the transfer hall beamlines shown in Fig. 1 is about 30 – 90%, which strongly depends on the emittance and the energy spread from ARIS. We installed a total of 18 viewer plates in the beamlines to measure the centroid and the spot size of the beam.

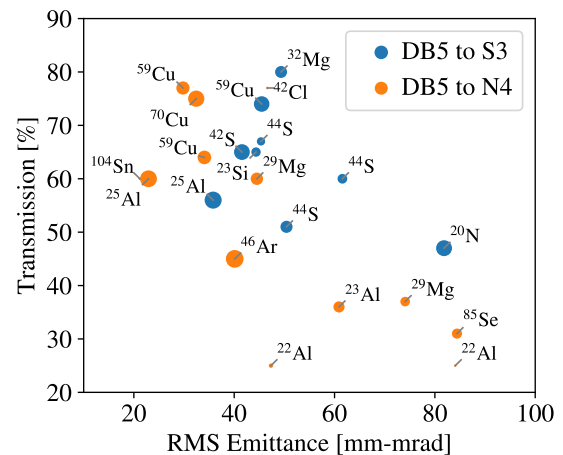


Figure 1: Transmission for user experiments from DB5 to S3 and N4 beamlines. The horizontal axis is the transverse RMS emittance at DB5, and the vertical axis is the transmission of the whole beam, including the fragment of interest (FOI), for each destination. Each dot shows the different experiments, and the dot sizes correspond to the purity of the label's FOI, which varies from 0.2% to 89.8%. Since we can measure the transmission of the whole beam only in most experiments on the fly, the transmission of the low-purity beams is less accurate.

BEAM TUNING

The beam tuning of the transfer hall is performed for each experiment, because the purity and the emittance of the beam from ARIS vary depending on the fragment of interest (FOI) required by the experiment.

As mentioned above, the purity of the fragment varies in experiments and could be lower than 1% in some cases. Also, the FOI is unevenly distributed with respect to the phase space of the entire beam. Therefore, the transmission

* Work supported by the U.S. Department of Energy, Office of Science, Office of Nuclear Physics and used resources of the Facility for Rare Isotope Beams (FRIB) Operations, which is a DOE Office of Science User Facility under Award Number DE-SC0023633 and DE-SC0024707.

[†] fukushim@frib.msu.edu

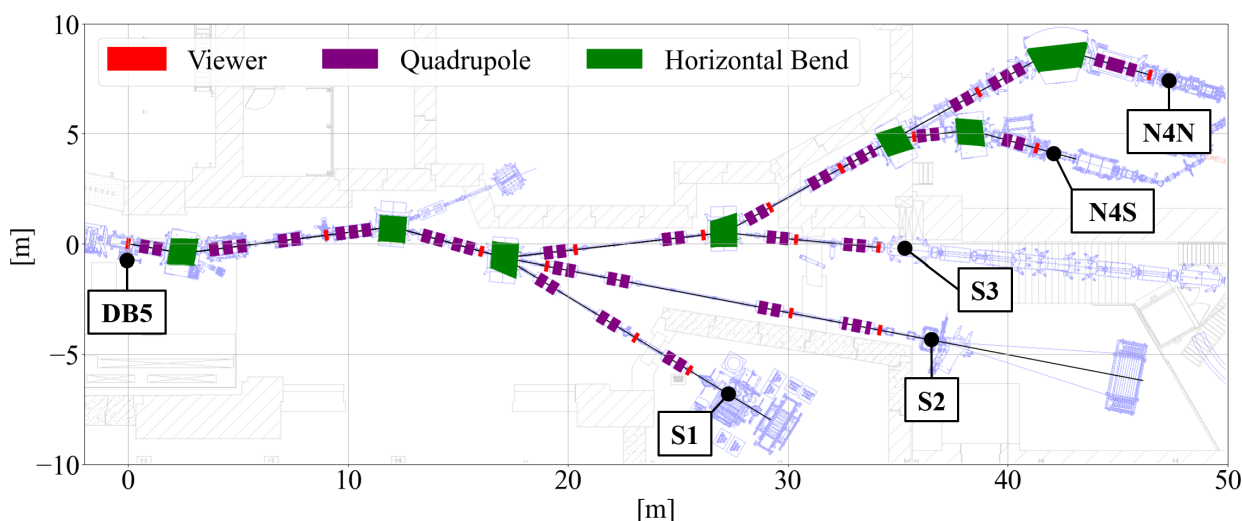


Figure 2: Transfer hall layout. The S1, S2, and S3 denote the south side, and the N4S/N denotes the north side beamlines.

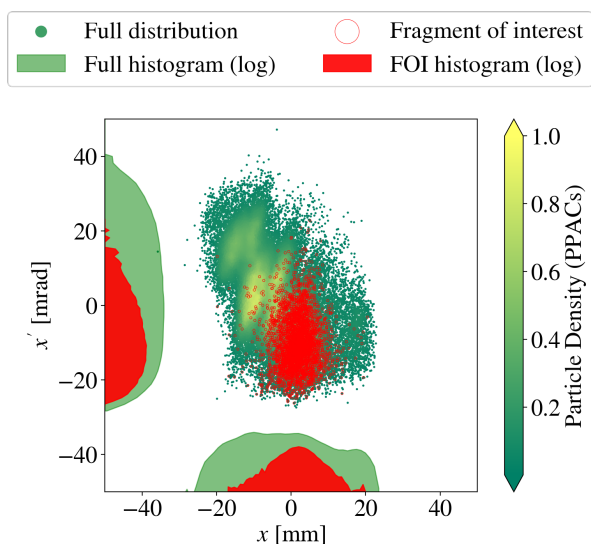


Figure 3: Horizontal (x) phase space distribution measured at DB5 PPACs. The green dots show the full beam distribution, and the red circles show the ^{99}Ag fragment of interest (FOI) distribution. The green and red histograms show the projections on each axis in a log scale. The centroid of the FOI is offset against the centroid of the whole beam.

of the entire beam does not necessarily match the transmission of the FOI. Figure 3 shows the measured phase space distribution of full and FOI (^{99}Ag) beams as an example.

To maximize the transmission of the FOI, we independently developed the pilot beam setting in the ARIS, which is the same magnetic rigidity, a high-purity, and similar phase space to the FOI. The beam tuning of the transfer hall is performed with this pilot beam, and then the separator setting is switched for the FOI. Figure 4 shows the measured phase space ellipses of the pilot beam and the FOI at the exit of the separator. In this example, the FOI is ^{128}Ag with 1.2% purity, and the pilot is ^{92}Kr cocktail with 96.8% pu-

urity. We match these phase spaces during the ARIS tuning to maximize the transmission of the FOI by using the pilot beam.

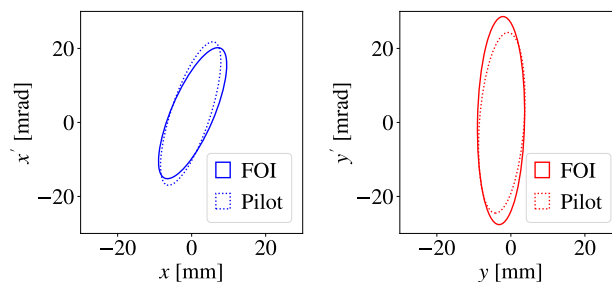


Figure 4: Measured phase space ellipses of FOI and Pilot beam. Horizontal (left) and Vertical (right) phase spaces are both matched between the FOI and pilot beams.

In the initial phase of transfer hall tuning, we measure the transverse phase space of FOI by using two parallel plate avalanche counters (PPACs) at DB5. Then, we reshape the phase space by changing the five quadrupoles around the DB5 to match the downstream beamline based on the simulation model. Next, we send the pilot beam to the viewer plates in the beamline and align the beam centroid by changing the switching dipoles and the steering magnets. In addition, the beam sizes on the viewer plates are checked with the FLAME [5,6] simulation. Figure 5 shows a typical viewer image in the transfer hall beamline. The beam size on the viewer plate is calibrated with the fiducial markers on the plate and converted pixels to physical units in real-time [7].

At the focal point of the beamline, we align the beam angle by minimizing the centroid shift on the viewer in conjunction with the offset of the upstream quadrupole field strength. Subsequently, we provide the beam to users. In some cases, the pilot beam is utilized to calibrate the user-side detector. Upon completion of detector calibration, the ARIS setting is

switched for FOI, and the user experiment is started. If the user has the beam position information from their detectors, we input it into our beamline simulation model and perform the fine-tuning of beamline magnets.

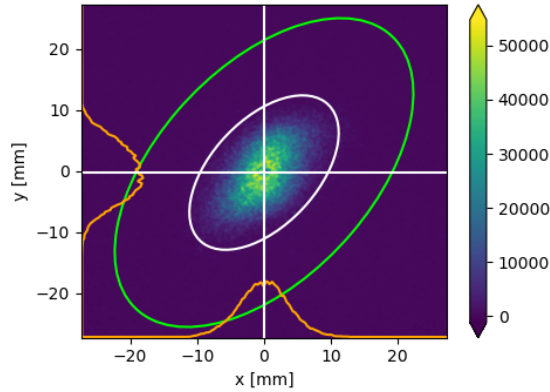


Figure 5: Viewer image in the transfer hall beamline. Horizontal and vertical white lines show the center of the beam. The white ellipse shows the 3-sigma, and the outer green ellipse shows the 6-sigma of the beam size. The orange lines show the projection of the beam to each axis.

BEAMLINE COMMISSIONING

We commissioned the S1 beamline in January 2025 and the S2 beamlines in April 2025. Figures 6 and 7 show the beam envelope of the S1 and S2 beamline. Measured beam sizes at the viewer plates agree with the simulation result. Since the beam commissioning of the S1 beamline, we have conducted five user experiments successfully in five months. User experiments with the S2 beamline will start in June 2025.

CONCLUSION

The isotope beam tuning approach based on the pilot beam efficiently worked for the user experiments. Since all beamlines consist of the smaller aperture quadrupoles and the switching dipoles, the acceptance is noticeably lower than the ARIS acceptance, which explains lower transmission at larger emittances at DB5. The beamline components remain unchanged since the original operation with the coupled cyclotrons at NSCL. By installing the High Rigidity Spectrometer (HRS) [8], we plan to improve the transmission by close to 100%. Also, there are plans to upgrade all beamlines with larger aperture quadrupoles and switching dipoles after the completion of the HRS project.

In addition, the beamline setup and the performance conducted to date are archived in centralized storage, and plans are underway to utilize these data to automate the fine-tuning based on the machine learning approach.

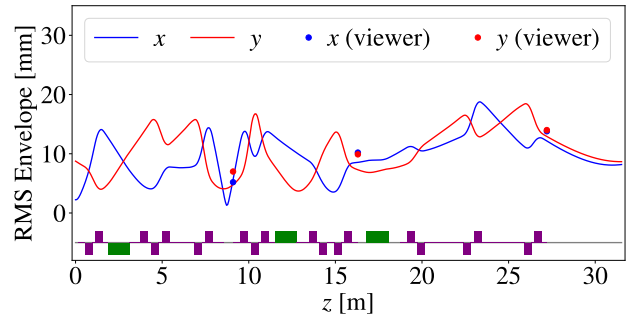


Figure 6: Beam envelope from DB5 to S1 beamline with ^{52}Fe pilot beam. The red line shows the horizontal envelope, and the blue line shows the vertical envelope. The red and blue dots show the measured beam size at the viewer plates.

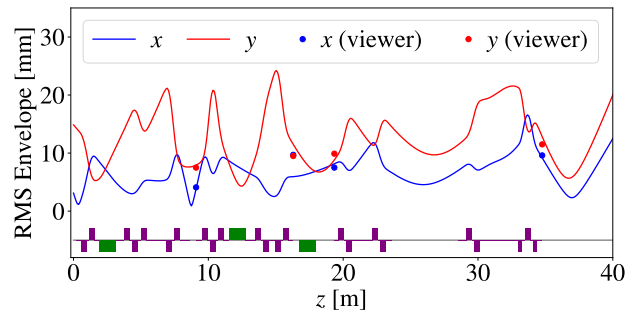


Figure 7: Beam envelope from DB5 to S2 beamline with ^{79}Ga pilot beam. Definitions of the lines and dots are the same as in Fig. 6.

ACKNOWLEDGMENT

We are grateful for the support and communications of the FRIB operation team and the laboratory-supported instrument teams, such as the S1, S2, S3, and N4 end stations.

REFERENCES

- [1] J. Wei *et al.*, “Accelerator commissioning and rare isotope identification at the Facility for Rare Isotope Beams”, *Mod. Phys. Lett. A*, vol. 37, no. 09, p.2230006, Mar. 2022. doi:10.1142/s0217732322300063
- [2] J. Wei *et al.*, “FRIB operations: first three years”, presented at HIAT25, East Lansing, MI, USA, Jun. 2025, Paper MOX01, this conference.
- [3] M. Hausmann *et al.*, “Design of the Advanced Rare Isotope Separator ARIS at FRIB”, *Nucl. Instrum. Methods Phys. Res., Sect. B*, vol. 317, pp. 349–353, Dec. 2013. doi:10.1016/j.nimb.2013.06.042
- [4] K. Fukushima *et al.*, “Simulation studies for beam commissioning at FRIB Advanced Rare Isotope Separator”, *Nucl. Instrum. Methods Phys. Res., Sect. B*, vol. 541, pp. 53–55, Aug. 2023. doi:10.1016/j.nimb.2023.04.038
- [5] Z. He, M. Davidsaver, K. Fukushima, G. Shen, M. Ikegami, and J. Bengtsson, “The fast linear accelerator modeling engine for FRIB online model service”, *Comput. Phys. Commun.*, vol. 234, pp. 167–178, Jan. 2019. doi:10.1016/j.cpc.2018.07.013

- [6] FLAME source code repository, <https://github.com/flame-simulation/FLAME>
- [7] Online Viewer Application (Viola) source code repository, <https://github.com/kryv/viola>
- [8] S. Noji *et al.*, “Design of the High Rigidity Spectrometer at FRIB”, *Nucl. Instrum. Methods Phys. Res., Sect. A*, vol. 1045, p. 167548, Jan. 2023.
doi:10.1016/j.nima.2022.167548

RARE-ISOTOPE PRODUCTION OPTICS OF ARIS PRESEPARATOR*

M. Portillo[†], Y. Choi, S. Cogan, E. Daykin, A. Dombos, X. Du, K. Fukushima, M. Hausmann, D. Kahl, E. Kwan, S. Lidia, S. Miller, P. Nariyoshi, I. Nesterenko, F. Pereira, P. Ostroumov¹, X. Rao, B.M. Sherrill¹, M.K. Smith, J. Song, M. Steiner, O.B. Tarasov, T. Xu, T. Zhang,

Facility for Rare Isotope Beams, MSU, East Lansing, MI, USA

¹also at the Department of Physics and Astronomy, MSU, East Lansing, MI, USA

Abstract

The Advance Rare Isotope Separator (ARIS) at FRIB provides in-flight purification of rare-isotope beams (RIB) generated by projectile fragmentation or fission on a target. Beams of stable ions from a driver linac impinge on a graphite target thin enough such that products maintain velocities close to that of the incident beam. The incident primary beam impinges on-target at about 200 MeV/u (for uranium and higher for lighter species). The energy may be lower than the maximum allowed, depending on the requirements of the experiment.

Using multi-charge state acceleration, the linac has most recently provided up to 20 kW on-target with a long-term goal of reaching 400 kW. Specialized magnets, collimators and other components have been integrated into the separator to withstand harsh conditions and facilitate maintenance. The optics properties at the beam dump are important since the power density must be kept low enough to avoid failure of the material. We describe the various optics modes that have been developed for safe operations and maximizing the beam power allowed for RIB production.

INTRODUCTION

The ARIS separator uses magnetic rigidity separation and momentum-loss achromat methods with wedged shaped degraders to purify beams of isotopes according to mass and atomic number Z [1].

The conceptual design was first introduced in a 2013 publication describing the optics and major components [2]. The layout addressed the major issues at the time, notably connecting the high-power driver linac (30 feet below ground level) to the existing experimental facility layout, while serving as a multi-stage in-flight separator. Figure 1 shows a schematic representation of the separator with labeled sections from target to diagnostic box DB5.

The description of each separation stage has already been described in detail by others [2, 3]. More details related to the separator role in operations at FRIB are also provided in these conference proceedings [4].

The focus here will be on the function of Stage 1 and the front-end optics solutions which have been developed for RIB operations. Details about beam transport after DB5 to experiments are described elsewhere [5].

Stage 1 Description

The first achromatic stage is often referred to as the vertical preseparator (PS). This stage is divided at wedge degrader position PSw, such that the front-end provides a momentum dispersion that is $\sim 1/3$ of that provided at the back-end, which ends at DB1. This is achieved by using 30° bend dipoles at the front-end and 50° at the back-end. A more detailed description of the magnets is provided in [6].

The latest optics solutions are very similar to the original design but have some slight differences due to slight changes during final construction. The first order matrix terms for the dispersion (x/d) and magnification (x/x) are listed in Table 1. The momentum compression factor can be determined to first order from the optics matrix terms using the following equation [7] :

$$\kappa = \frac{1}{(d/d)_{tot}} = -\frac{(x/d)_2}{(x/x)_2(x/d)_1} \quad (1)$$

Table 1: PS Optics Properties as Described in Text

Optics property	
$(x/d)_D$ Target to Dump [cm/%]	0.92
$(x/d)_1$ Target to PSw	-2.5
$(x/d)_2$ PSw to DB1	7.7
$(x/x)_2$	1.02
p-compression	3.0

The front-end components are exposed to the highest levels of beam loss and radiation from mainly target and beam dump. High power components of the beam are absorbed as much as possible in collimators and thermal shielding on magnets. Beam power after DB1 is typically well below a few watts.

Optics Modes

Three optics modes from target to PSw have been developed to maintain levels of power density to a minimum at beam dump while maximizing the power on-target. They are given names A, B, and C-optics and their first order properties are described by the plots in Fig. 2 and values listed in Table 2. The momentum resolving power is based on first order and a 1 mm beam spot at target.

* Work supported by the U.S. Department of Energy Office of Science under Cooperative Agreement DE-SC0023633, the State of Michigan, and Michigan State University.

[†] portillo@frib.msu.edu

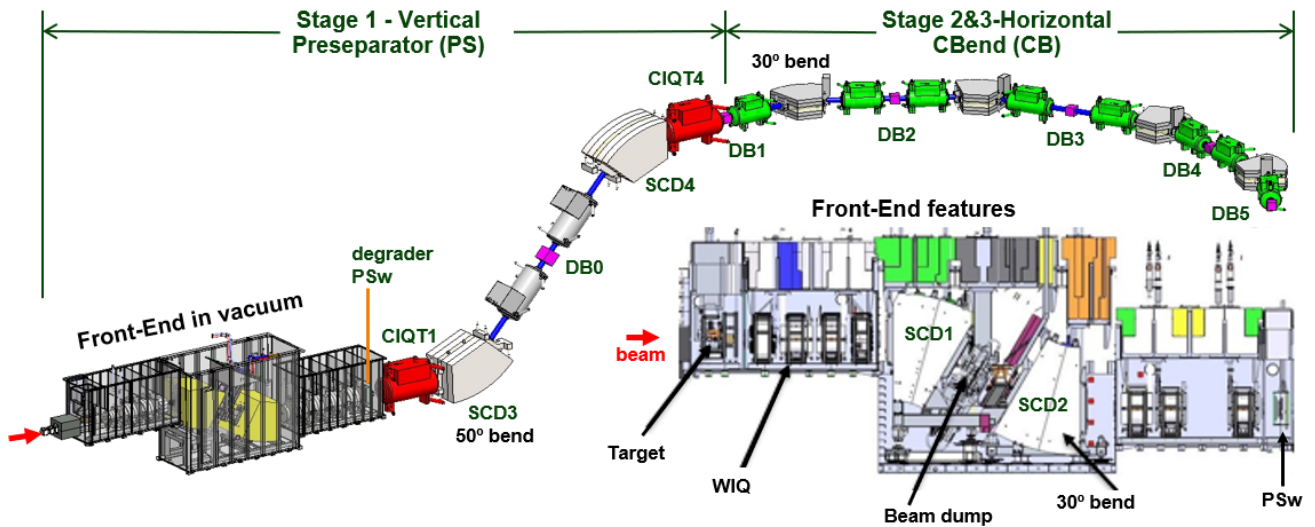


Figure 1: Layout of ARIS separator system from target to DB5. Three achromatic stages of separation purify the desired secondary beams to be delivered to experimental stations. The front-end magnets reside in vacuum and consist of WIQs. The rest of the quadrupoles are in cold-iron triplets (CIQT). See the text for more details.

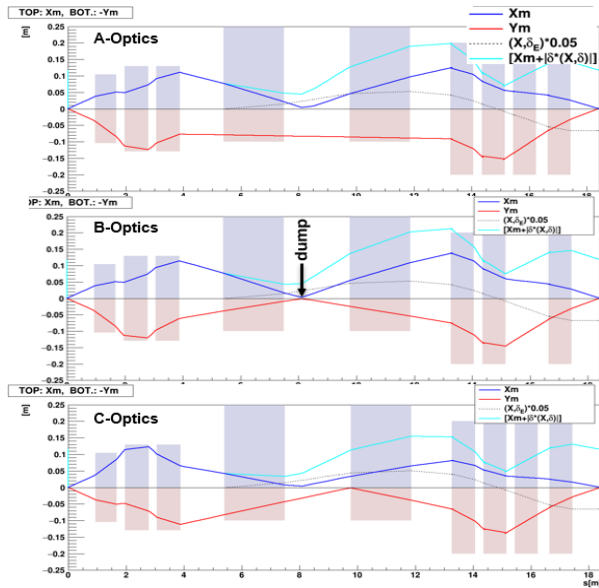


Figure 2: First order beam envelope plots of three solutions for PS target-to-wedge as described in the text.

Table 2: First Order Matrix Terms at PSw for Each Optics

Optics	(x/x)	(y/y)	R_p [mm]
A	1.50	-1.20	-1660
B	1.41	1.26	-1780
C	2.45	1.33	-1030

All three have the same dispersion of -2.5 cm/% and are used with the same back-end optics such that the compression factor remains the same to first order as evident by equation (1). As a result, the same wedge shape can be used to obtain achromatic focus at DB1.

All three modes have an x-focus at or close to the dump position. A-optics is closest to the original solution and is characterized by a parallel-y focus at dump position. B-

optics is optimized to have y-focus at dump, while C-optics has polarities flipped in the first three warm-iron quadrupoles (WIQs) to reduce the chromatic aberrations in y.

The effects of higher order aberrations can be seen by the x versus y beam spot distributions at dump position as depicted in Fig. 3. (Red-dashed lines depict the SCD1 dipole exit aperture boundaries.) The rays simulations were performed for 180 MeV/u ^{48}Ca primary beam. Only the 20+ charge state after an 8 mm graphite target was considered at various rigidity settings of the separator. The scale labeled dp/p at the top corresponds to the percentage difference from that centered on the optic axis. The simulations are carried out with fifth order maps evaluated using COSY INFINITY then imported into a LISE++ model as described elsewhere [8].

Notice that the beam widths in both x and y vary with dp/p setting such that small spot sizes result close to zero. High intensity RIB products tend to be close to the primary beam. When such products are selected it is necessary to choose the optics mode that will have size to minimize power density. Otherwise, the beam intensity needs to be limited to keep the estimated temperature on the beam dump below acceptable limits.

The expected beam widths for A-optics were confirmed with 1 kW operations using the so-called 20° beam dump, as described in [3]. This lends confidence to the simulation model. The larger incline of the currently used 6° beam dump allows for up to 20 kW operations, depending on the beam spot size [4].

The beam width behavior as a function of dp/p can be understood from the Taylor expansion terms of the map plotted in Fig. 4 as a function of the beam position up to PSw. Note that the A- and B-optics have a (y/bd) that swings wide and has a high slope for B-optics. This explains the large y-widths at the extremes. The C-optics has a reduced effect at the expense of a larger (x/ad) term which results in x-broadening of the beam at the extremes. Note that these simulations are for higher order correctors off.

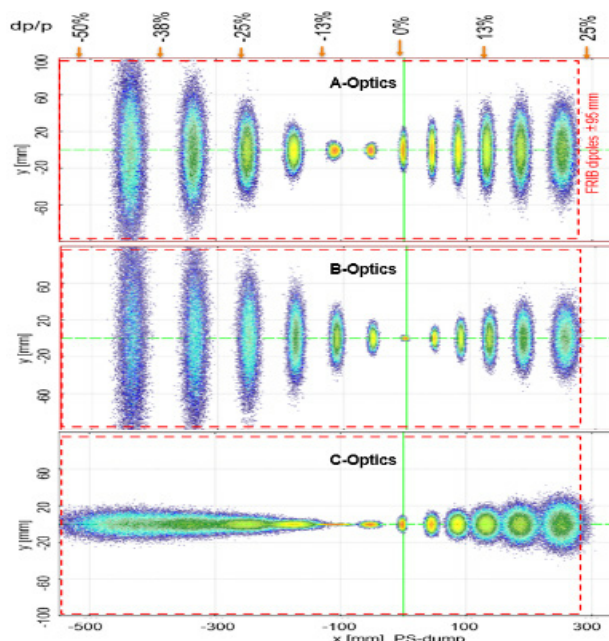


Figure 3: 5th order Monte Carlo simulation of rays from target to beam dump position as described in text.

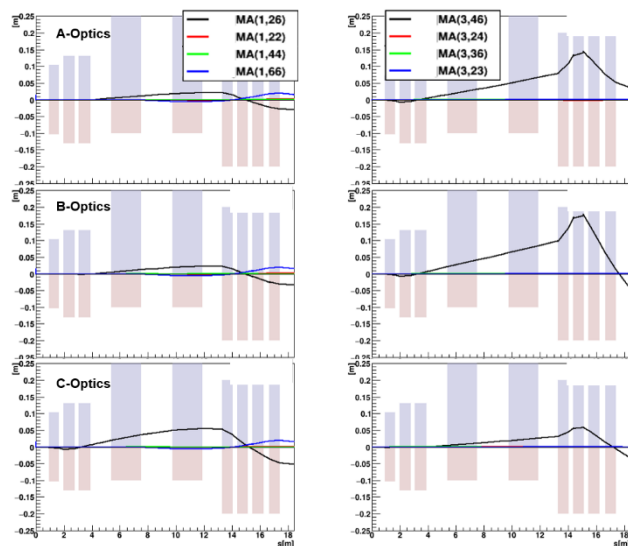


Figure 4: Plots of most prominent 2nd order map terms from target to PSw. (Left) x- and (Right) y-terms are such that terms $x \equiv 1$, $a \equiv 2$, $y \equiv 3$, $b \equiv 4$ and $d \equiv 6$.

Modes A and B have been used for routine operations over the past two years. The experience has been that A-optics tends to exhibit less purity when switching from B. Such effects have been most pronounced for cases of large phase space, such as fission products from ^{238}U . Transmission is very sensitive to quadrupole settings and reoptimizing may reduce the discrepancy. Further studies will be needed to confirm this.

The C-optics is a relatively new development and has not been tested yet since switching polarities at the first WIQ is not currently possible. A power supply switch is due to be installed during the Summer 2025 shut down which will allow the operation of this mode. This mode is expected to be needed below $dp/p \approx -40\%$ where undesired losses due to

large y-width occur. The trade-off is that the resolving power R_p can be $\sim 70\%$ less than that of the A and B modes. However, often such cases are for lower Z products for which high R_p is not required to obtain good purity anyway.

SUMMARY

Various optics modes for the ARIS separator front-end have been developed to support operational flexibility. All three optics modes developed have the same first order dispersion up to the preseparator wedge position, allowing the use of a common back-end optics that results in momentum compression factor of 3.

We have demonstrated that the higher order properties of each optics affects the primary beam spot size differently at the beam dump. The size varies depending on the beam deflection away from the optic axis and must be evaluated for each high-power beam setting before use. Temperature rise estimates are carried out to determine the maximum allowed power.

REFERENCES

- [1] K.-H. Schmidt, E. Hanelt, H. Geissel, G. Münzenberg, and J. P. Dufour, "The momentum-loss achromat — A new method for the isotopical separation of relativistic heavy ions," *Nucl. Instrum. Methods Phys. Res., Sect. A*, vol. 260, no. 2–3, pp. 287–303, Oct. 1987. doi:10.1016/0168-9002(87)90092-1
- [2] M. Hausmann *et al.*, "Design of the Advanced Rare Isotope Separator ARIS at FRIB," *Nucl. Instrum. Methods Phys. Res., Sect. B*, vol. 317, pp. 349–353, Dec. 2013. doi:10.1016/j.nimb.2013.06.042
- [3] M. Portillo *et al.*, "Commissioning of the Advanced Rare Isotope Separator ARIS at FRIB," *Nucl. Instrum. Methods Phys. Res., Sect. B*, vol. 540, pp. 151–157, Jul. 2023. doi:10.1016/j.nimb.2023.04.025
- [4] J. Wei *et al.*, "FRIB Operations: First three years", presented at HIAT'25, East Lansing, MI, Jun. 2025, paper MOX01, this conference.
- [5] K. Fukushima *et al.*, "Rare isotope beam tuning in FRIB", presented at HIAT'25, East Lansing, MI, Jun. 2025, paper FRA01, this conference.
- [6] Y. Choi *et al.*, "Overview of Fragment Separator Superconducting Magnets in the Facility for Rare Isotope Beams," *IEEE Trans. Appl. Supercond.*, vol. 33, no. 5, pp. 1–5, Aug. 2023. doi:10.1109/tasc.2023.3244141
- [7] L. Bandura *et al.*, "Fragment separator momentum compression schemes," *Nucl. Instrum. Methods Phys. Res., Sect. A*, vol. 645, no. 1, pp. 182–186, Jul. 2011. doi:10.1016/j.nima.2010.12.015
- [8] M. Portillo, M. Hausmann, and S. Chouhan, "Developments in magnet modeling and beam optics for the ARIS separator at FRIB," *Nucl. Instrum. Methods Phys. Res., Sect. B*, vol. 376, pp. 150–155, Jun. 2016. doi:10.1016/j.nimb.2016.01.029

PARTICLE IDENTIFICATION USING TRAJECTORY RECONSTRUCTION WITH THE ARIS SEPARATOR SYSTEM AT FRIB*

E. Kwan[†], S. Watters¹, O. B. Tarasov, A. C. Dombos, M. Hausmann, D. Kahl,
D. Kaloyanov¹, M. Portillo, B. M. Sherrill¹, M. K. Smith, M. Steiner

Facility for Rare Isotope Beams, Michigan State University, East Lansing, MI, USA

¹also at Department of Physics and Astronomy, Michigan State University, East Lansing, MI, USA

Abstract

The production of radioactive beams is crucial for advancing our understanding of the structure of atomic nuclei away from stability. The operation of the Facility for Rare Isotope Beams (FRIB) enables access to previously unreachable unstable nuclei. Radioactive beams produced at FRIB can be selected and purified using the Advanced Rare Isotope Separator (ARIS) for experimental studies. Ions are identified on based on measurements of energy loss (ΔE), magnetic rigidity ($B\rho$), gamma rays, time of flight (ToF), and total kinetic energy (TKE) using a suite of detectors. The transport of these cocktail beams to the end of ARIS can alter the ion path length and, consequently, the measured ToF. Such variations introduce uncertainty in the particle identification and can degrade the timing resolution if not properly accounted for. Characterizing ion optics with position-sensitive detectors enables corrections to the ions' flight paths. When combined with transfer matrices, this information allows for the reconstruction of ion trajectories, providing event-by-event corrections to the measured ToF.

In addition to improving the ToF resolution, trajectory reconstruction improves the precision of $B\rho$ measurements by enabling a more accurate determination of the momentum deviation ($\delta p/p$) based on reconstructed position and angle information. These corrections are essential for accurate charge-state identification, particularly in high-resolution optics modes. The impact of implementing this trajectory reconstruction method in ARIS operations will be presented.

INTRODUCTION

The production of radioactive beams is important for advancing our understanding of the evolution of nuclear structure in atomic nuclei far from stability and for enabling the study of key nuclei involved in stellar nucleosynthesis processes. At FRIB, radioactive beams are typically produced via projectile fragmentation or in-flight abrasion-fission using various primary beams, from oxygen to uranium. These beams impinge on carbon targets [1] to produce a wide range of nuclear fragments, which are predominantly lighter than the original projectile. These reaction products, which are produced at velocities close to that of the projectile and with a narrow momentum distribution, are then selected and purified using the ARIS separator [2]. The

LISE⁺⁺ package [3, 4] incorporates various reaction mechanisms using empirically determined parameters to model fragment production yields and charge-state distributions, to optimize separator settings based on simulated ion optics transport.

At FRIB energies, high- Z fragments are often produced in multiple charge states and may undergo further charge exchange in downstream material. Thus, high precision in the mass-to-charge ratio (A/q) is necessary to resolve neighboring isotopes with similar A/q values. A dedicated reconstruction method has been developed from scratch and has recently been implemented in ARIS. The following sections will present results demonstrating its impact on the particle identification resolution.

THE ADVANCED RARE ISOTOPE SEPARATOR

ARIS is a third-generation fragment separator located on the campus of Michigan State University, following the A1200 and A1900 fragment separators. ARIS is designed for multistage separation to reduce the rate of contaminants in the cocktail beam and supports selectable optical modes [5]. Diagnostic boxes (DBs) in the second stage of ARIS are equipped with a suite of detectors (see Ref. [6, 7]). DBs are positioned at both achromatic image planes, where ions with different momenta converge spatially, and dispersive planes, where ion positions vary with momentum. This configuration enables nearly simultaneous measurement of the kinematic properties of the ions, allowing trajectory reconstruction and identification of the atomic number (Z) and A/q .

Parallel-plate avalanche counters (PPACs) [8] are used to characterize ion optics by measuring the position, angle, and ToF of the ions as they traverse the separator. Information from the PPACs, in conjunction with forward and inverse ion-optics mapping, enables the local reconstruction of the ion phase-space vector, as well as the global reconstruction of the momentum and emission angle at the target. This also allows for confirmation of the phase space during tuning [9].

PARTICLE IDENTIFICATION

High-precision measurements of ToF, $B\rho$, ΔE , and TKE are essential to improve the resolution and separability of neighboring fragments, particularly for heavier masses. The particle identification using this approach has been thoroughly described in the appendix of Ref. [10].

* Work supported by the U.S. Department of Energy Office of Science under Cooperative Agreement DE-SC0023633, the State of Michigan, and Michigan State University.

[†] kwan@frib.msu.edu

The magnetic field strength B of dipole magnets with bending radius ρ enables determination of the ion momentum for a A/q , according to:

$$A/q = \frac{B\rho}{\beta\gamma} \frac{e}{cu}, \quad (1)$$

where β is the velocity of the ions relative to the speed of light, c , u is the atomic mass unit, e is the elementary charge, and γ is the Lorentz factor. Although the value of A/q is constant for a given ion, the achievable resolution in practice depends on the precision of the velocity and $B\rho$ measurements. As momentum acceptance increases, position measurements in the dispersive plane yield greater precision in the determination of $B\rho$. When this calculated $B\rho$ is used in conjunction with ion-optical transfer matrix elements determined from the trajectories of the particles, it is possible to improve the A/q resolution.

TRAJECTORY RECONSTRUCTION

Within the LISE⁺⁺ package, an extended configuration of ARIS was constructed to provide a granular view of the separator. In this setup, each magnet and drift section is treated as an individual optical block, enabling a detailed analysis of the system's aggregate optics. A dedicated utility was developed within the code to parse recorded experimental ARIS configuration files and automatically set the magnetic field strength of each magnet accordingly [11]. A second utility calculates second-order transfer matrices between any two optical blocks using TRANSPORT-based approximations [12], allowing localized matrix evaluation across arbitrary segments of the separator.

PPACs measure the cocktail beam's phase space at each diagnostic box, providing transverse positions (x, y) and angles (θ, ϕ) for each particle. These measurements define the phase-space vector (\vec{v}_i) at the initial location. The evolution of this vector to a subsequent position along the beamline is described by a transfer matrix (M), which characterizes the ion optical properties of the system. The final phase-space vector \vec{v}_f is obtained by applying the M to \vec{v}_i , following the standard formalism:

$$\vec{v}_f = M \cdot \vec{v}_i. \quad (2)$$

Using this equation, the momentum deviation ($\delta p/p$) and the path length difference relative to the central trajectory (ΔL) can be extracted for each particle along the specified beamline segment. As a specific example, the transfer matrix between DB3 and DB4 is used to estimate the angles in DB4, where only a single PPAC is available and angular measurements are not directly accessible. Similarly, the transfer matrix between DB4 and DB5 may be inverted, M^{-1} , to trace the particle trajectories from DB5 back to DB4. These forward and backward projection techniques serve as valuable cross-checks for both the optical model and detector calibrations.

Depending on the ARIS operation mode in the second stage of the separator, either high resolution with one dispersive plane at DB3 (CB1 optics), or high acceptance with

two dispersive planes at DB2 and DB4 (CB2 optics [2]), the appropriate reconstruction method must be applied to calculate the correct trajectories.

The impact of trajectory reconstruction on length is important in the CB1 mode. This is illustrated in Fig. 1, which shows the reconstructed A/q values for ^{198}Pt for different charge states with and without applying length corrections. When length corrections are applied, this correlation between A/q and $B\rho$ is effectively removed.

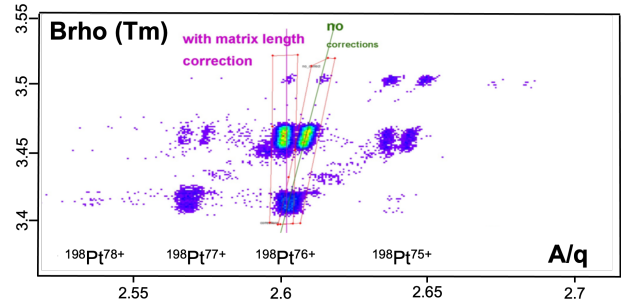


Figure 1: Effect of applying matrix length corrections in the trajectory reconstruction of ^{198}Pt charge states in CB1 mode on the A/q values used in the PID analysis of Ref. [13].

The effectiveness of trajectory reconstruction can also be evaluated by calculating the momentum spread ($\Delta B\rho/B\rho$). Figure 2 shows the three charge states of ^{198}Pt that reach DB5 in the same spectrometer setting. The y-axis represents the reconstructed $\Delta B\rho/B\rho$ using the DB3–DB5 PPACs, while the x-axis uses the DB1–DB3 PPACs. The linear correlation of the two segments of ARIS has a slope of approximately 1, indicating good agreement in the calculated dispersion and validating the reliability of our reconstruction method. Averaging these two values can further improve the PID resolution.

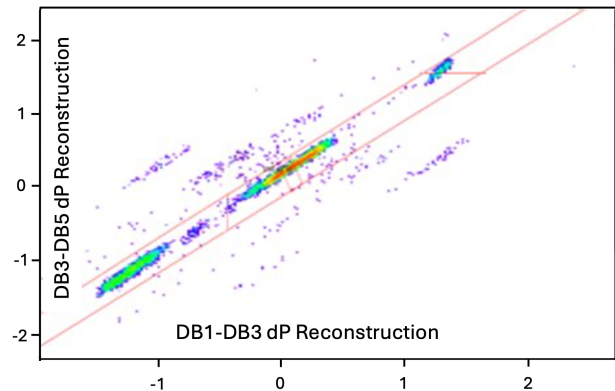


Figure 2: Calculated momentum spreads obtained with trajectory reconstruction for DB1-DB3 and DB3-DB5 segments in the same experiment as Ref. [13].

Figure 3 shows the quality of the separation of Z and $(A/q - 2) \cdot Z$ for the fragments of tin ($Z = 50$) to magnesium

($Z = 12$) in CB2 mode. Using the trajectory reconstruction described above, we achieved resolutions of 0.167 for Z and 0.0024 for A/q (standard deviations). These values correspond to a mass resolution of 0.105, evaluated using the combined quantity $(A/q - 2) \cdot Z$. An even better A/q resolution of approximately 0.001 was achieved using the CB1 optics mode.

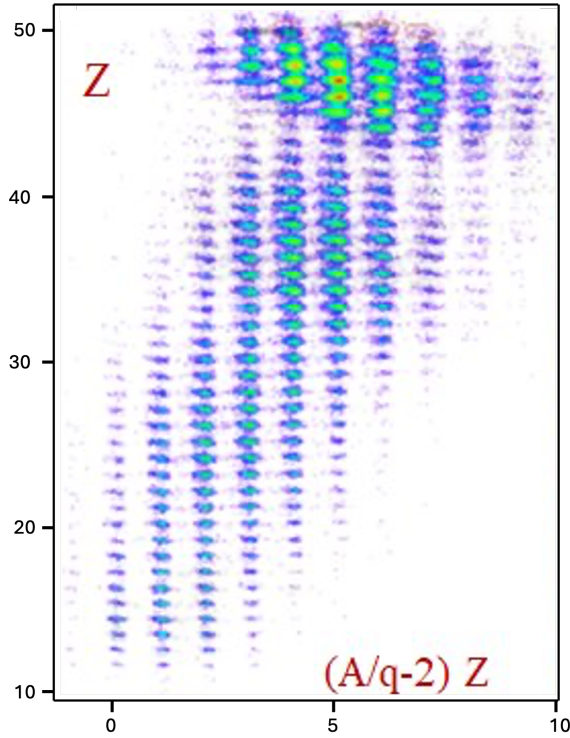


Figure 3: PID plot using trajectory reconstruction for selected fragments produced from the fragmentation of a 228 MeV/u ^{124}Xe on a 3.5 mm carbon target in CB2 optics.

The accuracy of trajectory reconstruction partly depends on the quality of the ion optics. Proper focus in DB3, DB4, and DB5 helps minimize correlations between A/q and phase-space parameters (x, y, θ, ϕ). Optical fine-tuning may be needed to correct small second-order aberrations, which can be calculated in LISE⁺⁺ or adjusted manually.

For optimal resolution, A/q should be independent of all phase-space variables. Figure 4 shows this for a single elemental mass chain: measured angles at DB3 (top row) and DB5 (middle row), and non-dispersive position and reconstructed $B\rho$ at DB4 (bottom row), each plotted against A/q . The near-vertical mass bands indicate a successful suppression of correlations.

REVERSE TRAJECTORY RECONSTRUCTION DOWN TO TARGET

In addition to local trajectory reconstruction (e.g., DB3–DB5), the LISE⁺⁺_{cute} code, using the extended ARIS configuration, enables global-scale reconstruction back to the production target. To obtain the reaction's kinematic

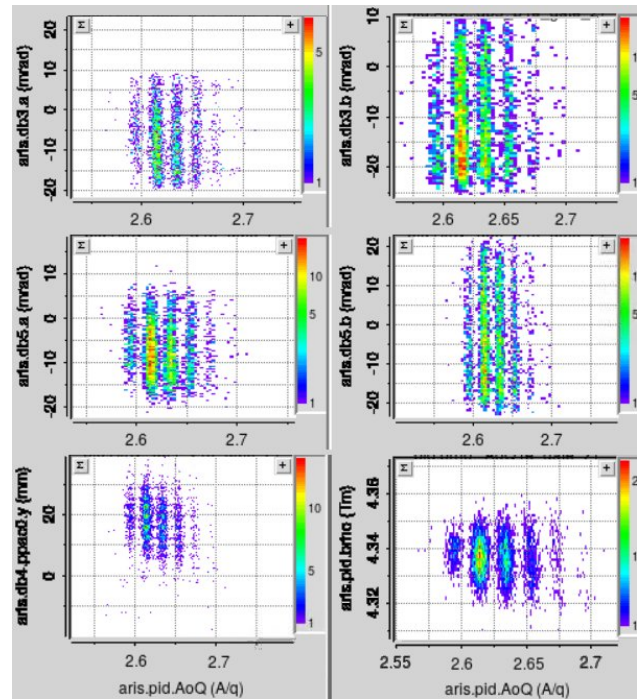


Figure 4: Phase space distributions of antimony isotopes produced via in-flight fission of ^{238}U at 177 MeV/u, shown at DB3, DB4, and DB5 as a function of A/q .

properties and constrain optical block apertures, this approach aims to infer the initial phase space at the target, which is information not directly accessible experimentally. See, for example, Ref. [14].

Global reconstruction in ARIS presents several unique challenges, including momentum compression in the pre-separator, rotation of the dispersive and non-dispersive planes, energy loss, and energy and angular straggling in the various materials downstream of the target. A comprehensive study of these effects and their impacts on the fidelity of the global trajectory reconstruction is currently in progress.

CONCLUSION

Trajectory reconstruction in ARIS has been used successfully to enhance the A/q resolution. We have demonstrated that the deduced A/q value can be made largely independent of the phase-space parameters including $B\rho$, by combining position measurements from PPACs with calculated transfer matrix elements. This approach significantly improves the PID resolution. An improvement in resolution by more than a factor of two was observed when comparing the high-resolution CB1 mode to the large-acceptance CB2 mode in the second stage of the ARIS. The continued optimization of these techniques is ongoing, as they are crucial for reliable charge-state identification in elements with $Z > 30$.

REFERENCES

- [1] J. S. Song *et al.*, “A single-slice rotating graphite target at FRIB”, presented at HIAT’25, East Lansing, MI, USA, Jun. 2025, paper TUB01, this conference.

- [2] M. Hausmann *et al.*, “Design of the Advanced Rare Isotope Separator ARIS at FRIB”, *Nucl. Instrum. Methods Phys. Res., Sect. B*, vol. 317, p. 349, Dec. 2013.
doi:10.1016/j.nimb.2013.06.042
- [3] O. B. Tarasov and D. Bazin, “LISE⁺⁺: Radioactive beam production with in-flight separators”, *Nucl. Instrum. Methods Phys. Res., Sect. B*, vol. 266, p. 4657–4664, Oct. 2008.
doi:10.1016/j.nimb.2008.05.110
- [4] O. B. Tarasov *et al.*, “LISE⁺⁺_{cute}, the latest generation of the LISE⁺⁺ package, to simulate rare isotope production with fragment-separators”, *Nucl. Instrum. Methods Phys. Res. B*, vol. 541, p. 4–7, 2023.
doi:10.1016/j.nimb.2023.04.039
- [5] M. Portillo *et al.*, “Rare-isotope production optics of ARIS preseparator”, presented at HIAT’25, East Lansing, MI, USA, Jun. 2025, paper FRA02, this conference.
- [6] M. K. Smith *et al.*, “Rare-Isotope Heavy-Ion Production with the ARIS separator system at FRIB”, presented at HIAT’25, East Lansing, MI, USA, Jun. 2025, paper MOP29, this conference.
- [7] A. C. Dombo *et al.*, “Updated magnetic rigidity calibration of ARIS”, presented at HIAT’25, East Lansing, MI, USA, Jun. 2025, paper MOP29, this conference.
- [8] S. Di Carlo and M. Cortesi, “Parallel-plate avalanche counters for heavy-ion beam tracking: History and mysteries”, *Phys. Rev. Accel. Beams*, vol. 27, p. 044801, Apr. 2024.
doi:10.1103/PhysRevAccelBeams.27.044801
- [9] K. Fukushima *et al.*, “Rare isotope beam tuning in FRIB”, presented at HIAT’25, East Lansing, MI, USA, Jun. 2025, paper FRA01, this conference.
- [10] O. B. Tarasov *et al.*, “Production of very neutron-rich nuclei with a ⁷⁶Ge beam”, *Phys. Rev. C* vol. 80, p. 034609, Sep. 2009. doi:10.1103/PhysRevC.80.034609
- [11] LISE⁺⁺ collaboration, “Exotic beam production – related topics”, <https://lise.frib.msu.edu/topics.html>
- [12] K. L. Brown, “A First- and Second-Order Matrix Theory for the Design of Beam Transport Systems and Charged Particle Spectrometers”, Stanford Linear Accelerator Center, Stanford, CA, USA, Rep. SLAC-75 (Rev. 4), Jun. 1982.
- [13] O. B. Tarasov *et al.*, “Observation of New Isotopes in the Fragmentation of ¹⁹⁸Pt at FRIB ⁷⁶Ge beam”, *Phys. Rev. Lett.* vol. 132, p. 072501, Feb. 2024.
doi:10.1103/PhysRevLett.132.072501
- [14] M. Bowry *et al.*, “Abrasion-fission reactions at intermediate energies”, *Phys. Rev. C*, vol. 108, p. 034604, Sep. 2023.
doi:10.1103/PhysRevC.108.034604

THE SPES-ISOLPHARM BEAMLINE FOR THE PRODUCTION OF MEDICAL RADIONUCLIDES AT INFN-LNL

A. Arzenton^{1,*}, D. Chen^{1,†}, M. Lunardon¹, S. Moretto¹,
G. S. Valli¹, INFN, Padova Division, Padova, Italy

A. Andrichetto, S. Corradetti, A. Leso², M. G. Martello, D. Serafini³,
INFN, Legnaro National Laboratories, Legnaro, Italy

E. Mariotti³, INFN, Pisa Division, Pisa, Italy

¹also at University of Padova, Department of Physics and Astronomy "G. Galilei", Padova, Italy

²also at University of Ferrara, Department of Physics and Earth Sciences, Ferrara, Italy

³also at University of Siena, Department of Physical Sciences, Earth and Environment, Siena, Italy

Abstract

The ISOLPHARM project, headed by the Legnaro National Laboratories of the Italian National Institute for Nuclear Physics (INFN-LNL), has the aim of developing innovative radiopharmaceuticals based on the radionuclides produced at the SPES Isotope Separation On-Line (ISOL) facility. Regarding the infrastructure, in late 2024 a key milestone of SPES was achieved: the production of the first radioactive ion beam by irradiating a silicon carbide target with an intermediate-energy proton beam. Moreover, the ISOLPHARM implantation station for radionuclide delivery to users, IRIS, is currently being installed online. Since its beginning in 2014, ISOLPHARM has built a broad network of universities, hospitals and research centers. The β^- emitter silver-111, in particular, obtainable using uranium carbide targets, has aroused a great interest in the collaboration as a theranostic candidate for targeted radionuclide therapy; a dedicated experimental campaign performed the first in-vitro tests and in-vivo imaging in 2024. This contribution will provide an overview on the status of the beamline and on the main results achieved by the preclinical experiments involving silver-111.

RADIOACTIVE ION BEAM PRODUCTION

SPES, standing for "Selective Production of Exotic Species", is an INFN project aimed at developing a second-generation ISOL facility at the LNL [1]. The facility hosts a B70 cyclotron (Fig. 1) produced by BEST Cyclotron Systems operating at proton beam energy of 30 to 70 MeV with intensity up to 750 μ A. Such beams can be used for direct activation or, if proper targets are used, to generate Radioactive Ion Beams (RIBs) with the ISOL technique. In SPES, these targets are made of 7 disks of fissile materials, such as uranium carbide (UC_x), or non-fissile materials, such as silicon carbide (SiC) and titanium carbide (TiC) [2]. The disks are spaced in a convenient way to obtain a uniform temperature distribution inside the box. The exotic species originating from the proton-induced nuclear reactions can leave the target box through a transfer line with a characteristic escape time depending on their chemical properties (*e.g.*,



Figure 1: SPES ISOL bunker at INFN-LNL.

their volatility). After that, they reach the ion source, where they can be ionized by three different mechanisms [3, 4]:

- surface ionization, occurring when atoms of the first group touch a hot surface;
- laser photo-ionization, based on stepwise excitation and subsequent ionization by interaction with laser beams tuned on a specific scheme of wavelengths for the element of interest;
- plasma ionization, consisting in an electron plasma hitting and ionizing all atoms with high efficiency and low selectivity.

Once ionized, the atoms can be accelerated by a high voltage and form the RIB. Finally, the beam passes through a Wien filter and becomes isobaric. This allows an extremely pure beam to be obtained, without isotopic contaminants of the desired radionuclides. The ISOLPHARM beamline, described in the next section, takes care of the collection of radionuclides of medical interest in dedicated substrates for subsequent radiochemical processing.

RADIONUCLIDE IMPLANTATION

The ISOLPHARM beamline, as shown in Fig. 2 (left), is installed in the low-energy experimental area of SPES. It is

* alberto.arzenton@pd.infn.it

† daiyuan.chen@phd.unipd.it

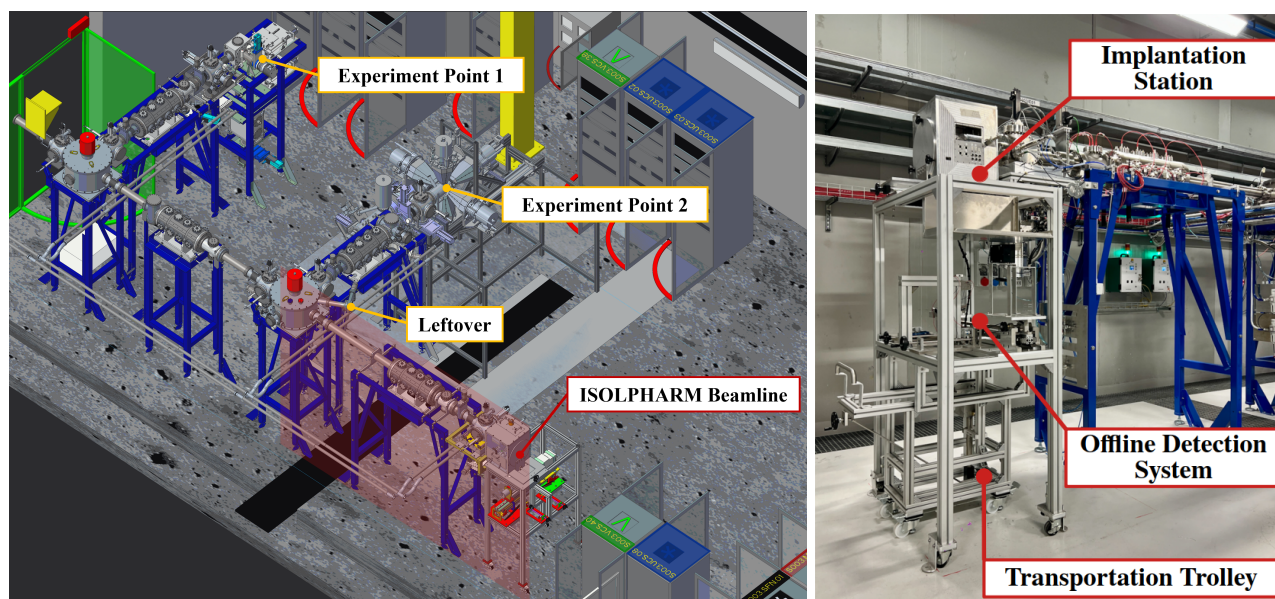


Figure 2: Layout of SPES low-energy experimental area (left) and on-site picture of the IRIS framework (right).

mainly made up of an electrostatic quadrupole and deflector intended for beam focusing and steering, a beam diagnostic box and the ISOLPHARM Radionuclide Implantation Station (IRIS), serving as the main device used for radionuclide collection and characterization. In recent years, Research and Development (R&D) activities have been carried out on the collection substrate and the IRIS, which has been installed in the SPES low-energy experimental area and is in the advanced stage of commissioning.

The collection substrate is the key element for implanting radionuclides of interest. The chemical and mechanical properties were taken into account in order to minimize the contamination while avoiding fracture during handling. The first candidates considered were sodium chloride or sodium nitrate. They were shown to be effective in depositing stable ions of silver [5, 6], though the presence of a large amount of salts could interfere with subsequent processes such as chemical purification [7]. In particular, Activated Carbon/PolyVinyl Alcohol (AC/PVA) substrates were developed for the collection of stable iodine, to avoid the difficulty in the quantification of deposited species caused by intrinsic contaminants [8]. Based on the preliminary study with the aforementioned materials, the pharmaceutical grade materials were given priority consideration, including water-soluble dextrates (sugars) and insoluble cellulose-based polymers [7]. In addition to its chemical compatibility with deposited radionuclides, the minimization of metallic contamination and a fair mechanical strength, recent studies suggest that the utilization of light materials could also mitigate the effect of self-sputtering [9]. The materials applied for the commissioning of the IRIS so far were dextrates.

The IRIS was designed to fulfill the tasks of automated substrate handling and on-site spectroscopic characterization at the irradiation stage. Meanwhile, a mechanism that allows for three implantations (five days per implantation within a

15-day beam cycle) to be performed was applied to make the most of the beam time. The IRIS framework is mainly made up of three subsystems (Fig. 2, right): 1) the Implantation Station (IS), 2) the Offline Detection System (ODS) and 3) the Transportation Trolley (TT). The periodic operational process begins with feeding the substrates into the system, before the IS takes care of substrate loading, alignment and unloading procedures with a motion system. The vacuum chamber allowing for the implantations to take place can also benefit an accurate beam shaping and diagnostics with a unit consisting of a Faraday cup and collimator. The irradiated sample will then descend to the ODS for Quality Control (QC) of the product. A High Purity Germanium (HPGe) detector and a scintillator detector made up of a Lanthanum BromoChloride (LBC) crystal are placed face-to-face for benchmark measurements. After the characterization finishes, the substrate will fall into a fixed vial placed in a shielded container and transported for post-processing with the (TT). In addition to the components described above, a high-vacuum system is used to maintain the proper working pressure (10^{-6} mbar) of the vacuum chamber, and three cameras are installed to provide visual monitoring of critical movements.

The IRIS control system is developed with the EPICS toolkit [10], to be fully integrated into the main control of SPES. It is responsible for driving the automated motion of the IS and the ODS, and interacting with the other supporting systems with EPICS Process Variables (PVs), such as the vacuum system, the beam diagnostic system and the SPES Machine Protection System (MPS). As for the user-end, the Graphic User Interface (GUI) is realized with the Control System Studio (CSS), to be consistent with other interfaces for apparatus control in the SPES facility.

Reliability and operational safety are regarded as the main concern in radionuclide implantation, as it takes place in a

highly regulated area with radiation exposure. In addition to the backup protocols established during the IRIS design stage, dedicated tests were performed on its subsystems individually. As for the IS, optimizations were implemented to prevent fatal errors that could lead to system blockage:

- the dimension of the entire passage and the compatibility with substrates were carefully investigated, and a proper thickness was determined;
- correction steps were introduced to the motors to compensate for the misalignment caused by routinely operational vibrations.

The two detectors used in the ODS were characterized in an offline bunker with different γ -ray sources to ensure optimal performance in terms of energy resolution and full-energy-peak efficiency. The HPGe detector exhibited a better energy resolution, implying a stronger capability of distinguishing contaminants, while a higher absolute efficiency and a fair energy resolution enable the LBC detector to be used for cross-checking.

PRECLINICAL APPLICATIONS

Moving to medical applications, the main focus since almost the very beginning of the project has been on silver-111, a β^- emitter with half-life of 7.45 d and decay properties suitable for nuclear medicine. In particular, its β^- radiation, with an average energy of about 360 keV, is very likely to be usable in radionuclide therapy, since its spectrum resembles those of lutetium-177, already approved by FDA and EMA [11], and mostly rhenium-186, currently being studied in phase I/II clinical trials [12]. In addition, de-excitation γ rays (main peaks at 245 keV and 342 keV with 1% and 7% intensities) emitted after the β^- decay can be used for Single-Photon Emission Tomography (SPECT) imaging, in such a way to obtain a real-time screening of the therapeutic approaches [13]. With the ISOL technique at SPES, the expectation is to produce ~ 1 GBq of highly pure silver-111 after a 6-hour irradiation cycle using a UC_x target, with the typical amount required for β therapy in human patients being a few gigabecquerels [14].

These features aroused the interest of several Italian research institutes, universities and hospitals, at the point that, while waiting for SPES to become fully operational, it has been decided to inaugurate an experimental campaign to study ^{111}Ag -labelled theranostic agents, characterize in advance their effects in vitro and in vivo and develop tailored imaging devices. To do this, small quantities of ^{111}Ag for preclinical research were and are currently produced at the Laboratory of Applied Nuclear Energy (LENA) of the University of Pavia, where a TRIGA Mark II nuclear reactor is available for research. To produce ^{111}Ag via radiative neutron capture, expensive palladium-110 enriched targets and a tough chemical separation procedure are necessary [15, 16]. This production route has been, together with the difficult chelation of silver due to its chemical properties, one of the main obstacles to the use of silver-111 in medicine up to

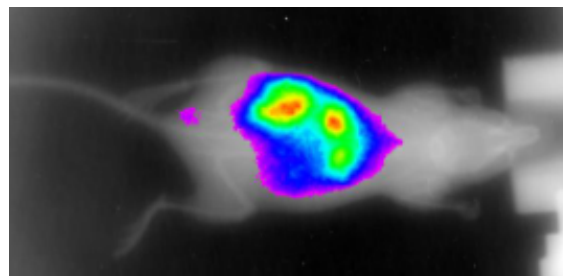


Figure 3: Digital autoradiography overlapped with an X-ray scan of a mouse injected with ^{111}Ag at the CAPIr labs of the University of Catania.

now [17]. However, after a preliminary phase characterized by in-vitro and in-vivo experiments aimed at developing radiopharmaceutical molecules and testing their stability in living systems [7, 18], it was possible to begin to use silver-111 first in phantoms [19] and then, for the first time in 2024, in cells and small animals. The experiments are still ongoing, but encouraging results come from in-vitro clonogenic assays and in-vivo imaging tests (see Fig. 3) using ^{111}Ag . To support these activities, several internal dosimetry simulations are performed [14] in cellular or murine geometries using Monte Carlo codes like GEANT4, PHITS and MCNP. Moreover, two imaging devices are being developed: a γ camera optimized for ^{111}Ag for clinical application in SPECT and a β imager, based on Monolithic Active Pixel Sensors (MAPS) and called "Detector Using MAPS for Beta-rays Observation" (DUMBO), for in-vitro uptake measurements.

CONCLUSION

This work describes the state of the art of the SPES-ISOLPHARM beamline at INFN-LNL, which has the aim of producing radionuclides of medical interest. The facility is almost ready to become operational, as the IRIS system was successfully moved online and is now being completed. Concerning medical applications, in the meanwhile a pre-clinical experimental campaign is ongoing using silver-111 produced via neutron activation at the LENA facility in Pavia. The theranostic properties of the free radionuclide are being characterized in vitro and in vivo, also with the help of novel β and γ imaging devices, and the next step will be the study of ^{111}Ag -loaded radiopharmaceutical candidates.

ACKNOWLEDGEMENTS

The authors wrote this proceeding on behalf of ISOLPHARM collaboration and acknowledge the valuable contribution of the mechanical workshops of INFN-LNL and INFN-Bologna.

REFERENCES

- [1] A. Andrighetto *et al.*, "Spes: An intense source of Neutron-Rich Radioactive Beams at Legnaro", *J. Phys. Conf. Ser.*, vol. 966, p. 012028, Feb. 2018.
doi: 10.1088/1742-6596/966/1/012028

- [2] M. Manzolaro *et al.*, “Thermal and Mechanical Characterization of Carbides for High Temperature Nuclear Applications”, *2D Mater.*, vol. 14, no. 10, p. 2689, May 2021. doi:10.3390/ma14102689
- [3] M. Manzolaro *et al.*, “Off-line ionization tests using the surface and the plasma ion sources of the SPES project”, *Rev. Sci. Instrum.*, vol. 83, no. 2, p. 02A907, Feb. 2012. doi:10.1063/1.3666172
- [4] O. S. Khwairakpam *et al.*, “Resonant Laser Ionization and Fine-Structure Study of Silver in an Ablation Plume”, *Appl. Sci.-Basel*, vol. 13, no. 1, p. 309, Dec. 2022. doi:10.3390/app13010309
- [5] M. Ballan *et al.*, “Preliminary evaluation of the production of non-carrier added ^{111}Ag as core of a therapeutic radiopharmaceutical in the framework of ISOLPHARM_Ag experiment”, *Appl. Radiat. Isot.*, vol. 164, p. 109258, Oct. 2020. doi:10.1016/j.apradiso.2020.109258
- [6] M. Ballan *et al.*, “Development of implantation substrates for the collection of radionuclides of medical interest produced via ISOL technique at INFN-LNL”, *Appl. Radiat. Isot.*, vol. 175, p. 109795, Sep. 2021. doi:10.1016/j.apradiso.2021.109795
- [7] E. Vettorato *et al.*, “A new production method of high specific activity radionuclides towards innovative radiopharmaceuticals: the ISOLPHARM project”, *RAD Conf. Proc.*, vol. 6, pp. 8–14, 2022. doi:10.21175/radproc.2022.02
- [8] F. Borgna *et al.*, “A preliminary study for the production of high specific activity radionuclides for nuclear medicine obtained with the isotope separation on line technique”, *Appl. Radiat. Isot.*, vol. 127, pp. 214–226, Sep. 2017. doi:10.1016/j.apradiso.2017.06.022
- [9] M. Deseyn, “Maximizing the radionuclide collection efficiency at CERN-MEDICIS: A case study on terbium collections and sputtering”, Masters thesis, KU Leuven, Leuven, Belgium, Jun. 2023.
- [10] EPICS – Experimental Physics and Industrial Control System, <https://epics-controls.org>
- [11] A. M. Denis-Bacelar *et al.*, “Phase I/II trials of ^{186}Re -HEDP in metastatic castration-resistant prostate cancer: post-hoc analysis of the impact of administered activity and dosimetry on survival”, *Eur. J. Nucl. Med. Mol. Imaging*, vol. 44, no. 4, pp. 620–629, Oct. 2016. doi:10.1007/s00259-016-3543-x
- [12] J. Zhang-Yin, “Lutetium-177-Prostate-Specific Membrane Antigen Radioligand Therapy: What Is the Value of Post-Therapeutic Imaging?”, *Biomedicines*, vol. 12, no. 7, p. 1512, Jul. 2024. doi:10.3390/biomedicines12071512
- [13] C. Blackadar *et al.*, “SPECT/CT Imaging of ^{111}Ag for the Preclinical Evaluation of Silver-Based Antimicrobial Nanomedicines”, *ACS Appl. Mater. Interfaces*, vol. 14, no. 23, pp. 26382–26393, Jun. 2022. doi:10.1021/acsami.2c03609
- [14] A. Arzenton, “Towards ^{111}Ag as a medical radionuclide: from production and laser photo-ionisation to cell dosimetry and radiation biophysics in the context of the ISOLPHARM project”, PhD thesis, University of Siena, Siena, Italy, Nov. 2024. doi:10.25434/arzenton-alberto_phd2024-11-11
- [15] L. Morselli *et al.*, “Production and characterization of ^{111}Ag radioisotope for medical use in a TRIGA Mark II nuclear research reactor”, *Appl. Radiat. Isot.*, vol. 197, p. 110798, Jul. 2023. doi:10.1016/j.apradiso.2023.110798
- [16] M. Tosato and M. Asti, “Lights and Shadows on the Sourcing of Silver Radioisotopes for Targeted Imaging and Therapy of Cancer: Production Routes and Separation Methods”, *Asian J. Pharm. Sci.*, vol. 16, no. 7, p. 929, Jun. 2023. doi:10.3390/ph16070929
- [17] M. Tosato *et al.*, “Highly Stable Silver(I) Complexes with Cyclen-Based Ligands Bearing Sulfide Arms: A Step Toward Silver-111 Labeled Radiopharmaceuticals”, *Acta Chem. Scand. Ser. A*, vol. 59, no. 15, pp. 10907–10919, Jul. 2020. doi:10.1021/acs.inorgchem.0c01405
- [18] M. Verona *et al.*, “Preliminary Study of a 1,5-Benzodiazepine-Derivative Labelled with Indium-111 for CCK-2 Receptor Targeting”, *Molecules*, vol. 26, no. 4, p. 918, Feb. 2021. doi:10.3390/molecules26040918
- [19] D. Serafini *et al.*, “ ^{111}Ag phantom images with Cerenkov Luminescence Imaging and digital autoradiography within the ISOLPHARM project”, *Appl. Radiat. Isot.*, vol. 215, p. 111562, Jan. 2025. doi:10.1016/j.apradiso.2024.111562

REACCELERATING LONG-LIVED RADIOISOTOPES AT FRIB*

A. Henriques[†], S. Nash, X. Chen, N. Gamage, C. Izzo, A. Lapierre, S. Schwarz, H.J. Son,
C. Sumithrarachchi, A.C.C. Villari, Q. Zhao

Facility for Rare Isotope Beams, Michigan State University, East Lansing, MI, USA

Abstract

The ReAccelerator at Facility for Rare Isotope Beams (FRIB) started the stand-alone program in May 2021. Several technical upgrades were implemented to expand the scientific capabilities, including a new BMIS source, a room-temperature rebuncher, and the ReA6 accelerator with its corresponding experimental vault.

Following the commissioning of these upgrades, over 25 beams were delivered to experiments, including six long-lived RIBs: Be-7, Be-10, Al-26, Si-32, Ni-56 and As-73.

In this contribution, we outline the key steps that led to the success of the stand-alone program, including a description of the upgrades, results from the ReA6 commissioning, approaches to mitigating isobaric contamination, and future activities for the ReA stand-alone program.

INTRODUCTION

The ReAccelerator (ReA) [1] at FRIB [2] at Michigan State University has proven to be a unique facility, reaccelerating stopped beams produced by in-flight fragmentation.

In 2021, when the Coupled Cyclotron Facility at National Superconducting Cyclotron Laboratory [3] ceased operations to accommodate preparations for FRIB, ReA continued operations in a stand-alone mode. Ever since FRIB started its scientific program in May 2022, stand-alone beams have been also available to users.

At FRIB, rare isotopes produced by in-flight fragmentation are stopped using linear gas stoppers [4]. These beams can be used for stopped beam experiments or injected into the reaccelerator. Additional sources like the hot-cathode discharge source or surface ionization source, and the Batch Mode Ion Source (BMIS) [5] provide stable and long-lived rare isotope beams (RIB), respectively.

At the ReA front-end, an Electron Beam Ion Trap (EBIT) [6] defines the ion charge state for reacceleration. Ions at 12 keV/u pass through a Q/A separator ($R \sim 600$) and into the Multi-Harmonic Buncher, before being injected into a 80.5 MHz four-rod RFQ. After, the beam enters the ReA3 superconducting linac with three cryomodules housing 80.5 MHz quarter-wave resonators ($\beta = 0.041$ and 0.085) and solenoids for transverse focusing.

Beams up to 1.4 Tm in rigidity can be transported to the ReA3 experimental area where three beam lines can be used for experiments. Beams can also be directed to the ReA6 linear accelerator. This third step of acceleration doubles the

beam energy using eight 80.5 MHz quarter-wave resonators ($\beta = 8.5\%$).

The current configuration was ready at start of the stand-alone program: BMIS enabled delivery of both stable and long-lived RIBs, and the beam energy available was doubled with the ReA6 accelerator, a new vault, and two beamlines. A new room-temperature re-buncher was also developed and installed.

UPGRADES FOR THE REA STAND-ALONE OPERATION

Batch Mode Ion Source

The Batch Mode Ion Source (BMIS) was installed near the two gas cells, making use of existing beam lines to deliver beams to both the low-energy and ReA areas (Fig. 1).

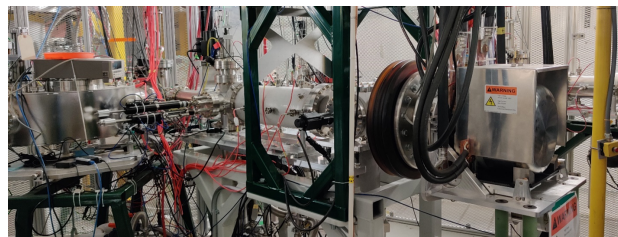


Figure 1: BMIS module and extraction beam line.

The sample material is placed in an oven capable of reaching temperatures up to 2000 °C. Heating the oven initiates the evaporation of the sample. It has a gas handling system for introducing a reactive and/or support gas on-line to enhance this process. The resulting atoms are diffused through a transfer tube, which is maintained at an even higher temperature to facilitate the transport of ions to the ionizer. Various types of ionizers can be employed, such as a Forced Electron Beam-Induced Arc Discharge (FEBIAD) ionizer or a surface ionizer. These devices supply electrons to ionize the neutral atoms. The resulting ions are then extracted using an extraction electrode. The efficiency of beam extraction depends on several factors, including ion source parameters, oven temperature, physical and chemical properties of sample compound, and the operating pressure of the support gas.

BMIS beam development starts with the study of the optimal chemical form to extract the RIB from the source. The desired chemical form is selected and synthesized to have a melting point within the operational range, optimized to reduce melting points and provide the desired yields, while simultaneously not enhance yields of other species that may be also present in the sample [7]. A stable isotope of the

* This material is based upon work supported by the U.S. Department of Energy, Office of Science, Office of Nuclear Physics and used resources of the Facility for Rare Isotope Beams (FRIB) Operations, which is a DOE Office of Science User Facility under Award Number DE-SC0023633.

[†] henrique@frib.msu.edu

same species is used to test the method. When a method is established, the analogue form is synthesized for the radioactive sample used for the beam production.

BMIS has provided beams for the ReA stand-alone program for testing, beam tuning and experiments, among those beams are stable isotopes as well as the long-lived isotopes Be-7, Be-10, Al-26, Si-32, Ni-56 and As-73. Among those isotopes, Ni-56 has the shortest half-life of 6 days while Be-10 has the longest with 1 million years. The availability of isotope, acquisition of isotope under the regulation limits and the complex chemical preparation techniques restrict the beam availability in the stand-alone program.

The ReA6 Upgrade

A new room-temperature rebuncher was developed to improve longitudinal beam matching between the ReA3 and ReA6 cryomodels. Optimized for beams energies above 1.5 MeV/u, the $\beta_{opt} = 0.1$ quarter-wave resonator was installed upstream of ReA6. Operating at the second harmonic (161 MHz), it minimizes its power use and supports up to 180 kV bunching voltage at 4 kW input, based on FRIB's H-type rebunchers. It was successfully commissioned in May 2021 as shown on the buncher response to different amplitudes in Fig. 2.

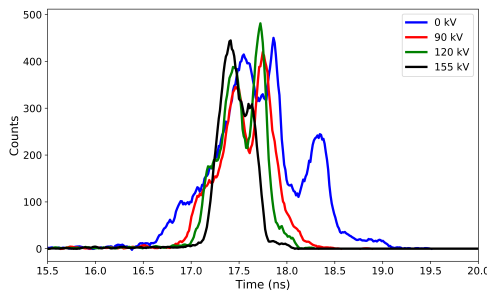


Figure 2: Rebuncher amplitude effect on bunching time structure using N-15 beam, 155 kV is the nominal voltage for operation.

The ReA6 linac employs an FRIB-type $\beta = 0.085$ quarter-wave-resonator cryomodel [8], providing beam energies up to 12 MeV/u for an A/q of 2. This cryomodel is composed of eight 80.5 MHz quarter-wave-resonators and three superconducting solenoids.

BEAM CHARACTERIZATION

User experiments at ReA usually request one isotope with high purity. The rate requested is dependent on the experimental setup used and the type of measurement performed. For example, gas detectors can handle limited rates and will request high purities. When sending the beam to an experiment, these properties have to be verified to not only ensure beam quality but optimize the time for science.

To identify and determine the composition of the beam, silicon detectors in combination with degrader foils are strategically positioned along the ReA beam lines [9]. By selecting degrader foils of appropriate thicknesses, it becomes

possible to separate and identify the beam of interest and contaminants. For this, two systems are routinely used: one consists of two independently actuated drives holding aluminum foils followed by a surface-barrier silicon detector; the other places an aluminum foil with a central aperture in front of a silicon detector. Both operate on the same principle. After acceleration, isotopes share the same energy per nucleon, but lose different amounts of energy in a thin foil due to their atomic number. This results in different kinetic energies, which are measured by the silicon detector. These energy differences enable identification of beam contaminants, and in particular isobars.

CONTAMINANT SUPPRESSION

Given the limited resolution of the Q/A, beams accelerated in ReA may be contaminated by isobars or isotopes with similar Q/A ratios. These contaminants are typically stable isotopes originating from materials in the sources or decay products of the rare isotope beams themselves. Reducing the rate of contaminants is important to limit the detection system dead time and becomes determinant when the detectors resolution is limited impeding the identification of the events of interest from contamination background. Several methods have been employed to suppress the background.

Selecting the appropriate charge state after the EBIT charge breeder is critical to both acceleration efficiency and beam purity. For example, choosing Be-7(4+) instead of Be-7(3+) helps avoid contamination from Li-7(3+). Nevertheless, choosing the optimal charge state cannot address all cases, such as the suppression of B-10 isobaric contamination from the decay of Be-10 in the Be-10 beam.

A beam with the long-lived rare isotope Be-10 was delivered from the BMIS source but highly contaminated with B-10 and N-15. The beam contaminants had origin in a BMIS source insulator and also the EBIT as shown in Fig. 3.

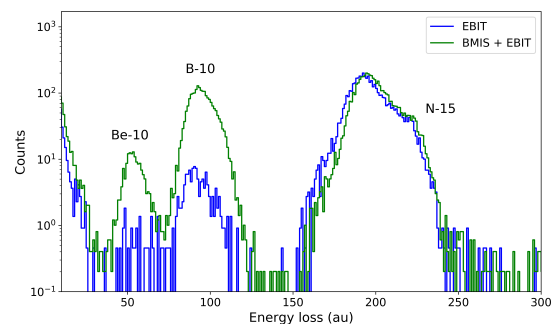


Figure 3: Energy loss spectra of residual beam from the EBIT (blue) and beam from the BMIS and EBIT (green).

While BMIS contributed B-10, the EBIT contribution alone was mainly N-15. Adjusting the oven temperature and the reactive gas (NF₃) pressure allowed to have a detectable quantity of Be-10 amidst the B-10 background. To address a maximum total rate limitation of 1E4 pps defined by the experiment, inserting a 2.75 μ m carbon stripper foil on the

beam path improved the beam purity. The nominal foil thickness provided by the supplier (2.75 ± 0.28) μm was used to estimate the new beam rigidity after the foil, and scale the beam line accordingly. Hence, the beamline was used as a spectrometer. The effect of stripping is shown in Fig. 4 where it is also compared to no stripping. Stripping increased the beam purity from below 1% to 60%. In addition, the N-15 contamination was reduced by increasing the ions breeding time in the EBIT.

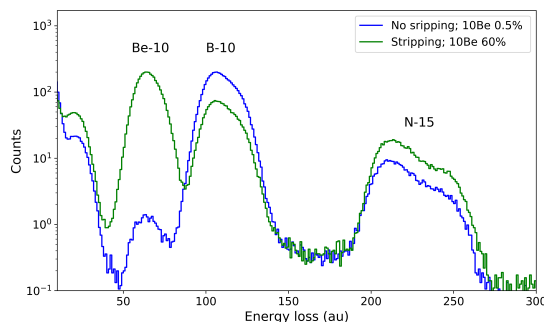


Figure 4: Energy loss spectra comparison for a Be-10 beam without stripping (blue) and when stripping using a 2.75 μm carbon stripper foil (green).

A similar strategy was used for a Si-32 beam and is reported in [9, 10]. With a half-life of 163 years, this long-lived isotope was contaminated with its S-32 isobar and Mo-96.

The chemical form of Si-32 played a significant role in the presence of contaminants. For example, the selection of Si-32 oxygen adducts of $M=32, 48, 64$, and 96 at the mass spectrometer of low energy beam line (D-line) varies the contamination level of the final beam. In Fig. 5, we observe the presence of S-32, Si-32 and Mo-96. While $A=32$ and $A=96$ show a similar composition, when selecting $A=48$, it is clearly seen that the Si-32 extraction efficiency from the source is enhanced. The beam rate achieved for all the S-32 experiments was 1E6 pps at a 95% purity and this value was kept steady for the science program.

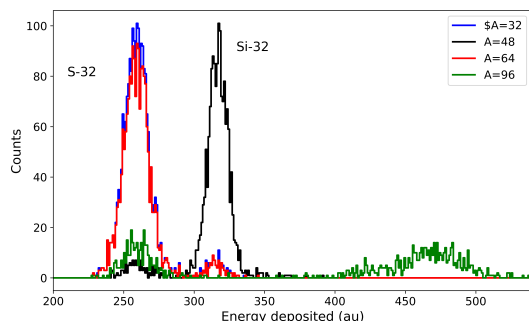


Figure 5: Energy deposited for Si-32 beam for different D-line mass separator selections [5]. Mass 48 is chemically more efficient for Si-32.

The long-lived Al-26 isotope has a half-life close to one million years is also an excellent candidate to develop from

the BMIS. A rate of 1E6 pps was requested and delivered to an experiment. Without any optimization, at the beginning of the beam characterization measurements the Al-26 beam was contaminated by Mg-26 at a level of 60%. The oven temperature as well as the pressure of the reactive gas were identified as key parameters to the successful outcome. Optimizing on these parameters led to a beam purity of 90% for a mass selection of 26 at the D-line mass analyzer. The key parameter for this successful outcome was the oven temperature as shown in Fig. 6.

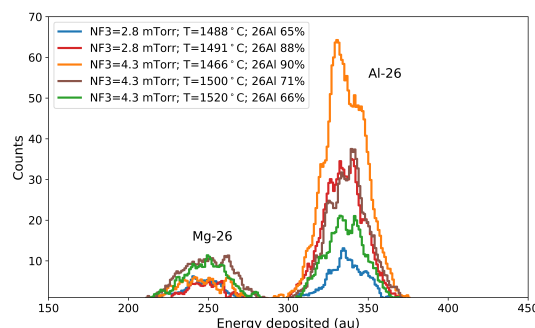


Figure 6: Silicon detector spectra obtained for Al-26. The two peaks are Mg-26 (left) and Al-26 (right). Beam purity was studied for different support gas pressures and oven temperatures.

BMIS FUTURE ACTIVITIES FOR REA EXPERIMENTS

In addition to the scientific research using long-lived rare isotopes, BMIS plays a key role to providing stable analogue beams to set up the ReA accelerator, beam lines, calibrate detectors and perform quick validations of users' detection systems.

BMIS is aiming to extend the availability of isotopes in the mid-mass range of long-lived isotope complementing the production of ISOL facilities. Examples are P-32, S-35, Ti-44 and V-49. In addition, isotopes collected from FRIB harvesting program [11] will be used to produce unique beams for the science program and applications. Ultimately, the SOL project, a solid-stopper prototype, will be able to provide low-Z radioactive beams at high intensities of interest for fundamental symmetry and p-capture reactions studies.

ACKNOWLEDGEMENTS

This material is based upon work supported by the U.S. Department of Energy, Office of Science, Office of Nuclear Physics and used resources of the Facility for Rare Isotope Beams (FRIB) Operations, which is a DOE Office of Science User Facility under Award Number DE-SC0023633.

REFERENCES

- [1] A. C. C. Villari *et al.*, "Commissioning and first accelerated beams in the Reaccelerator (Rea3) of the National Super-

- conducting Cyclotron Laboratory MSU”, in *Proc. IPAC’16*, Busan, Korea, May 2016, pp. 1287–1290.
doi:10.18429/JACoW-IPAC2016-TUPMR024
- [2] FRIB, <https://frib.msu.edu/>.
- [3] NSCL, <https://nscl.msu.edu/>.
- [4] A. C. C. Villari *et al.*, “Gas stopping and reacceleration techniques at the Facility for Rare Isotope Beams (FRIB)”, *Nucl. Instrum. Methods Phys. Res. B*, vol. 541, pp. 350–354, Aug. 2023. doi:10.1016/j.nimb.2023.05.037
- [5] C. S. Sumithrarachchi *et al.*, “The new batch mode ion source for stand-alone operation at the Facility for Rare Isotope Beams (FRIB)”, *Nucl. Instrum. Methods Phys. Res. B*, vol. 541, pp. 301–304, Aug. 2023. doi:10.1016/j.nimb.2023.05.061
- [6] A. Lapierre *et al.*, “On-line operation of the EBIT charge breeder of the ReA post-accelerator”, *AIP Conf. Proc.*, 2018, p. 070002. doi:10.1063/1.5053344
- [7] K. A. Domnanich *et al.*, “Preparation of stable and long-lived source samples for the stand-alone beam program at the Facility for Rare Isotope Beams”, *Appl. Radiat. Isot.*, vol. 200, p. 110958, Oct. 2023. doi:10.1016/j.apradiso.2023.110958
- [8] T. Xu *et al.*, “FRIB cryomodule design and production”, in *Proc. LINAC2016*, East Lansing, MI, USA, Sep. 2016, pp. 673–678. doi:10.18429/JACoW-LINAC2016-WE2A02
- [9] A. Henriques *et al.*, “Quantification and purification of isotopic contamination at the ReAccelerator of the Facility for Rare Isotope Beams”, *Rev. Sci. Instrum.*, vol. 94, no. 10, p. 103306, Oct. 2023. doi:10.1063/5.0165850
- [10] A. C. C. Villari *et al.*, “ReAccelerator upgrade, commissioning and first experiments at the National Superconducting Cyclotron Laboratory (NSCL) / Facility for Rare Isotope Beams (FRIB)”, in *Proc. IPAC’22*, Bangkok, Thailand, Jun. 2022, pp. 101–103. doi:10.18429/JACoW-IPAC2022-MOPOST021
- [11] E. P. Abel *et al.*, “Isotope harvesting at FRIB: additional opportunities for scientific discovery”, *J. Phys. G: Nucl. Part. Phys.*, vol. 46, no. 10, p. 100501, Aug. 2019. doi:10.1088/1361-6471/ab26cc